BULGARIAN CHEMICAL

COMMUNICATIONS

Journal of the Chemical Institutes

of the Bulgarian Academy of Sciences

and of the Union of Chemists in Bulgaria

ANNOTATION

The present issue of the Bulgarian Chemical Communications contains selected papers based on presentations at the 15th National Conference on Catalysis organised by Bulgarian Catalysis Club and Institute of Catalysis of the Bulgarian Academy of Sciences in memoriam of Professor Atanas Andreev who left the catalysis community in 1997. He was a prominent Bulgarian chemist with important contributions to fundamental and applied catalysis.

Submitted papers by Bulgarian and foreign scientists in the field of catalysis are a tribute to Professor A. Andreev for his achievements as a leading representative of the Bulgarian school of catalysis. We are indebted to all contributors for their effort to accomplish this issue.

This issue of the Bulgarian Chemical Communications is published with the kind financial support from Bulgarian Catalysis Club and Institute of Catalysis of the Bulgarian Academy of Sciences.

The Editors

Physicochemical properties of monometallic Rh and Ni and bimetallic RhNi catalyst materials supported on unmodified and yttrium-modified alumina

R. Palcheva, I. Shtereva, Y. Karakirova, G. Tyuliev, S. Damyanova*

Institute of Catalysis, Bulgarian Academy of Sciences, G. Bonchev St., Bldg. 11, 1113 Sofia, Bulgaria

The effect of Y_2O_3 addition to γ-alumina carrier on the structure and surface and reductive properties of supported monometallic Rh and Ni bimetallic RhNi materials was studied. Various techniques for physicochemical characterization were used, such as N_2 adsorption-desorption isotherms, XRD, UV-vis DRS, XPS, EPR, and TPR. XRD, UV-vis DRS, and XPS results of calcined samples showed the presence of Ni^{2+} ions in different environment: octahedral and tetrahedral coordination. Well-dispersed yttrium and rhodium oxide species were detected. EPR and TPR data indicated a strong interaction between Ni and yttria, as revealed by higher temperature of reduction of nickel oxide species. Rh promoting effect on the reduction of Ni oxide species was related to hydrogen spillover effect of the noble metal.

Key words: nickel catalysts, rhodium, yttrium, characterization.

INTRODUCTION

Due to high availability and low cost, alumina-supported nickel catalyst materials have been widely used for hydrogen production by reforming processes of ethanol [1,2] and for synthesis gas or hydrogen-rich synthesis gas production by reforming of methane with CO_2 [3]. On the other hand, methane and carbon dioxide are greenhouse gases that cause the global climate change and considerable attention has been given to control and utilize these gases [4,5]. It is well known that Ni-based catalysts supported on alumina suffer from carbon deposition over the active phase. Different studies have been focused on problems how to eliminate coke formation on Ni catalysts including use of suitable additives or supports to modify the physicochemical properties of Ni/Al_2O_3 with beneficial features, such as high metal dispersion, high number of basic sites, and superior reducible nature [6–8]. Another promising alternative to obtain highly active and coke resistant Ni-based catalysts is addition of small amount of noble metal [9–12]. The aim of the present work was to study the effect of yttrium addition to γ-alumina carrier and of Rh introduction to supported Ni catalysts on their structure and surface and reductive properties. Sample physicochemical properties were examined by applying N_2 adsorption-desorption isotherms, X-ray diffraction (XRD), UV-vis diffuse reflectance spectroscopy (UV-vis DRS), X-ray photoelectron spectroscopy (XPS), electron paramagnetic resonance (EPR), and temperature-programmed reduction (TPR).

EXPERIMENTAL

Sample preparation

Modified alumina support with yttrium was prepared by impregnation of γ-Al_2O_3 with an aqueous solution of $Y(NO_3)_3.6H_2O$. Monometallic Ni and Rh catalysts were prepared by impregnation of unmodified and yttrium modified alumina with aqueous solution of $Ni(NO_3)_2.6H_2O$ and ethanol solution of $RhCl_3.3H_2O$ salt, respectively. Supported bimetallic NiRh samples were prepared by co-impregnation of unmodified and modified alumina with solutions of rhodium chloride and nickel nitrate salts in ethanol. Obtained solids were dried at 110 °C for 12 h and calcined at 550 °C for 4 h. The theoretical content of Y, Ni, and Rh was 10, 10, and 1 wt.%, respectively. The samples were denoted as Y-Al, Ni/Al, Rh/Al, Ni/Y-Al, RhNi/Al, and RhNi/Y-Al.

Methods

N_2 adsorption-desorption isotherms of samples were recorded at 77 K by means of a Quantachrome Instruments NOVA 1200e (USA) 3000 apparatus. Beforehand the samples were outgassed under vacuum at 200 °C for 18 h. The surface area was calculated according to the BET method. XRD analysis was performed according to step scanning procedure (step size 0.02°; 0.5 s) with a computerized Seifert 3000 diffractometer, using Ni-filtered CuKα (λ = 0.15406 nm) radiation and a PW 2200 Bragg-Brentano θ/2θ goniometer equipped with a

* To whom all correspondence should be sent
E-mail: sonia.damyanova@yahoo.com

bent graphite monochromator and an automatic slit. The assignment of the various crystalline phases was based on JPDS powder diffraction file cards. UV-vis DRS spectra of the samples were recorded in the range of 200–800 nm at room temperature using a Varian Cary 5000 UV-vis spectrometer equipped with an integration sphere. XPS measurements of the samples were carried out on an ESCALAB-MkII (VG Scientific) spectrometer with a base pressure in the analysis chamber of $\sim 10^{-8}$ Pa. The spectra were excited with an Al Kα radiation (hν = 1253.6 eV) at total instrumental resolution of ~ 0.9 eV as measured by FWHM of Ag $3d_{5/2}$ photoelectron line. The binding energy (BE) scale of the spectrometer was calibrated with respect to the Au $4f_{7/2}$ peak of gold fixed at 83.98 eV and the BE's of O 1s, Al 2p, Ni 2p, Y 3d, and Rh 3d electrons were referenced to the O1s band at 531.5 eV. Peak decomposition was performed using Casa XPS program (Casa Software, UK) assuming 85/15 Gaussian/Lorentzian product function. EPR spectra of calcined (550 °C in air) and reduced (550 °C in 10% H_2/N_2 flow) samples were recorded as a first deri-vative of the absorption signal of JEOL JES-FA 100 EPR spectrometer at room temperature. The spectrometer operated in X-band equipped with a standard TE_{011} cylindrical resonator. The samples were placed in a special quartz reactor and fixed in the cavity centre. A variable temperature controller ES-DVT4 was used to permit detection of EPR spectra at temperatures from 123 to 298 K. Desired temperature could be easily obtained by moving liquid nitrogen at a certain temperature controlled by the EPR spectrometer data system computer to the sample area. The reduction temperature of the various phases in the oxide form of the samples was determined by the method of TPR. The reducing mixture containing 10% H_2 in Ar was deoxygenated over Pt/asbestos filter at 130 °C, dried in a molecular sieve 5A filter, and then fed into the a tubular quartz reactor at a flow rate of 25 cm^3/min. The program started from room temperature at a ramp rate of 10 deg/min up to 1000 °C. Catalyst sample amount charged in the reactor was 0.1 g. The TPR set-up was equipped with a thermal conductivity detector.

RESULTS AND DISCUSSION

Structure and surface properties

Nitrogen adsorption-desorption isotherms of calcined samples (not shown) were classified as a type IV isotherm according to IUPAC, which is typical of mesoporous materials [13]. Specific surface area (S_{BET}), total pore volume (V_p), and average pore diameter (D_p) values are summarized in Table 1.

Table 1. Textural properties of calcined monometallic and bimetallic RhNi samples

Sample	S_{BET} (m^2/g)	Vp (cm^3/g)	Pore diameter (nm)
Al_2O_3	232	0.90	15.5
Y-Al	183	0.79	17.2
Ni/Al	187	0.55	11.7
Ni/Y-Al	163	0.66	16.2
Rh/Y-Al	185	0.72	15.7
NiRh/Al	161	0.65	16.2
NiRh/Y-Al	171	0.70	16.2

A decrease in specific surface area and pore volume of the alumina carrier was observed after addition of yttrium or nickel (from 232 to 183 and 187 m^2/g for Y-Al and Ni/Al, respectively, Table 1) due to blockage of alumina pores by yttrium or nickel oxide species. The S_{BET} of modified Y-Al support continued to decrease for Y-Al$_2$O$_3$-supported monometallic Ni and Rh samples and it is more obvious with the former one. The bimetallic NiRh samples have the lowest specific surface area. It is interesting to note that with exception of Ni/Al the mean pore diameter of the supported samples is higher than that of pure alumina (Table 1). Probably, this is caused by the presence of particles with larger pores and owing to possible blockage of the small pores by yttrium oxide species.

XRD patterns of unmodified and Y-modified alumina and supported monometallic and bimetallic samples are shown in figure 1. Pure alumina exhibited peaks at 2θ = 37.2^o, 39.7^o, 46.2^o, and 66.4^o, which are due to γ-Al$_2$O$_3$ (JCPDS 86-1410). Modification of alumina with yttrium or addition of nickel and/or Rh led to a change of intensity and modification of the shape of the alumina lines because of changes in crystallinity of the samples.
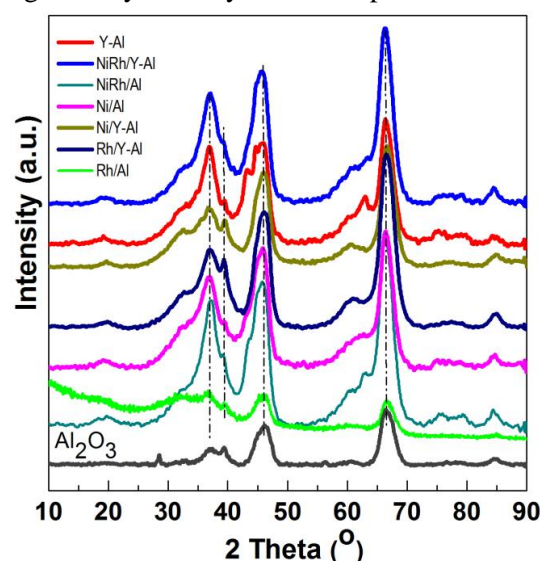

Fig. 1. XRD of supported monometallic Rh and Ni and bimetallic RhNi samples.

Diffraction lines of Y_2O_3 at $2\theta = 33.77^o$, 48.54^o, and 57.6^o (JCPDS 65-3178) were not detected in yttrium modified samples, which is an indication of the amorphous nature of the compound. In spite of the absence of peaks characteristic of $NiAl_2O_4$ phase, the presence of some surface spinel species cannot be excluded. In addition, the peaks of $NiAl_2O_4$ overlap with those of γ-Al_2O_3. For Ni/Al and NiRh/Y-Al samples XRD lines at $2\theta = 37^o$, 43.2^o, 62.9^o, and 76° are registered, which could be related to the presence of cubic NiO species (JCPDS 47-1049). However, these lines were not definitely detected with other samples. Since the main characteristic peaks of rhodium oxide species in the 2θ interval of 16–18° [14] were absent, it could be assumed that these species were well dispersed.

UV-vis DR spectra of calcined samples in the wavelength ranges of 200−800 nm and 500−800 nm are displayed in figure 2. Supported bimetallic RhNi/Y-Al sample manifested a strong absorption at 200−350 nm with a maximum at about 260 nm related to $O^{2-} \rightarrow Ni^{2+}$ charge transfer transition.
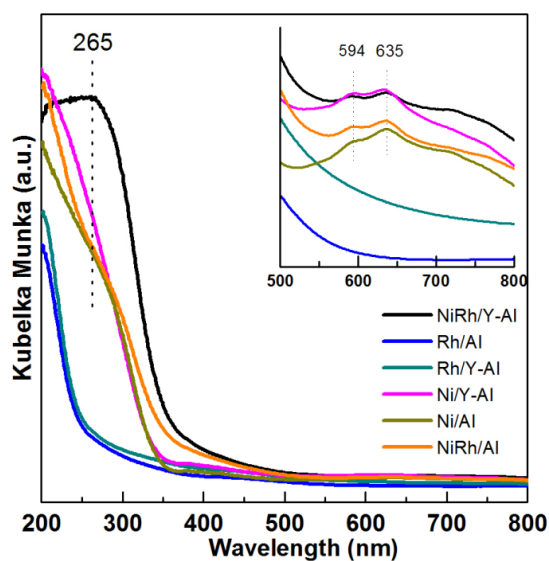

Fig. 2. UV-vis-DRS of supported monometallic Rh and Ni and bimetallic RhNi samples.

A doublet at 594 and 635 nm in the wavelength range of 500−800 nm (Fig. 2) indicates presence of Ni^{2+} ions in tetrahedral coordination of $NiAl_2O_4$ spinel like structure [15]. A broad absorption at about 720−780 nm means that Ni^{2+} ions are in octahedral coordination that is typical of NiO species. It can be concluded that the nickel ions occurred in different environment: tetrahedral and octahedral coordination.

Binding energy (BE) values of Y $3d_{5/2}$, Ni $2p_{3/2}$, and Rh $3d_{5/2}$ as well as XPS atomic ratios for calcined samples are listed in Table 2. The BE values of Y $3d_{5/2}$ electrons for Y-containing samples (158.8−159.2 eV) are higher compared to that of the bulk Y_2O_3 (157.9 eV, Table 2) which should be related to certain interaction of supported yttrium oxide species with alumina or with Rh or Ni. For Ni/Al sample the BE of Ni $2p_{3/2}$ electrons at 856.4 eV characterizes the Ni^{2+} ions in nickel oxide species, which can be ascribed to the presence of dispersed NiO species as well as of surface $NiAl_2O_4$ like species [16,17]. This is in accordance with the UV-vis DRS results (Fig. 2). However, there is some increase of the BE value of Ni $2p_{3/2}$ to 857.0 eV for NiRh/Y-Al sample, most likely due to a change in coordination and/or reflection effects in the presence of Rh and Y oxide species.

The BE values of Rh $3d_{5/2}$ electrons at 310.0–310.4 eV could be ascribed to Rh^{3+} species [18], though these values are slightly higher than that of bulk Rh_2O_3 (309.0 eV). The observed shift in binding energy values may arise from a smaller size of the supported rhodium oxide species.

XPS atomic ratios calculated from the intensities of the peak normalized by atomic sensitivity factor [19] are summarized in Table 2. Nickel oxide dispersion on alumina increased after introduction of the noble metal to Ni/Al. However, the presence of Y in monometallic Ni/Y-Al and in bimetallic RhNi/Y-Al caused a decrease in the XPS atomic Ni/Al + Y + Rh ratio values due to some agglomera-

Table 2. XPS characteristics of calcined monometallic Rh and Ni and bimetallic RhNi samples supported on unmodified and yttrium modified alumina

Sample	Y $3d_{5/2}$	Ni $2p_{3/2}$	Rh $3d_{5/2}$	Y/Al+Ni+Rh	Ni/Al+Y+Rh	Rh/Al+Y+Ni
b. Y_2O_3	157.9	-		-	-	-
Y-Al	159.2	-		0.074	-	-
Ni/Al	-	856.4		-	0.053	-
Ni/Y-Al	158.8	856.4		0.067	0.051	-
Rh/Al	-	-	310.0	-	-	0.005
Rh/Y-Al	159.1	-	310.2	0.070	-	0.005
NiRh/Al	-	856.7	310.4	-	0.058	0.003
NiRh/Y-Al	158.8	857.0	310.1	0.058	0.048	0.003

tion of nickel oxide species. Yttrium oxide species were well dispersed on pure alumina. However, addition of other elements led to a decrease of the accessibility of Y-containing species, which is more pronounced for the bimetallic RhNi/Y-Al sample (Table 2). Rh oxide species were well dispersed on the surface of unmodified and Y-modified alumina. A decrease of the atomic XPS Rh/Al+Y+Ni values with the bimetallic RhNi samples was observed (Table 2), probably due to some Rh coverage, bearing in mind nickel higher concentration. It has been reported [20] that yttrium oxide species had no important impact on oxidation state and dispersion of metallic centres, but substantially altered support acid-base properties.

Reductive properties

EPR spectra of reduced Ni/Al_2O_3, $Ni-Y/Al_2O_3$, $Ni-Rh/Al_2O_3$, and $Ni-Rh/Y-Al_2O_3$ samples at room temperature are given in figure 3. The spectra consist of two overlapping EPR signals denoted as Si1 and Si2. A narrow signal Si1 detected in the spectrum of Ni/Al_2O_3 is characterized by a g factor of 2.1993 and a linewidth of 32.6 mT. In the presence of yttrium and rhodium the *g* factor decreased to 2.1676 and 2.1480, respectively, and the value of the linewidth increased to about 42−46 mT for Si1 because of change in atom surrounding. Based on previous EPR studies of supported Ni samples the signal Si1 can be assigned to Ni^{2+} ions in octahedral symmetry [21−23]. The electronic configuration of Ni^{2+} is d^8 and postulated coupling would lead to a spin-paired system. This signal probably had never been detected in samples containing only nickel ions. Thus, it can be stated that signal Si1 is due to the presence of paramagnetic species evidently related to the interaction among aluminium, yttrium or rhodium, and Ni^{2+} ions. A broader Si2 line in Ni-Al sample has g value of 2.3791 and linewidth of 102.8 mT. The EPR parameters of this signal were changed after modification of the sample with yttrium and rhodium to g of 2.2299 and 2.2195 and to ΔH of 90.0 and 135.3 mT for Ni/Y-Al and NiRh/Al, respectively. In view of the literature data [23], the most probable reason for the appearance of the signal Si2 is the presence of ferromagnetic metallic nickel. Compared with other samples, the signal Si1 of Ni/Y-Al is dominant. Therefore, a small number of nickel ions were reduced to metallic nickel for this sample. It may be concluded that nickel and yttrium interacted with each other and this led to a decrease of the reduced capacity of nickel oxide species. Addition of rhodium to the samples increased the reduction of Ni^{2+} to Ni^0, which was confirmed by the more pronounced signal Si2 in the

EPR spectrum of Ni-Rh/Al sample that is caused by the hydrogen spillover effect.
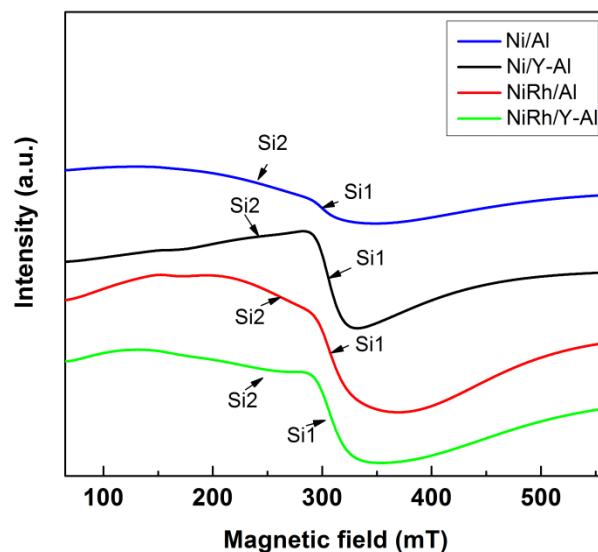

Fig. 3. EPR of reduced Ni-containing samples.

TPR profiles of calcined mono and Ni, Rh, and bimetallic NiRh samples are shown in figure 4. At a temperature above 450 °C a high hydrogen consumption with poorly resolved maxima at about 526, 600, 700, and 797 °C is observed for Ni/Al sample. Both higher temperature maxima should be related to hard reduction of nickel oxide species in strong interaction with alumina surface or to the presence of agglomerated NiO particles, whereas the lower temperature peaks at 526 and 600 °C are associated with the presence of small weakly bonded NiO species to the support. Addition of yttrium to Ni/Al gave rise to a shift of the latter two peaks to higher temperatures: from 700 to 725 °C and from 797 to 833 °C, respectively (Fig. 4).
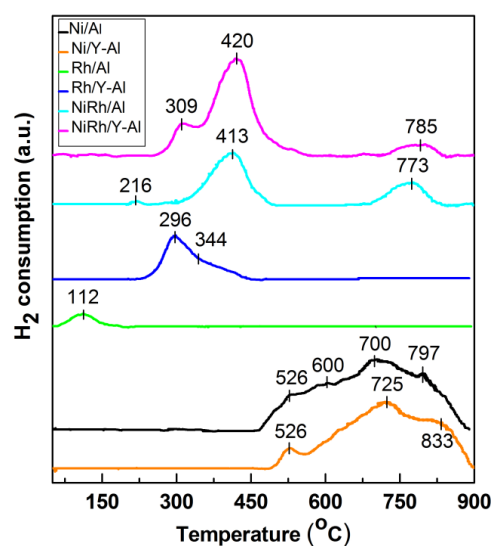

Fig. 4. TPR profiles of supported monometallic Rh and Ni and bimetallic RhNi samples.

The high temperature shift suggests a strong interaction between nickel oxide species and alumina support modified with yttrium. A TPR profile of Rh/Al sample demonstrated a small peak at around 112 °C assigned to reduction of rhodium oxide species. After introduction of yttrium to alumina, the TPR profile of Rh/Y-Al sample displayed a main signal at 296 °C with a shoulder at about 344 °C that corresponds to reduction of rhodium oxide species of different extent of interaction with yttrium-modified alumina support. No peaks were registered in the TPR profile of alumina modified with Y. As can be seen in figure 4, Rh improved Ni reducibility in the bimetallic RhNi sample by decreasing significantly the reduction temperature of nickel oxide species to 413 and 420 °C for NiRh/Al and NiRh/Y-Al, respectively, due to hydrogen spillover effect. It can be concluded that yttrium presence makes difficult the reduction of nickel and rhodium oxide species.

SUMMARY

Investigated monometallic Rh and Ni and bimetallic RhNi samples exhibited mesoporous structure. Supported yttrium oxide species were in amorphous state. Detected Ni^{2+} ions occurred in tetrahedral and octahedral configuration, similarly to surface $Ni_2Al_2O_4$ spinel structure and NiO, respectively. A strong interaction between yttrium oxide species and alumina was detected. A couple of Ni^{2+}/Ni^0 ions was defined in reduced Ni-containing samples based on EPR study. The reducibility of nickel oxide species increases in the presence of noble metal.

REFERENCES

1. J. R. Rostrup-Nielsen, J. H. B. Hansen, *J. Catal.*, **144**, 38 (1993).
2. H. Braga, J. B. O. Santos, J. M. C. Bueno, S. Damyanova, *Bulg. Chem. Commun.*, **49**, 45 (2017).
3. S. Damyanovaa, B. Pawelec, R. Palcheva, Y. Karakirova, M. C. Capel Sanchez, G. Tyuliev, E. Gaigneaux, J. L. G. Fierro, *Appl. Catal. B: Environ.*, **225**, 340 (2018).
4. N. Wang, K. Shen, L. Huang, X. Yu, W. Qian, W. Chu, *ACS Catal.*, **3**, 1638 (2013).
5. I. Luisetto, S. Tuti, C. Battocchio, S. Lo Mastro, A. Sodo, *Appl. Catal. A: Gen.*, **500**, 12 (2015).
6. M. L. Dieuzeide, M. Laborde, N. Amadeo, C. Bonura, F. Frusteri, *Int. J. Hydrogen Energy*, **41**, 157 (2016).
7. A. N. Fatsikostas, D. I. Kondarides, X. E. Verykios, *Catal. Today*, **75**, 145 (2002)
8. F. Can, A. Le Valant, N. Bion, F. Epron, D. Duprez, *J. Phys. Chem.*, C **112,** 14145 (2008).
9. S. Damyanova, B. Pawelec, K. Aristirova, J. L. G. Fierro, C. Sener, T. Dogu, *Appl. Catal. B: Environ.*, **92**, 250 (2009).
10. S. Damyanova, B. Pawelec, K. Arishtirova, J. L. G. Fierro, *Int. J. Hydrogen Energy*, **36**, 10635 (2011).
11. J. Zhang, H. Wang, A. K. Dalai, *J. Catal.*, **249**, 300 (2007).
12. Z. Hou, P. Chen, H. Fang, X. Zheng, T. Yashima, *Int. J. Hydrogen Energy*, **31**, 555 (2006).
13. G. Leofanti, M. Padovan, G. Tozzola, B. Venturelli, *Catal. Today*, **41**, 207 (1998).
14. A. Saric, S. Popovic, R. Trojko, S. Music, *J. Alloys Comp.*, **320**, 140 (2001).
15. Tisoaga, D. Visinescu, B. Jurca, A. Ianculescu, O. Carp, *J. Nanopart. Res.*, **13**, 6397 (2011).
16. K. T. Ng, D. M. Hercules, *J. Phys. Chem.*, **80**, 2094 (1976).
17. Y. Oh, H. Roh, K. Jun, Y. Baek, *Int. J. Hydrogen Energy*, **28**, 1387 (2003).
18. S. Eriksson, S. Rojas, M. Boutonnet, J. L. G. Fierro, *Appl. Catal. A: Gen.*, **326**, 8 (2007).
19. C. D. Wagner, L. E. Davis, M. V. Zeller, J. A. Taylor, R. H. Raymond, L. H. Gale, *Surf. Interface Anal.*, **3**, 21 (1981).
20. F. Can, A. Le Valant, N. Bion, F. Epron, D. Duprez, *J. Phys. Chem., C*, **112**, 14145 (2008).
21. A. J. A. Konings, W. L. J. Brentjens, D. C. Koningsrerger., V. H. J. De Beer, *J. Catal.*, **67**, 145 (1981).
22. D. S. Thakur, B. Delmon, *J. Catal.*, **91**, 308 (1985).
23. S. Damyanova, A. A. Spojakina, D. M. Shopov, *Appl. Catal.*, **48**, 177 (1989).

ФИЗИКОХИМИЧНИ СВОЙСТВА НА МОНОМЕТАЛНИ Ni И Rh И БИМЕТАЛНИ NiRh КАТАЛИТИЧНИ МАТЕРИАЛИ, НАНЕСЕНИ ВЪРХУ НЕМОДИФИЦИРАН И МОДИФИЦИРАН С ИТРИЙ АЛУМИНИЕВ ОКСИД

Р. Палчева, И. Щерева, Й. Каракирова, Г. Тюлиев, С. Дамянова*

Институт по катализ, Българска академия на науките, ул. „Акад. Г. Бончев", блок 11, 1113 София, България

(Резюме)

Изучен е ефектът на Y_2O_3, добавен в носител γ-Al_2O_3, върху структурата, повърхностните и редукционните свойства на нанесени монометални Rh и Ni и биметални RhNi каталитични материали. Използвани са различни техники за тяхното физикохимично охарактеризиране: адсорбционни-десорбционни изотерми на азот, дифузно отражателна и рентгенова фотоелектронна спектроскопия, електронен парамагнитен резонанс и температурно програмирана редукция. Установено е, че Ni^{2+} йони в накалени образци са в октаедрично и тетраедрично обкръжение, съответстващо на това в NiO и $NiAl_2O_4$ шпинел. Присъствието на двойка йони Ni^{2+}/Ni^0 е регистрирано с помощта на ЕПР в оксидни Ni-съдържащи образци. Наблюдавано е силно взаимодействие между Ni и Y_2O_3, проявяващо се в по-трудна редукция на никелови оксидни частици. Промотиращият ефект на Rh върху високата редуцируемост на NiO до Ni^0 се дължи на спиловер ефект на благородния метал.

Y-doped ceria-supported gold and palladium mono- and bimetallic catalysts for complete propene oxidation

P. Ts. Petrova[1,*], G. Pantaleo[2], A. M. Venezia[2], L. F. Liotta[2], Z. Kaszkur[3], T. T. Tabakova[1], L. I. Ilieva[1]

[1] Institute of Catalysis, Bulgarian Academy of Sciences, 1113 Sofia, Bulgaria
[2] Istituto per lo Studio dei Materiali Nanostrutturati (ISMN)-CNR, 90146, Palermo, Italy
[3] Institute of Physical Chemistry, Polish Academy of Sciences, Kasprzaka 44/52, 01-224 Warsaw, Poland

Monometallic Au and Pd as well as bimetallic Pd-Au particles deposited on Y-doped ceria supports were studied in complete propene oxidation (CPO), which was used as a probe reaction for aliphatic hydrocarbons abatement. Y-modified ceria supports (1 wt.% Y_2O_3) were prepared by impregnation and coprecipitation. Gold (3 wt.% Au) and palladium (1 wt.% Pd) containing samples were prepared by deposition-precipitation method. Bimetallic Pd-Au catalysts were prepared by adding palladium to already deposited gold. Catalyst samples were characterized by BET, XRD, TPR, and XPS techniques. In general, the catalytic activity in CPO did not differ significantly in the presence of Y dopant and because of synthesis method of mixed oxide support. Total propene conversion over gold catalysts was reached at 220 °C. Pd-based catalysts demonstrated a higher oxidation activity in comparison with Au-based samples showing 100% propene conversion at 200 °C. The lowest temperature of total propene oxidation of 180 °C was achieved over the bimetallic Pd-Au catalysts and long-term catalytic performance showed good stability with no loss of catalytic activity.

Key words: *Au, Pd, and Pd-Au catalysts, Y-doped ceria, complete propene oxidation.*

INTRODUCTION

Treatment of gaseous emissions containing volatile organic compounds (VOCs) has been an increasing concern in the last years. Catalytic combustion is considered a promising way to convert VOCs, especially of low concentration, into harmless CO_2 and water. Selection of catalytic materials for the reduction of VOCs is not easy because several factors such as support type, active sites distribution, and synthesis methods would influence catalyst activity and catalyst lifetime.

Gold-based catalysts are already well known as promising candidates for the total oxidation of VOCs at relatively low temperatures [1]. Rapid change in cerium oxidation state ($Ce^{4+}\leftrightarrow Ce^{3+}$) makes ceria a suitable reducible support, which is also able to stabilize finely dispersed gold particles. Due to the formation of oxygen vacancies, CeO_2 modification with metal dopant of proper oxidation state and concentration could lead to further increase of oxygen mobility in ceria-based catalysts. Own results of gold deposited on ceria doped with MeO_x (Me = Fe, Mn, Co, and Sn) have shown an effect of mixed oxide support composition and structure on the catalytic behaviour in complete benzene oxide-tion [2,3]. Recent results have shown a beneficial effect on the catalytic performance in complete benzene oxidation in the case of Au deposited on Y-doped ceria support (1 wt.% Y_2O_3) prepared by impregnation as compared to gold on bare ceria [4].

Catalysts containing both highly dispersed gold and palladium particles were reported as very effective in many reactions including organic compounds oxidation. A higher catalytic activity in the case of bimetallic formulation as compared to the corresponding monometallic Au and Pd catalysts for catalytic destruction of *p*-aniline [5] and toluene [6] was observed. An important role of metal loading sequence was established [7,8]. Catalysts prepared by palladium introduction to already deposited gold, containing Pd(shell)–Au(core) particles, exhibited the best catalytic activity in toluene and propene oxidation [7]. In accordance with these observations, the highest complete benzene oxidation activity has been reported for Pd-Au catalyst prepared by impregnation of Fe-doped ceria support when Pd loading followed gold deposition [9].

The present study is focused on the complete oxidation of propene, the latter being selected as a probe molecule for aliphatic hydrocarbon combustion. The activity of mono- (Au, Pd) and bimetallic Pd-Au particles (Pd added to deposited Au particles) supported on differently prepared Y-doped ceria (1

* To whom all correspondence should be sent
E-mail: petia@ic.bas.bg

wt.% dopant) in the complete propene oxidation (CPO) was investigated. Modification of Au, Pd, and Y oxidation state before and after catalytic work was elucidated

EXPERIMENTAL

Sample preparation

Three series of catalysts containing Au (3 wt.%), Pd (1 wt.%), and Pd (1 wt.%)-Au (3 wt.%) supported on bare ceria, Y-doped ceria prepared by impregnation (IM), and Y-doped ceria prepared by co-precipitation (CP) were synthesised. Yttria dopant amount was 1 wt.%.

Ceria was prepared by precipitation of aqueous solution of $Ce(NO_3)_3.6H_2O$ with K_2CO_3 at 60°C and constant pH = 9.0. The resulting precursor was aged at the same temperature for 1 h, filtered and carefully washed until NO_3^- ions removal, dried in vacuum at 80 °C, and calcined in air at 400 °C for 2 h. Using IM method ceria was impregnated with aqueous solution of appropriate amount of $Y(NO_3)_3.6H_2O$ under vigorous stirring at room temperature for 4 h. Then, the suspension was evaporated under vacuum at 70 °C in a rotary evaporator until water was completely removed. By CP method a solution of Y and Ce nitrates at an appropriate ratio were co-precipitated with a solution of K_2CO_3 at constant pH = 9.0 and temperature of 60 °C. The precipitates were aged at the same temperature for 1 h, filtered, and washed until removal of NO_3^- ions. All resulting precursors were dried in vacuum at 80 °C and calcined in air at 400 °C for 2 h. Before metal deposition, the support was dispersed in water and activated in an ultrasound disintegrator.

Gold was deposited by deposition-precipitation method from $HAuCl_4.3H_2O$ and K_2CO_3 precursors under vigorous stirring. The precipitation was carried out under full control of all parameters of preparation (constant pH = 7, T = 60 °C, stirring speed = 250 rpm, reactant feed flow rate = 0.15 $l.h^{-1}$, etc.). After filtering and careful washing, the solid was dried under vacuum and calcined in air at 400 °C for 2 h. The gold catalysts were denoted as AuCe, AuYCeIM, and AuYCeCP.

Pd-containing samples were prepared from $Pd(NO_3)_2.xH_2O$ precursor following aforementioned preparation method and calcination procedure for gold catalysts. These samples were denoted as PdCe, PdYCeIM, and PdYCeCP.

Sequential deposition-precipitation was applied for the preparation of bimetallic Pd-Au catalysts. Palladium was loaded on already prepared and calcined Au/Y-doped ceria. After Pd deposition calcination in air at 400 °C for 2 h was carried out. The samples were denoted as Pd-AuCe, Pd-AuYCeIM, and Pd-AuYCeCP.

Sample characterization

Sample BET surface area (S_{BET}) was evaluated by performing nitrogen adsorption/desorption experiments on a Carlo Erba Sorptomat 1900 instrument. Prior to the measurements, each sample was outgassed at 200 °C for 1 h under vacuum. Computerized analysis of the nitrogen adsorption isotherm at −196 °C allowed estimating the specific surface areas of the samples in the standard pressure range of 0.05–0.3 P/P_0.

X-ray powder diffraction (XRD) measurements were performed using a D5000 diffractometer (Bruker AXS), with Cu sealed tube operating at 40 kV and 40 mA. The setup employed Bragg-Brentano focusing geometry with 1° beam divergence and LynxEye strip detector. Data were analysed using PeakFit program (Jandel Scientific) and fityk (Copyright 2001–2014 Marcin Wojdyr) fitting XRD profiles to K_α 1,2 doublets having PEARSON VII analytical form. The CeO_2 phase was analysed on the basis of 14 well measured reflections and Williamson-Hall plot [10,11] to calculate the average crystal size. Gold particle crystal size was estimated based on the strongest (111) reflection as the only one detectable. The procedure is described in detail elsewhere [4].

X-ray photoelectron spectroscopy (XPS) analysis was performed by VG Microtech ESCA 3000 Multilab equipped with a dual Mg/Al anode [12]. The spectra were excited by unmonochromatized Al Kα source (1486.6 eV) run at 14 kV and 15 mA. The analyser was operated in the constant analyser energy (CAE) mode. For the individual peak energy regions, a pass energy of 20 eV set across the hemispheres was used. Sample powders were pelletized and mounted on a double-sided adhesive tape. The pressure in the analysis chamber was in the range of 10^{-8} Torr during data collection. Constant charging of the samples was removed by referencing all the energies to the C1s set at 285.1 eV arising from adventitious carbon. Peak analysis was performed with software provided by VG based on non-linear least squares fitting program using a weighted sum of Lorentzian and Gaussian component curves after background subtraction according to Shirley and Sherwood [13,14].

Temperature-programmed reduction (TPR) measurements were carried out by means of an apparatus described elsewhere [15]. A cooling trap (–40 °C) for removing water formed during reduction was mounted in the gas line prior to the thermal

conductivity detector. A hydrogen-argon mixture (10% H_2), dried over a molecular sieve 5A (−40 °C), was used to reduce the samples at a flow rate of 24 ml.min^{-1}. The temperature was linearly raised at a rate of 15 °C min^{-1}. The amount of sample used was 0.05 g based on a criterion proposed by Monti and Baiker [16]. Hydrogen consumption during the reduction process was calculated using preliminary calibration of the thermal conductivity detector performed by reducing different amounts of NiO to Ni^0, NiO – 'analytical grade' being calcined at 800 °C for 2 h to avoid presence of non-stoichiometric oxygen).

Catalytic activity measurements in CPO

The catalytic activity in CPO, expressed as degree of propene conversion, was evaluated in the temperature range of 100–300 °C after catalyst pretreatment using 50 ml.min^{-1} of 5% O_2 in He for 1 h at 350 °C. The measurements were carried out in U-shaped quartz reactor under reactive gas mixture containing 1500 ppm C_3H_6 + 4.2% O_2 (He as balance) at weight hourly space velocity (WHSV) of 60000 ml.h^{-1}.g^{-1}. The reactants and products were examined by IR analysers (ABB Uras 14) for CO and CO_2 species, while oxygen concentration in the feed was measured by ABB paramagnetic analyser. Propene conversion was evaluated taking into account the CO_2 formed during the reaction.

RESULTS AND DISCUSSION

Catalytic activity measurements

The catalytic results of CPO over the studied catalysts as a function of reaction temperature are compared in figure 1. In all cases, detected CO was negligible and no intermediate products of partial propene oxidation were registered. The effect of monometallic (Au and Pd) and bimetallic Pd-Au deposition on combustion activity is clearly seen in the figure. In general, the Pd-based catalysts exhibited a higher catalytic activity than the matching

Au-containing samples. A higher activity of Pd as compared to Au catalysts in total oxidation of propene and methyl ethyl ketone has been shown in a comparative study of Au and Pd deposited on titanium oxide nanotubes [17]. In a recent investigation of toluene catalytic oxidation over Au and Pd supported on macro-mesoporous metal-doped titania, it has been reported that Pd-containing systems also exhibited a better performance [18]. Formation of highly dispersed Pd^{2+} species on different oxides as supports was considered responsible for the propene oxidation at lower temperatures by Gil *et al*. [19].

The present results indicated the same catalytic behaviour in CPO over Pd and Pd-Au catalysts on bare ceria. The effect of Y was negligible for the monometallic gold and palladium catalysts and slightly positive with the bimetallic samples. However, a definitive positive effect of the palladium deposition after gold loading was observed for Y-doped ceria supports. The reason for higher catalytic activity over bimetallic Pd-Au catalysts as reviewed above is still not exactly clarified. Enache *et al*. [20] supposed that gold influenced electronically the catalytic properties of Pd. Hosseini *et al*. [7] have proposed a Langmuir-Hinshelwood mechanism for toluene and propene oxidation over Pd-Au/TiO_2 catalysts, suggesting that a VOC molecule and oxygen from a [Pd–O] complex compete for adsorption. The authors explained the higher activity of the Pd(shell)–Au(core) as compared to the Au(shell)–Pd(core) system by easier [Pd–O] formation and low adsorption of oxygen on gold due to its lower ability to polarize the O=O bond as compared to Pd.

In the present study, the lowest temperature of total propene conversion was achieved at 180 °C over both Pd-AuYCeIM and Pd-AuYCeCP catalysts. Bimetallic Pd-Au entity on IM support demonstrated better activity at a lower temperature (150 °C) as compared to Pd-Au on CP support (see Fig. 1). Long lasting tests (72 h) in CPO at 180 °C performed over Pd-AuYCeIM sample showed that the catalyst was stable with no loss of oxidation activity.
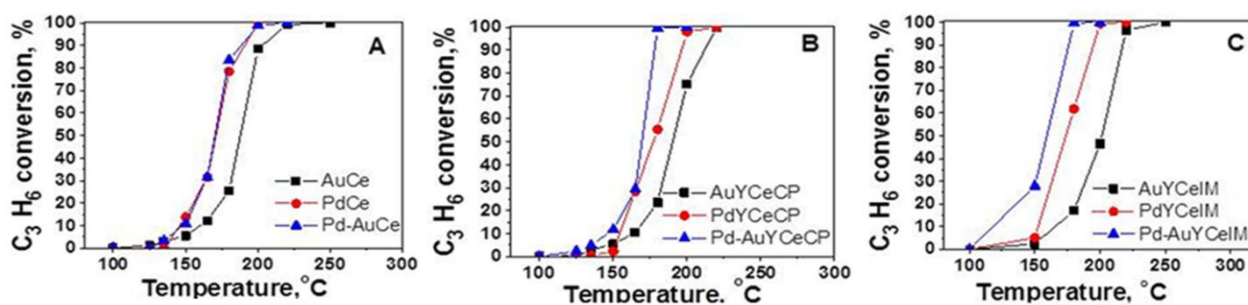

Fig. 1. Effect of monometallic (Au and Pd) and bimetallic Pd-Au loading on ceria (A) and Y-doped ceria supports (B and C) on propene conversion degree.

Sample characterization

Specific surface area (S_{BET}) values are given in table 1. All S_{BET} values are ranging around 100 ± 10 $m^2.g^{-1}$. No substantial differences between mono- and bimetallic catalysts were observed; slightly lower values were found in the case of CP supports.

Table 1. Specific surface area (S_{BET}), and hydrogen consumption of the studied catalysts

Catalyst	S_{BET} ($m^2.g^{-1}$)	HC ($mmol.g^{-1}$)	
		to 250 °C	to 800 °C
AuCe	102.4	0.5	0.5
PdCe	101.9	0.6	1.0
Pd-AuCe	108.5	0.6	1.2
AuYCeCP	90.0	0.7	0.7
PdYCeCP	99.6	0.7	1.4
Pd-AuYCeCP	90.0	0.7	1.1
AuYCeIM	107.2	0.6	0.6
PdYCeIM	105.0	0.7	1.2
Pd-AuYCeIM	105.5	0.5	1.1

X-ray diffractograms of all the studied catalysts showed typical reflections of face-centred cubic fluorite-type structure of CeO_2 (Fig. 2). A separate Y_2O_3 phase was not visible. Pd was not detectable in the Pd containing samples. For the gold containing samples a weak Au(111) peak was registered at $2\theta = 38.2°$ suggesting absence of alloying between Au and Pd. As expected ceria and gold average particle sizes were in accord with those obtained previously using the same synthesis procedure [4].
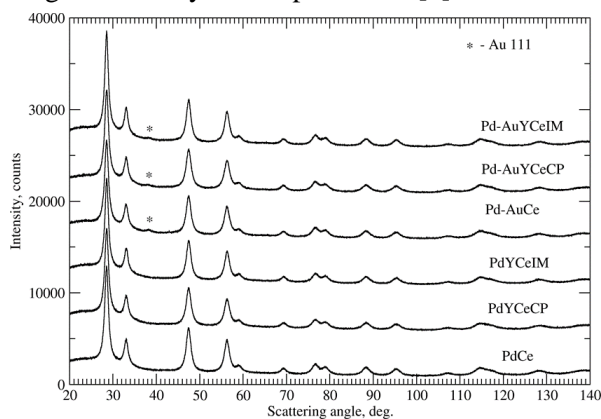
Fig. 2. XRD patterns of the studied Pd and Pd-Au catalysts.

The average particle size of bare ceria, Y-doped ceria prepared by IM, and Y-doped ceria prepared by CP was 5.7, 7.1, and 8.1 nm, respectively, whereas the average particle size of gold in Au and Pd-Au entities on bare ceria, Y-doped ceria prepared by IM, and Y-doped ceria prepared by CP was 4.1, 4.0, and 5.8 nm, correspondingly.

As reported before, based on HRTEM/HAADF analyses evaluated gold average particle size in AuCe, AuYCeIM, and AuYCeCP (valid for the Pd-Au samples as well) was 2.1, 2.6, and 3.2 nm, respectively [21]. Measurements of interplanar distances in selected HRTEM images of AuYCeIM catalyst evidenced the presence of Y_2O_3 crystals (not detectable by XRD) even in the case of 1 wt.% dopant content [21]. HRTEM measurements of Pd-containing samples are not reported. Due to similarity in lattice distances of PdO and CeO_2 it was difficult to distinguish unambiguously between ceria and PdO crystals by HRTEM [9].

Sample reducibility was evaluated by means of TPR measurements. The reduction of ceria proceeds in two steps: surface layer reduction at around 500 °C and bulk reduction above 800 °C [22]. It is known that the presence of noble metals is beneficial for the ceria reduction. Such effect has also been observed for gold when supported as nanoparticles. Many studies have confirmed the first observations of the research groups of Stephanopoulos [23] and Andreeva [24] that the role of nanogold is to lower substantially the temperature of the ceria surface layer reduction. Doping ceria with low concentration of Y^{3+} ions leads to random oxygen vacancies formation accompanied by enhanced reduction of Au/Y-doped ceria catalysts [4 and references therein].

TPR profiles of Au, Pd, and Pd-Au on ceria and Y-doped ceria supports are illustrated in figure 3. The TPR profiles of bare ceria supported mono- and bimetallic catalysts are compared in figure 3A. The T_{max} of the peak assigned to surface ceria reduction of AuCe (contribution of positively charged gold particles can be neglected) was 120 °C and the reduction process was finished up to 200 °C. Differently from samples with nanosized gold favouring ceria surface layer reduction [24], low intense broad peaks at higher temperatures could be seen in the presence of Pd. They were related to enhanced reduction of deeper ceria layers caused by palladium. The first TPR peaks in the profiles of Pd and Pd-Au catalysts should be assigned to the reduction of both ceria surface layers and oxidized palladium (revealed by XPS data on fresh catalysts). Compared with the TPR peak of AuCe, the peaks of Pd containing samples were narrower and located at lower temperatures, especially in the case of Pd-AuCe (T_{max} at 43 and 23 °C, respectively). The same tendency was observed on comparing the TPR profiles of Au, Pd, and Pd-Au on Y-doped ceria prepared by CP and IM (Figs. 3B and C). The lowest T_{max} at 20 °C was registered for Pd-AuYCeIM, however, a lower intensity of this peak was noticeable.

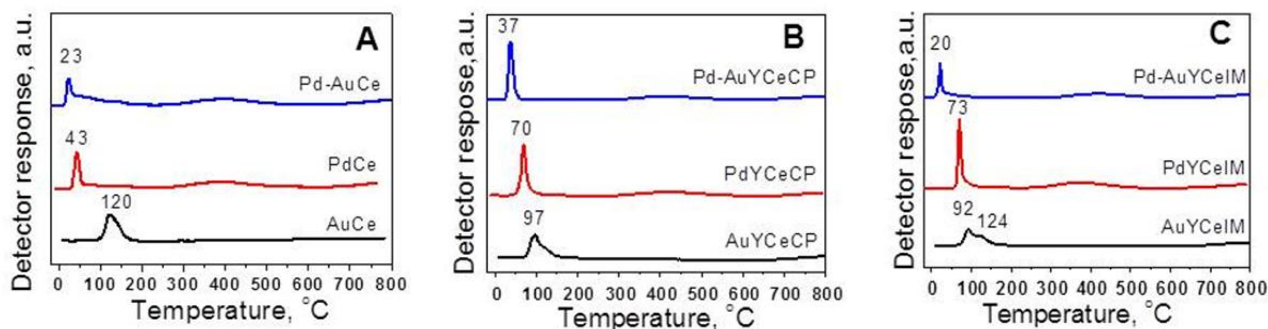Sample reduction behaviour was also evaluated based on calculated hydrogen consumption (HC).

Fig. 3. TPR profiles of the studied ceria- (A) and Y-doped ceria-supported (B and C) monometallic (Au and Pd) and bimetallic Pd-Au catalysts.

Table 1 presents experimental HC values during TPR up to 250 and 800 °C. In agreement with literature data, theoretical HC values for ceria surface layer reduction without changes in ceria bulk structure are limited to 17% [25] or 20% [26]. This means stoichiometric HC values of 0.49–0.58 and 0.49–0.57 mmol.g^{-1} for bare ceria and ceria doped with 1 wt.% Y_2O_3, respectively. Hydrogen consumption of AuCe was in the frame of the theoretical values for ceria surface layer reduction; a relatively higher HC in the case of CP method as compared to the IM mode was observed (even HC of the AuYCeCP catalysts exceeded 20% reduction).

For palladium containing catalysts, bearing in mind that the calculated HC value needed for the process $PdO + H_2 \rightarrow Pd^0$ is 0.08 mmol.g^{-1}, the HC for ceria surface layers reduction up to 250 °C was almost the same as for the matching gold catalysts. These close results justify the similarity of the CPO activities regardless of support nature. However, there existed differences in the oxidation activities determined by the type of loaded metal. The bimetallic catalysts exhibited the best performance irrespective of support composition. Sample activities followed an inverse trend of the reduction T_{max}: the C_3H_6 conversion varied with the supported metal catalysts as Pd-Au > Pd > Au. The TPR T_{max} of the catalysts followed the order T_{max} of Pd-Au catalysts $< T_{max}$ of Pd catalysts $< T_{max}$ of Au catalysts. Such an inverse relationship confirmed the important role of the oxygen being supplied by the support. Indeed the T_{max} of the TPR peak is indicative of the easiness with which the oxygen from ceria can be extracted.

A lower HC value obtained for Pd-AuYCeIM catalyst, which was mentioned above in relation to TPR peak intensity, is not in agreement with its highest CPO activity up to 180 °C, the latter being the temperature at which complete oxidation was also achieved over Pd-AuYCeCP. Tabakova *et al.* have observed a similar discrepancy for bimetallic catalyst of best catalytic performance in a study of Pd-Au deposited on Fe-modified ceria for complete benzene oxidation [9]. Based on XPS evidence for metallic Pd particles at the onset of the low temperature TPR peak, the authors explained unexpectedly decreased reducibility by the formation of inactive Au_xPd_y alloy species in the hydrogen flow [9].

XPS data on fresh and used samples in CPO are summarized in table 2. All samples contained Ce^{4+} and a minor percentage of Ce^{3+} ions. A certain amount of Ce^{3+} in the fresh samples could be related to X-ray beam induced reduction during XPS analysis. For a fresh AuCe catalyst, the Au $4f_{7/2}$ binding energy (BE) was typical of metallic Au^0 [27]. Yttrium presence induced a slight increase of the BE especially for AuYCeCP catalyst sample, thus indicating occurrence of partly positively charged $Au^{\delta+}$. Charged $Au^{\delta+}$ particles were also registered in Pd-Au catalysts. Calculated atomic ratios showed that the Au catalysts exposed a gold-enriched surface of nominal Au/Ce of 0.03. After palladium deposition over gold, the Au/Ce ratio in the Pd-Au catalysts became closer to the nominal value. The monometallic palladium catalysts were characterized by Pd $3d_{5/2}$ BE of 337.1 eV that is typical of Pd^{2+} [28]. The bimetallic samples exhibited somewhat higher Pd 3d binding energy as compared to the monometallic ones, which may be attributed to a charge transfer from palladium to the more electronegative gold species. The Pd/Ce atomic ratio was always much higher than the nominal one (0.016) showing a strong surface segregation of palladium.

The binding energy of Y $3d_{5/2}$ at 157.6 ± 0.2 eV is typical of Y^{3+}. In the palladium containing samples, another Y $3d_{5/2}$ component at a lower energy (about 153.3 ± 0.3 eV) was registered. Such a component assigned to partially reduced yttrium ($Y^{(3-\delta)+}$) has been related to alloying effect in the presence of the noble metal [29]. Enrichment of the ceria surface by yttrium was evidenced by the Y/Ce atomic ratio values, which were larger than the analytical one (0.016).

XPS analysis of samples after reaction was carried out for the best performing bimetallic cata-

13

lysts. As shown in table 2, gold in the used samples was slightly more reduced as compared to the fresh catalysts. Palladium exhibited two components, one at high energy typical of oxidized palladium and the other due to reduced palladium.

Pd 3d and Y 3d spectra of the bimetallic fresh and spent catalysts are displayed in figures 4 and 5. It was interesting to observe that the largest amount of reduced palladium was found in the Pd-AuYCeIM catalyst as compared to the other two ca-
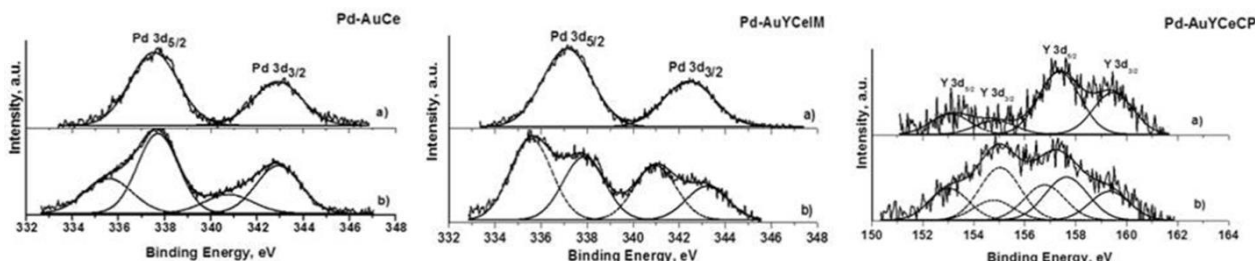

Fig. 4. Pd 3d XP spectra of Pd-Au catalysts: a) fresh,
b) after CPO.
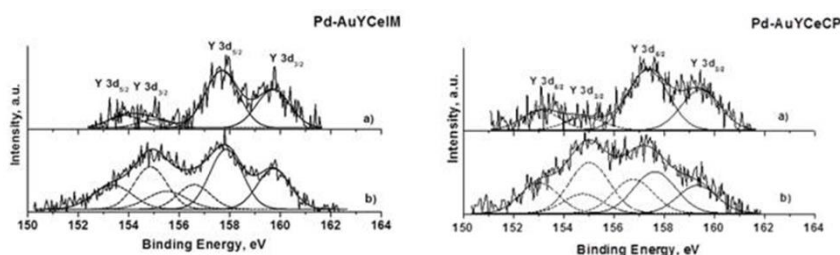
Fig. 5. Y 3d XP spectra of Pd-Au catalyst: a) fresh,
b) after CPO.

Table 2. XPS data in terms of binding energy and atomic ratio

Sample	Au 4f$_{7/2}$ eV	Pd 3d$_{5/2}$ eV	Y 3d$_{5/2}$ eV	O 1s eV	Pd/Ce (0.016)	Au/Ce (0.03)	Y/Ce (0.016)
AuCe	84.3			529.3 (57%) 531.6 (43%)		0.06	
AuYCeCP	85.1		157.7 (66%) 153.8 (34%)	529.5 (79%) 532.0 (21%)		0.06	0.09
AuYCeIM	84.5		157.4	529.4 (77%) 532.0 (23%)		0.06	0.15
PdCe*		337.1		529.6 (80%) 531.4 (20%)	0.14		
PdYCeCP*		337.2	157.5 (57%) 153.4 (43%)	529.6 (73%) 532.2 (27%)	0.49		0.25
PdYCeIM*		337.1	157.7 (81%) 153.2 (19%)	529.4 (78%) 531.7 (22%)	0.36		0.21
Pd-AuCe	84.5	337.6		529.5 (76%) 531.8 (24%)	0.25	0.03	
Pd-AuCe spent in CPO	84.2	337.7 (76%) 335.3 (24%)		529.3 (69%) 531.5 (20%) 533.2 (11%)	0.20	0.02	
Pd-AuYCeCP	84.8	337.5	157.4 (70%) 153.2 (30%)	529.4 (82%) 531.5 (18%)	0.32	0.04	0.04
Pd-AuYCeCP spent in CPO	84.2	337.8 (70%) 335.6 (30%)	157.6 (33%) 155.1 (37%) 153.1 (30%)	529.5 (60%) 531.8 (24%) 533.5 (16%)	0.27	0.02	0.15
Pd-AuYCeIM	84.8	337.2	157.6 (63%) 153.7 (37%)	529.3 (64%) 531.4 (36%)	0.33	0.04	0.07
Pd-AuYCeIM spent in CPO	84.2	337.9 (44%) 335.6 (56%)	157.8 (45%) 155.9 (33%) 153.2 (22%)	529.3 (60%) 531.7 (24%) 533.2 (16%)	0.19	0.04	0.17

talysts. On the contrary, in the bimetallic catalysts the Y 3d appeared more reduced for the CP Y-doped ceria with respect to the IM Y-doped ceria.

A Langmuir-Hinshelwood mechanism is generally claimed to operate in the catalytic oxidation of hydrocarbons over Pd-containing catalysts, although a redox Mars-van Krevelen mechanism cannot be excluded [30]. As it was already mentioned, Hosseini *et al.* [7] proposed Langmuir-Hinshelwood mechanism for the propene oxidation over bimetallic gold and palladium catalysts on titania. The present XPS observation of increased reduction after CPO over palladium, particularly with Pd-AuYCeIM sample, would further support the formation of a complex between the organic molecule and Pd-O species followed by reduction of palladium and oxidation of organic molecule. Enhanced reduction of palladium in this particular catalyst is attributed to the presence of gold and yttrium acting in synergy.

CONCLUSIONS

Mono- (Au, Pd) and bimetallic Pd-Au particles (Pd loaded over already deposited Au) in Y-modified (1 wt.% Y_2O_3) ceria supports exhibited a high catalytic activity in the reaction of CPO. Y dopant presence in the cerium oxide and synthesis method of mixed oxide support (impregnation or coprecipitation) did not significantly affect the catalytic performance.

These results are in agreement with catalyst reducibility evaluated from hydrogen consumption data during TPR. Moreover, CPO activity was affected by Au, Pd, or Pd-Au presence. Generally, the Pd catalysts were more active than matching Au catalysts. The bimetallic catalysts exhibited the best CPO activity. This function of activities correlated well with oxygen mobility through ceria surface layers. Modification of the oxidation state of gold, palladium, and yttrium after catalysis revealed a redox character of propene oxidation over the studied catalysts. A relatively low temperature of total propene oxidation of 180 °C, reached over Pd-Au catalysts on Y-doped ceria, and manifested good stability during longstanding catalytic performance make the bimetallic catalysts promising for reducing the energy requirements for VOCs abatement.

REFERENCES

1. S. Scire, L. F. Liotta, *Appl. Catal. B,* **125,** 222 (2012) and references therein.
2. L. Ilieva, P. Petrova, T. Tabakova, R. Zanella, Z. Kaszkur, *React. Kinet. Mech. Catal.*, **105,** 23 (2012).
3. L. Ilieva, P. Petrova, T. Tabakova, R. Zanella, M. V. Abrashev, J. W. Sobczak, W. Lisowski, Z. Kaszkur, D. Andreeva, *Catal. Today*, **18,** 30 (2012).
4. L. Ilieva, P. Petrova, L. F. Liotta, J. W. Sobczak, W. Lisowski, Z. Kaszkur, G. Munteanu, *Catalysts,* **6,** 99 (2016) .
5. S. S. Shao, H. Wang, M. Zhang, D. D. Ma, S. T. Lee, *Appl. Phys. Lett.,* **93,** 243110 (2008).
6. D. S. Lee, Y. W. Che, *J. Taiwan Inst. Chem. Eng.*, **44,** 40 (2013).
7. M. Hosseini, T. Barakat, R. Cousin, A. Aboukaïs, B.-L. Su, G. De Weireld, S. Siffert, *Appl. Catal. B*, **111–112,** 218 (2012).
8. H. Takatani, H. Kago, Y. Kobayashi, F. Hori, R. Oshima, *Trans. Mater. Res. Soc. Jpn.,* **28,** 871 (2003).
9. T. Tabakova, L. Ilieva, P. Petrova, A. M. Venezia, G. Avdeev, R. Zanella, Y. Karakirova, *Chem. Eng. J.,* **260,** 133 (2015).
10. G. K. Williamson, W. H. Hall, *Acta Metall.*, **1,** 22 (1953).
11. V. D. Mote, Y. Purushotham, B. N. Dole, *J. Theor. Appl. Phys.,* **6,** 6 (2012).
12. M. Ousmane, L. F. Liotta, G. Di Carlo, G. Pantaleo, A. M. Venezia, G. Deganello, L. Retailleau, A. Boreave, A. Giroir-Fendler, *Appl. Catal. B*, **101,** 629 (2011).
13. D. A. Shirley, *Phys. Rev. B*, **5,** 4709 (1972).
14. P. M. A. Sherwood, in: Practical Surface Analysis, D. Briggs, M. P. Seah (Eds.), Wiley, New York, 1990, p. 555.
15. N. Kotzev, D. Shopov, *J. Catal.*, **22,** 297 (1971).
16. D. A. M. Monti, A. Baiker, *J. Catal.,* **83,** 323 (1983).
17. H. L. Tidahy, S. Siffert, V. Idakiev, T. Tabakova, Z. Y. Yuan, R. Cousin, A. Aboukais, B. L. Su, *Stud. Surf. Sci. Catal.,* **175**, 743 (2010).
18. T. Barakat, V. Idakiev, R. Cousin, G.-S. Shao, Z.-Y. Yuan, T. Tabakova, S. Siffert, *Appl. Catal. B*, **146**, 138 (2014).
19. S. Gil, J. M. Garcia-Vargas, L. F. Liotta, G. Pantaleo, M. Ousmane, L. Retailleau, A. Giroir-Fendler, *Catalysts,* **5,** 671 (2015).
20. D. I. Enache, J. K. Edwards, P. Landon, B. Solsona-Espriu, A. F. Carley, A. A. Herzing, M. Watanabe, C. J. Kiely, D. W. Knight, G. J. Hutchings, *Science,* **311,** 362 (2006).
21. L. Ilieva, P. Petrova, G. Pantaleo, R. Zanella, L. F. Liotta, V. Georgiev, S. Boghosian, Z. Kaszkur, J. W. Sobczak, W. Lisowski, A. M. Venezia, T. Tabakova, *Appl. Catal. B*, **188,** 154 (2016).
22. H. C. Yao, Y. F. Yu Yao, *J. Catal.,* **86,** 254 (1984).
23. Q. Fu, A. Weber, M. Flytzani-Stephanopoulos, *Catal. Lett.,* **77,** 87 (2001).
24. D. Andreeva, V. Idakiev, T. Tabakova, L. Ilieva, P. Falaras, A. Bourlinos, A. Travlos, *Catal. Today*, **72,** 51 (2002).
25. M. G. Sanchez, J. L. Gazquez, *J. Catal.,* **104**, 120 (1987).
26. A. Laachir, V. Perrichon, A. Bardi, J. Lamotte, E.

Catherine, J. C. Lavalley, J. El Faallah, L. Hilaire, F. le Normand, E. Quemere, G. N. Sauvion, O. Touret, *J. Chem. Soc. Faraday Trans.*, **87,** 1601 (1991).

27. M. P. Casaletto, A. Longo, A. Martorana, A. Prestianni, A. M. Venezia, *Surf. Interface Anal. B*,

38, 214 (2006).

28. A. M. Venezia, R. Murania, G. Pantaleo, G. Deganello, *J. Catal.*, **251,** 94 (2007).

29. X. He, H. Yang, *Appl. Clay Science*, **101**, 339 (2014).

30. L. F. Liotta, *Appl. Catal. B*, **100**, 403 (2010).

МОНОМЕТАЛНИ (Au, Pd) И БИМЕТАЛНИ Pd-Au ЧАСТИЦИ, НАНЕСЕНИ ВЪРХУ Y-ДОТИРАНИ ЦЕРИЕВООКСИДНИ НОСИТЕЛИ ЗА ПЪЛНО ОКИСЛЕНИЕ НА ПРОПЕН

П. Цв. Петрова[1, *], Д. Панталео[2], А. М. Венеция[2], Л. Ф. Лиота[2], З. Кашкур[3], Т. Т. Табакова[1], Л. И. Илиева[1]

[1] Институт по катализ, Българска академия на науките, 1113 София, България
[2] Институт по наноструктурни материали, CNR, Палермо, Италия
[3] Институт по физикохимия, Полска академия на науките, Каспжак 44/52, 01-224 Варшава, Полша

(Резюме)

Монометални (Au, Pd) и биметални Pd-Au частици, нанесени на Y-дотирани цериевооксидни носители, са изследвани в моделната реакция на пълно окисление на пропен за пречистване на въздух от алифатни въглеводороди. Y-модифицираните цериевооксидни носители (1 тегл.% Y_2O_3) са синтезирани чрез импрегниране или съутаяване. Злато- (3 тегл.% Au) и паладий-съдържащите (1 тегл.% Pd) катализатори са получени по метода на отлагане чрез утаяване. Биметалните Pd-Au катализатори са синтезирани чрез добавяне на паладий към предварително нанесено злато. Получените катализатори са охарактеризирани с помощта на ниско-температурна адсорбция на азот (БЕТ), рентгенова дифракция, температурно-програмирана редукция и рентгенова фотоелектронна спектроскопия. Каталитичната активност не зависи съществено от наличието на Y-допант и метода на синтез на смесенооксиден носител. Пълното окисление на пропен в присъствие на златните катализатори е при 220 °C. Pd-съдържащите катализатори проявяват по-висока окислителна активност в сравнение със златните, показвайки 100% окисление на пропен при 200 °C. Най-ниската температура за пълното окисление на пропен, 180 °C, е постигната в присъствие на биметалните Pd-Au катализатори и проведеният продължителен каталитичен тест показва стабилна работа без загуба на каталитична активност.

Silver-based catalysts for preferential CO oxidation in hydrogen-rich gases (PROX)

S. Zh. Todorova[1]*, H. G. Kolev[1], M. G. Shopska[1], G. B. Kadinov[1], J. P. Holgado[2], A. Caballero[2]

[1] Institute of Catalysis, Bulgarian Academy of Sciences, Acad. G. Bonchev St., Block 11, 1113 Sofia, Bulgaria,
[2] Instituto de Ciencia de Materiales and Dpto. Química Inorgánica, CSIC-University of Sevilla, Sevilla, Spain

Silver samples were prepared by impregnation of different supports (SiO_2, CeO_2, and MnO_2) with aqueous solution of $AgNO_3$. The catalysts were characterized by X-ray diffraction, X-ray photoelectron spectroscopy, temperature-programmed reduction, temperature-programmed desorption of oxygen, high resolution SEM, in situ diffuse reflectance infrared Fourier transform spectroscopy of adsorbed CO, and tested in the reaction of preferential CO oxidation in H_2-rich gases. A 15%Ag/SiO_2 sample pretreated in pure oxygen showed the best catalytic performance. It is suggested that oxidative pretreatment leads to the formation of surface and subsurface oxygen species, which rearrange the silver surface thus increasing significantly silver catalyst activity for CO oxidation in hydrogen-rich gases.

Key words: Ag/SiO_2 catalyst, Ag/CeO_2 catalyst, Ag/MnO_2 catalyst, CO oxidation, PROX.

INTRODUCTION

CO preferential oxidation in hydrogen-rich gases (PROX process) has been studied for application to polymer electrolyte membrane fuel cells (PEMFCs) to reduce CO in the fuel gases below 10 ppm. The catalysts, proposed so far for the PROX process, are based mainly on noble metals such as Pt, Rh, and Ru, deposited on different supports with or without promoters [1–9]. The working temperature of these catalysts is within the range of 130–200 °C [10–12]. It seems to be too high to match subsequent reaction in a PEMFC, which is usually carried out at 50–125 °C [13]. Decreasing the reaction temperature and search for more economic catalysts for PROX are challenging objectives for the near future. IB-group metals, supported on suitable metal oxides, are very promising as PROX catalysts. Highly dispersed gold exhibits an extraordinarily high activity in low-temperature CO oxidation [14–19], however, it deactivates rapidly during long-term operation [20–22]. A very promising catalytic system that has received a great attention during the last years is the copper-cerium mixed oxide composites [23–24]. These oxides show a practically constant and high selectivity towards CO oxidation within a wide temperature interval. However, satisfactory CO conversion (about 90%) is obtained at a temperature above 150 °C [25–28]. Silver, another member of group IB, has been scarcely investigated as a PROX catalyst in spite of its high activity in low temperature CO oxidation in absence of hydrogen [29–31]. Reports concerning utilization of Ag as catalyst for selective CO oxidation are few and they examine only mono-metallic silver supported on SiO_2 or carbon [32–34] and composites like Ag/Co and Ag/Mn oxides [35, 36]. Qu and co-workers [31–33] have observed that SiO_2 and siliceous mesoporous materials, such as MCM-41 and SBA-15, are suitable supports for active PROX catalysts. An increase in Si/Al ratio of H-ZSM-5-supported catalysts results in a decrease in activity due to strong interaction between Ag atoms and Al ions in the zeolite framework. The authors communicate a maximal conversion of about 40% at 45 °C. Zhang et al. [37] have found that the Si/Al ratio of the support has an important effect on the structure of Ag catalysts and as a consequence on the catalytic activity and selectivity in preferential CO oxidation. Derekaya and co-authors found that a 50/50 (mol.%) Ag-Co mixed oxide sample calcined at 200 °C was the most active catalyst and a 50/50 (mol.%) Co-Ce mixed oxide sample calcined at 200 °C was the most selective catalyst for PROX process [35]. Very active and stable Ag/OMS-2 catalysts were obtained by Hu *et al.* [38] through a simple reflux method. It was found that addition of a small amount of Al is beneficial to the formation of small sized highly dispersed Ag metal particles.

This paper is a first part of our research targeting at the influence of metal oxides of high oxygen capacity as CeO_2 and MnO_x on the properties of silver catalysts in the reaction of selective CO oxidation in hydrogen-rich gases. Preliminary catalytic tests showed that silica is the most suitable support. The main objective of the present study is to investigate the effect of silver loading on the activity and selectivity of Ag/SiO_2 in PROX process.

---

* To whom all correspondence should be sent
E-mail: todorova@ic.bas.bg

EXPERIMENTAL

Catalysts preparation

Silver catalysts were prepared by addition of respective support (SiO_2, CeO_2 or MnO_2) to an aqueous solution of $AgNO_3$ to obtain 5, 10, and 15 wt.% Ag on SiO_2 (Aerosil, S_{BET} = 147 m^2/g), and 5 wt.% Ag on CeO_2 (S_{BET} = 130 m^2/g) and MnO_2 (Fluka, S_{BET} = 58 m^2/g). Reference data [32] and preliminary catalytic measurements showed that pretreatment in oxygen at high temperatures increased the catalytic activity. For this reason, all samples were calcined and pretreated in pure O_2 for 2 h at 450 °C before the catalytic tests.

Catalyst characterization

Powder XRD patterns were collected at room temperature in a step-scan regime (step = 0.05°, count time = 2 s) on a Siemens D-501 diffractometer using CuK_α radiation (λ = 1.5718 Å). XRD data processing was performed by using X'Pert HighScore program. SEM images were recorded by a field emission scanning electron microscope (FE-SEM) model S5200. Temperature-programmed reduction (TPR) was carried out by an equipment described elsewhere [38] using a flow mixture of 5% H_2 in Ar at a flow rate of 10 ml/min, and a temperature ramp of 10 °C /min up to 900 °C. Prior to TPR experimental run the samples were treated in He for 30 min at 150 °C. Temperature-programmed desorption of oxygen (TPD-O_2) experiments were performed on the same experimental setup. Oxygen desorbed from the samples was determined by means of a mass spectrometer (QMS-422 Baltzers) and a thermal conductivity detector. Before TPD-O_2 experiment each sample was pretreated in oxygen flow for 2 h at 450 °C, cooled down to room temperature in oxygen followed by 30 min in He. Desorption of O_2 was carried out in He flow until reaching 900 °C at a ramp rate of 20 °C/min.

X-ray photoelectron measurements were conducted on an ESCALAB MkII (VG Scientific) electron spectrometer at a base pressure in the analysis chamber of 5.10^{-10} mbar using a twin anode MgKα/AlKα X-ray source with excitation energies of 1253.6 and 1486.6 eV, respectively. Passing through a 6-mm slit (entrance/exit) of a hemispherical analyser, electrons of 20 eV energy were detected by a channeltron. Because of small concentration and natural width of the AgMNN peak, 50 eV pass energy was used. The spectra were recorded with a total instrumental resolution (as measured with the FWHM of $Ag3d_{5/2}$ photoelectron line) of 1.06 and 1.18 eV for MgKα and AlKα excitation sources, respectively. The energy scale was calibrated by normalizing the Si2p line to 103.3 eV. Spectra processing included subtraction of X-ray satellites and Shirley-type background [39]. Peak positions and areas were evaluated by a symmetrical Gaussian-Lorentzian curve fitting. Relative concentrations of the different chemical species were determined by normalization of the peak areas to their photoionization cross-sections calculated by Scofield's approach [40].

Carbon monoxide adsorption on 15% Ag/SiO_2 catalyst was studied by *in situ* diffuse reflectance infrared Fourier transform spectroscopy (DRIFTS) using a Nicolet 6700 spectrometer equipped with a high temperature/vacuum chamber installed in Collector II accessory (Thermo Spectra-Tech). The CO was adsorbed from CO + Ar mixture flow at room temperature. Experiments were carried out on oxidized or calcined samples, being pretreated in O_2 + Ar for 2 h at 450 °C or in air for 2 h at 450 °C, respectively.

Catalytic activity measurements

The catalytic activity tests were carried out in a continuous flow type glass reactor at atmospheric pressure with a catalyst bed loading of about 0.8 cm^3 (fraction 0.25–0.31 mm). The gas mixture consisted of 1 vol.% CO, 1 vol.% O_2, 40 vol.% H_2, and He as balance to 100 vol.%. External mass transfer limitations were minimized by working at high GHSV (18750 h^{-1}). The reaction temperature was measured by an internal thermocouple. Converted gas mixture analysis at the outlet was performed by a HP5890 series II gas chromatograph equipped with a thermal conductivity detector and Carboxen-1000 column. Helium was used as a carrier gas. Aalborg mass flow controllers were used to regulate gas flow rates. Before catalytic test each sample was calcined and pretreated in oxygen for 2 h at 450 °C.

Carbon monoxide conversion was calculated based on changes in CO concentration:

$$CO_{conversion} = ([CO]_{in} - [CO]_{out})*100/[CO]_{in}, \ \%$$

Oxygen conversion degree was based on O_2 consumption:

$$O_{2conversion} = ([O_2]_{in} - [O_2]_{out})*100/[O_2]_{in}, \ \%$$

Finally, the selectivity for CO oxidation (S_{CO}) was calculated based on the oxygen mass balance as follows:

$$S_{CO} = 0.5*([CO]_{in} - [CO]_{out})*100/([O_2]_{in} - [O_2]_{out}) \ \%$$

RESULTS AND DISCUSSION

Preliminary tests with 5% Ag on a different

support, SiO_2, CeO_2, and MnO_2, indicated that 5% Ag/SiO_2 and 5% Ag/CeO_2 samples reached a maximal activity in the temperature range of 60–100 °C (Fig. 1A). A maximum of catalytic activity (20% CO conversion) with Ag/MnO_2 was observed at a higher temperature – 130 °C. Since the catalyst of better performance was Ag/SiO_2, silica was the selected support for future preparation of samples of different Ag loading (5, 10, 15 wt.%). As it was mentioned in the Experimental section, all samples

were pretreated in oxygen before catalytic tests. Figure 1B presents CO and O_2 conversions, and selectivity to CO_2 with temperature on silica-supported catalysts of different Ag loading. The conversion curves are 'volcano-shaped' and a maximum was reached within the temperature interval of 70–100 °C. The activity increased with the increase in Ag loading. For all samples, the selectivity to CO_2 decreased with temperature rise.
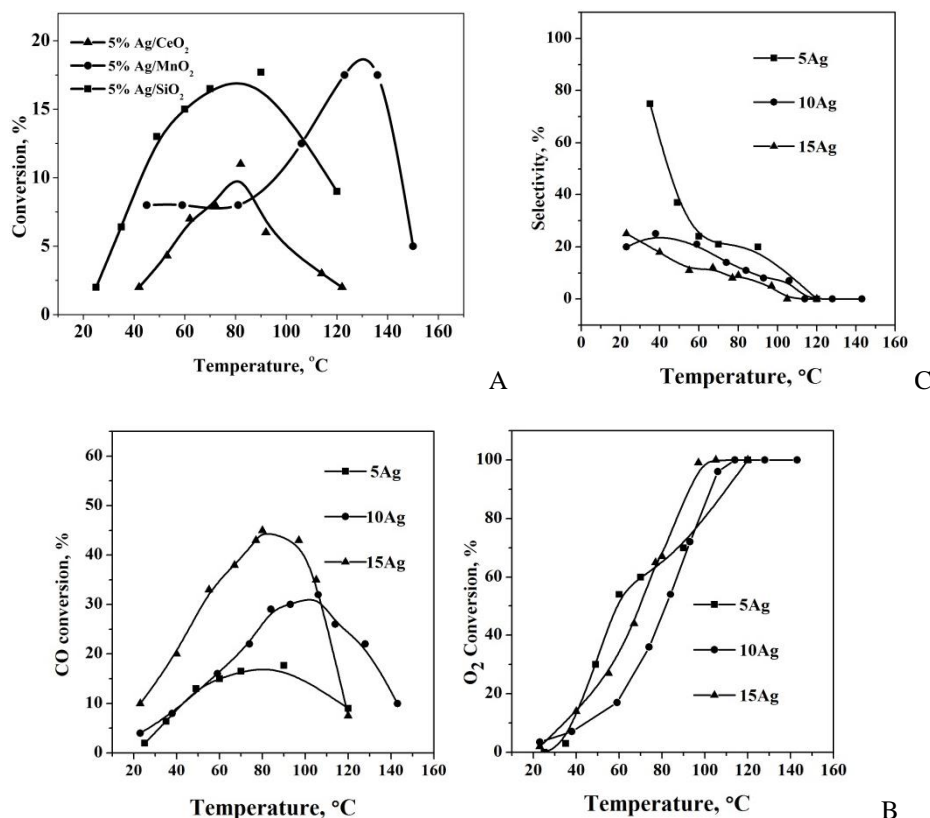
Fig. 1. A. CO conversion degree with catalyst bed temperature on Ag supported on different oxides; B. CO (a) and O_2 (b) conversion degrees with temperature on silica-supported catalysts of different Ag loading; (c) selectivity to CO_2.

A drop in CO_2 selectivity observed with all samples and compatible with results reported in the literature is attributed to the fact that the activation energy of H_2 oxidation was found to be considerably higher than that of CO oxidation [41,42]. A sample of the most active catalyst, 15% Ag/SiO_2, reached a maximum activity of 60% within 70–90 °C, i.e. it dropped down. This catalyst was further examined by different physicochemical methods.

According to XRD data, silver was in the form of Ag^0 (01-087-0719) in all silver samples after pretreatment in oxygen. Calculated silver particles size by using Scherrer equation showed increasing values with increasing loading from 5 nm for 5% Ag up to 23 and 47 nm for 10% Ag and 15% Ag, respectively (Fig. 2).
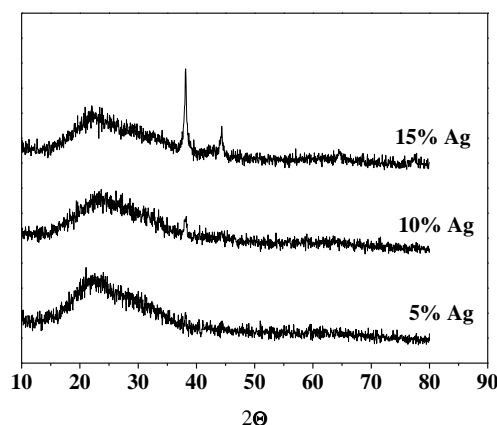
Fig. 2. XRD patterns of monometallic silver samples after treatment in oxygen flow at 450 °C.

Figure 3 displays SEM images obtained from backscattered electrons for 15% Ag. As is known, these images depend on the atomic number contrast among the different constituents of the sample. Bright zones represent heavy elements, while dark ones correspond to light elements. Thus, the bright zones can be assumed to be silver, while the dark counterparts correspond to the support. Spherical silver particles with mean diameter of 20–40 nm are visible in the micrograph of 15% Ag/SiO$_2$ sample and this manifests good coincidence with XRD data.
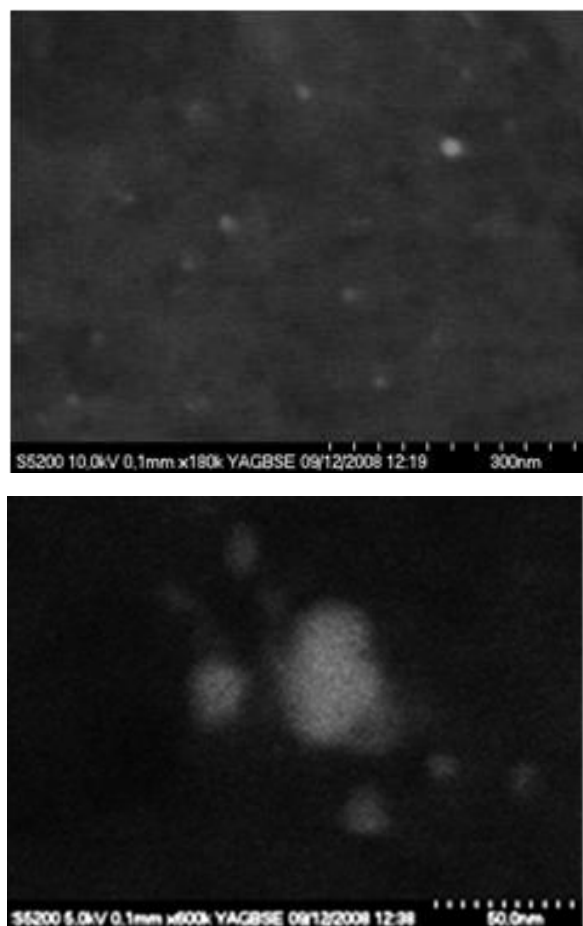
Fig. 3. SEM images of 15% Ag/SiO$_2$ after calcination.

O$_2$-TPD was used to study oxygen interaction with the silver surface. Four desorption peaks are visible in the spectrum (Fig. 4A): a very low intensity peak at 130 °C, and peaks at 410, 493, and 750 °C. Desorption temperatures of molecular, atomic, and lattice oxygen have been reported to be 150–470, 550–650, and over 750 °C, respectively [43–44]. Qu *et al.* observed two desorption peaks of oxygen in the TPD spectrum of Ag/SiO$_2$ catalyst pretreated with oxygen at 500 °C [32]. A peak at about 500 °C is assigned to desorption of bulk oxygen species (O$_\beta$), which diffuses *via* an interstitial diffusion mechanism.

The desorption peak at higher temperatures (≈700 °C) is attributed to subsurface oxygen (O$_\gamma$) [45–46]. Based on the results cited above, we suppose that the low temperature peaks at 120 and 401 °C arise from desorption of adsorbed molecular oxygen, the peak at 493 °C originates from atomic oxygen desorption, and the peak at 750 °C comes from desorption of subsurface oxygen species. Two reduction peaks at 92 and 113 °C are observed in the TPR profile of 15% Ag/SiO$_2$ catalyst (Fig. 4B). According to some authors [47], a peak at 108 °C can be ascribed to reduction of oxygen species on finely dispersed silver. Taking into account that XRD data are pointing to the presence of metallic silver only, hydrogen consumption at 92 and 113 °C is ascribed to the reduction of surface oxygen species.
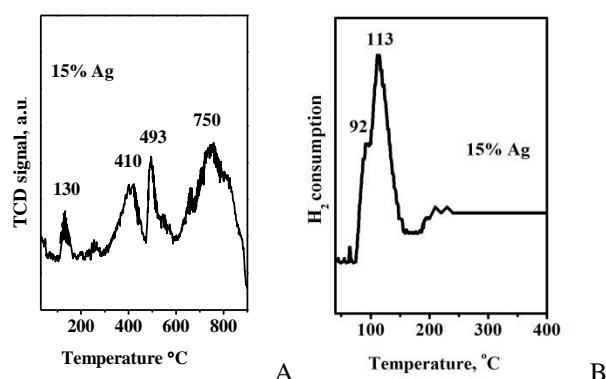
Fig. 4. O$_2$-TPD (A) and TPR (B) patterns of 15% Ag/SiO$_2$ catalyst pretreated with oxygen at 450 °C.

XPS experiments were carried out on calcined and oxidized 15% Ag/SiO$_2$ samples in order to estimate silver oxidation state on the surface (Fig. 5). As the characteristic 3d states of oxidized and metallic silver are closely positioned together (within 0.5 eV) [46], the binding energy values of Ag3d do not identify unambiguously silver particle oxidation state.

Auger parameter (ά = EK(AgMNN) + EB(Ag3d$_{5/2}$)) was used for precise determination of the chemical state of Ag, thus eliminating surface effects of electrostatic charging [49,50]. Two Auger peaks are visible in the XPS spectrum of 15% Ag sample oxidized for 2 h at 450 °C and the ά parameters are 724.0 eV (356.1 + 367.9 eV) and 726.1 eV (358.2 + 367.9 eV), respectively. Since the Auger parameters of Ag^0 and Ag$^+$ are 726.0 eV and 724.5 eV [50], it is clear that part of the surface silver species in the 15% Ag sample after pretreatment in oxygen are in the form of Ag$^+$ and some occur as Ag^0, i.e. both Ag$^+$ and Ag^0 species are present on the surface of the monometallic silver sample after oxidative pretreatment.
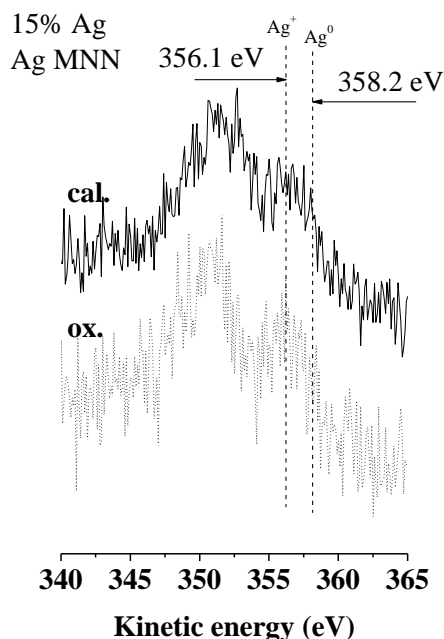
Fig. 5. XP spectra of Ag MNN registered on oxidized (2 h, 450 °C in oxygen) and calcined silver samples.
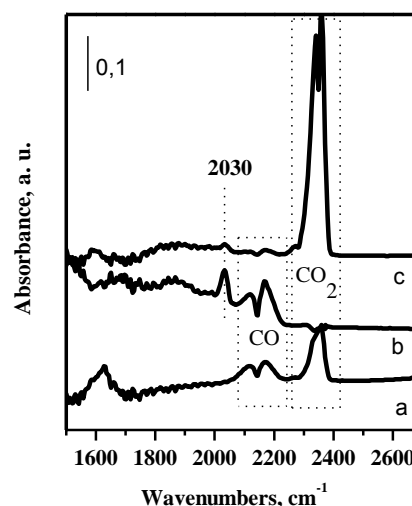

Fig. 6. Diffuse-reflectance infrared spectra of CO adsorbed at room temperature on 15% Ag/SiO_2 after different pretreatments: a - 20 h exposure to CO after calcination; b - 1 h exposure to CO after oxidation; c - 20 h exposure to CO after oxidation.

Qu *et al*. [32] claim that oxygen pretreatment leads to the formation of subsurface oxygen, which induces rearrangement of the silver surface, facilitates the formation of active sites for CO oxidation, and enhances the ability of the catalyst to adsorb CO and activate oxygen. Carbon monoxide was found to interact directly with subsurface oxygen species at room temperature, which might be one of the reasons for high activity of the catalyst for CO oxidation. In view of this, DRIFT spectroscopy of adsorbed CO was applied to shed some additional light on the state of the catalyst surface.

It is well known that in situ DRIFT spectroscopy is one of the most powerful techniques to obtain information about the type of the active sites, their stability and reactivity, chemical state of the surface under static and dynamic conditions within a wide temperature range and after different kinds of pretreatment. The most frequently used probe molecule to study supported catalysts is carbon monoxide due to $\nu(C-O)$ sensitivity to the chemical state of the metal atom(s) to which it is being coordinated.

We made an attempt to gain further information on the state of the catalyst surface by adsorption of CO after various pretreatments. The IR spectra of CO adsorbed on calcined and oxidized 15% Ag/SiO_2 samples are shown in figure 6. Only gas-phase spectra are visible after CO adsorption from $CO + N_2$ mixture on the calcined sample. After 20 h exposure at room temperature a band for gaseous CO_2 appeared (2300–2400 cm^{-1}) indicating that the CO oxidation occurred at room temperature.

Most probably, CO reacted with surface or subsurface oxygen formed during calcination in air. No O_2-TPD was carried out after calcination, however, it can be assumed that some oxygen surface and subsurface species were formed after this pretreatment. The picture was completely different after adsorption of CO on oxidized surface: the band at 2030 cm^{-1} is visible in the IR spectra. There are few FTIR studies dedicated to the adsorption of CO on supported Ag^0 particles as summarized by Müslehiddinolu and Vannice [51]. Before their study, literature data mainly concluded about the absence of IR bands after adsorption of CO at 300 K. [52–54]. According to Müslehiddinolu and Vannice about 10% of the total amount of Ag^0 sites are able to adsorb CO and they are either on very specific planes or on steps [51]. Gravejat *et al.* [55] have established by volumetric measurements that the total amount of adsorbed CO species count for a small fraction of the superficial sites of reduced Ag particles implying that they are adsorbed on defect sites. According to the above-mentioned data [51–55] a band in the frequency range of 2020–2055 cm^{-1} is due to formation of monocarbonyl CO-Ag^0 species depending on pretreatment or CO partial pressure. Surface faceting has been observed in the case of thin films, single crystals, and supported catalysts after oxygen treatment [56,57]. Morphological changes of silver following a high-temperature treatment in oxygen have been directly observed in SEM micrographs by Nagy *et al*. [58].

Based on the assumption given above we can state that pretreatment in oxygen at 450 °C gave rise to silver surface rearrangement leading to the forma-

tion of sites suitably exposed to linear CO bonding. After 20 h exposure at room temperature in $CO + N_2$ mixture, the band for $CO–Ag^0$ decreased its intensity along with the appearance of a band due to gaseous CO_2 to demonstrate interaction between adsorbed CO and subsurface oxygen. The band of linearly adsorbed carbon monoxide disappeared completely after a purge thus revealing its low stability.

CONCLUSIONS

According to the results presented above, we can conclude that supported silver catalysts are promising systems for selective oxidation of CO at low temperatures. Among all studied supports, silica was the most suitable. Oxidation pretreatment led to the formation of surface and subsurface oxygen species that rearranged the silver surface and signifycantly affected silver catalyst activity for CO oxidation in hydrogen-rich gases.

REFERENCES

1. P. V. Snytnikov, V. A. Sobyanin, V. D. Belyaev, P. G. Tsyrulnikov, N. B. Shitova, D. A. Shlyapin, *Appl. Catal. A: General,* **239**, 149 (2003).
2. T. İnce, G. Uysal, A. N. Akin, R. Yildirim, *Appl. Catal. A-Gen,* **292**, 171 (2005).
3. D. Teschner, A. Wootsch, O. Pozdnyakova-Tellinger, J. Kröhnert, E. M. Vass, M. Hävecker, S. Zafeiratos, P. Schnörch, P. C. Jentoft, A. Knop-Gericke, R. Schlögl, *J. Catal.*, **249**, 316 (2007).
4. P. V. Snytnikov, V. A. Sobyanin, V. D. Belyaev, P. G. Tsyrulnikov, N. B. Shitova, D. A. Shlyapin, *Appl. Catal. A-Gen,* **239**, 149 (2003).
5. M. Kipnis, E. Volnina, *Appl. Catal. B-Environ,* **98**, 193 (2010).
6. D. Teschner, A. Wootsch, O. Pozdnyakova-Tellinger, J. Kröhnert, E. M. Vass, M. Hävecker, S. Zafeiratos, P. Schnörch, P. C. Jentoft, A. Knop-Gericke, R. Schlögl, *J. Catal.,* **249**, 316 (2007).
7. R. H. Liu, N. S. Gao, F. Zhen, Y. Y. Zhang, L. Mei, X. W. Zeng, *Chem. Eng. J.* **225**, 245 (2013).
8. F. G. Wang, K. F. Zhao, H. J. Zhang, Y. M. Dong, T. Wang, D. N. He, *Chem. Eng. J.* **242**, 10 (2014).
9. L. Wang, J. Chen, A. Patel, V. Rudolph, Z. Zhu, *Appl. Catal. A: Gen.,* **447–448**, 200 (2012).
10. H. Igarashi, H. Uchida, M. Suzuki, Y. Sasaki, M. Watanabe, *Appl. Catal. A: Gen.,* **159**, 159 (1997).
11. M. J. Kahlich, H. A. Gasteiger, R. J. Behm, *J. Catal.* **171**, 93 (1997).
12. O. Korotkikh, R. Farrauto, *Catal. Today,* **62**, 249 (2000).
13. M. J. Kahlich, H. A. Gasteiger, R. J. Behm, *J. Catal.*, **182**, 430 (1999).
14. S. Kandoi, A. A. Gokhale, L. C. Grabow, J. A. Dumesic, M. Mavrikakis, *Catal. Lett.* **93**, 93 (2004).
15. G. Avgouropoulos, M. Manzoli, F. Boccuzzi, T. Tabakova, J. Papavasiliou, T. Ioannides, V. Idakiev, *J. Catal.,* **256**, 237 (2008).
16. G. Avgouropoulos, T. Ioannides, Ch. Papadopoulou, J. Batista, S. Hocevar, H. K. Matralis, *Catal. Today,* **75**, 157 (2002).
17. S. S. Pansare, A. Sirijaruphan, J. G. Goodwin, *J. Catal.,* **234**, 151 (2005).
18. C. Rossignol, S. Arrii, F. Morfin, L. Piccolo, V. Caps, J. Rousset, *J. Catal.*, **203**, 476 (2005).
19. A. Luengnaruemitchai, S. Osuwan, E. Gulari, *Int. J. Hydrogen Energy*, **29**, 429 (2004).
20. A. Luengnaruemitchai, D. T. K. Thoa, S. Osuwan, E. Gulari, *Int. J. Hydrogen Energy,* **30,** 981 (2005).
21. M. Schubert, M. Kahlich, H. Gasteiger, R. Behm, *J. Power Sources,* **84**, 175, (1999).
22. G. Avgouropoulos, Th. Ioannides, H. K. Matralis, J. Batista, St. Hocevar, *Catal. Lett.,* **73**, 33 (2001).
23. P. Y. Peng, I. Jin, T. C. K. Yang, C. M. Huang, *Chem. Eng. J.*, **251**, 228 (2014).
24. E. Moretti, L. Storaro, A. Talon, M. Lenarda, P. Riello, R. Frattini, M. del V. Martínez de Yuso, A. Jiménez-López, E. Rodríguez-Castellón, F. Ternero, A. Caballero, J. P. Holgado, *Appl. Catal. B-Env.*, **102**, 627 (2011).
25. F. Marin, C. Descorme, D. Duprez, *Appl. Catal. B-Env.,* **58**, 175 (2005).
26. A. Martínez-Arias, A. B. Hungría, G. Munuera, D. Gamarra, *Appl. Catal. B-Env.,* **65**, 207 (2006).
27. P. Ratnasamy, D. Srinivas, C. V. V. Satyanarayana, P. Manikandan, R. S. Senthil Kumaran, M. Sachin, V. N. Shetti, *J. Catal.*, **221**, 455 (2004).
28. G. Avgouropoulos, J. Papavasiliou, T. Tabakova, V. Idakiev, T. Ioannides, *Chem. Eng. J.*, **124**, 41 (2006).
29. S. Imamura, H. Yamada, K. Utani, *Appl. Catal. A-Gen.,* **192**, 221 (2000).
30. K. Song, S. Kang, S. D. Kim, *Catal. Lett.*, **49**, 65 (1997).
31. Z. Qu, S. Zhou, W. Wu, Can Li, X. Bao, *Catal. Lett.*, **101**, 21 (2005).
32. Z. Qu, M. Cheng, W. Huang, X. Bao, *J. Catal.*, **229**, 446 (2005).
33. Z. Qu, M. Cheng, C. Shi, X. Bao, *J. Mol. Catal. A-Chem.,* **239**, 22 (2005).
34. L. Chen, D. Ma, X. Li, X. Bao, *Catal. Lett.*, **111**, 133 (2006).
35. G. Güldür F. Balikçi, *Int. J. Hydrogen Energy,* **27**, 219 (2002).
36. F. B. Derekaya, G. Güldür, *Int. J. Hydrogen Energy,* **35**, 2247 (2010).
37. R. Hu, C, Yan, L. Xie, Yi Cheng, D. Wang, *Int. J Hydrogen Energy,* **36**, 64 (2011).
38. P. Malet, A. Caballero, *J. Chem. Soc. Faraday Trans.*, **84**, 2369 (1988).
39. D. Shirley, *Phys. Rev. B,* **5**, 4709 (1972) .
40. J. H. Scofield, *J. Electron Spectrosc. Relat. Phenom.,* **8**, 129 (1976).
41. S. Scire, C. Crisafulli, S. Minico, G. G. Condorelli,

A. Di Mauro, *J. Mol. Catal. A-Chem.,* **284**, 24 (2008).

42. M. J. Kahlich, H. A. Gasteiger, R. J. Behm, *J. Catal.,* **182**, 430 (1999).

43. Y.-E. Sung, W. Y. Lee, H.-K. Rhee, H.-I. Lee, *Kor. J. Chem. Eng.*, **6**, 300 (1989).

44. C. Backx, C. P. M. de Groot, P. Biloen, W. M. H. Sachtler, *Surf. Sci.*, **128**, 81 (1983).

45. X. H. Bao, J. Barth, G. Lempfuhl, R. Schuster, Y. Uchida, R. Schlögl, G. Ertl, *Surf. Sci.,* **284**, 14 (1993).

46. A. J. Nagy, G. Mestl, D. Herein, G. Weinberg, E. Kitzelmann, R. Schlögl, *J. Catal.,* **182**, 417 (1999).

47. F. Boccuzzi, A. Chiorino, M. Manzoli, D. Andreeva, T. Tabakova, L. Ilieva, V. Iadakiev, *Catal. Today,* **75**, 169 (2002).

48. L. J. Kundakovic, M. Flytzani-Stephanopoulos, *Appl. Catal. A-Gen.*, **183**, 35 (1999).

49. C. D. Wagner, *Faraday Discuss. Chem. Soc.,* **60**, 291 (1975).

50. G. Atanasova, D. Guergova, D. Stoychev, A. Naydenov, P. Stefanov, *Reac. Kinet. Mech. Catal.,* **101**, 397 (2010).

51. J. Müslehiddinoğlu, M. A. Vannice, *J. Catal.*, **213**, 305 (2003).

52. G. W. Keulks, A. Ravi, *J. Phys. Chem.,* **74**, 783 (1970).

53. A. N. Pestryakov, A. A. Davydov, L. N. Kurina, *Russ. J. Phys. Chem.,* **62**, 926 (1988).

54. Y. Y. Huang, *J. Catal.,* **32**, 482 (1974).

55. P. Gravejat, S. Derrouiche, D. Farrussengn, K. Lombaert, C. Mirodatos, D. Bianchi, *J. Phys. Chem., C*, **111**, 9496 (2007).

56. R. A. Marbrow, R. M. Lamber, *Surf. Sci.,* **71**, 107 (1978)

57. D. Herein, A. Nagy, H. Schubert, G. Weinberg, E. Kitzelmann, E. R. Schlögl, *Z. Phys. Chem.,* **197**, 67 (1996).

58. A. J. Nagy, G. Mestl, D. Herein, G. Weinberg, E. Kitzelmann, E. R. Schlögl, *J. Catal.,* **182**, 417 (1999).

КАТАЛИЗАТОРИ НА ОСНОВАТА НА СРЕБРО ЗА СЕЛЕКТИВНО ОКИСЛЕНИЕ НА СО В БОГАТИ НА ВОДОРОД СМЕСИ

С. Ж. Тодорова[1]*, Х. Г. Колев[1], М. Г. Шопска[1], Г. Б. Кадинов[1], Н.-Р. Холгадо[2], А. Кабалеро[2]

[1] *Институт по катализ, Българска академия на науките, ул. „Акад. Г. Бончев", бл. 11, 1113 София, България*

[2] *Институт за изследване на материали и департамент по неорганична химия, CSIC-Университет в Севиля, Севиля, Испания*

(Резюме)

Получени са сребърни катализатори посредством импрегниране на различни носители (SiO_2, CeO_2 и MnO_2) с воден разтвор на $AgNO_3$. Те са охарактеризирани с помощта на различни методи: рентгенова дифракция, рентгенова фотоелектронна спектроскопия, температурно програмирана редукция, температурно програмирана десорбция на кислород, сканираща електронна спектроскопия с висока резолюция, *in situ* дифузно-отражателна инфрачервена спектроскопия на адсорбиран СО. Образците са тествани в реакция на селективно окисление на СО в богати на водород смеси. Установено е, че проба с най-добра каталитична активност е предварително обработен в чист кислород образец Ag/SiO_2. Предположено е, че използването на окислителна предварителна обработка води до образуване на повърхностни и подповърхностни кислородни форми и преструктуриране на повърхността на сребърните частици, което значително увеличава активността на катализатора в изследваната реакция.

Structure and activity of M-Al layered double hydroxides in CO$_2$ methanation reaction as function of the divalent metal

M. V. Gabrovska[1]*, D. Crişan[2], D. A. Nikolova[1], I. Z. Shtereva[1], L. P. Bilyarska[1], M. Crişan[2], R. M. Edreva-Kardjieva[1]

[1] *Institute of Catalysis, Bulgarian Academy of Sciences, Acad. G. Bonchev St., Bldg. 11, 1113 Sofia, Bulgaria*
[2] *Ilie Murgulescu Institute of Physical Chemistry, Romanian Academy, Splaiul Independentei 202, 060021 Bucharest, Romania*

The effect of divalent metal (Ni or Co) on the structure, phase composition, thermal stability, and reducibility of co-precipitated Al-containing layered double hydroxides (LDHs) as catalyst precursors for CO$_2$ removal by methanation reaction was examined. The catalytic activity was estimated by varying reduction and reaction temperature and space velocity as well. It was observed that the divalent metal in Al-containing LDHs affects the crystallisation degree of the formed layered compounds, their specific surface area, and temperature of LDH decomposition with parallel phase transformation to resultant mixed metal oxides. It was found that Co^{2+} ions stabilised in CoAl$_2$O$_4$ spinel structure hampered their reduction to metal state, thus leading to deficiency of Co^0 active metal surface phase. This phenomenon determined a low activity of Co/Al$_2$O$_3$ catalyst, especially at low reduction temperatures. In contrast, the interaction between Ni^{2+} and Al^{3+} ions resulted in generation of readily reducible Ni^{2+}-O species, which favoured a higher activity of Ni/Al$_2$O$_3$ catalyst after reduction at the same temperatures. Spinel-type phases were formed at different temperatures as a function of the divalent metal and determined catalyst activity in the purification of H$_2$-rich streams from traces of CO$_2$ by methanation reaction.

Key words: CoAl and Ni-Al layered double hydroxides, structure, mixed metal oxides, reducibility; CO$_2$ methanation.

INTRODUCTION

Carbon dioxide (CO$_2$) is a major greenhouse gas and makes a significant contribution to global warming and climate change. The pressing necessity for greenhouse gas emissions control concentrates scientists' attention to decrease CO$_2$ accumulation in the atmosphere. On this occasion, mitigation and effective utilisation of the CO$_2$ emissions have become major areas of research worldwide [1,2]

Among catalysed reactions, the catalytic hydrogenation of CO$_2$ over transition metal catalysts to form methane, simply called methanation (CO$_2$ + 4H$_2$ = CH$_4$ + 2H$_2$O), is one of the most appropriate and efficient techniques for CO$_2$ removal. Direct synthesis of methane from CO$_2$ is favourable not only for reduction of greenhouse gas emissions, but also for fuel and chemicals production [2,3]. Moreover, CO$_2$ methanation is used as a promising technique for purification of H$_2$-rich streams from traces of CO$_2$ to prevent catalyst poisoning especially in the ammonia synthesis industry [4] and in the fuel cell anode technology [5].

Although many different metals supported on various oxide carriers have been used, nickel and ruthenium are two of the most effective. Despite the highest activity observed of Ru metal, it is not of practical interest due to its high cost [6]. Nickel catalysts at a large scale of concentrations (25−77 wt.%) are a choice of the industrial methanation because of their high activity, effectivity, selectivity toward methane formation in preference to other hydrocarbons, and relatively low cost [7−9].

Layered double hydroxides are lamellar materials belonging to a great group of natural or synthetic inorganic layered compounds, named anionic clays or hydrotalcite-like materials, because of the similarity existing between their structures and that of mineral hydrotalcite, (Mg$_6$Al$_2$(OH)$_{16}$CO$_3$·4H$_2$O). The structure of LDHs can be expressed by the general formula [M$^{2+}_{1-x}$ M$^{3+}_x$ (OH)$_2$]$^{x+}$ [A$^{n-}_{x/n}$ mH$_2$O]$^{x-}$, where bivalent M^{2+} (Mg^{2+}, Ni^{2+}, Co^{2+}, Zn^{2+}, etc.) and trivalent M^{3+} (Al^{3+}, Cr^{3+}, In^{3+}, etc.) metal cations are located in the brucite-like hydroxide layers. Due to charge disequilibrium, a substituted trivalent M^{3+} cation for a M^{2+} ion gives rise to infinite repetition of positively charged sheets alternating with A^{n-} ions which are required to balance the net positive charges of the hydroxide layers. The charge compensating exchangeable anions A^{n-}, such as CO$_3^{2-}$, NO$_3^-$, SO$_4^{2-}$, Cl$^-$, etc., as well as water molecules,

are situated in the interlayer gallery of the layered structure. Herewith, x represents the fraction of the M^{3+} cation, more precisely $x = M^{3+}/(M^{3+} + M^{2+})$, the most reliable composition range being approximately $0.2 \leq x \leq 0.4$, and m is the number of co-intercalated water molecules which prevent inter-anion repulsion. The LDH compounds are characterised by uniform homogeneous distribution of the M^{2+} and M^{3+} metal cations at the octahedral sites of the brucitelike layer on an atomic level. The cations are crosslinked through hydroxyl groups to form a bimetal hydroxide sheet similar to that of brucite [10−13].

Our research efforts have been directed to assess the potential use of Ni-Al layered systems as catalysts for CO_2 removal in place of conventional Ni-based catalysts. It has been established that depending on the Ni^{2+}/Al^{3+} molar ratio and temperature of treatment in hydrogen ambience, Ni-Al LDHs are promising precursors for catalysts for fine CO_2 removal from hydrogen-rich gas streams through the CO_2 methanation reaction both as-synthesised [14] and after thermal treatment to cause formation of finely dispersed Ni-Al mixed oxides [15].

While numerous studies have been focused on CO_2 methanation over Ni catalysts, there are only scarce attempts to elucidate the role of Co catalysts in the same reaction [16,17].

In this regard, the object of the present investigation is to elucidate the effect of divalent cation, Ni^{2+} and Co^{2+}, in co-precipitated Al-containing LDHs on phase composition, structure, thermal stability, reducibility, and activity estimation in CO_2 methanation by varying reduction and reaction temperature and space velocity as well.

Until now, an extensive comparative study of CO_2 methanation on non-calcined co-precipitated Co-Al and Ni-Al LDH has not been reported in the literature.

EXPERIMENTAL

Sample preparation

Carbonate forms of LDH precursors of identical composition (M^{2+}/Al^{3+} molar ratio of 3.0, M^{2+} = Co^{2+} or Ni^{2+}) were obtained by co-precipitation of mixed Co-Al or Ni-Al aqueous nitrate solution with Na_2CO_3 as precipitating agent at constant pH = 8 and temperature of 80 °C under vigorous stirring. The initial salts of analytical grade, provided by Alfa Aesar (USA), were used as received without further purification. Detailed description of the preparation procedure is presented in Ref. 14. The obtained precipitate was further dried at 80 °C for 20 h, named as-synthesised precursor, and designated

as CoAl or NiAl (Table 1). After reaction run, the spent catalysts were labelled as CoAl-s or NiAl-s.

Dried layered systems were step-wise treated in air for 2 h in the temperature range 200−1000 °C at a heating rate of 3 °C/min in order to understand phase composition changes.

Sample characterisation

The chemical composition of the as-synthesised materials was determined by inductively coupled plasma atomic emission spectroscopy (ICP-AES) using JY (Jobin Yvon) 38 spectrometer.

Specific surface areas were measured employing the single point BET method using a FlowSorb II 2300 Micromeritics apparatus with a N_2/He mixture (30/70) at the boiling temperature of liquid nitrogen.

Thermal analysis (DTA-TG) was carried out simultaneously on a Stanton Redcroft conventional TG-DTA system. Measurements were carried out under airflow (ca. 3 ml/h) at a heating rate of 10 deg/min.

The phase composition of as-synthesised, calcined, and spent samples was established by powder X-ray diffraction (PXRD) analysis. Data were collected on a Bruker D8 Advance powder diffractometer employing CuKα radiation. Crystalline phases were identified by means of International Centre for Diffraction Data (ICDD) powder diffraction files.

The temperature-programmed reduction (TPR) behaviour of the investigated samples (~0.025 g) was evaluated by means of a laboratory setup using a thermal conductivity detector. The temperature was linearly raised from 25 to 850 °C at a heating rate of 10 deg/min. The TPR experiments were accomplished by a gaseous mixture of 10% H_2 in Ar at a flow rate of 25 cm³/min. The samples were heated in nitrogen to 80 °C at a rate of 30 deg/min to remove adsorbed water. Then the nitrogen was replaced by a gaseous mixture of 10% H_2 in Ar and the temperature was raised again at a rate of 10 deg/min up to 850 °C. The selected conditions were compatible with the criteria proposed by Monti and Baiker [18] that avoid mass transfer and temperature control limitations.

Gas-phase hydrogenation of CO_2 to CH_4 was carried out in a fixed-bed flow reactor setup under atmospheric pressure. For each catalytic measurement, 0.8 g of as-synthesised precursor of 0.4–0.8 mm particle size were loaded into a quartz reactor. Quartz glass pellets of 1.0–1.25 mm size were used to fill up reactor to eliminate mass transfer effects. Catalyst activation was successively performed by *in situ* reduction at 400, 450, 530, and 600 °C for 3 h with pure hydrogen (Messer MG, Chimco Gas) at a constant gas hourly space velocity (GHSV) of 2000

h^{-1} and a heating rate of 1.7 deg/min. The catalytic activity measurements were accomplished by CO$_2$/H$_2$/Ar gaseous mixture (0.65/34.35/65 vol.%, Messer MG, Chimco Gas) in the temperature interval 220–400 °C and GHSV from 3000 to 22000 h^{-1} after each reduction temperature. Residual CO$_2$ was determined using an online-connected Uras 3G gas analyser (Hartmann-Braun AG) in the range 0–0.0050 vol.% CO$_2$ (0–50 ppm). During reaction water was removed by a cooling trap (–40 °C) between the reactor and the gas analyser. The catalytic activity was evaluated by the GHSV value at which CO$_2$ residual concentration at the reactor outlet was 10 ppm, the latter being an admissible limit in the feedstock of industrial ammonia production. In addition, it satisfies the requirements for safety work of the fuel cell anodes.

Mass-gas analysis of the outlet gas mixture was performed on a MS-10 spectrometer with precision of 1×10^{-4} vol.%.

RESULTS AND DISCUSSIONS

Chemical analysis data of the samples listed in Table 1 reveal that the M^{2+}/Al^{3+} molar ratio of the dried precipitates is consistent with that of the initial mixed Co-Al and Ni-Al nitrate solutions.

For better understanding of the effect of divalent cation (Ni^{2+} or Co^{2+}) on phase composition, structure, thermal stability, and reducibility of the corresponding co-precipitated Al-containing LDHs, a number of physicochemical characterisations were performed.

Table 1. Sample notation, chemical composition, and colour of the as-synthesised hydrotalcite-like samples

Notation	Chemical composition as M^{2+}/Al^{3+} (molar ratio)		Colour
	theoretical	experimental	
CoAl	3.0	2.87	green
NiAl	3.0	2.98	beige

PXRD patterns of the as-synthesised precursors (Fig. 1a) exhibit common features with reflections located at the angles typical of a hydrotalcite-like phase that contains carbonate anions in the interlayer space (ICDD-PDF file 00-014-0191): sharp and symmetrical for (003), (006), (110), and (113), and broad and asymmetrical for (009), (015), and (018), respectively. Applying PXRD data processing, the average crystallite sizes (*L*) from full-width at half-maximum values of the most intensive diffraction line (003) and the lattice parameters of the precursors were estimated (Table 2).
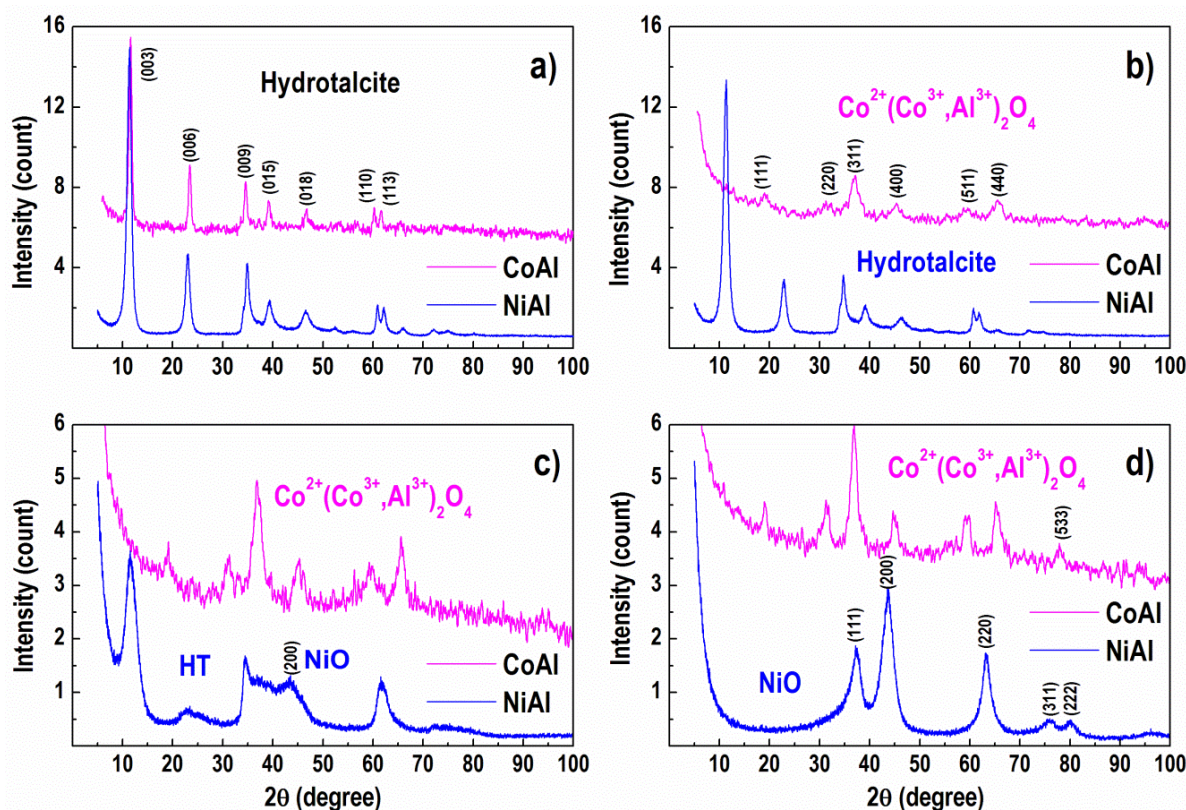
Fig. 1. PXRD patterns of the precursors thermally treated at 80 °C (a), 200 °C (b), 250 °C (c), and 350 °C (d).

Table 2. Lattice parameters, specific surface area, and average particle size of the as-synthesized samples

Sample	a (nm)	c (nm)	V (nm³)	SSA (m²/g)	$L_{(003)}$ (nm)
CoAl	0.3076 ± 0.0019	2.311 ± 0.002	0.189 ± 0.041	60	15.7
NiAl	0.3044 ± 0.0002	2.310 ± 0.001	0.186 ± 0.001	71	11.0
hydrotalcite*	0.3070	2.3230	0.190		

*JCPDS file 01-014-0191

Collected data in Table 2 indicate that the CoAl sample demonstrates larger LDH crystallites than NiAl that are in conformity with narrower diffraction lines and lower specific surface area (SSA) values. The NiAl sample has smaller unit cell a and c parameters than the CoAl one. Differences in the a-parameter can be attributed to a smaller octahedral ionic radius of the Ni^{2+} ions (0.069 nm) compared to Co^{2+} (0.074 nm) [19].

Furthermore, different values of c-parameter can be ascribed to carbonate and water molecule amount in the interlayer space, which is apparently affected by the divalent ion present in the octahedral brucite-like hydroxide layers of the HT structure [11]. Variations of the lattice parameters were in good agreement with octahedral ionic radii of the metal ions present in the layered network. A double effect of Co^{2+} partial oxidation to Co^{3+} ions in the brucite-like layer during synthesis of the CoAl material should also be noticed. On the one hand, the Co^{3+} ions, having a greater ionic radius (0.063 nm) with respect to Al^{3+} (0.050 nm), cause an increase in the a-parameter value by comparison with standard hydrotalcite (Table 2). On the other hand, Co^{3+} higher oxidation state enhances positive charge density of the brucite-like layer to require an excess of carbonate anions for charge compensation and water molecules to prevent interanionic repulsion in the interlayer gallery (c-parameters). As previously reported [20], Co^{3+} ion presence is supported by the beige colour of the CoAl sample (Table 1). It should also be considered that the samples under study were prepared at 80 °C followed by aging in the mother liquor at the same temperature for 60 min. Obviously, the preparation temperature is a precondition to realise partial oxidation. Partial oxidation of Co^{2+} to Co^{3+} ions during preparation of the Co-Al layered materials has also been reported [21].

Carbonate-containing CoAl and NiAl samples were thermally decomposed (Fig. 2) by two transitions routes each of them being realised in two stages accompanied by weight losses, which is in agreement with that reported for stable layered compounds with molar ratio of M^{2+}/M^{3+} = 2–3 [21,22]. During low-temperature transition at 182 °C (CoAl) and 195 °C (NiAl) a reversible dehydration of the interlayer space occurred that is attributed to re-

moval of adsorbed water (<100 °C), and elimination of interlayer structural water (100–200 °C). The second decomposition step is irreversible and takes place at higher temperatures, namely 230 and 336 °C for CoAl and NiAl, respectively, due to simultaneous dehydroxylation (removal of water from the brucite sheet) and decarbonation (CO_2 loss from the interlayer carbonate anion) of the HT framework.
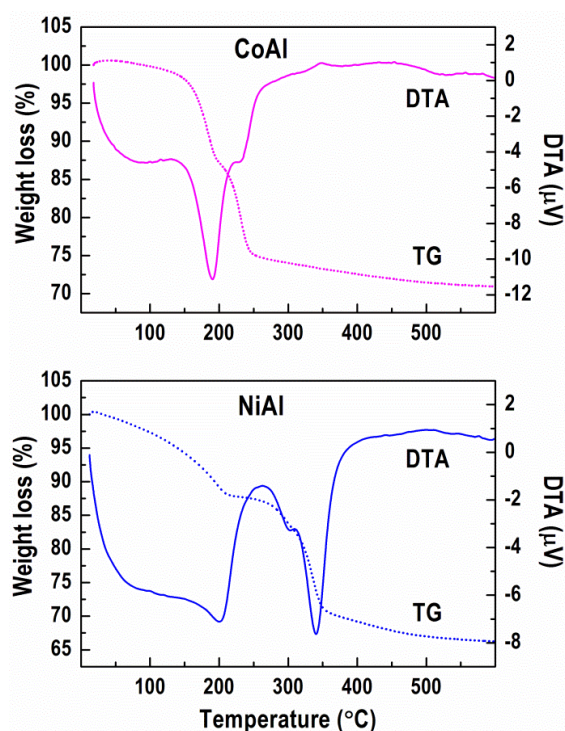
Fig. 2. DTA-TG profiles of the as-synthesised precursors.

Dehydroxylation results in destruction of the HT layer structure accompanied by formation of CoAl and NiAl mixed metal oxides.

In brief, the layered structure collapses at a lower temperature with CoAl (250 °C) than NiAl (350 °C). Thermal analysis data reveal that the total weight loss over the entire temperature range was higher with NiAl (34.0%) than CoAl (29.0%). This finding shows specifically the effect of divalent metal type on the thermal behaviour of the layered solids: the presence of Ni^{2+} ions in the NiAl layered system increases the temperature of sample decomposition in comparison with CoAl. The result indicates a relatively low stability of the CoAl solid and attributes it to oxidation of Co^{2+} ions.

27

In accordance with PXRD data, the characteristic diffraction lines of HT layered structure disappear completely after treatment of the CoAl sample at 200 °C (Fig. 1b) suggesting dehydroxylation of the brucite-type layers and decarbonation of the interlayer space because of destroyed layered structure. New reflections were registered that can be related to a spinel-like Co$_3$O$_4$ phase (ICDD-PDF file 00-043-1003) and/or a spinel-like mixed oxide Co^{2+}(Co^{3+},Al^{3+})$_2$O$_4$, attributable to facile oxidisability of the Co^{2+} ion, and thermodynamic stability of Co$_3$O$_4$ in air [23]. An isomorphous replacement of some of the larger Co^{3+} ions, located at Oh sites of the Co$_3$O$_4$ phase, by the smaller Al^{3+} ions causes the formation of a non-stoichiometric very stable spinel-like mixed oxide Co^{2+}(Co^{3+},Al^{3+})$_2$O$_4$ [24,25]. Both spinel-like phases demonstrate similar reflections and intensities, thus it is not possible to distinguish between them. In contrast, PXRD patterns of NiAl sample calcined at 200 °C (Fig. 1b) display reflections similar to that of the as-synthesised counterpart signifying stability of the layered structure up to 200 °C. A decrease in peak intensity with concomitant shifting of the reflections to higher angles was observed that might be attributed to interlayer water molecule losses [26]. While the thermal treatment of CoAl sample at 250 °C only enhances the crystallinity of spinel-like mixed oxide Co^{2+}(Co^{3+},Al^{3+})$_2$O$_4$, (Fig. 1c), the same temperature induces creation of an intermediate meta-stable dehydrated HT layered phase and appearance of additional broad diffraction lines of cubic NiO phase (ICDD-PDF file 00-047-1049) for NiAl solid. A further increase of the decomposition temperature to 350 °C (Fig. 1d) and especially to 800 °C (Fig. 3a) provokes better resolution of the diffraction peaks of Co^{2+}(Co^{3+},Al^{3+})$_2$O$_4$ phase for CoAl, indicating that Al^{3+} cations are no more statistically distributed as they are located mainly at Oh positions of the mixed oxide spinel-like structure. Characteristics reflections of the HT layered structure disappeared completely after treatment of NiAl solid at 350 °C (Fig. 1d). Rather amorphous calcination products such as NiO phase were formed showing collapse of the layered structure [26,27]. PXRD patterns of NiAl sample calcined at 800 °C (Fig. 3a) exhibited reflections of a single oxide cubic NiO phase. The Al^{3+} ions can be incorporated either in an amorphous nickel aluminate phase, or in a separate amorphous alumina phase [27].

A further increase of the annealing temperature to 1000 °C (Fig. 3b) promoted crystallisation as seen by the sharper diffraction lines of a mixed spinel-like Co^{2+}(Co^{3+},Al^{3+})$_2$O$_4$ oxide phase, while the pattern of the NiAl solid treated at the same

temperature shows the co-existence of two phases: a dominating NiO entity and a NiAl$_2$O$_4$ one.
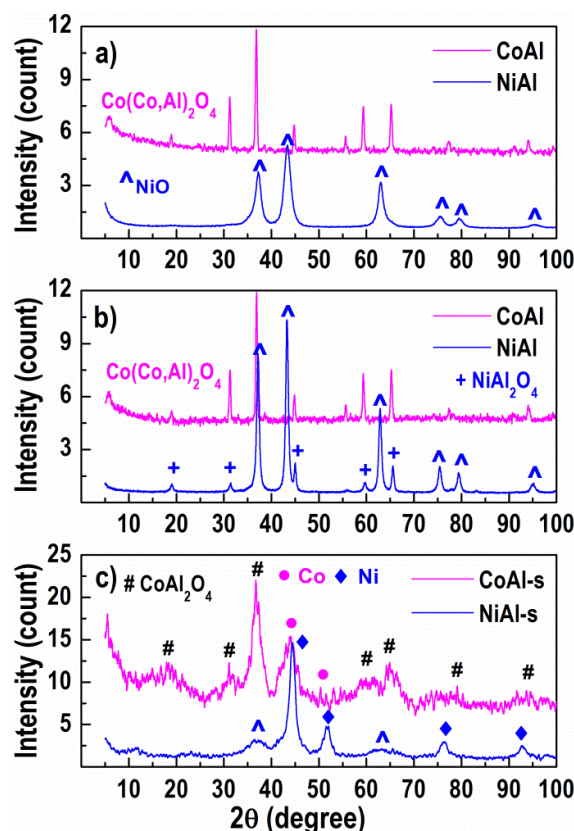
Fig. 3. PXRD of the precursors calcined at 800 °C (a) and 1000 °C (b), and of the spent catalysts preliminary reduced at 600 °C (c).

Briefly, while thermal decomposition of the CoAl precursor gave rise to CoAl$_2$O$_4$ spinel formation, NiO and NiAl$_2$O$_4$ spinel phases were the final products upon destruction of the NiAl sample.

A TPR technique was applied to investigate reducibility of the as-synthesised precursors. Experiments were carried out to elucidate reducible metal–O species present in the samples and to reveal the effect of divalent metals on the reduction of layered materials.

Since the reduction process was carried out dynamically at increasing temperatures by starting from the as-prepared state of the precursor, it is obvious that two parallel processes such as thermal decomposition and reduction of the obtained oxides take place during the TPR experiments. It has been reported that the thermal decomposition of the carbonate containing LDHs occurs in a similar range of temperatures either in air or hydrogen ambience [28].

The TPR profile of CoAl sample (Fig. 4) is characterised by low and high temperature regions between 180 and 400 °C and above 650 °C. Reduction in the former region is typically attributed to

transformation of Co$_3$O$_4$ or spinel-like mixed oxide Co^{2+}(Co^{3+},Al^{3+})$_2$O$_4$ to CoO phase (Co^{3+} → Co^{2+}), followed by reduction of Co^{2+} ions to metal Co^0 state (Co^{2+} → Co^0). Reduction of Co-Al spinels, Co$_2$AlO$_4$ → CoAl$_2$O$_4$, is typical of the latter region [29−31]. Higher temperatures imply a stronger interaction between the Co and Al species, as in the reduction of cobalt aluminate [32,33]. It has been suggested that the Al^{3+} ions polarise the more or less covalent Co−O bonds in the spinel-like mixed oxide thus increasing the effective charge of the Co ions [34] and, consequently, the lattice energy and the reduction temperature are increased as stated in Ref. 29.
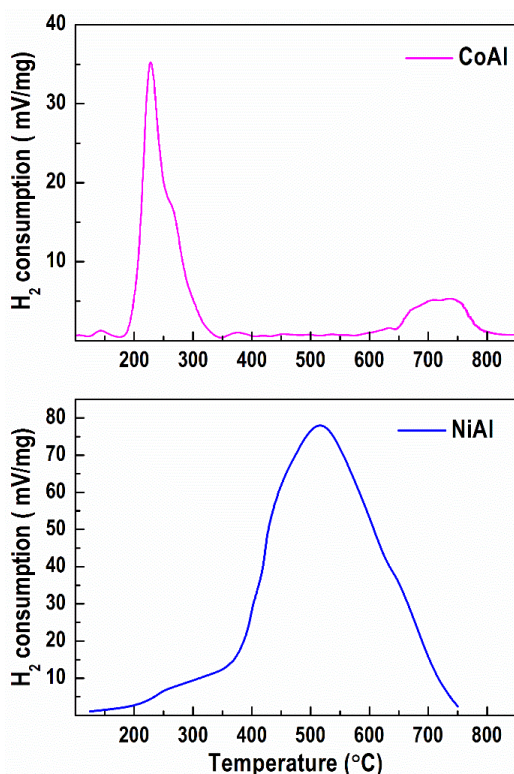
Fig. 4. TPR profiles of the as-synthesizsed precursors.

Contrary to CoAl, a broad asymmetric TPR profile spreading throughout a wide temperature range from 200 to 750 °C was registered with the NiAl sample. Low-temperature shoulders at ≈250, 400, and 430 °C, a well-resolved temperature maximum (T$_{max}$) at ≈520 °C as well as a high-temperature shoulder at ≈630 °C could be distinguished. A common explanation of the TPR results is searched in models proposed for decomposition and reduction of Ni-Al LDH compounds [35,36]. It was suggested that Ni-Al LDH give rise to mixed oxides that contain: (i) a NiO phase, which has a small amount of Al^{3+} ions; (ii) a quasi-amorphous non-stoichiometric Ni-Al spinel-like phase, which hypothetically

is located at the interface between NiO and the alumina-type phase, and (iii) an alumina-type phase doped with small amounts of Ni^{2+} ions, probably 'grafted' on the spinel-like phase. Based on this the low-temperature shoulders and T$_{max}$ can be ascribed to reduction of NiO intimately mixed with a small quantity of Al^{3+} ions (i). The high-temperature shoulder is attributed to reduction of a poorly organised Ni–Al spinel-like phase (ii). A small amount of alumina-type phase doped with Ni^{2+} ions (iii) may also be present.

In general, TPR profiles of the studied solids suggest two types of species, namely readily and hardly reducible entities. It is anticipated that their amounts and ratio may have impact on catalytic performance. In this connection, the layered compounds were reduced at 400, 450, 530, and 600 °C and then the methanation activity was evaluated. The measurements disclosed that both catalysts hydrogenate CO$_2$ successfully to 0−10 ppm at reaction temperatures between 400 and 320 °C and GHSV within 3000–22000 h^{-1} (not shown). Bearing in mind that lower temperatures are thermodynamically favourable for the reaction, the activity of the catalysts is presented for reaction temperatures from 300 to 220 °C (Fig. 5 and 6).

Figures 5a-d show that the NiAl catalyst hydrogenated CO$_2$ to levels below 4 ppm at 300 °C and GHSV up to 22000 h^{-1} irrespective of reduction temperature. In contrast to this, the Co-Al catalyst demonstrated a very low activity after reduction at 400 °C (Fig. 5a). Reduction at 600 °C, however, gave comparable levels of purification with both catalysts (Fig. 5d).

A similar activity was observed at 280 °C after reduction at each selected temperature if the activity was estimated by GHSV at which the concentration of CO$_2$ at reactor outlet is 10 ppm (Fig. 6a). Unlike CoAl, the NiAl catalyst remained active at a higher GHSV (20500 h^{-1}) after reduction at 400 °C, whereas the former showed some activity at a lower GHSV (6.500 h^{-1}). Reduction at 600 °C gave priority to NiAl because of 0-ppm CO$_2$ levels. Gradually the activity of the CoAl catalyst increased reaching a GHSV of 15500 h^{-1} after reduction at 600 °C (Fig. 6a). A reaction temperature as low as 260 °C (Fig. 6b) caused a decrease in overall activity of both catalysts. The NiAl catalyst manifested a higher activity after reduction in the range 400–530 °C, however, at a lower GHSV. Almost equal CO$_2$ hydrogenation levels with both catalysts were achieved upon raising the reduction temperature up to 600 °C.
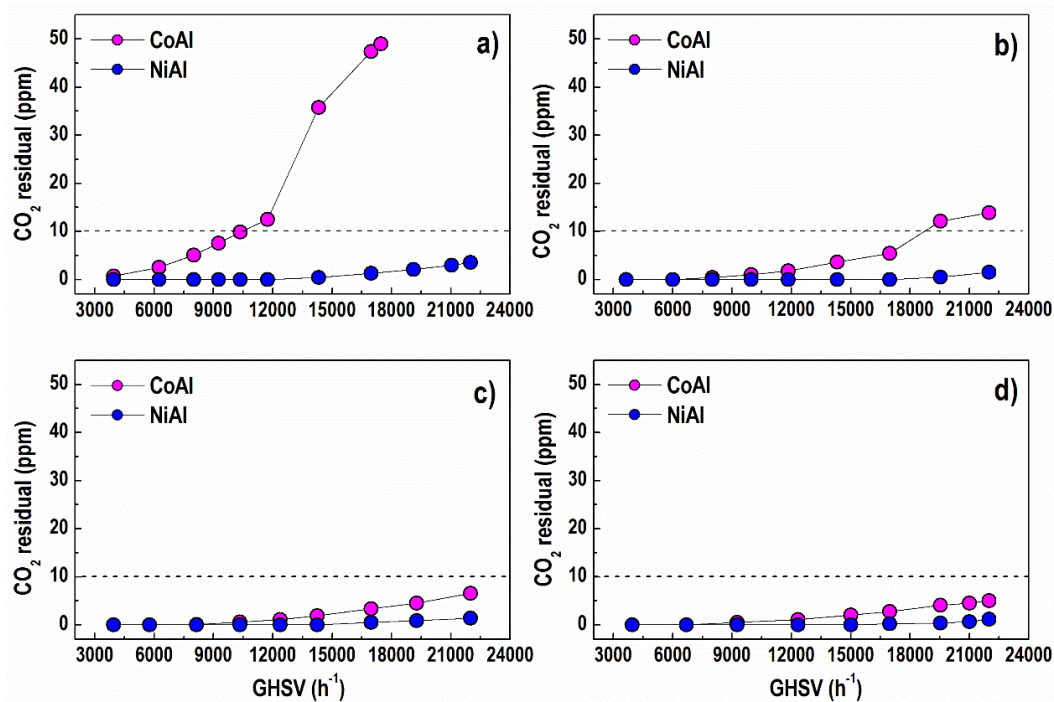
Fig. 5. Methanation activity of the catalysts at 300 °C after reduction: 400 °C (a), 450 °C (b), 530 °C (c), and 600 °C (d).
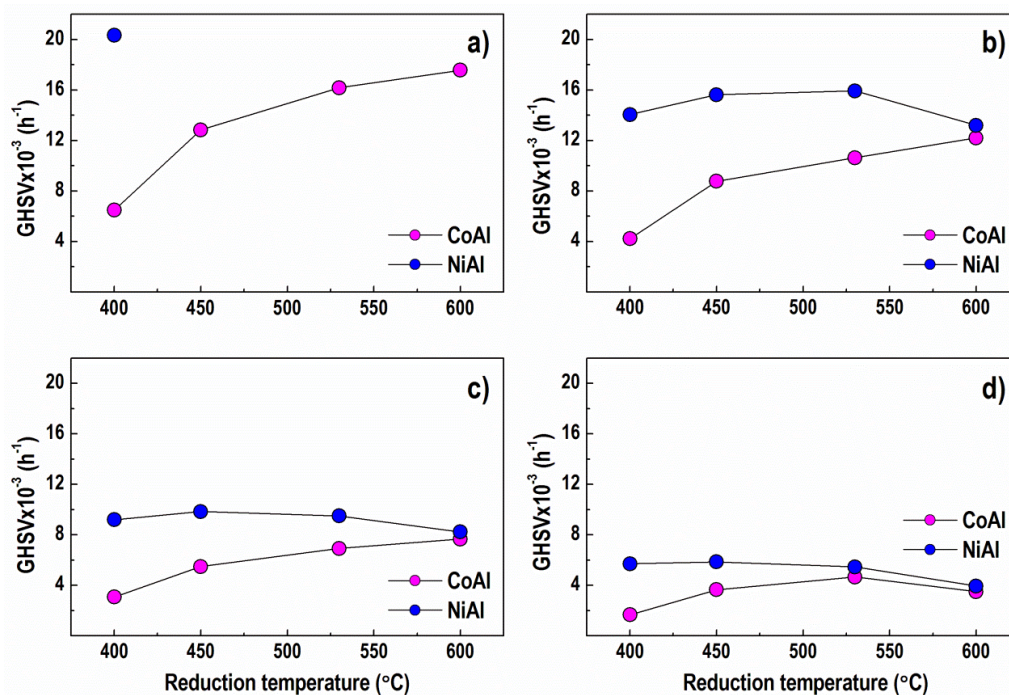

Fig. 6. Catalyst methanation activity at a 10-ppm level of CO_2 at a variable reaction temperature: 280 °C (a), 260 °C (b), 240 °C (c), and 220 °C (d).

Further decrease of the reaction temperature to 240 °C (Fig. 6c) enabled another drop of purification activity at the same degree. Experiments revealed that at the lowest reaction temperature of 220 °C (Fig. 6d) both catalysts exhibited a poor methanation activity independent of reduction temperature. CO_2 purification reached similar levels for both catalysts at higher temperatures of reduction (530 and 600 °C). Obviously, kinetic limitations play a decisive role.

PXRD patterns of the spent CoAl catalyst (CoAl-s) (Fig. 3c) display reflections of low crystallinity mostly of $CoAl_2O_4$ phase and metal Co^0 phase. In contrast to them, PXRD patterns of the

NiAl-s catalyst exhibit diffraction lines characteristic mainly of metallic nickel phase Ni^0 (ICDD-PDF file 00-004-850) as well as low intensity reflections of NiO phase (ICDD-PDF file 00-047-1049).

Differences in the catalytic performance of both catalysts are explained by different divalent metal presence and different redox properties of the metal species. A possible understanding of the methanation activity may be found in the TPR and PXRD data. Reduction of the Ni or Co ions in the precursor samples proceeds at different temperatures. This is attributed to different strength of interaction between Ni/Co and the Al^{3+} moieties. The TPR profile of the NiAl sample displays significantly higher hydrogen consumption than the CoAl solid suggesting a facilitated reduction of Ni^{2+}-O species. The NiAl catalyst showed a higher activity after reduction at lower temperatures (400 and 450 °C), which is ascribed to readily reducible Ni^{2+}-O species. The occurrence of the latter in the solid was expected, because the formation of a hardly reducible $NiAl_2O_4$ spinel-like phase was accomplished at temperatures over 800 °C (PXRD, Fig. 3a,b). This phenomenon determines the existence of non-spinel Ni^{2+} ions that are reduced at lower temperatures to favour a higher activity of the NiAl catalyst in comparison with CoAl at the same reduction temperatures. Further reduction treatment of NiAl at high temperatures (530 and 600 °C) induced aggregation or sintering of the reduced metal Ni^0 thus leading to diminished CO_2 removal. Oppositely, the PXRD and TPR techniques indi-cated that Co^{2+} and Al^{3+} ions form a $CoAl_2O_4$ normal spinel at 350 °C. A lower activity of CoAl catalyst could be discussed as a probability that a small fraction of Co^{2+} ions would be reduced to the metal state. The remainder Co^{2+} ions would be included in stable and hardly reducible cobalt aluminate phases prevailing in thermally treated or reduced samples at temperatures over 300 °C.

On the other hand, it is known that the catalytic activity is directly related to the number of available metal sites on the surface [37,38]. Consequently, a forming Co-Al spinel phase would hamper the reduction of Co^{2+} ions and reduce the number of metal active Co^0 sites that are obtained during reduction-activation. Moreover, SSA data on spent catalysts reveal that NiAl-s possesses an almost twofold higher surface area (94 m²/g) than that of CoAl-s catalyst (50 m²/g). Overall characteristics of the catalysts point out a smaller number of active sites on the surface of the CoAl catalyst in comparison with NiAl, which determine a low methanation activity of the CoAl solid. This assumption was confirmed by the results of the activity tests at each applied reaction temperatures especially after reduction of CoAl at lower temperatures.

Mass-gas analysis

The NiAl catalyst manifested a high level of CO_2 removal, which causes some doubt that this activity includes some partial hydrogenation of CO_2 to CO. For this purpose, the outlet gas mixture after the catalytic tests was collected and analysed. Data indicated that methane was the single reaction product thus confirming that CO_2 hydrogenation was the only reaction that proceeded on the catalysts at great excess of hydrogen.

CONCLUSIONS

Results from the study of Co-Al and Ni-Al layered double hydroxides discovered a strong dependence of structure, phase composition, thermal stability, and reducibility on the nature of divalent metal in the Al-containing samples Divalent metal ions affect the crystallisation degree of the formed layered compounds, their specific surface area, and the thermal decomposition process of the layered structure accompanied by concomitant phase transformation to mixed metal oxides.

Formation of the spinel-type phases proceeded at different temperatures as a function of the type of divalent metal thus defining catalyst properties in the reaction of CO_2 methanation. Co^{2+} ions stabilised in spinel structures hamper their reduction to metal state, leading to deficiency of active Co^0 phase on the surface. This phenomenon determined a low activity of Co/Al_2O_3 catalyst, especially at low reduction temperatures. In contrast, interaction between Ni^{2+} and Al^{3+} ions generated readily reducible Ni^{2+}-O species, which favoured a higher activity of Ni/Al_2O_3 catalyst at the same reduction temperatures. The overall hydrogenation activity of Ni/Al_2O_3 makes the catalyst appropriate for low temperature CO_2 methanation.

REFERENCES

1. C. Song, *Catal. Today*, **115**, 2 (2006).
2. W. Wang and J. Gong, *Front. Chem. Sci. Eng.*, **5**, 2 (2011).
3. W. Wang, Sh. Wang, X. Ma, J. Gong, *Chem. Soc. Rev.*, **40**, 3703 (2011).

4. K. Xavier, R, Sreekala, K. Rashid, K. Yusuff, B. Sen, *Catal. Today*, **49**, 17 (1999).
5. G. Xu, X. Chen, Z.-G. Zhang, *Chem. Eng. J*., **121**, 97 (2006).
6. M. Duyar, A. Ramachandran, C. Wan, *J. CO₂ Util*., **12**, 27 (2015).
7. H. Takano, K. Izumiya, N. Kumagai, K. Hashimoto, *Appl. Surf. Sci.*, **257**, 8171 (2011).
8. G. Garbarino, P. Riani, L. Magistri, G. Busca, *Int. J. Hydrogen Energy*, **39**, 11557 (2014).
9. P. Frontera, A. Macario, M. Ferraro, P-L. Antonucci, *Catalysts*, **7**, 59 (2017).
10. R. Allmann, *Chimia*, **24**, 99(1970).
11. F. Cavani, F. Trifirò, A. Vaccari, *Catal. Today*, **11**, 173 (1991).
12. A. Vaccari, *Catal. Today*, **41**, 53(1998).
13. A. Vaccari, Appl. Clay Sci., **14**, 161 (1999).
14. M. Gabrovska, R. Edreva-Kardjieva, D. Crişan, P. Tzvetkov, M. Shopska, I. Shtereva, *React. Kinet. Mech. Cat.*, **105**, 79 (2012).
15. M. V. Gabrovska, R. M. Edreva-Kardjieva, D. D. Crişan, K. K. Tenchev, D. A. Nikolova, M. Crişan, *Bulg. Chem. Commun.,* **45**, 617 (2013).
16. J. Janlamool, P. Praserthdam, B. Jongsomjit, *J. Nat. Gas Chem.*, **20**, 558 (2011).
17. G. Zhou, T. Wu, H. Xie, X. Zheng, *Int. J. Hydrogen Energy*, **38**, 10012 (2013).
18. D. Monti, A. Baiker, J. *Catal*., **83**, 323 (1983).
19. R. Shannon, *Acta Crystallogr*. A, **32**, 751 (1976).
20. M. Gabrovska, R. Edreva-Kardjieva, K. Tenchev, P. Tzvetkov, A. Spojakina, L. Petrov, *Appl. Catal. A: Gen.,* **399**, 242 (2011).
21. M. Ulibarri, J. Fernández, F. Labajos, V. Rives, *Chem. Mater*., **3**, 626 (1991).
22. S. Kannan, S. Velu, V. Ramkumar, C. Swamy, *J. Mater. Sci*., **30**, 1462 (1995).
23. T. Sato, U. Fujita, T. Endo, M. Shimada, A. Tsunashima, *Reactivity of Solids*, **5**, 219 (1988).
24. S. Kannan, C. Swamy, *Catal. Today*, 53**,** 725 (1999).
25. J. Pérez-Ramírez, G. Mul, F. Kapteijn, J. Moulijn, *J. Mater. Chem*., **11**, 821 (2001).
26. S. Kannan, A. Narayanan, C. Swamy, *J. Mater. Sci*., **31**, 2353 (1996).
27. J. Pérez-Ramírez, G. Mul, J. Moulijn, *Vib. Spectrosc*., **27**, 75 (2001).
28. O. Lebedeva, D. Tichit, B. Coq, *Appl Catal. A: Gen*., **183**, 61 (1999).
29. P. Arnoldy, J. Moulijn, *J. Catal*., **93**, 38 (1985);
30. S. Velu, K. Suzuki, T. Osaki, *Catal. Lett.*, **69**, 43 (2000).
31. A. Alvarez, S. Ivanova, M. Centeno, J. Odriozola, *Appl. Catal. A: Gen*., **431–432**, 9 (2012).
32. S. Rane, O. Borg, J. Yang, E. Rytter, A. Holmen, *Appl. Catal. A: Gen*., **388**, 160 (2010).
33. M. de Beer, A. Kunene, D. Nabaho, M. Claeys, E. van Steen, *J. South. Afr. Inst. Min. Metall*., **114**, 157 (2014).
34. H. Kung, *J. Catal*., **73**, 387 (1982).
35. O. Clause, B. Rebours, E. Merlen, F. Trifiro, A. Vaccari, *J. Catal*., **133**, 231 (1992).
36. F. Trifiro, A. Vaccari, O. Clause, *Catal. Today*, **21**, 185 (1994).
37. J. Lahtinen, T. Anraku, G. Somorjai, *Catal. Lett*., **25**, 241 (1994).
38. G. Fröhlich, U. Kestel, J. Lojewska, T. Lojewski, G. Meyer, M. Voß, D. Borgmann, R. Dziembaj, G. Wedler, *Appl. Catal. A: Gen.*, **134**, 1 (1996).

СТРУКТУРА И АКТИВНОСТ НА M-Al СЛОЕСТИ ДВОЙНИ ХИДРООКИСИ В РЕАКЦИЯТА НА МЕТАНИРАНЕ НА CO$_2$ КАТО ФУНКЦИЯ НА ДВУВАЛЕНТНИЯ МЕТАЛ

М. В. Габровска[1]*, Д. Кришан[2], Д. А. Николова[1], И. Ж. Щерева[1], Л. П. Билярска[1], М. Кришан[2],
Р. М. Едрева-Кърджиева[1]

[1] *Институт по катализ, Българска академия на науките, ул. Акад. Г. Бончев, бл. 11, 1113 София, България*
[2] *Институт по физикохимия „Илие Мъргулеску", Румънска академия, 202 бул. „Индепенденцей",
060021 Букурещ-12, Румъния*

(Резюме)

Изследван е ефектът на вида на двувалентния метал (Ni или Co) върху структурата, фазовия състав, термичната стабилност и редуцируемостта на съутаени Al-съдържащи слоести двойни хидроксиди (СДХ) като прекурсори на катализатори за фино очистване от CO$_2$ чрез реакцията на метаниране. Направена е оценка на каталитичната активност чрез промяна на температурата на редукция, реакционната температура и обемната скорост. Разкрито е, че природата на двувалентния метал в Al-съдържащите СДХ влияе върху кристалността на образуваните СДХ, специфичната им повърхност и температурата на разлагане на слоеста структура до съответните смесени метални оксиди. Установено е, че стабилизирането на Co^{2+} йоните в шпинелната CoAl$_2$O$_4$ структура възпрепятства редукцията им до метално състояние, което води до недостатъчно количество от активна метална Co^0 фаза на повърхността. Този факт определя ниската метанираща активност на Co/Al$_2$O$_3$ катализатор, особено при по-ниски температури на редукция. В контраст на това, взаимодействието между Ni^{2+} и Al^{3+} йоните предизвиква формиране на лесно редуцируеми Ni^{2+}–O структури, което благоприятства по-висока активност на Ni/Al$_2$O$_3$ катализатор при същите температури на редукция. Образуването на шпинело-подобни фази е функция на вида на двувалентния метал и е определящо за активността на катализаторите при фино очистване от CO$_2$ на богати на водород газови смеси чрез реакцията на метаниране.

Catalytic behaviour of nanostructured Ce-Mn oxide catalysts in ethyl acetate oxidation

R. N. Ivanova*, G. S. Issa, M. D. Dimitrov, T. S. Tsoncheva

Institute of Organic Chemistry with Centre of Phytochemistry, Bulgarian Academy of Sciences, 1113 Sofia, Bulgaria,

Ce-Mn mixed oxide catalysts were prepared by co-precipitation method and used as catalysts for complete oxidation of ethyl acetate. The influence of Ce/Mn ratio was in the focus of the discussion in close relation with their catalytic activity. The obtained materials were characterised by different techniques, such as nitrogen physisorption, XRD, UV-Vis, and temperature-programmed reduction with hydrogen. A higher specific surface area favouring a higher catalytic activity as compared with pure CeO_2 and MnOx was established for all binary oxides. A strong effect of sample composition on dispersion and redox behaviour of the binary oxides was also found.

Key words: catalytic combustion, ethyl acetate, manganese oxide, ceria.

INTRODUCTION

Volatile organic compounds (VOCs) are one type of toxic pollutants to environment that are produced in variety of small and medium size industries. Among VOCs, ethyl acetate is a commonly used solvent, which can cause several environmental hazards. It can be completely oxidized to CO_2 by Pd, Pt supported catalyst at about 220–320 °C [1]. Some other papers [2–4] also reported attempts to eliminate low concentration of the ethyl acetate existing in gas steams. Recently, transition metal/metal oxides have been extensively studied for VOCs elimination as an alternative of the expensive noble based catalysts [5], but here the problem with the formation of products of partial oxidation, which are often very harmful for the human health, still exists. Among them, CeO_2-Mn_xO_y mixed oxides have been developed as environmentally friendly catalysts for the abatement of contaminants in both liquid and gas phases, such as oxidation of ammonia [6], pyridine [7], phenol [8], and acrylic acid [9]. Incorporation of manganese ions into ceria lattice greatly improved the oxygen storage capacity of cerium oxide as well as the oxygen mobility on the surface of the mixed oxides [10].

The present study deals with the effect of Ce/Mn ratio in CeO_2-Mn_xO_y mixed oxides on the catalytic behaviour of the latter in total oxidation of ethyl acetate. For this purpose, the catalysts were characterised by nitrogen physisorption, XRD, UV-Vis, and temperature-programmed reduction with hydrogen. A complicated relationship among sample structure, texture, redox properties, and catalytic activity was discussed.

EXPERIMENTAL

Materials

Manganese-cerium mono- and bi-component oxides of different composition were prepared by co-precipitation method. 1M NH_3 was added to an aqueous solution containing known amounts of $Mn(NO_3)_2 \cdot 4H_2O$ and/or $Ce(NO_3)_2 \cdot 6H_2O$ at room temperature until the pH of the solution was about pH=9.02. After 1 hour, the resulting precipitate was filtered, washed with distilled water, and dried at 373 K for 24 h. Metal oxide samples were obtained after calcination in air at 773 K for 5 h. The obtained catalysts were denoted as xCeyMn where x/y represents the Ce/Mn mol ratio.

Methods of characterisation

Powder X-ray diffraction patterns were collected on a Bruker D8 Advance diffractometer equipped with Cu Kα radiation and LynxEye detector. Nitrogen sorption measurements were recorded on a Quantachrome NOVA 1200e instrument at 77 K. Before physisorption measurements, the samples were outgassed overnight at 423 K under vacuum. UV-Vis spectra were recorded on a Jasco V-650 UV-Vis spectrophotometer equipped with a diffuse reflectance unit. TPR/TG (temperature-programmed reduction/thermogravimetric) analyses were performed on a Setaram TG92 instrument. Typically, 40 mg of the sample were placed in a microbalance crucible and heated in a flow of 50 vol.% H_2 in Ar

($100 \, cm^3 min^{-1}$) up to 773 K at 5 $Kmin^{-1}$ and a final hold-up of 1-h tests. The catalytic oxidation of ethyl acetate was carried out in a flow type reactor (0.030 g of catalyst) with a mixture of ethyl acetate and air (1.21 mol%) at WHSV of 100 h^{-1}. Before the catalytic experiments the samples were treated in argon at 373 K for 1 h. Experimental data were acquired under temperature-programmed regime in the range of 473–773 K. Gas chromatographic analyses were made on a HP 5890 apparatus using carbon-based calibration. Products distribution was calculated as CO_2 (S_{CO2}), acetaldehyde (S_{AA}), ethanol (S_{Et}), and acetic acid (S_{AcAc}) selectivity by the equation: $S_i = Y_i/X*100$, where S_i and Y_i were selectivity and yield of (i) product, respectively, and X was conversion. For a precise comparison, the conversion was normalised to unit surface area (SA = X/A, where X was the conversion at 650 K and A was the specific surface area of the sample).

RESULTS AND DISCUSSION

Nitrogen physisorption measurements were conducted in order to elucidate sample textural properties (Fig. 1, Table 1). All isotherms were of type IV according to IUPAC classification that is typical of mesoporous materials. They were characterised by well-pronounced step at about 0.6–0.8 relative pressure due to capillary condensation of nitrogen into the pores. The shape of the hysteresis loop indicated presence of uniform cage-like pores for 2Ce1Mn with average pore diameter about 5 nm.

Slit-like pores of very wide size distribution was detected for all other metal oxide materials. The obtained binary oxides possessed a higher specific surface area as compared to the individual oxides and it increased almost linearly upon decrease of the manganese content in the samples. This could indicate formation of homogeneous metal oxide phase and further information about this was provided by XRD measurements of the samples (Fig. 2). The XRD pattern of pure manganese oxide contained intensive diffraction reflections at $2\theta = 23.1°$, $33.1°$, $38.2°$, $55.2°$, and $65.9°$ due to well crystallised Mn_2O_3 phase (JCDS 41–1442) with relatively large crystallites. The latter provoked low surface area and pore volume for this material (Table 1). Additional weak reflections indicated presence of other crystalline phases, probably MnO_2, Mn_3O_4, which is in accordance with literature data [11,12]. Characteristic reflections at $2\theta = 28.5°$, $33.1°$, $47.5°$, and $56.4°$ in the XRD pattern of pure ceria matched crystal planes of (111), (200), (220), and (311) in cubic fluorite structure of CeO_2 (JCPDS 43-1002). Similar but broader reflections were also observed in the patterns of all bi-component samples. Here, no reflections of any manganese oxide phase could be detected. Thus, formation of ceria-manganese mixed oxide phase could be assumed [13]. Obviously, the incorporation of manganese in ceria rendered difficult the agglomeration of individual metal oxide phases, which provided an increase in dispersion (Fig. 2) and BET surface area (Table 1) of the composites.
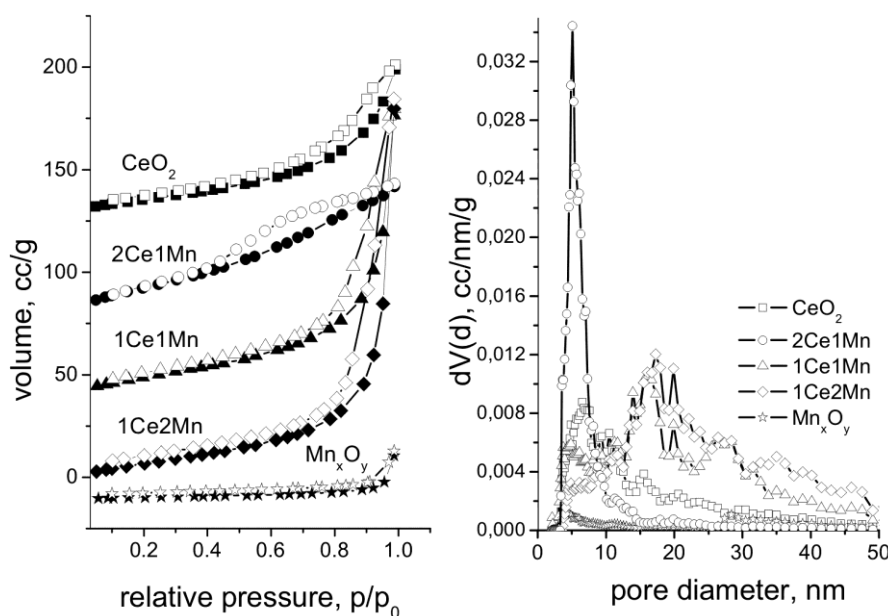
Fig. 1. Nitrogen physisorption isotherms (left) and pore size distribution (right) for pure and mixed metal oxide samples.
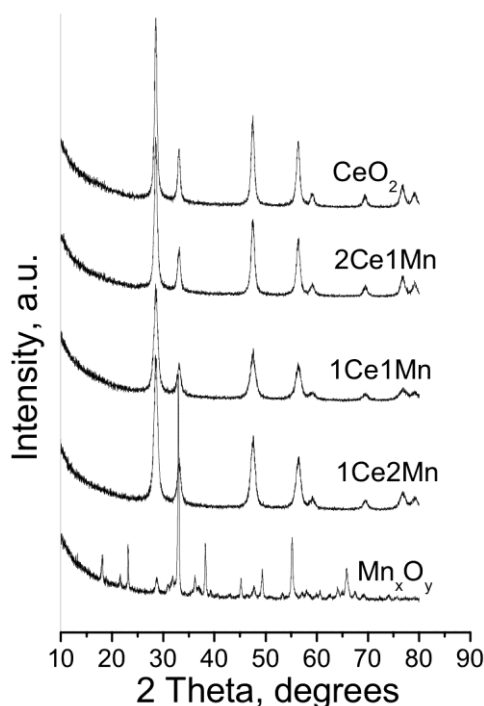
Fig. 2. XRD patterns of the studied samples.

Table 1. Texture parameters of the obtained oxides determined by low temperature nitrogen physisorption (specific surface area S_{BET}; total pore volume Vt, and specific activity SA)

Sample	S_{BET}, m^2g^{-1}	V_t, cm^3g^{-1}	Conversion, 610 K	SA, 610 K
CeO_2	47.5	0.12	60	1.26
2Ce1Mn	82.2	0.10	81	0.98
1Ce1Mn	66.9	0.21	90	1.35
1Ce2Mn	57.6	0.26	84	1.46
Mn_xO_y	7.4	0.025	88	11.89

UV-Vis spectra were recorded to characterise precisely the oxidation state of metal oxide species (Fig. 3). The spectrum of manganese oxide represented a continuous absorption feature, which is due to variations in manganese oxidation state (Mn^{2+}, Mn^{3+}, and Mn^{4+}). The absorption band at about 250 nm was attributed to a charge transfer between O^{2-} and Mn^{2+}. Absorption at approximately 300 nm was related to Mn^{4+} and the continuous absorption above 300 nm is assigned to $O^{2-} \rightarrow Mn^{3+}$ charge transfer and d-d transition for d4 electronic configuration in octahedral field [14]. Simultaneous presence of MnO_2 and Mn_2O_3 after precursor decom-position in air at a temperature above 623 K was also reported by Milella *et al.* [15]. The spectrum of pure ceria represented two maxima at about 250 and 305 nm that could be attributed to $Ce^{4+} \leftarrow O^{2-}$ charge transfer (CT) and interband transitions, respectively [16]. The latter peak was also assigned to lattice defects. The former band was broad and it may be superposed together with the band of $Ce^{3+} \leftarrow O^{2-}$ charge

transfer transition. The observed features in the spectra of bi-component materials could not be simply assigned to superposition of the spectra of single oxides. These results confirmed changes in the environment and/or oxidation state of metal ions probably due to formation of solid solution.
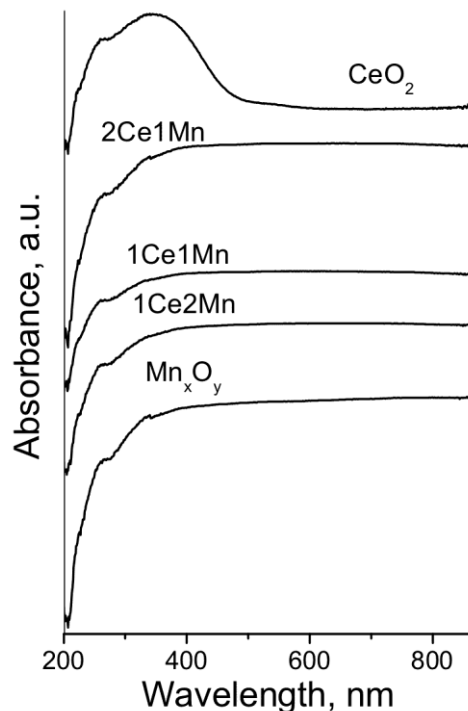
Fig. 3. UV-Vis spectra of the studied samples.

Further information for about the redox properties of the studied materials was obtained by temperature-programmed reduction (TPR) with hydrogen (Fig. 4). The reduction effects over 570 K for pure CeO_2 were generally assigned to surface Ce^{4+} to Ce^{3+} transition [17]. The reduction degree was about 4% (Table 2).

The DTG-TPR profiles of Mn_xO_y sample (Fig. 4, right) consisted of two reduction effects for low and high temperature regions. They are generally assigned to step-wise reduction of MnO_2 (or Mn_2O_3) to Mn_3O_4 and further reduction of Mn_3O_4 to MnO, respectively [18, 19]. A decrease in the overall reduction degree upon ceria increase in the binary materials (Table 2) indicated stabilised Mn-O bonds near Ce^{4+} ions. However, here the reduction transformations were broader and shifted to lower initial temperatures. This observation, combined with an increase in the ratio of the low temperature to high temperature reduction effects could be an indication for the increased Mn^{4+} content at the expense of manganese ions of lower oxidation state in the samples. In accordance with the XRD and UV-Vis data, this could be provoked by stabilisation of Mn^{4+} ions *via* incorporation in the ceria lattice. Changes

in the reduction degree (Table 2) showed that the portion of Mn^{4+} ions shared with Ce^{4+} could be controlled by the Ce/Mn ratio and it seemed to be the highest for 1Ce2Mn (Table 2).

Fig. 5 gives temperature dependencies of catalytic activity in ethyl acetate (EA) oxidation for all studied samples. CO_2, ethanol (Et), acetaldehyde (AA), and acetic acid (AcAc) in different proportion with temperature rise were registered. For all samples, ethyl acetate oxidation was initiated over 500 K and an 80–100% conversion was achieved

above 650 K combined with high CO_2 selectivity. Between the pure oxides, manganese oxide exhibited a higher catalytic activity. According to their catalytic activity, the bi-component mixed oxide materials are arranged in the following order: 1Ce1Mn > 2Ce1Mn ≈ 1Ce2Mn. All of them provided a higher catalytic activity than the mono-component samples, which could be due to the existence of a synergistic effect between the ceria and manganese oxide species and/or owing to higher dispersion and specific surface area.
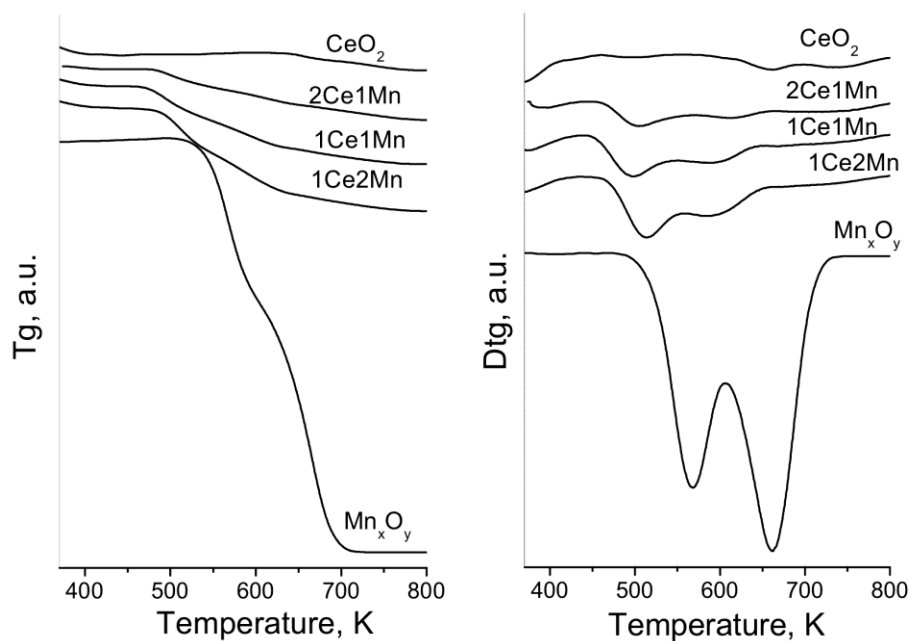
Fig. 4. TG (left) and DTG (right) data on the samples.

Table 2. TPR data for all samples (T_{ini}-initial reduction temperature, T_{max} - maximum of the reduction peak $Mn^{3+} \rightarrow Mn^{2+}$; $Mn^{4+} \rightarrow Mn^{2+}$)

Sample	T_{ini}, K	T_{max}, K	Weight loss, theoretical, mg	Weight loss, experimental, mg	Reduction degree, %
Mn_xO_y	482	565, 662	4.05 (Mn_2O_3)	4.73	116
			2.79 (Mn_3O_4)		169
			9.01 (MnO_2)		52
			(to Mn^{2+})		
1Ce2Mn	458	515, 596	0.94 (Mn_2O_3)	1.12	119
			0.68 (Mn_3O_4)		164
			1.62 (MnO_2)		69
1Ce1Mn	445	497, 592	0.91 (Mn_2O_3)	0.86	95
			0.8 (Mn_3O_4)		107
			2.08 (MnO_2)		41
2Ce1Mn	460	503, 620	0.90 (Mn_2O_3)	0.58	64
			0.46 (Mn_3O_4)		126
			1.58 (MnO_2)		37
CeO_2	577	660, 738	3.72 (Ce^{4+} to Ce^{3+})	0.14	4
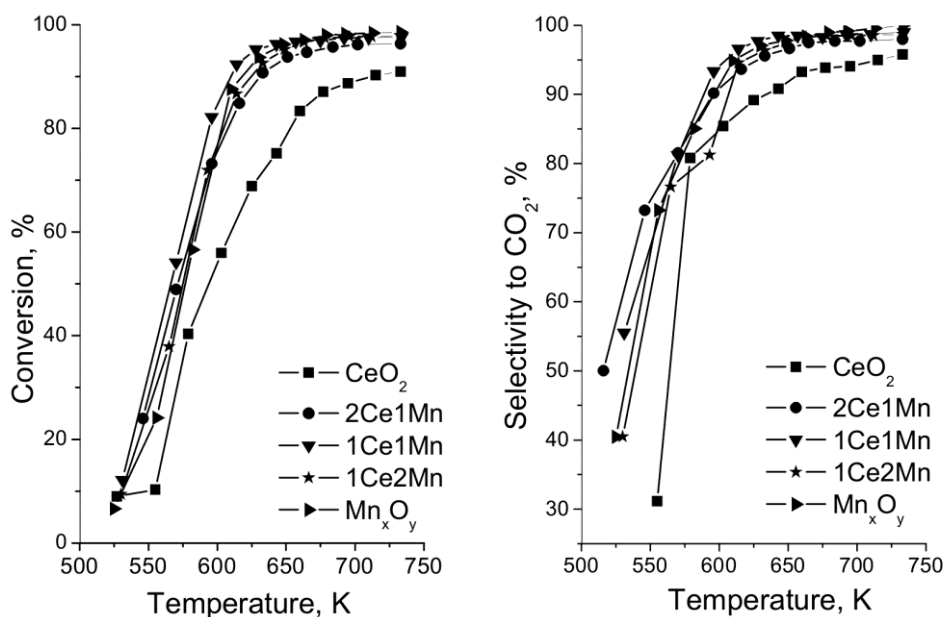
Fig. 5. Temperature dependence of ethyl acetate total oxidation (left) and selectivity to CO_2 (right) for the studied samples.

Over 80% selectivity to CO_2 for all samples was detected (Table 3). A slight tendency to form by-products (acetaldehyde and ethanol) with the the binary oxides was observed. Specific catalytic activity (SA) per unit BET surface area was calculated as a measure of conversion to elucidate the impact of textural parameters on sample catalytic behaviour (Table 1). Note an extremely high SA value for pure Mn_xO_y, which clearly indicates the decisive role of the oxidation state of the manganese ions in the samples. The SA values for all binary materials were much lower than expected if the samples were simple mechanical mixtures of individual oxides.

Table 3. Results from the catalytic tests: selectivity to acetaldehyde (S_{AA}), ethanol (S_{Et}), acetic acid (S_{AcAc}), and CO_2 (S_{CO2}) at 50% conversion of ethyl acetate.

Sample	Conversion, %	S_{AA} %	S_{Et} %	S_{AcAc} %	S_{CO2} %
Mn_xO_y	50	12	2		86
1Ce2Mn	50	13	5	1	81
1Ce1Mn	50	17	1		82
2Ce1Mn	50	11	6	1	82
CeO_2	50	7	6	1	86

Thus, the enhanced catalytic activity of the binary materials could mainly be related to both increased dispersion and specific surface area. In accordance with the TPR data, the decrease in SA for the binary materials could be due to stabilisation of the lattice oxygen ions *via* formation of shared Mn-O-Ce bonds, which renders difficult the EA oxidation *via* Mars-van-Krevelen mechanism [20].

The TPR data also revealed that the increase in SA with the increase of Mn content in the binary oxides could be due to stabilised Mn^{4+} ions *via* their incorporation in the ceria lattice.

CONCLUSIONS

Binary manganese-cerium oxides exhibited higher dispersion and higher specific surface area, but suppressed reduction ability as compared to the individual oxides. Catalytic activity and selectivity in ethyl acetate combustion could be regulated by variation of the Ce/Mn ratio in the samples. Formation of shared Ce-O-Mn bonds and an increase of the Mn content facilitated the formation of more active Mn^{4+}-Mn^{3+} pairs in ethyl acetate oxidation.

REFERENCES

1. Y. Yang, X. Xu, K. Suna, *J. Hazard. Mater. B,* **139**, 140 (2007).
2. P. Papaefthimiou, T. Ioannides, X. Verykios, *Appl. Thermal Eng.*, **18**, 1005 (1998).
3. P. Papaefthimiou, T. Ioannides, X. Verykios, *Appl. Catal. B.,* **15**, 75 (1998).
4. X. Wang, M. Landau, H. Rotter, *J. Catal.* **222**, 565 (2004).
5. P. Lin, M. Skoglundh, L. Lowendahl, *Appl. Catal. B,* **6**, 237 (1995).
6. Z. Ding, L. Wade, E. Gloyna, *Ind. Eng. Chem. Res.*, **37**, 1707 (1998).

7. S. Aki, M. Abraham, *Ind. Eng. Chem. Res.,* **38**, 358 (1999).
8. H. Chen, A. Sayari, A. Adnot, F. Larachi, *Appl. Catal. B*, **32**, 195 (2001).
9. A. Silva, R. Marques, R. Quinta-Ferreira, *Appl. Catal. B,* **47**, 269 (2004).
10. X.Tang, Y. Li, X. Huang, Y. Xu, H. Zhu, J. Wang, W. Shen, *Appl. Catal. B*, **62**, 265 (2006).
11. S. Todorova, A. Naydenov, H. Kolev, K. Tenchev, G. Ivanov, G. Kadinov, *J. Mater. Sci.*, **46**, 7152 (2011).
12. S. Kanungo, *J. Catal.,* **58**, 419 (1979).
13. M. Machida, M. Uto, D. Kurogi, T. Kijima, *Chem. Mater.*, **12**, 3158 (2000).
14. Y. Lin, S. Ming, Y. Jian, Y. Qian, H. Zhifeng, L.

Chaosheng, *Chin. J. Catal.,* **29**, 1127 (2008).
15. F. Milella, J. Gallardo-Amores, M. Baldic, G. Busca, *J. Mater. Chem.,* **8**, 2525 (1998).
16. A. Kambolis, H. Matralis, A. Trovarelli, C. Papadopoulou, *Appl. Catal. A,* **377,** 16 (2010).
17. L. Shi, W. Chu, F. Qu, J. Hu, M. Li, *J. Rare Earths,* **26**, 836 (2008).
18. Y. Du, Q. Meng, J. Wanga, J. Yan, H. Fan, Y. Liu, H. Dai, *Micropor. Mesopor. Mater.* **162**, 199 (2012).
19. D. Delimaris, T. Ioannides, *Appl. Catal. B*, **84**, 303 (2008).
20. P. Larsson, A. Andersson, *Appl. Catal. B,* **24**, 175 (2000).

КАТАЛИТИЧНИ СВОЙСТВА НА НАНОСТРУКТУРИРАНИ Ce-Mn ОКСИДНИ КАТАЛИЗАТОРИ ЗА ОКИСЛЕНИЕ НА ЕТИЛАЦЕТАТ

Р. Н. Иванова*, Г. С. Исса, М. Д. Димитров, Т. С. Цончева

Институт по органична химия с Център по фитохимия, БАН, 1113 София, България

(Резюме)

За настоящото изследване бяха получени Ce-Mn смесени оксидни катализатори за изгаряне на етилацетат чрез метод на съутаяване. Специално внимание бе обърнато на влиянието на съотношението на Ce/Mn, което е в тясна връзка с каталитичната им активност. Получените материали бяха характеризирани с помощта на различни методи, сред които азотна физисорбция, прахова рентгенова дифракция, УВ-видима спектроскопия и температурно-програмирана редукция с водород. Резултатите от физикохимичните изследвания показаха, че бинарните материали притежават по-висока специфична повърхност, което благоприятства по-високата каталитична активност в сравнение с еднокомпонентните оксиди. Беше установен значителен ефект на състава на образците върху тяхната дисперсност и редокси свойства.

Biogenic iron-containing materials synthesised in modified Lieske medium: composition, porous structure, and catalytic activity in *n*-hexane oxidation

M. Shopska*, G. Kadinov, D. Paneva, I. Yordanova, D. Kovacheva[1], A. Naydenov[1], S. Todorova, Z. Cherkezova-Zheleva, I. Mitov

Institute of Catalysis, Bulgarian Academy of Sciences, Acad. G. Bonchev St., Bldg. 11, 1113 Sofia, Bulgaria
[1] *Institute of General and Inorganic Chemistry, Bulgarian Academy of Sciences, Acad. G. Bonchev St., Bldg. 11, 1113 Sofia, Bulgaria*

Leptothrix genus bacteria were cultivated in Lieske medium modified by the presence of inorganic material. Two modifiers were used: a fibrous 0.3% Pd/mesoporous silica-alumina catalyst and a one-side anodic oxidised aluminium foil. Obtained biomasses (named LieskeV and LieskeA, respectively) were studied by the methods of infrared and Mössbauer spectroscopy, X-ray diffraction, nitrogen adsorption, and chemical analysis. Examination of fresh samples revealed that LieskeA contained γ-FeOOH, α-FeOOH, and Fe_3O_4, whereas LieskeV comprised γ-FeOOH, α-FeOOH, and γ-Fe_2O_3 of various ratios. Elemental analysis indicated 0.003% Pd and proved that some amount of the modifier is incorporated in the LieskeV material. Registered transformations in original (biogenic or chemical) iron oxide/hydroxide phases after catalytic activity tests confirmed that LieskeV samples contained a larger amount of γ-Fe_2O_3 obtained from biogenic precursor, and some γ-FeOOH. LieskeV biomass was found to be more active in the reaction of *n*-hexane oxidation. This material also impeded incomplete oxidation to carbon monoxide. Despite very small amounts of palladium present in LieskeV samples, the latter process is probably assisted since palladium is an active catalyst for CO oxidation. Carbon monoxide oxidation in the case of LieskeV samples was stimulated by two components, which exhibit a certain activity in the studied process. Biogenic γ-Fe_2O_3 showed some intrinsic activity in CO oxidation and its dominance is a second reason for control of the incomplete hexane oxidation. A third feature of the Pd-modified samples, determining their relatively higher activity, is the presence of slightly larger pores that allow enhanced mass transfer of the reagents inside the catalytic particles.

Key words: *Leptothrix* sp., biogenic iron-containing material, hexane oxidation.

INTRODUCTION

Volatile organic compounds (VOCs) as low molecular weight hydrocarbons and oxygen containing compounds are main air pollutants. They are precursors of ozone formation in the air ground layer and have influence on processes of greenhouse gas oxidation and formation in troposphere. Volatile organic compounds together with fine dust particles cause photochemical smog formation. The smog has a harmful effect on the human health and plants. Hexane is a representative of the volatile hydrocarbons group and is widely used in a number of chemical productions as solvent or reagent, e.g. glue production, leather treatment, and pharmaceutical industry. It participates in radical reactions in the air and the formed products become involved in a photochemical smog. Hexane is included in Directive 2008/50/EC list about air quality as a compound referred to be strictly monitored and measured because it is a precursor for ozone formation [1].

One way to decrease and/or eliminate hexane emissions is their catalytic oxidation to carbon dioxide and water. The catalysts applied in this process should exhibit high activity in a wide range of reaction temperature even in the presence of various contaminants, stable performance over a large variety space velocities and substance concentrations, resistance to deactivation, and ability for regeneration [2]. There are three groups of oxidation catalysts: i) supported noble metals; ii) metal oxides and supported metal oxides; iii) mixtures of noble metal and metal oxide. The most explored catalysts for complete oxidation contain mono- and bimetallic Pt, Pd, and Rh [3,4]. They satisfy to high extent above-mentioned requirements, however, high cost and easy particle agglomeration encourage search for other active materials. Single and mixed metal oxides of Cu, Mn, Cr, Fe, and Ni can be applied as catalytic materials to this process [5,6]. Transition metal oxide catalysts are moderately resistant to sulphur poisoning and are less active at low temperatures than noble metals but a combination of several oxides could result in highly thermally stable catalysts of satisfactory activity. Transition

---

* To whom all correspondence should be sent
E-mail: shopska@ic.bas.bg

metal oxides of Mn, Fe, and Co are most active in the oxidation of volatile organic compounds [7]. Single metal oxides, amongst them Fe_xO_y, have also been used for this purpose [8]. It has been found that nanosized iron oxides show high activity in CO, CH_4, C_3H_8, and C_3H_6 oxidation, selective oxidation of alcohols and olefins, and ethylbenzene dehydrogenation [9]. They are also active in soot removal. However, published investigations on hexane oxidation in the presence of iron oxide catalysts are few.

Mixed valence oxides containing divalent and trivalent cations of transition metals form stable spinel structures of the AB_2O_4 type, in particular Fe_3O_4. Cations with multiple oxidation states having close values of the crystal field stabilisation energy of octahedral and tetrahedral sites are the main reason for existing abundant defective spinel structures and non-stoichiometry [10]. Me_2O_3 oxides (e.g. γ-Fe_2O_3) crystallise in metastable spinel structures. Corundum is an exception because it is thermodynamically stable. Non-stoichiometric cation-deficient spinel structures are known for different transition metal oxides. These materials have been applied as oxidation catalysts and electrode materials [11–14].

Metal oxide bulk and surface oxygen mobility is significant to enhance catalyst performance in oxidation reactions. A fast electron exchange in the Fe^{2+}/Fe^{3+} couple in magnetite (Fe_3O_4) is directly related to oxygen mobility that facilitates redox reactions. Iron oxide nanoparticles have largely a defect crystal structure, which is energy uncompensated. Particle sizes, smaller than about 15 nm, induce a unique magnetic property of superparamagnetism. The latter has attracted much attention because of useful applications in different fields of science and practice.

Iron oxide compounds can be synthesised by different abiotic and biotic methods. Conventional techniques (chemical, mechanical) use toxic and expensive chemicals and devices, and require high-energy consumption and detoxification of waste flows that raise catalyst costs [15–19]. However, obtained products are of good purity and have well-defined properties. Bio-inspired technologies imitate natural processes of iron mineralisation by inclusion of different mediators. One trend is to exploit different bacteria. These microorganisms are widespread in nature and their possibilities are not fully investigated and used [15,20]. Iron biomineralisation through bacteria is clean, simple, nontoxic, low-cost, and needs ambient conditions. Produced iron oxide materials are cheap. This kind of synthesis does not use dangerous reagents. Cultivation of iron bacteria for biogenic iron (oxy)(hydr)oxides synthesis takes part in diluted feeding solutions till their nutrition components are running low or their concentration decreases under critical values related to microorganism life support. Because of that, there is no evolution of toxic products and this approach enables material preparation without evolving hazardous waste. Thus, biomineralisation methods are definitely environmentally friendly [15,18,21–30]. Ferric ion deposition by bacteria is relatively a slow process in comparison with other methods but it is not associated with energy supply because the bacteria are natural cell metabolites and no, or at least very low, energy consumption is necessary for synthesis [21–27].

Biogenic iron-containing materials are applicable to heterogeneous catalysis as catalyst precursors, active components, catalyst supports, and immobilising carriers. Studies are concentrated on different reactions and one of them is oxidation [18,19,22,28–37]. Own previously published results have shown that biogenic iron-containing materials obtained by cultivation of *Leptothrix* sp. in different feeding media exhibit a certain activity in the reaction of CO oxidation and it was found that maghemite obtained from lepidocrocite bioprecursor was more active than other bioproducts (goethite and lepidocrocite) [35]. In view of aforementioned, it is reasonable to study hexane complete oxidation in presence of biogenic iron-containing materials as a model reaction and the present work is focused on this problem.

EXPERIMENTAL

Biogenic materials were prepared by *Leptothrix* genus bacteria cultivation in Lieske medium, which contained different inorganic materials. The medium was modified by introduction of 0.3% Pd/Al-Si-O fibrous material or anodised Al foil (anodic Al_2O_3/Al). 0.3% Pd/Al-Si-O was obtained by sol-gel method [38], reduced at 400 °C, and then kept in air. The fibrous material was sterilised for 15 min by autoclaving at 1 atm and 120 °C. The aluminium foil was one-side covered with alumina by anodic oxidation in 0.3M $H_2C_2O_4$ electrolyte [39]. Lamellae of this material were cold sterilised by UV light. After immersing the modifiers into the feeding solutions, the latter were infected with 10% inoculum from *Leptothrix* genus bacteria. Cultivation was realised under static conditions at 20 °C for a period of 36(40) days. The produced precipitates were separated by decantation, washed with distilled water and filtered, and then dried at 40 (105) °C. The materials thus prepared are denoted as LieskeV (obtained in presence of 0.3% Pd/Al-Si-O) and LieskeA (in presence of anodic Al_2O_3/Al).

Powder X-ray diffraction patterns of the biogenic materials were collected within the range from 5.3

to 80° 2θ with a constant step of 0.02° 2θ on a Bruker D8 Advance diffractometer with Cu Kα radiation and LynxEye detector. Phase identification was performed by Diffrac*plus* EVA using ICDD-PDF2 Database.

Mössbauer spectra were recorded at room temperature by means of Wissenschaftliche Elektronik GmbH electromechanical apparatus (Germany), operating at a constant acceleration mode. An α-Fe standard and a [57]Co/Rh source were used. Parameters of hyperfine interactions of the obtained spectral components: isomer shift (IS), quadrupole splitting (QS), hyperfine effective field (H_{eff}), line width (FW), and component relative weight (G) were determined by CONFIT program. Computer fitting was based on the least squares method.

FTIR spectra of the materials were recorded on a Nicolet 6700 FTIR spectrometer (Thermo Electron Corporation, USA) in the far and middle IR regions. The method of dilution of studied material in a KBr pellet (0.5% of studied substance) was used. Spectra were collected using 100 scans and resolution of 4 (data spacing 1.928 cm^{-1}).

Specific surface area of both biogenic materials was measured according to the BET method (adsorption of N_2 at −196 °C) by a NOVA-1200e high-speed gas sorption analyser (Quantachrome Instruments, USA). Prior to measurements, each sample was evacuated at 100 °C. Pore size distribution was also estimated using the BJH method based on the isotherm desorption branch.

Catalytic measurements were carried out in an isothermal continuous flow type quartz-glass reactor (6.0 mm inner diameter) at atmospheric pressure. The catalyst was fixed in the reactor between plugs of quartz wool. Applied test conditions were: 0.63−0.8 mm catalyst fraction, 0.5 cm^3 catalyst volume, and gas hourly space velocity (GHSV) of 60.000 h^{-1}. The GHSV value was selected in order to minimise external mass transfer limitations. Reactant gases were supplied through electronic mass flow controllers. Reactant inlet concentrations were 334 ppm *n*-hexane and 20 vol.% oxygen. The gas mixture was balanced to 100% with nitrogen of 99.99% purity. Analysis of the gaseous flows was performed using a mass-spectrometer CATLAB system (Hiden Analytical, UK) by on-line gas-ana-lysers of $CO/CO_2/O_2$ (Maihak), and a flame ionisa-tion detector (Horiba) of the total hydrocarbon con-tent. The studied materials were preliminary treated in the reaction flow for 30 min at 400 °C in order to obtain constant composition, which would not change during the catalytic examinations.

LieskeV biogenic material elemental composi-tion was determined on Li-tetraborate pellets using laser ablation inductively coupled plasma-mass spec-trometry. Spot analysis was done using an UP-193FX excimer laser (system) (New Wave Research Inc., USA) attached to a ELAN DRC-e quadrupole induct-ively coupled plasma-mass spectrometer (Perkin-Elmer Inc.). A standard reference material NIST SRM 610, a 'squid' smoothing device, He carrier gas, energy density on sample ca. 7.3−7.6 J.cm^{-2}, repeti-tion rate of 10 and ablation craters 75 μm were used. The analysis was carried out in one block starting and ending with two NIST SRM 610 measurements and two measurements of the sample, which were then averaged. Two separate measurement experi-ments were performed in order to obtain a precise result. NIST SRM 612 was used for internal control of a possible systematic error.

RESULTS AND DISCUSSION

Elemental analysis was used to determine the amount of modifying additive, which is included in LieskeV final biogenic material. Results showed the following composition: 79.41 wt.% Fe, 8.32 wt.% Al, 9.69 wt.% Si, 0.003 wt.% Pd.

Fresh samples were studied by means of the BET method (Fig. 1). Analysis of isotherm hysteresis showed that it is of D type (or 2) [40]. This kind of hysteresis is due to heterogeneous capillaries that have large main body radii and many size-varying short necks. Pore size distribution results indicate mesoporous materials with predominant size of 4 nm. Diameters of 5–24 nm are also widely repre-sented. Larger pores within 14–7-nm diameter are less in the case of LieskeA sample (Fig. 1B). A uni-form decrease in number of pores of increasing size was found with LieskeV sample (Fig. 1B). The mea-sured total pore volume was 0.21 cm^3/g for LieskeA and 0.25 cm^3/g for LieskeV samples. The average pore size was 11 and 10.5 nm for LieskeA and LieskeV samples, respectively. However, LieskeV biomass exposed a higher specific surface area of 95 m^2/g compared to 76 m^2/g of LieskeA counterpart.

Transmission infrared spectra of as-prepared bio-genic materials ('fresh' samples) are shown in Fig. 2. Characteristic bands of lepidocrocite, goethite, and maghemite were recorded [25,41,42]. They are denoted γ, α, and m, respectively. Band intensity and band intensity ratios vary for the materials. Bands characteristic of feeding medium residues were also registered [43].

X-ray diffraction patterns of as-prepared samples (Fig. 3) disclose lines of the following phases: lepidocrocite (PDF01-070-8045), goethite (PDF00-029-0713), maghemite (PDF00-039-1346), and magnetite (PDF01-071-6336). Quantitative analysis results are given in Table 1.
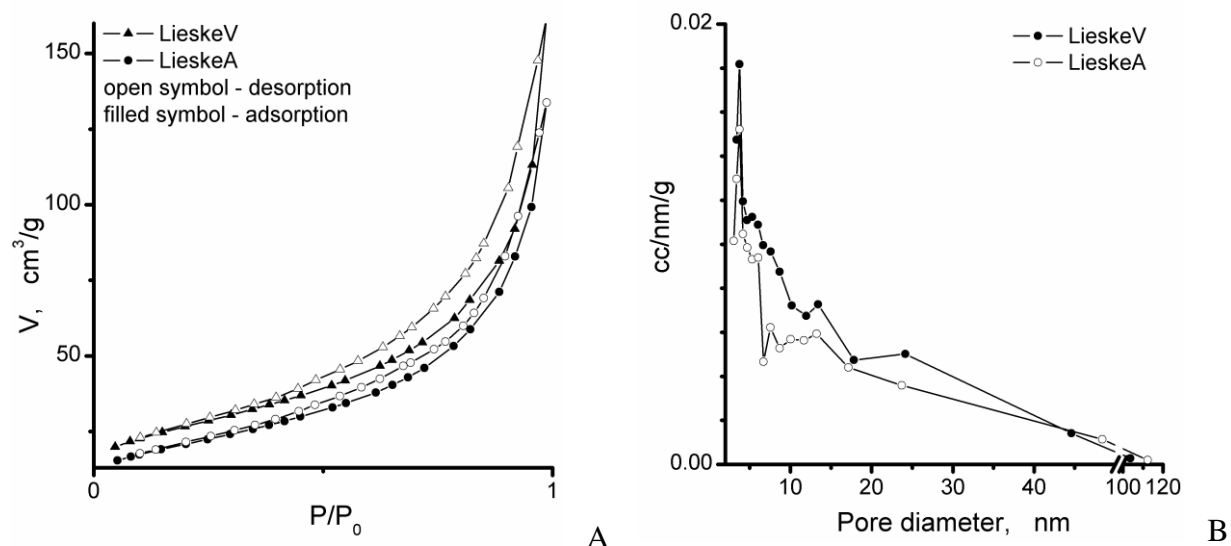
Fig. 1. Adsorption-desorption isotherms (A) and pore size distribution (B).
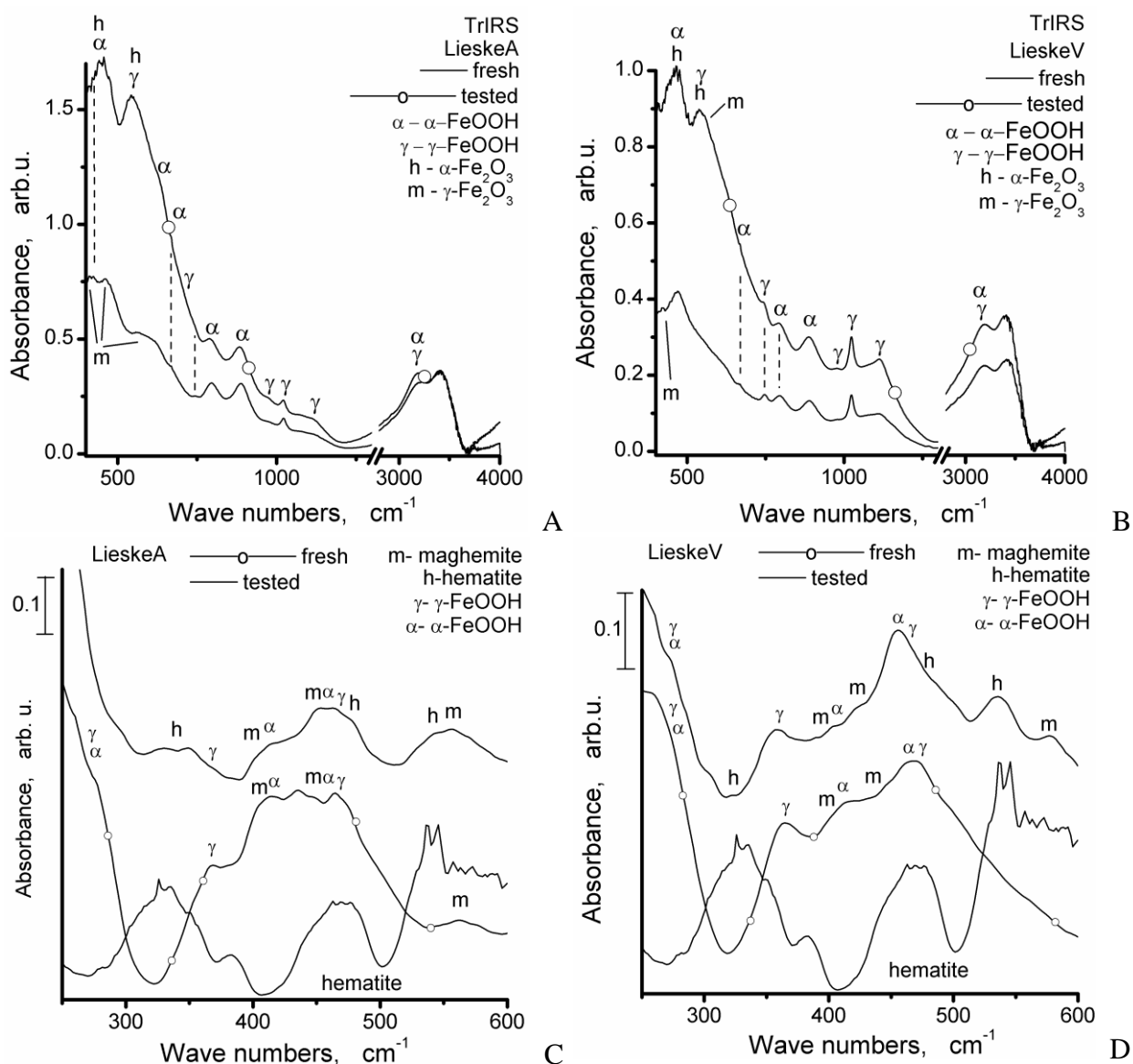

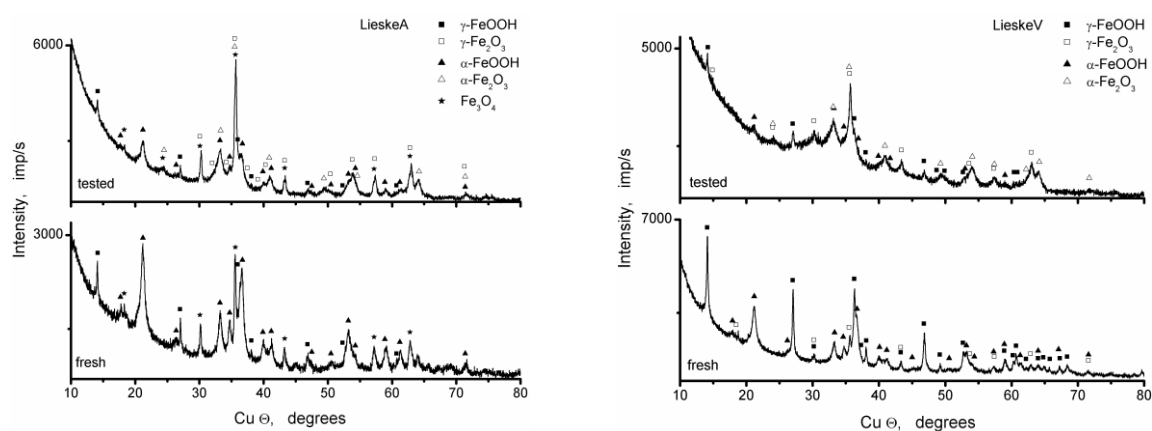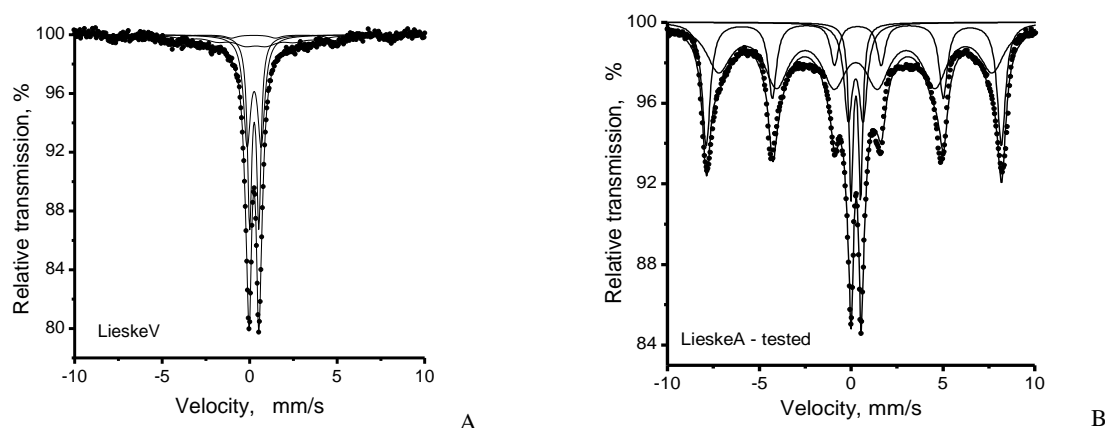Fig. 2. IR spectra of fresh and tested samples: A, C – LieskeA, B, D – LieskeV.

Table 1. Quantitative X-ray analysis data (XRD) and Mössbauer component relative weight (G_{MS})

| Component | XRD/GMS, % | | | |
| | LieskeV | | LieskeA | |
	fresh	tested	fresh	tested
Fe_3O_4			17 / 38	
γ-Fe_2O_3	7 / 7	39 / 55		23 / 53
α-Fe_2O_3		36 / 21		44 / 27
α-FeOOH	60 / 17	18 / -	76 / 39	25 / -
γ-FeOOH	32 / 39	7 / 11	7 / 23	8 / 10
SPM	37	13		10

Mössbauer spectra of fresh samples were composed of doublet and sextet components and the mathematical model for calculation includes such elements. A spectrum of LieskeV sample is shown in Fig. 4A to illustrate experimental results. Isomer shift values for LieskeV samples are characteristic of octahedrally coordinated ferric ions, while in the case of LieskeA samples, Fe^{3+} ions are tetrahedrally coordinated and $Fe^{2.5+}$ ions are positioned at octahedral sites (Table 2). Calculated parameters allow allocation of iron ions between several phases with particle sizes above 10 nm: oxyhydroxides (α-FeOOH and γ-FeOOH) and oxides (γ-Fe_2O_3 and Fe_3O_4). Some

Fe^{3+} ions in LieskeV samples are involved in oxide compounds of small particle size, below 10 nm, thus being superparamagnetic. A critical size of iron (oxy)(hydr)oxide particles that exhibit superparamagnetic properties is about 10–12 nm. In this case, the spectral components and their parameters correspond to a mixture of iron oxide compounds of two types of particles: superparamagnetic particles with sizes below 10 nm (doublets) and larger particles subjected to the model of collective magnetic excitement (CME) (sextuplets).

The biogenic materials were examined in the reaction of *n*-hexane oxidation (Fig. 5). Analyses of the reaction products showed that the process runs to CO_2 and partially to CO without any other intermediates. Analysis of the catalytic curves showed the same behaviour which is assigned to a similar reaction mechanism. The results demonstrate that LieskeV biomass is the more active material. In addition, on this type of samples, the incomplete oxidation of *n*-hexane to CO occurs to a lower extent. Despite small amount of palladium (0.003%), this modifier probably assists both processes. Palladium is well known as active catalyst for CO oxidation [44] as well for hydrocarbons oxidation [3,4].

Fig. 3. X-ray diffraction patterns of fresh and tested samples.

Fig. 4. Mössbauer spectra of fresh and tested samples: A – LieskeV (fresh), B – LieskeA (tested).

Table 2. Mössbauer parameters of hyperfine interaction

Sample	Components	IS, mm/s	QS, mm/s	Heff, T	FW, mm/s	G, %
LieskeV fresh	Sx1 - Fe^{3+}_{octa}, γ-Fe_2O_3	0.32	0.00	49.6	0.80	7
	Sx2 - Fe^{3+}_{octa}, α-FeOOH	0.33	−0.12	23.5	1.50	17
	Db1 - Fe^{3+}_{octa}, γ-FeOOH	0.36	0.53	-	0.30	39
	Db2 - Fe^{3+}_{octa}, SPM - oxides and hydroxides	0.36	0.81	-	0.49	37
LieskeV tested	Sx1 - Fe^{3+}_{octa}, α-Fe_2O_3	0.36	−0.11	49.9	0.52	21
	Sx2 - Fe^{3+}_{octa}, γ-Fe_2O_3	0.32	0.01	45.1	1.75	55
	Db1 - Fe^{3+}_{octa}, γ-FeOOH	0.36	0.56	-	0.31	11
	Db2 - Fe^{3+}_{octa}, SPM - iron oxides and hydroxides	0.34	0.97	-	0.64	13
LieskeA fresh	Sx1 - Fe^{3+}_{tetra}, Fe_3O_4	0.29	0.00	49.6	0.46	17
	Sx2 - $Fe^{2.5+}_{octa}$, Fe_3O_4	0.64	0.00	46.4	0.90	21
	Sx3 - Fe^{3+}_{octa}, α-FeOOH	0.33	−0.12	25.5	1.00	14
	Db1 - Fe^{3+}_{octa}, γ -FeOOH	0.37	0.50	-	0.28	23
	Db2 - Fe^{3+}_{octa}, α -FeOOH	0.37	0.74	-	0.46	25
LieskeA tested	Sx1 - Fe^{3+}_{octa}, α-Fe_2O_3	0.36	−0.11	50.0	0.53	27
	Sx2 - Fe^{3+}_{octa}, γ-Fe_2O_3	0.34	0.01	46.3	1.61	53
	Db1 - Fe^{3+}octa, γ-FeOOH	0.36	0.53	-	0.30	10
	Db2 - Fe^{3+}_{octa}, SPM - iron oxides and hydroxides	0.35	0.81	-	0.54	10

Samples subjected to catalytic tests ('tested') were studied by XRD, infrared and Mössbauer spectroscopy. XRD results showed that the tested samples contain lepidocrocite (PDF01-070-8045), goethite (PDF00-029-0713), maghemite (PDF00-039-1346), and hematite (PDF01-089-0596). Quota of compounds is displayed in Table 1. Bands characteristic of lepidocrocite, goethite, maghemite, and hematite (denoted as 'h') were recorded in the infrared spectra [25,37,45]. Band intensity and band intensity ratios vary with both samples (Fig. 2, 'tested'). The Mössbauer spectra of tested and fresh samples are composed of doublet and sextet components, the second element being dominant. Spectral computation was performed following the same model. A spectrum of LieskeA sample after catalytic experiment is displayed as illustration in Fig. 4B. IS parameter values are typical of octahedrally coordinated ferric ions (Table 2). Sets of hyperfine interaction parameters are related to iron ions in α-FeOOH, γ-FeOOH, and γ-Fe_2O_3 with particle sizes above 10 nm. Fe^{3+} ions, which are included in oxide compounds with particles below 10 nm, exhibit superparamagnetic properties and amount to 10–13%. Discussion on the results obtained by the three methods revealed that most probably the superparamagnetic phase found through Mössbauer spectra analysis of tested samples is goethite. Infrared characteristic bands displayed in Fig. 2 ('tested') and diffraction lines denoted in Fig. 3 as 'tested' identify this compound. Hematite presence in the tested samples implies a transformation that has been realised during pretreatment and/or during reaction. This result is not surprising since thermal transitions of iron compounds are well-known to follow the order oxyhydroxides → oxides → hematite [25,45,46].
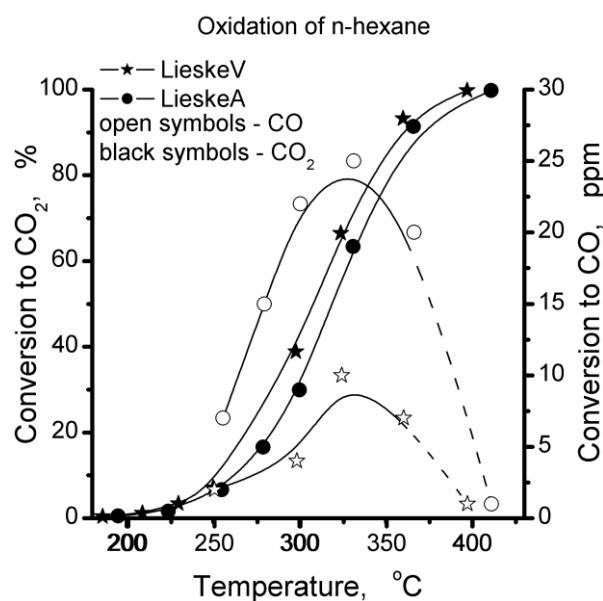
Fig. 5. Results of catalytic tests.

It is known that biomass obtained during cultivation of neutrophillic bacteria contains various iron compounds (α-FeOOH, γ-FeOOH, and β-FeOOH, and Fe_xO_y) at different ratios [41]. In addition, under selected conditions (liquid phase composition, neutral pH, and room temperature) the process of Fe^{2+} transformation to Fe^{3+} is of biogenic as well chemical nature. Iron oxides are formed in the feeding medium because of chemical reactions [47–53], however, *Leptothrix* genus participates mostly in the formation of iron oxyhydroxides [41]. Thermal conversion of goethite and lepidocrocite determines formation of biogenic maghemite.

45

Tested catalysts have almost the same composition, the differences being negligibly small. Bearing in mind possible transformations of iron (oxy)(hydr)oxide phases and whether they have biogenic or chemical origin [25,41,45,46], it can be affirmed that the LieskeV biomass contains a larger amount of maghemite originating from a biogenic precursor. The amount of this precursor (lepidocrocite) in fresh LieskeA biomass is less. Biogenic maghemite manifests some intrinsic activity in CO oxidation [35]. Together with available traces of palladium in LieskeV, it is reasonable to expect impeded *n*-hexane incomplete oxidation to CO. Carbon monoxide oxidation in the case of LieskeV samples is stimulated to a higher extent depending on two components that are active in this process. These special features of LieskeV biomass composition determine its higher activity at lower temperatures.

Pore structure of the studied systems has some influence on the catalytic behaviour. Although the textural features were determined for fresh samples, they could be used to explain the catalytic behaviour already discussed above. It has been found that biogenic iron is a hybrid product structured composed of iron oxide units and organic residues of bacterial origin [54-60]. It has been suggested that bacterially formed mineral deposits have wall structure, which contains iron (oxy)hydroxide spheres stabilized by organic carbon inclusions [54–57]. This structure is sterically stable to different impacts [15,28,32,34,61–63]. The LieskeV samples are characterised by relatively larger pores. This facilitates hexane molecules contact with the catalyst surface for long residence time. As a result, *n*-hexane transformation to CO_2 proceeds to a much higher extent in comparison with conversion to carbon monoxide.

CONCLUSIONS

Biogenic material, synthesised in Lieske cultivation medium in the presence of 0.3% Pd/Al-Si-O fibrous catalyst, was more active in the reaction of *n*-hexane oxidation than a counterpart material synthesised in the same medium in the presence of anodic oxidised aluminium foil. Incomplete oxidation to CO was also registered, however, to a lower extent if compared with the latter biomass. Beneficial catalytic properties were determined by two basic factors: (i) presence of traces of the 0.3% Pd/Al-Si-O fibrous material, which actually corresponds to 0.0003% Pd in the biomass and (ii) larger amount of maghemite obtained from a biogenic precursor in comparison with the material formed in presence of alumina/Al lamellae. Contribution by relatively larger pores and higher specific surface area is also suggested.

REFERENCES

1. Directive 2008/50/EC of the European Parliament and of the Council of 21 May 2008 on ambient air quality and cleaner air for Europe, *Official Journal of the European Union*, **L 152**, 1–44 (11.6.2008).
2. R.M Heck, R.J. Farrauto, Catalytic Pollution Control, second ed., Wiley-Interscience, New York, 2002.
3. S. C. Kim, W. G. Shim, *Appl. Catal. B: Environ.*, **92**, 429 (2009).
4. L. F. Liotta, *Appl. Catal. B: Environ.*, **100**, 403 (2010).
5. K. Everaert, J. Baeyens, *J. Hazard. Mater.*, **109**, 113 (2004).
6. J. J. Spivey, *Ind. Eng. Chem. Res.*, **26**, 2165 (1987).
7. U. Zavyalova, P. Scholz, B. Ondruschka, *Appl. Catal. A: General*, **323**, 226 (2007).
8. S. Scirè, S. Minicò, C. Crisafulli, S. Galvagno, *Catal. Commun.*, **2**, 229 (2001).
9. M. Baldi, V. S. Escribano, J. M. G. Amores, F. Milella, G. Busca, *Appl. Catal. B-Environ.*, **17**, L175 (1998).
10. A. Wells, Structural Inorganic Chemistry, 5th ed., Clarendon Press, Oxford, 1986, Ch. 13.
11. H. Hung, *Stud. Surf. Sci. Catal.*, **45**, 171 (1989).
12. J. Barrault, C. Renard, *Appl. Catal.*, **14**, 133 (1985).
13. T. Baird, K. Campbell, P. Holliman, R. Hoyle, D. Stirling, B. Williams, M. Morris, *J. Mater. Chem.*, **7**, 319 (1997).
14. A. C. Tavares, M. A. Cartaxo, M. I. Pereira, F. M. Costa, *J. Electroanal. Chem.*, **464**, 187 (1999).
15. A. B. Seabra, P. Haddad, N. Duran, *IET Nanobiotechnol.*, **7**, 90 (2013).
16. K. B. Narayanan, N. Sakthivel, *Adv. Coll. Interface Sci.*, **156**, 1 (2010).
17. H. Jung, J.-W. Kim, H. Choi, J.-H. Lee, H.-G. Hur, *Appl. Catal. B: Environ.*, **83**, 208 (2008).
18. B. Kazprzyk-Hordern, M. Ziolek, J. Nawrocik, *Appl. Catal. B: Environ.*, **46**, 639 (2003).
19. T. Shahwan, S. Abu Sirriah, M. Nairat, E. Boyaci, A. E. Eroglu, T. B. Scott, K. R. Hallam, *Chem. Eng. J.*, **172**, 258 (2011).
20. T. Ema, Y. Miyazaki, I. Kozuki, T. Sakai, H. Hashimoto, J. Takada, *Green Chem.*, **13**, 3187 (2011).
21. H. Hashimoto, S. Yokoyama, H. Asaoka, Y. Kusano, Y. Ikeda, M. Seno, J. Takada, T. Fujii, M. Nakanishi, R. Murakami, *J. Magnet. Magnet. Mater.*, **310**, 2405 (2007).
22. T. Sakai, Y. Miyazaki, A. Murakami, N. Sakamoto, T. Ema, H. Hashimoto, M. Furutani, M. Nakanishi, T. Fujiia, J. Takada, *Org. Biomol.Chem.*, **8**, 336 (2010).

23. B. Xin, D. Zhang, X. Zhang, Y. Xia, F. Wu, S. Chen, L. Li, *Bioresour. Technol.*, **100**, 6163 (2009).

24. J. A. Rentz, I. P. Turner, J. L. Ullman, *Water Res.*, **43**, 2029 (2009).

25. R. Cornell, U. Schwertmann, Iron Oxides, Wiley-VCH Verlag, Weinheim, Germany, 2003.

26. R. W. Fitzpatrick, R. Naidu, P. G. Self, in: Biomineralization Processes of Iron and Manganese - Modern and Ancient Environments, Catena Supplement 21, H. C. W. Skinner, R. W. Fitzpatrick (eds.), Catena Verlag, Reiskirchen, Germany, 1992, p. 263.

27. D. A. Ankrah, E. G. Sogaard, in: 13th Int. Water Technol. Conf., IWTC 13, Hurghada, Egypt, 2009, p. 999.

28. T. Ema, Y. Miyazaki, I. Kozuki, T. Sakai, H. Hashimoto, J. Takada, *Green Chem.*, **13**, 3187 (2011).

29. A. Alharthi, R. A. Blackley, T. H. Flowers, J. S. J. Hergreaves, I. D. Pulford, J. Wigzell, W. Zhou, *J. Chem. Technol. Biotechnol.*, **89**, 1317 (2014).

30. G. E. Hoag, J. B. Collins, J. L. Holcomb, J. R. Hoag, M. N. Nadagouda, R. S. Varma, *J. Mater. Chem.,* **19**, 8671 (2009).

31. H. Jung, H. Park, J. Kim, J.-H. Lee, H.-G. Hur, N. V. Myung, H. Choi, *Environ. Sci. Technol.*, **41**, 4741 (2007).

32. K. Mandai, T. Korenaga, T. Ema, T. Sakai, M. Furutani, H. Hashimoto, J. Takada, *Tetrahedron Lett.*, **53**, 329 (2012).

33. R. A. Maithreepala, R.-A. Doong, *Chemosphere*, **70**, 1405 (2008).

34. B. Kumar, K. Smita, L. Cumbal, A. Debut, *J. Saudi Chem. Soc.*, **18**, 364 (2014).

35. M. Shopska, D. Paneva, G. Kadinov, S. Todorova, M. Fabian, I. Yordanova, Z. Cherkezova-Zheleva, I. Mitov, *React. Kinet. Mech. Catal.*, **118**, 179 (2016).

36. M. Shopska, Z. Cherkezova-Zheleva, D. Paneva, M. Iliev, G. Kadinov, I. Mitov, V. Groudeva, *Cent. Eur. J. Chem. (Open Chemistry),* **11**, 215 (2013).

37. M. G. Shopska, D. G. Paneva, H. G. Kolev, G. B. Kadinov, R. Ilieva, M. Iliev, Z. P. Cherkezova-Zheleva, I. G. Mitov, *Helv. Chim. Acta*, **100**, e1700172 (2017).

38. L. Spasov, P. Dimitrov, Ch. Vladov, V. Zhelyazkov, Ch. Bonev, L. Petrov, in: Heterogeneous Catalysis (Proc. 8th Int. Symp. Heterogen. Catal., Varna, 5−9 October 1996), Institute of Catalysis, Bulgarian Academy of Sciences, Sofia, 1996, p. 751.

39. B. R. Tzaneva, A. I. Naydenov, S. Zh. Todorova, V. H. Videkov, V. S. Milusheva, P. K. Stefanov, *Electrochim. Acta*, **191**, 192 (2016).

40. A. Adamson, Physical Chemistry of Surfaces, 3rd ed., Z. M. Zorin, V. M. Muller (eds.), Mir, Moscow, 1979.

41. M. Shopska, D. Paneva, G. Kadinov, Z. Cherkezova-Zheleva, I. Mitov, M. Iliev, *Appl. Biochem. Biotechnol.*, **181**, 867 (2017).

42. B. Weckler, H. D. Lutz, *Eur. J. Solid State Inorg. Chem.*, **35**, 531 (1998).

43. L. H. Little, Infrared spectra of adsorbed species, Academic Press Inc., London, New York, 1966.

44. O. V. Krylov, Heterogeneous Catalysis: Textbook, Akademkniga, Moscow, 2004.

45. H. Lepp, *Am. Miner. (Notes and News),* **42**, 679 (1957).

46. A. U. Gehring, A. M. Hofmeister, *Clays Clay Miner.*, **42**, 409 (1994).

47. H. L. Ehrlich, D. K. Newman, Geomicrobiology, USA: CRC Press - Taylor & Francis Group, 2009.

48. A. Kappler, K. L. Straub, Geomicrobiological Cycling of Iron, In: Molecular Geomicrobiology (J. F. Banfield, J. Cervini-Silva, K. H. Nealson, Eds.), Reviews in Mineralogy and Geochemistry, vol. 59 (J. J. Rosso, Series ed.), Mineralogical Society of America (Geochemical Society), 2005.

49. M. Shopska, S. Todorova, I. Yordanova, S. Mondal, G. Kadinov, *Bulg. Chem. Commun.*, **47** (Special issue C), 73 (2015).

50. D. Emerson, J. V. Weiss, *Geomicrobiol. J.*, **21**, 405 (2004).

51. S. Vollrath, T. Behrends, C. Bender Koch, P. Van Cappellen, *Geochim. Cosmochim. Acta*, **108**, 107 (2013).

52. E. D. Melton, E. D. Swanner, S. Behrens, C. Schmidt, A. Kappler, *Nature Reviews. Microbiology*, **12**, 797 (2014).

53. Z. Cherkezova-Zheleva, M. Shopska, D. Paneva, D. Kovacheva, G. Kadinov, I. Mitov, *Hyperfine Interact.*, **237**, (2016).

54. C. S. Chan, S. C. Fakra, D. S. Edwards, D. Emerson, J. F. Banfield, *Geochim. Cosmochim. Acta,* **73**, 3807 (2009).

55. F. G. Ferris, R. O. Hallberg, B. Lyven, K. Pedersen, *Appl. Geochem.*, **15**, 1035 (2000).

56. K. Benzerara, T. H. Yooh, T. Tyliszczak, B. Constantz, A. M. Spormann, G. E. Brown, Jr., *Geobiology,* **2**, 249 (2004).

57. D. Emerson, H. Lin, L. Agulto, L. Lin, *Bioscience,* **58**, 925 (2008).

58. T. Suzuki, H. Hashimoto, H. Ishihara, T. Kasai, H. Kunoh, J. Takada, *Appl. Environ. Microbiol.,* **77**, 7873 (2011).

59. M. Furutani, T. Suzuki, H. Ishihara, H. Hashimoto, H. Kunoh, J. Takada, *Minerals,* **1**, 157 (2011).

60. M. G. Shopska, Z. P. Cherkezova-Zheleva, D. G. Paneva, V. Petkova, G. B. Kadinov, I. G. Mitov, *Croat. Chem. Acta,* **87**, 161 (2014).

61. T. Shahwan, S. Abu Sirriah, M. Nairat, E. Boyaci, A. E. Eroglu, T. B. Scott, K. R. Hallam, *Chem. Eng. J.*, **172**, 258 (2011).

62. M. Harshiny, C. N. Iswarya, M. Matheswaran, *Powder Technol.*, **286**, 744 (2015).

63. T. Ema, Y. Miyazaki, T. Taniguchi, J. Takada, *Green Chem.*, **15**, 2485 (2013).

БИОГЕННИ ЖЕЛЯЗО-СЪДЪРЖАЩИ МАТЕРИАЛИ СИНТЕЗИРАНИ В МОДИФИЦИРАНА СРЕДА НА ЛИСКЕ – СЪСТАВ, ПОРИСТА СТРУКТУРА И КАТАЛИТИЧНА АКТИВНОСТ В ОКИСЛЕНИЕТО НА n-ХЕКСАН

М. Шопска*, Г. Кадинов, Д. Панева, Ил. Йорданова, Д. Ковачева[1], Ант. Найденов[1], С. Тодорова, З. Черкезова-Желева, Ив. Митов

Институт по катализ, Българска академия на науките, ул. „Акад. Г. Бончев" бл. 11, 1113 София, България
[1] *Институт по обща и неорганична химия, Българска академия на науките, ул. „Акад. Г. Бончев" бл. 11, 1113 София, България*

(Резюме)

Бактерии от род *Leptothrix* са култивирани в среда на Лиске модифицирана с неорганичен материал. Използвани са два вида модификатори: 0.3% Pd/мезопорест Al-Si-O влакнест катализатор и едностранно анодно окислено алуминиево фолио. Получените биомаси (означени съответно ЛискеВ и ЛискеА) са изследвани чрез методите инфрачервена и Мьосбауерова спектроскопия, Рентгенова дифракция, адсорбция на азот и каталитични изпитания. Охарактеризирането на свежи образци показа, че ЛискеА съдържа γ-FeOOH, α-FeOOH и Fe₃O₄, докато ЛискеВ се състои от γ-FeOOH, α-FeOOH и γ-Fe₂O₃ в различни съотношения. Чрез елементен анализ бе доказано, че малко количество от модифициращия материал е включено в ЛискеВ и образецът съдържа 0.003% Pd. Регистрирани превръщания на изходните (биогенни и абиотични) желязооксидни/хидроксидни фази след участието на материалите в каталитичните изпитания потвърдиха, че образец ЛискеВ съдържа по-голямо количество γ-Fe₂O₃, получен от биогенен прекурсор, както и малко количество γ-FeOOH. Беше установено, че материалът ЛискеВ е по-активен в реакцията на окисление на n-хексан. Освен това, в присъствие на този образец непълното окисление до CO протича в по-малка степен. Въпреки, че паладият присъства в много малко количество в образец ЛискеВ, той най-вероятно подпомага каталитичния процес, тъй като е активен катализатор за окислението на CO. При употребата на образец ЛискеВ окислението на CO се стимулира от два компонента, които са активни в изследвания процес. Активност в окислението на CO е присъща и на биогенния γ-Fe₂O₃, а по-високото му съдържание в образеца е втората причина за по-ниската степен на непълно окисление на C₆H₁₄. Трета особеност на образец ЛискеВ, която определя неговата относително по-добра активност, е присъствието на малко по-широки пори, което позволява подобрен масопренос на реагентите в катализаторните частици.

Modification and characterization of iron-containing biogenic materials as catalysts for the reaction of CO oxidation

T. M. Petrova*, D. G. Paneva, S. Zh. Todorova, Z. P. Cherkezova-Zheleva, D. G. Filkova, M. G. Shopska, N. I. Velinov, B. N. Kunev, G. B. Kadinov, I. G. Mitov

Institute of Catalysis, Bulgarian Academy of Sciences, Acad. G. Bonchev St., Bldg. 11, 1113 Sofia, Bulgaria

The present study is focused on the preparation of modified iron-containing biogenic materials and testing them as catalysts for the reaction of CO oxidation. Modification was performed by impregnation of biogenic material obtained in Lieske cultivation medium. Impregnation was done using solutions of palladium chloride, cobalt nitrate, and manganese nitrate. Samples were characterized by X-ray diffraction, infrared spectroscopy, and Mössbauer spectroscopy. XRD results revealed that the starting biogenic material was X-ray amorphous, however, the presence of mixtures of low-crystalline iron oxyhydroxides, goethite and lepidocrocite, could not be excluded. Heating of Pd- and Co-modified materials led to the formation of oxide phases of Co_3O_4, γ-Fe_2O_3, and α-Fe_2O_3. Infrared spectra confirmed metal oxyhydroxide complete transformation to metal oxides in thermally treated samples. Mössbauer spectra of samples preheated at 300 °C indicated that the formed materials had a low degree of crystallinity, which is a specific feature of highly dispersed oxide materials. Doublet components in the Mössbauer spectra are indicative of nanosized highly dispersed particles demonstrating superparamagnetic behaviour. A ferrite $MnFe_2O_4$ phase was formed during synthesis of Mn-modified sample. Mössbauer spectra recorded at the temperature of liquid nitrogen showed a decrease of doublet part, which is typical of iron oxide particles of sizes below 4–10 nm. All the prepared samples were active in the reaction of CO oxidation, most active being manganese-modified catalyst. A synergistic effect was proposed between iron and manganese oxide components. Sample analysis after catalytic tests by means of Mössbauer spectroscopy revealed no changes in phase composition and dispersion.

Key words: biogenic iron-containing materials, chemical modification, X-ray diffraction, Infrared spectroscopy, Mössbauer spectroscopy, CO oxidation.

INTRODUCTION

Biogenic iron-containing materials are products of iron-transforming bacteria lifecycle [1–3]. Iron-containing bacteria of the *Sphaerotilus-Leptothrix* group are typical water representatives. In presence of these bacteria, Fe^{2+} ions are transformed into Fe^{3+} containing compounds [2,4–6]. These compounds are insoluble and the iron is deposited in the form of oxides, hydroxides, and salts [2,7–10], which have different phase composition, and different shape and size (globules, tubes, etc.). These materials demonstrate high specific surface area and high reactivity, which facilitate adsorption and decomposition of various contaminants [7–9,11–18]. Specific physical, chemical, and biological features of nanomaterials have motivated researchers for intensive studies. Iron oxides/hydroxides are a particular class of biocompatible compounds having natural biogenic analogues. Such materials being developed by various methods of synthesis are widely applied as catalysts. Many synthetic techniques for the production of various types of iron oxide nanoparticle materials (hematite, magnetite, goethite, etc.) are well established. However, most of these methods are costly and involve the use of hazardous chemicals [19]. Therefore, there is growing necessity to develop ecological and sustainable methods, such as biosynthesis [20]. Various studies have found that biogenic iron oxides, especially those of bacterial origin, are low crystalline aggregates composed of smaller species [7–10,17,21–23]. Biogenic iron specific properties are crucial for its application as an active component in catalysis in gaseous and liquid media [13,19,23–31], catalyst precursors [19,32], and catalysts [33]. In the course of the catalytic process, the stability of the biogenic materials is a very important property. In previous studies, it was found that their catalytic activity was preserved or slightly decreased after repeated use [26,32–35]. Actually, chemical modification of the biogenic materials is focused on improving some chemical properties.

This work is aimed at modifying iron containing biogenic materials by Pd, Co, and Mn and studying their catalytic behaviour in the reaction of CO oxidation.

EXPERIMENTAL

Synthesis

Pd, Co, or Mn were deposited separately or in combination (Pd+Co) on biogenic iron-containing material by impregnation with solutions of $PdCl_2$, $Co(NO_3)_2.6H_2O$, and $Mn(NO_3)_2.4H_2O$, respectively. Basic biogenic material (BM) was prepared by *Leptothrix* genus bacteria cultivation in Lieske medium, which contained 0.3% Pd/Al-Si-O fibrous material. Proper concentrations of the selected salts were used so that chemical modifier content was 1 mass% Pd, 20 mass% Co, and 20 mass% Mn. Selected salts were dissolved in distilled water at room temperature under constant stirring. Three drops of 1N hydrochloric acid were added to the $PdCl_2$ solution to complete dissolution. Evaporation of the water was carried out at 60 °C and continuous stirring. The samples were further heated at the same temperature for 24 hours for complete drying. The same technique was applied for Co deposition on a sample containing 1% Pd. The samples are denoted as Pd/BM, Pd+Co/BM, Co/BM, and Mn/BM.

Before catalytic tests, the samples were calcined in air at 300 °C for 2 hours at a heating rate of 10 deg/min.

Characterization

Powder X-ray diffraction (XRD) patterns were collected by a TUR M62 diffractometer with Co Kα radiation. Phase identification was performed using ICDD-PDF2 database. Experimental XRD profiles of the studied ferrites were processed by using PowderCell-2.4 software and appropriate corrections for instrumental broadening.

Infrared (IR) spectra of the samples were recorded on a Nicolet 6700 FTIR spectrometer (Thermo Electron Corporation, USA) using the method of dilution in KBr pellets (0.5% of studied substance). The spectra were collected in the middle IR region using 100 scans at a resolution of 4 (data spacing 1.928 cm^{-1}).

Mössbauer spectra (MS) were registered in air at room temperature (RT) by means of Wissel (Wissenschaftliche Elektronik GmbH, Germany) electromechanical spectrometer working in a constant acceleration mode. A ^{57}Co/Rh (activity $\cong$ 20 mCi) source and α-Fe standard were used. Experimentally obtained spectra were fitted using special software. The parameters of hyperfine interaction, such as isomer shift (IS), quadruple splitting (QS), effective internal magnetic field (Heff), line widths (FWHM), and relative weight (G) of the partial components in the spectra were determined.

Catalytic measurements

The catalytic measurements were carried out in an isothermal continuous flow type quartz-glass reactor (6.0 mm inner diameter) at atmospheric pressure. The catalysts were fixed in the reactor between plugs of quartz wool. The following conditions were applied: catalyst fraction 0.63–0.8 mm, catalyst volume 0.3 cm^3, and gas flow mixture of 108 ml/min at $CO:O_2$:He ratio of 4:5:91 vol.%. The reactant gases were supplied through Aalborg electronic mass flow controllers. Analysis of inlet and outlet gas flows was performed online on a HP 5890 gas chromatograph equipped with a thermal conductivity detector and a Carboxen-1000 column. Helium was used as a carrier gas.

RESULTS AND DISCUSSION

Sample XRD patterns are presented in figure 1, which reveal that the starting biogenic material was X-ray amorphous. This is evidence that the biogenic material contained low-crystalline iron oxyhydroxides (probably goethite and lepidocrolite). No characteristic lines of the modifying medium component 0.3% Pd/Al-Si-O in the spectra were registered. This result implies that no significant amount of the modifier was mixed with the biomaterial during cultivation.
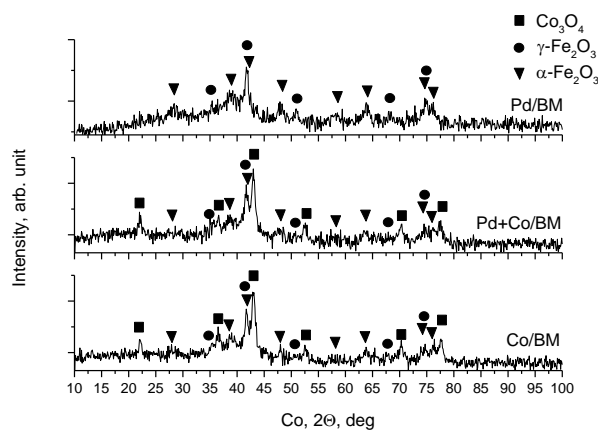
Fig. 1. X-ray diffraction patterns of modified samples thermally treated at 300 °C.

An overall pattern of all measured spectra of the modified biogenic material after calcination at 300 °C indicated chemical phases of low degree of crystallinity, which are characteristic of ultra- and highly dispersed oxide materials. Only iron-containing phases of hematite and maghemite were present in the spectrum of Pd-modified sample, the lines of hematite (α-Fe_2O_3) slightly higher intensity.

XRD patterns for Co_3O_4 (PDF 01-076-1802), γ-Fe_2O_3 (PDF 00-039-1346) and α-Fe_2O_3 (PDF 01-084-0310) are detectable in a Pd+Co/BM sample.

50

No diffraction peaks for Pd and PdO were visible in the XRD spectrum revealing fine dispersion of the noble metal. The main characteristic lines of the two iron oxide modifications are approximately of the same intensity. The diffraction lines are broad and low intense owing to high dispersion of the iron oxides. The linewidths indicate that the formed materials are ultra- or highly dispersed.

IR results are displayed in figure 2a. A spectrum of Pd/BM sample shows bands characteristic of goethite (3182, 886, 792, 668, 470 cm^{-1}) and lepidocrocite (3182, 1112, 1023, 976, 745 cm^{-1}) as well as surface carbonates (1482 plateau, 1639, 1656, 718 cm^{-1}).

The spectra of Pd+Co/BM, Co/BM, and Mn/BM show bands characteristic of lepidocrocite (3203, 1115, 745, 1021 cm^{-1}), nitrates (825, 1382 cm^{-1}), and surface carbonates (1657, 1640, 1474, 1454, 719 cm^{-1}). Although not all characteristic goethite bands were observed, its presence in the studied systems should be assumed. The materials treated at 300°C were also investigated. The IR spectra are presented in figure 2b. Bands characteristic of Fe-O vibration (under 500 cm^{-1}) prove the presence of iron oxides and Co_3O_4.

meters of the spectra are given in Table 1. Results of XRD and Mössbauer spectroscopy studies confirmed the presence of hematite and maghemite in the samples before catalysis. Most spectra except those of Mn/BM and Pd+Co/BM-LNT fit well with a model of two sextets and two doublets. The parameters of both sextets correspond to the two modifications of iron oxide - hematite (α-Fe_2O_3) and maghemite (γ-Fe_2O_3), that of maghemite being more intensive. Both sextets have reduced H_{eff} values of about 10−20 T, which indicated that the particles were highly dispersed. Doublet components in the Mössbauer spectra are indicative of nanosized highly dispersed particles, which demonstrate superparamagnetic behaviour. Polymorph phases ratio of iron oxides before heating to those obtained after heating at 300 °C can be related to thermal decomposition dynamics of the various iron hydroxides.

Fig. 2. Infrared spectra of modified samples before (a) and after (b) thermal treatment at 300 °C.

Mössbauer spectra of samples before and after catalytic test are shown in figure 3. Calculated para-
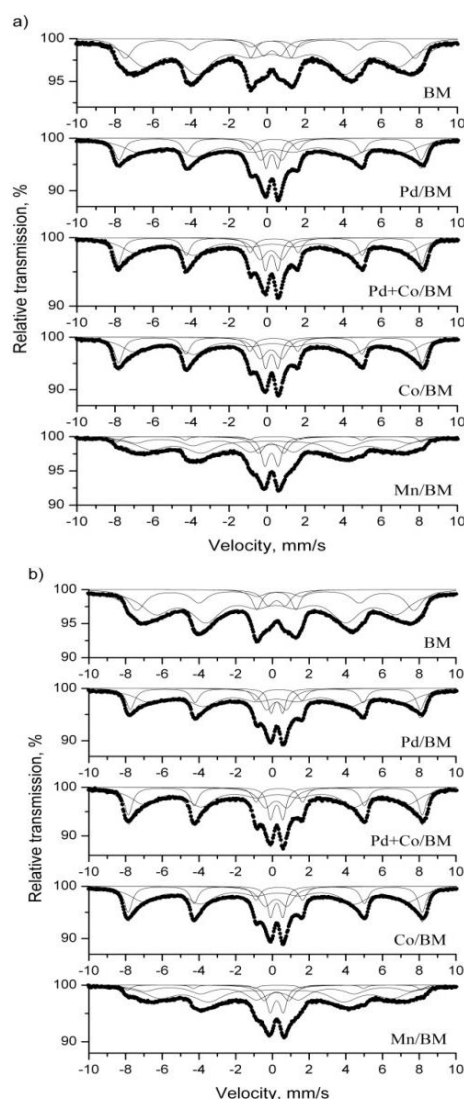
Fig. 3. Room temperature Mössbauer spectra of modified samples thermally treated at 300 °C (a) and after catalytic test (b).

Table 1. Mössbauer parameters of modified samples thermally treated at 300 °C and after CO oxidation reaction

Sample	Components	IS, mm/s	QS, mm/s	H_{eff}, T	FWHM, mm/s	G, %
BM TS300	$Sx1 - \alpha\text{-}Fe_2O_3$	0.37	-0.10	47.3	0.90	18
	$Sx2 - \gamma\text{-}Fe_2O_3$	0.33	0.00	41.8	1.98	70
	Db1 – SPM	0.36	0.90	-	0.73	6
	Db2 – SPM	0.32	2.13	-	0.56	6
Pd/BM TS300	$Sx1 - \alpha\text{-}Fe_2O_3$	0.36	-0.11	49.4	0.60	22
	$Sx2 - \gamma\text{-}Fe_2O_3$	0.33	0.03	43.3	2.00	58
	Db1 – SPM	0.34	0.61	-	0.40	9
	Db2 – SPM	0.32	1.10	-	0.76	11
Pd+Co/BM TS300	$Sx1 - \alpha\text{-}Fe_2O_3$	0.36	-0.11	49.6	0.52	25
	$Sx2 - \gamma\text{-}Fe_2O_3$	0.33	0.00	44.7	1.71	51
	Db1 – SPM	0.33	0.66	-	0.41	11
	Db2 – SPM	0.30	1.15	-	0.80	13
Pd+Co/BM TS300, LNT	$Sx1 - \alpha\text{-}Fe_2O_3$	0.47	-0.11	52.3	0.39	33
	$Sx2 - \gamma\text{-}Fe_2O_3$	0.41	0.03	49.7	0.90	61
	Db1 – SPM	0.42	0.84	-	0.75	7
Co/BM TS300	$Sx1 - \alpha\text{-}Fe_2O_3$	0.36	-0.10	49.6	0.54	26
	$Sx2 - \gamma\text{-}Fe_2O_3$	0.33	0.01	44.6	1.67	51
	Db1 – SPM	0.33	0.66	-	0.42	10
	Db2 – SPM	0.30	1.15	-	0.79	13
Mn/BM TS300	$Sx1 - \alpha\text{-}Fe_2O_3$	0.33	-0.11	49.8	0.40	5
	$Sx2 - MnFe_2O_4$	0.38	0.00	44.8	1.39	31
	$Sx3 - MnFe_2O_4$	0.31	0.00	39.3	2.00	45
	Db1 – SPM	0.33	0.70	-	0.46	10
	Db2 – SPM	0.32	1.32	-	0.69	9
BM TS300, after CO oxidation	$Sx1 - \alpha\text{-}Fe_2O_3$	0.37	-0.10	47.0	1.07	22
	$Sx2 - \gamma\text{-}Fe_2O_3$	0.31	0.00	40.8	2.00	66
	Db1 – SPM	0.34	0.95	-	0.75	6
	Db2 – SPM	0.33	2.12	-	0.59	6
Pd/BM TS300, after CO oxidation	$Sx1 - \alpha\text{-}Fe_2O_3$	0.36	0.10	49.2	0.56	21
	$Sx2 - \gamma\text{-}Fe_2O_3$	0.34	0.00	43.1	2.00	59
	Db1 – SPM	0.33	0.63	-	0.40	8
	Db2 – SPM	0.33	1.07	-	0.79	12
Pd+Co/BM TS300, after CO oxidation	$Sx1 - \alpha\text{-}Fe_2O_3$	0.36	-0.11	49.8	0.52	24
	$Sx2 - \gamma\text{-}Fe_2O_3$	0.33	0.01	45.0	1.76	53
	Db1 – SPM	0.33	0.67	-	0.43	10
	Db2 – SPM	0.30	1.18	-	0.89	13
Co/BM TS300, after CO oxidation	$Sx1 - \alpha\text{-}Fe_2O_3$	0.36	-0.10	49.6	0.54	26
	$Sx2 - \gamma\text{-}Fe_2O_3$	0.33	0.01	44.6	1.67	51
	Db1 – SPM	0.33	0.66	-	0.42	10
	Db2 – SPM	0.30	1.15	-	0.79	13
Mn/BM TS300, after CO oxidation	$Sx1 - \alpha\text{-}Fe_2O_3$	0.33	-0.11	49.8	0.40	5
	$Sx2 - MnFe_2O_4$	0.38	0.00	45.0	1.41	30
	$Sx3 - MnFe_2O_4$	0.31	0.00	39.4	2.00	47
	Db1 – SPM	0.35	0.71	-	0.48	10
	Db2 – SPM	0.32	1.33	-	0.73	8

IS - isomer shift, QS - quadrupole splitting, H_{eff} - effective internal magnetic field, FWHM - line widths, G - relative weight of the partial components in the spectra, LNT- spectra measured at liquid nitrogen temperature

Mössbauer spectrum recorded at the temperature of liquid nitrogen (LNT) showed a decrease of doublet part, which is typical of iron oxide particles of sizes below 4–10 nm (figure 4).

The spectrum of Mn-modified sample preheated at 300 °C differs from the spectra of other samples by lower content of iron phase, which is hematite rhombohedral polymorph ($\alpha\text{-}Fe_2O_3$). In the synthesis of Mn-modified sample, a ferrite $MnFe_2O_4$ phase was formed. It is presented in the spectrum by two sextet components with zero value of the quadruple split, indicating that the ferrite $MnFe_2O_4$ phase has a cubic symmetry. The two components in the spectra correspond to two types of differently coordinated iron ions, tetrahedral and octahedral, and are characteristic of inverse type spinel structure of the fer-

rites. Ferrite phase lines are broad and asymmetrical and the values of the internal magnetic field are reduced. This is due to a size dependent magnetic effect of the particles, which is explained by the presence of finely dispersed structure of the Mn-modified biogenic material.
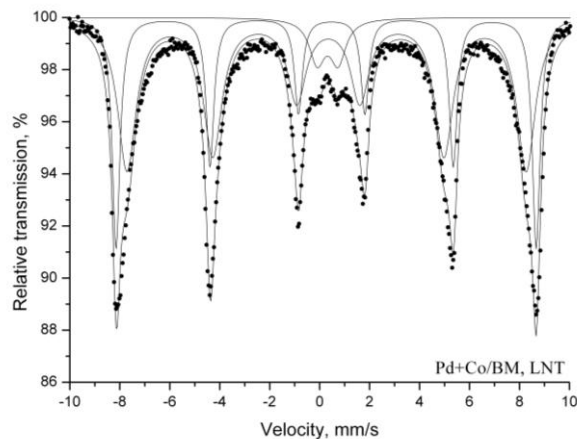
Fig. 4. Liquid nitrogen temperature Mössbauer spectrum of Pd+Co/BM sample thermally treated at 300 °C.

The spectra of all samples measured before and after catalysis are of the same type and matched by the values of calculated superfine parameters. The relative ratio of sextets to doublets was preserved, which indicated that no recrystallization and agglomeration processes occurred at the temperature of catalytic tests.

Temperature dependences of the CO oxidation over unmodified and modified biogenic catalysts are shown in figure 5. Doping with palladium, cobalt, or manganese increased the catalytic activity. The order of activity was Mn/BM > Pd+Co/BM > Co/BM > Pd/BM > BM. As is seen, unmodified biogenic material is active in the studied reaction. The reaction started at about 200 °C and a maximum of 70% conversion was reached at 275 °C. According to literature data, iron oxide materials have been found to be good/proper candidates as cheap and efficient catalysts, especially in environmental processes [36, 37]. As was shown above, the maghemite (γ-Fe$_2$O$_3$ 70%) is a predominant iron oxide in the initial biogenic material. According to some authors [38] γ-Fe$_2$O$_3$ has exhibited a low activity at temperatures lower than 300 °C. Addition of Pd resulted in displacement of the conversion curve to a lower temperature indicating a better catalytic activity. Liu *et al.* [39] claim that the promoting effect of iron oxide in the case of Pd-FeO$_x$ catalysts is related to the ability of the iron oxide species, located in close proximity to the palladium, to provide adsorption sites for oxygen that can subsequently react with CO molecules adsorbed on adjacent Pd sites. Thus, we can

conclude that because of the high dispersion of Pd and close interaction between Pd and Fe$_2$O$_3$ in Pd/BM sample, more surface oxygen species is provided to the palladium, thus improving its catalytic activity. Modification of Pd/BM sample with cobalt caused a further increase in activity. This is not surprising because unsupported cobalt oxide is a very active species in the field of air pollution control of CO [40,41]. It is known that cobalt catalysts are active for CO oxidation at low temperatures (-70 °C) if pre-oxidised before activity measurement [42, 43].
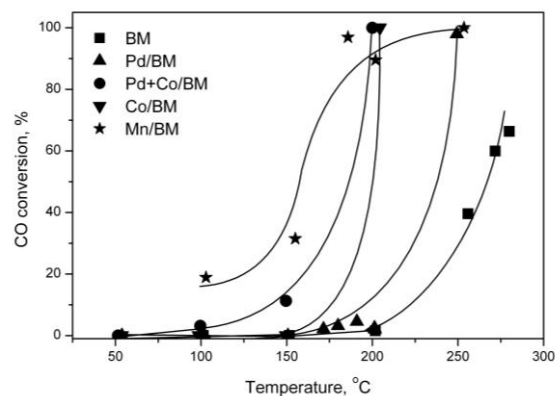
Fig. 5. Conversion vs. temperature in the reaction of CO oxidation.

Mn-modified BM sample manifested the highest catalytic activity. A synergistic effect could be proposed between iron and manganese oxide components. As was shown by Mössbauer spectroscopy a ferrite MnFe$_2$O$_4$ phase was formed. Formation of solid solutions or Fe$_x$Mn$_y$O$_4$ spinels has been proposed by Kedesdy and Tauber [44]. It has also been observed that transition metals such as manganese in the spinel lattice can strongly modify the redox properties of the ferrites and therefore activity. To obtain adequate explanation of the synergistic effect further in-depth study of this system is necessary.

CONCLUSIONS

Starting biogenic material is an X-ray amorphous mixture of goethite and lepidocrocite iron oxyhydroxides having ultradispersed nanosized particles with adsorbed surface nitrate and carbonate groups. Modification of the biogenic material with Pd, Pd+Co, and Co and subsequent calcination led to the formation of Co$_3$O$_4$, γ-Fe$_2$O$_3$, and α-Fe$_2$O$_3$. A highly dispersed MnFe$_2$O$_4$ ferrite phase was formed in Mn-modified sample. It has a cubic symmetry, spinel structure, and inverse ion distribution. It was proved by Mössbauer spectroscopy that the iron oxides and MnFe$_2$O$_4$ ferrite were nanosized highly dispersed entities. Metal ions oxidation state, phase composition, and dispersion of the test samples did not

change during catalytic tests. Catalytic measurements showed that all prepared samples were active in the reaction of CO oxidation and the catalytic properties depended on dopant type. A synergistic effect was proposed between iron and manganese oxide components.

REFERENCES

1. D. Ellis, Microbiology of the Iron-depositing Bacteria, Wexford College Press, Palm Springs, CA, 2003.
2. A. Kappler, K. L. Straub, *Rev. Miner. Geochem.*, **59**, 85 (2005).
3. Z. Cherkezova-Zheleva, D. Paneva, M. Shopska, R. Ilieva, M. Iliev, D. Kovacheva, G. Kadinov, *Hyperfine Interact.,* **239**, 6 (2018).
4. M. Shopska, D. Paneva, Z. Cherkezova-Zheleva, G. Kadinov, I. Mitov, V. Grudeva, *Nanoscience & Nanotechnology*, **14**, 21 (2014).
5. D. Emerson, E. J. Fleming and J. M. McBeth, *Annu. Rev. Microbiol.*, **64**, 561 (2010).
6. H. L. Ehrlich, D. K. Newman, Geomicrobiology, CRC Press, Boca Raton, 2009.
7. C. Chan, S. Fakra, D. Edwards, D. Emerson, J. Banfield, *Geochim. Cosmochim. Acta*, **73**, 3807 (2009).
8. F. G. Ferris, R. O. Hallberg, B. Lyven, K. Pedersen, *Appl. Geochem.*, **15**, 1035 (2000).
9. K. Benzerara, T. Yooh, T. Tyliszczak, B. Constantz, A. Spormann, G. Brown, Jr., *Geobiology*, **2**, 249 (2004).
10. T. Ema, Y. Miyazaki, I. Kozuki, T. Sakai, H. Hashimoto, J. Takada, *Green Chem.*, **13**, 3187 (2011).
11. X. Wang, M. Zhu, S. Lan, M. Ginder-Vogel, F. Liu, X. Feng, *Chem. Geol.*, **415**, 37 (2015).
12. Z. Cherkezova-Zheleva, M. Shopska, D. Paneva, D. Kovacheva, G. Kadinov, I. Mitov, *Hyperfine Interact.*, **237**, 56 (2016).
13. T. Sakai, Y. Miyazaki, A. Murakami, N. Sakamoto, T. Ema, H. Hashimoto, M. Furutani, M. Nakanishi, T. Fujiia, J. Takada, *Org. Biomol. Chem.*, **8**, 336 (2010).
14. P. C. Francisco, T. Sato, T. Otake, T. Kasama, *Am. Mineral.*, **101**, 2057 (2016).
15. J. A. Rentz, Phosphorus Removal Potential Using Biogenic Iron Oxides, WERF Research Report Series, vol. 10, IWA Publishing, London, 2010.
16. D. Pragnesh, C. Lakhan, *J. Nanotechnol.*, Article ID 398569 (2014).
17. M. Shopska, D. Paneva, G. Kadinov, S. Todorova, M. Fabian, I. Yordanova, Z. Cherkezova-Zheleva, I. Mitov, *Reac. Kinet. Mech. Catal.*, **118**, 179 (2016).
18. M. Shopska, D. Paneva, G. Kadinov, Z. Cherkezova-Zheleva, I. Mitov, M. Iliev, *Appl. Biochem. Biotechnol.*, **181**, 867 (2017).
19. M. Shopska, Z. Cherkezova-Zheleva, D. Paneva, M. Iliev, G. Kadinov, I. Mitov, V. Groudeva, *Cent. Eur. J. Chem.*, **11**, 215 (2013).
20. K. B. Narayanan, N. Sakthivel, *Adv. Colloid Interface Sci.*, **156**, 1 (2010).
21. H. Hashimoto, S. Yokoyama, H. Asaoka, Y. Kusano, Y. Ikeda, M. Seno, J. Takada, T. Fujii, M. Nakanishi, R. Murakami, *J. Magnet. Magnet. Mater.*, **310**, 2405 (2007).
22. D. Emerson, H. Lin, L. Agulto, L. Lin, *Bioscience*, **58**, 925 (2008).
23. J. S. J. Hargreaves, A. I. Alharthi, *J. Chem. Technol. Biotechnol.*, **91**, 296 (2016).
24. B. Kazprzyk-Hordern, M. Ziolek, J. Nawrocik, *Appl. Catal. B.*, **46**, 639 (2003).
25. T. Shahwan, S. Abu Sirriah, M. Nairat, E. Boyaci, A. E. Eroglu, T. B. Scott, K. R. Hallam, *Chem. Eng. J.*, **172**, 258 (2011).
26. B. Kumar, K. Smita, L. Cumbal, A. Debut, *J. Saudi. Chem. Soc.*, **18**, 364 (2014).
27. G. E. Hoag, J. B. Collins, J. L. Holcomb, J. R. Hoag, M. N. Nadagouda, R. S. Varma, *J. Mater. Chem.*, **19**, 8671 (2009).
28. H. Jung, H. Park, J. Kim, J-H Lee, H-G Hur, N. V. Myung, H. Choi, *Environ. Sci. Technol.*, **41**, 4741 (2007).
29. M. G. Shopska, G. B. Kadinov, J. Briancin, I. D. Yordanova, H. G. Kolev, M. Fabian, *Bulg. Chem. Commun.*, **47** (Special Issue C), 79 (2015).
30. M. Shopska, S. Todorova, I. Yordanova, S. Mondal, G. Kadinov, *Bulg. Chem. Commun.*, **47** (Special Issue C), 73 (2015).
31. S. Y. Lee, M. H. Baik, H-R Cho, E. C. Jung, J. T. Jeong, J. W. Choi, Y. B. Lee, Y. J. Lee, *J. Radioanal. Nucl. Chem.*, **296**, 1311 (2013).
32. A. Alharthi, R. A. Blackley, T. H. Flowers, J. S. J. Hergreaves, I. D. Pulford, J. Wigzell, W. Zhou, *J. Chem. Technol. Biotechnol.*, **89**, 1317 (2014).
33. K. Mandai, T. Korenaga, T. Ema, T. Sakai, M. Furutani, H. Hashimoto, J. Takada, *Tetrahedron Lett.*, **53**, 329 (2012).
34. M. Harshiny, C. N. Iswarya, M. Matheswaran, *Powder Technol.*, **286**, 744 (2015).
35. T. Ema, Y. Miyazaki, T. Taniguchi, J. Takada, *Green Chem.*, **15**, 2485 (2013).
36. M. Mohapatra, S. Anand, *Int. J. Eng. Sci. Technol.*, **2**, 127 (2010).
37. S. C. Kwon, M. Fan, T. D. Wheelock, B. Saha, *Sep. Purif. Technol.*, **58**, 40 (2007).
38. L. C. A. Oliveira, J. D. Fabris, R. R. V. A. Rios, W. N. Mussel, R. M. Lago, *Appl. Catal. A: Gen.*, **259**, 253 (2004).
39. L. Liu, F. Zhou, L. Wang, X. Qi, F. Shi, Y. Deng, *J. Catal.*, **274**, 1 (2010).
40. Y. J. Mergler, J. Hoebink, B. E. Nieuwenhuys, *J. Catal.*, **167**, 305 (1997).
41. J. Jansson, *J. Catal.*, **194**, 55 (2000).
42. P. Thormählen, M. Skoglundh, E. Fridell, B. Andersson, *J. Catal.*, **188**, 300 (1999).

43. D. A. H. Cunningham, T. Kobayashi, N. Kamijo, M. Haruta, *Catal. Lett.*, **25**, 257 (1994).

44. H. H. Kedesdy, A. Tauber, *J. Americ. Ceram. Soc.*, **39**, 425 (1956).

МОДИФИЦИРАНЕ И ОХАРАКТЕРИЗИРАНЕ НА ЖЕЛЯЗОСЪДЪРЖАЩИ БИОГЕННИ МАТЕРИАЛИ КАТО КАТАЛИЗАТОРИ ЗА РЕАКЦИЯТА НА ОКИСЛЕНИЕ НА CO

Т. М. Петрова*, Д. Г. Панева, С. Ж. Тодорова, З. П. Черкезова-Желева, Д. Г. Филкова, М. Г. Шопска, Н. И. Велинов, Б. Н. Кунев, Г. Б. Кадинов, Ив. Г. Митов

Институт по катализ, Българска академия на науките, ул. „Акад. Г. Бончев", бл. 11, 1113 София, България

(Резюме)

Настоящото изследване е насочено към получаване на модифицирани желязо-съдържащи биогенни материали и тяхното изпитване като катализатори в реакцията на окисление на CO. Модифицирането е осъществено чрез импрегниране на биогенен материал, получен в хранителна среда Lieske. Импрегнирането е извършено с използване на разтвори на паладиев хлорид, кобалтов нитрат и манганов нитрат. Пробите са охарактеризирани с рентгенова дифракция (XRD), инфрачервена и Мьосбауерова спектроскопия. Резултатите от XRD показват, че изходният биогенен материал е рентгеноаморфен, но въпреки това не се изключва наличието на смес от нискокристални железни оксихидроксиди гьотит и лепидокрокит. Нагряване на Pd- и Co-модифицирани материали води до образуване на фази от Co_3O_4, γ-Fe_2O_3 и α-Fe_2O_3. В термично третираните проби, инфрачервените спектри потвърждават пълно трансформиране на оксихидроксидите до оксиди. Мьосбауерови спектри на проби обработени при 300 °C показват, че образуваните материали имат ниска степен на кристалност, която е специфична характеристика за наноразмерни високо дисперсни оксидни материали. Дублетни компоненти в Мьосбауеровите спектри са показателни за наличието на наноразмерни високо-дисперсни частици демонстриращи суперпарамагнитно поведение. При синтеза на образец модифициран с манган се формира феритна $MnFe_2O_4$ фаза. Мьосбауеров спектър, регистриран при температурата на течен азот, показва намаляване на дублетната част, което е типично за железни оксидни частици с размер под 4–10 nm. Всички изследвани образци показват активност в реакцията на окисление на CO, като най-високо активен е катализаторът модифициран с манган. Анализ на Мьосбауеровите спектри на пробите след каталитични тестове не показва промени във фазовия състав и дисперсността.

Levulinic acid esterification on SO₃H-modified mesoporous silicas

H. I. Lazarova[1]*, M. D. Popova[1], A. Szegedi[2], B. Likozar[3], V. Dasireddy[3], N. Novak-Tusar[3]

[1] Institute of Organic Chemistry with Centre of Phytochemistry, Bulgarian Academy of Science, 1113 Sofia, Bulgaria,
[2] Research Centre for Natural Sciences, Institute of Materials and Environmental Chemistry, Hungarian Academy of Sciences, 1117 Budapest, Magyar tudósok körútja 2, Hungary
[3] National Institute of Chemistry, Hajdrihova 19, 1001 Ljubljana, Slovenia

Ordered mesoporous SBA-15 silica and a nanosized KIL-2 material with textural mesoporosity were synthesised and modified with sulphonic groups. Functionalisation with SO₃H groups was performed by a two-step procedure, in which mercapto-modified mesoporous silicas were obtained first in reaction with mercaptosilane followed by treatment in H_2O_2 to result SO₃H-modified mesoporous silicas. Initial and SO₃H-containing mesoporous materials were characterised by X-ray diffraction (XRD), N_2 physisorption, TG analysis, and TPD of ammonia. The catalytic performance of the SO₃H/SBA-15 and SO₃H/KIL-2 catalysts was studied in levulinic acid esterification with ethanol. A sulphonic-functionalised SBA-15 mesoporous material showed a higher conversion of levulinic acid to ethyl levulinate.

Key words: levulinic acid esterification, mesoporous silicas, KIL-2, SBA-15, biomass valorisation.

INTRODUCTION

The growing energy crisis and environmental concerns have prompted the utilisation of readily available lignocellulosic biomass materials as an alternative to the limited fossil resources [1,2]. Levulinic acid and its esters are promising platform chemicals for the production of a wide range of sources for biofuel, polymer, and fine chemicals industry [3−7]. Levulinic acid (LA) is generally produced by acid-catalysed hydrolysis of cellulose, and can be converted into levulinate esters, g-valerolactone, 1,4-pentanediol, and 5-nonanone (*via* pentanoic acid) as well as diphenolic acid as an intermediate for the synthesis of epoxy resins and polycarbonates [8−12]. Levulinate esters are also valuable compounds that can be used as fuel additives, solvents, and plasticisers. In particular, up to 5 wt.% ethyl levulinate can directly be used as a diesel miscible biofuel in regular diesel engines without modification because of its physicochemical properties similar to those of biodiesel, i.e., fatty acid methyl esters (FAME) [8]. Therefore, it has the potential to decrease the consumption of petroleum-derived fossil fuels. Generally, levulinate esters are produced by esterification of LA with several alcohols using mineral acids like HCl, H_2SO_4, and H_3PO_4 as catalysts, to give a high yield of corresponding products within a short reaction time. However, such homogenous acid catalysts cannot be recycled and always lead to technological problems (e.g., use of a large volume of base for neutralisation and corrosion of equipment). Their replacement with heterogeneous analogues, which are easily separable and reusable, is thus highly desirable. Various solid acids have been used for the esterification of levulinic acid with alcohols, e.g., zeolites and sulphated mixed oxides (sulphated zirconia ($SO_4^{2−}/ZrO_2$), niobia ($SO_4^{2−}/Nb_2O_5$), titania ($SO_4^{2−}/TiO_2$), and stannia ($SO_4^{2−}/SnO_2$) [8−12]. The number and the strength of acid sites and the applied preparation conditions are the key parameters for catalyst activity. One possible strategy to increase catalyst activity is to use a neutral, high surface area support, e.g., mesoporous silica materials, in order to ensure fine dispersion of the supported active phase. This approach may enhance the catalytic activity of the obtained catalysts in liquid-phase reactions by accelerating mass transport of reactant and product molecules as well.

In the present study mesoporous SBA-15 and KIL-2 materials were prepared and modified with SO₃H groups and studied in liquid phase esterification of levulinic acid with ethanol. The effect of the structural, textural, and acid properties of the obtained materials on their catalytic activity and stability was discussed.

EXPERIMENTAL

Synthesis of mesoporous KIL-2 silica

In the first step, the silica source (tetraethyl orthosilicate, 98% TEOS, Acros) as well as the templates (triethanolamine (99% TEA, Fluka) and tetra-

---

* To whom all correspondence should be sent
E-mail: lazarova@orgchm.bas.bg

ethylammonium hydroxide (20% TEAOH, Acros)) were mixed with a molar composition of 1.0 TEOS : 0.5 TEA : 0.1 TEAOH : 11 H_2O to obtain a homogeneous gel. The gel was aged overnight at room temperature and then dried in an oven for 24 h at 323 K. In the second step, the gel was solvothermally treated in ethanol in Teflon-lined stainless steel autoclaves at 423 K for 48 h. Removal of the template was performed by calcination at 773 K for 10 h using a ramp rate of 1 K/min in air flow.

Synthesis of mesoporous SBA-15 silica

In principle, Pluronic P123 (12.0 g) were dissolved in a solution containing 365.8 g distilled H_2O and 37.1 g 37% HCl under vigorous stirring at 308 K. After the surfactant was completely dissolved, 24.0 g TEOS were added and agitation continued for 24 hours. The obtained gel was placed into an autoclave and kept at 373 K for another 24 hours followed by filtration, washing with distilled water, and drying at room temperature. For template removal, the obtained powder sample was calcined at a temperature ramp of 1 K/min up to 823 K and dwelling times of 2 hours at 563 K and 6 hours at 823 K.
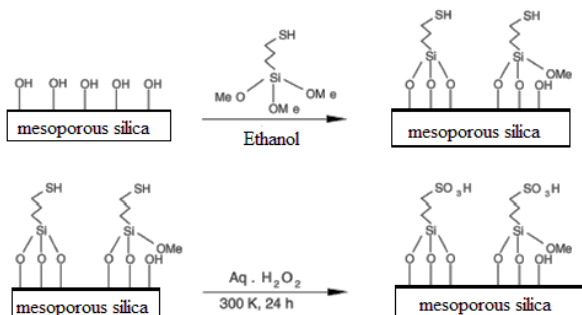
Scheme 1. Functionalisation of mesoporous silicas by SO_3H groups.

Functionalisation of KIL-2 and SBA-15 by SO_3H groups

The initial SBA-15 and KIL-2 materials were functionalised with 3-mercaptopropyl trimethoxysilane by dispersing in toluene at refluxed condition for 6 h and then filtered, washed, and dried in oven at 328 K for 3 h. Further, the obtained mercapto-modified mesoporous silicas were dispersed in H_2O_2 and stirred for 24 h at room temperature. The oxidised materials were filtered and dried in a vacuum oven at 323 K for 8 h and denoted as SO_3H/SBA-15 and SO_3H/KIL-2, respectively.

Methods of characterization

X-ray powder diffraction (XRD) patterns were recorded on a PANalytical X'Pert PRO (HTK) high-resolution diffractometer using Cu Ka1 radiation (1.5406 E) in the 2 q range from 5 to 80 (100 s per

step 0.016) for the samples and from 10 to 80 (100 s per step 0.016) for the sample holder using a fully opened X'Celerator detector.

Nitrogen physisorption measurements were carried out at 77 K using a Tristar 3000 Micromeritics volumetric adsorption analyser. Before adsorption analysis, the samples were outgassed under vacuum for 2 h at 473 K in the port of the adsorption analyser. BET specific surface areas were calculated from adsorption data in the relative pressure range from 0.05 to 0.21 [13]. The total pore volume was estimated based on the amount adsorbed at a relative pressure of 0.96 [14]. Mesopore and micropore volumes were determined using the t-plot method [15]. Pore size distributions (PSDs) were calculated from nitrogen adsorption data using an algorithm based on the ideas of Barrett, Joyner, and Halenda (BJH) [16]. The mesopore diameters were determined as the maxima on the PSD for the given samples.

Thermogravimetric analysis (TGA) was performed by a DTA-TG SETSYS2400, SETARAM analyser under the following conditions: temperature range 293−1273 K, static air atmosphere, heating rate of 5 K/min.

Ammonia temperature-programmed desorption (NH_3-TPD) was carried out using a Micromeritics 2920 Autochem II chemisorption analyser. In the NH_3-TPD experiments, the catalyst was pretreated at 773 K under a stream of helium for 60 min. After that, the temperature was decreased to 353 K. A mixture of 9.8% NH_3 in He as passed over the catalyst at a flow rate of 25 ml/min for 60 min. Excess ammonia was removed by purging with helium for 25 min. The temperature was then raised gradually to 1173 K by ramping at 10 K/min under helium flow and desorption data were collected. The TCD signals were calibrated using various gas concentrations of ammonia ranging within 0−10% in He. The quantity of desorbed ammonia was calculated from a detailed deconvolution of NH_3-TPD profile. In the TPD profile of the prepared catalysts, weak acidic sites were observed at 372–673 K as well as moderate acidic sites at 673–873 K and strong acidic sites above 873 K.

Catalytic experiments

Prior to catalytic measurements, the materials were pretreated *ex-situ* for 1 h at 413 K under static conditions in ambient air. A batch reactor with magnetic stirrer was used to perform the esterification reaction. In a typical experiment, the reactor was charged with 2 g LA and 0.050 g powder catalyst (2.5 wt.% catalyst/LA), the LA/ethanol weight ratio being 1:5. The reactor was heated to the desired

reaction temperature (343 K) for 1 h. Analysis of the reaction products was performed using HP-GC with FID and a WCOT fused silica 25 m 0.25 mm coating CP-SIL 43CB column. Mass balance was made based on carbon-containing products.

RESULTS AND DISCUSSION

Physicochemical properties

Low-angle powder XRD patterns of KIL-2 and SBA-15 indicate that KIL-2 had a disordered meso-porous structure, whereas SBA-15 demonstrated an ordered 2D hexagonal (p6mm) pore arrangement (not shown). A somewhat decreased intensity and some broadened reflections were observed for the SO_3H-modified silicas indicating a certain structural disorder. To gain information about textural characteristics of the studied materials nitrogen physic-sorption measurements were carried out (Table 1).

The isotherms of the SBA-15 samples were of type IV with a H1 type hysteresis loop between 0.6 and 0.7 (Fig. 1) relative pressures, typical of SBA-15 structure.

The KIL-2 samples exhibited adsorption iso-therms of IV type with a relatively narrow hysteresis loop at a higher relative pressure, which is due to textural mesoporosity. A significant decrease of the textural parameters, such as surface area and total pore volume of the SO_3H-mesoporous samples was registered. The surface area of $SO_3H/KIL-2$ was diminished from 668 to 465 m^2/g, whereas more significant surface area reduction from 878 to 463 m^2/g was observed for $SO_3H/SBA-15$ catalyst (Table 1). These data indicate that a substantial part of propyl sulphonic groups was located inside the channels of mesoporous supports.

TG plots of sulphonic functionalised SBA-15 and KIL-2 samples are presented in Fig. 2. The TG profiles show that the weight losses over 723 K were 7.6 and 8.6 wt.% for the $SO_3H/SBA-15$ and $SO_3H/KIL-2$ samples, respectively (Table 1), which was due to decomposition of SO_3H groups. A TG peak for $SO_3H/SBA-15$ was shifted to a higher temperature in comparison with that for $SO_3H/KIL-2$. Despite the differences in pore structure, the amount of the formed propyl sulphonic groups was similar.

Fig. 1. Nitrogen adsorption/desorption isotherms of SBA-15 and KIL-2 silicas and their sulphonic analogues.
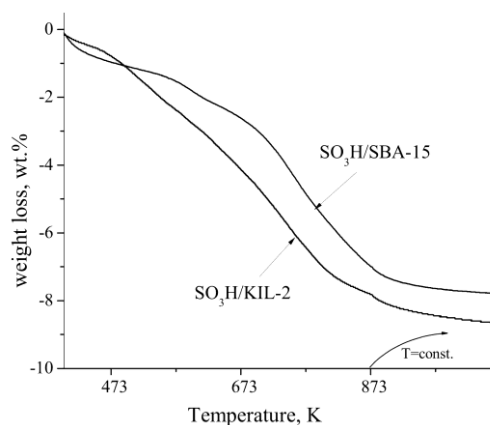
Fig. 2. TGA of $SO_3H/SBA-15$ and $SO_3H/KIL-2$ samples.

Table 1. Physicochemical properties of the studied samples.

Sample	S_{BET} m^2/g	Pore volume cm^3/g	Pore diameter[a] nm	SO_3H amount[b], wt.%	SO_3H amount[c], wt.%	Desorbed NH_3[d], mmol/g
SBA-15	878	1.14	5.5	-	-	-
KIL-2	668	1.45	15.2	-	-	-
$SO_3H/SBA-15$	463	1.00	5.1	7.6	7.3	0.60
$SO_3H/KIL-2$	465	1.10	14.4	8.6	8.2	0.45

[a] Pore diameter was calculated by the BJH method (desorption branch) for SBA-15 samples and by NLDFT method for KIL-2 samples (adsorption branch); [b] determined by TG analysis of fresh catalyst; [c] determined by TG analysis of spent catalyst; [d] calculated by TPD of ammonia.

Characterisation of the acidic properties by TPD of adsorbed ammonia.

TPD of ammonia was performed to determine the amount and strength of acid sites (Fig. 3). The

quantity of desorbed ammonia was calculated from a detailed deconvolution of the NH_3-TPD profile (Table 1). The most intensive peak over 773 K in the TPD curves could probably be associated with strong Brönsted acidity of the samples and with

partial decomposition of SO₃H groups. The TPD peak for the SO$_3$H/SBA-15 sample was more intensive then that for SO$_3$H/KIL-2.
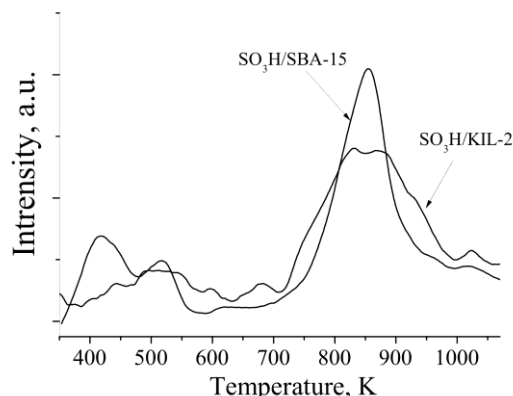
Fig. 3. TPD-NH3 of SO$_3$H/SBA-15 and SO$_3$H/KIL-2 samples.

It can be concluded that the acid sites formed on the two supports possess the same strength regardless of silica. Silica texture influences mainly the amount of acid sites formed.

Catalytic activity for LA esterification with ethanol

Samples were investigated in the esterification of levulinic acid with ethanol. The only registered products were ethyl levulinate and water. (Fig. 4). After 6 hours of reaction time over both samples, a conversion of about 22−30% was attained and in the next 2 hours, the catalysts kept the same catalytic activity.
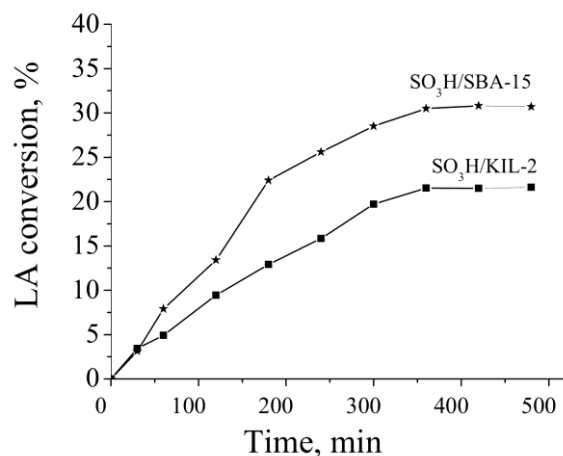
Fig. 4. Catalytic activity of SO$_3$H/SBA-15 and SO$_3$H/KIL-2 samples in levulinic acid esterification with ethanol at 343 K.

The highest catalytic activity was observed for the sulphonic-modified SBA-15 samples resulting in a conversion of 31% after 6 h. This effect could be attributed to the presence of SO$_3$H groups on the surface of the catalyst, which leads to an increase in Brönsted acidity. Formation of a higher amount of

acid sites can be due to the presence of a higher amount of accessible silanol groups in SBA-15 during the functionalisation process in comparison with KIL-2, where the grafting silane can be easily blocked in the nanoparticles aggregates of SO$_3$H/KIL-2. Ziarani *et al.* [17] also found that SO$_3$H/SBA-15 was a highly active green recyclable catalyst in various acid reactions. A stable activity for LA esterification in three reaction cycles was determined for the SO$_3$H/SBA-15 catalyst (Fig. 5).
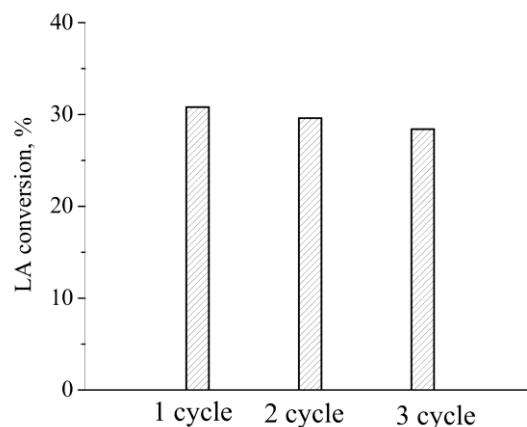
Fig. 5. Catalytic activity of SO$_3$H/SBA-15 sample.

The stable catalytic activity of the SO$_3$H/SBA-15 samples can be explained by easier accessibility of the reactants to the strong Brönsted acid sites in straight 2D channels of SBA-15 structure. The SO$_3$H/SBA-15 sample showed (Fig. 5) a LA conversion of 28.4% after three reaction cycles, whereas it was 30.8% in the first cycle. Catalyst reusability and stability are of key importance for practical applications as the catalyst lifetime predetermines the cost of the overall process. No leaching of sulphonic groups was registered on the SO$_3$H/SBA-15 samples after the third reaction cycle (Table 1) which could be a possible reason for excellent reusability with only a slight loss in catalytic activity.

Acquired catalytic data on activity and stability of the sulphonic-modified mesoporous SBA-15 silica material indicate that this catalyst is efficient, reusable, and stable solid acid for levulinic acid esterification.

CONCLUSIONS

Sulphonic-modified mesoporous SBA-15 and KIL-2 silicas were prepared by post synthesis method and investigated in levulinic acid esterification with ethanol. The obtained materials exhibited a high catalytic activity due to the formation of strong Brönsted acid sites. SO$_3$H/SBA-15 type mesoporous silica with its straight, easily accessible channels and affordable amount of silanol groups for post synthesis modification is a better choice as

a catalyst for the studied reaction compared with SO₃H/KIL-2 structure possessing textural meso-porosity. A good catalytic stability and resistance of the SO₃H/SBA-15 catalyst toward sulphonic groups leaching were also demonstrated.

REFERENCES

1. J. N. Chheda, G. W. Huber, J. A. Dumesic, *Angew. Chem.-Int. Ed.*, **46**, 7164 (2007).
2. G. W. Huber, S. Iborra, A. Corma, *Chem. Rev.*, **106**, 4044 (2006).
3. Handbook of Biofuels Production: Processes and Technologies (Woodhead Publishing Series in Energy), No. 15, R. Luque, J. Campelo, J. Clark, Eds. Woodhead Publishing, 2013.
4. C. S. K. Lin, L. A. Pfaltzgraff, L. Herrero-Davila, E. B. Mubofu, S. Abderrahim, J. H. Clark, A. Koutinas, N. Kopsahelis, K. Stamatelatou, F. Dickson, S. Thankappan, Z. Mohamed, R. Brocklesby, R. Luque, *Energy Environ. Sci.,* **6**, 426 (2013).
5. J. H. Clark, V. Budarin, Th Dugmore, R. Luque, *Catal. Commun.*, **9**, 1709 (2008).
6. D. R. Fernandes, A. S. Rocha, E. F. Mai, C. J. A. Mota, V. Teixeira da Silva, *Appl. Catal. A,* **425-426**, 199 (2012).
7. F. M. A. Geilen, B. Engendahl, A. Harwardt, W. Marquardt, J. Klankermayer, W. Leitner, *Angew. Chem. Int. Ed.*, **49**, 5510 (2010).
8. X.-R. Chen, Y.-H. Ju, C.-Y. Mou, J. *Phys. Chem.* C, **111**, 18731 (2007).
9. A. Corma, S. Iborra, A. Velty, *Chem. Rev.*, **107**, 2411 (2007).
10. A. A. Peterson, F. Vogel, R. P. Lachance, M. Froling, M. J. Antal Jr., J. W. Tester, *Energy Environ*. Sci., **1**, 32 (2008).
11. F. D. Pileidis, M. Tabassum, S. Coutts, M.-M. Titirici, *Chin. J. Catal.*, **35**, 929 (2014).
12. J. N. Chheda, G. W. Huber, J. A. Dumesic, *Angew. Chem. Int. Ed.*, **46**, 7164 (2007).
13. S. Brunauer, P. H. Emmett, E. Teller, *J. Am. Chem. Soc.*, **60**, 309 (1938).
14. K. S. W. Sing, D. H. Everett, R. A. Haul, L. Moscou, R. A. Pirroti, J. Rouquerol, T. Siemieniewska, *Pure Appl. Chem.*, **57**, 603 (1985).
15. B. C. Lippens, J. H. de Boer, *J. Catal.*, **4** (3), 319 (1965).
16. E. P. Barrett, L. G. Joyner, P. P. Halenda, *J. Am. Chem. Soc.*, **73**, 373 (1951).
17. G. M. Ziarani, N. Lashgari, A. Badiei, *J. Mol. Catal. A*, **397**, 166 (2015).

ЕСТЕРИФИКАЦИЯ НА ЛЕВУЛИНОВА КИСЕЛИНА ВЪРХУ SO₃H-МОДИФИЦИРАНИ МЕЗОПОРЕСТИ СИЛИКАТИ

Хр. Ил. Лазарова[1*], М. Д. Попова[1], А. Сегеди[2], Б. Ликозар[3], В. Дасиреди[3], Н. Новак-Тушар[3]

[1] *Институт по органична химия с център по фитохимия, Българска академия на науките, 1113 София, България,*

[2] *Изследователски център за природни науки, Институт за материалите и химия на околната среда, Унгарска академия на науките, 1117 Будапеща, Унгария*

[3] *Национален институт по химия, 1001 Любляна, Словения*

(Резюме)

Мезопорести SBA-15 и KIL-2 материали бяха синтезирани и модифицирани със сулфонови функционали групи, с цел получаване на хетерогенни кисели катализатори. Функционализирането със SO₃H групи се извършваше чрез двустепенна процедура, при която първоначално се получава меркапто-модифицирани мезо-порести силикати и в последваща обработка в H₂O₂ се получава модифицирани със SO₃H групи мезопорести силикати. Получените материали бяха охарактеризирани с рентгенова дифракция (XRD), N₂ физисорбция и температурнопрограмирана десорбция на амоняк. Каталитичното поведение на SO₃H/SBA-15 и S0₃H/KIL-2 е изследвано в реакцията на естерификация на левулинова киселина с етанол. Функционализираният със SO₃H групи SBA-15 мезопорест катализатор показа по-висока каталитична активност в тази реакция до етиллевулинат.

Supported palladium containing perovskite catalysts for methane combustion

S. G. Stanchovska[1]*, D. N. Guergova[2], G. M. Ivanov[1], R. K. Stoyanova[1], E. N. Zhecheva[1], A. I. Naydenov[1]

[1] *Institute of General and Inorganic Chemistry, Bulgarian Academy of Sciences, Acad. G. Bonchev Str., Bldg. 11, 1113 Sofia, Bulgaria*

[2] *Rostislaw Kaischew Institute of Physical Chemistry, Bulgarian Academy of Sciences, Acad. G. Bonchev Str., Bldg. 11, 1113 Sofia, Bulgaria*

Citrate solution method is very suitable for preparation of multielement perovskites in the form of powders and thin layers. In this study, we demonstrate the feasibility of the method for deposition of perovskite-based materials on conventional γ-alumina and industrial metal carriers. A perovskite-based entity of $La(Co_{0.8}Ni_{0.1}Fe_{0.1})_{0.85}Pd_{0.15}O_3$ composition manifested a high catalytic activity in the methane combustion reaction. Preliminary data on the practical applicability of the perovskite-based material supported on monolithic VDM®Aluchrom Y Hf carrier are reported. Taking into account the high thermal stability of the catalytically active phase it is concluded that the prepared material can serve as a basis for further development of an effective technology for abatement of methane emissions..

Key words: palladium, cobalt perovskites, methane, complete oxidation.

INTRODUCTION

The European Union (EU) is planning reduction in the greenhouse gas emissions by 20% in 2020 as compared to 1990 [1]. Methane is a greenhouse gas (GHG) that contributes to significant share of the total amount of GHG emissions [2]. Abatement of methane emissions can be achieved by applying the method of complete catalytic oxidation. Catalysts used for methane combustion are based on palladium in combination with different metal oxides, however, the main problem related to deactivation is not solved yet.

Perovskite-type metal oxides are considered promising as catalysts for methane combustion due to their thermal stability. There has been an increasing interest in the perovskite catalysts due to the development of the so-called 'intelligent' three-way catalysts based on Pd-containing perovskite oxides [3,4], the catalytic behaviour of these catalysts being defined by palladium chemical state and redox behaviour.

Catalysts for methane combustion are usually used in the form of monoliths coated by an active phase of metal or ceramic films. The main advantages of the metal monolithic catalysts are high mechanical strength, high thermal conductivity and low thermal inertia, and low weight [5].

In this study, we present new data on synthesis and catalytic behaviour of Pd-containing Co-based perovskite oxides deposited on different industrial supports: Fe-Cr-Al – alloy wire and VDM® Aluchrom Y Hf. For comparison, conventional γ-alumina (Rhone Poulenc) was also used. The prepared catalytic systems were investigated in the reaction of complete oxidation of methane.

EXPERIMENTAL

Prior to deposition γ-alumina support was modified by SiO_2. The procedure involved impregnation of γ-alumina with silica sol (colloidal silica, 40% aqueous solution), silica content being 2 wt.% with respect to γ-alumina. Metal ions (La, Co, Ni, Fe, and Pd) from citrate solution were deposited *via* wet impregnation on silica-modified/γ-alumina support. Details on solution preparation are given elsewhere [6,7]. Pd content was 15%, while perovskite nominal composition was $La(Co_{0.8}Ni_{0.1}Fe_{0.1})_{0.85}Pd_{0.15}O_3$. The impregnated support was heated first in air at 400 °C for 3 h to decompose the citrate salts, and then the obtained solid residue was annealed in air at 600 °C for 3 h. Selected thermal treatment procedure was compatible with our own previous study on the formation of multiple-substituted perovskites having high specific surface area [6]. The weight amount of the deposited perovskite was 10%.

Industrial carriers based on Al-containing Fe-Cr alloys were used for catalyst preparation. For this purpose, Fe-Cr-Al alloy foil (or wire) was pre-oxidized at 950 °C for 10 hours to form α-alumina layer on the metal surface. The prepared catalyst carrier was coated with γ-alumina layer prepared by

sol-gel method. On the so formed washcoat the perovskite active phase was supported by wet impregnation method.

X-ray structural analysis was performed by a Bruker Advance 8 diffractometer using CuKα radiation. Step-scan recordings for structure refinement by Rietveld's method were carried out using 2θ steps of 0.02° and 5 s duration. A FULLPROF computer program was used for calculations

TEM investigations were performed on a TEM JEOL 2100 instrument at accelerating voltage of 200 kV. Specimens were prepared by grinding and then suspending in ethanol by ultrasonic treatment for 6 min. The suspensions were dripped on standard holey carbon/Cu grids. TEM micrographs were made using digital image analysis of reciprocal space parameters. The analysis was carried out by Digital Micrograph software.

XPS measurements were carried out in the UHV chamber of ESCALAB MkII (VG Scientific) electron spectrometer applying an AlKα excitation source. Spectra calibration was performed by using the C 1s line of adventitious carbon centred at a binding energy (BE) of 285.0 eV.

Specific surface area of the catalyst samples was determined by low temperature adsorption of nitrogen according to the BET method using Nova 1200 (Quantachrome) apparatus. Temperature-programmed reduction (TPR) experiments were carried out in the measurement cell of a SETARAM DSC-111 differential scanning calorimeter directly connected to a gas chromatograph (GC), within the 300–973 K range at a 10 K/min heating rate in Ar/H_2 flow of 9:1, the total flow rate being 20 ml/min. A cooling trap between DSC and GC removed the water obtained during the reduction. To obtain *ex situ* XRD patterns of partially reduced oxides the reduction process was interrupted at selected temperatures, and then the samples were cooled down to room temperature in Ar/H_2 flow followed by argon treatment for 10 min.

The catalytic experiments were carried out at atmospheric pressure in a continuous flow type reactor equipped with mass spectrometer. The monolithic catalysts were tested as single channel reactors with inner diameter of 2.5–3.5 mm and length of 90–115 mm. For this purpose, they were placed in an isothermal tubular flow reactor. To compensate the adiabatic effect of the reaction the catalyst bed temperature was kept constant with deviations within +/–1 °C. Pressure drop of the catalyst bed was measured to be less than 1 kPa. Reactant inlet concentrations were adjusted as methane feed concentration 0.1 vol.%, oxygen 20.9 vol.%, and the feed gas mixtures were balanced to 100% with nitrogen (4.0). Gas analysis was performed using the mass spectrometer of CATLAB (Hiden Analytical) system, on-line CO/CO_2/O_2 gas analysers (Maihak), and THC-FID (total hydrocarbon content with a flame ionization detector, Horiba).

RESULTS AND DISCUSSION

Catalyst morphology was examined by SEM/EDS techniques. SEM images of perovskites supported on γ-alumina and monolithic VDM®Aluchrom Y Hf carrier are compared in figure 1. Deposition on γ-alumina involved formation of plate-like aggregates on the surface, however, small particles are also observable. EDS analysis indicated that the smaller particles contained mainly Pd, while the aggregates were composed of all other elements, such as La, Co, Ni, Fe, and Pd at a ratio which did not coincide with that known for nominal perovskite composition. This fact implies that during impregnation there occurs formation of a mixture of phases comprising, most probably, oxides of palladium and other metals in addition to the pure perovskite phase.

Deposition on the monolithic carrier was accomplished in the same way as in the case of γ-alumina support: there were plate-like aggregates composed of La, Co, Ni, Fe, and Pd at a ratio matching a mixture of perovskite phase and oxides of palladium, lanthanum, and transition metals. Comparison between supported catalysts shows that the deposition of the active phase on the monolithic substrate was rather inhomogeneous (Fig. 1). Needle-like network is due to the γ-alumina formed as an intermediate layer, on which the active catalytic phase of plate-like aggregates is deposited. It is important to note that irrespective of support type Pd average content in the catalysts was almost the same: 1.7 ± 0.2 wt.% on γ-alumina support and 1.2 ± 0.5 wt.% on VDM®Aluchrom Y Hf monolithic carrier.

Results from the catalytic tests are displayed in figure 2. The highest activity was observed when the perovskite phase was supported on γ-alumina in the form of irregular shaped particles (fraction 0.5–0.8 mm, Rhone Poulenc, France) followed by Fe-Cr-Al-wire (length 2.7 m, diameter 0.15 mm), the latter being used in this case as a model carrier of so called 'wire-knitted' catalysts.
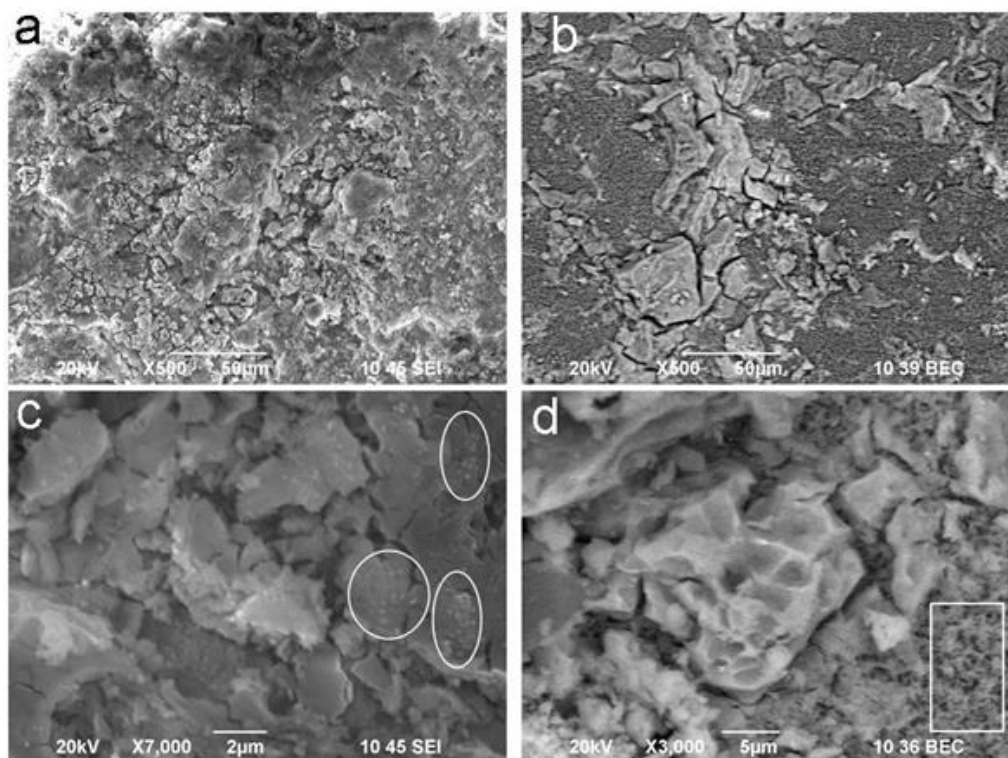
Fig. 1. SEM images of different magnification for γ-alumina (*a,c*) and monolithic VDM®Aluchrom Y Hf (*b,d*) supported catalyst. The circles indicate small particles enriched in Pd and the square points to an intermediate layer of monolithic support due to γ-alumina.
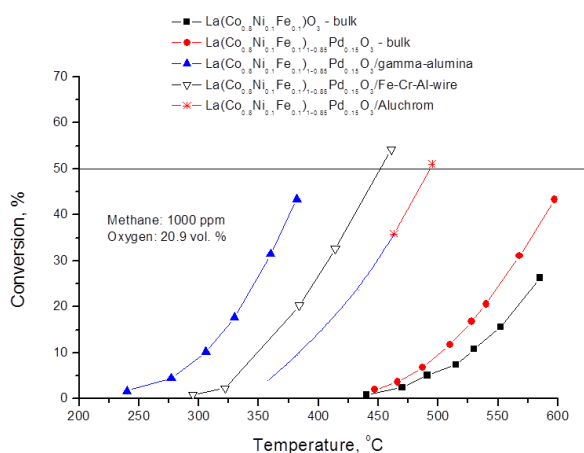
Fig. 2. Temperature dependence of conversion during complete oxidation of methane on the investigated perovskite-based catalysts.

Preliminary studies on the reaction kinetics showed that the reaction pathway over the prepared catalysts occurs most probably through Mars-van Krevelen mechanism, where water molecules compete with methane molecules for oxidized adsorption sites. The rate-determining step is reduction of the active sites except for the case of low oxygen concentration where reoxidation is the slower process. Despite relatively large deviation of experimental data from what is expected in the case of Eley-Rideal mechanism where the methane is impinging from the gas phase this mechanism cannot be entirely excluded since the observed reaction order to methane is close to unity.

It should be pointed out that it was assumed for both γ-alumina and Fe-Cr-Al-wire that the operation occurs under conditions of intensive mass transfer due to well-mixed gas-solid conditions (turbulent gas flow). However, for achieving methane abatement the practice requires operation with large amounts of waste gases, hence application of monolithic reactors is required. Therefore, possible application of Aluchrom is considered highly promising. Despite relatively high temperature for 50% conversion (T_{50}), about 490 °C at GHSV of 30000 h^{-1}, a combination between high thermal stability of the Pd-containing perovskite active phase and well improved thermal and corrosive resistance of Aluchrom could lead to reliable solution of the Pd-deactivation problem in parallel with low pressure drop of the catalytic element. Hence, the experimental data obtained by the Aluchrom-based monolithic catalytic tests were used for model calculations, performed by using a two-dimensional heterogeneous model for monolithic reactor, accounting for both external and internal mass transfer effects (assuming first order kinetics during isothermal operation). The principles of applied reactor modelling have been published by Belfiore [8].

Furthermore, it is of interest to calculate the needed catalyst amount for achieving a desirable degree of waste gases purification. For this purpose, the experimental results obtained by isothermal laboratory reactor were used to simulate abatement of methane containing gases under adiabatic conditions.

a)

b)

c)
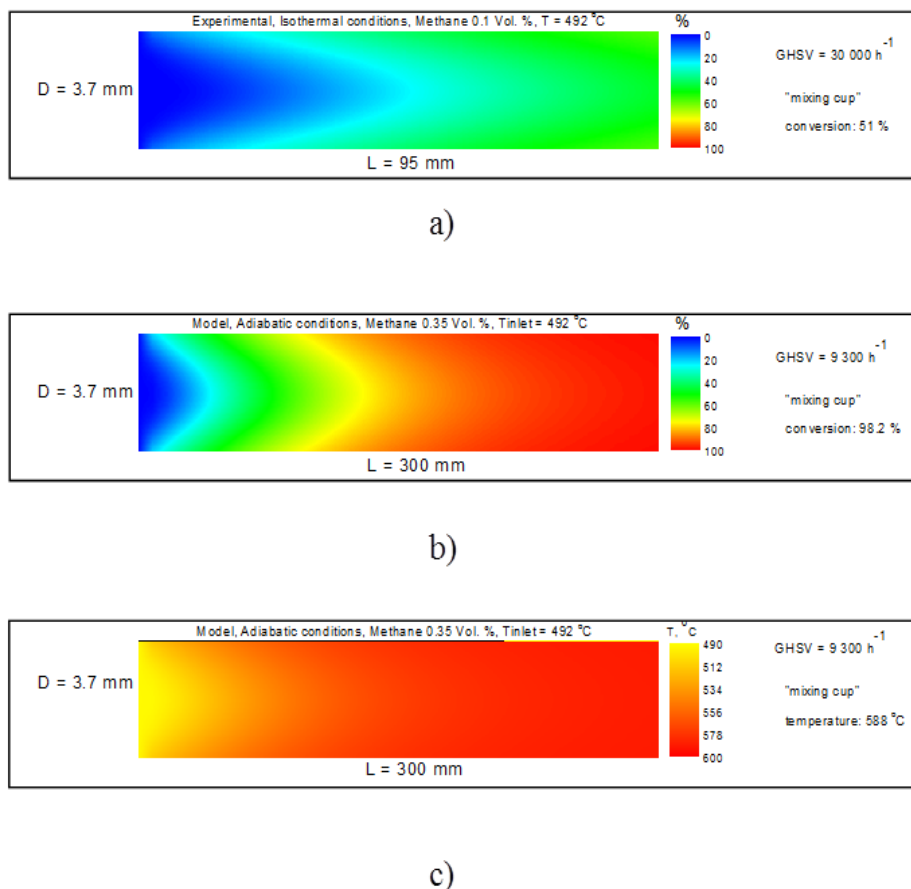
Fig. 3. Experimental data on $La(Co_{0.8}Ni_{0.1}Fe_{0.1})_{1-0.85}Pd_{0.15}O_3$/Aluchrom activity under isothermal conditions (a) and calculation of catalyst amount needed for 98.2% purification of waste gas (air) containing 0.35 vol.% methane under adiabatic conditions, (b), (c) – conversion and temperature profiles, respectively.

Due to adiabatic effect of the exothermal reaction (combustion of 0.35 vol.% methane), the temperature at reactor outlet was increased from 492 to 588 °C. Numerical investigation showed that desired conversion over 98% can be realized when the length of the monolithic element is about threefold longer than that used for laboratory experiments described above.

Experimental catalytic results and model calculations demonstrated benefits of the developed method for preparation of highly active catalysts for methane combustion.

CONCLUSIONS

Perovskite-based materials were successfully deposited on conventional γ-alumina and industrial metal carriers by impregnation using citrate solutions containing La, Co, Ni, Fe, and Pd elements. The nominal weight of deposited perovskites was 10 wt.% with respect to the support. Irrespective of support type, the average Pd content in the catalysts was almost the same: 1.7 ± 0.2 wt.% on γ-alumina support and 1.2 ± 0.5 wt.% on monolithic VDM®Aluchrom Y Hf carrier. A uniform distribution of the active phase was achieved over the γ-alumina support.

Preliminary data on the practical applicability of $La(Co_{0.8}Ni_{0.1}Fe_{0.1})_{0.85}Pd_{0.15}O_3$ material supported on monolithic VDM®Aluchrom Y Hf carrier were obtained. Considering the high thermal stability of the active phase it is concluded that the prepared catalyst composite is a basis for further development of an effective technology for abatement of methane emissions.

Established correlations concerned with synthesis history, structure, and morphology of the catalysts and their catalytic activities are of significance in order to design more effective monolith catalysts for the reaction of methane combustion at relatively low temperatures.

REFERENCES

1. European Commission Global Methane Reduction Actions, Ref. Ares (2013) 2843722 – 06/08/2013.
2. Federal Register/ Vol. 78, No. 63 / Tuesday, April 2, 2013 / Proposed Rules, Environmental Protection Agency, 40 CFR Part 98, 2013 Revisions to the Greenhouse Gas Reporting Rule and Proposed Confidentiality Determinations for New or Substantially Revised Data Elements.
3. Y. Nishihata, J. Mizuki, T. Akao, H. Tanaka, M. Uenishi, M. Kimura, T. Okamoto, N. Hamada, *Nature*, **418**, 164 (2002).
4. H. Tanaka, M. Taniguchi, M. Uenishi, N. Kajita, I. Tan, Y. Nishihata, J. Mizuki, K. Narita, M. Kimura, K. Kaneko, *Angewandte Chemie*, **45**, 5998 (2006).
5. V. G. Milt, S. Ivanova, O. Sanz, M. I. Domínguez, A. Corrales, J. A. Odriozola, M. Centeno, *Appl. Surf. Sci.*, **270**, 169 (2013).
6. S. Stanchovska, R. Stoyanova, E. Zhecheva, A. Naydenov, *Bulg. Chem. Commun.*, **49**, 107 (2017).
7. S. Stanchovska, P. Markov, K. Tenchev, R. Stoyanova, E. Zhecheva, A. Naydenov, *React. Kinet. Mech. Catal.*, **122**, 931 (2017).
L. A. Belfiore, Transport Phenomena for Chemical Reactor Design, John Wiley & Sons, Inc., (2003).

НАНЕСЕНИ ПАЛАДИЙ СЪДЪРЖАЩИ ПЕРОВСКИТОВИ КАТАЛИЗАТОРИ ЗА ПЪЛНО ОКИСЛЕНИЕ НА МЕТАН

С. Г. Станчовска[1], Д. Н. Гергова[2], Г. М. Иванов[1], Р. К. Стоянова[1], Е. Н. Жечева[1], А. И. Найденов[1]

[1] *Институт по обща и неорганична химия, БАН, ул. „Акад. Г. Бончев“, бл. 11, 1113 София, България*
[2] *Институт по физикохимия „Академик Ростислав Каишев“, БАН, ул. „Акад. Г. Бончев“, бл. 11, 1113 София, България*

(Резюме)

Методът на основата на цитратни разтвори е подходящ за получаване на многоелементни перовскити под формата на прахове и тънки слоеве. В това изследване показваме приложимостта на този метод за отлагане на перовскит-съдържащи материали върху конвенционални γ-алуминиеви и промишлени метални носители. Перовскитовият катализатор с номинален състав на активния компонент $La(Co_{0.8}Ni_{0.1}Fe_{0.1})_{0.85}Pd_{0.15}O_3$ показва висока каталитична активност в реакцията на изгаряне на метан. Представени са предварителни данни за практическата приложимост на катализатор с монолитен носител VDM®Aluchrom Y Hf. Благодарение на високата си термична стабилност, предложената активна фаза може да служи като основа за разработване на ефективна технология за намаляване на емисиите на метан.

Catalytic abatement of CO and VOCs in waste gases over alumina-supported Cu-Mn catalysts modified by cobalt

E. N. Kolentsova[1], D. Y. Dimitrov[1], D. B. Karashanova[2], Y. G. Karakirova[3], P. Ts. Petrova[3], T. T. Tabakova[3],*, G. V. Avdeev[4], K. I. Ivanov[1]

[1] Department of Chemistry, Agricultural University, 4000 Plovdiv, Bulgaria
[2] Institute of Optical Materials and Technologies, Bulgarian Academy of Sciences, 1113 Sofia, Bulgaria
[3] Institute of Catalysis, Bulgarian Academy of Sciences, 1113 Sofia, Bulgaria
[4] Institute of Physical Chemistry, Bulgarian Academy of Sciences, 1113 Sofia, Bulgaria

Production of formaldehyde by selective oxidation of methanol is an important industrial process. The main by-products in the waste gases are CO and dimethyl ether (DME). Currently, rational design of new catalytic materials with improved efficiency in the removal of air pollutants is a topic of appreciable research. The aim of this study was to combine advantages of both Cu-Mn and Cu-Co catalytic systems by obtaining a new mixed Cu-Mn-Co catalyst of high activity and selectivity in the simultaneous oxidation of CO, methanol, and DME. XRD, TEM, EPR and TPR techniques were used to characterise prepared samples.

Key words: Copper-manganese-cobalt catalyst, CO and VOCs oxidation.

INTRODUCTION

Catalytic oxidation is a widely applied and effective method of removing toxic components such as CO and volatile organic compounds (VOCs) emitted by transport activities, and petrochemical and chemical industries [1–4], including formalin production by selective oxidation of methanol [5]. Many studies have shown that precious metals such as Pt, Pd, Au, and Ag [2,3] demonstrate high activity at a relatively low temperature, but are more expensive and some of the problems associated with their industrial exploitation (such as low stability, particle agglomeration, and susceptibility to poisoning) limit their wide application. On the other hand, transition metal oxides (Fe_2O_3, Co_3O_4, NiO, Cr_2O_3, CuO, and MnO_2) are subject to significant studies [2,4,6]. Advantages of these catalysts are related to lower costs, but also to higher thermal stability and resistance to catalytic poisons, which is essential for their performance [4,7]. At low temperatures, they are less active than precious metal catalysts; however, some specific combinations of metal oxides may improve their activity in VOC elimination reactions [2]. For example, Faure *et al*. [8] have investigated Cu-Co catalysts for catalytic oxidation of model VOCs (toluene and ethyl acetate) prepared by the precipitation method. The results indicated the presence of synergistic effect between copper and cobalt in the mixed Cu-Co oxide catalysts, which showed a higher activity compared to copper oxide or cobalt oxide. According to the authors, finely divided copper particles on a Co_3O_4 surface especially in the Cu-Co spinel is the most likely reason of increased specific surface area and improved catalytic activity regarding VOC oxidation. According to other authors, mixed spinel-type Co-Mn oxides that have better oxidation properties than Co_3O_4 concerned with VOC complete oxidation [9] are produced by partial replacement of cobalt by manganese. Cu-Mn catalysts have also been shown to be effective in the oxidation reaction of CO [10–12], a wide range of VOCs [13–15], water-gas shift reaction [16], methanol steam reforming [17], etc. Own studies [15] have revealed that alumina-supported mixed Cu-Mn oxide catalysts manifest an increased activity with respect to the oxidation of CO, methanol and DME. A synergistic interaction between copper and manganese species was observed to increase the activity for total oxidation of tested toxic components compared to the activity of CuO/γ-Al_2O_3 and MnO_x/γ-Al_2O_3 catalysts. It has been found that carrier type, calcination temperature, and active phase composition are important factors influencing the catalytic activity [15]. Due to mentioned properties nanosized mixed spinel-type oxides have been extensively studied in recent decades [1,13]. Improved properties of mixed oxides against individual oxides are well known especially in environmental catalysis [1,15]. Spinel

materials, however, are quite sensitive to synthesis conditions, which may affect both morphological and structural properties [1,10]. Therefore, one of the major challenges associated with this type of material is to find appropriate preparation methods leading to defects in nanocrystalline particles, which may favour catalytic performance [1].

The main idea of this study is to combine advantages of the Cu-Mn and Cu-Co catalytic systems by producing new mixed Cu-Mn-Co oxide catalysts with spinel structure that exhibit high activity and selectivity for simultaneous oxidation of CO, methanol, and DME, which are waste products in formaldehyde production.

EXPERIMENTAL

Catalyst preparation

A copper-rich Cu-Mn/γ-Al$_2$O$_3$ sample of Cu/Mn molar ratio of 2:1 and a manganese-rich sample of Cu-Mn molar ratio of 1:5 were selected for this investigation. Manganese in these samples was replaced by cobalt in the entire concentration range. Catalyst preparation was carried out by impregnation of γ-alumina support (80 wt.%, fraction 0.6–1.0) with aqueous solution of copper, cobalt, and manganese nitrates of different composition. The total amount of active phase was 20 wt.%. Before impregnation, the carrier was calcined for 2 hours at 450 °C in a ceramic furnace. After keeping at room temperature, earlier prepared solutions of copper, manganese, and cobalt nitrates were added. The support remained immersed in the salt solution for 12 hours at 80 $^{\rm o}$C. After the impregnation, the samples were dried and calcined in the following sequence: drying for 12 h at room temperature, heating at 120 $^{\rm o}$C for 10 h, and raising the temperature at 10 $^{\rm o}$C/min to 450 $^{\rm o}$C where it was held for 4 hours.

Analytical techniques for sample characterisation

X-ray powder diffraction (XRD) patterns for phase identification were recorded on a Philips PW 1050 diffractometer equipped with Cu Kα tube and scintillation detector. Data on cell refinements were collected in θ-2θ step-scan mode in the angle interval from 10 to 90$^{\rm o}$ (2θ) at steps of 0.03$^{\rm o}$ (2θ) and counting time of 3 s/step. The cell refinements were obtained with PowderCell program. Size-strain analysis was carried out using BRASS-Bremen Rietveld Analysis and Structure Suite.

Transmission electron microscopy (TEM) measurements were performed by a JEOL JEM 2100 instrument at accelerating voltage 200 kV. Selected Area Electron Diffraction (SAED) was also

employed to gain information on the nature of the crystalline phases.

Temperature-programmed reduction (TPR) of the samples was carried out in a flow system under the following conditions: hydrogen-argon gas mixture (10 vol.% H$_2$), temperature ramp of 15 °C/min, flow rate of 24 ml/min, and sample amount of 0.05 g.

EPR spectra were recorded on a JEOL JES-FA 100 EPR spectrometer operating in X-band with standard TE$_{011}$ cylindrical resonator under the following conditions: modulation frequency of 100 kHz, microwave power of 1 mW, modulation amplitude of 0.2 mT, sweep of 500 mT, time constant of 0.3 s, and sweeping time of 4 min.

The catalytic measurements of single compounds oxidation were performed by continuous flow equipment with a four-channel isothermal stainless steel reactor containing 1.0 ml catalyst at atmospheric pressure and space velocity (GHSV) of 10000 h^{-1} allowing simultaneous examination of four samples under the same conditions. A flow of ambient air (40–50% humidity) and CO (final concentration of 2.0%), and mass flow controllers (GFC Mass Controller AABORG, Germany) were used. Liquid methanol was cooled to 0 $^{\rm o}$C in evaporator through which a stream of air was passed. Additional air was added after the evaporator to final concentration of methanol 2.0 vol.%. DME (final concentration 0.8–1.0 vol.%) was obtained by dehydration of methanol in nitrogen flow on γ-Al$_2$O$_3$ in tubular isothermal reactor. Gas mixtures at reactor inlet and outlet were analysed by means of a HP 5890 Series II gas chromatograph equipped with FID and TCD detectors, Porapak Q column (for methanol, CO$_2$, and DME), and MS-5A column (for CO, oxygen, and nitrogen).

RESULTS AND DISCUSSION

Powder X-ray diffraction

Samples of the Cu-Mn/γ-Al$_2$O$_3$ series of Cu/Mn ratio in the active phase of 2:1 or 1:5, in which manganese was partly or completely replaced by cobalt, were analysed by XRD. The samples were selected after evaluation of the catalytic behaviour in CO, methanol, and DME oxidation.

X-ray diffraction patterns of the Cu-Mn/γ-Al$_2$O$_3$ series samples with Cu/Mn in the active phase of 1:5 (a), in which manganese was replaced by cobalt (40, 60, and 100%), are shown in Fig. 1 (A). For comparison, XRD patterns of samples containing alumina-supported MnO$_2$ (e) or Co$_3$O$_4$ (f) as well as of the γ-Al$_2$O$_3$ support (h) are presented. The intensity of the peaks due to formation of separate phase

of Co_3O_4 (Ref. Code 98-015-0805) at $2\theta = 31.2$, 36.9, 44.7, 55.8, 59.5, and 65.5° increased upon increasing its amount, however, comparison with $Co_3O_4/\gamma\text{-}Al_2O_3$ sample (f) revealed a higher dispersion of the Co_3O_4 phase in the Cu-Mn-Co/γ-Al_2O_3 samples. Replacement of Mn by Co caused a significant decrease of the reflections of MnO_2 at $2\theta = 28.6$, 37.2, 42.8, and 56.5°.

XRD patterns of the Cu-Mn/γ-Al_2O_3 samples (Cu/Mn ratio of 2:1 or 1:5) in which manganese was completely replaced by cobalt are compared in Fig. 1 (B). The dominating reflections for the Co_3O_4 phase are well visible in the pattern of the sample of 1:5 ratio. The most intense reflections at $2\theta = 35.6$ and 38.8°, typical of CuO, were registered in the patterns of the Cu-Co sample of 2:1 ratio.

Transmission electron microscopy

Results of transmission electron microscopy of

Cu-Mn/γ-Al_2O_3 sample of Cu/Mn ratio of 1:5 modified with 60 wt.% Co are presented in Fig. 2. Phase identification of SAED patterns revealed the presence of a new spinel $CuCo_2O_4$ phase co-existing with Co_3O_4 (Table 1).

Table 1. Indexing of SAED patterns according to PDF 01-1155 for $CuCo_2O_4$ and PDF 78-1969 for Co_3O_4.

No	D, Å	hkl
1	2.85	(220) $CuCo_2O_4$
2	2.43	(311) $CuCo_2O_4$
3	2.02	(400) Co_3O_4
4	1.55	(511) $CuCo_2O_4$
5	1.42	(440) $CuCo_2O_4$

Co_3O_4 formation was in agreement with the results of XRD analysis. However, it was suggested that a low amount or rather high dispersion of the $CuCo_2O_4$ spinel phase was the reason for missing signal in the XRD patterns.
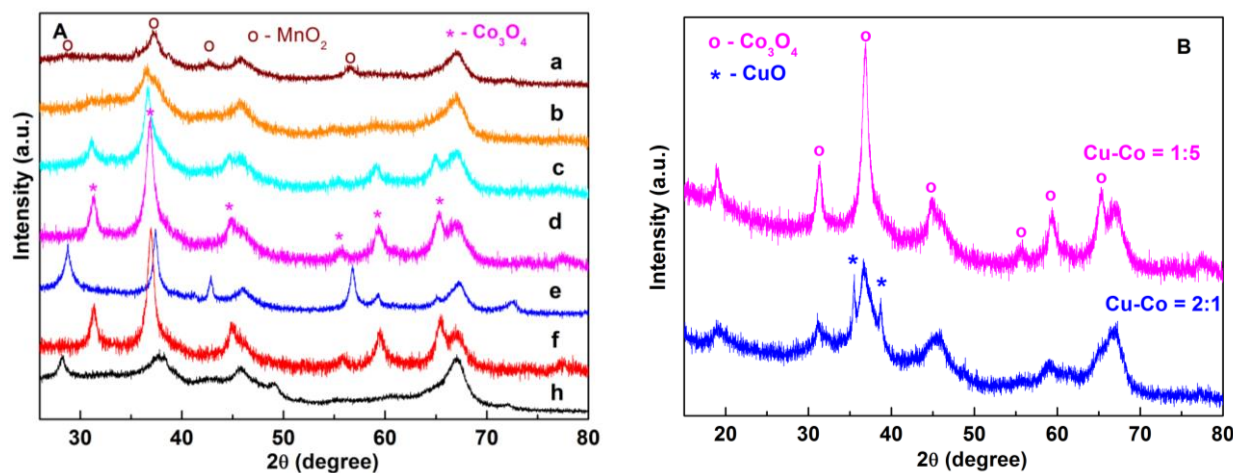
Fig. 1. XRD patterns of the studied samples: (section A) Cu-Mn/γ-Al_2O_3 catalysts of Cu/Mn ratio of 1:5 (a); after replacement of Mn by 40 wt.% Co (b); after replacement of Mn by 60 wt.% Co (c); after complete replacement of Mn by Co (d); MnO_2/γ-Al_2O_3 (e); Co_3O_4/γ-Al_2O_3 (f), and γ-Al_2O_3 (h); and (section B): Cu-Mn/γ-Al_2O_3 catalysts of Cu/Mn ratio of 1:5 and 2:1 after complete replacement of Mn by Co.
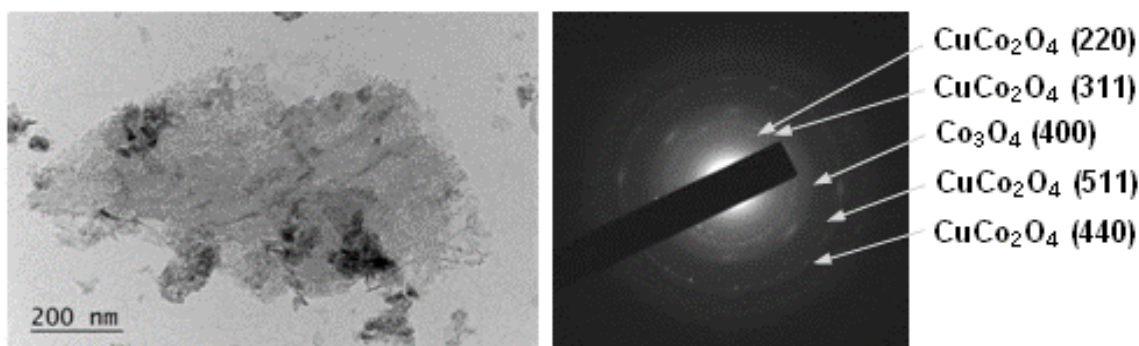
Fig. 2. TEM image and SAED pattern of Cu-Mn/γ-Al_2O_3 catalysts of Cu/Mn ratio of 1:5 (60% of Mn replaced by Co) at magnification 25000 x.

Electron paramagnetic resonance

Figure 3 (A) shows EPR spectra of Cu-Mn/γ-Al$_2$O$_3$ sample of Cu/Mn ratio of 2:1 and 1:5, and of modified samples prepared by replacing manganese by Co in various concentration from 40 to 100%. Due to coupling between electron spin and nuclear spin of the Cu^{2+} ions (S = 1/2, I = 3/2) an EPR spectrum with four parallel and four perpendicular hyperfine components could be expected. Despite this the signal showed a poorly resolved hyperfine splitting for the parallel band characteristic of isolated Cu^{2+} ions and unresolved for the perpendicular band. Parameters of the EPR spectra (g$_\parallel$, g$_\perp$, linewidth, and intensity) are listed in Table 2.

It was observed that the g-values remained constant upon increase of the Co concentrations from 40% to 60% in the Cu-Mn sample of 1:5 ratio. Similar parameters were found in the case of Cu-Mn (2:1) when manganese was completely replaced by cobalt. This result suggests that interactions among Cu and Co ions were rather weak which implied that they were randomly distributed in the Al$_2$O$_3$ matrix without clustering. A weak decrease in the g values of Cu-Mn (1:5) catalyst with manganese completely replaced by cobalt was related to changes in the chemical environment of the Cu ions in the presence of cobalt and probably due to a new phase formed between copper and cobalt ions.

EPR signal intensity (I) and linewidth ($_\Delta$H) parameters evolution of the EPR absorption for Cu-Mn (1:5) catalysts are shown in Fig. 3 (B). As seen, increased cobalt content in the samples leads to an increase of I. The increased signal intensity evidenced a higher total amount of Cu^{2+} ions. At the same time, ΔH decreased with increasing the cobalt

content of the studied samples and remained relatively constant for higher x values. This can be related to improved distribution of isolated Cu^{2+} ions. Comparing Cu-Co (2:1) and Cu-Co (1:5) intensities and linewidths it was observed that the linewidth of cooper-rich sample was higher than that of manganese-rich sample. This finding could be associated with interacting Cu^{2+} ions, which caused a decrease in the amount of isolated Cu^{2+} ions in Cu-Co (2:1) in agreement with decreased intensity of the EPR spectra. In many cases, the enhanced catalytic activity is explained by the presence of higher total amount of Cu^{2+} ions and increased amount of isolated Cu^{2+} ions. However, in this study such a relationship was not observed. It could be suggested that chemical composition, in particular presence of different amounts of Co$_3$O$_4$ and CuCo$_2$O$_4$, initiated a stronger effect on the catalytic properties.

Table 2. Calculated EPR parameters: *g*-factor, linewidth and intensity.

Samples	g$_\parallel$	g$_\perp$	ΔH, mT	I, a.u.
Cu-Co = 2:1	2.3567	2.0935	29.07	2225.60
Cu-Co = 1:5	2.3560	2.0896	25.39	3251.43
Cu:Mn 1:5 (Co 60%)	2.3567	2.0932	25.39	1862.00
Cu:Mn 1:5 (Co 40%)	2.3565	2.0934	25.47	1792.23

Temperature-programmed reduction (TPR)

Cu-Mn/γ-Al$_2$O$_3$ samples of Cu/Mn ratio of 2:1 or 1:5, in which manganese was partly or completely replaced by Co$_3$O$_4$, were studied by temperature-programmed reduction. Fig. 4 (A) shows TPR profiles of CuO-Co$_3$O$_4$/γ-Al$_2$O$_3$ samples of Cu/Co ratio of 2:1 and 1:5.
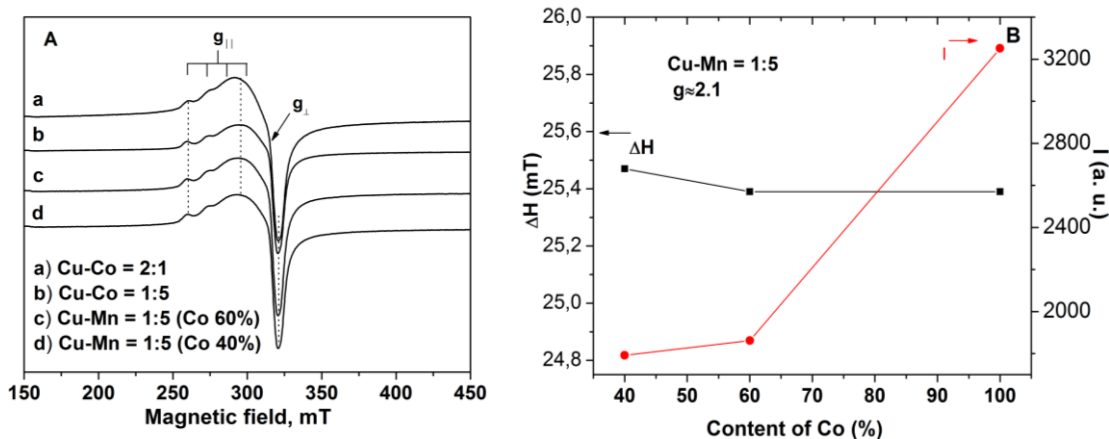
Fig. 3. (A) EPR spectra of Cu-Mn/γ-Al$_2$O$_3$ catalysts of Cu:Mn ratio of 2:1 and 1:5 after partial or total replacement of Mn with Co; (B) dependence of EPR signal intensity and linewidth on cobalt amount in Cu-Mn/γ-Al$_2$O$_3$ of Cu:Mn ratio of 1:5.

The TPR profile of alumina-supported Co_3O_4 is also given for comparison. An intense peak with T_{max} at about 217 °C registered for the Cu-Co (2:1) sample may be associated with reduction of CuO separate phase whose presence was confirmed by XRD analysis. A small shoulder on the higher-temperature side of the profile could be related to reduction of some of the available Co^{3+} ions in $CuCo_2O_4$. In the cobalt-rich Cu-Co (1:5) sample a complex profile with two maxima at 255 and 284 °C was recorded due to $Co_3O_4 \rightarrow CoO \rightarrow Co$ reductive transitions. The better reducibility of this sample was substantially facilitated by the presence of finely divided copper particles.

Fig. 4 (B) shows the TPR profiles of Cu-Mn/Al_2O_3 samples of Cu/Mn ratio of 1:5 in which Mn was completely replaced (Cu-Co) or partially replaced by 40 and 60 wt.% cobalt. The profile of unmodified Cu-Mn/γ-Al_2O_3(1:5) is given for comparison. There is an apparent tendency to shift the temperature maximum to a lower temperature because of partial replacement of Mn by Co (from 290 to 242 °C). Improved reducibility of these samples could contribute to higher catalytic activity.

Activity measurements

Fig. 5 displays results obtained in the complete oxidation of CO on Cu-Mn-Co/γ-Al_2O_3 samples of Cu-Mn ratio of 2:1 (A) and 1:5 (B) where manganese was replaced by cobalt over the entire concentration range from 0 to 100%. The results presented in Fig. 5 (A) indicate that the catalytic reaction started at a temperature of about 80 °C, and full oxidation was reached at 200 °C with all samples except Cu-Co (2:1) (containing 100% of cobalt). For samples containing cobalt within 0–60 wt.%, no clearly notable difference in catalytic acti-

vity was observed. The most significant difference in activity was found at 160 °C for samples of 1:5 ratio (Fig. 5, B). At this temperature, the sample modified by 60 wt.% cobalt exhibited over 80% conversion in CO oxidation, while the latter was only 10% over a sample in which manganese was completely replaced by cobalt. The results clearly show that manganese had a favourable effect on catalytic activity and its complete replacement played a negative role on activity. However, the copper-rich sample demonstrated better catalytic properties in the oxidation of CO and methanol. The registered temperatures for 50% conversion of CO (T_{50} = 170 °C) and methanol (T_{50} = 175 °C) were significantly lower than those for Cu-Co (1:5), T_{50} = 210 °C in the oxidation of CO and T_{50} = 200 °C in the oxidation of methanol, respectively. Comparison between the TPR profiles of these two samples revealed improved reducibility of the Cu-Co (2:1) sample and enabled correct explanation of the catalytic results.

Considering methanol oxidation, again no significant difference in activity of the tested samples was observed with both catalysts having a ratio of 2:1 (C) and 1:5 (D). The results demonstrated that full oxidation was achieved at T = 220 °C with all catalysts.

Regarding DME oxidation, there was a tendency of decreasing activity with the increase in cobalt content (Fig.5, E and F). In both groups of catalysts, the highest activity was exhibited by the unmodified samples, and this effect was more pronounced for catalysts of 2:1 ratio. Partial replacement of manganese by 60 wt.% cobalt in catalysts of 1:5 ratio led to a slight increase in activity probably due to formation of spinel structures in the active phase, which was confirmed by TEM measurements.
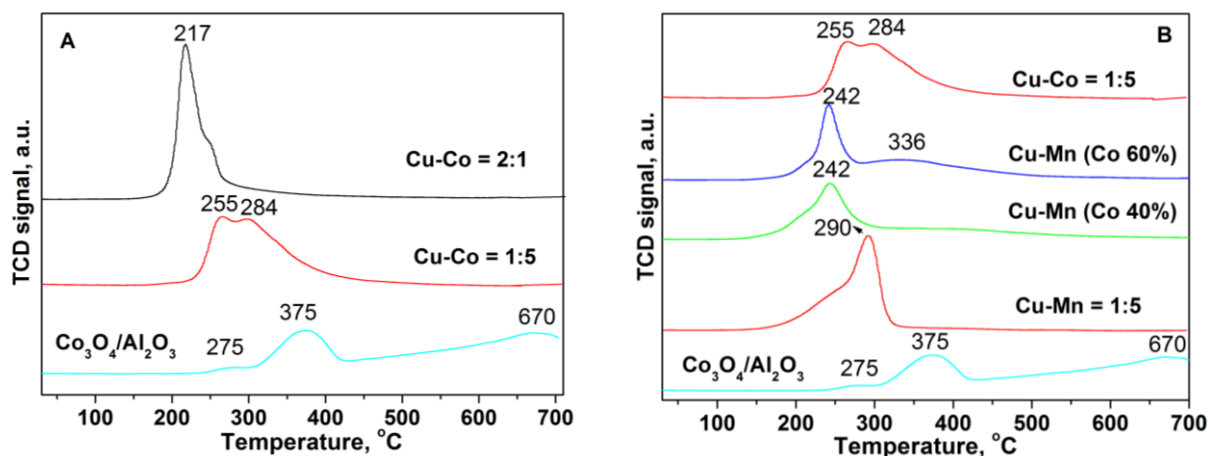
Fig. 4. TPR profiles of Cu-Co/γ-Al_2O_3 catalysts of Cu:Co ratio of 1:5 and 2:1 (A), and Cu-Mn/γ-Al_2O_3 catalysts of Cu:Mn ratio of 1:5 after partial or total replacement of Mn by Co (B).
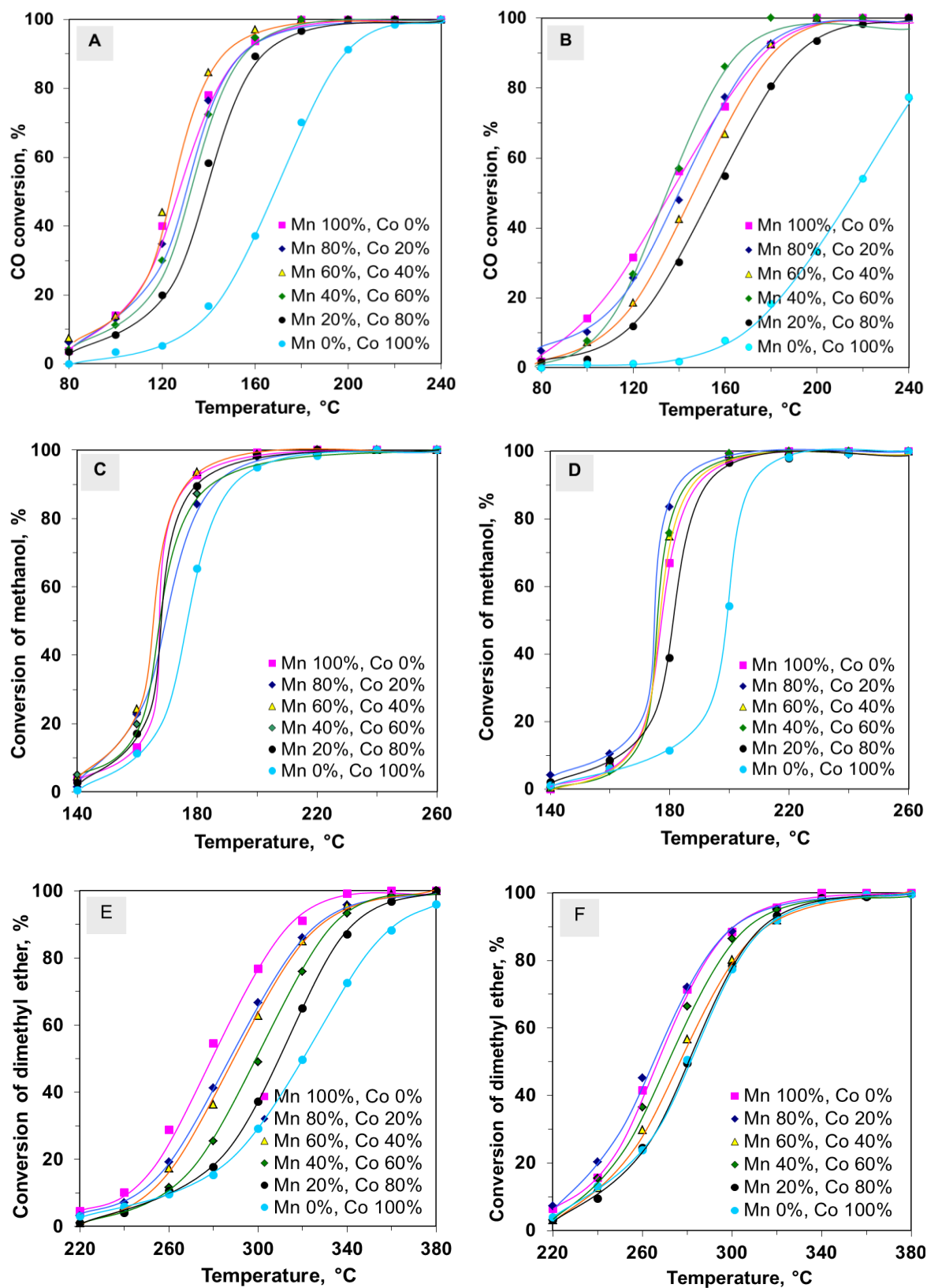
Fig. 5. Temperature dependence: CO oxidation over Cu-Mn-Co/γ-Al$_2$O$_3$ catalyst of Cu:(Mn+Co) ratio of 2:1 (A) and Cu-Mn-Co/γ-Al$_2$O$_3$ catalyst of Cu:(Mn+Co) ratio of 1:5 (B); methanol oxidation over Cu-Mn-Co/γ-Al$_2$O$_3$ catalyst of Cu:(Mn+Co) ratio of 2:1 (C) and Cu-Mn-Co/γ-Al$_2$O$_3$ catalyst of Cu:(Mn+Co) ratio of 1:5 (D); DME oxidation over Cu-Mn-Co/γ-Al$_2$O$_3$ catalyst of Cu:(Mn+Co) ratio of 2:1 (E) and Cu-Mn-Co/γ-Al$_2$O$_3$ catalyst of Cu:(Mn+Co) ratio of 1:5 (F).

.

Results of the catalytic measurements (Fig. 6, A and B) showed a general trend of increasing activity toward CO and methanol oxidation and decreasing activity toward DME oxidation with the increase of cobalt amount up to 60% for both groups of catalyst. This tendency, however, manifested specific features depending on catalyst composition and nature of the

oxidised gas. The catalytic activity of samples of Cu:(Mn+Co) ratio of 2:1 was gradually changed with increasing cobalt content. The activity of samples of Cu:(Mn+Co) ratio of 1:5 passed through a maximum for 60% manganese replacement by cobalt probably owing to formation of highly dispersed Co-based spinel structures (Co_3O_4 and $CuCo_2O_4$).
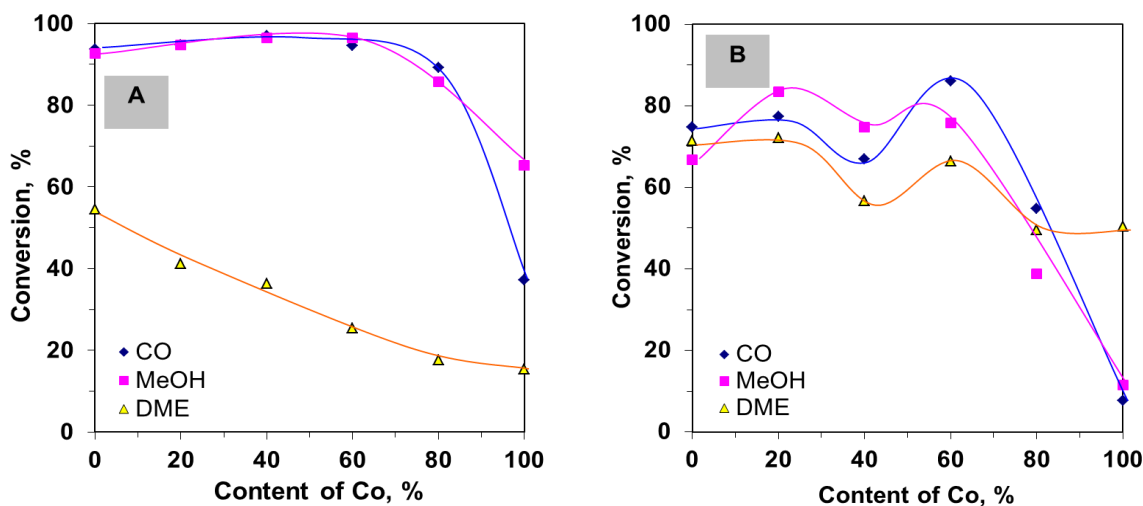
Fig. 6. Effect of manganese replacement by cobalt in Cu-Mn(Co)/γ-Al_2O_3 catalyst of Cu:(Mn+Co) ratio of 2:1 (A) and Cu:(Mn+Co) ratio of 1:5 (B) on CO, CH_3OH, and DME oxidation (T_{CO} = 160 ^{o}C, T_{MeOH} = 180 ^{o}C, T_{DME} = 280 ^{o}C).

CONCLUSIONS

The present study demonstrated that chemical composition strongly affected the catalytic properties, this effect being quite variable with regard to different processes. Successful oxidation of CO, CH_3OH, and DME was achieved over a sample of Cu-Mn ratio of 1:5 and partial replacement of manganese by 60 wt.% cobalt in the active component. Analysis of XRD and TEM data (including SAED) indicated at least three compounds in this sample: Co_3O_4, MnO_2, and $CoCu_2O_3$. Study of the effect of modification by cobalt upon variation of its content in Cu-Mn/γ-Al_2O_3 showed that a Cu-Mn-Co)/γ-Al_2O_3 composition of Cu:(Mn+Co) 1:5 ratio with 60 wt.% Co appeared beneficial for catalytic performance. The activity of the best-performing sample could also be related to improved reducibility.

REFERENCES

1. S. Hosseini, D. Salari, A. Niaei, F. Deganello, G. Pantaleo, Pejmanhojati, *J. Envir. Sci. Health*, Part A,

46, 291(2011).
2. A. Ulukardesler, *Energy Sources*, Part A, **35**, 1218 (2013).
1. G. Rattan, R. Prasad, R. C. Katyal, 21th Int. Conf. Thai Inst. Chem. Engn. Appl. Chem. (TIChE 2011), Hatyai, Songkhla, Thailand, 2011.
2. W. Tang, W. Li, D. Li, G. Liu, X. Wu, Y. Chen, *Catal. Lett.*, **144**, 1900 (2014).
3. T. Tsoncheva, K. Ivanov, D. Dimitrov, *Can. J. Chem.*, **5**, 583 (2011).
4. B. White, PhD Thesis, Graduate School of Arts and Sciences, Columbia University, New York (2007).
5. R. Prasad, P. Singh, *Catal. Rev.: Sci. Eng.*, **54**, 224 (2012).
6. B. Faure, P. Alphonse, *Appl. Catal. B*, **180**, 715 (2016).
7. S. Todorova, I. Yordanova, A. Naydenov, H. Kolev, Z. Cherkezova-Zhelev, K. Tenchev, B. Kunev, *Rev. Roum. Chim.*, **59**, 259 (2014).
8. E. C. Njagi, C. H. Chen, H. Genuino, H. Galindo, H. Huang, S. L. Suib, *Appl. Catal. B*, **99**, 103 (2010).
9. L. N. Cai, Y. Guo, A.-H. Lu, P. Branton, W.-C. Li, *J. Molec. Catal. A*, **360**, 35 (2012).
10. G. Hutchings, A. Mirzaei, R. Joyner, M. Siddiqui, S. Taylor, *Appl. Catal. A*, **166**, 143 (1998).
11. S. Behar, P. Gonzalez, P. Agulhon, F. Quignard, D. Srwierczynrski, *Catal. Today*, **189**, 35 (2012).
12. M. Morales, B. Barbero, L. Cadus, *Appl. Catal. B*, **67**, 229 (2006).
13. K. Ivanov, E. Kolentsova, D. Dimitrov, *Int. J. Chem.*

Molec. Nuclear Mater. Metallurg. Eng., **9**, 548 (2015).

14. K.-D. Zhi, Q.-S. Liu, Y.-G. Zhang, S. He, R.-X. He, *J. Fuel Chem. Technol.*, **38** (4), 445 (2010).

15. J. Papavasiliou, G. Avgouropoulos, T. Ioannides, *Catal. Commun.*, **6**, 497 (2005).

КАТАЛИТИЧНО ОЧИСТВАНЕ НА ОТПАДЪЧНИ ГАЗОВЕ ОТ CO И ЛЕТЛИВИ ОРГАНИЧНИ СЪЕДИНЕНИЯ ВЪРХУ Cu-Mn/γ-Al₂O₃ КАТАЛИЗАТОРИ МОДИФИЦИРАНИ С КОБАЛТ

Е. Н. Коленцова[1], Д. Я. Димитров[1], Д. Б. Карашанова[2], Й. Г. Каракирова[3], П. Цв. Петрова[3], Т. Т. Табакова[3]*, Г. В. Авдеев[4], К. И. Иванов[1]

[1] *Катедра „Обща химия", Аграрен университет, 4000 Пловдив, България*
[2] *Институт по катализ, Българска академия на науките, 1113 София, България*
[3] *Институт по оптични материали и технологии, Българска академия на науките, 1113 София, България*
[4] *Институт по физикохимия, Българска академия на науките, 1113 София, България*

(Резюме)

Производството на формалдехид чрез селективно окисление на метанол е важен промишлен процес. Основните странични продукти в отпадните газове са CO и диметилов етер (ДМЕ). Понастоящем дизайнът на нови каталитични материали с подобрена ефективност за отстраняване на замърсители на въздуха е предмет на значителни проучвания. Целта на това изследване е да се съчетаят предимствата на Cu-Mn и Cu-Co каталитични системи, като се получи нов смесен Cu-Mn-Co катализатор с висока активност и селективност за едновременно окисление на CO, метанол и ДМЕ. Катализаторните образци са охарактеризирани с рентгено-структурен анализ, трансмисионна електронна микроскопия, електронен парамагнитен резонанс и температурно-програмирана редукция.

Hexane and toluene oxidation on LaCoO₃ and YCoO₃ perovskite catalysts

M. Markova-Velichkova*, Ts. Lazarova, G. Ivanov, A. Naydenov, D. Kovacheva

Institute of General and Inorganic Chemistry, Bulgarian Academy of Sciences, 1113 Sofia, Bulgaria

Solution combustion technique was applied to prepare perovskite-type $LaCoO_3$ and $YCoO_3$ catalysts supported on α-Al_2O_3. X-ray diffraction and scanning electron microscopy were used for physicochemical and morphological characterisation of fresh and worked catalysts. Sample catalytic activity was studied with respect to complete oxidation of hydrocarbons (*n*-hexane and toluene). It was found that *n*-hexane is difficult to oxidise as compared to toluene. Reaction kinetics tests and experiments on so-called 'depletive' oxidation were conducted to establish reaction mechanism. Experimental results showed that Eley-Rideal and Mars-van Krevelen mechanisms were unlikely. The methods applied indicated that toluene complete oxidation on both catalysts proceeded *via* Langmuir-Hinshelwood mechanism by dissociative adsorption of oxygen, the reacting hydrocarbon and oxygen being adsorbed on different active sites. The result proved that lanthanum-containing samples exhibited a higher activity than yttrium catalysts. Different A-positioned cations of perovskite catalysts are discussed about their effect on structural, morphological, and catalytic properties.

Key words: perovskite catalyst, combustion synthesis, hydrocarbon oxidation.

INTRODUCTION

Perovskite-type oxides have been extensively studied over the last decades in terms of their application as catalysts in reactions of hydrocarbon oxidation. They possess some advantages such as low cost, stability at high temperature, and excellent catalytic activity [1–3]. Perovskites have been tested as catalysts for CO oxidation, oxidation of methane to syngas, oxidation of volatile organic compounds and CO + NO reactions [4–6]. Perovskite type oxides have general formula ABO_3. The structure is named after the naturally occurring mineral perovskite ($CaTiO_3$) and is usually described in pseudocubic form. This type of structure offers two positions for the cations. The cation with a large ionic radius (usually rare-earth or alkali-earth metal) occupies A site, while a cation with a smaller ionic radius (for example 3-d transition metal) occupies B site. The number of potentially interesting perovskites in the oxidation reactions is very great owing to the number of A and B cations that can be accomodated into this structure. Lattice distortion magnitude depends on the kind of A cations. In all cobalt-containing perovskites, the cobalt ion is surrounded by weakly distorted oxygen CoO_6 octahedra, whereas the rare-earth ions are situated in distorted cubo-octahedra formed of 12 oxygen ions. The coordination of A cation comprises 12 Ln-O bonds, three of them are long bonds, six are medium-length bonds, and the rest three are short bonds. Cell volume change follows lanthanide contraction. It is well established that on decreasing ionic radius of A cation the perovskite changes from higher to lower symmetry like from cubic to orthorhombic. An increasing rotation of the CoO_6 octahedra with decreasing A ionic radius reduces the Co-O-Co bond angles from 180° in ideal cubic perovskite to 164–146° in almost all $LnCoO_3$. On the other hand, the Co-O bond remains almost constant except for Ln = La with a broad maximum for lanthanide ionic radius about 1.1 Å. The crystal structure of $LaCoO_3$ is different from all other members of the $LnCoO_3$ series. At room temperature, $LaCoO_3$ has a rhombohedrally distorted cubic perovskite structure with unit cell belonging to the space group R-3c and two formulas per unit cell. Replacement of La^{3+} ion of smaller ionic radius by La^{3+} induces a chemical pressure on the CoO_3 array that allows cooperative rotations of CoO_6 octahedra, which relieve the compressive stress on the Co-O bond. Consequently, the Co-O bond length changes a little with ionic size [7]. The structure of $LnCoO_3$ perovskites is very sensitive to temperature changes. Structural distortion magnitude changes significantly with changes in temperature. Evolution of the structure of perovskite rare-earth cobaltites versus temperature governs their magnetic, catalytic, and transport properties. A neutron diffraction study of $LaCoO_3$ versus temperature [8] has shown that there is no deviation from the R-3c symmetry, but the bond lengths exhibit significant anomalies. Many synthesis procedures have been developed in order to produce perovskite mixed oxides of high specific surface area, namely

---

* To whom all correspondence should be sent
E-mail: markova@svr.igic.bas.bg

co-precipitation [9], citrate complexation [10], spray drying [11], freeze drying [12], flame hydrolysis [13], etc. As an alternative to the above-mentioned methods, solution combustion synthesis offers several attractive advantages such as short time to obtain final product, simplicity of laboratory procedures, high degree of homogeneity of the final product of small crystallite size, cheapness due to energy saving. Solution combustion synthesis has a special advantage of simultaneous synthesis of the desired ceramic phase and its adhesion to the support. In this work, solution combustion technique was applied to prepare perovskite-type $LaCoO_3$ and $YCoO_3$ catalysts supported on α-Al_2O_3. Catalytic activity measurements were performed in the reactions of complete oxidation *n*-hexane and toluene.

EXPERIMENTAL

Sucrose-assisted solution combustion method was applied to prepare $LaCoO_3$ and $YCoO_3$ catalysts [14,15]. La_2O_3 (Fluka) or Y_2O_3 (Merck) and $Co(NO_3)_2.6H_2O$ (Merck) were used as initial compounds. Stoichiometric amounts of matching oxide and cobalt nitrate were dissolved in distilled water. The rare-earth oxides were transformed into nitrate form by addition of certain amount of nitric acid. According to described method the nitrate solutions were further mixed with aqueous solution of sucrose at an oxidizing to reducing power ratio of corresponding nitrate and organic fuel of 1:1 [14,15]. The solutions were placed on a heating plate until evaporation of the water. After that, a foamy mass was formed, which burnt to produce an amorphous powder oxide material. As-prepared materials were thermally treated at 400 °C for 1 h in air. Then, the materials were ground for homogeneity. The final synthesis procedure included heat treatment of the catalysts in air at 700 °C for 1 h. At this temperature, the $LaCoO_3$ sample was a single phase, while $YCoO_3$ showed some residual Y_2O_3. Single phase $YCoO_3$ was obtained after additional grinding and heat treatment at 800 °C for 1 h. After the synthesis, a ball milling in a planetary mill for 1 h in isopropanol was applied to both perovskite samples. Spherical pellets of α-Al_2O_3 (with average diameter of 0.9 mm and negligible specific surface area) were used as support. The carrier was dipped into the suspension of perovskite phase and isopropanol. After dipping, the catalysts were dried at 100 °C and heated at 700 °C for 30 min. As a result, the active phase is regularly distributed on the external spherical surface of the support. Powder X-ray diffraction was used at every stage of perovskite phase

preparation as well as after deposition on the carrier and catalytic tests. Powder diffraction pat-terns were taken at room temperature on a Bruker D8 Advance diffractometer using CuK_α radiation and LynxEye detector. Measurement range was 10° to 80° 2θ with a step of 0.04° 2θ. XRD data were evaluated by means of EVA and TOPAS 4.2 program packages. SEM photographs of perovskite catalysts were made on a JEOL-JSM-6390 scanning electron microscope.

The catalytic measurements were carried out in a flow type reactor at atmospheric pressure. The test conditions (catalyst volume of 1.0 cm³, α-alumina spherical particles, fraction of 0.9 ± 0.1 mm, reactor diameter of 10.0 mm, quartz-glass, GHSV of 30000 h⁻¹) were selected after preliminary experiments by applying GHSV from 15000 h⁻¹ to 40000 h⁻¹. The measurements were compensated for adiabatic effect by keeping the reaction temperature measured at inlet and outlet of the catalyst bed within ±1 °C. Pressure drop was measured to be below 0.2 m water and was not taken into account. Therefore, the geometrical characteristics of the catalytic reactor permitted to consider it close to isothermal plug flow reactor. The inlet concentrations of reactants were varied as follows: hexane and toluene 115–715 ppm; oxygen 2–21 vol.%; all gas mixtures were balanced to 100% with nitrogen (4.0) and no additional water vapour was added to the gas mixtures. Experiments on so-called 'depletive' oxidation [16] were performed under the same conditions as for the kinetics tests. The nitrogen used for this experiment was of 99.99% purity. Gas analysis was carried out by on-line analysers of $CO/CO_2/O_2$ (Maihak) and THC (total hydrocarbon content, Horiba). A possible formation of organic by-products was monitored by model AL7890A GC-MS apparatus.

RESULTS AND DISCUSSION

Figures 1 and 2 present XRD powder patterns of two catalysts before and after catalytic tests. X-ray data on synthesized perovskites show that the active material is single phase without impurities. $LaCoO_3$ and $YCoO_3$ perovskites crystallize in rhombohedral R-3c space group, and orthorhombic Pnma space groups, respectively. The unit cell parameters of perovskite phases have values which are close to the literature data [ICDD PDF-2 (2009) Card No: $LaCoO_3$ – 48-0123, $YCoO_3$ – 75-7970]. Average crystallite sizes of as deposited catalysts were determined by TOPAS 4.2 program and are 63(3) and 88(4) nm for $LaCoO_3$ and $YCoO_3$, respectively (Figs. 1a, 2a). The results can be explained by different synthesis conditions needed to produce single-

phase perovskite materials. Powder XRD patterns of the catalysts manifested also diffraction peaks of the α-Al$_2$O$_3$ carrier. Rietveld quantification applied to the powder diffraction patterns revealed that active phase amount was 1.5 and 4.8 (±0.4) mass% for LaCoO$_3$ and YCoO$_3$, respectively (Figs. 1b, 2b). After catalytic tests a slight narrowing of the diffraction peaks was observed, which can be associated with increased crystallite size of the working catalysts (Figs. 1c, 2c).
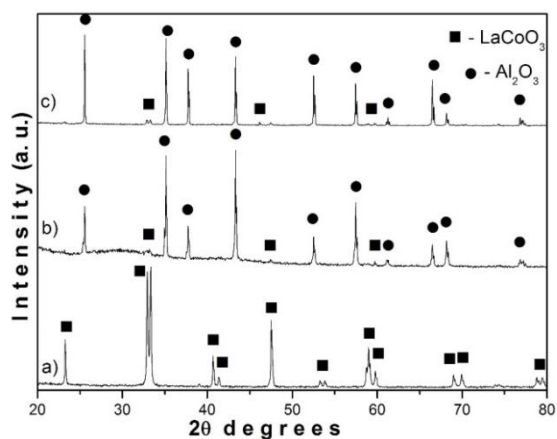
Fig. 1. XRD patterns of: a) initial LaCoO$_3$ perovskite, b) LaCoO$_3$ deposited on α-Al$_2$O$_3$, and c) LaCoO$_3$/α-Al$_2$O$_3$ catalytic tests.
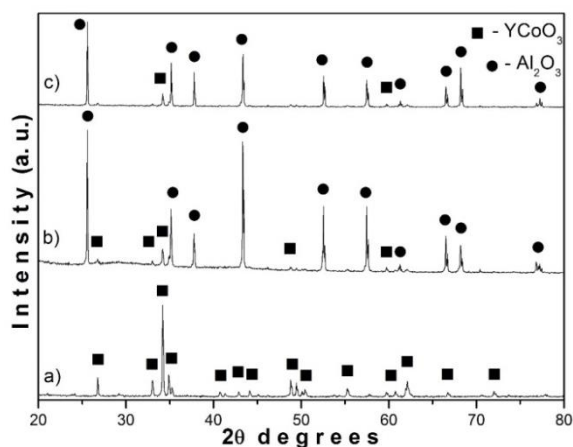
Fig. 2. XRD patterns of: a) initial YCoO$_3$ perovskite, b) YCoO$_3$ deposited on α-Al$_2$O$_3$, and c) YCoO$_3$/α-Al$_2$O$_3$ catalytic tests.

SEM images of different magnification of as-prepared catalysts are shown in figure 3. It is seen that deposition technique leads to uniform distribution of perovskite phase onto the surface of the carrier. Photographs of higher magnification revealed catalyst microstructure. Particles of the active phase at the surface are about 1–3 μm in size and many pores exist in the interstice among them. The specific surface area of both samples is about 10–15 m^2/g. A difference in particle morphology is also seen. For La sample, the shape of the particles is

predominantly plate-like, while the Y sample exposes aggregates of small grain-like particles.
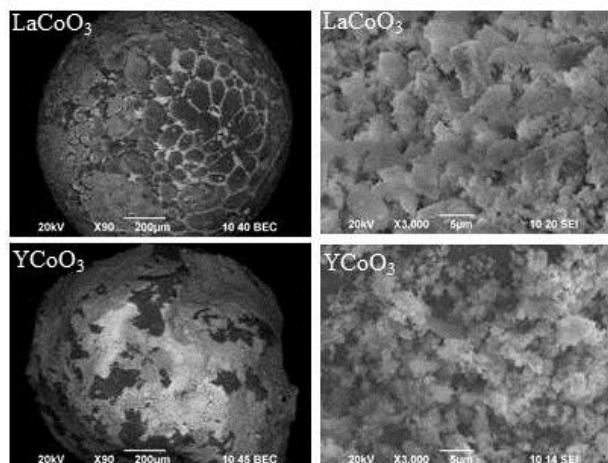
Fig. 3 SEM images of different magnification of the Al$_2$O$_3$-supported perovskite catalysts.

Results from catalytic activity measurements of complete oxidation of toluene and *n*-hexane are displayed in figures 4–6. Obviously, the activities of the two catalyst samples are very different, LaCoO$_3$ being more active than YFeO$_3$. An explanation for the significant difference in catalytic activity between LaCoO$_3$ and YCoO$_3$ should be found in structural peculiarities due to the presence of different A cations and their influence on perovskite phase stability and catalytic activity. In the present study difference between the two perovskite structures originates mainly from difference in A cation size, being 1.36 Å for La^{3+} and 1.075 Å for Y^{3+} of the same coordination. For comparison, the ionic radius of O^{2-} is 1.35 Å. Several factors have been proposed to evaluate the stability of the perovskite structures [17,18]. Based on crystal structure data on LaCoO$_3$ and YCoO$_3$, calculated tolerance factor, being equal to 1 for ideal perovskite structure, is 1.0112 for LaCoO$_3$ and 0.9049 for YCoO$_3$. As it can be seen the Y-containing perovskite has more deformed structure and smaller tolerance factor than the La-containing counterpart has. This means that the Y-containing structure is more unstable towards external mechanical, thermal, or chemical influence [19]. LaCoO$_3$ structure stability indicates that this oxide can easily accommodate certain amount of cation and anion defects without structural changes. It is well known that this compound can be synthesized with some deviation from stoichiometry [20]. Previous studies [21] revealed a clear distinction in thermal expansion between LaCoO$_3$ and YCoO$_3$. The Co-O-Co bond angles in YCoO$_3$ decrease with temperature above the onset of spin transition in contrast to LaCoO$_3$, where the Co-O-Co angles constantly increase with temperature. A more

active catalytic behaviour of $LaCoO_3$ can be ex-plained with less deformed (and less deformable) crystal structure compared to that of $YCoO_3$. The Co-O-Co bond angle of $YCoO_3$ is very small (about 148°) and practically remains stable up to 600 K, followed by a decrease with temperature above the onset of spin transition. This leads to a slightly larger expansion of the CoO_6 octahedra compared to lattice expansion. On the other hand, at room tem-perature the Co-O-Co bond angle in $LaCoO_3$ is about 164° and monotonically increases with tem-perature, which results in a slightly smaller expan-sion of the CoO_6 octahedra with respect to lattice expansion [21]. Such a different behaviour has been attributed to a higher symmetry of the $LaCoO_3$ structure compared to $YCoO_3$ (Pbnm) [19]. Cata-lytic tests showed that sample activity towards tolu-ene was significantly higher than that with hexane (Fig. 4) and further investigation was concentrated on toluene combustion.
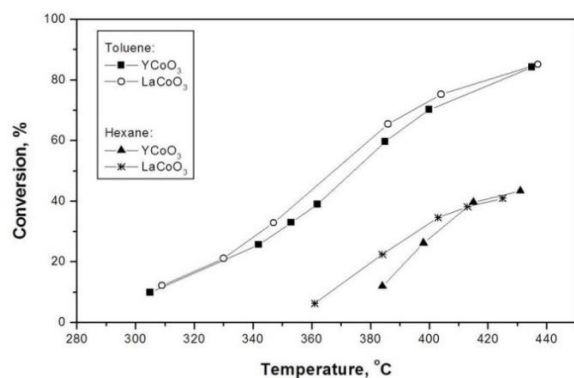
Fig. 4. Complete oxidation of toluene and hexane in air on alumina-supported $YCoO_3$ and $LaCoO_3$: effect of reaction temperature on hydrocarbon conversion degree.

For calculation of kinetics parameters, inlet con-centrations of both hydrocarbon and oxygen react-ants were varied. Concentration dependence on con-version leads to the conclusion that first order kine-tics should be excluded. An Eley-Rideal mechanism should not be considered since the reaction is not first order in oxygen. Regarding Mars-van Krevelen mechanism (oxi-redox) bulk oxygen from the active phase must take part in the reaction. In order to find out which mechanism is more probable, experi-ments on so-called 'depletive' oxidation were per-formed [16]. The latter involve measurements of the formation of oxidation products (CO and CO_2) when oxygen supply to the gas mixture is stopped after achieving stationary conditions at a temperature for 33% conversion. The reason for these experiments is to find out whether oxygen from the catalyst participates in the oxidation process. Results from the 'depletive' oxidation are presented in figure 5.
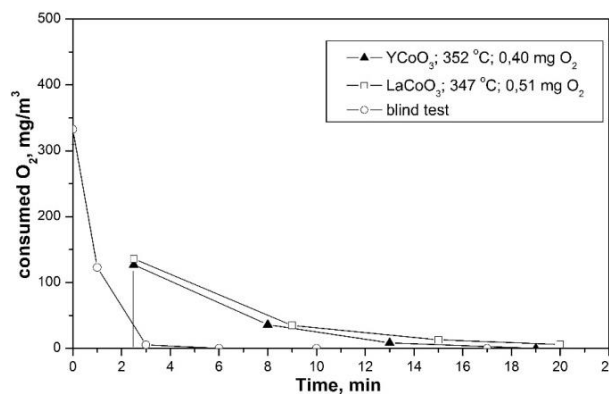
Fig. 5. 'Depletive' oxidation at temperatures for 33% conversion of toluene.

Following termination of the oxygen supply to the gas feed, formed amount of $CO+CO_2$ in each test was calculated from the area under the transient curves. The surface or lattice oxygen, which takes part in the reaction, was estimated based on formed $CO+CO_2$ quantities during 'depletive' oxidation, experiment duration being 20 min. Very small amounts of surface or lattice oxygen (0.3–0.5 mg, below 1.5% of active phase) and the absence of phase transformations after the catalytic tests reveal that bulk oxygen from the active phase is not involved in the reaction, i.e. the Mars-van Krevelen mechanism should not be considered likely. Finally, power law kinetics (PWL) and four mechanistic models (Langmuir-Hinshelwood, bimolecular reac-tion, surface reaction being the rate-determining step) were fitted with the experimental data. Fitting of the kinetics parameters was performed applying of an integrated computer program for simultaneous solu-tion of the material balance in isothermal plug flow reactor and numerical nonlinear optimization pro-cedure based on iterative gradient reduction. For finding a global minimum, residuals squared sum (RSS) between experimental data and model pre-dictions was minimized upon starting from several different initial values of the varying parameters. As an additional measure, the absence of trends in the RSS distribution was controlled and the square of correlation coefficient (R^2) was calculated.

Two Langmuir-Hinshelwood models assume that the hydrocarbon and the oxygen are adsorbed on different sites and oxygen adsorption is non-disso-ciative (LH-DS-ND) or dissociative (LH-DS-D). Other two LH models suppose competitive adsorp-tion of hydrocarbon and oxygen on one-type sites and non-dissociative (LH-OS-ND) or dissociative (LH-OS-D) adsorption of oxygen. Kinetics parame-ters are given in Table 1.

Table 1. Reaction rate expressions and kinetics parameters for applied power law and Langmuir-Hinshelwood models

PWL

$$r = kP_{voc}^m P_{ox}^n$$

Catalyst	k_o	E_a	m	n			RSS	R^2
YCoO$_3$	1.35E+06	75 656	0.29	0.33			2.05	0.99
LaCoO$_3$	2.36E+06	78 260	0.31	0.19			1.79	0.99

LH-DS-ND

$$r = \frac{kK_{voc}K_{ox}P_{voc}P_{ox}}{(1+K_{voc}P_{voc})(1+K_{ox}P_{ox})}$$

Catalyst	k_o	E_a	$k_{o,voc}$	ΔH_{voc}	$k_{o,ox}$	ΔH_{ox}	RSS	R^2
YCoO$_3$	5.41E+06	93720	2.71E-03	-60644	2.40E+01	-1269	3.77	0.975
LaCoO$_3$	2.74E+07	101219	7.95E-05	-77677	2.80E+02	+7396	1.12	0.992

LH-DS-D

$$r = \frac{kK_{voc}P_{voc}K_{ox}^{1/2}P_{ox}^{1/2}}{(1+K_{voc}P_{voc})(1+K_{ox}^{1/2}P_{ox}^{1/2})}$$

Catalyst	k_o	E_a	$k_{o,voc}$	ΔH_{voc}	$k_{o,ox}$	ΔH_{ox}	RSS	R^2
YCoO$_3$	3.80E+07	99839	4.21E-04	-70751	1.03E-01	-15724	2.22	0.985
LaCoO$_3$	6.46E+07	104294	4.72E-05	-80584	1.12E+00	-16995	0.75	0.995

LH-OS-ND

$$r = \frac{kK_{voc}K_{ox}P_{voc}P_{ox}}{(1+K_{voc}P_{voc}+K_{ox}P_{ox})^2}$$

Catalyst	k_o	E_a	$k_{o,voc}$	ΔH_{voc}	$k_{o,ox}$	ΔH_{ox}	RSS	R^2
YCoO$_3$	5.06E+07	97888	9.44E-03	-51410	1.87E-03	-45118	6.52	0.960
LaCoO$_3$	7.56E+06	87572	4.08E-02	-45523	1.71E-05	-73715	4.65	0.967

LH-OS-D

$$r = \frac{kK_{voc}K_{ox}^{1/2}P_{voc}P_{ox}^{1/2}}{(1+K_{voc}P_{voc}+K_{ox}^{1/2}P_{ox}^{1/2})^2}$$

	k_o	E_a	$k_{o,voc}$	ΔH_{voc}	$k_{o,ox}$	ΔH_{ox}	RSS	R^2
YCoO$_3$	2.27E+08	101208	3.87E-03	-52372	6.30E-04	-37006	2.41	0.984
LaCoO$_3$	9.49E+07	99285	4.37E-04	-65667	1.97E-01	-20287	1.01	0.993

E_{ai}, J/mol; ΔH_i, J/mol; k_{oi}, atm^{-1}; $k = k_o \cdot \exp(-E_a/RT)$; $K_i = k_{o,(voc,ox)} \cdot \exp(-\Delta H_{i,voc,ox}/RT)$; $\Delta H_i = E_{ad} - E_{des}$

Figure 6 displays model consistency as a difference between standard measurement error of conversion and RSS.
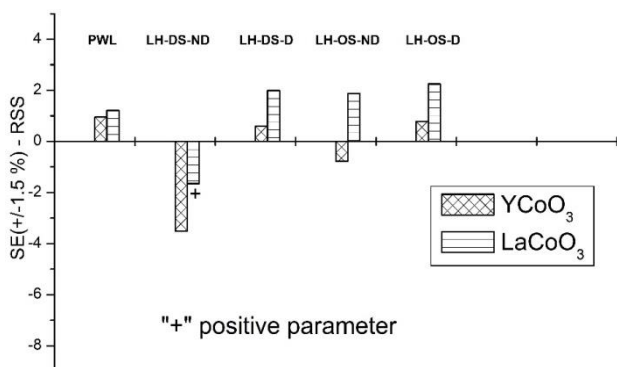
Fig. 6. Consistency of model prediction with catalytic test errors.

Evidently, four of the models (PWL, LH-DS-ND, LH-DS-D, LH-OS-D) are consistent with measurement confidence interval, while LH-OS-ND should be considered non-satisfactory. In addition, the latter model suggests non-dissociative adsorption of the oxygen. With one of the models (LH-DS-ND and LaCoO$_3$) the obtained value for ΔH of the oxygen adsorption is positive, which has no physical sense and is a reason to reject this model. It is obvious that a fit that is more adequate was obtained with the models which predict dissociative adsorption of oxygen. Among considered Langmuir-Hinshelwood models, the values for RSS with LH-DS-D are the lowest, which can be taken as supplementing information to conclude that the hydrocarbons and oxygen are adsorbed on different sites and oxygen adsorption is dissociative.

CONCLUSIONS

Two perovskite-type catalysts (LaCoO$_3$ and YCoO$_3$, supported on α-Al$_2$O$_3$ spherical particles) were synthesized *via* sucrose-assisted solution combustion method. Mean crystallite size varied between 63(3) nm for LaCoO$_3$ and 88(4) nm for YCoO$_3$. Catalytic activity measurements with respect to complete oxidation of hydrocarbons (*n*-hexane and toluene) showed that aliphatic hydrocarbon was found to be difficult to oxidize, while with aromatic compound (toluene) a promising activity was observed. LaCoO$_3$ more active catalytic behaviour of could be explained by less deformed (and less

deformable) crystal structure compared to YCoO$_3$. It can be concluded that the reaction of complete oxidation of toluene on perovskite-type catalysts (LaCoO$_3$ and YCoO$_3$, supported on α-Al$_2$O$_3$) proceeds *via* Langmuir-Hinshelwood mechanism with dissociative adsorption of oxygen, the reacting hydrocarbon and oxygen being adsorbed on different sites.

REFERENCES

1. R. Zhang, H. Alamdari, S. Kaliaguine, *Appl. Catal. B: Environ.,* **72**, 331 (2007).
2. M. Natile, E. Ugel, C. Maccato, A. Glisenti, *Appl. Catal. B: Environ.*, **72**, 351 (2007).
3. S. Hosseini, M. Sadeghi, A. Alemi, A. Niaei, D. Salari, L. Kafi-Ahmadi, *Chin. J. Catal.*, **31**, 747 (2010).
4. E. Arenolt, A. Maione, A. Klisinska, A. Sanz, M. Montes, S. Shares, J. Blanco, *Appl. Catal. A: General,* **339**, 1 (2008).
5. G. Pecchi, P. Reyes, R. Zamora, C. Campos, L. Cadus, B. Barbero, *Catal. Today*, **133-135**, 420 (2008).
6. J. Dacquin, C. Lancelot, C. Dujardin, P. Da Costa, G. Djega-Mariadassou, P. Beaunier, S. Kaliaguine, S. Vaudreuil, S. Royer, P. Granger, *Appl. Catal. B: Environ.*, **91**, 596 (2009).
7. J.-S. Zhou, J.-Q. Yan, J. B. Goodenough, *Phys. Rev. B*, **71**, 220103(R), (2005).
8. G. Maris, Y. Ren, V. Volotchaev, C. Zobel, T. Lorenz, T. T. M. Palstra, *Phys. Rev. B*, **67**, 224423 (2003).
9. P. K. Gallagher, *Mater. Res. Bull.*, **3**, 225, (1967).
10. H.-M. Zhang, Y. Teraoka, N. Yamazoe, *Chem. Lett.*, 665 (1987).
11. R. J. H. Voorhoeve, D. W. Johnson, J. P. Remeika, P. K. Gallagher, *Science*, **195**, 827 (1977).
12. J. Kirchnerova, D. Klvana, *Int. J. Hydrogen Energy*, **19,** 501 (1994).
13. R. A. M. Giacommuzi, M. Portinari, I. Rossetti, L. Forni, *Stud. Surf. Sci. Catal.*, **130**, 197 (2000).
14. S. Biamino, C. Badini, *J. Eur. Ceram. Soc.*, **21**, 3021 (2004).
15. S. Biamino, P. Fino, D. Fino, N. Russo, C. Badini, *Appl. Catal. B: Environ.*, **61**, 297 (2005).
16. C. Brooks, *J. Catal.*, **8**, 272 (1967).
17. A. Mineshige, M. Inaba,T. Yao, Z. Ogumi, *J. Solid State Chem.*, **121**, 423 (1996).
18. J. E. Sunstrom IV, K. V. Ramanujachary, M. Greenblatt, M. Croft, *J. Solid State Chem.*, **139**, 388 (1998).
19. M. James, D. Cassidy, D. J. Goossens, R. L. Withers, *J. Solid State Chem.*, **177**, 1886 (2004).
20. J. Mira, J. Rivas, M. Vázquez, J. M. García-Beneytez, J. Arcas, R. D. Sánchez, M. A. Señarís-Rodríguez, *Phys. Rev. B*, **59**, 123 (1999).
21. P. G. Radaelli, S.-W. Cheong, *Phys. Rev. B*, **66**, 094408 (2002).

ОКИСЛЕНИЕ НА ХЕКСАН И ТОЛУЕН ВЪРХУ LaCoO₃ И YCoO₃ ПЕРОВСКИТОВИ КАТАЛИЗАТОРИ

М. Маркова-Величкова*, Ц. Лазарова, Г. Иванов, А. Найденов, Д. Ковачева

Институт по обща и неорганична химия, Българска академия на науките, 1113 София, България.

(Резюме)

Перовскитови LaCoO₃ и YCoO₃ катализатори бяха синтезирани по метода на изгаряне от разтвор и нанесени на α-Al₂O₃ носител. Физикохимично и морфологично охарактеризиране на получените и работили катализатори беше извършено с методите рентгенова дифракция и сканиращата електронна микроскопия. Каталитичната активност е изследвана по отношение на пълното окисление на въглеводороди (хексан и толуен). Установено е, че хексанът се окислява по-трудно в сравнение с толуена. Реакционният механизъм беше изследван с кинетични тестове и чрез опити върху така нареченото „деплетивно" окисление. Получените резултати показват, че механизмите на Ели-Ридиъл и Марс-ван Кревелен не са вероятни, а най-висока степен на предвиждане на опитните резултати се постига при прилагане модела на Лангмюр-Хиншелуд (дисоциативна адсорбция на кислород, реагиращите въглеводород и кислород се адсорбират на различни активни центрове). От сравнителен анализ е установено, че пробата, съдържаща лантан, притежава по-висока активност, отколкото тази, съдържаща итрий. Дискутирана е ролята на различните катиони в А позиция върху структурните, морфологични и каталитични свойства на перовскитовите катализатори.

Nanosized mesoporous titania composites promoted with ceria and zirconia as catalysts for ethyl acetate oxidation: effect of preparation procedure

G. S. Issa[1]*, M. D. Dimitrov[1], D. G. Kovacheva[2], T. S. Tsoncheva[1]

[1] *Institute of Organic Chemistry with Centre of Phytochemistry, Bulgarian Academy of Sciences, Acad. G. Bonchev St., Bldg. 9, 1113 Sofia, Bulgaria,*

[2] *Institute of General and Inorganic Chemistry, Bulgarian Academy of Sciences, Acad. G. Bonchev St., Bldg. 11, 1113 Sofia, Bulgaria*

The aim of the current investigation was to develop a series of titania-based nanosized mesoporous binary materials promoted with Ce and Zr and to test them as catalysts for total oxidation of ethyl acetate. Metal oxide materials were synthesised by template-assisted hydrothermal approach and homogeneous precipitation with urea. The main aspect of the study was to find a relationship between preparation procedure and structure, texture, surface, and catalytic properties of the obtained materials. These materials were characterised by low temperature nitrogen physisorption, XRD, Raman and UV-Vis spectroscopy, and temperature-programmed reduction with hydrogen. The hydrothermal method enabled formation of mesoporous materials of better homogeneity as compared to urea-synthesised counterparts where certain microporosity was registered as well. Doping agents affected preparation procedures. Improved texture parameters of ZrTi binary oxides obtained by the hydrothermal technique facilitated their catalytic activity as compared to urea analogues. Just an opposite effect of preparation was observed for CeTi materials.

Key words: mesoporous catalysts, Ce-pomoted titania, Zr-promoted titania, ethyl acetate oxidation.

INTRODUCTION

Volatile organic compounds (VOCs) are important environmental pollutants produced from refineries, fuel storage and loading operations, motor vehicles, solvent cleaning, printing and painting operations [1]. VOCs are regarded as critical precursors for the potential formation of tropospheric ozone and photochemical smog. Examples of common VOCs are ethyl acetate, benzene, toluene, acetone, and ethanol [2]. In particular, ethyl acetate is one of the most common VOCs, used in printing operations, glues, and nail polish removers, often employed as a model compound for VOCs oxidation [3,4]. Catalytic oxidation seems to be very promising for VOCs elimination. Practical realisation of each of these catalytic processes requires the development of effective catalysts remarkable not only for their activity, stability, and selectivity, but for their low cost and ability to operate at relatively low temperatures. In recent years, efforts in this direction were focused on obtaining new porous materials based on transition metal oxides [5]. Improved methods for their synthesis have led to new materials of different morphology, high specific surface area, and well developed porous structure. These materials contain pores of different size, shape, and topology, and in some cases functionalise the surface of the metal oxide to acquire tunable surface properties [5−10]. Moreover, multicomponent nanosized metal oxide materials are subject of even greater interest for improving their properties via exhibited synergism among the individual components, i.e. one of the metal oxides may change the properties of another one because of electronic and structural impacts. Recently titania has received much attention owing to its non-toxicity, chemical and biological inertness, availability, and low cost. Preparation of nanodisperse mesoporous titania and its doping with different metal oxides provide good opportunities not only for improved catalytic behaviour, but also for formation of new stable composites, which could manifest completely different physicochemical and catalytic properties [6]. Titania-ceria materials represent undoubted interest due to an important role of the cerium dopant to decrease particle size, and to cause a strong effect on metal oxide reducibility, high degree of synergistic interaction between components, and favourable modification of structural and catalytic properties [8]. It has been established that isomorphous substitution of cerium ions into the TiO_2 lattice generates oxygen vacancies, which stabilise the anatase phase, increases the specific surface area and the dispersion of the metal oxide particles [8]. It has been demonstrated that addition

---

* To whom all correspondence should be sent
E-mail: *Issa@abv.bg*

of zirconia to titania can significantly increase surface acidity by formation of OH groups and the acid-base properties can be substantially influenced by the Ti/Zr ratio [9]. It has been shown that individual components in these binary oxides interact to form $ZrTiO_4$ [9]. The aim of this investigation is to obtain nanosized mesoporous ceria-titania and zirconia-titania binary materials and to test them as catalysts for complete oxidation of ethyl acetate. The materials were synthesised by template-assisted hydrothermal approach (HT) and homogeneous precipitation with urea (U). A principal aspect in the study was to find a relationship between preparation procedure and structure, texture, and catalytic properties of the obtained materials.

EXPERIMENTAL

Mono and bi-component titania, ceria, and zirconia materials were synthesised by hydrothermal procedure (HT) using cetyltrimethylammonium bromide (CTAB) as a structure-directing template [10] and by homogeneous precipitation with urea (U) [11]. Samples were denoted as xCeyTi M and xZryTi M, where x/y was metal to mol ratio, which in the bi-component samples was 5:5, and M was the preparation method used. Textural characteristics were acquired from nitrogen adsorption-desorption isotherms measured at 77 K using a Coulter SA3100 instrument. Powder X-ray diffraction patterns were collected on a Bruker D8 Advance diffractometer with Cu Kα radiation using a LynxEye detector. UV-Vis spectra were recorded on a Jasco V-650 UV-Vis spectrophotometer. Raman spectra were registered on a DXR Raman microscope applying a 780-nm laser. TPR/TG analyses were performed on a Setaram TG92 instrument in a flow of 50 vol.% H_2 in Ar. Catalytic oxidation of ethyl acetate (EA) was conducted in a flow type reactor with a mixture of EA and air. Gas chromatographic analyses were made on a HP 5890 apparatus using carbon-based calibration

RESULTS AND DISCUSSION

Table 1 presents nitrogen physisorption data on ceria-titania and zirconia-titania materials. Addition of zirconia or ceria to TiO_2 led to an increase of both specific surface area and pore volume. The urea-prepared materials exhibited up to 5 times lower values of pore volume as compared to the HT samples due to mainly smaller mesopores and to a certain amount of micropores because of interparticle interaction. The best texture characteristics were registered for 5Zr5Ti obtained by hydrothermal method. Thus, the development of mesoporous structure was strongly dependent on the preparation technique. The latter was mostly controlled by the organic template during the hydrothermal procedure and by interparticle interaction on using urea for homogeneous precipitation. These effects were better pronounced for the binary oxides.

Table 1. Nitrogen physisorption and XRD data of CeTi and ZrTi materials.

Sample	Phase composition	Unit cell parameters, Å	Cristallite size, nm	S_{BET}, m²g⁻¹	V_t, cm³g⁻¹
TiO_2 HT	anatase, syn tetragonal body-centred I41/amd	3.7861 9.493	17	85	0.29
TiO_2 U	anatase, syn tetragonal body-centred I41/amd	3.7855 9.507	13	97	0.19
CeTi HT	cerium oxide face-centred cubic Fm-3m	5.403	12	99	0.45
CeTi U	anatase, syn tetragonal body-centred I41/amd cerium oxide face-centred cubic Fm-3m	3.770 9.51 5.401	5 7	117	0.30
CeO_2 HT	cerium oxide face-centred cubic Fm-3m	5.416	10	46	0.26
CeO_2 U	cerium oxide face-centred cubic Fm-3m	5.4144	13	76	0.07
ZrTi HT	amorphous			248	0.69
ZrTi U	amorphous			204	0.16
ZrO2 HT	tetragonal ZrO_2	3.591 5.183	13	67	0.32
	monoclinic ZrO_2	5.303 5.163 5.197 β = 99.17	14		
ZrO2 U	tetragonal ZrO_2	3.6006 5.1859	30	2	0.02

81

Figure 1 displays XRD patterns of both series of samples, while phase composition, unit cell parameters, and average crystallite size are shown in Table 1. The diffraction peaks in the pattern of TiO_2 HT and TiO_2 U at 25.5°, 38.2°, 47.8°, 54.3°, and 62.8° 2θ are indexed to a pure anatase phase of titania with average crystallite size of about 8 nm and 13 nm, respectively (Table 1) [6].

The XRD patterns of both CeO_2 samples consist of intensive diffraction peaks at 28.5°, 33.1°, 47.6°, 56.5°, and 59.2° 2θ. They are indexed to a face-centred fluorite type structure [7] with average crystallite size of 10−13 nm. Ceria with average crystallite size of 12 nm was only registered for CeTi HT, while a mixture of anatase and ceria with average crystallite size of 5 and 7 nm, respectively, was found for CeTi U. A slight decrease in unit cell parameters accompanied with an increase of the ceria average particle size as compared to the individual CeO_2 sample was observed. This could be evidence for a Ce-O-Ti interface layer formation *via* incurporation of smaller Ti^{4+} ions in the ceria [8]. The XRD patterns of pure zirconia samples showed strong reflections at $2\theta = 30.17°$, 49.81°, 50.07°, and 60.15° that are typical of the crystalline planes of tetragonal zirconia phase. Additional reflections at $2\theta = 28.19°$, 31.48°, 34.19°, 45.52°, 49.26°, and 54.1° for ZrO_2 HT correspond to the crystalline planes of monoclinic zirconia (Figure 1b) [9]. The average crystallite size of zirconia was 13−14 nm for the hydrothermally obtained sample and about 30 nm for the urea one, which indicates that the former technique is more appropriate to prepare nanodispersed zirconia. Despite the preparation method used, XRD patterns of mixed ZrTi oxides demonstrate a broad hump, which is typical of amorphous materials. Here, a plateau in the XRD patterns indicates the formation of very finely dispersed oxides, which well correlates with an extremely high surface area for these materials (Table 1).
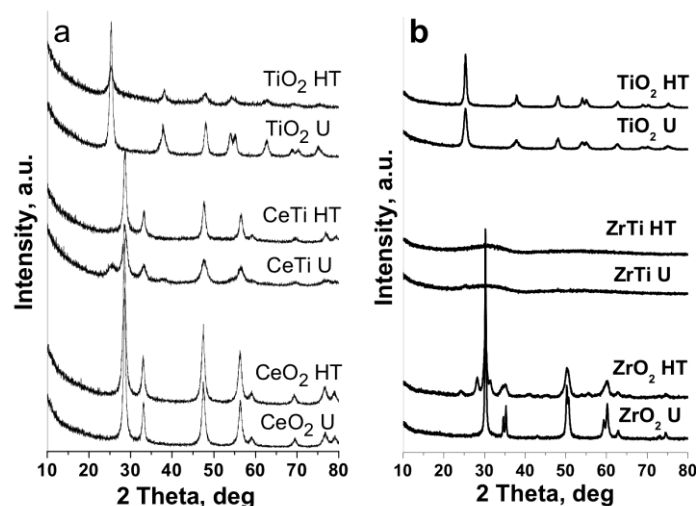
Fig. 1. XRD patterns of CeTi (a) and ZrTi (b) materials.

The UV-Vis spectra of both series of samples prepared by hydrothermal and urea treatment are displayed in Figures 2a and 2b. A strong absorption feature in the spectra of both titania samples at 350 nm is typical of anatase [12], which is also consistent with the XRD data. The UV-Vis spectra of pure CeO_2 HT and CeO_2 U demonstrate absorption at 240, 285, and 330 nm which can be attributed to $O_2 \rightarrow Ce^{3+}$ charge transfer (CT), $O_2 \rightarrow Ce^{4+}$ CT, and interband transitions, respectively (Fig. 2a) [13]. The latter band is related to defect lattice sites as well. A shift of the main absorption edges with both individual cerium oxides indicates higher dispersion for the hydrothermally obtained materials.

Changes in the 350–500 nm region of both bi-component CeTi materials confirm the assumption made above of strong interaction between metal ions and/or increase in metal oxide dispersion (Fig. 2a). The spectra of both zirconia samples show two absorption bands at around 208 and 230 nm as expected for m-ZrO_2 (Fig. 2b). The second feature in the spectra at absorption threshold position around 320 nm reveals coexistence of t-ZrO_2 [14]. In consistence with the XRD data (Fig. 1b, Table 1) a slight red shift in the position of the main feature for ZrO_2 HT and appearance of additional absorption bands at about 300 and 450 nm could be assigned to higher dispersion of the zirconia phase. The overall absorption of mixed ZrTi materials is significantly higher as compared to pure zirconia samples. The observed features could not be simply assigned to superposition of the spectra of the single metal oxides. According to Ref. [15] and in consistence with nitrogen physisorption and XRD

results these features could be attributed to formation of amorphous phase and modification of the titania lattice because of Zr^{4+} ion incorporation.

Figure 3 gives Raman spectra of CeTi materials prepared by various procedures. Raman shifts at 143, 195, 396, 514, and 637 cm^{-1} in the spectra of both titania samples demonstrate presence of pure anatase phase (Fig. 3a) [16]. Anatase bands at 396 and 639 cm^{-1} are ascribed to Ti−O stretching vibrations and to Eg mode of O−Ti−O bending vibration, res-

pectively [16]. Only one Raman-active F2g mode, centred at about 463 cm^{-1}, which is typical of cubic structure, was detected for both ceria materials (Fig. 3b) [8,17]. The appearance of second less prominent and broad band at about 600 cm^{-1} is usually assigned to defect-induced longitudinal optical mode of ceria due to formation of oxygen vacancies [17]. The main Raman active mode is broader for ceria prepared by urea technique, which in accordance with the XRD data could be due to a decrease of crystallite size.
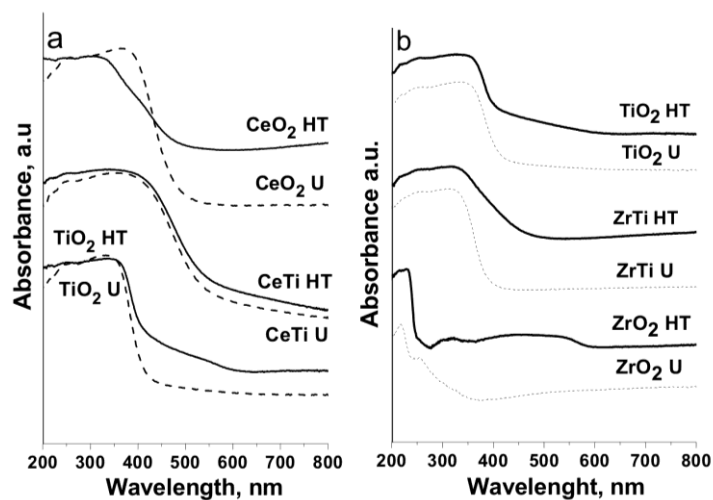
Fig. 2. UV-Vis spectra of CeTi (a) and ZrTi (b) materials, prepared by urea (dash lines) and template hydrothermal (solid lines) methods.
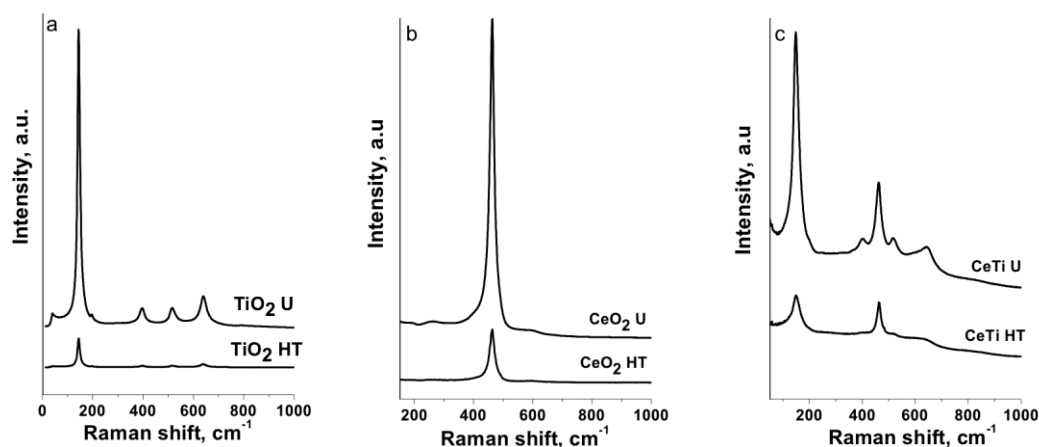
Fig. 3. Raman spectra of titania (a), ceria (b), and CeTi (c) materials.

The Raman spectra of binary oxides reveal that they represent a mixture of ceria and anatase phases, the latter being of higher amount for the urea-prepared sample (Fig. 3c), which is in agreement with the XRD data. A slight blue shift of the Raman E1g mode to 150 cm^{-1} could indicate changes in the environment of titanium ions in anatase lattice. A shift of the main signal to higher wavenumber values with the bi-component samples is due to shortening of the Ce−O bond because of incorporation of

titanium ions into the cerium oxide lattice. E1g band widening could be attributed to a decrease of crystallite size, which is in accordance with reported XRD and UV-Vis data.

Figure 4 shows Raman spectra of the obtained ZrTi samples. The bands at 142, 270, 317, 458, and 643 cm^{-1} in both spectra of ZrO_2 are compatible to tetragonal zirconia (Fig. 4a) [18]. In consistence with the XRD study additional Raman bands at 176, 192, 478, and 612 cm^{-1} in the spectrum of ZrO_2 HT

indicate co-existence of monoclinic zirconia.

Not well defined peaks are visible in the Raman spectra of ZrTi samples, which can be attributed to the amorphization of the crystal structure and increased concentration of defects arising from the incorporation of zirconium ions in titania and/or to the significant particle size decrease (Fig. 4b). The observed slight shifting and broadening of the main Raman-active mode of anatase accompanied with a decrease in its intensity could be assigned to metal oxide bonds shortening and formation of smaller crystallites with defect structure due to the replacement of titanium ions with zirconium ones.

TPR-TG profiles of hydrothermally synthesised and urea-precipitated CeTi samples were compared in the 500–750 K region (not shown). A weight loss agreed with reduction of Ce^{4+} to Ce^{3+}, being about 10 and 4% for CeO_2 HT and CeO_2 U, respectively. Reduction started at a lower temperature with the bi-components samples and the effects were larger in comparison with the pure ceria samples. In accord-ance with other physicochemical measurements, an increased mobility of lattice oxygen in these materials could be due to increased dispersion as well as owing to distortion of the ceria lattice during titanium incorporation. The reduction behaviour of the mixed materials was not simply related to their specific surface area. Thus, a facile reduction of the hydrothermally obtained samples is probably related to their higher dispersion, well-developed mesoporous structure, and homogeneous phase composition. Not all zirconia-containing samples manifested reduction ability in the studied temperature interval.

Figure 5 gives temperature dependencies of total oxidation of EA on various materials. Temperatures at which a 50% conversion over various samples was achieved are compared in Table 2. Beside CO_2, which is the most important product of EA oxidation, (Fig. 5b), ethanol, acetaldehyde, acetic acid, and ethene were also registered as by-products. All materials were catalytically active above 500−525 K, and 80−100% conversion was achieved at 600−670 K
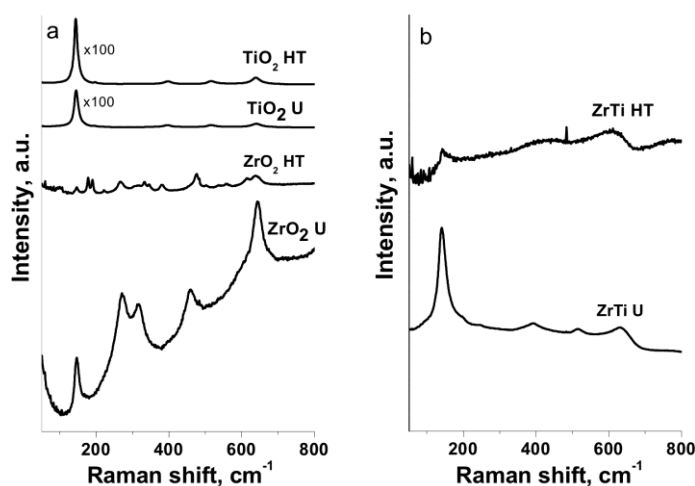
Fig. 4. Raman spectra of zirconia and titania (a) and ZrTi (b) materials.
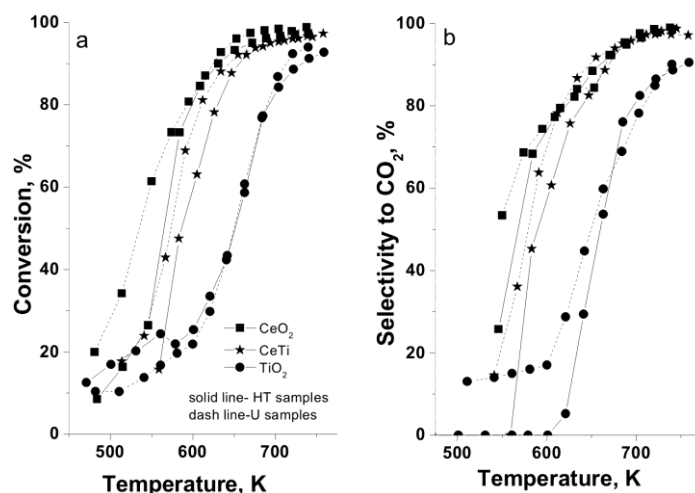
Fig. 5. Ethyl acetate conversion (a) and selectivity to CO_2 (b) of CeTi materials.

(Fig. 5a). Titania exhibited a notably low catalytic (Table 2) activity combined with high ability to form by-products, mainly acetaldehyde, ethanol, and ethane. Just the opposite, both mono-component ceria samples manifested high activities, but low selectivity to CO_2 due to the formation of ethanol as by-product (Table 2). Ceria-titania binary materials possessed a lower catalytic activity as compared to pure CeO_2 (Table 2, Fig. 5a) and a higher selectivity for total oxidation of ethyl acetate to CO_2 which could be due to improved redox ability. A common feature was a higher activity of all urea-precipitated materials as compared to their hydrothermally prepared analogues.

Table 2. Temperatures for 50% conversion of ethyl acetate and specific catalytic activity for CeTi and ZrTi materials

Sample	$T_{50\%}$, K	SA, EA mol.m^{-2}	Sample	$T_{50\%}$, K	SA, EA mol.m^{-2}
TiO_2 HT	660	0.29	TiO_2 HT	650	0.56
TiO_2 U	651	0.23	TiO_2 U	650	0.52
CeTi HT	586	0.60	ZrTi HT	629	0.26
CeTi U	574	0.65	ZrTi U	660	0.21
CeO_2 HT	560	1.74	ZrO_2 HT	650	0.78
CeO_2 U	535	1.09	ZrO_2 U	713	1.7

To ignore any effect of different specific surface area of the samples (Table 1), specific catalytic activity (SA) was calculated as conversion at a selected temperature per unit surface area (Table 2). Here, the urea samples exhibited lower or similar SA to the HT analogues indicating that the observed catalytic behaviour was strongly related to increased surface area during urea synthesis.

Figure 6a presents temperature dependencies of catalytic activity in ethyl acetate oxidation for the ZrTi materials. The mono-component zirconia sample exhibited the lowest activity, a relatively low selectivity of ethyl acetate oxidation to CO_2, and formation of significant amount of ethanol as by-product (Fig. 6b). This was probably due to a higher hydrolysis degree of ethyl acetate on the acid/base sites of zirconia, which is generally assumed as a first step in ethyl acetate oxidation [19]. The bicomponent samples manifested a higher catalytic activity and CO_2 selectivity than the corresponding mono-component materials (Fig. 6a). Taking into account the physicochemical data, we ascribe this result to a specific interaction between the individual oxides and increased surface area of the mixed oxide materials. The catalytic activity of the hydrothermally prepared composites was higher as compared to the urea samples.
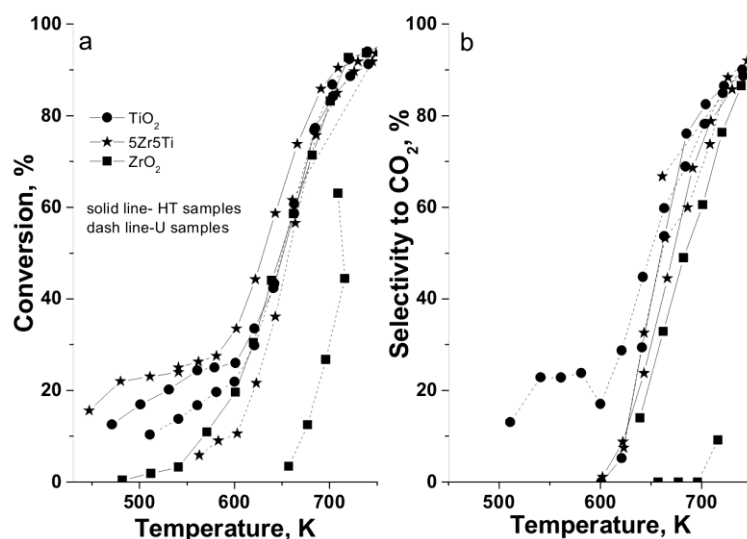
Fig. 6. Ethyl acetate conversion (a) and selectivity to CO_2 (b) of ZrTi materials.

The binary materials showed a lower specific catalytic activity as compared to the individual metal oxides (Table 2). In accordance with the XRD, UV-Vis, and Raman data, significant changes in the nature of the active sites due to incorporation of zirconium ions into titania lattice could be proposed and this could be successfully controlled by the preparation procedure used.

CONCLUSIONS

Highly dispersed titania doped with ceria and zirconia materials were successfully prepared by using a template-assisted hydrothermal procedure and homogeneous precipitation with urea. The effect of the preparation technique on the properties of the obtained binary titania-based materials was depend-

ent on the nature of dopant. In the case of ceria doping, the template-assisted hydrothermal synthesis facilitated formation of more homogeneous materials, but exhibiting lower dispersion and lower specific surface area. This provided a lower catalytic activity for complete oxidation of ethyl acetate. In contrast, the zirconia dopant significantly improved the texture characteristics of titania and enhanced the catalytic activity of hydrothermally synthesised materials.

REFERENCES

1. W. G. Tucker, Digital Engineering Library, @ McGraw-Hill, New York, 2004.
2. F. I. Khan, A.K. Ghoshal, *J. Loss Prev. Process Ind.*, **13**, 527 (2000).
3. S. Akram, Z. Wang, L. Chen, Q. Wang, G. Shen, N. Han, Y. Chen, G. Ge, *Catal. Commun.*, **73,** 123 (2016).
4. S. Carabineiro, M. Konsolakis, G. Marnellos, M. Asad, O. Soares, P. Tavares, M. Pereira, J. Órfão, J. Figueiredo, *Molecules*, **21,** 644 (2016).
5. S. Yuesong , Z. Dahai, Y. Bo, N. Songbo, Z. Shemin, *J. Rare Earths*, **30**, 431 (2012).
6. M. Altomare, M. Dozzi, G. Chiarello, A. Paola, L. Palmisano, E. Selli, *Catal. Today*, **252**, 184 (2015).
7. D. W. Wheeler, I. Khan, *Vib. Spectrosc.*, **70**, 200 (2014).
8. J. Fang, X. Bi, D. Si, Z. Jiang, W. Huang, *Appl. Surf. Sci.*, **253**, 8952 (2007).
9. B. Neppolian, Q. Wang, H. Yamashita, H. Choi, *Appl. Catal. A: Gen.*, **333,** 264 (2001).
10. T. Tsoncheva, I. Genova, M. Dimitrov, E. Sarcadi-Priboczki, A. M. Venezia, D. Kovacheva, N. Scotti, V. dal Santo, *Appl. Catal. B: Environ.,* **165**, 599 (2015).
11. J. Subrt, V. Stengl, S. Bakardjieva, L. Szatmary, *Powder Technol.*, **169**, 33 (2006).
12. M. N. Iliev, V. G. Hadjiev, A. P. Litvinchuk, *Spectroscopy*, **64**, 148 (2013).
13. A. Kambolis, H. Matralis, A. Trovarelli, Ch. Papadopoulou, *Appl. Catal. A: Gen.*, **377**, 16 (2010).
14. S. Damyanova, B. Pawelec, K. Arishtirova, M. V. Martinez Huerta, J. L. G. Fierro, *Appl. Catal. A: Gen.*, **337,** 86 (2008).
15. M. Fernàndez-García, A. Martínez-Arias, J. C. Hanson, J. A. Rodriguez, *Chem. Rev.*, **104**, 4063 (2004).
16. K. C. Silva, P. Corio, J. J. Santos, *Vib. Spectrosc.,* **86**, 103 (2016).
17. D. R. Sellick, A. Aranda, T. García, J. M. López, B. Solsona, A. M. Mastral, D. J. Morgan, A. F. Carley, S. H. Taylo, *Appl. Catal. B: Environ.*, **132–133**, 98 (2013).
18. W. Zhu, N. Sugano, G. Pezzotti, *J. Biomed. Opt.*, **18**, 127 (2013).
19. P.-O. Larsson, A. Andersson, *Appl. Catal. B: Environ.*, **24**, 175 (2000).

ВЛИЯНИЕ НА МЕТОДА НА ПОЛУЧАВАНЕ ВЪРХУ ФОРМИРАНЕТО НА НАНОСТРУКТУРИРАНИ МЕЗОПОРЕСТИ CeO$_2$-TiO$_2$ И ZrO$_2$-TiO$_2$ КАТАЛИЗАТОРИ ЗА ПЪЛНО ОКИСЛЕНИЕ НА ЕТИЛАЦЕТАТ

Г. С. Исса[1], М. Д. Димитров[1], Д. Г. Ковачева[2], Т. С. Цончева[1]

[1] *Институт по органична химия с Център по фитохимия, БАН, 1113 София, България*
[2] *Институт по обща и неорганична химия, БАН, 1113 София, България*

(Резюме)

Цел на настоящото изследване е получаване на наноразмерни мезопорести смесени материали на основата на промотиран с Ce и Zr титанов оксид и тестването им като катализатори в реакция на пълно окисление на етилацетат. Получените оксиди бяха синтезирани чрез хидротермален синтез в присъствието на органичен темплейт и хомогенно утаяване с карбамид. Основен аспект в изследването е изясняване на връзката между използвания метод на получаване и текстурата, структурата и окислително-редукционните свойства на получените материали. Образците бяха характеризирани чрез физична адсобция на азот, рентгеноструктурен анализ, UV-Vis и Раманова спектроскопия, както и температурно програмирана редукция. Хидротермалният метод благоприятства формирането на мезопорести и по-хомогенни материали в сравнение със синтезираните с карбамид образци, където се регистрира и известна микропористост. Ефектът от процедурата на получаване зависи от вида на металооксидната добавка към TiO$_2$. Подобрените текстурни характеристики на смесените ZrTi оксиди, получени чрез хидротермален метод благоприятстват тяхната каталитична активност в сравнение с получените с карбамид аналози. Точно обратният ефект се наблюдава при CeTi материалите.

Synthesis, structure, and catalytic properties of $SrFe_{12}O_{19}$ hexaferrite

K. V. Koleva[1]*, N. I. Velinov[1], I. G. Genova[2], T. S. Tsoncheva[2], V. S. Petkova[3,4]

[1] Institute of Catalysis, Bulgarian Academy of Sciences, 1113 Sofia, Bulgaria

[2] Institute of Organic Chemistry with Centre of Phytochemistry, Bulgarian Academy of Sciences, 1113 Sofia, Bulgaria

[3] Institute of Mineralogy and Crystallography, Bulgarian Academy of Sciences, 1113 Sofia, Bulgaria

[4] New Bulgarian University, Department of Natural Sciences, 21 Montevideo St., 1618 Sofia, Bulgaria

M-type $SrFe_{12}O_{19}$ hexaferrites were synthesised by means of co-precipitation method followed by annealing at 600 °C and 850 °C. A portion of a sample, treated at 850 °C, was further subjected to high-energy ball milling for 1 and 5 hours. TG-DTG-DTA, X-ray powder diffraction, and ^{57}Fe Mössbauer spectroscopy were used for samples characterisation. A well-crystallised $SrFe_{12}O_{19}$ hexaferrite phase and small amount of secondary hematite (α-Fe_2O_3) phase were observed after annealing at 850 °C. Changes in the structure and a decrease in crystallite size of $SrFe_{12}O_{19}$ from 47 nm to 22 nm were observed after one-hour ball-milling treatment. Prolongation of the milling time induced separation of hematite phase and the highest amount was achieved after 5 hours of treatment. All samples exhibited good catalytic activity and CO selectivity in methanol decomposition. Mössbauer study of catalytically tested materials demonstrated stability of the hexaferrite phase under reductive reaction conditions.

Key words: M-type hexaferrites, Mössbauer spectroscopy, methanol decomposition.

INTRODUCTION

Hexaferrite materials are in the focus of many investigations due to their superior electrical and magnetic properties. The M-type $SrFe_{12}O_{19}$ hexaferrite material has hexagonal crystal structure of $P6_3/mmc$ space group. This structure is built by divalent alkaline earth metals, such as Sr, Ca or Ba, and Fe^{3+} ions that occupied tetrahedral (4f1), octahedral (12k, 2a, 4f2), and hexahedral (2b) crystallographic sites in the oxygen lattice.

Different methods for preparation of hexaferrite powders, such as sol-gel [1], sol-gel auto combustion [2], glass ceramic [3], hydrothermal synthesis [4], co-precipitation [5], and ball milling [6−8] have been reported. Among them ball-milling procedures provide the production of powders, consisting of fine particles, being smaller than the single-domain size, by simple operation and handy experimental equipment [9].

Catalytic processes successfully solve a number of contemporary problems related to environmental and energy demands. Recently, methanol decomposition has received much attention as a potential source of clean and efficient fuel for gas turbines, fuel cells, and vehicles [10−12]. Morphology and structure features of metal oxide materials with spinel structure regarding their catalytic behaviour in methanol decomposition have already been re-

ported [13−16]. To the best of our knowledge, studies of strontium hexaferrites materials as catalysts for methanol decomposition have not been published so far.

The goal of the present work was to synthesise $SrFe_{12}O_{19}$ hexaferrite materials of tunable particle size using the method of mechanochemical treatment. Synthesis parameters impact on catalytic activity and selectivity of the obtained materials in methanol decomposition is in the focus of the study.

EXPERIMENTAL

Synthesis

$SrFe_{12}O_{19}$ samples were synthesised by co-precipitation method followed by thermal treatment. $Sr(NO_3)_2$ and $Fe(NO_3)_3.9H_2O$ supplied by Alfa Aesar were used as starting materials at an appropriate molar ratio. A mixed nitrate solution was precipitated dropwise by NaOH. The precipitate was dried at room temperature to form a precursor powder. The thermal treatment was carried out in static air at two temperatures: 600 and 850 °C with a hold of four hours. After heating at 850 °C, the powder was milled for 1 and 5 hours using a Fritsch Planetary miller in a hardened steel vial together with fifteen grinding balls of diameters ranging from 3 to 10 mm. The balls-to-powder mass ratio was 10:1. The abbreviations used in sample names are: HF – hexaferrite, TS – thermal synthesis, MS – mechano-che-

mical synthesis, and MD − after methanol decomposition.

Characterisation

Dried precursor powders (HC) were analysed by thermogravimetry and differential thermal analysis (TG-DTA) using a Stanton Redcroft instrument in static air at a heating ramp rate of 10 °C/min. Powder X-ray diffraction (XRD) samples were recorded by use of a TUR M62 diffractometer with Co Kα radiation. Average crystallite size (D, nm), degree of microstrain (e), and lattice parameters (a) of the studied hexaferrites were calculated from experimental XRD profiles by using PowderCell-2.4 software [17]. The Mössbauer spectra were registered at room temperature (RT) on a Wissel (Wissenschaftliche Elektronik GmbH, Germany) electromechanical spectrometer working in a constant acceleration mode. A ^{57}Co/Rh (activity $\cong$ 50 mCi) source and an α-Fe standard were used. Experimentally obtained spectra were fitted using CONFIT2000 software [18]. Parameters of hyperfine interactions, such as isomer shift (IS, mm/s), quadrupole splitting (QS, mm/s), effective internal magnetic field (H_{eff}, T), line widths (FWHM, mm/s), and relative weight (G, %) of the partial components in the spectra were determined.

Catalytic test

Methanol decomposition was carried out in a flow reactor at methanol partial pressure of 1.57 kPa and argon as a carrier gas (50 ml/min). The catalysts (0.055 g) were tested under temperature-programmed regime within the range of 77−500 °C at a heating ramp rate of 1 °C/min. On-line gas chromatographic analyses were performed on a PLOT Q column using flame ionisation and thermal conductivity detectors. An absolute calibration method and a carbon based material balance were used to calculate conversions and yields of the obtained products. Products selectivity was calculated as $Y_i/X*100$, where Y_i is the current yield of product i and X is methanol conversion.

RESULTS AND DISCUSSION

TG-DTG-DTA analysis of dried precursor powder is shown in Fig. 1. A significant endo-thermal effect up to 400 °C combined with sample mass loss could be associated with dehydration. Two exothermal peaks at 576 and 820 °C are due to crystallisation of hematite and hexaferrite phase, respectively [19,20].
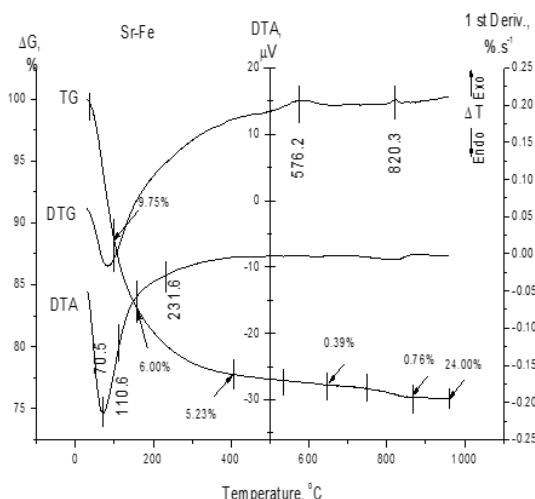
Fig. 1. TG-DTG-DTA investigation of SrFe₁₂O₁₉ dried precursor sample.

Powder X-ray diffraction patterns of heat-treated and ball-milled SrFe₁₂O₁₉ samples are shown in Fig. 2. In accordance with DTA analysis, diffractions of the precursor powder and of the sample obtained at 600 °C correspond to hematite - α-Fe₂O₃ (S.G.: R3c). Well defined reflexes of highly crystalline SrFe₁₂O₁₉ (Fig. 2b) were registered after 4-h treatment at 850 °C (ICDD, PDF 80-1198). Calculated average crystallite size, microstrain degree, and lattice parameters are given in Table 1.

Table 1. Average crystallites size (D), degree of microstrain (e) and lattice parameters determined from XRD patterns of SrFe₁₂O₁₉.

Sample	Phases	D, nm	e 10³ a.u	a, c, Å		%
HF TS850	SrFe₁₂O₁₉	47.38	1.14	a = 5.87	c = 23.04	93
	α-Fe₂O₃	66.58	1.26	a = 5.03	c = 13.73	7
HF TS850/MS1	SrFe₁₂O₁₉	24.98	5.67	a = 5.87	c = 23.04	88
	α-Fe₂O₃	35.83	1.66	a = 5.02	c = 13.72	12
HF TS850/MS5	SrFe₁₂O₁₉	25.07	7.81	a = 5.87	c = 23.13	57
	α-Fe₂O₃	25.03	5.63	a = 5.04	c = 13.75	43
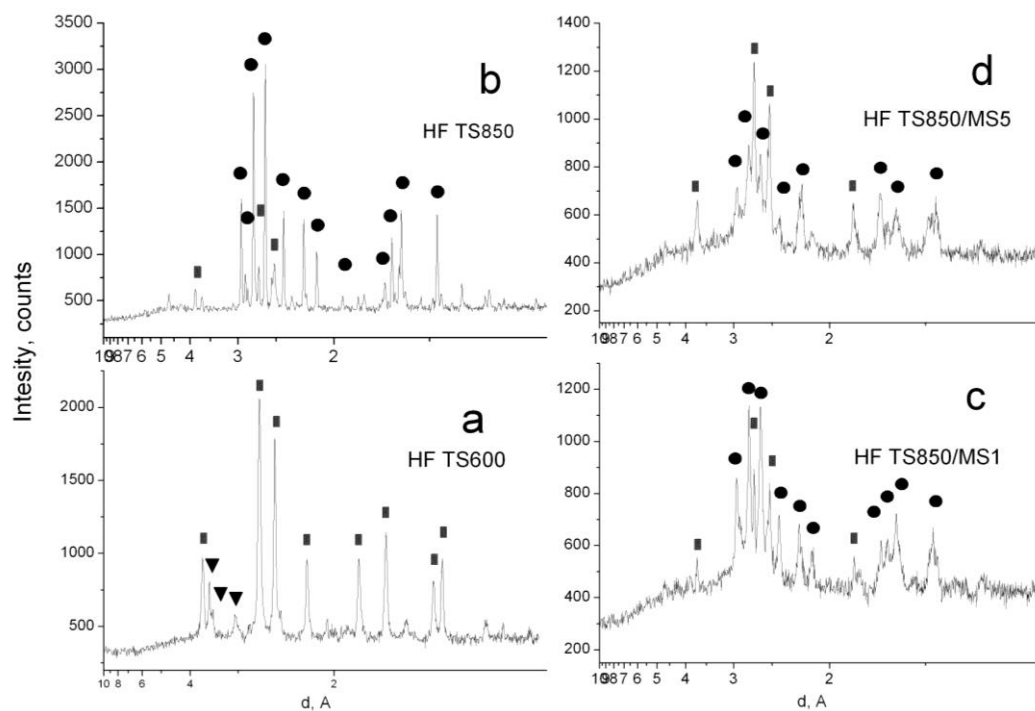
Fig. 2. X-ray analysis of thermally synthesised (a, b) and mechanochemically obtained (c, d) SrFe$_{12}$O$_{19}$ samples (●- SrFe$_{12}$O$_{19}$, ■- α-Fe$_2$O$_3$ and ▼-SrCO$_3$).
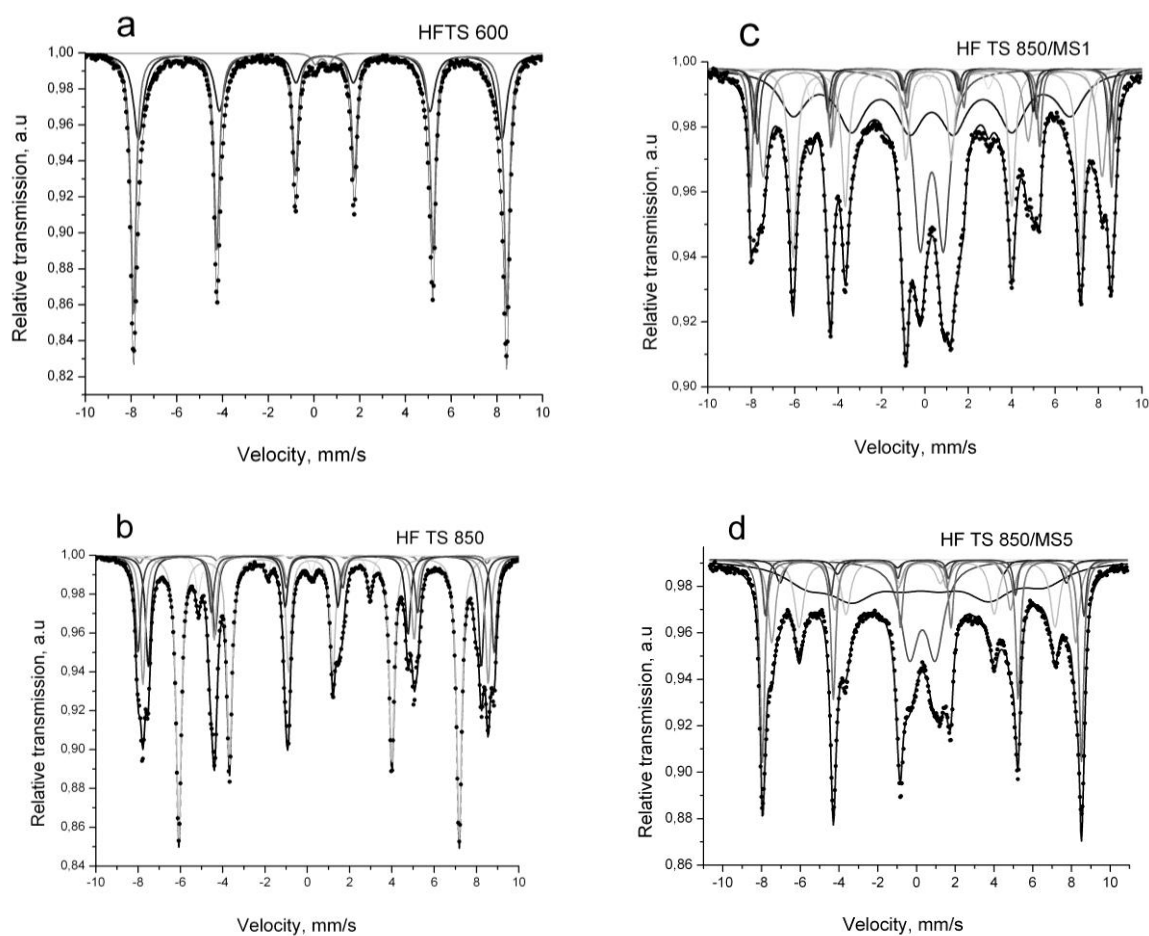
Fig. 3. Mössbauer spectra of thermally (a, b) and mechanochemically (c, d) synthesized SrFe$_{12}$O$_{19}$ samples.

Table 2. Mössbauer parameters of SrFe$_{12}$O$_{19}$ samples.

Sample	Components	IS, mm/s	QS, mm/s	Heff, T	FWHM mm/s	G, %
HF TS600	Sx1 Fe$_2$O$_3$	0.37	-0.21	50.7	0.28	64
	Sx2 Fe$_2$O$_3$	0.36	-0.20	49.3	0.53	35
	Db	0.34	0.58	-	-	1
HF TS850	octahedral (4f2)	0.38	0.07	52.3	0.30	14
	octahedral (2a)	0.35	0.06	50.7	0.29	17
	tetrahedral (4f1)	0.27	0.15	48.9	0.30	18
	octahedral (12k)	0.35	0.39	41.2	0.29	44
	bipyramidal (2b)	0.28	2.23	40.8	0.29	6
	Fe$_2$O$_3$	0.38	-0.20	51.0	0.29	1
HF TS850/MS1	octahedral (4f2)	0.45	0.14	51.2	0.28	6
	octahedral (2a)	0.28	0.04	50.8	0.25	4
	tetrahedral (4f1)	0.30	0.12	48.5	0.47	13
	octahedral (12k)	0.36	0.38	41.2	0.39	21
	bipyramidal (2b)	0.20	2.10	40.5	0.40	3
	Sx	0.31	0.27	39.7	1.60	30
	Db	0.31	1.07	-	0.72	16
	Fe$_2$O$_3$	0.38	-0.20	51.6	0.23	7
HF TS850/MS5	octahedral (4f2)	0.38	0.07	51.1	0.28	5
	octahedral (2a)	0.34	0.06	48.7	0.46	12
	tetrahedral (4f1)	0.27	0.15	45.9	0.50	4
	octahedral (12k)	0.36	0.36	41.1	0.57	13
	bipyramidal (2b)	0.28	2.20	40.7	0.30	1
	Sx	0.35	0.27	38.0	2.85	30
	Db	0.29	1.33	-	1.07	16
	Fe$_2$O$_3$	0.37	-0.20	51.2	0.29	19
HF TS850MD	octahedral (4f2)	0.38	0.09	52.1	0.35	15
	octahedral (2a)	0.36	0.06	50.5	0.33	20
	tetrahedral (4f1)	0.27	0.15	48.8	0.30	15
	octahedral (12k)	036	0.39	41.1	0.30	44
	bipyramidal (2b)	0.29	2.21	40.6	0.28	6
HF TS850/MS1MD	octahedral (4f2)	0.39	0.09	51.3	0.40	8
	octahedral (2a)	0.33	0.05	50.1	0.36	12
	tetrahedral (4f1)	0.30	0.06	48.4	0.43	19
	octahedral (12k)	0.36	0.38	40.9	0.32	17
	bipyramidal (2b)	0.23	2.07	40.5	0.30	3
	Sx	0.33	0.07	40.2	1.38	41
HF TS850/MS5MD	octahedral (4f2)	0.37	0.07	50.6	0.30	4
	octahedral (2a)	0.35	0.06	48.7	0.40	8
	tetrahedral (4f1)	0.27	0.15	46.7	0.80	13
	octahedral (12k)	0.37	0.33	40.6	0.66	18
	bipyramidal (2b)	0.28	2.20	41.2	0.30	1
	Sx	0.35	0.14	34.3	1.54	21
	Fe$_2$O$_3$	0.38	-0.20	50.9	0.38	35

Significant transformations with the SrFe$_{12}$O$_{19}$ TS850 sample occurred after mechanochemical activation (Fig. 2c and d, and Table 1). Even after 1-h ball milling a decrease of the crystallite size from 47 nm to 24 nm and an increase of the microstrain degree from 1.14×10^{-3} to 5.67×10^{-3} were observed. Increasing the milling time up to five hours resulted in the appearance of almost 50% secondary hematite phase.

Mössbauer spectra of the obtained samples and matching calculated parameters are given in Fig. 3 and Table 2, respectively. In the case of HF TS600 the best fitting model consists of two sextet

components and a doublet with IS = 0.34 mm/s and QS = 0.58 mm/s parameters indicating presence of amorphous phase. The appearance of more than one sextet component is associated with hematite phase of different particle size. M-type SrFe$_{12}$O$_{19}$ was detected after a temperature rise up to 850°C. The spectrum represented five well visible magnetically split components, indicating different cation environment around the Fe^{3+} ion in the hexagonal structure S.G.: P6$_3$/mmc [21]. The sextet parameter of the lowest IS (IS = 0.27 mm/s) is due to iron ion in tetrahedral position (FeO$_4$), while the component with the largest QS (around 2.20 mm/s) is typical of

a site of the lowest symmetry - trigonal bipyramidal [22]. Octahedrally coordinated Fe^{3+} are described as 4f2, 2a and 12k Wyckoff positions. Results from Mössbauer spectroscopy show a change in the material that occurred within one hour of milling. The observed collapse in the magnetic hyperfine structure in this case indicated significant changes in the sample. Appearance of additional magnetically split component with large width (FWHM = 1.6 and 2.85 mm/s for 1 and 5 hours milling, respectively) could be due to formation of highly defective and finely divided hexaferrite particles [23]. After mechanical activation, the appearance of non-magnetic component in the spectrum is evidence for the formation of highly dispersed material as well. About 16% of the total spectral area represents a doublet with parameters of the Fe^{3+} oxidation state, due to superparamagnetism phenomenon [24]. Thus, a short time grinding provides reduction in the particles size of less than 10 nm. Elongation of milling time induced separation of hematite phase.

All materials were catalytically active in methanol decomposition above 300 °C and at 350 °C about an 80–100% conversion was achieved. According to their catalytic activity, the samples arrange in the following order: HF TS850 < HF TS850 MS1 < HF TS850 MS5 (Fig. 4).
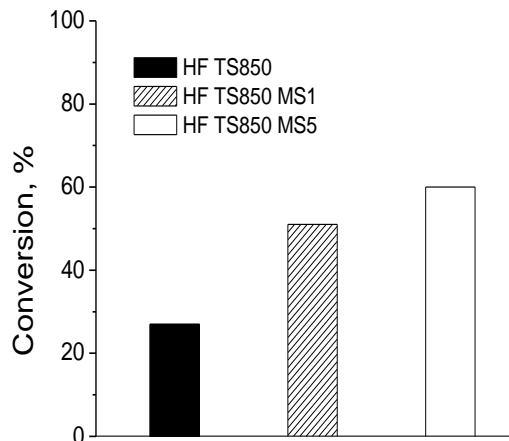
Fig. 4. Methanol decomposition at 330 °C on various samples.

For all materials, the selectivity to CO was about 80% and CO_2 and methane were registered as by-products. After catalysis, Mössbauer analysis of the samples was carried out. Parameters of hyperfine interaction are presented in Table 2. Despite strong reductive reaction atmosphere, no changes in phase composition of the initial materials were observed. None second hematite phase was registered only in the case of HF TS 850. A missing doublet component in the spectra of the milled samples indicates particle aggregation during the catalytic reaction.

CONCLUSIONS

Nanocrystalline M-type SrFe$_{12}$O$_{19}$ hexaferrite was successfully synthesised by thermal method combined with a ball-milling procedure. Powder X-ray diffraction and ^{57}Fe Mössbauer spectroscopy analyses indicated a facile effect of shorter milling time on the formation of homogeneous and finely divided SrFe$_{12}$O$_{19}$ hexaferrite and an increase of second hematite phase. The ball-milling procedure enhanced the catalytic activity of the samples in methanol decomposition and no significant effect of the milling time was detected. Mössbauer study of the catalysts after tests indicated that the hexaferrite phase remained stable even under highly reductive conditions.

REFERENCES

1. J. Qiu, L. Lan, H. Zhang, M. Gu, *J. Alloys Compd.,* **453**, 261 (2008).
2. A. Baykal, S. Yokuş, S. Güner, H. Güngüneş, H. Sözeri, Md. Amir, *Ceram. Int.*, **43**, 3475 (2017).
3. J. H. de Araur, F. A. O. Cabral, M. F. Ginani, J. M. Soares, F. L. A. Machado, *J. Non-Cryst. Solids,* **352**, 3518 (2006).
4. L. Lechevalliera, J. M. Le Breton, J. F. Wangc, I. R. Harris, *J. Magn. Magn. Mater.*, **269**, 192 (2004).
5. V. Luna, S. A. Palomares-Sanchéza, F. Ruíza, *Catal. Today*, **266**, 110 (2016).
6. I. Bsoul, S. Mahmood, A. F. Lehlooh, *Alloys Compd.*, **498**, 157 (2010).
7. I. Bsoul, S. Mahmood, *J. Alloys Compd.*, **489**, 110 (2010).
8. I. Bsoul, S. Mahmood, *Jordan J. Phys.,* **2**, 171 (2009).
9. A. Awadallaha, S. H. Mahmooda, Y. Maswadeha, I. Bsoulb, M. Awawdehc, Q. I. Mohaidatc, H. Juwharia, *Mater. Res. Bull.*, **74**, 192 (2016).
10. M. Ni, D. Y. C. Leung, M. K. H. Leung, *Int. J. Hydrogen Energy*, **32**, 3238 (2007).
11. H. Muroyama, R. Nakase, T. Matsui, K. Eguchi, *Int. J. Hydrogen Energy*, **35**, 1575 (2010).
12. F. Frusteri, S. Freni, L. Spadoro, V. Chiodo, G. Bonura, S. Donato, S. Cavallaro, *Catal. Commun.*, **5**, 611 (2004).
13. I. Genova, T. Tsoncheva, M. Dimitrova, D. Paneva, B. Tsyntsarski, R. Ivanova, Z. Cherkezova-Zheleva, T. Budinova, D. Kovacheva, I. Mitov, N. Petrov, *Catal. Commun*, **55**, 43 (2014).
14. N. Velinov, E. Manova, T. Tsoncheva, Claude Estoumes, D. Paneva, K. Tenchev, V. Petkova, K. Koleva, B. Kunev, I. Mitov, *Solid State Sci.*, **14**, 1092 (2012).
15. K. Koleva, N. Velinov, T. Tsoncheva, I. Mitov,

Hyperfine Interact., **226**, 89 (2014).

16. N. Velinov, K. Koleva, T. Tsoncheva, E. Manova, D. Paneva, K. Tenchev, B. Kunev, I. Mitov, *Catal. Commun.*, **32**, 41 (2012).

17. W. Kraus, G. Nolze, PowderCell for Windows, Federal Institute for Materials Research and Testing, Berlin, 2000.

18. T. Žák, Y. Jirásková, CONFIT: Mössbauer Spectra fitting program, *Surf. Interface Anal.*, **38**, 710 (2006).

19. E. Darezereshki, *Mater. Lett.*, **65**, 642 (2011).

20. M. V. Bukhtiyarova, A. S. Ivanova, E. M. Slavinskaya, L. M. Plyasova, V. A. Rogov, V. V. Kaichev, A. S. Noskov, *Fuel*, **90**, 1245 (2011).

21. I. A. Auwal, H. Güngüneş, A. Baykal, S. Güner, S. E. Shirsath, M. Sertkol, *Ceram. Int.*, **42**, 8627 (2016).

22. S. K. Chawla, R. K. Mudsainiyan, S. S. Meena, S. M. Yusuf, *J. Magn. Magn. Mater.*, **350**, 23 (2014).

23. V. Šepelák, M. Myndyk, R. Witte, J. Röder, D. Menzel, R. H. Schuster, H. Hahn, P. Heitjans, K.-D. Becker, *Faraday Discuss.*, **170**, 121 (2014).

24. M. Sorescu, A. Grabias, L. Diamandescu, D. Tarabasanu, *J. Mater. Synth. Process.*, **8**, 2 (2000).

СИНТЕЗ, СТРУКТУРА И КАТАЛИТИЧНИ СВОЙСТВА НА SrFe$_{12}$O$_{19}$ ХЕКСАФЕРИТ

К. В. Колева[1]*, Н. И. Велинов[1], И. Г. Генова[2], Т. С. Цончева[2], В. С. Петкова[3,4]

[1] *Институт по катализ, БАН, 1113 София, България*
[2] *Институт по органична химия с център по фитохимия, БАН, 1113 София, България*
[3] *Институт по минералогия и кристалография, БАН, 1113 София, България*
[4] *Нов български университет, 1618 София, България*

(Резюме)

Хексаферитната структура от М-тип (MeFe$_{12}$O$_{19}$) се състои от редуващи се шпинелни и хексагонални блокове, което поражда голямо разнообразие от разпределение на йоните в кристалната решетка. Елементарната клетка на този вид съединения е изградена от двувалентни алкалоземни метали Ca, Sr, Ba, а също така и метали от преходния ред (Co, Cu, Cr). Fe^{3+} йоните са разположени в пет кристалографски позиции: тетраедрична-FeO$_4$ (4f1), октаедрична-FeO$_6$ (12k, 2a, 4f2) и бипирамидална-FeO$_5$ (2b).

Цел на настоящото изследване е синтез на хексаферитни материали от М-тип (SrFe$_{12}$O$_{19}$) при ниска температура и контрол на размера на частиците чрез механохимично третиране, както и определяне на влиянието на структурните особености на образците върху техните каталитични свойства в реакция на разлагане на метанол.

Феритните материали са получени по метода на съутаяване с последваща термична обработка при 600 °C и 850 °C. На образец, получен при 850 °C, е приложено механично въздействие чрез смилане 1 и 5 часа. Образците са охарактеризирани с помощта на ДТА, рентгенофазов анализ и Мьосбауерова спектроскопия. Термично обработен при 850 °C образец е високо кристален SrFe$_{12}$O$_{19}$ хексаферит с наличие на втора фаза - хематит. Установено е редуциране на частиците по размер от 47 нм до 21 нм след един час механохимична обработка. Изследваните материали показват добра каталитична активност и селективност по СО в реакцията на разлагане на метанол. Образци, изследвани с Мьосбауерова спектроскопия след катализ, се отличават със стабилна хексаферитна фаза в силно редукционната среда на разлагане на метанол.

Mechanochemically assisted solid state synthesis and catalytic properties of CuWO₄

M. N. Gancheva*, P. M. Konova, G. M. Ivanov, L. I. Aleksandrov, R. S. Iordanova, A. I. Naydenov

*Institute of General and Inorganic Chemistry, Bulgarian Academy of Science,
Acad. G. Bonchev St., Bldg. 11, 1113 Sofia, Bulgaria*

The synthesis and catalytic properties of nanostructured copper tungstate have been investigated in this study. A mixture of CuO and WO_3 at a molar ratio of 1:1 was subjected to intensive mechanical treatment in air using a planetary ball mill for different periods of time. Structural and phase transformations were monitored by X-ray diffraction analysis, differential thermal analysis, and infrared spectroscopy. Mechanochemical treatment promoted progressive amorphisation of the initial oxides. Full amorphisation was achieved after 7 h milling time and remained up to 20 h milling time. DTA measurements of amorphous sample showed that the crystallization temperature was 430 °C. A pure nanostructured $CuWO_4$ phase was prepared after thermal treatment of amorphous phase at 400 °C. Nanostructured $CuWO_4$ was tested in the reactions of complete oxidation of C_1-C_4 hydrocarbons and the highest temperature for 10% conversion (T10) was measured with methane. Repeated addition of one further carbon atom to the methane molecule led to a decrease in T10 by about 70 °C (from methane to propane) and further by 30 °C from propane to *n*-butane. Calculated apparent activation energies for the reaction of complete oxidation decreased from methane to *n*-butane, and this effect correlated with diminished strength of the weakest C-H bond of the corresponding hydrocarbon.

Key words: mechanochemistry, nanoparticles, catalytic activity, preparation of single phase $CuWO_4$.

INTRODUCTION

$CuWO_4$ is a member of metal tungstate oxides (AWO_4) group, which have received much attention due to their application in various fields as catalysts [1–3], optical devices [4], sensors [5], and magnetic properties [6]. AWO_4 (A = Ni, Fe, Zn, and Cu) tungstate family oxides exhibit a wolframite-type of monoclinic structure, where both A and W atoms are bonded to six surrounding oxygen atoms by forming octahedral chains [7]. Like-filled octahedra share edges, but unlike octahedra share vertex. In this way edge-sharing distorted WO_6 octahedra form W_2O_8 structural units. Among these tungstates only $CuWO_4$ crystallizes in a triclinic wolframite-type of structure at room temperature composed by CuO_6 and WO_6 octahedra distorted by the first-order and second-order Jahn-Teller effects, respectively [8–10]. Some authors have suggested that the CuO_6 octahedra possess a pseudo-tetragonally elongated geometry [10,11]. Ruiz-Fuertes *et al.* [12] have established that $CuWO_4$ undergoes phase transition from a low temperature triclinic phase to a monoclinic one with wolframite-type of structure at 10 GPa involving a change in the magnetic order. Different methods for $CuWO_4$ preparation as sol-gel [5], coprecipitation [2,4,10], solid state reaction [10,11], sonochemistry [3], microwave-assisted synthesis [13], polyol-mediated approach [1], electrochemical synthesis [14], and hydrothermal route [5,15,16] have been developed. There are some disadvantages concerned with metal salts used as raw materials (necessity of anion removal), strictly controlled synthesis media, high costs, and thermal treatment after synthesis. Up to now, mechanochemical synthesis of $CuWO_4$ compound from initial oxides has not been studied. It is well known that the mechanochemical activation is a suitable method for preparation of complex inorganic oxides [16–18]. It is characterized by lower synthesis temperature, chemical homogeneity, high purity, and sample crystallite size and morphology control. Careful regulation of milling parameters is a promising way to improve the physicochemical properties of the final products as compared to conventional routes. We have found out that ball milling is an appropriate approach to synthesis different inorganic materials like ZnO, $NiWO_4$, $ZnWO_4$, $ZrMo_2O_8$, Bi_2WO_6, and $MgWO_4$ [19–24]. Our investigations showed that metal tungstates ($MgWO_4$ and Bi_2WO_6) obtained by mechano-chemical activation exhibit a moderate catalytic activity for oxidation of CO and volatile organic compounds (VOCs) [23,24]. This motivated us to continue experiments in the same field. The aim of this study was to investigate the catalytic activity of nanopowder $CuWO_4$ prepared *via* mechanochemically assisted solid-state synthesis.

* To whom all correspondence should be sent
E-mail: m.gancheva@svr.igic.bas.bg

EXPERIMENTAL

CuO (Merck, 99.9%) and WO$_3$ (Aldrich, 99.9%) starting materials at a molar ratio of 1:1 were subjected to intense mechanical treatment using a planetary ball mill (Fritsch-Premium line-Pulverisette No. 7). Both vials and balls were made of stainless steel. The following milling conditions were used: air atmosphere; milling speed of 500 rpm; ball to powder weight ratio of 10:1, and milling time varying from 0 to 20 h. To avoid excessive temperature rise within the grinding chamber, 15 min of ball milling duration were followed by a pause of 5 min. Milled amorphous samples were heated at 400 °C for 6 h in air atmosphere. X-ray diffraction (XRD) patterns were registered on a Bruker D8 Advance diffractometer using Cu-Kα radiation in the 2θ range of 10–80°. Average crystallite sizes (D) resulting from X-ray diffraction line broadening were determined using Scherrer' equation: $D = K\lambda/\beta cos\theta$, where D is the crystallite size in nm, K is a constant, conventionally accepted to be 1.0, λ is the Cu-Kα radiation wavelength (1.5406 Å), β is the full width at half maximum (FWHM) of the diffraction line, and θ in radians is the corresponding diffraction peak is 2θ = 19.00°. Differential thermal analysis (DTA) was performed in air by SETARAM LabsysEvo apparatus, at a heating rate of 5 °C.min^{-1}, in an open corundum crucible. Specific surface areas (BET method) were determined by low-temperature (77.4 K) nitrogen adsorption in NOVA 1200e surface area & pore analyzer at relative pressures p/p_0 = 0.1–0.3 using BET equation. Infrared spectra were recorded in the range of 1200–400 cm^{-1} on a Nicolet-320 FTIR spectrometer using the KBr pellet technique. Catalytic activity tests were carried out in a continuous flow type reactor. The following conditions were applied: catalyst bed volume of 0.5 cm^3 (0.3 cm^3 catalyst and 0.2 cm^3 quartz-glass particles of same size), iregular shaped particles having an average diameter of 0.45 ± 0.15 mm, reactor diameter of 6.0 mm, and quartz-glass ($D_{reactor}/D_{particles} \geq 10$). The gaseous hourly space velocity (GHSV) was fixed to 100 000 h^{-1}. Inlet concentration for each one of the individually tested hydrocarbons (methane, ethane, propane, and butane) was set to 0.10 vol.%, while oxygen supply was kept at 20.0 vol.%. All gas mixtures were balanced to 100% with nitrogen (4.0). Gas analysis was performed using on-line gas-analyzers of CO/CO$_2$/O$_2$ (Maihak) and THC-FID (total hydrocarbon content with a flame ionization detector, Horiba). To compensate adiabatic effect of the reaction, the catalyst bed temperature was kept almost constant. Pressure drop of the catalytic bed was measured to be less than 2 kPa

and it was not taken into account. Axial dispersion effect was neglected as the catalyst bed matched a chain of more than 10 ideal mixing cells along the reactor axis. Therefore, the geometrical characteristics and the flow conditions of the catalytic reactor justify a conclusion that the reactor was close to the case of isothermal plug flow reactor (PFR) except for the effect of radial velocity profile inside the catalyst bed.

RESULTS AND DISCUSSION

XRD analysis was used to monitor phase transformation during mechanochemical treatment (Fig. 1). The diffraction lines indexed with monoclinic CuO (JCPDS 01-072-0677) and monoclinic WO$_3$ (JCPDS 01-072-0677) became broadened and less intense after 1 h milling time (Fig. 1b).
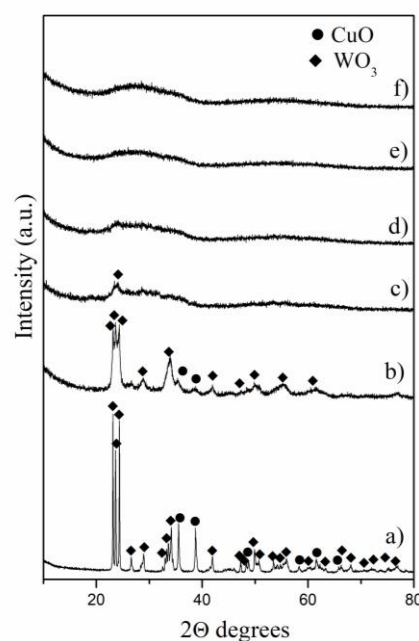
Fig. 1. X-ray diffraction patterns of mechanochemically activated mixture of CuO and WO$_3$ at: (a) 0 h; (b) 1 h; (c) 3 h; (d) 7 h; (e) 10 h; (f) 20 h.

All reflections of CuO disappeared after 3 h of milling time interval, while reflections of WO$_3$ were still observed (Fig. 1c). This indicates that CuO amorphisation was easier than that of WO$_3$. Complete amorphisation of the samples was observed after 7 h milling time (Fig. 1d). Further mechanochemical treatment up to 20 h did not promote chemical reaction and production of any new compound (Fig. 1f). Thermal analysis was used to determine the reaction temperature between mechanochemically activated reagents.

Fig. 2 shows a TG/DTA curve of a sample after 20 h milling time in air atmosphere. The presence of one strong exothermal peak at 430 °C could be

attributed to the formation of $CuWO_4$. All reflection lines typical of triclinic $CuWO_4$ (JCPDS-01-080-5325) were observed in the diffraction patterns of amorphous samples heated at 400 °C for 6 h (Fig. 3).
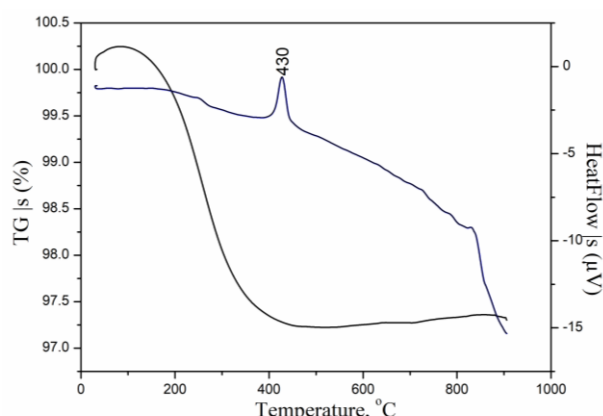
Fig. 2. TG/DTA curves of $CuWO_4$ sample after 20 h milling time.
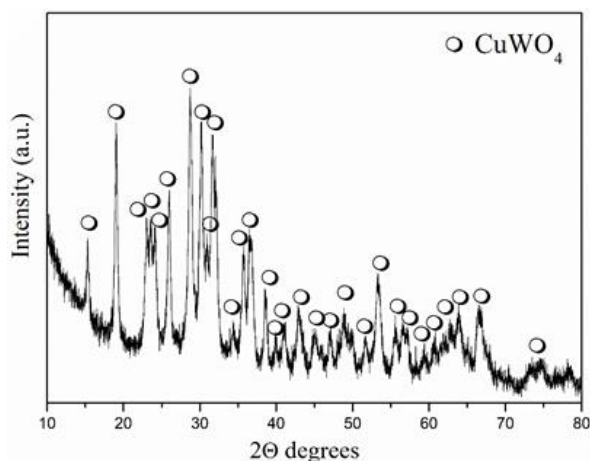
Fig. 3. XRD pattern of $CuWO_4$.

This temperature was considerably lower as compared to the temperature needed for traditional solid-state reaction (800 °C) [10]. Well-defined diffraction peaks suggest a high degree of crystallinity of the final product. As-prepared $CuWO_4$ had an average crystallite size of 24 nm according to the Scherrer equation with specific surface area of 13 m^2/g.

Structural arrangement during mechanochemical treatment and formation of $CuWO_4$ were investigated by IR spectroscopy (Fig. 4). IR spectrum of non-activated sample shows the characteristic bands of the initial oxides. The bands at 830 and 780 cm^{-1} are assigned to stretching vibrations of W–O–W bridge bonds between WO_6 octahedra in WO_3 [25,26]. The absorption bands at 590, 530, and 480 cm^{-1} are due to a stretching vibration of Cu–O bond of monoclinic CuO phase [27].

Mechanochemical treatment of the sample had strong influence on bands intensity and position.

After 1 h milling time the bands at 780, 590, and 530 cm^{-1} disappeared, the bands at 840 and 480 cm^{-1} were broadened, and their intensity was decreased (Fig. 4b). This fact is a result of destruction of the long-range order and partial amorphisation of the reagents. On the other hand a new absorption band at 625 cm^{-1} appeared that could be attributed to a vibration of Cu–O bond typical of Cu_2O phase [28,29].
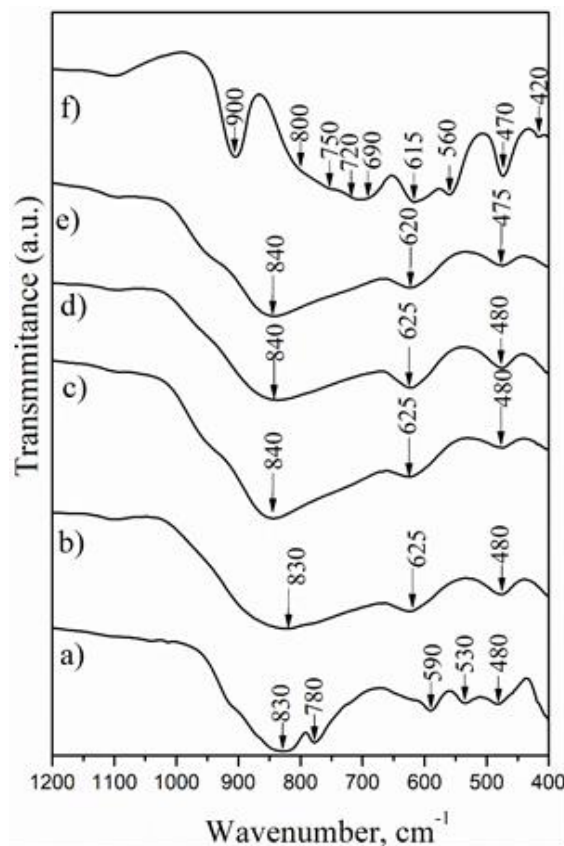
Fig. 4. IR spectra of mechanochemically activated mixture of CuO and WO_3 at: (a) 0 h; (b) 1 h; (c) 3 h; (d) 7 h; (e) 20 h; (f) sample heated at 400 °C after 20 h milling time.

It was established that mechanochemical treatment induced partial transformation of CuO to Cu_2O phase. A similar result has been reported by Sheibani *et al.* [30]. According to the X-ray diffraction analysis sample amorphisation induced by ball milling completed after 7 h milling time and the IR spectrum contains bands at 840, 620, and 480 cm^{-1} (Fig. 4d–f). Annealing of amorphous sample at 400 °C led to significant changes in the FTIR spectrum. The observed absorption bands are in good agreement with previously reported IR data on this compound [2–4,30,31]. Band assignment was carried out based on structural data on $CuWO_4$, X-ray absorption fine structure (EXAFS) analysis [6,10,32], and vibration data on AWO_4 (A = Ni, Zn, and Mg) phase of wolframite type of structure [21,24,33,34].

95

The bands at 800 and 750 cm^{-1} are due to the vibrations of WO_2 entity present in W_2O_8 groups. The bands at 720, 690, and 615 cm^{-1} are typical of the asymmetric stretching vibrations of a two-oxygen bridge type species (W_2O_2). The band below 600 cm^{-1} arised from vibrations of CuO_6 polyhedra [21, 24,33,34].

To examine synthesized $CuWO_4$ applicability as combustion catalyst, the reactions of complete oxidation of different hydrocarbons (methane, ethane, propane, and butane) were investigated. Reproducibility and confidence intervals for measured conversion values were the subject of preliminary tests, which involved repeating of tests under conditions similar but not identical to separate experimental runs presented in the study. Calculated standard deviation SD = +/−1.5% was based on the average of six measurements for each one of the experimental points. The reported results are based on the average values for conversion degree within two parallel measurements. Data on conversion-temperature dependencies were used to fit kinetics parameters by applying the method described by Duprat [35] and Harriot [36]. In brief, this method consists of direct integration of the reaction rate based on data on temperature-conversion curves by using one-dimensional pseudo-homogeneous model of plug-flow isothermal reactor. The residual squared sum (RSS) between experimental data and model predictions was minimized (optimization criterion) and the square of correlation coefficient (R2) was calculated. The following margin values of the kinetics parameters were established: methane R2 = 0.99, SD = ±3.6%; ethane R2 = 0.99, SD = ±2.9%; propane R2 = 0.99, SD = ±5.3%; and butane R2 = 0.99, SD = ±4.0%. The obtained results are displayed in Figure 5.
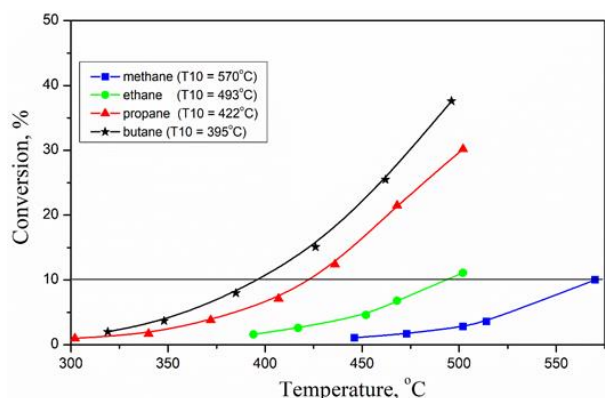
Fig. 5. Conversion-temperature dependence for complete oxidation of different hydrocarbons (methane, ethane, propane, and butane) over CuWO₄ catalyst.

It is seen that the highest temperature for 10% conversion was observed for methane combustion (T10 = 570 °C) due to the known stability of this compound. As it is well known [37], the highest temperature to achieve 10% conversion (T10) is required for methane combustion and addition of carbon atoms to methane molecule and up to C_4 leads to a decrease in T10. For our $CuWO_4$ catalyst, this reduction is higher than 170 °C from methane to *n*-butane.

To calculate pre-exponential factor (k_o) and apparent activation energy (E_{app}), data on conversion degrees below 45% were utilized. For such cases, calculated values for average effectiveness factor (accounting for irregular shaped catalyst particles) were within the limits of 0.95–0.99 and therefore the effect of internal diffusion effect had to be implemented in the reactor model by applying of iterative approach. Table 1 gives apparent activation energy values and the calculated rate constants for complete oxidation of the investigated hydrocarbons over $CuWO_4$ catalyst.

Table 1. Reaction parameters (pre-exponential factors k_o and the apparent activation energies E_{app}), for the complete oxidation of hydrocarbons on $CuWO_4$ catalyst.

Hydrocarbon	k_o, s^{-1}	E_{app}, kJ/mol	ΔH_{C-H}, kJ/mol
methane	$2.08×10^6$ ($±1.0×10^5$)	88.4 ($±5$)	433
ethane	$5.80×10^6$ ($±1.1×10^5$)	86.0 ($±4$)	410
propane	$7.99×10^6$ ($±1.4×10^5$)	80.5 ($±4$)	394
n-butane	$3.43×10^6$ ($±2.2×10^5$)	73.0 ($±3$)	394

As can be seen the apparent activation energy are decreased from methane to butane, which could be correlated with the strength of the weakest H–C bond of the corresponding *n*-alkane [38,39]. It should be pointed out that a similar trend of decrease in apparent activation energy was reported earlier [40].

CONCLUSIONS

A single $CuWO_4$ phase was synthesized by thermal treatment at 400 °C of mechanically activated mixture of copper and tungsten oxides. Several effects were established during the ball milling processes including full amorphisation of the initial oxides, lack of chemical reaction after prolonged activation up to 20 h, and partial transformation of CuO to Cu_2O phase. The formation of amorphous phase favoured obtaining of $CuWO_4$ nanopowder of 24 nm crystallite size. The prepared nanostructured $CuWO_4$ was tested for possible application as catalyst for abatement of waste gases containing alkanes in a reactions of complete oxidation of C_1–C_4 hydrocarbons. The highest temperature for 10% conversion (T10) was measured for methane, while one further carbon added the to the

C$_1$ hydrocarbon molecule led to a decrease in T10 by about 70 °C (from methane to propane) and further by 30 °C from propane to *n*-butane. Calculated apparent activation energies for the reaction of complete oxidation decreased from methane to *n*-butane, and this effect was associated decreased strength of the weakest C–H bond of the corresponding alkane.

REFERENCES

1. P. Schmitt, N. Brem, S. Schunk, C. Feldmann, *Adv. Funct. Mater.*, **21**, 3037 (2011).
2. S. J. Naik, A. V. Salker, *Catal. Commun.*, **10**, 884 (2009).
3. E. L. S. Souza, J. C. Sczancoski, I. C. Nogueira, M. A. P. Almeida, M. O. Orlandi, M. S. Li, R. A. S. Luz, M. G. R. Filho, E. Longo, L. S. Cavalcante, *Ultrasonic Sonochem.*, **38**, 256 (2017).
4. S. M. Pourmortazavi, M. Rahimi-Nasrabadi, M. Khalilian-Shalamazi, H. R. Chaeni, S. S. Hajimirsadeghi, *J. Inorg. Organomet. Polym.*, **22**, 333 (2014).
5. M. A. Damian, Y. Rodriguez, J. L. Solis, W. Estrada, *Thin Solid Film*, **444**, 104 (2003).
6. M. V. Lalic, Z. S. Popovic, F. R. Vukajlovic, *Comp. Mater. Sci.*, **50**, 1179 (2011).
7. K. Sieber, R. Kershaw, K. Dwight, A. Wold, *Inorg. Chem.*, **22**, 2667 (1983).
8. L. Kihlborg, E. Geber, *Acta Cryst. B*, **26**, 1020 (1970).
9. O. Yu. Khyzhuna, T. Strunskusb, S. Crammc, Yu. M. Solonina, *J. Alloys Compnd.*, **389**, 14 (2005).
10. J. Timoshenko, A. Anspoks, A. Kalinko, A. Kuzmin, *Phys. Scr.*, **89**, 044006 (2014).
11. O. Yu. Khyzhun, V.L. Bekenev, Yu.M. Solonin, *J. Alloys Compnd.*, **480**, 184 (2009).
12. R. Ruiz-Fuertes, A. Friedrich, J. Pellicer-Porres, D. Errandonea, A. Segura, W. Morgenroth, E. Haussuhl. C.-Y. Tu, A. Polian, *Chem. Mater.*, **23**, 4220 (2011).
13. D. Kumar, S. Karuppuchamy, *Ceram. Inter.*, **40**, 12397 (2014).
14. S. M. Pourmortazavi, M. Rahimi-Nasrabadi, Y. Fazli, M. Mohammad-Zadeh, *Int. J. Refract. Met. Hard Mater.*, **51**, 29 (2015).
15. S. Kannan, K. Mohanraj, G. Sivakumar, *Chem. Select*, **2**, 4484 (2017).
16. T. Raghua, R. Sundaresan, P. Ramakrishnan, T. R. Rama Mohan, *Mater. Sci. Engin. A*, **304–306**, 438, (2001).
17. A. F. Fuentes, L. Takacs, *J. Mater. Sci.*, **48**, 598 (2013).
18. X. Cuo, D. Xiang, G. Duan. P. Mou, *Waste Manage.*, **30**, 4 (2010).
19. Y. Dimitriev, M. Gancheva, R. Iordanova, *J. Alloys Compd.*, **519**, 161 (2012).
20. M. Mancheva, R. Iordanova, D. Klissurski, G. Tyuliev, B. Kunev, *J. Phys. Chem. C*, **111**, 1101 (2007).
21. M. Mancheva, R. Iordanova, Y. Dimitriev, *J. Alloys Compd.*, **509**, 15 (2011).
22. R. Iordanova, M. Mancheva, Y. Dimitriev, D. Klissurski, G. Tyuliev, B. Kunev, *J. Alloys Compd.*, **485**, 104 (2009).
23. M. Gancheva, R.Iordanova, Y. Dimitriev, D. Nihtianova, P. Stefanov, A. Naydenov, *J. Alloys Compd.*, **570**, 34 (2013).
24. M. Gancheva, A. Naydenov, R. Iordanova, D. Nihtianova, P. Stefanov, *J. Mater. Sci.*, **50**, 3447 (2015).
25. M. F. Daniel, B. Desbat, J. C. Lassegues, B. Gerand, M. Figlarz, *J. Solid State Chem.*, **67**, 235 (1987).
26. C. L. Veenas, L. R. Asitha, V. C. Bose, A. S. A. Raj, G. Madhu, V. Biju, *Mater. Sci. Engin.*, **73**, 012119 (2015).
27. S. Wang, H. Xu, L. Qian, X. Jia, J. Wang, Y. Liu, W. Tang, *J. Solid State Chem.*, **182**, 1088 (2009).
28. K. Borgohain, J. B. Singh, M. V. Rama Rao, T. Shripahi, S. Mahamuni, *Phys. Rev.*, **61**, 11093 (2000).
29. M. Kouti, L. Matouri, *Transaction F, Nanotechnology*, **17**, 73 (2010).
30. C. Wei, Y. Huang, X. Zhang, X. Chen, J. Yan, *Electrochim. Acta*, **220**, 156 (2016).
31. G. M. Clark, W. P. Doyel, *Spectrochim. Acta*, **22**, 1441 (1966).
32. O. Yu. Khyzhun, V. L. Bekenev, Yu. M. Solonin, *J. Alloys Compd.*, **480**, 184 (2009).
33. V. V. Fomichev, O. I. Kondratov, *Spectrochim. Acta A*, **50**, 1113 (1994).
34. M. Daturi, G. Busca, M. M. Borel, A. Leclaire, P. Piaggio, *J. Phys. Chem.*, **101**, 4358 (1997).
35. F. Duprat, *Chem. Eng. Sci.*, **57**, 901 (2002).
36. P. Harriot, Chemical Reactor Design, Marcel Dekker, Inc., 2003.
37. F. G. Dwyer, *Catal. Rev. Sci. Eng.*, **6**, 261 (1972).
38. M. Zboray, A. T. Bell, E. Iglesia, *J. Phys. Chem. C*, **113**, 12380 (2009).
39. P. Deshlahra, E. Iglesia, *J. Phys. Chem. C*, **120**, 16741 (2016).
40. Y. Xin, H. Wang, C. K. Law, *Combust. Flame*, **161**, 1048 (2014).
41. L. Van De Beld, M. P. G. Bijl, A. Reinders, B. Van Der Werf, K. R. Westerterp, *Chem. Eng. Sci.*, **49**, 4361 (1994).

МЕХАНОХИМИЧЕН АКТИВИРАН ТВЪРДОФАЗЕН СИНТЕЗ И КАТАЛИТИЧНИ СВОЙСТВА НА CuWO₄

М. Н. Ганчева*, П. М. Конова, Г. М. Иванов, Л. И. Александров, Р. С. Йорданова, А. И. Найденов

Институт по обща и неорганична химия, Българска академия на науките,
ул. „Акад. Георги Бончев", бл. 11, 1113 София, България

(Резюме)

Изучено е получаването и каталитичните свойства на наноструктуриран меден волфрамат. Смес от CuO и WO₃ в молно отношение 1:1 бе подложена на механохимично активиране на въздух използвайки планетарна топкова мелница за различен период от време. Структурните и фазовите трансформации бяха проследени чрез рентгенофазов анализ, диференциален термичен анализ (ДТА) и инфрачервена спектроскопия. Механохимичното третиране доведе до прогресивно аморфизиране на изходните оксиди. Пълна аморфизация бе осъществена след 7 часа механохимична обработка и се запази до 20 часа време на активиране. ДТА на аморфния образец показа, че температурата на кристализация е 430 °C. Монофазен наноструктуриран CuWO4 бе синтезиран след термична обработка на аморфната фаза при 400 °C. CuWO₄ бе тестван в реакция на пълно каталитично окисление на C₁-C₄ въглеводороди, като най-високата температура за постигане на степен на превръщане 10% (T10) бе установена при метана, а добавянето на всеки следващ въглероден атом към метановата молекула води до понижаване на T10 с около 70 °C (от метан до пропан) и с около 30 °C от пропан до *n*-бутан. Изчислените стойности на наблюдаваната активираща енергия за реакцията на пълно каталитично окисление показа понижение в реда от метан до *n*-бутан, като ефектът е в корелационна зависимост от енергията за разкъсване на най-слабата C–H връзка в съответния въглеводород.

98

Mesoporous nanostructured $Ti_xSn_{1-x}O_4$ mixed oxides as catalysts for methanol decomposition: effect of Ti/Sn ratio

I. Genova[1]*, T. Tsoncheva[1], M. Dimitrov[1], D. Kovacheva[2]

[1] *Institute of Organic Chemistry with Centre of Phytochemistry, Bulgarian Academy of Sciences, 1113 Sofia, Bulgaria*
[2] *Institute of General and Inorganic Chemistry, Bulgarian Academy of Sciences, 1113 Sofia, Bulgaria*

The aim of the current investigation is to elucidate the impact of the Ti/Sn ratio in $Ti_xSn_{1-x}O_4$ mixed oxides on their textural, structural, redox, and catalytic features. Mesoporous mixed oxides of different Ti/Sn ratio were synthesised by template-assisted hydrothermal technique. The obtained materials were characterised by a complex of physicochemical techniques, such as nitrogen physisorption, XRD, Raman, UV–Vis, FTIR, and TPR with hydrogen. Methanol decomposition to syngas was used as a test reaction. The catalytic activity of the binary materials was affected in a complicated way by their phase composition. The latter was improved due to an increase in material specific surface area and pore volume and strongly suppressed because of significant structural changes.

Key words: tin-titania binary oxides, template-assisted hydrothermal synthesis, methanol decomposition.

INTRODUCTION

In last decades, hydrogen was considered most effective fuel, but the problem with its safety storage and transport is still a matter of challenge. One reliable solution is to apply various chemical compounds, which in case of need easily release hydrogen. Among them, methanol gains much interest because it possesses high H/C ratio, releases hydrogen at relatively low temperatures, and can be synthesised from valuable and renewable sources by well-developed technologies. An important step in the control of this catalytic process is to develop highly efficient catalysts with regulated properties. Titania has received much attention due to its superior optical, electrical, mechanical, and catalytic properties combined with non-toxicity and cost effectiveness [1]. Dopant introduction into titania lattice is well known procedure to improve its dispersion and redox and catalytic properties due to a specific interaction and/or synergism between components [2]. It has been shown that incorporation of Sn^{4+} ions into the titania lattice increases its dispersion, provides significant structural and texture changes [3−5], and improves the photocatalytic activity [6].

Much effort has been focused on the preparation of Sn-Ti metal oxides with porous structure, high specific surface area, and good crystallinity by various synthetic routes, such as sol-gel, solvothermal, direct oxidation, electrodeposition, chemical/physical vapour deposition, emulsion or hydrolysis precipitation, etc. [7−10]. Among these procedures, the hydrothermal technique is considered suitable to prepare mesoporous mixed oxide materials of high surface area and pore volume [11]. However, to our knowledge no data on the preparation of binary titania-tin oxide materials by template-assisted hydrothermal technique have been reported. The aim of the present investigation was to prepare a series of titania-tin oxide materials of different Ti/Sn ratio. The effect of phase composition on their textural, structural, and redox properties was studied using a complex of various physicochemical techniques, such as nitrogen physicsorption, XRD, Raman, UV–Vis, FTIR, and TPR. The potential of application of these materials as catalysts was tested in methanol decomposition to syngas.

EXPERIMENTAL

Materials

TiO_2 and SnO_2 materials were synthesised by template-assisted technique using hexadecyl-N,N,N-trimethyl ammonium bromide (CTAB) as a template, hydrothermal treatment at 373 K, and calcination at 773 K [12]. The same synthesis was applied to prepare bi-component metal oxides. The samples were denoted as xTiySn, where x/y is the metal mol ratio, which was 2:8, 5:5, or 8:2.

Methods of characterisation

Specific surface area (A_{BET}) and total pore volume (V_{tot}) were measured by nitrogen adsorption-desorption isotherms at 77 K on a Beckman

Coulter SA 3100 apparatus. Powder X-ray diffraction patterns were collected by a Bruker D8 Advance diffractometer with CuKα radiation and LynxEye detector; the average crystallite size was evaluated according to Scherrer equation. FTIR spectra (KBr pellets) were recorded on a Bruker Vector 22 FTIR spectrometer at a resolution of 1–2 cm^{-1} by accumulating 64–128 scans. Raman spectra were acquired by a DXR Raman microscope using a 780-nm laser. UV–Vis spectra were recorded on a Jasco V-650 UV–Vis spectrophotometer equipped with a diffuse reflectance accessory. Temperature-programmed reduction and thermogravimetric (TPR-TG) analysis was performed in a Setaram TG92 instrument in a flow of 50 vol.% H$_2$ in Ar (100 cm^3 min^{-1}) at a heating rate of 5 K.min^{-1}.

Catalytic tests

Methanol decomposition was carried out in a fixed-bed reactor at atmospheric pressure. The catalyst (0.055 mg) of 0.2–0.8-mm particle size was diluted with a three-fold higher amount (by volume) of glass spheres. Each catalyst was tested under conditions of a temperature-programmed regime within the range of 350–770 K at a heating rate of 1 K.min^{-1}. During the experiments, the reactant (methanol) as well as all carbon-containing products (CO, CO$_2$, methane, methyl formate, and dimethyl ether) were in the gaseous phase. Their amounts were determined by on-line GC analyses on a HP apparatus equipped with flame ionisation and thermal conductivity detectors, and a 30-m PLOT Q column using an absolute calibration method and a carbon-based material balance.

RESULTS AND DISCUSSION

To gain information about textural characteristics of the studied materials, nitrogen physisorption measurements were conducted (Fig. 1a, Table 1). The isotherms were characterised as type IV according to IUPAC classification, which is typical of mesoporous materials, with a hysteresis loop attributed to cage-like mesopores. All the materials were characterised by high specific surface area and total pore volume (Table 1). The binary materials demonstrated higher specific surface area in comparison with the individual metal oxides, which was the highest for 5Sn5Ti. Besides, formation of smaller and uniform mesopores was observed with the binary oxides. There was no simple relation between texture parameters (Table 1) and sample composition, which could be evidence for absence of mechanical mixture of the separate oxides. XRD patterns of TiO$_2$–SnO$_2$ mixed oxides are presented in Fig. 1b and data on phase composition, unit cell parameters, and average crystallite size are listed in Table 1.
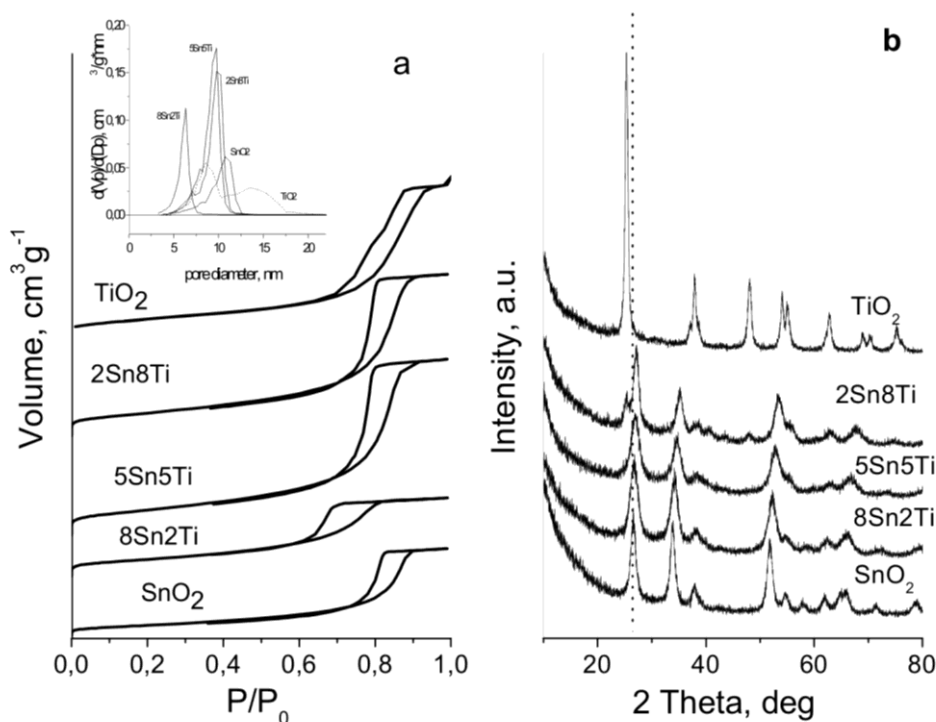
Fig. 1. Nitrogen physisorption isotherms (a) and pore size distribution (a, insert) and XRD patterns (b) for all Ti-Sn oxides.

For pure titania, only reflections of anatase (2θ = 25.6º, 38.3º, 47.8º, and 62.5º) were detected (pdf 01086-1157) [13]. The diffraction pattern of unmixed tin dioxide showed reflections at 2θ = 27.2° and 34.4° referred to SnO$_2$ with cassiterite tetragonal structure (ICDD card No. 41-1445) of space group P42/mnm. Weak reflections of anatase were still detected in the pattern of 8Ti2Sn, but well-defined reflections of cassiterite were also observed.

On further increase of tin content (5Ti-5Sn and 2Ti-8Sn samples) only reflections of well crystal-lised cassiterite were registered. These reflections were slightly shifted to higher Bragg angles indi-cating a decrease in cassiterite unit cell parameters.

Taking into account that Ti^{4+} and Sn^{4+} ion radii are 0.74 and 0.84 Å, respectively, the latter observation could be assigned to incorporation of the smaller Ti^{4+} ions into SnO$_2$ lattice [3]. A slight increase in anatase unit cell parameters was also detected with 2Sn8Ti (Table 1) probably due to incorporation of Sn^{4+} ions [3, 4]. XRD reflections of all the binary materials are broader as compared to the pure tin dioxide and titania, which is evidence for higher dispersion of the former (Table 1).

To obtain further information about the oxidation state of the various metal oxide species, UV-Vis, FTIR, and Raman spectroscopy measurements were also made (Fig. 2).

Table 1. Nitrogen physisorption and XRD data on Ti-Sn oxides of different composition.

Sample	A_{BET}, * m^{2}g^{-1}	V_{tot}, ** cm^{3}g^{-1}	Space group	Unit cell	Particle size, nm	SA***
TiO$_2$	85	0.29	anatase, I41/amd	3.7862(4) 9.493(1)	17	0.46
2Sn8Ti	98	0.30	cassiterite, P42/mnm	4.670(4) 3.059(2)	7	0.28
			anatase, I41/amd	3.803(3) 9.528(8)	10	
5Sn5Ti	107	0.32	cassiterite, P42/mnm	4.664(2) 3.096(2)	5	0.05
8Sn2Ti	72	0.14	cassiterite, P42/mnm	4.707(2) 3.154(1)	6	0.18
SnO$_2$	43	0.16	cassiterite, P42/mnm	4.738(1) 3.186(1)	9	0.21

*A_{BET} -specific surface area (BET method), **V_{tot}- total pore volume, ***SA - specific catalytic activity calculated per unit surface area at T = 700 K
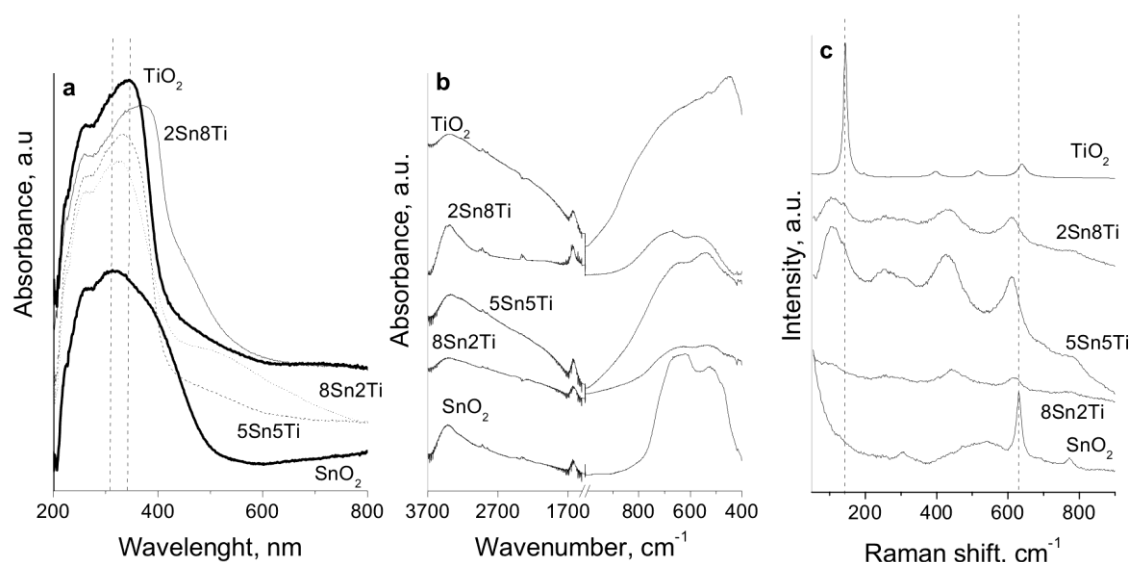
Fig. 2. UV-vis spectra (a), FTIR spectra (3700–1500 cm^{-1} and 1000–400 cm^{-1}) (b), and Raman spectra of the Ti-Sn oxides (c).

A strong absorption feature at 350 nm in the UV-Vis spectrum (Fig. 2a) of titania sample is due to d-d electronic transition between Ti^{4+} ions and O$_2$-

ligands in anatase [15]. The UV–Vis spectrum of pure tin dioxide represents an absorption in the 200–350-nm range, which is characteristic of a valence-

conduction interband transition. Increased absorption could be ascribed to the presence of defects in the SnO$_2$ lattice [16]. A maximum at about 230 nm could be due to surface Sn^{4+} species [15 and refs therein]. A well-defined red shift of the absorption edges was observed for all binary materials, which indicates changes in the environment and/or of the oxidation state of the tin ions.

FTIR spectra of TiO$_2$–SnO$_2$ materials are shown in Fig. 2b. The IR bands at about 460, 620 cm^{-1} and the shoulder at 910 cm^{-1} are close to reported reference vibration modes of Ti–O in anatase phase TiO$_2$ lattice [17]. Changes in the shape and intensity of the shoulder at 910 cm^{-1} in the IR spectra of the bi-component materials reveal interaction between tin dioxide and titania phases, which is in good agreement with XRD and nitrogen physisorption data. In consistence with the UV-Vis data (Fig.2a), the broad band in the 400–680 cm^{-1} region could be ascribed to superposition of vibration stretching modes of bridged Sn−O−Sn, Ti−O−Ti, and Ti−O−Sn bonding [17]. Broad bands centred at about 3400 and 1600 cm^{-1}, which are generally assigned to stretching and bending vibrations of physically adsorbed water and hydroxyl groups, respectively, were registered as well [18,19].

To get more information on the interaction between the metal oxide nanoparticles, Raman spectra were also recorded (Fig. 2c). The spectrum of titania sample (Fig. 2c) displays the main peaks at 149, 198, 398, 515, and 644 cm^{-1} that are typical of anatase TiO$_2$ structure [20]. The spectrum of tin dioxide consists of an intense band at 630 cm^{-1} and a weak band at 774 cm^{-1}, which could be assigned to [21] A1g and B2g modes of symmetric and asymmetric stretching vibrations of Sn−O bonds, respectively [22, 23].

A slight shift and broadening of the main Raman-active modes combined with a decreased intensity were observed with the bi-component materials (Fig. 2c), which could be assigned to partial incorporation of titanium ions into the SnO$_2$ lattice. The latter resulted in significant changes in dispersion and structure [21−23].

Fig. 3 shows data on TPR analyses. Reduction of tin dioxide sample was initiated above 440 K. A further temperature increase up to 773 K caused a weight loss associated with about 100% (или: with almost complete) reduction of Sn^{4+} to Sn^0 (Fig. 3a).

The TPR-DTG effect on the bi-component samples was smaller in comparison with unmixed tin dioxide and shifted to higher temperature. In accordance with the UV–Vis data, this could be assigned to the formation of hardly reducible Ti-O-Sn species. 5Sn5Ti manifested the lowest reducibility. Note that this material exhibited the highest dispersion and specific surface area (Table 1). In this way, the equimolar Ti/Sn ratio in the binary materials facilitated the formation of homogeneous mixed oxide phase.

Temperature dependencies of methanol conversion and the selectivity to CO for the titania and tin oxide materials are presented in Fig. 4a, b.
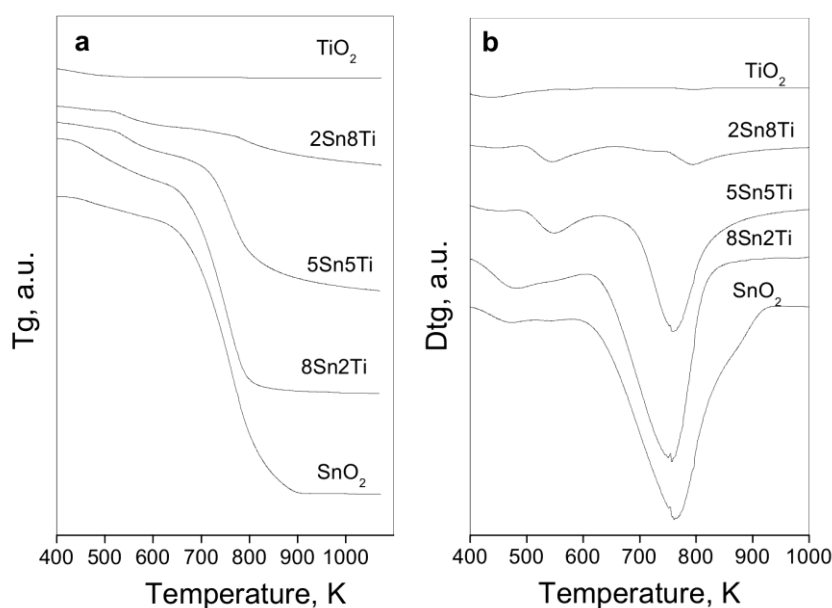
Fig. 3. TPR-TG (a) and TPR-DTG (b) profiles of the Ti-Sn mixed oxides.
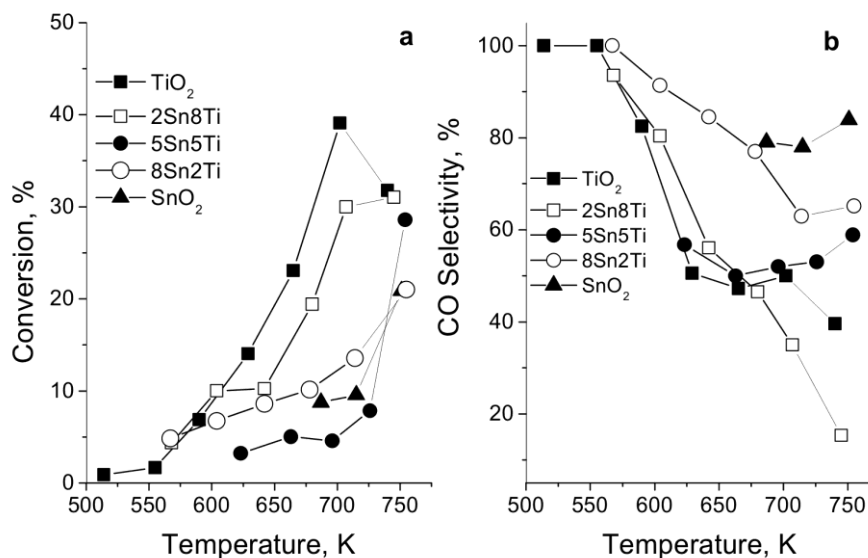
Fig. 4. Methanol conversion vs temperature (a) and selectivity to CO (b) for the Sn-Ti oxides.

Except for CO, which is directly associated with hydrogen production from methanol, CO_2, CH_4, and dimethyl ether (DME) were registered as by-products. All samples exhibited catalytic activity above 550 K. It was the highest for pure titania and strongly decreased upon SnO_2 addition. No simple relation between catalytic activity and samples composition was observed. Moreover, the sample having the highest dispersion and specific surface area (5Sn5Ti) demonstrated the lowest catalytic activity. Specific catalytic activity per unit surface area (SA) was calculated to disregard the impact of sample texture parameters on the catalytic properties (Table 1). Again, the highest value was found for titania, whereas 5Sn5Ti demonstrated an extremely low value. At the same time, significant differences in products distribution were observed. The main by-product on titania was DME (about 40%), which could be assigned to high Lewis acidic functionality [25]. The highest CO selectivity (85%) was detected for pure tin dioxide. All binary materials showed a relatively high selectivity to CO_2 (up to 10%) and methane (25−47%) formation. These results clearly demonstrate changes of the catalytic sites in the binary materials. In view of the XRD, TPR, UV-Vis, and Raman and FTIR spectral data, formation of shared Sn−O−Ti active sites can be proposed. Obviously, this formation is associated with sample composition, being to a higher extent for the sample with Ti/Sn equimolar ratio.

CONCLUSIONS

High surface area mesoporous SnO_2-TiO_2 binary materials can be successfully synthesized using template assisted hydrothermal technique. It was found that the binary oxide materials exhibit higher dispersion and specific surface area, but lower specific catalytic activity and selectivity in methanol decomposition to CO as compared to the individual metal oxides. This could be assigned to the formation of shared Sn−O−Ti structures, the process being directed by the Ti/Sn ratio.

REFERENCES

1. O. Cap, C. L. Huisman, A. Reller, *Prog. Solid State Chem.*, **32**, 33 (2004).
2. S. G. Seong, E. J. Kim, Y. Kim, K. Lee, S. Hahn, *Appl. Surf. Sci,.* **256,** 1 (2009).
3. M. F. Abdel-Messih, *J. Photochem. Photobiol. A: Chem.,* **260**, 1 (2013).
4. E. Arpac, F. Sayılkan, M. Asiltürk, P. Tatar, Nadir Kiraz, H. Sayılkan, *J. Hazard. Mater.,* **140**, 69 (2007).
5. Y. Tu, S. Huang, J. Sang, X. Zou , *J. Alloys Compd.,* **482**, 382 (2009).
6. E. M. El-Maghraby, *Physica B,* **405,** 2385 (2010).
7. H. Gleiter, *Acta Mater.*, **48** 1 (2000).
8. M. Fernandez-Garcıa, A. Martınez-Arias, J. C. Hanson, J. A. Rodriguez, *Chem. Rev.* **104**, 4063 (2004).
9. B. L. Cushing, V. L. Kolesnichenko, C. J. O'Connor, *Chem. Rev.* **104**, 3893 (2004).
10. X. Wang, J. Zhuang, Q. Peng, Y. D. Li, *Nature* **437**, 121 (2005).

11. Y. Ju-Nam, J. R. Lead, *Sci. Total Environ.* **400**, 396 (2008).
12. I. T. Weber, A. Valentini, L. F. D. Probst, E. Longo, E. R. Leite, *Mater. Lett.* **62**, 1677 (2008).
13. T. Tsoncheva, L. Ivanova, D. Paneva, I. Mitov, C. Minchev, M. Fröba, *Micropor. Mesopor. Mater.,* **120**, 389 (2009).
14. M. Altomare, M. V. Dozzi, G. L. Chiarello, A. D. Paola, L. Palmisano, E. Selli, Catal. Today, **252**, 184 (2015).
15. Q. Shen, H. Yang, Q. Xu Qian, Y. Yang, R. Hao, *Mater. Lett.* **64**, 442 (2010).
16. I. Nitoi, P. Oancea, M. Raileanu, M. Crisan, L. Constantin, I. Cristea, *J. Ind. Eng. Chem.,* **21**, 677 (2015).

17. D. A. Popescu, J.-M. Herrmann, A. Ensuque, F. Bozon-Verduraz, *Phys. Chem. Chem. Phys.,* **3**, 2522 (2001).
18. Y. A. Cao, W. S. Yang, W. F. Zhang, G. Z. Liu, P. Yue, *New J. Chem.,* **28**, 218 (2004).
19. C. P. Sbu, S. R. Kumar, P. Mukundan, K. G. K. Warrier, *Chem. Mater.* **14**, 2876 (2002).
20. H. Nur, Mater. *Sci. Eng. B – Sol,* **133**, 49 (2006).
21. W. Wang, *Appl. Surf. Sci.,* **261**, 890 (2012).
22. S. Cui, *J. Mater. Chem. A,* **1**, 4462 (2013).
23. T. Jia, *Mater. Sci. Eng. B,* **189**, 32 (2014).
24. X. Liu, J. Iqbal, Z. Wu, B. He, R. Yu, *J. Phys. Chem. C,* **114**, 4790 (2010).
25. G. Issa, A. Mileva, M. Dimitrov, J. Henych, V. Štengl, T. Tsoncheva, *Nanosci & Nanotech.,* **17**, 18 (2017).

НАНОСТРУКТУРИРАНИ МЕЗОПОРЕСТИ Ti$_X$Sn$_{1-X}$O$_4$ СМЕСЕНИ ОКСИДИ КАТО КАТАЛИЗАТОРИ ЗА РАЗПАДАНЕ НА МЕТАНОЛ: ЕФЕКТ НА СЪОТНОШЕНИЕТО Ti/Sn

И. Генова[1]*, Т. Цончева[1], М. Димитров[1], Д. Ковачева[2]

[1] *Институт по органична химия с Център по фитохимия, БАН, 1113 София, България*
[2] *Институт по обща и неорганична химия, БАН, 1113 София, България*

(Резюме)

Целта на настоящето изследване е да се изясни влиянието на Ti / Sn съотношението на смесени Ti$_x$Sn$_{1-x}$O$_4$ оксиди върху техните структурни, редукционни и каталитични свойства. Мезопорести смесени оксиди с различно съотношение Ti/Sn са синтезирани чрез хидротермална техника в присъствие на органичен темплейт. Получените материали са характеризирани с комплекс от физикохимични техники, като асорбция на азот, рентгенофазов анализ, Раманова, УВ-видима и ИЧ спектроскопия и ТПР с водород. Като каталитична тест-реакция е използвана реакция на разпадане на метанол до синтез газ. Каталитичната активност на бинарните материали зависи по сложен начин от техния фазов състав. Той е подобрен благодарение на увеличаването на специфичната повърхност и обема на порите, но силно потиснат поради значителните структурни промени.

Synthesis, characterization and photocatalytic performance of brannerite-type LiVMoO$_6$

M. K. Milanova*, R. S. Iordanova, M. N. Gancheva

Institute of General and Inorganic Chemistry, Bulgarian Academy of Sciences, Acad. G. Bonchev St., Bldg. *11, 1113 Sofia, Bulgaria*

Crystalline LiVMoO$_6$ with brannerite structure was synthesized by mechanochemically assisted solid-state synthesis. A mixture of Li$_2$CO$_3$; V$_2$O$_5$, and MoO$_3$ of oxide 1:1:2 molar ratio was subjected to intense mechanical treatment for 10 min in air using a planetary ball mill (Fritsch-Premium line-Pulversette No 7) and zirconia vials and balls (5 mm in diameter). The mechanically treated mixture of the metal oxides was subsequently heated for 1 hour at 450 °C. XRD, Raman spectroscopy, and SEM investigations were performed to examine phase formation, local structure, and morphology of the obtained product. Preliminary mechanical activation of the reagents led to the formation of highly reactive precursor and annealing of the latter formed submicron-sized particles of LiVMoO$_6$ with irregular shape, which were highly agglomerated. Photocatalytic results showed that adsorption of Malachite Green dye (MG) on the LiVMoO$_6$ surface is a prerequisite for its photodegradation. Degradation percentage of Malachite Green in the presence of LiVMoO$_6$ photocatalyst was about 70% after 210 min of UV irradiation time.

Key words: mechanochemistry, Raman spectroscopy, photocatalysis.

INTRODUCTION

Over the last decades, photocatalysis has been extensively explored as a process to efficiently conduct oxidation of organic compounds, mainly pollutants. In this sense, TiO$_2$ has been preferred by far over other materials as photocatalyst. Despite the proven efficiency of titania, some issues still challenge the scientific community dedicated to photo-catalysis. Recently, scientific efforts have been directed to design titania-free visible-light active photocatalysts. For example, monoclinic and perovskite materials, such as InMO$_4$ (M = V, Nb, Ta), BiVO$_4$, AgTaO$_3$, AgNbO$_3$, and Ag$_3$VO$_4$, have been confirmed to be active visible-light responsive photocatalysts [1–4]. In this context, some other monoclinic systems may deserve special attention. Among them, brannerite-type LiMoVO$_6$ compound calls the attention due to its electrochemical properties and recognised application as a positive electrode material for lithium secondary batteries [5–7]. The aim of the present study was to obtain LiMoVO$_6$ compound by mechanochemically assisted solid-state synthesis and to explore its structural and photocatalytic properties.

EXPERIMENTAL

Crystalline LiVMoO$_6$ with brannerite structure was prepared by mechanochemically assisted solid-state synthesis. A mixture of Li$_2$CO$_3$, V$_2$O$_5$, and MoO$_3$ of oxide 1:1:2 molar ratio was subjected to intense mechanical treatment for 10 min in air using a planetary ball mill (Fritsch-Premium line-Pulversette No 7) and zirconia vials and balls (5 mm in diameter). Balls to powder weight ratio was 10:1. The mechanically treated mixture of the reagents was subsequently heated for 1 hour at 450 °C. Phase formation was checked by XRD (CuKα, Ultima IV; Rigaku Corp.). Room temperature Raman spectroscopy measurements of LiVMoO$_6$ were performed in the range of 200–1200 cm^{-1} on a micro-Raman system of Jobin-Yvon Horiba (LABRAM HR-800) spectrometer with green laser (wavelength of 532 nm). LiVMoO$_6$ morphology and microstructure were investigated by JEOL JSM-5300 scanning electron microscope. The photocatalytic activity of the obtained LiVMoO$_6$ was evaluated toward the degradation of a model aqueous solution of Malachite Green (MG) oxalate (Sigma-Aldrich) under UV irradiation at room temperature. A MG solution (150 ml, 5 ppm, pH = 7) containing 0.1 g of as-prepared powder was placed into a glass beaker. Before turning on the light, the solution was ultrasonicated for 10 min and after that stirred for 10 min to ensure adsorption-desorption equilibrium in the solid/solution system. A solution of 3 ml volume was taken at regular time intervals and separated through centrifugation (5000 rpm, 5 min). Then MG

---

concentration in the centrifugate was measured by an Evolution 300 UV-VIS (Thermo Scientific, 50–60 Hz, 150 VA) spectrophotometer. The photo-degradation percentage of MG was calculated by Eq. (1).

$$R = (1 - C_t/C_0) \times 100, \% \quad (1)$$

Where C_0 and C_t are MG initial concentration and concentration after certain period of irradiation time (ppm), respectively.

RESULTS AND DISCUSSION

Figure 1 presents X-ray diffraction patterns of $Li_2CO_3 + V_2O_5 + MoO_3$ mixture before mechanical treatment (Fig. 1a), initial mixture after mechanical treatment for 10 minutes (Fig. 1b), and mixture of mechanically treated precursors for 10 min, and subsequently calcined for 1 h at 450 °C (Fig. 1c).
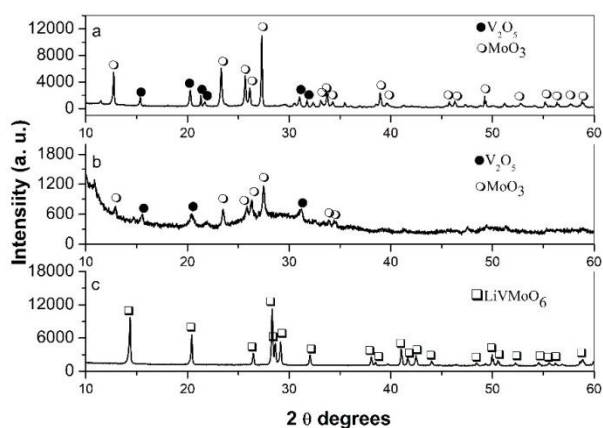
Fig. 1. XRD patterns of $Li_2CO_3 + V_2O_5 + MoO_3$ mixture: a) before mechanical treatment; b) after 10 min mechanical treatment under rotation speed of 500 rpm; c) after 10 min mechanical treatment and calcination at 450 °C for 1 hour.

The initial XRD pattern (Fig. 1a) shows all peaks corresponding to MoO_3 (JCPDS No 47-01320) and V_2O_5 (JCPDS No 75-0457), while the reflections of the initial Li-containing compounds are present at the background level due to weak scattering ability of the lithium atoms. The diffraction peaks of the reactants gradually decreased with milling. More-over, partial amorphisation of the initial oxides was observed during the milling process (Fig. 1b). XRD data indicate the formation of single phase $LiVMoO_6$ with brannerite-type structure by mechanochemical treatment of the precursor for 10 min followed by heat treatment for 1 h at 450 °C (Fig. 1c). The dif-fraction pattern of the obtained $LiVMoO_6$ was indexed using 'Index' software assuming a C2/m symmetry that corresponds to the monoclinic citing of the brannerite structure and shows no traces of

impurity phases [8]. The diffraction peaks are intense and symmetrical evidencing the formation of a well crystallized $LiVMoO_6$ product.

The obtained material was characterized by applying Raman spectroscopy and SEM. Raman features show (Fig. 2) vibrational modes of the various MeO_6 (Me = V, Mo, Li) octahedral units building the lattice. The assignment of the observed Raman bands is shown in Table 1.
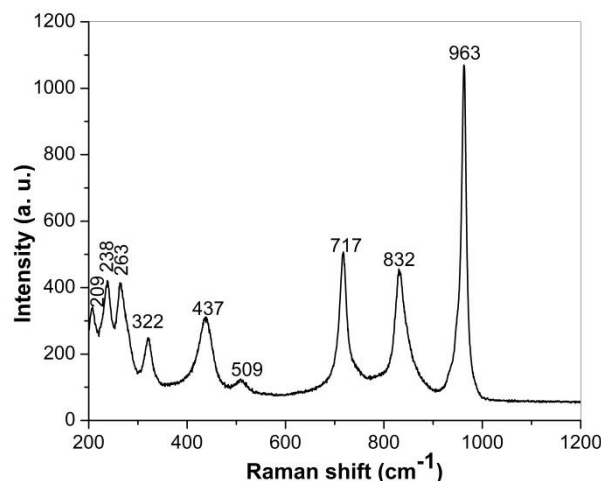
Fig. 2. Raman spectra of $LiVMoO_6$ obtained after mechanical activation of $Li_2CO_3 + V_2O_5 + MoO_3$ mixture for 10 min and subsequent heat treatment for 1 hour at 450 °C.

Table 1. Observed Raman bands and their assignment for $LiVMoO_6$, obtained by mechanochemically assisted solid state synthesis.

Raman band position, cm⁻¹	Assignments	Refs.
963	ν(Me=O; Me=V, Mo)	9–11
832	ν_{as} (Me-O-Me)	9–11
717	ν_{as} (Me-O-Me)	9–11
437	ν_{as} (Me-O-Me)	9–11
322	δ(Me-O-Me)	9, 10
263	δ(Me-O-Me) + ν(LiO₆)	9–11

SEM images of $LiVMoO_6$ of different magnifi-cation are displayed in figure 3. SEM photographs evidenced that the sample consists of dense agglo-merates formed from irregular shaped and small submicron-size particles.

The MG dye was used as a model pollutant to investigate the photocatalytic activity of the prepared sample. The strongest absorption peak of MG dye at 615 nm was selected to monitor the photocatalytic degradation process (Fig. 4). After UV illumination, the absorption band at 615 nm decreased rapidly and new absorption bands in the ultraviolet and visible range were not registered. This observation is in marked contrast with the data
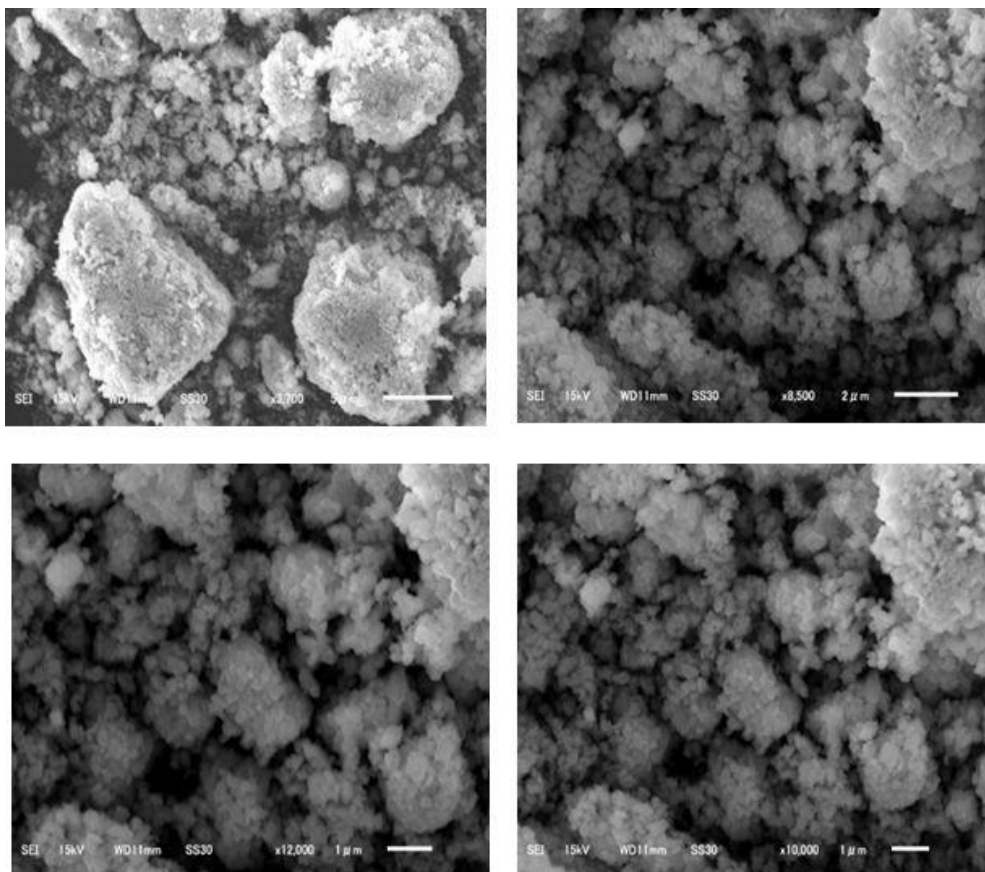
Fig. 3. SEM images of $LiVMoO_6$ at different magnification obtained after mechanical activation of
$Li_2CO_3 + V_2O_5 + MoO_3$ mixture for 10 min and subsequent heat treatment for 1 hour at 450 °C.

reported in the literature concerned with photocatalyzed degradation of many organic compounds in the presence of TiO_2 under UV irradiation, in which intermediates are easily detected by absorption spectra [12]. These photocatalytic results also show that MG is firstly absorbed on the $LiVMoO_6$ surface and then photodegraded. MG degradation percentage in the presence of $LiVMoO_6$ photocatalyst was about 70% after 210 min of irradiation time.
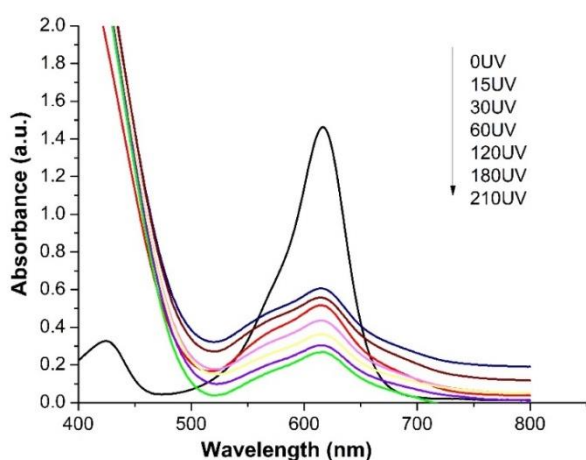
Fig. 4. Evolution of absorption spectra of MG dye solution over $LiVMoO_6$ powder under UV-vis irradiation.

CONCLUSIONS

Single phase $LiVMoO_6$ was successfully prepared by applying mechanochemically assisted solid-state synthesis. Preliminary mechanical activation of a mixture of metal oxides in a planetary ball mill led to the formation of highly reactive precursors. Annealing of the latter caused formation of submicron-sized highly agglomerated particles of $LiVMoO_6$ with irregular shape. Photocatalytic results show that adsorption of Malachite Green is a prerequisite for $LiVMoO_6$-assisted photodegradation of MG under UV light irradiation. MG degradation percentage in the presence of $LiVMoO_6$ photocatalyst was about 70% after 210 min of irradiation time.

REFERENCES

1. J. Ye, Z. Zou, H. Arakawa, M. Oshikiri, M. Shimoda, A. Matsushita, T. Shishido, *J. Photochem. Photobiol. A: Chem.*, **148**, 79 (2002).
2. X. Zhang, Z. Ai, F. Jia, L. Zhang, X. Fan, Z. Zou, *Mater. Chem. Phys.,* **103**, 162 (2007).
3. H. Kato, H. Kobayashi, A. Kudo, *J. Phys. Chem. B,* **106**, 12441 (2002).
4. R. Konta, H. Kato, H. Kobayashi, A. Kudo, *Phys. Chem. Chem. Phys.,* **5**, 3061 (2003).
5. C. Julien, *Ionics,* **6**, 30 (2000).
6. L. Zhou, Y. Liang, L. Hu, X. Han, Z. Yi, J. Sun, S. Yang, *J. Alloys Comp.,* **457**, 389 (2008).
7. M. Milanova, R. Iordanova, M. Tatsumisago, A. Hayashi, P. Tzvetkov, D. Nihtianova, P. Markov, Y. Dimitriev, *J. Mater. Sci.,* **51**, 3574 (2016).
8. R. Run, A. Wadsley, *Acta Cryst.,* **21**, 974, (1966).
9. N. Amdouni, H. Zarrouk, F. Soulette, C. Julien, *J. Mater. Chem.,* **13**, 2374 (2003).
10. L. Hurtado, E. Torres-García, R. Romero, A. Ramírez-Serrano, J. Wood, R. Natividad, *Chem. Eng. J.,* **234**, 327 (2013).
11. E. Baran, C. Cabello, A. Nord, *J. Raman Spectrosc.,* **18**, 405, (1987).
12. H. Hidaka, J. Zhao, E. Pelizzetti, N. Serpone, *J. Phys. Chem.,* **96**, 2226 (1992).

СИНТЕЗ, ОХАРАКТЕРИЗИРАНЕ И ФОТОКАТАЛИТИЧНИ СВОЙСТВА НА LiVMoO$_6$

М. К. Миланова*, Р. С. Йорданова, М. Н. Ганчева

Институт по обща и неорганична химия, Българска академия на науките, ул. „Акад. Г. Бончев", блок 11, 1113 София, България

(Резюме)

Монофазен кристален LiVMoO$_6$ със структура от Бранеритов тип е получен успешно чрез механохимично активиран твърдофазен синтез. Смес от Li$_2$CO$_3$, V$_2$O$_5$ и MoO$_3$ в молно съотношение на оксидите 1:1:2 е подложена на интензивна механична обработка за 10 минути във въздушна среда в планетарна топкова мелница (Fritsch-Premium line-Pulversette No 7). Механично обработената смес от прекурсорите е нагрята за 1 час при 450 °C. Така полученият образец е охарактеризиран чрез Рентгенова дифракция, Раманова спектроскопия и сканираща електронна микроскопия. Установено е, че предварителното механично третиране на сместа от реагенти в планетарна топкова мелница, води до значително активиране на реакционната смес от изходни компоненти и след последващо нагряване за кратък период от време (1 час) се получава кристален LiVMoO$_6$, съдържащ кристалити със субмикронен размер. Фотокаталитичната активност на полученият LiVMoO$_6$ беше изследвана чрез разграждане на органичното багрило Малахитово Зелено под ултравиолетово облъчване. Фотокаталитичните резултати показват, че органичното багрило първо се адсорбира на повърхността на LiVMoO$_6$ и след това започва неговото разграждане. След 210 минути време на облъчване, процентът на разграждане на Малахитово Зелено в присъствие на LiVMoO$_6$ е около 70%.

Properties of mechanochemically synthesised N-doped Fe$_2$O$_3$-ZnO mixed oxide

N. G. Kostova*[1], M. Fabian[2], E. Dutkova[2], N. Velinov[1], Y. Karakirova[1], M. Balaz[2]

[1] Institute of Catalysis, Bulgarian Academy of Sciences, 1113 Sofia, Bulgaria
[2] Institute of Geotechnics, Slovak Academy of Sciences, 04001 Kosice, Slovakia

This work reports synthesis and characterisation of N-doped Fe$_2$O$_3$-ZnO mixed oxide and the ability of this material to decolourise Methyl Orange organic dye in aqueous solution under visible light irradiation. The photocatalytic material was prepared using eco-friendly simple mechanochemical synthesis. The photocatalysts were characterised by X-ray diffraction (XRD), UV-vis diffuse reflectance spectroscopy (DRS), photoluminescence spectroscopy (PL), and electron paramagnetic resonance (EPR) methods as well as Mössbauer spectroscopy. XRD analysis showed that employed mechanochemical synthesis promoted changes in crystallite size. A lower band gap was observed. The lower band gap and an improved photocatalytic activity under visible light irradiation of the mechanochemically synthesised nitrogen-doped Fe$_2$O$_3$-ZnO mixed oxide were registered in comparison with ZnO. A lower intensity in the PL spectra of N-Fe$_2$O$_3$-ZnO confirmed better separation and lower electron-hole recombination rate and accordingly higher photodecolourisation performance than initial ZnO.

Key words: mechanochemistry, photocatalysis, dye discolouration, Methyl Orange.

INTRODUCTION

Heterogeneous photocatalysis has been widely investigated as a technique for environmental detoxification in both water and air [1]. Semiconductors are widely studied as photocatalysts for degradation of organic contaminants in wastewaters [2]. Many semiconductors such as metal oxides and metal sulphides have been employed to study photocatalytic reduction of pollutants in water [3]. ZnO is often used as a solid photocatalyst [4]. The zinc oxide has higher efficiency in photocatalytic performance than TiO$_2$ due to its high quantum efficiency [5]. Zinc oxide in the wurtzite phase is the most used metal oxide as photocatalyst due to its electronic band structure. ZnO is a wide band gap semiconductor (E$_g$ = 3.37 eV) that utilises only the UV portion (about 5%) of solar energy. Therefore, considerable effort has been applied to extend the response of ZnO to photodegradation of pollutants by visible-light irradiation [6]. This disadvantage is overcome in two ways, namely: by coupling with another metal oxide [7] or by doping with non-metal [8].

Hematite (α-Fe$_2$O$_3$) is a promising candidate for photocatalytic applications due to its narrow band gap of 2.2 eV [9]. Furthermore, hematite absorbs light up to 600 nm, collects up to 40% of the solar spectrum energy. Being stable in most aqueous solutions, it is one of the cheapest available semiconductor materials [10]. Development of coupled semiconductor photocatalysts is a significant advancement in catalytic functional materials [11]. Mixed oxides show a considerably higher photocatalytic activity for dye removal from wastewater under visible light irradiation than that of a single semiconductor [12]. The mixed oxides have been fabricated by different techniques such as hydrothermal-thermal decomposition [11], sol-gel [12], reflux condensation [13], homogeneous precipitation [14], and mechanochemical methods [15]. High-energy milling is one of the most powerful techniques for synthesis of photocatalysts [16].

Nitrogen doping represents an important strategy to modulate the optical and photocatalytic properties of metal oxides [17]. Nitrogen doping is more effective than carbon/sulphur doping to achieve a high visible-light response [18]. Highly intensive homogenisation by milling of the mixture of interacting components makes mechanochemical synthesis easier [19].

In this work N-doped Fe$_2$O$_3$-ZnO mixed oxide prepared by mechanochemical synthesis was investigated to evaluate photodecolourisation of Methyl Orange (MO) as a dye model system. Here, N-doping of mixed Fe$_2$O$_3$-ZnO oxide was studied as a low cost alternative to enhance ZnO photoactivity in visible light irradiation by slowing down photogenerated charge recombination.

---

* To whom all correspondence should be sent
E-mail: nkostova@ic.bas.bg

EXPERIMENTAL

Materials

Commercial ZnO was purchased from Himsnab Company (Bulgaria). Hematite (Aldrich) and ammonia reagents of analytical grade were used without further purification. Samples of N-doped Fe$_2$O$_3$-ZnO mixed oxide were prepared by mechanochemical synthesis using a high-energy planetary ball mill Pulverisette 6 (Fritsch, Germany). The precursors were milled for 0.5 h at 550 rpm in ambient atmosphere using a chamber (250 cm^3) with 21 balls (10 mm in diameter) both made of zirconia. The ball-to-powder mass ratio was 40:1. After milling, the powdered mixture was calcined at 673 K in air for 2 h.

Methods of investigation

X-ray diffraction (XRD) patterns were recorded on a D8 Advance diffractometer (Brucker, Germany) using CuKα radiation. Diffraction data were collected over angular range of $20° < 2\Theta < 65°$ with steps of 0.02° and a counting time of 9 s/step. Commercial Diffrac^{plus} Topas was utilised for Rietveld analysis.

Diffuse reflectance UV-vis spectra for evaluation of photophysical properties were recorded in the diffuse reflectance mode and transformed to absorption spectra through the Kubelka-Munk function [20]. A Thermo Evolution 300 UV-vis spectrophotometer, equipped with a Praying Mantis device with Spectralon as the reference was used.

Photoluminescence (PL) spectra at room temperature were acquired at right angle on a photon counting spectrofluorometer PC1 (ISS) with a photoexcitation wavelength of 325 nm. A 300-W xenon lamp was used as the excitation source. For measuring the PL intensity, the powders were suspended in absolute ethanol.

Room temperature Mössbauer spectra were registered by measurements with a Wissel (Wissenschaftliche Elektronik GMBN, Germany) electromechanical spectrometer working in a constant acceleration mode. A 57 Co/Rh (activity = 50 mCi) source and α-Fe standard were used. Parameters of hyperfine interaction, such as isomer shift (δ), quadrupole splitting (Δ), magnetic hyperfine field (B), line widths (FWHM), and relative weight (G) of partial components in the spectra were determined according to Ref. [21].

EPR spectra were recorded at room temperature on a JEOL JES-FA 100 EPR spectrometer operating in the X-band equipped with a standard TE$_{011}$ cylindrical resonator. The samples were placed in quartz tubes and fixed in the cavity centre. The instrumental settings using the above spectrometer were modulation frequency of 100 kHz, sweep 500 mT, time constant 0.3 s, sweep time 2 min, microwave power 1 mW, and amplitude of the magnetic field modulation of 0.2 mT.

Photocatalytic test

Methyl Orange adsorption on initial ZnO and mechanochemically synthesised Fe$_2$O$_3$-ZnO and N-doped Fe$_2$O$_3$-ZnO samples was measured in the dark. In each experiment, 100 mg of sample were added to dye aqueous solution. Then the suspension was magnetically stirred for 30 min at room temperature in the dark in the absence of oxygen to attain adsorption-desorption equilibrium [22]. The photocatalytic activity of all samples was determined by photodecolourisation of Methyl Orange organic dye under visible light illumination. Moreover, 0.10 g of prepared photocatalyst was suspended in 100 ml of MO solution. The obtained mixture was subjected to stirring in the dark for 30 min to achieve adsorption-desorption equilibrium. Then, the mixed suspension was kept under visible light illumination. At a given time interval, 6 ml of mixed suspension was sampled and centrifuged to eliminate the photocatalyst. The residual concentration of MO was estimated at 463 nm using a SPEKOL 11 (Carl Zeiss Jenna) spectrophotometer.

RESULTS AND DISCUSSION

X-ray data analysis

Powder X-ray diffraction (XRD) analysis was used to identify the crystal phase of the samples. The XRD patterns of pure ZnO and mechanochemically synthesised N-doped Fe$_2$O$_3$-ZnO samples after heat treatment are shown in Fig. 1.
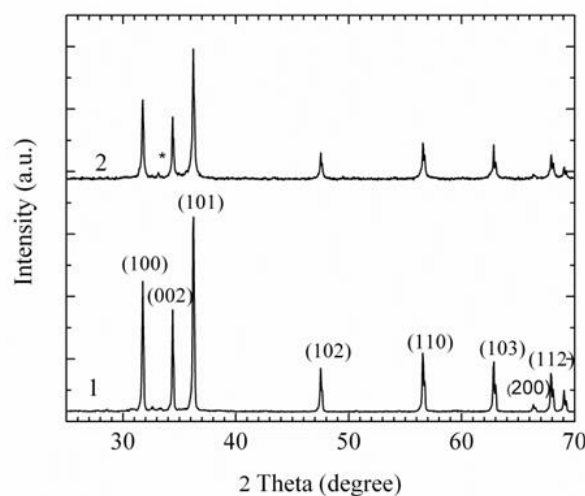
Fig. 1. XRD pattern of initial ZnO (1) and mechanochemically synthesised N-Fe$_2$O$_3$-ZnO sample (2).

Identification of the registered peaks was performed using the JCPDS card 36-1451 for ZnO. The three most intensive peaks at $2\Theta = 31.74$, 34.38, and $36.2°$ were assigned to (100), (002), and (101) reflections of ZnO, indicating that the samples were of hexa-gona wurtzite structure. For the mechanochemically synthesised N-Fe$_2$O$_3$-ZnO sample an additional diffraction peak of α-Fe$_2$O$_3$ appeared at $2\theta = 33.15°$ reflection (104) that is typical of hematite (JCPDS card No 33-0664). The XRD pattern confirmed the formation of nanocrystalline mixed oxide. No peaks consistent with another N-containing phase were detected in the XRD pattern of mechanochemically synthesised sample. The peak intensities of the mechanochemically synthesised sample were lower along with certain broadening (Fig. 1). Thus, mechanochemical synthesis promotes changes in crystallite size of the ZnO material. The average crystallite size of ZnO decreased from 168 nm to about 90 nm.

Diffuse reflectance spectra

UV-vis diffuse reflectance spectra are shown in Fig. 2. A pure ZnO sample could absorb only ultraviolet light. A spectrum of N-doped Fe$_2$O$_3$-ZnO sample demonstrated a reflectance, covering wavelengths from 200 to 800 nm. A decrease of the reflectance was observed for doped mixed oxide compared with pure ZnO.
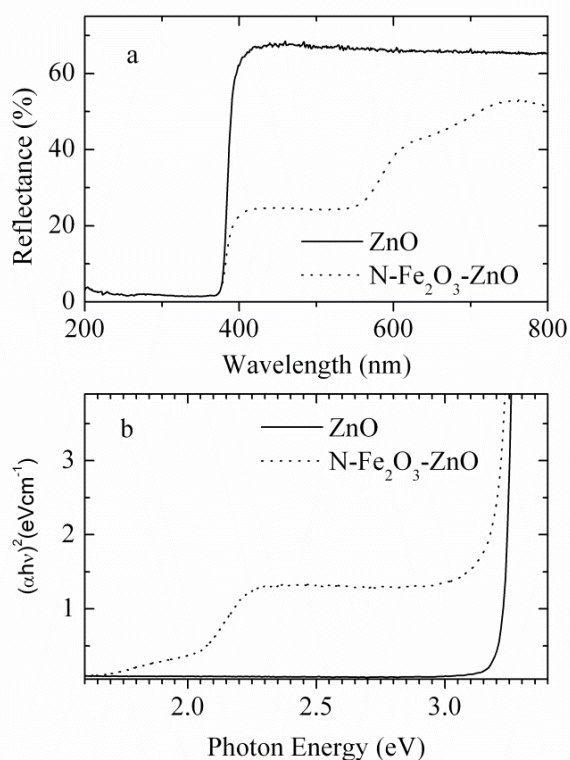
Fig. 2. Diffuse reflectance spectra (a) and plot of $(\alpha h\nu)^2$ versus energy (b) of pure ZnO and mechanochemically synthesised N-doped Fe$_2$O$_3$-ZnO sample.

The reflectance edge of mechanochemically synthesised N-doped Fe$_2$O$_3$-ZnO sample manifested a red shift. Electronic interactions between ZnO and Fe$_2$O$_3$ induced a shift of the band gap absorption to longer wavelengths [23]. This result suggested that the N-doped Fe$_2$O$_3$-ZnO sample had a potential for photocatalysis using the visible part of the spectrum.

The band gap energy of all samples was calculated from the diffuse reflectance spectra by performing a Kubelka-Munk analysis using the following equation:

$$F(R) = (1-R)^2/2R, \qquad (1)$$

where R is the diffuse reflectance. According to this function the band gap energy can be obtained by plotting the $F(R)^2$ vs. the energy in electron volts. The linear part of the curve was extrapolated to $F(R)^2 = 0$ to calculate the direct band gap energy. The results are presented in Fig. 2b. The band gap of the initial ZnO was 3.38 eV, whereas that of the mechanochemically synthesised N-doped Fe$_2$O$_3$-ZnO sample was 1.98 eV. A red shift was attributed to sp-d exchange interactions between the band electrons and the localised d electrons of Fe ions.

Photoluminescence

Because of its high sensitivity and nondestructive nature, photoluminescence (PL) spectroscopy was applied to obtain significant information about the structure of active sites of metal oxides [24]. Room temperature PL spectra of samples were also recorded to study sample defects. Fig. 3 shows PL spectra of the starting ZnO and prepared N-Fe$_2$O$_3$-ZnO samples excited by UV-ray wavelength of 325 nm (photon energy of 3.81 eV) that usually leads to ZnO emission. They exhibit a strong ultraviolet emission at 391 nm and a weak green-yellow emission at 530 nm. The UV emission is attributed to a free excitonic recombination through free excitons transition process [25].

In the spectrum of mechanochemically synthesised N-Fe$_2$O$_3$-ZnO sample, the PL intensity drastically decreased while the line width increased with a shift of emission maximum towards longer wavelengths. This spectrum could be decomposed into PL bands, one in the green, and another in the yellow region. The green luminescence arises from a radiative recombination involving an intrinsic defect located at the surface [26]. The peak intensity of PL spectra correlate with the recombination rate of electron-hole pairs. As the PL emission is the result of the recombination of excited electrons and holes, a lower PL intensity indicates a decrease in recombination rate and thus higher photocatalytic activity [27]. Therefore, it is deduced that the Fe^{3+}

ions trapped the photogenerated electrons, while nitrogen trapped the photogenerated holes, leading to enhanced quantum efficiency and photocatalytic activity [28].

An increase in oxygen vacancies that acted as electron donors in the ZnO lattice promoted better charge separation. Reduction of emission intensity signified a high efficiency of charge separation and transfer between N, Fe$_2$O$_3$, and ZnO.
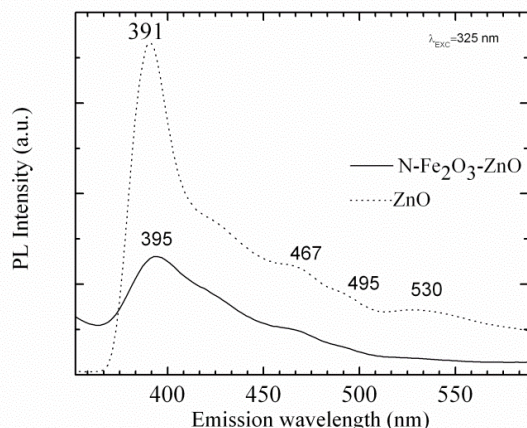
Fig. 3. Photoluminescence spectra of initial ZnO (dot line) and mechanochemically synthesised N-Fe$_2$O$_3$-ZnO sample (solid line).

Mössbauer spectroscopy

57Fe Mössbauer spectra of initial α-Fe$_2$O$_3$ and mechanochemically synthesised N-Fe$_2$O$_3$-ZnO samples are displayed in Fig. 4 and consequent parameters of the materials are listed in Table 1.

The Mössbauer spectrum of pure Fe$_2$O$_3$ was fitted with one sextet with IS of 0.37 mm/s, H$_{eff}$ = 51.5 T, and a negative QS which could be assigned to hematite. The result agrees well with the data from XRD analysis. The Mössbauer spectrum of the N-Fe$_2$O$_3$-ZnO sample is a combination of sextet and doublet (Table 1). Sextet parameters respond to octahedrally coordinated Fe^{3+} ions in antiferromagnetic hematite, while doublet ones reconcile to Fe^{3+} ions in octahedral coordination in paramagnetic or superparamagnetic oxide phase. An approximative phase ratio in the sample can be assumed based on the ratio between calculated relative weights of the components G (Table 1). The doublet with QS = 0.75 mm/s can be ascribed to α-Fe$_2$O$_3$ particles, the sizes of which are below the critical one for the

transition of ferromagnetic to superparamagnetic behaviour [29].
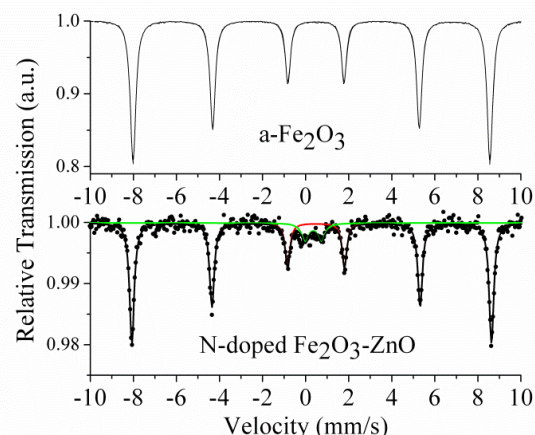
Fig. 4. Mössbauer spectra of initial α-Fe$_2$O$_3$ and N-Fe$_2$O$_3$-ZnO samples.

Electron paramagnetic resonance spectroscopy

Typical EPR spectra of initial ZnO and mechanochemically synthesised N-doped ZnO and N-Fe$_2$O$_3$-ZnO samples are given in Fig. 5. The EPR spectrum of pure Fe$_2$O$_3$ is characterised by a wide line with g value of 2.6997. This line is due to paramagnetic Fe^{3+} ions. The reason for the very wide signal and movement of the g factor to lower magnetic field in comparison with that reported in the literature is a high concentration of ferrous ions and their spin-spin interactions.
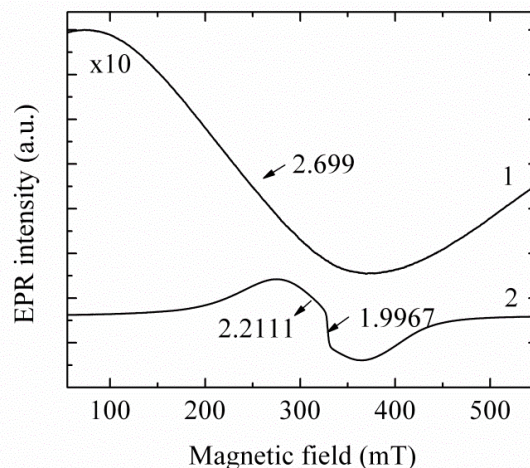
Fig. 5. EPR spectra of α-Fe$_2$O$_3$ (1) and mechanochemically synthesised N-Fe$_2$O$_3$-ZnO sample (2).

Table 1. Room temperature Mössbauer parameters

Sample	Component	IS, mm/s	QS, mm/s	H$_{eff}$, T	FWHM, mm/s	G, %
α-Fe$_2$O$_3$	Sx-α-Fe$_2$O$_3$-Fe^{3+}	0.37	−0.21	51.5	0.30	100
N-Fe$_2$O$_3$-ZnO	Sx-α-Fe$_2$O$_3$-Fe^{3+}	0.38	−0.20	51.9	0.26	90
	Db-Fe^{3+}	0.36	0.75	-	0.40	10

The EPR spectrum of mechanochemically prepared N-Fe_2O_3-ZnO sample can be regarded as superposition of two overlapping EPR signals. One of the signals is wide with g factor around 2.211 and $\Delta H = 87.74$ mT due to octahedrally coordinated Fe^{3+} ions of more finely dispersed iron oxide species [30]. The other signal with $\Delta H = 4.48$ mT and g value of 1.9967 is generally attributed to an unpaired electron trapped on an oxygen vacancy site [31].

Photocatalytic activity

The photocatalytic activities of the samples were evaluated by photodecolourisation of MO in aqueous solutions under visible light irradiation. A preliminary test showed that the direct photolysis process is very slow and can be considered negligible in the same time. Fig. 6a shows decolourisation of MO as a function of irradiation time for the pure ZnO and mechanochemically synthesised N-Fe_2O_3-ZnO samples. Compared to undoped ZnO, the N-Fe_2O_3-ZnO sample showed a considerably enhanced photoactivity. The N-Fe_2O_3-ZnO sample demonstrated discoloration efficiency of 42% in 120 min irradiation that was higher than the ZnO efficiency for the same time duration. The electronic configuration obtained after coupling the two semi-conductors reduces recombination through efficient electron transfer from Fe_2O_3 to ZnO, thus justifying the observed photocatalytic activity results [23].
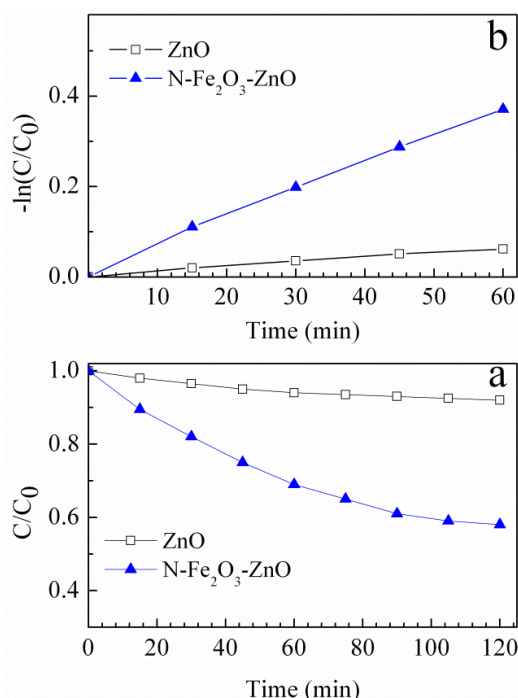
Fig. 6. (a) Degree of decolourisation of Methyl Orange dye and (b) dependence of the rate constants of photo-catalytic decolourisation of Methyl Orange over pure ZnO and mechanochemically synthesised N-Fe_2O_3-ZnO samples under visible light irradiation.

Some researchers have reported that the kinetic behaviour of photocatalytic reaction can be described by a pseudo-first order model. It has been noted that the plot of $\ln(C_0/C)$ versus illumination time represents a straight line and the slope of linear regression can be equal to the apparent pseudo-first order rate constant k. The rate constants for the mechanochemically synthesised N-Fe_2O_3-ZnO and pure ZnO samples were 0.372 and 0.06 h^{-1}, respectively. These results indicated that the localised electron states of Fe_2O_3 serve as charge carrier traps for photogenerated charge carriers under visible light irradiation [32]. According to the literature, the trapped electron or hole will be migrated to the catalyst surface where it will participate in a redox reaction with the dye molecules, thereby suppressing the electron-hole recombination and hence substantially increasing the photodecolourisation efficiency [33].

Furthermore, it is suggested that the different photocatalytic activity behaviours depend on several factors such as crystallite size and band gap. According to the XRD measurements in the present study N-dopant and Fe_2O_3 in mechanochemically prepared samples led to reduction of the crystallite size. In large crystallites of ZnO, recombination is dominant and can be inhibited by decreasing the particle size by ball milling. The pronounced photo-catalytic effect is ascribed to the reduced band gap (DRS) and lower recombination rate (PL) of ZnO.

CONCLUSION

In this study, N-doped Fe_2O_3-ZnO photocatalyst was prepared by a combination of mechanoche-mical/thermal treatment and was used as a catalyst in the process of photodecolourisation of Methyl Orange as a dye model. A lower PL intensity of the mechanochemically synthesised samples in compa-rison with the initial ZnO indicated a lower recom-bination rate of excited electrons and holes. Initial ZnO possessed low PL intensity under visible light irradiation. The mechanochemically synthesised samples exhibited a higher photocatalytic decolouri-sation of Methyl Orange under visible light in comparison with initial ZnO, indicating that visible light generates photon-induced electrons and holes in N-doped Fe_2O_3-ZnO due to appearance of elec-tron level in the band gap. The visible light res-ponsive photocatalyst showed effective activity in the decolourisation process of Methyl Orange and up to 42% for 120 min by increasing the doping level.

REFERENCES

1. M. Janczarek, E. Kowalska, *Catalysts,* **7**, 317 (2017).
2. W. Chiron, A. Fernandes-Cilba, A. Rodriguez, E. Garcia-Calvo, *Water Res*., **34,** 366 (2000).
3. K. M. Lee, Ch. W. Lai, K. S. Ngai, J. Ch. Juan, *Water Res*., **88**, 428 (2016).
4. A. di Mauro, M. E. Fragala, V. Privitera, *Mat. Sci. Semicon. Proc.*, **69**, 44 (2017).
5. C. Tian, Q. Zhang, A. Wu, M. Jiang, Z. Liang, *Chem. Commun*., **48**, 2858 (2012).
6. Z. Wang, Y. Liu, B. Huang, Y. Dai, Z. Lou, G. Wang, X., Zhang, X. Qin, *Phys. Chem. Chem. Phys*., **16**, 2758 (2014).
7. K. Mageshwari, D. Nataraj, T. Pal, R. Sathymoorthy, J. Park, *J. Alloys Comp*., **625**, 362 (2015).
8. G. T. S. T. da Silva, K. T. G. Carvalho, O. F. Lopes, E. S. Gomes, A. R. Maliagutti, V. R. Mastelaro, C. Ribeiro, H. A. J. L. Mourao, *Chemcatchem*, **9**, 3795 (2017).
9. P. S. Bassi, L. H. Wong, J. Barber, *Phys. Chem. Chem. Phys*., **16**, 11834 (2014).
10. M. Mishra, D.-M. Chun, *Appl. Catal. A: General* **498**, 126 (2015).
11. S. Balachandran, M. Swaminathan, *J. Phys. Chem. C*, **116**, 26306 (2012).
12. M. Dorraj, M. Alizadeh, N. A. Sairi, W. J. Basirun, B. T. Goh, P. M. Woi, Y. Alias, *Appl. Surface Sci*., **414**, 251 (2017).
13. K. Madeshwari, D. Nataraj, T. Pal, R. Sathyamoorthy, J. Park, *J. Alloys Comp*. **625**, 362 (2015).
14. R. K. Sharma, D. Kumar, R. Ghose, *Ceram. Int*., **42**, 4090 (2016).
15. V. Sepelak, A. Duvel, M. Wilkening, K. D. Becker, *Chem. Soc. Rev*., **42**, 7507 (2013).
16. M. P. Tsvetkov, K. L. Zaharieva, Z. P. Cherkezova-Zheleva, M. M. Milanova, I. G. Mitov, *Bulg. Chem. Commun*., **47**, 354 (2015).
17. V. Polliotto, E. Albanese, S. Livraghi, G. Pacchioni, E. Giamello, *J. Mater. Chem. A*, **5**, 13062 (2017).
18. W. Wang, M. O. Tade, Z. Shao, *Prog. Mater. Sci.*, **92**, 33 (2018).
19. K. Jiratova, A. Spojakina, L. Kaluza, R. Palcheva, J. Balabanova, G. Tyuliev, *Chinese J. Catal*., **37**, 258 (2016).
20. D. R. Cummins, H. B. Russell, J. B. Jasinski, M. Menon, K. M. Sunkara, *Nano Lett*., **13**, 2423 (2013).
21. T. Žák, Y. Jirásková, CONFIT: Mössbauer spectra fitting program, *Surf. Interface Anal.*, **38**, 710 (2006).
22. V. I. Iliev, D. V. Tomova, V. F. Georgiev, S. K. Rakovski, *Bulg. Chem. Commun*., **49** Special Issue L, 17 (2017).
23. H. Lachheb, F. Ajala, A. Hamrouni, A. Houas, F. Parrino, L. Palmisano, *Catal. Sci. Technol*., **7**, 4041 (2017).
24. M. Anpo, S. Dzwigaj, M. Che, *Adv. Catal*., **52**, 1 (2009).
25. N. S. Portillo-Velez, A. Hernando-Gordillo, M. Bizarro, *Catal. Today*, **287** 106 (2017).
26. M. Scepanovic, T. Sreckovic, K. Vojisavljevic, M. M. Ristic, *Sci. Sinter*., **38**, 169 (2006).
27. H. Ozaki, S. Iwamoto, M. Inoue, *J. Phys. Chem. C***, **111**, 17061 (2007).
28. Y. Cong, J. L. Zhang, F. Chen, M. Anpo, D. N. He, *J. Phys. Chem. C*, **111,** 10618 (2007).
29. T. Tsoncheva, R. Ivanova, M. Dimitrov, D. Paneva, D. Kovacheva, J. Heynych, P. Vomacka, M. Kormunda, N. Velinov, I. Mitov, V. Stengl, *Appl. Catal. A*: *General*, **528**, 24 (2016).
30. S. S. R. Putluru, S. Mossin, A. Riisager, R. Fehrmann, *Catal. Today*, **176**, 292 (2011).
31. H. Kaftelen, K. Ocakoglu, R. Thomann, S. Tu, S. Weber, E. Erdem, *Phys. Rev. B*, **86**, 014113 (2012).
32. L. G. Devi, N. Kottam, B. Narasimha, B. N. Murthy, S. G. Kumar, *J. Mol. Catal. A: Chem.*, **328**, 44 (2010).
33. R. Chauhan, A. Kumar, R. P. Chaudhary, P. Ram, *Spectrochim. Acta Part A: Mol. Biomol. Spectrosc.,* **98**, 256 (2012).

СВОЙСТВА НА МЕХАНОХИМИЧНО СИНТЕЗИРАН ДОТИРАН С АЗОТ Fe$_2$O$_3$-ZnO СМЕСЕН ОКСИД

Н. Г. Костова*[1], М. Фабиан[2], Е. Дуткова[2], Н. Велинов[1], Й. Каракирова[1], М. Балаж[2]

[1] *Институт по катализ, Българска академия на науките, 1113 София, България*
[2] *Институт по геотехника, Словашка академия на науките, 04001 Кошице, Словакия*

(Резюме)

Настоящата статия се отнася до получаването и охарактеризирането на дотиран с азот Fe$_2$O$_3$-ZnO смесен оксид и способността на този материал да обезцвети органичното багрило Метил Оранж във воден разтвор при облъчване с видима светлина. Фотокаталитичният материал беше получен чрез екологичен механохимичен метод на синтез. Фотокатализаторите бяха охарактеризирани с рентгенофазов анализ (РФА), УВ-видима дифузно-отражателна спектроскопия (ДОС), фотолуминесцентна спектроскопия (ФЛ), електронен парамагнитен резонанс (ЕПР) и Мьосбауерова спектроскопия. РФА показа, че прилагането на механохимичен синтез промотира промени в размера на кристалитите. Беше регистрирано стесняване на забранената зона на механохимично синтезирания дотиран с азот Fe$_2$O$_3$-ZnO смесен оксид и подобряване на фотокаталитичната активност при облъчване с видима светлина в сравнение с изходния ZnO. Пониженият интензитет във фотолуминесцентния спектър на N-Fe$_2$O$_3$-ZnO свидетелства за подобрено разделяне на зарядите, по-ниска скорост на рекомбиниране на електрон-дупка и съответно по-висока фотокаталитична активност в сравнение с изходния ZnO.

Mineralization of pharmaceutical drugs by ZnO photocatalysts under UV light illumination

N. Kaneva*, A. Bojinova, K. Papazova, D. Dimitrov

Laboratory of Nanoparticle Science and Technology, Department of General and Inorganic Chemistry, Faculty of Chemistry and Pharmacy, University of Sofia, 1164 Sofia, Bulgaria

Zinc oxide films were obtained by simple suspension method through mixing commercial ZnO powder, ethanol, and polyethylene glycol. Samples were deposited with one and five layers by dip coating. Film efficiency was evaluated by decolourisation of the pharmaceutical drugs Paracetamol and Chloramphenicol. Drugs mineralisation kinetics in distilled water upon UV light illumination was studied as a model system for contaminated wastewater. Photocatalytic experiments with commercial ZnO powders (unannealed and annealed) were also investigated. The films and the powders were characterised by SEM, XRD, BET, and UV-vis spectroscopy. The effects of catalysts amount and annealing temperature were examined. ZnO showed higher photocatalytic efficiency in Paracetamol degradation as compared to that of Chloramphenicol.

Key words: ZnO, thin films, powders, photocatalysis, pharmaceutical drugs.

INTRODUCTION

Zinc oxide is one of the most important inorganic, multifunctional, and promising materials in the family of wide-gap semiconductors due to its unique properties, such as chemical, radiation and thermal resistance, optical transparency, and high piezoelectric and photocatalytic properties. It has been extensively used in industrial and medical applications such as UV light emitting diodes [1], UV laser [2], solar cells [3], gas sensors [4], photo-catalysts [5], photovoltaic devices [6], toxicological materials [7], etc. It is well known that the proper-ties of nanomaterials depend not only on the composition but also on the structure. There are various ZnO nanostructures, such as nanoparticles [8], nanorods [9], nanoflowers [10], nanowires [11], and nanosheets [12], which have been successfully synthesised by different approaches: thermal decom-position [13,14], sol-gel method [15], microwave method [16], chemical precipitation method [17], hydrothermal method [18], etc.

ZnO is widely utilised semiconductor catalyst that exhibits an attractive and promising property. In regarding to its high photocatalytic activity, ZnO nanostructures have attracted a considerable atten-tion, which is due to their superior performance in the range of ultraviolet and visible light compared with well-known catalysts such as titania [19]. Zinc oxide nanomaterials exhibit unique properties owing

to their complicated structure, among which photo-catalysis is the most important for degradation of organic pollutants in aqueous solution: dyes [20,21], pesticides [22], pharmaceutical drugs [23–25], etc.

Pharmaceutical products are considered harmful pollutants in the aquatic ecosystem even at low concentrations due to their continuous input and accumulation in the environment. They have been detected worldwide in environmental matrices indicating their ineffective removal from waste-waters using conventional purification methods. To prevent this contamination several processes of drug removal have been studied [26]. Heterogeneous photocatalysis of organic pollutants in wastewater is an advanced method for environmental protection. As a well-known photocatalyst, ZnO has the poten-tial for degradation and complete mineralisation of environmental pollutants [27]. Besides photopuri-fication of water suspensions seems more promising (high scores and degree of photodegradation and a greater amount of treated solution), there are crucial limitations for its application in practice: unsolved problems like light penetration into solutions and final separation of the catalysts from treated solu-tion. Therefore, the purification of contaminated water *via* photocatalytic films is still preferable for practical application.

In this study, nanostructured ZnO photocatalysts (powders and thin films, prepared by dip coating from suspensions) were characterised and tested for the photocatalytic degradation of two commonly used drugs: Paracetamol (PCA) and Chloramphe-nicol (CA). Photomineralisation kinetics of drugs in

* To whom all correspondence should be sent
E-mail: nina_k@abv.bg

water upon UV light illumination was studied as a model system for purification of contaminated pharmaceutical wastewater.

EXPERIMENTAL

Reagents and materials

Commercial zinc oxide powder and absolute ethanol (>99.0%) were supplied from Fluka. Polyethylene glycol (PEG 4000) was kindly provided from the Institute of Pure Compounds (University of Sofia, Bulgaria). Glass slides (ca. 76 mm×26 mm), used for substrates of ZnO films, were delivered by ISO-LAB (Germany). Distilled water was used for all experiments.

Paracetamol ($C_8H_9NO_2$, λ_{max} = 243 nm, ≥99.0% purity, Actavis) and Chloramphenicol ($C_{11}H_{12}Cl_2N_2O_5$, λ_{max} = 278 nm, ≥99.0% purity, Actavis) were used as model contaminants in the photocatalytic activity experiments. The former drug belongs to a group of medicines known as analgesics or painkillers. It is used to relieve mild-to-moderate fever, headache, migraine, toothache, muscle pain, or early stages of flu. It is also useful for lowering a raised temperature, such as after childhood immunisation. In combination with other drugs, it enhances pharmacological and side effects. The latter pharmaceutical product is an antibiotic useful for the treatment of a number of bacterial infections. Chloramphenicol is a broad spectrum antibiotic with antibacterial and bacteriostatic type of action against Gram positive and Gram-negative bacteria. It is applied only to treat or prevent simple infections (e.g. cold, flu, throat infections), if safer and effective medicines can be used. The side effects of both pharmaceutical drugs are shown in Table 1.

Preparation and characterization of ZnO powder photocatalysts
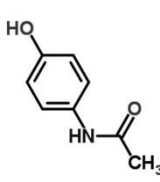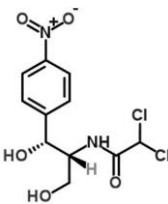
The commercial ZnO powder (Fluka) to be tested as a photocatalyst was annealed for 1 h at 500 °C. To prepare the respective thin films polyethyleneglycol (PEG-4000) was dissolved in absolute ethanol upon constant stirring and then heated for 30 min at 70 °C until a homogenous solution was formed. Pure (unannealed) ZnO powder was dispersed in ethanol (60 ml) and mixed with the PEG-4000 solution. The obtained suspension was stirred for 10 min and sonicated (15 kHz) for additional 30 min. To prepare the films, glass substrates were dipped in the suspension and withdrawn at a rate of 0.9 cm/min at room temperature [28]. Films with different number of coatings (one and five) were manufactured. The films were dried at 80 °C for 30 min after each coating. The dried films were an-

nealed at 500 °C for 1 h in order to decompose the organics and to get the final ZnO films for photocatalytic tests. The photocatalyst samples were characterised by means of SEM (JSM-5510 JEOL), XRD (Siemens D500 with CuKα radiation within 2θ range of 10−80 deg at a 0.05-deg step and counting time of 2 s/step), BET analysis before and after annealing (N_2 adsorption), and UV-vis spectroscopy (Evolution 300 Thermo Scientific).

Photocatalytic procedure

The photocatalytic tests [29] were carried out in cylindrical glass reactors of 250-ml and 150-ml volume for powders and films, respectively, equipped with magnetic stirrer and UV lamp (maximum emission at 370 nm) and placed at 10 cm above the purified solution. Light power density at the sample position measured with a research radiometer (Ealing Electro-optics) was 0.66 mW/cm^2. PCA and CA photodegradation was monitored by UV-vis absorbance spectroscopy after aliquot sampling at regular time intervals. Each sample was turned back to the reaction mixture after spectrophotometrical measurement. All photocatalytic experiments were performed at a constant stirring rate of 500 rpm at room temperature (23 ± 2°C). The initial concentrations of pollutants were as follows: (i) 50 and 25 ppm (PCA and CA) in case of powder photocatalysts, and (ii) 15 and 8 ppm (PCA and CA) in case of films.

Table 1. Side effects of Paracetamol and Chloramphenicol.

Drugs	Formula	Side effects
Paracetamol		• high doses: hepatotoxicity, skin, liver, and kidney damage; • prolonged use: changes the effect of other pharmaceutical drugs (Rifampicin, Cimetidine, Chloramphenicol, Busulfan).
Chloramphenicol		• high doses: violation of blood-forming apparatus; haemolytic anemia leukemia, nausea, vomiting, diarrhea, stomatitis (gastrointestinal) reactions, headache, depression (neurotoxic effects), rash, itching, burning, redness, swelling, fever (allergic); • Prolonged use: development of fungal infections and resistance of microorganisms to the product.

RESULTS AND DISCUSSION

Characterisation of ZnO photocatalysts

The morphology, composition, and structure of the commercial ZnO powder (unannealed and annealed at 500 °C) were examined by scanning electron microscopy (Fig. 1 a, b). The SEM images show particles of various sizes and shape. Sintering (densification) of the ZnO particles and an increased share of large agglomerates in the range of 0.4–0.6 μm were observed in the case of annealing.

The SEM investigation indicated that the ZnO films had a homogenous morphology (Fig. 1 c, d). The film surface is uniform and porous. After annealing, the layer did not peel off. This is due to the PEG, which acts as a stabiliser. Higher magnification revealed a fine granular structure of the film morphology. No significant difference in the morphology of films prepared with different number of coatings could be observed. However, the films obtained by five coatings were thicker (4 μm) then those obtained by one coating (2 μm).

Phase analysis and crystallinity of the prepared ZnO powder samples, unannealed and annealed at 500 °C, and ZnO thin films, with one or five layers, were determined by XRD analysis (Fig. 2).

All diffraction peaks can be indexed to a hexagonal structure of ZnO, in agreement with the literature data. No characteristic peaks of any impurities are observed. The three characteristic peaks ((left to right) (100) - $2\theta = 31.76°$; (002) - $2\theta = 34.39°$; and (101) - $2\theta = 35.67°$) correspond to the different crystallographic orientations of the crystal lattice of ZnO wurtzite. They are narrow with high intensity, which indicate that the ZnO nanostructures have high crystallinity. The crystallite size of the commercial ZnO powder was 30 nm as calculated by the Scherer equation. The XRD spectrum of annealed ZnO powder shows that annealing caused an increase of the crystallite sizes from 30 to 100 nm. The results of X-ray diffraction were confirmed by BET analysis. The specific surface area of unannealed powder was lower (9.1 m^2/g) compared to annealed zinc oxide (10.3 m^2/g). This parameter affected the photocatalytic efficiency for degradation of pharmaceutical drugs.
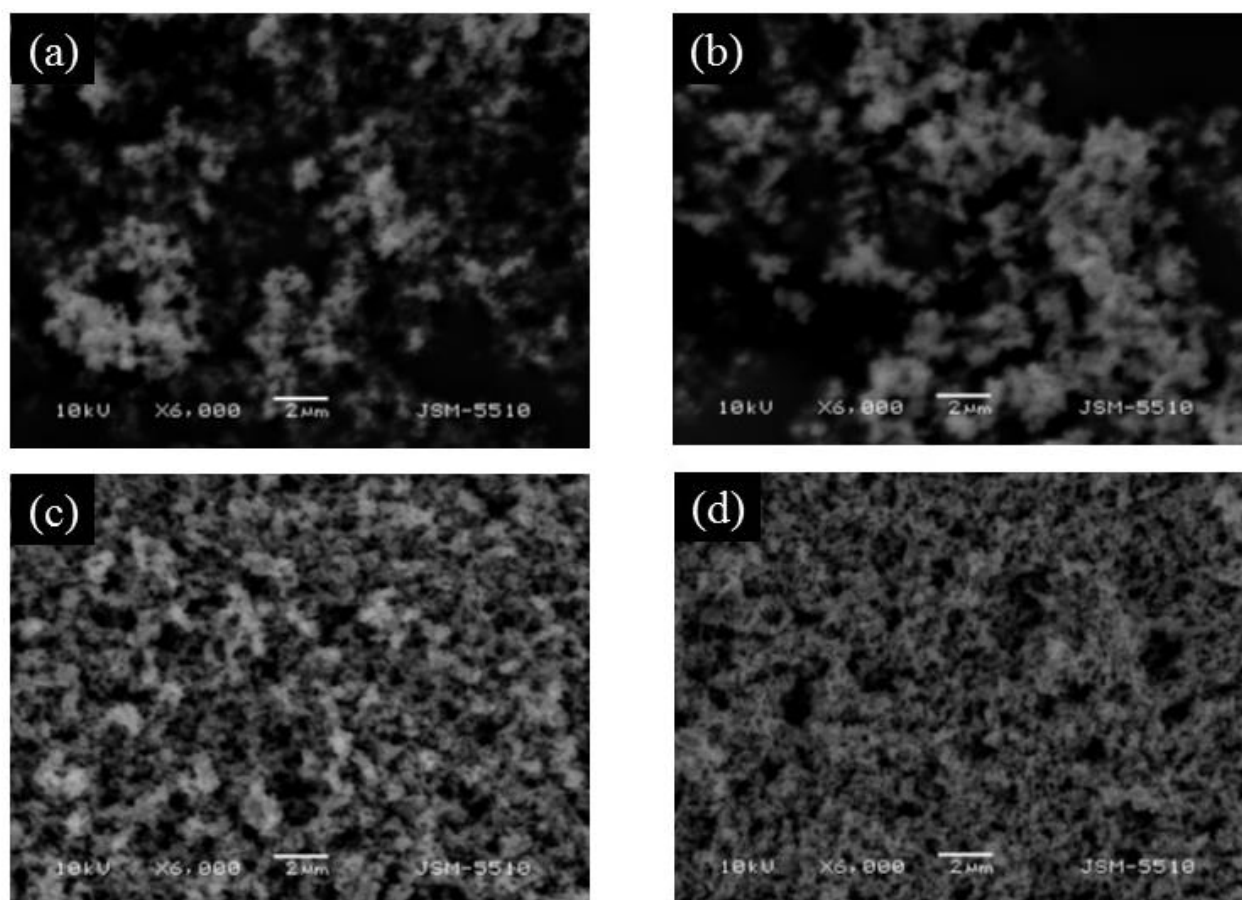
Fig. 1. SEM images: (a) unannealed ZnO powder, (b) annealed ZnO powder, (c) ZnO film with one coat, and (d) ZnO film with five coats.
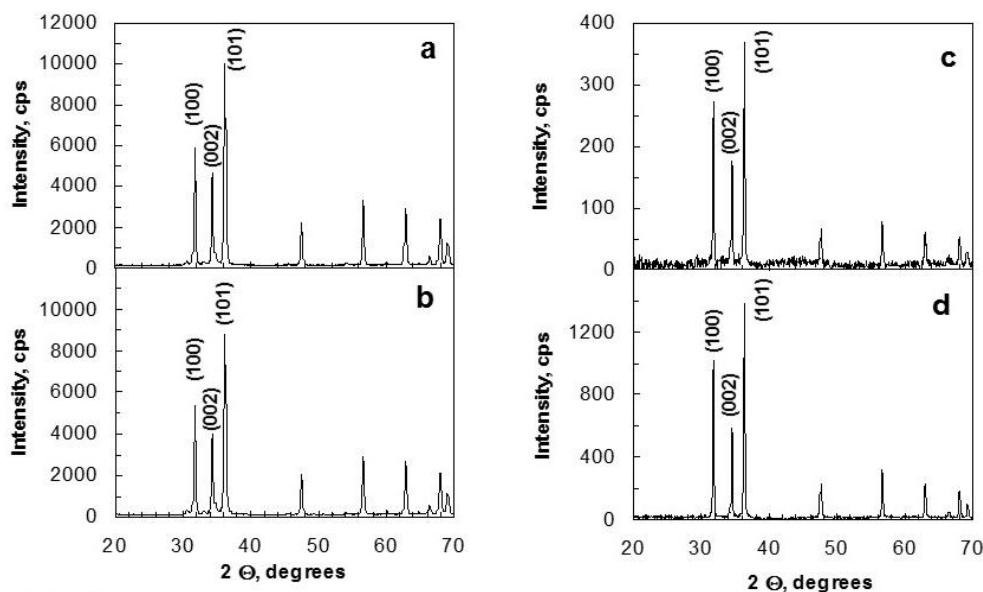
Fig. 2. XRD spectra of: (a) non-annealed ZnO powder, (b) annealed ZnO powder; (c) ZnO film with one coat; (d) ZnO film with five coats.

Degradation of pharmaceutical drugs by ZnO photocatalysts

In our research, Paracetamol and Chloramphenicol are used as model contaminants in the catalytic experiments. Figure 3 displays the PCA and CA degradation kinetics in aqueous solution using ZnO powders and UV light illumination. Annealing influences crystallinity degree, particle size, surface morphology, and therefore, the photocatalytic efficiency of the ZnO nano-particles. As seen, the annealed powders demonstrate higher efficiency, 96.67% (PCA) and 80.86% (CA) for two hours, in comparison with unannealed ZnO: 90.40% (PCA) and 72.51% (CA) for two hours. The photocatalytic results are in good agreement with calculated values of the rate constants k.

Changes in the mineralisation degree of the pharmaceutical pollutants during photocatalysis for 240 min are presented in Fig. 4. As seen the intensity of the main peaks smoothly decreased with illumination time without any formation of new peaks due to intermediates or by-products. The latter confirms complete mineralisation of the drugs by annealed ZnO powders.

The relationship between drug degradation and irradiation time (240 min) is illustrated in Fig. 5. It is evident that the light-induced mineralisation activity increases upon increasing powder film thickness.
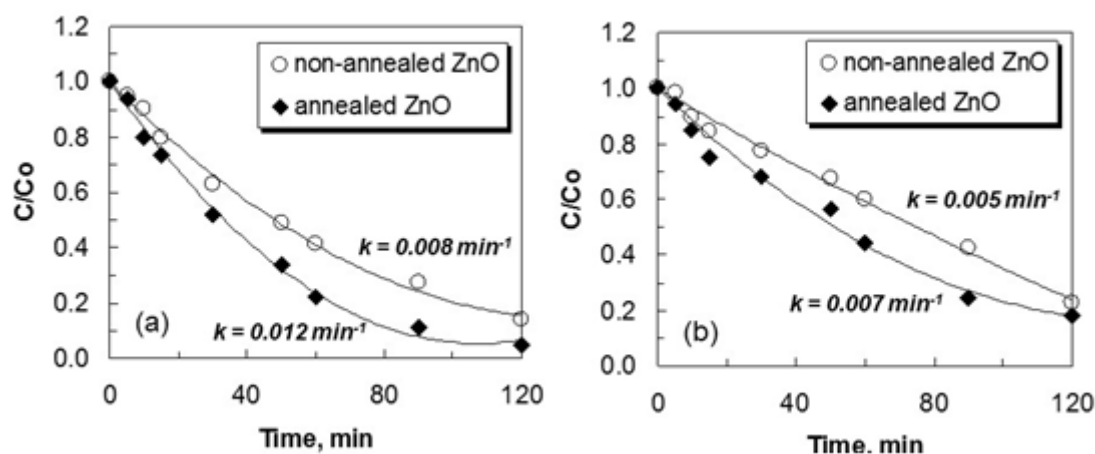
Fig. 3. Decrease in (a) Paracetamol and (b) Chloramphenicol concentration versus time upon UV light illumination with annealed and unannealed ZnO powders.

119
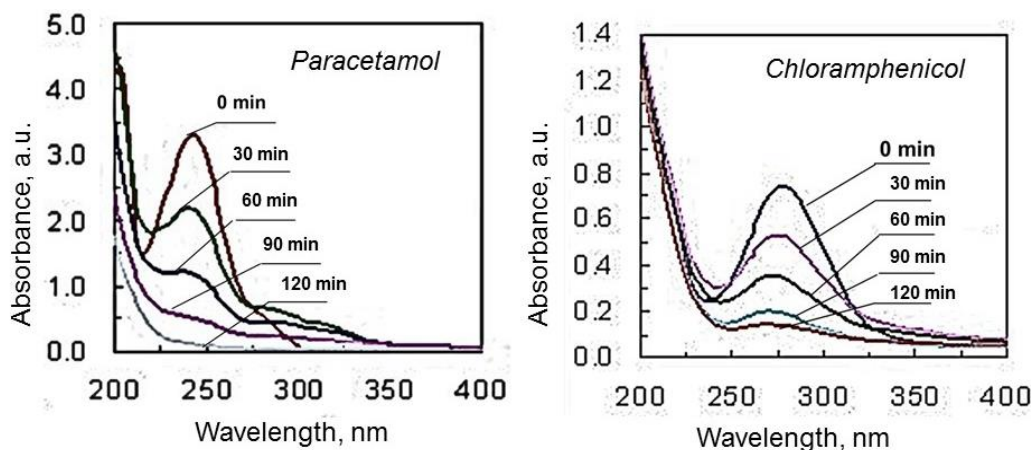
Fig. 4. Mineralisation of Paracetamol (50 ppm) and Chloramphenicol (25 ppm) with photocatalysis time.

The reason for this effect is a larger amount of zinc oxide deposited on the glass substrate. Nanostructure films manifested a higher degradation percentage of Paracetamol (D_{5coats} = 81.15% for 4 h) compared to Chloramphenicol (D_{5coats} = 68.48% for 4 h) under UV light illumination.
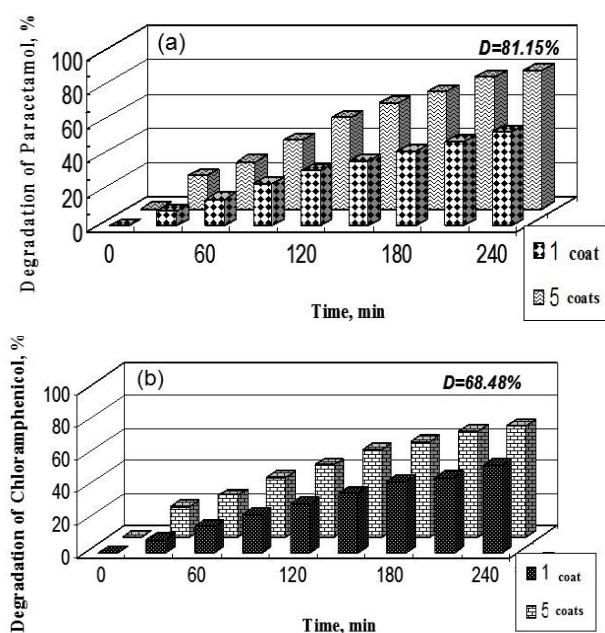
Fig. 5. Paracetamol (a) and Chloramphenicol (b) bleaching kinetics by ZnO films with one and five coats.

A faster mineralisation of Paracetamol by ZnO photocatalysts in comparison with that of Chloramphenicol is related to different drug molecule structures (Table 1) and degradation pathways. PCA photodegradation is a result of successive hydroxylation at the benzene ring moiety of paracetamol, which finally leads to its rupture. The process is initiated by highly reactive hydroxyl radicals formed after irradiation of ZnO and includes a number of products: hydroquinone, monohydroxy paracetamol, dihydroxy paracetamol, and aliphatic carboxylic acids (fumaric and malic) at the end [30]. CA photodecomposition is a more complicated process of two stages: dechlorination and denitrification [31]. According to the literature the nitro group in nitroaromatics can easily be eliminated *via* electrophilic substitution of the •OH radicals at the *para* position in the aromatic ring. Then the NO_2^- group can be oxidised to NO_3^-. Chloramphenicol can undergo also a reductive degradation pathway. Before forming nitrate ions, the nitro group may be reduced to an amine group on the ring and then released as ammonia.

CONCLUSIONS

This work demonstrates a simple dip-coating method for synthesis of zinc oxide powder films with one or five layers from suspension. The films and the respective powders were characterised by scanning electron microscopy, X-ray diffraction, and specific surface area measurements. SEM images showed that the films were composed of compact and dense layers. The powder films expressed a granular morphology without any crack. XRD results revealed that all powders and films were of hexagonal wurtzite structure of ZnO. The crystallite size of the zinc oxide powders increased with annealing temperature. BET analysis confirmed these results. Photocatalytic reaction kinetics was systematically studied for degradation of pharmaceutical drugs under UV light illumination. The ZnO photocatalysts mineralised Paracetamol faster in comparison with the antibiotic. Thin films prepared by five layers from suspension exhibited a higher efficiency than those prepared by one layer.

The photocatalytic activity of the powders was enhanced with annealing temperature.

REFERENCES

1. Ch. Huang, J. Lai, *Org. Electron.*, **32**, 244 (2016).
2. P. Shewale, Y. Yu, *Ceram. Int.*, **42**, 7125 (2016).
3. J. Tang, Z. Tseng, L. Chen, S. H. Chu, *Sol. Energ. Mat. Sol. C*, **154**, 18 (2016).
4. V. Galstyan, E. Comini, C. Baratto, G. Fagilia, G. Sberveglieri, *Ceram. Int.,* **41**, 14239 (2015).
5. Y. Weng, K. Hsiao, *Int. J. Hydrogen Energ.*, **40**, 3238 (2015).
6. A. Sharma, J. Franklin, B. Singh, G. Andersson, D. Lewis, *Org. Electron.,* **24**, 131 (2015).
7. R. Roy, M. Das, P. Dwivedi, *Mol. Immunol.*, **63**, 184 (2015).
8. K. Omri, I. Najeh, L. Elmir, *Ceram. Int.,* **42**, 8940 (2016).
9. C. Yilmaz, U. Unal, *Appl. Surf. Sci.*, **368**, 456 (2016).
10. A. Umar, H. Algarni, S. Kim, M. Al-Assiri, *Ceram. Int.,* **42**, 13215 (2016).
11. R. Bahramian, A. Moshaii, H. Eshghi, *Mater. Lett.*, **179**, 222 (2016).
12. J. Yang, Y. Wang, J. Kong, H. Jia, Z. Wang, *Opt. Mater.*, **46**, 179 (2015).
13. I. Kontopoulou, A. Angelopoulou, N. Bouropoulos, *Mater. Lett.*, **165**, 87 (2016).
14. N. Kaneva, A. Bojinova, K. Papazova, D. Dimitrov, *Catal. Today*, **252**, 113 (2015).
15. T. Demes, C. Ternon, D. Riasseto, H. Roussel, L. Rarenne, I. Gelard, C. Jimenez, V. Stambouli, M. Langlet, *J. Phys. Chem. Solids*, **95**, 43 (2016).
16. Q. Al-naser, J. Zhou, G. Liu, L. Wang, *Ceram. Int.,* **42**, 828 (2016).
17. R. Suntako, *Mater. Lett.*, **158**, 399 (2015).
18. Y. Sun, H. Guo, W. Zhang, T. Zhou, Y. Qiu, K. Xu, B. Zhang, H. Yang, *Ceram. Int.,* **42**, 9648 (2016) .
19. H. Maleki-Ghaleh, M. Shahzadeh, S. Hoseinizadeh, A. Arabi, E. Aghaie, M. SIladati, *Mater. Lett.*, **169**, 140 (2016).
20. H. Seo, H. Shin, *Mater. Lett.*, **159**, 265 (2015).
21. L. Saikia, D. Bhuyan, M. Saikia, B. Malakar, D. Dutta, P. Sengupta, *Appl. Catal. A: General*, **490**, 42 (2015).
22. S. Navarro, J. Fenoll, N. Vela, E. Ruiz, G. Navarro, *J. Hazard. Mater.*, **172**, 1303 (2009).
23. M. Shakir, M. Faraz, M. Sherwani, S. Al-Resayes, *J. Lumin.*, **176**, 159 (2016).
24. M. El-Kemary, H. El-Shamy, I. El-Mehasseb, *J. Lumin.*, **130**, 2327 (2010).
25. B. Peake, R. Braund, L. Tremblay, A. Tong, in: The Life-Cycle of Pharmaceuticals in the Environment, Elsevier Ltd., 2016, Ch. 6, pp. 153-202.
26. M. Klavarioti, D. Mantzavinos, D. Kassinos, *Environ. Int.*, **35**, 402 (2009).
27. S. Rehman, R. Ullah, A. Butt, N. Gohar, *J. Hazard. Mater.*, **170**, 560 (2009).
28. C. Dushkin, S. Stoianov, A. Bojinova, S. Russev, *Ann. Univ. Sofia, Fac. Chimie*, **98-99**, 73 (2006).
29. N. Kaneva, I. Stambolova, V. Blaskov, Y. Dimitriev, A. Bojinova, C. Dushkin, *Surf. Coat. Tech.*, **207**, 5 (2012).
30. E. Moctezuma, E. Leyva, C. A. Aguilar, R. A. Luna, C. Montalvo, *J. Hazard. Mater.*, **243**, 130 (2012).
31. A. Chatzitakis, C. Berberidou, I. Paspaltsis, G. Kyriakou, T. Sklaviadis, I. Poulios, *Water Res.*, **42**, 386 (2008).

МИНЕРАЛИЗАЦИЯ НА ЛЕКАРСТВА С ФОТОКАТАЛИЗАТОР ZnO И УВ-ОБЛЪЧВАНЕ

Н. Канева*, А. Божинова, К. Папазова, Д. Димитров

*Лаборатория „Наука и технология на наночастиците", катедра „Обща и неорганична химия",
Факултет по химия и фармация, Софийски университет, бул. „Джеймс Баучер" 1, 1164 София, България*

(Резюме)

Получени са филми от цинков оксид чрез прост суспензионен метод – смес от търговски ZnO на прах, етанол и полиетилен гликол. Пробите са отложени с един и пет слоя, използвайки метода на потапяща се подложка. Ефективността на филмите е изследвана с разграждане на фармацевтичните лекарства – Парацетамол и Хлорамфеникол. Изследвана е кинетиката на минерализация на лекарствата в дестилирана вода в присъствие на УВ светлина като моделна система за пречистване на замърсени отпадъчни води. Проведени са и фотокаталитичните опити с търговски ZnO прахове (ненакалени и накалени). Филмите и праховете са охарактеризирани със СЕМ, рентгеноструктурен анализ, метода БЕТ и УВ-видима спектроскопия. Изследван е ефектът на количеството катализатор и температурата на накаляване. Цинковият оксид показва по-висока фотокаталитична ефективност при разграждане на Парацетамол в сравнение с Хлорамфеникол.

Characterisation of mechanochemically synthesised N-doped TiO$_2$

N. G. Kostova*,[1], M. Fabian[2], E. Dutkova[2], M. Balaz[2], M. Shipochka[3]

[1] *Institute of Catalysis, Bulgarian Academy of Sciences, 1113 Sofia, Bulgaria*
[2] *Institute of Geotechnics, Slovak Academy of Sciences, 04001 Kosice, Slovakia*
[3] *Institute of General and Inorganic Chemistry, Bulgarian Academy of Sciences, 1113 Sofia, Bulgaria*

N-doped TiO$_2$ photocatalyst (P25-u) was prepared by combined mechanochemical/thermal synthesis. Urea was used as nitrogen source. Wet grinding experiments have been conducted on titanium dioxide P25 Degussa in a high-energy planetary mill. As-milled samples were calcined at 400 °C. The samples were characterised by X-ray diffraction (XRD), N$_2$ adsorption-desorption isotherms, UV-vis diffuse reflectance spectroscopy (DRS), X-ray photoelectron spectroscopy (XPS), and photoluminescence spectroscopy (PL) analysis. XRD results showed that art of phase anatase transforms to rutile during wet milling. All XRD peaks were broadened indicating that the crystallite size was within the nanometre range. P25-u samples possessed lower S$_{BET}$ values than the initial P25 Degussa. Milling in the wet environment resulted in deterioration of the porous structure. A lower photoluminescence intensity of mechanochemically synthesised P25-tu samples in comparison with the initial P25 ones indicated a lower recombination rate of photoexcited electrons and holes. Estimated E$_{bg}$ value for P25-u was 2.36 eV. This result suggests a possibility to apply as-prepared material as a photocatalyst in degradation process with visible light irradiation. Mechanochemically synthesised N-doped TiO$_2$ samples using urea exhibited a higher decolourisation rate of Methyl Orange dye than the commercially available TiO$_2$ Degussa powder under visible light irradiation.

Key words: mechanochemistry, photocatalysis, titanium dioxide, N-doping, Methyl Orange, photoluminescence.

INTRODUCTION

Titanium dioxide has been widely investigated because of its low cost, good physical and chemical stability, and environmental compatibility [1]. TiO$_2$ absorbs only a small fraction of the solar spectrum emission due to its band gap energy value. Photocatalysts that can exhibit high reactivity under visible light should be developed to use the main part of the solar spectrum. Thus, anion-doped TiO$_2$ has attracted considerable attention due to its manifested activity under visible light. Among all, N-doped TiO$_2$ seems to be a promising photocatalyst [2]. Different techniques have been used for doping titania with non-metal ions, e.g. sol-gel technology [3], magnetron sputtering deposition method [4], chemical vapour deposition [5], decomposition of N-containing metal organic precursors [6,7], etc. Nitrogen can be doped into titania by using different organic compounds, e.g. Refs. [8−10].

Commercially available TiO$_2$ (Degussa P 25), which is a standard material in the field of photocatalytic reactions, contains anatase and rutile phases [11]. The rutile phase with a band gap of 3.0 eV is the most thermodynamically stable form of crystalline titania, while anatase with band gap of 3.2 eV is

a metastable form of TiO$_2$. The presence of rutile in the samples reduces the recombination effect toward enhancing the photocatalytic performance in comparison with pure single phase of titania [12]. Anatase absorption affinity for organic compounds is higher than that of rutile [13]. This phase exhibits lower rates of recombination in comparison with rutile due to its higher rates of hole trapping [14]. The anatase is generally regarded as the more photochemical active phase of titania, presumably due to the combined effect of lower rate of recombination and higher surface adsorption capacity.

Mixed-phase materials (A+R) exhibit a higher photocatalytic activity than either pure phase alone [15]. Due to the higher activity of pure-phase anatase compared to rutile, anatase is conventionally considered the active component in mixed-phase catalysts with rutile serving passively as an electron sink. These mixed-phase materials exhibit increased photo-efficiencies and are activated by lower energy light [16].

In this study, pure and N-doped TiO$_2$ P25 Degussa as possible photocatalysts were studied. As-prepared samples were synthesised by a mechanochemical approach. Urea was used as nitrogen source. Photodecomposition of Methyl orange (MO) under visible light irradiation was used as a model reaction. An improved photocatalytic activity was

---

* To whom all correspondence should be sent
E-mail: nkostova@ic.bas.bg

found for all N-doped TiO₂ Degussa P25 samples. The aim of the present study was to investigate the influence of doping and of the local structure variation of titania on its photocatalytic properties.

EXPERIMENTAL

Mechanochemical synthesis

Commercial TiO₂ P25 (Degussa, Holand) and urea of analytical grade were used without further purification. N-doped TiO₂ samples were prepared by addition of urea as modifier to TiO₂ P25 Degussa by mechanochemical/thermal synthesis using a high-energy planetary ball mill Pulverisette 6 (Fritsch, Germany). Titania powder was mixed with 5 wt.% urea before being placed in the reactor vessel. Wet milling was performed in presence of 1.2 ml distilled water. The sample was milled for 30 min at 550 rpm under argon using a chamber (250 cm^3 in volume) with 21 balls (10 mm in diameter) both made of zirconia. The ball-to-powder mass ratio was 40:1. To remove residual urea, the yellowish sample of N-doped TiO₂ P25 Degussa was calcined at 400 ^{o}C in air for 1 h. According to urea modifier, the N-doped samples were denoted as P25-u. An original TiO₂ P25 powder was also used as a reference sample (P25).

Characterisation techniques

The crystal structure was characterised by using a D8 Advance X-ray diffractometer (Bruker, Germany) in the Bragg-Brentano geometry working with a CuK$_\alpha$ radiation ($\lambda = 0.15406$ nm) and a scintillation detector. Data were collected over the angular range of $20^o < 2\theta < 65^o$ with scanning steps of 0.020^o and a measurement step time interval of 9 s. For data processing, commercial Bruker tools were used. Specifically, Diffrac^{plus} Eva database was utilised for phase identification.

A nitrogen adsorption apparatus NOVA 1200e Surface Area & Pore Size Analyzer (Quantachrome Instruments, United Kingdom) was employed to record adsorption-desorption isotherms. Specific surface area (S$_{BET}$) values were calculated using Brunauer-Emmett-Teller (BET) equation. The pore size distribution was calculated using the Barrett-Joyner-Halenda (BJH) method. The measurements were performed at the liquid nitrogen temperature.

Diffuse reflectance UV-vis spectra for evaluation of photophysical properties were recorded in the diffuse reflectance mode (R) and transformed to absorption spectra through the Kubelka-Munk function [17]. A Thermo Evolution 300 UV-vis spectrophotometer (Thermo Scientific, USA) equipped with a Praying Mantis device with Spectralon as the refer-

ence was used. Reflectance data were obtained as a relative percentage reflectance to a non-absorbing material (spectralon) which could optically diffuse light.

Sample composition and electronic structure were investigated by X-ray photoelectron spectroscopy (XPS). The measurements were carried out on an AXIS Supra electron - spectrometer (Kratos Analitycal Ltd., Japan) using monochromatic AlK$_\alpha$ radiation with photon energy of 1486.6 eV and charge neutralisation system. Binding energies (BE) were determined with an accuracy of ± 0.1 eV. The chemical composition of the films was determined by monitoring the areas and binding energies of C1s, O1s, and Ti2p photoelectron peaks using an asymmetric Gaussian-Lorentzian function fit. Applying commercial data-processing software of Kratos Analytical Ltd. concentrations of the different chemical elements (as atomic %) were calculated by normalising the areas of the photoelectron peaks to their relative sensitivity factors.

Photoluminescence (PL) spectra at room temperature were acquired at right angle on a photon counting spectrofluorometer PC1 (ISS, USA) with a photoexcitation wavelength of 325 nm. A 300-W xenon lamp was used as the excitation source. For measuring the PL intensity, the powders were suspended in absolute ethanol.

Sample photocatalytic activity in the reaction of Methyl orange decolourisation was measured under visible light illumination. The photocatalytic experiments were carried out in a semi-batch photoreactor equipped with a magnetic stirrer as reported in previous work [18]. Methyl Orange dye was used as reactant with a concentration of 10 mg/L. The suspension was prepared by adding N-doped TiO₂ sample (100 mg) to 100 ml of Methyl Orange solution. MO degree of decolourisation could be easily monitored by optical absorption spectroscopy. Prior to deposition, the suspension of MO with N-doped TiO₂ was sonicated for 5 min to obtain an optimally dispersed system using an UP200S ultrasound processor (Hielscher, Germany) at 24 Hz in a pulse mode. The suspension was magnetically stirred in the dark for 30 min to ensure an adsorption-desorption equilibrium. Then the light was turned on and this was considered to be the initial moment (t = 0 s) of the photocatalytic reaction. The suspension was irradiated by a Philips TUV lamp (4 W) at UV-C monochromatic radiation ($\lambda = 254$ nm). All experiments were performed at a constant stirring rate of 400 rpm at room temperature. During the photo-catalytic reaction the concentration of MO was determined by monitoring the changes of the main absorbance peak at $\lambda = 463$ nm. MO decolourisation reaction course

was monitored after aliquot sampling at regular time intervals. Each aliquot sample was returned to the reaction mixture immediately after spectrophotometric measurement (operation under constant volume) and the illumination was switched on again.

RESULTS AND DISCUSSION

X-ray data analysis

Powder XRD patterns of initial TiO$_2$ P 25 as well as of ball-milled and N-doped TiO$_2$ P 25 Degussa nanopowders are presented in Fig. 1. Diffraction peaks due to anatase and rutile (for the P25 and P25-u samples) are clearly observed. All XRD peaks are broadened indicating that crystallite sizes were within the nanometre range. Anatase transformation to rutile phase during ball milling was in agreement with a study of Begin-Colin *et al.* [19]. Phase content of the particular samples was calculated from the integrated intensity of the anatase (101) and rutile (110) peaks. The mass fraction of anatase (W$_a$) and rutile (W$_r$) could be calculated from

$$W_a = K_a A_a/(K_a A_a + A_r) \text{ and} \tag{1}$$

$$W_r = A_r/(K_a A_a + A_r), \tag{2}$$

where A$_a$ and A$_r$ are the integrated intensities of the anatase (101) and rutile (110) peaks, respectively. W$_a$ and W$_r$ represent the weight fractions of anatase and rutile, respectively. The optimised correction coefficient K$_a$ has a value of 0.886 [20].

Fig. 1 illustrates that the relative peak intensities ascribed to a rutile phase increased from P25 to P25-u, to indicate more progression of anatase transformation to rutile phase. Sample crystallite sizes were calculated using the Debye-Scherrer equation [21]. They are given in Table 1. From Rietveld analysis of XRD data, it can be deduced that the anatase/rutile ratio was changed and the average crystallite size decreased after doping. All diffracttion peaks were broadened because of the nanosize crystals [22] as well as due to structural disorder introduced by milling procedure [23].

Specific surface area

The specific surface area (S$_{BET}$) values for all the

studied samples are listed in Table 1. It is known that specific surface area is an important factor influencing activity of TiO$_2$ particles [24]. The specific surface area of the standard sample P25 was 52 m^2/g in good agreement with [25]. The sample P25-u possessed lower S$_{BET}$ value indicating that milling in the wet environment resulted in deterioration of the porous structure. In our experiments distilled water was in the wet milling process. The reduction of S$_{BET}$ value for TiO$_2$ upon milling was also reported in [26] and the lowest value was registered for the wet-milled sample in methanol. The adsorption-desorption isotherms of two samples were recorded in whole p/p$_0$ interval to examine the surface properties in more detail (Fig. 2).
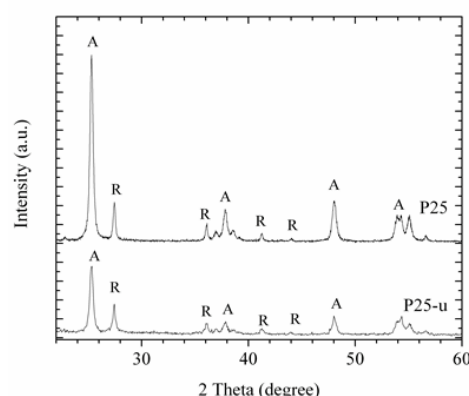
Fig. 1. XRD patterns of initial P25 and P25-u.
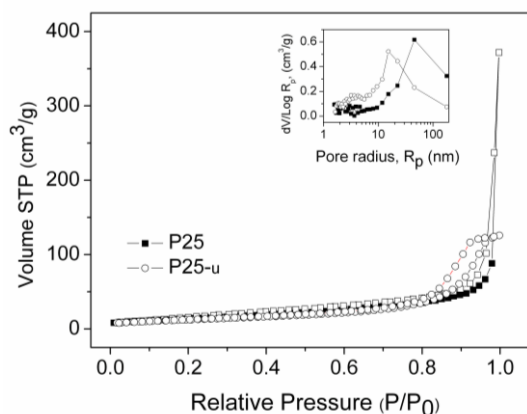
Fig. 2. N$_2$ adsorption-desorption isotherms of all samples (full shapes correspond to the adsorption curve and empty ones to the desorption curve) and Pore size distribution calculated from the N$_2$ desorption isotherm (insert).

Table 1. Sample composition (A = anatase and R = rutile); phase composition, average crystalline size; BET surface area, band gap (E_g), chemical composition obtained by XPS, and the reaction rate constant (k') of P25 reference and mechanochemically synthesized samples.

Sample	Phase, %		Crystallite size, nm		S$_{BET}$, m^{2}g^{-1}	Band gap, eV	Chemical composition at.%			$k \times 10^2$ min^{-1}
	A	R	A	R			Ti	O	N	
P 25	82	18	24	34	52	3.2	31.6	68.4	-	0.3
P25-u	70	30	20	30	38	2.36	31.9	68.0	0.1	9.4

It can be seen that all isotherms contain a hysteresis loop, which is evidence for presence of mesopores in their structures. P25 sample isotherm shape in the area of relative pressures around 1 hints to the presence of macropores. According to the classification of Sing *et al.* [27] the shape of the isotherm is on the borderline between types II and IV. The isotherm of the P25-u sample fits into type IV. The hysteresis loop can be classified as H3. Analysis of the pore size distribution (Fig. 2 insert) provided further information on pore types.

It can be seen that the pore size distribution of the P25-u sample is significantly different. Whereas the P25 sample contains mainly big mesopores and macropores, the P25-u sample is almost completely mesoporous. Smaller pores with maximum in pore radius distribution around 8 nm were observed with P25-u sample. Its pore size distribution profile is similar to that reported in Ref. [28].

XPS analysis

Samples were also analysed by XPS to evaluate the surface chemical species taking into account both the Ti2p and O1s regions. The latter allows investigation of both quality and abundance of OH surface species, which is fundamental in the photocatalytic process [29]. XPS survey spectra of initial P25 and P25-u are displayed in Fig. 3a. The binding energies were calibrated with respect to the C1s peak at 284.5 eV. XPS analysis showed that the P25 and P25-u particles had C, O, and Ti elements on their surface. Moreover, N element was also present because of P25 co-milling with urea. The chemical composition of the samples is given in Table 1.

Ti $2p_{1/2}$ and Ti $2p_{3/2}$ spin orbital splitting photoelectrons of both samples were localised at binding energies of 464.8 and 459 eV, respectively, as seen in Fig. 3c. A peak separation value of 5.8 eV between the Ti$2p_{1/2}$ and Ti$2p_{3/2}$ signals is in agreement with literature data on Ti^{4+} [30,31]. No peaks of titanium oxidation state other than 4+ were found in the spectrum of the P25-u sample. The absence of broad and shoulder peaks made it reasonable to conclude that only Ti^{4+} species was bonded to O^{2-} in the TiO$_2$ lattice on the surface.

The shape of the O1s peaks in the XPS spectra of both P25 and P25-u samples are similar and have a slight asymmetry at the higher binding energy side of the peaks. The O1s peaks could be deconvoluted in two components (Fig. 3b). The component of lower binding energy at ~530.2 eV is attributed to oxygen bonded to tetravalent Ti ions (Ti-O$_L$), whereas that of ~531.4 eV is ascribed to oxygen atoms in hydroxyl groups [32].

Diffuse reflectance spectra

Diffuse-reflectance spectra (DRS) in both the ultra-violet and visible ranges were recorded in order to investigate the optical properties of as-prepared samples as shown in Fig. 4. The TiO$_2$ P25 Degussa sample has a wide absorption band in the range from 200 to 380 nm (see Fig. 4). An absorption edge for the mechanically activated TiO$_2$ P25 Degussa is red shifted and the absorption tail is extended to 420 nm. The yellowish N-doped mechanochemically synthesised P25-u sample shows two absorption edges at around 408 nm and 550 nm. The former edge is the same as for P25 after mechanical activation. The latter edge seems to indicate the formation of a new N2p-based band, which is located above the O2p-based valence band [33].
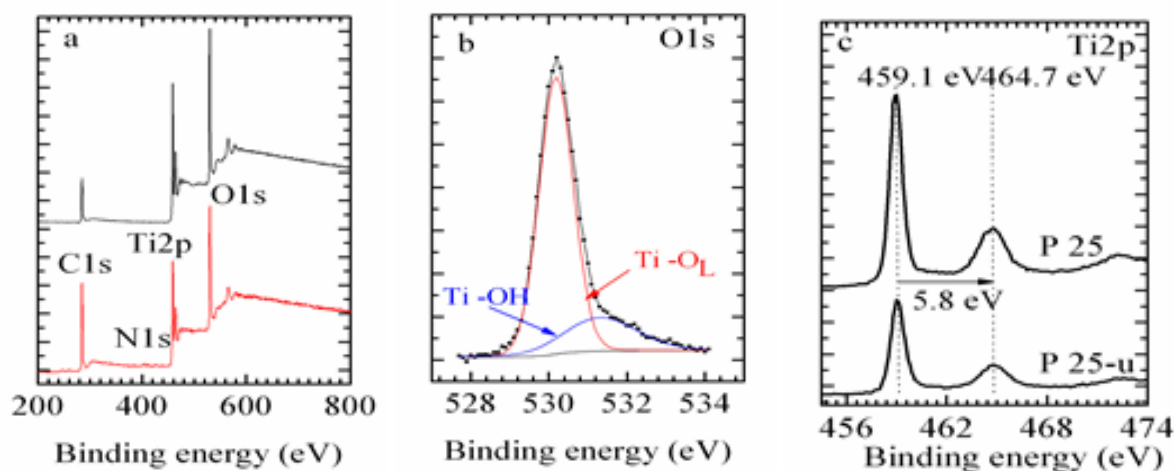
Fig. 3. XPS survey spectra of initial P25 and P25-u (a), XPS collected from P25 and P25-u samples for O1s (b) and Ti2p (c) core levels.

N-doping resulted in an intense increase in absorption in the visible light region and a red shift in the absorption edge of TiO$_2$ P25. Mixing of the N2p states with the valence band of TiO$_2$ was found to contribute to an increase of the valence band [34]. This led to band gap narrowing in the N-doped sample mechanochemically synthesised using urea.
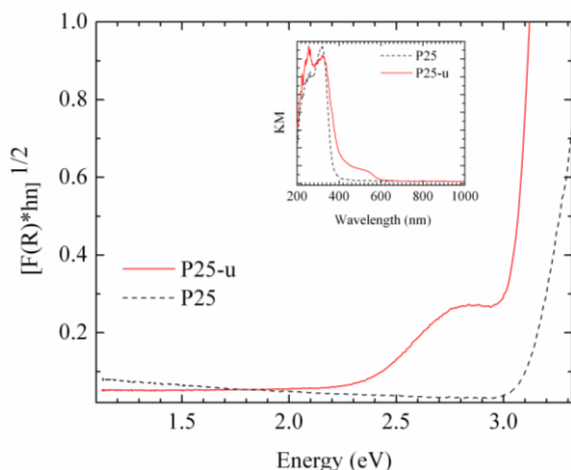
Fig. 4. DRS spectra of initial P25 and P25-u samples and corresponding Tauc's plot (insert).

In addition, the UV-vis diffuse reflectance spectroscopy was employed to estimate the band gap energies of as-prepared samples. Band gap values were calculated using the UV-vis spectra from the following equation:

$$\alpha(h\nu) = A(h\nu - E_{bg})^{\frac{1}{2}}, \tag{3}$$

where α is the absorption coefficient and *hν* is the photon energy. The band gap energies were calculated by extrapolating a straight line to the abscissa axis. The value of hν extrapolated to α = 0 gives an absorption energy, which corresponds to a band gap energy. Sample band gaps obtained through Kubelka-Munk plots are listed in Table 1. A value of 3.20 eV was found for initial P25. The mechanically activated TiO$_2$ P25 Degussa has energy band gap E$_{bg}$ = 3.05 eV (Fig. 4). Narrowing of the band gap was observed after modification of P25 with urea.

Furthermore, a new band with maximum at 2.9 eV appeared in the spectra of P25-u samples. The estimated E$_{bg}$ value for P25-u was 2.36 eV. The red shift is attributed to creation of additional electronic states in the band gap of TiO$_2$ P25 [35]. These results suggest a possible application of the as-prepared material as a photocatalyst for degradation process with lower energetic requirements than TiO$_2$.

Photoluminescence

The PL behaviour of TiO$_2$ photocatalysts in presence of various kinds of reactant molecules has already been investigated [36]. PL intensity dependence on atmosphere was explained in terms of surface band bending of titania particles.

The PL measurements were performed to analyse the photogenerated carrier separation efficiency of the doped samples. PL emission intensity of a semiconductor is proportional to the photoinduced electron-hole recombination rate. TiO$_2$ is a semiconductor with an indirect band gap. Titania exhibits a broad visible luminescence spectrum, which is related to transition of a trapped charge carrier in the oxygen vacancy to the TiO$_2$ valence band [37].

All samples were photoexcited by a light at wavelength 325 nm. It corresponds to photon energy of 3.81 eV, which is higher than the band gap energy of titania. This energy is absorbed by exciting transition of valence band electrons to the conduction band. The PL spectra of the initial TiO$_2$ P 25 Degussa and P25-u are displayed in Fig. 5. Intensive peaks in the spectrum of TiO$_2$ P 25 Degussa with maxima in the blue region at about 416 nm (2.98 eV) and 464 nm (2.67 eV) can be ascribed to emission of a photon having a slightly lower energy than the band gap width of the anatase and rutile phases in P25 TiO$_2$. This is evidence for direct recombination of a photoexcited electron and a positively charged hole [38−39]. A contribution of rutile particles of sample P25 to the excitation band is higher than that of anatase [40]. Rutile particles of sample P25-u have lower photoluminescence efficiency than the initial P25. A charge transfer between the anatase and rutile phases can explain this. Some electrons in the anatase particles that are excited from the valence band to the conduction band are transferred to the rutile particles because the energy level of conduction band in anatase particles is higher than that in the rutile entities [41]. The peak at 464 nm in the visible region is attributed to defects in the samples, namely the oxygen-ion vacancies, which provide acceptor levels near the conduction-band edge [42].

In the mechanochemically prepared P25-u sample, PL emission peaks were observed within blue (370−480 nm) and green (490−565 nm) regions. In the blue region, a peak at 404 nm and shoulders at 416 and 366 nm were registered that are characteristic of rutile and anatase phases, respectively. The peak at 404 nm in PL spectrum of P25-u sample is attributed to emission of band gap transition [43] and arises from radiative annihilation of excitons (band to band recombination) [44]. The intensity of PL signal for P25-u was lower than that of P25 sample. The differences are due to a different content of defects and/or oxygen vacancies by preparation methods. This demonstrates the fact that co-

existence of rutile and anatase phases is responsible for changes in PL intensity and superior photocatalytic activity of the N-doped P25-u samples. In addition, a low intensity emission peaks appeared at higher wavelengths of 464 and 530 nm. In the observed PL spectra, the peak at 464 nm is related to self-trapped excitons (STE) and a peak at 530 nm is associated with oxygen vacancies [45]. We suppose that band-band PL emissions of heterojunctions were broadened due to nanocrystalline nature and mixed contribution from individual rutile-anatase phases.
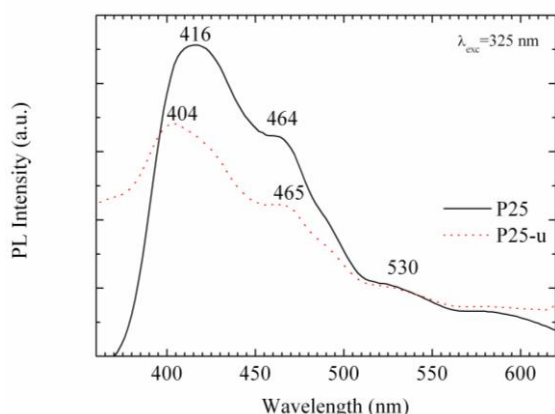
Fig. 5. Photoluminescence spectra of P25 (1) and P25-u (2) samples.

Photocatalytic properties

The photocatalytic activity of mechanochemically synthesised samples was evaluated by degradation of representative industrial dye Methyl Orange in aqueous solution under visible irradiation. All experiments were performed under room temperature. For comparative purpose, the activity of TiO₂ P25 Degussa was also investigated under the same conditions. Temporal changes in the concentration of MO were monitored by examining the variation in maximal absorption in UV-vis at 464 nm.

In a region where Lambert-Beer law is valid the concentration of MO dye is proportional to the absorbance as shown in Fig. 6. It can be seen that P25 demonstrated the smallest adsorption of MO (only 1%), while the P25-u sample showed a higher value (3%). It has been documented that preliminary adsorption of dye on the photocatalytic surface is a prerequisite for highly efficient oxidation [46]. The photocatalytic efficiency (C/C_o) in presence of P25 and P25-u photocatalysts is represented on Fig. 6 where C_o is the initial concentration of MO. Based on blank experiments self-photolysis of MO could be neglected. TiO₂ P25 Degussa was taken as reference for comparison and in this case, the MO degradation was about 2% after 120 min. The P25-u sample manifested higher photodegradation activity

with a MO conversion of 60% after 120 min irradiation. As shown in Fig. 6, the photocatalytic degradation curves of MO followed a pseudo-first order kinetic model, as given in Eq. 4:

$$\ln (C_o/C_t) = k't, \tag{4}$$

where: k' (min⁻¹) is the reaction rate constant, C_o is the initial MO concentration, and C_t is the MO concentration at a certain time (min). The reaction rate constant k could be estimated from Eq. 4 by plotting $\ln(C_o/C_t)$ versus irradiation time. Values of the reaction rate constant are presented in Table 1.

The reaction rate constant of the mechanochemically synthesised P25-u sample was higher than that of initial P25 (0.094 min⁻¹). Enhanced photocatalytic activity of the mechanochemically prepared P25-u samples containing anatase and rutile phases is due to difference in conducting band edges of the anatase and rutile phases. This may promote interfacial electron transfer from rutile to anatase and resulting energy barrier would suppress back electron transfer, which decreases the probability of the charge carrier recombination, confirmed by the low PL intensity (see Fig. 5).
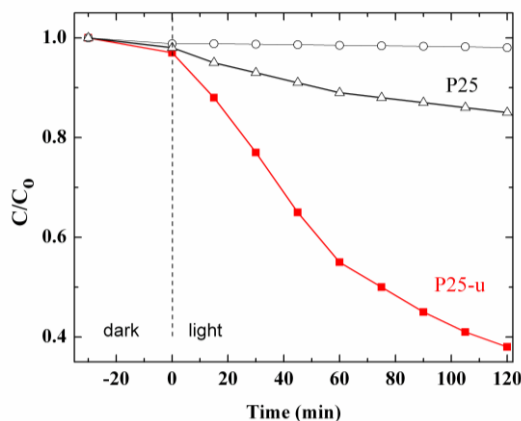
Fig. 6. Photodegradation of MO as a function of irradiation time of blank experiment without photocatalyst (○), commercial P25 (Δ) and mechanochemically synthesized sample P25-u (■).

Photocatalysis is a process, which depends on numerical parameters such as particle size, porous structure, crystallinity, surface area, and dopant. The presence of mixed phase improves the photochemical performance of the samples through reducing the recombination of photogenerated holes and electrons.

CONCLUSIONS

An eco-friendly one-step mechanochemical method to prepare N-doped TiO₂ samples for efficient photocatalytic decolourisation was established. During the mechanical activation, a transformation of anatase to rutile was established. Whereas the

initial P25 contained mainly big mesopores and macropores, the P25-u samples were almost completely mesoporous. A broadened absorption edge and a narrowed energy band gap were observed. The results show that titania phase composition is an important factor determining the PL intensities and photocatalytic activity in photodecolourisation of Methyl Orange of the mechanochemically synthesised samples.

REFERENCES

1. M. R., Hoffmann, S. T. Martin, W. Y. Choi, D. W. Bahnemann, *Chem. Rev.*, **95,** 69 (1995).
2. R. Marschal, L. Wang, *Catal. Today*, **225,** 111 (2014).
3. Y. Hu, H. Liu, X. Kong, X. Guo, *J. Nanosci. Nanotechnol.*, **14**, 3532 (2014).
4. M. Kitano, K. Funatsu, M. Matsuoka, M. Ueshima, M. Anpo, *J. Phys. Chem,* C, **110**, 25266 (2006).
5. L. Youssef, A. J. K. Leoga, S. Roualdes, J. Bassil, M. Zakhour, V. Rouessac, A. Ayral, M. Nakhl, *J. Eur. Ceram. Soc.,* **37**, 5289 (2017).
6. S. Yang, L. Gao, *J. Amer. Ceram. Soc.*, **87,** 1803 (2004).
7. T. Sano, N. Degushi, T. Takeshi, S. Matsuzawa, *J. Mater. Chem.*, **14,** 380 (2004).
8. G. Liu, X. Wang, L. Wang, Z. Chen, F. Li, G. Lu, H.-M. Chen, *J. Coll. Interface Sci.*, **334**, 171 (2009).
9. S. Livraghi, A. M. Czoska, M. C. Paganini, E. Giamello, *J. Solid. State Chem.*, **182**, 160 (2009).
10. K. Kobayakawa, Y. Murakami, Y. Sato, *J. Photochem. Photobiol. A: Chemistry*, **170**, 177 (2005).
11. T. Ohno, K. Sarukawa, K. Tokieda, M. Matsumura, *J. Catal.*, **203**, 82 (2001).
12. M. Anpo, *Bull. Chem. Soc. Jpn*, **77**, 1427 (2004).
13. U., Stafford, K. A. Gray, P. V. Kamat, A. Varma, *Chem. Phys. Lett.*, **205**, 55 (1995).
14. G. Riegel, J. R. Bolton, *J. Phys. Chem.*, **99**, 4215 (1995).
15. R. P. Busca, J. Kiwi, *Appl. Catal. B-Environ.*, **16**, 19-(1998).
16. S. M. El-Sheikh, T. M. G. Zhang, V. Vogiazi, A. A. Ismail, K. O'Shea, D. D. Dionysiou, *Chem. Eng. J.* **310,** 428 (2017).
17. Z. C. Orel, M. K. Gunde, B. Orel, *Prog. Org. Coat.,* **30**, 59 (1997).
18. N. G. Kostova, E. Dutkova, *Bulg. Chem. Commun.*, **46**, Special issue C, 87 (2015).
19. S. Begin-Colin, T. Girot, *J. Solid State Chem.*, **149**, 41 (2000).
20. H. Zhang, J. F. Banfield, *J. Phys. Chem.* B, **104**, 3481 (2000).
21. A. L. Patterson, *Phys. Rev.*, **56,** 978 (1939).
22. J. Z. Niu, W. W. Xu, H. B. Shen, S. Li, H. Z. Wang, L. S. Li, *Korean Chem. Soc.*, **33**, 393 (2012).
23. P. Baláž, M. Achimovičová, M. Baláž, P. Billik, Z. Cherkezova-Zheleva, J. M. Craido, F. Delogu, E. Dutková, E. Gaffet, F. J. Gotor, R. Kumar, I. Mitov, T. Rojac, M. Senna, A. Streletskii, K. Wieczorek-Ciurowa, *Chem. Soc. Rev.*, **42**, 7571 (2013).
24. S. J. Xiong, Y. Tang, H. S. Ng, X. Zhao, Z. Jiang, Z. Chen, K. W. Ng, S. C. J. Loo, *Toxicology*, **304**, 132 (2013).
25. W. Li, C. Ni, H. Lin, C. P. Huang, S. Ismat Shah, *J. Appl. Phys.*, **96**, 6663 (2004).
26. P. Dulian, M. Buras, W. Zukowski, *Polish J. Chem. Technol.*, **18**, 68 (2016).
27. K. S. W. Sing, D. H. Everett, R. A. W. Haul, L. Moscou, R. A. Pierott, J. Rouquerol. T. Sieminiewska, *Pure Appl. Chem.*, **57**, 603 (1985).
28. V. Nadtochenko, N. Denisov, A. Gorenberg, Yu. Kozlov, P. Chubukov, J. A. Rengifo, C. Pulgarin, J. Kiwi, *Appl. Catal. B-Environ.*, **91**, 460 (2009).
29. S. Ardizzone, C. L. Bianchi, G. Cappelleti, S. Gialanella, C. Parola, V. Ragaini, *J. Phys. Chem.* C, **111,** 13222 (2007).
30. E. McCafferty, J. P. Wightman, *Surf. Interface Anal.* **26**, 549 (1998).
31. W. Zhang, Y. Li, S. Zhu, F. Wang, *Chem. Phys. Lett.* **373**, 333 (2003).
32. T. Tsoncheva, R. Ivanova M. Dimitrov, D. Paneva, D. Kovacheva, J. Henych, P. Vomacka, M. Kormunda, N. Velinov, I. Mitov, V. Stengl, *Appl. Catal. A:* General, **528**, 24 (2016).
33. R. Asahi, T. Morikawa, T. Ohwaki, K. Aoki, Y. Taga, *Science*, **293**, 269 (2001).
34. M. Hamadanan, A. Reisi-Vanani, A. Majedi, *Mater. Chem. Phys.*, **116**, 376 (2009).
35. S. G. Kumar, L.G. Devi, *J. Phys. Chem.* A **115**, 13211 (2011).
36. M. Anpo, M. Che, *Adv. Catal.*, **44,** 119 (2000).
37. M. Tahir, N. S. Amin, *Appl. Catal. B. Environ.*, **162**, 98 (2015).
38. S. Liu, X-J. Zhao, Q. Zhao, X. He, J. Feng, *J. Electron Spectrosc. Relat. Phenom.,* **148**, 158 (2005).
39. D. Dastan, P. U. Loundhe, N. B. Chaure, *Mater. Sci.-Mater. Electr.*, **25**, 3473 (2014).
40. H. Nakajama, T. Mori, Q. Shen, T. Toyada, *Chem. Phys. Lett.*, **409**, 81 (2005).
41. J. Yu, J. C. Yu, W. Ho, Z. Jiang, *New J. Chem.* **26,** 607 (2002).
42. J. Liqiang, Q. Yichun, W. Baiqi, L. Shudan, J. Baojiang, *Sol. Energy Mater. Sol. Cell.*, **90,** 1773 (2006).
43. K. L. L. Li, *J. Mol. Catal.* A, **356**, 78 (2012).
44. J. Xu, L. Li, *J. Colloids Interface Sci.*, **318**, 29 (2008).
45. J. Preclikova, P. Galar, *J. Appl. Phys.*, **108**, 113502 (2010).
46. Y. M. Xu, C. H. Langford, *Langmuir*, **17**, 897 (2001).

ОХАРАКТЕРИЗИРАНЕ НА МЕХАНОХИМИЧНО СИНТЕЗИРАН ДОТИРАН С АЗОТ TiO₂

Н. Г. Костова*,[1], М. Фабиан[2], Е. Дуткова[2], М. Балаж[2], М. Шипочка[3]

[1] *Институт по катализ, Българска академия на науките, 1113 София, България*
[2] *Институт по геотехника, Словашка Академия на науките, 04001 Кошице, Словакия*
[3] *Институт по неорганична химия, Българска академия на науките, 1113 София, България*

(Резюме)

Дотиран с азот TiO₂ фотокатализатор (P25-u) е получен чрез комбиниран механохимичен/термичен синтез. Като източник на азот е използван карбамид. Опитите с влажно смилане бяха проведени с титанов диоксид P25 Дегуса във високоенергийна планетарна мелница. След смилане образецът беше накален при 400 °C. Образците са охарактеризирани с помощта на рентгенов фазов анализ (РФА), азотни адсорбционни-десорбционни изотерми, ултравиолетова-видима дифузионно-отражателна спектроскопия (ДОС), рентгенова фотоелектронна спектроскопия (РФЕС) и фотолуминесцентен спектроскопски (ФС) анализ. Резултатите от рентгенофазовия анализ показаха, че част от фазата анатаз се трансформира в рутил по време на влажното смилане. Всички дифракционни линии бяха уширени, което свидетелства, че размерът на кристалитите е в нанометричната област. Образецът P25-u показа по-ниска специфична повърхност от тази на изходния образец P25 Дегуса. Смилането във влажна среда довежда до влошаване на порестата структура на образеца. По-ниският интензитет на фотолуминесцентния спектър на механохимично синтезирания образец P25-tu в сравнение в изходния P25 свидетелства за по-ниска скорост на рекомбиниране на фото-възбудените електрони и дупки. Определена беше стойността на енергията на забранената зона E_{bg} на образеца P25-u (2.36 eB). Този резултат навежда на мисълта за възможното приложение на така получения материал като фотокатализатор в процеса на разграждане на багрила чрез облъчване с видима светлина. Механохимично синтезираният дотиран с азот титанов диоксид с прекурсор карбамид показа по-висока скорост на обезцветяване на багрилото Метил Оранж при облъчване с видима светлина в сравнение с търговския прахообразен TiO₂ Дегуса.

Synthesis and investigation of composite photocatalysts on the base of nickel and zinc oxides

K. I. Milenova[1]*, K. L. Zaharieva[1], S. V. Vassilev[2], S. S. Dimova[3], I. D. Stambolova[4], V. N. Blaskov[4]

[1] *Institute of Catalysis, Bulgarian Academy of Sciences, Acad. G. Bonchev St., Bldg. 11, 1113 Sofia, Bulgaria*

[2] *Institute of Electrochemistry and Energy Systems, Bulgarian Academy of Sciences, Acad. G. Bonchev St., Bldg. 10, 1113, Sofia, Bulgaria*

[3] *Institute of Polymers, Bulgarian Academy of Sciences, Acad. G. Bonchev St., Bldg. 103A, 1113 Sofia, Bulgaria*

[4] *Institute of General and Inorganic Chemistry, Bulgarian Academy of Sciences, Acad. G. Bonchev St., Bldg. 11, 1113 Sofia, Bulgaria*

Photocatalytic activities of $NiO_{0.8}ZnO_{0.2}$-ZnO samples obtained by precipitation from various starting materials (chlorides and nitrates) followed by thermal treatment at two different temperatures (450 °C or 650 °C) were compared. Powder X-ray diffraction and FTIR spectroscopy were used to characterize the investigated catalysts. Oxidative photodegradation of Malachite Green dye on $NiO_{0.8}ZnO_{0.2}$-ZnO catalysts over a period of 2 hours using UV light was studied. Photodegradation degree of the Malachite Green dye using $NiO_{0.8}ZnO_{0.2}$-ZnO obtained from chlorides and treated at 450 °C or 650 °C, are 89 and 86%, respectively. Samples from nitrate precursors calcined at 450 °C or 650 °C exhibited a higher photocatalytic degradation activity 99 and 94%, respectively.

Key words: photocatalysts, photodegradation, Malachite Green, dye, pollutant.

INTRODUCTION

Synthetic dyes are one of the most important pollutants from the textile industry [1]. They may cause serious health and environmental problems because of their stability, and toxicity [2]. Heterogeneous photocatalysis, being highly efficient advanced oxidation means, has been applied as an environmentally friendly, cost effective, and green process for successful degradation of many harmful organic compounds [3]. Recently there has been an increasing tendency of applying thermally and chemically stable semiconductor metal oxides as photocatalysts in aqueous systems [4]. In the recent years, scientists are excited by the opportunity to create low cost photocatalytic materials of high catalytic activity [5]. Due to modified electronic and structural properties, nanocomposites can possess enhanced photocatalytic activity in comparison with monocomponent oxides [6]. The role of incorporated foreign material such as metal/metal oxide, ceramic or polymer is to trap and transfer photoexcited electrons on the semiconductor surface and overcome the problem of recombination of the electron-hole pairs. NiO-ZnO coupled systems have demonstrated excellent photocatalytic efficiency under UV and visible light irradiation, when compared to individual ZnO and NiO due to the effective separation of photogenerated electron-hole pairs. [7]. Low lattice mismatch between NiO and ZnO is important for the formation of p-n heterojunction [8]. Zinc oxide hybrid photocatalyst [9] and NiO-ZnO composites [10] were also studied as photocatalysts for water pollutant degradation.

NiO photocatalytic activity for bleaching of Rose Bengal [11] and degradation of Rhodamin-B dye under visible light has also been examined [12]. NiO-ZnO composites have been investigated for photodecomposition of Methylene Blue under UV [13] and visible light [14,15] irradiation and of Methyl Orange under UV light [4,16]. NiO-coupled ZnO photocatalysts have been tested for degradation of 2,4-dichlorophenol [7]. Introduction of Ni as dopant into ZnO can be efficient way to improve the activity of ZnO photocatalyst [17,18]. Composites on the base of ZnO-NiO supported on zeolites were also studied [3,19].

The aim of this work was to compare the photocatalytic activities towards degradation of Malachite Green dye of $NiO_{0.8}ZnO_{0.2}$-ZnO samples prepared from different precursors (chlorides and nitrates) and calcined at a different temperature (450 or 650 °C).

---

* To whom all correspondence should be sent
E-mail: kmilenova@ic.bas.bg

EXPERIMENTAL

Sample preparation and physicochemical investigation

Composite samples on the base of mixed nickel oxide and zinc oxide powders were synthesized by precipitation of nickel and zinc nitrates, or nickel and zinc chlorides of Ni to Zn salt solution ratio of 1:2. For this purpose aqueous solutions of 0.25M $Ni(NO_3)_2 \cdot 6H_2O$ (VWR Prolabo BDH chemicals), 0.25M $Zn(NO_3)_2 \cdot 6H_2O$ (Valerus Co.), 0.25M $NiCl_2 \cdot 6H_2O$ (Valerus Co.), and 0.25M $ZnCl_2$ (Valerus Co.) were applied. An aqueous solution of 0.75M NaOH (Valerus Co.) used as a precipitant was added dropwise to the mixture upon stirring until pH = 12 and kept further under stirring for an hour. The precipitates were filtered, washed with distilled water several times, dried at 35 °C, and calcined in air at 450 °C or 650 °C for 3 hours and 30 minutes. Samples obtained from nitrates and calcined at 450 °C and 650 °C were denoted as H450 and H650, respectively. Those obtained from chloride precursors and calcined at 450 °C and 650 °C are indicated as X450 and X650, accordingly.

Physicochemical characterization of the samples was performed applying FTIR spectroscopy and powder X-ray diffraction (PXRD) analysis. FTIR spectra were recorded on a Bruker-Vector 22 instrument in the range of 400–4000 cm^{-1} using KBr discs of studied material. PXRD patterns of the samples were collected on a Philips PW 1050 apparatus with Cu K$_\alpha$ radiation. ICDD database was used for phase determination.

Photocatalytic study

Oxidative photodegradation of aqueous solution of Malachite Green dye of 5 ppm concentration was investigated in a semi-batch slurry reactor using 0.15 g of $NiO_{0.8}ZnO_{0.2}$-ZnO catalysts catalyst and 150 ml of dye solution under constant stirring in air flow. The photocatalytic experiments were performed using a UV-Vis absorbance spectrophotometer in the wavelength range from 200 to 800 nm (λ_{max} = 615 nm) and polychromatic UV-A lamp illumination (18 W) with maximum of the emission at 365 nm and illumination intensity of 0.66 mW.cm^{-2}. Tested systems were left in the dark for about 30 min before switching on the UV irradiation for 2 hours in order to reach adsorption-desorption equilibrium state. First, sample aliquots of the suspension were taken from the reaction vessel and second the powder was separated from the aliquot solution by centrifugation.

Dye degradation degree was calculated using the dependence $((C_0 - C)/C_0) \times 100$, where C_0 and C are initial concentration before turning on the illumination and residual concentration of the dye solution after illumination for selected time interval, respectively.

RESULTS AND DISCUSSION

PXRD patterns of the investigated samples are presented in figure 1. $NiO_{0.8}ZnO_{0.2}$ (PDF-750271) and ZnO (PDF-897130) phases were determined in the materials.
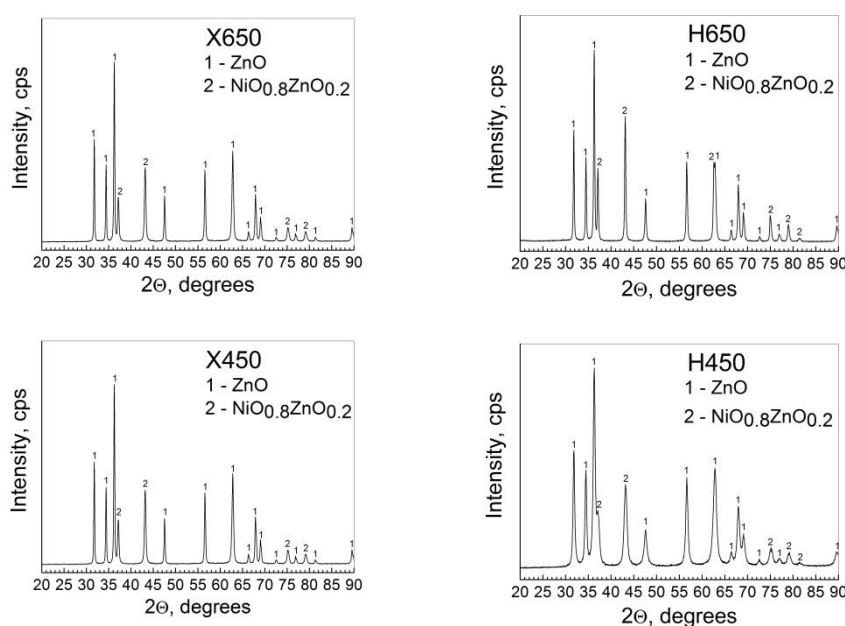
Fig. 1. PXRD patterns of $NiO_{0.8}ZnO_{0.2}$-ZnO materials calcined at 450 and 650 °C.

FT-IR spectra of the investigated materials in the range of 400–4000 cm^{-1} are displayed in figure 2. Absorption bands at about 3432–3442 and 1636 cm^{-1} were observed in the infrared spectra of $NiO_{0.8}ZnO_{0.2}$-ZnO samples ascribed to the stretching and bending vibrations of O–H bonds [20,21]. The presence of vibrational bands registered at around 1058 and 1197 cm^{-1} could be due to other admixtures in the investigated materials. The bands observed in the region above 436 cm^{-1} belong to the stretching vibrations of zinc oxide [22,23]. The results obtained by FT-IR spectroscopy are in agreement with data from PXRD analysis.
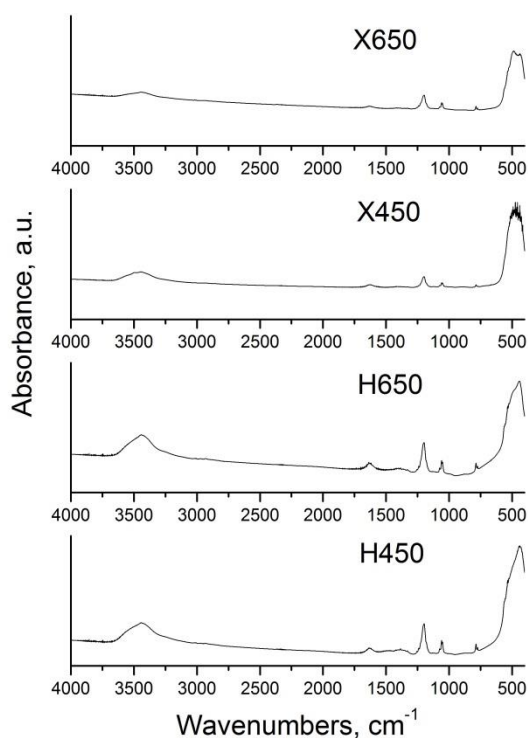
Fig. 2. FTIR spectra of $NiO_{0.8}ZnO_{0.2}$-ZnO samples calcined at 450 and 650 °C.

Adsorption capacity of the investigated materials was calculated using the formula:

$$Q = \frac{(C_0 - C).V}{m}$$

where C_0 is initial dye concentration, C is dye concentration after 30 minutes in the dark, V is solution volume, and m is photocatalyst weight.

Sample adsorption capacity (Figure 3) decreased in the following order: H450 (0.051 mg/g) > X450 (0.044 mg/g) > H650 (0.040 mg/g) > X650 (0.025 mg/g). Samples calcined at 450 °C had higher adsorption capacity than those treated at 650 °C.

Figure 4 presents C/C_0 concentration ratio of MG dye degradation with UV illumination time. Calculated degradation degree of Malachite Green dye increases in the order: X650 (86%) < X450 (89%) <

132

H650 (94%) < H450 (99%) (Table 1). Data on apparent rate constants (calculated using logarithmic linear dependence ($-\ln(C/C_0)$ = k.t) of the studied catalysts are given in Table 1. Apparent rate constant values of $NiO_{0.8}ZnO_{0.2}$-ZnO, 450 °C, chlorides and $NiO_{0.8}ZnO_{0.2}$-ZnO, 650 °C, chlorides are 11.8×10^{-3} min^{-1} and 13.9×10^{-3} min^{-1}, respectively, while those of $NiO_{0.8}ZnO_{0.2}$-ZnO, 450 °C, nitrates and $NiO_{0.8}ZnO_{0.2}$-ZnO, 650 °C, nitrates increased to 26.0×10^{-3} min^{-1} and 17.9×10^{-3} min^{-1}, accordingly.
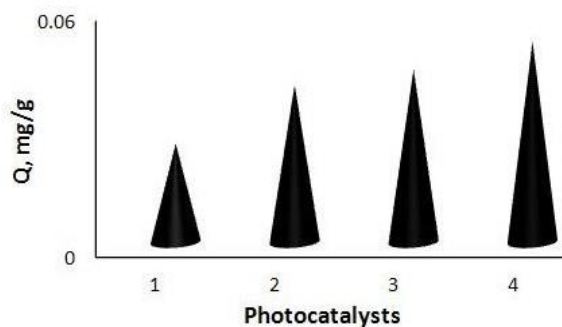
Fig. 3. Comparison of photocatalyst adsorption capacities: 1-X650, 2-H650, 3-X450, and 4-H450 for degradation of Malachite Green dye.
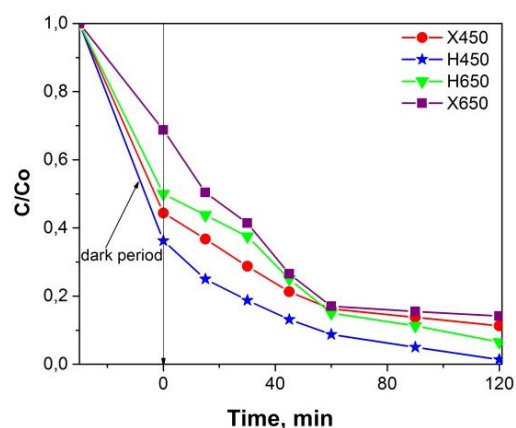
Fig. 4. Concentration C/C_0 ratio of Malachite Green dye with UV illumination time.

Table 1. Calculated apparent rate constants of investigated photocatalysts and degradation degree of tested dye

Sample	k (x10^{-3} min^{-1})	Degree of degradation, %
X450	11.8	89
H450	26.0	99
H650	17.9	94
X650	13.9	86

Materials prepared by nitrate precursors possessed higher photocatalytic activity in comparison with those prepared by chloride precursors. The photocatalytic reactivity decreases on rising the temperature of calcination of one type precursor samples. An increase from 400 to 500 °C caused a decrease in photocatalytic activity of ZnO-NiO sup-

ported on zeolite semiconductors due to changes in crystallite phase and particle size [3]. Under UV [24] and solar irradiation [25] commercial ZnO showed degradation of Malachite Green dye below 90%. We can conclude that the photocatalytic behaviour of $NiO_{0.8}ZnO_{0.2}$-ZnO materials for degradation of Malachite Green dye under UV-light irradiation is dependent on different synthesis conditions. The high photocatalytic activity of NiO-ZnO composite is probably due to increased separation rate of photogenerated electrons and holes [8,10].

CONCLUSIONS

A precipitation method was used to obtain composite $NiO_{0.8}ZnO_{0.2}$/ZnO photocatalysts using two types of precursors, chlorides and nitrates, followed by calcination at 450 °C or 650 °C. XRD analysis confirmed the presence of ZnO (wurtzite) and $NiO_{0.8}ZnO_{0.2}$ crystallographic phases. Photocatalytic activities of $NiO_{0.8}ZnO_{0.2}$-ZnO catalysts prepared under different synthesis conditions for dye degradation for a period of 2 hours using UV light were compared. All photocatalysts manifested a high catalytic activity. Among them, samples obtained from nitrate precursors treated at 450 °C photodegrade Malachite Green dye by 99% after 2 hours of illumination. Samples from chloride precursors exhibited a lower photocatalytic activity. An increase of the calcination temperature to 650 °C slightly decreased the degradation activity of samples prepared from the same precursor. Composite $NiO_{0.8}ZnO_{0.2}$-ZnO photocatalysts, synthesized from nitrate precursors could be suitable for purification of water polluted with Malachite Green textile dye.

REFERENCES

1. K. M. Lee, C. W. Lai, K. S. Ngai, J. C. Juan, *Water. Res.*, **88**, 428 (2016).
2. K. M. Reza, A. S. W. Kurny, F. Gulshan, *Appl. Water. Sci.*, **7**, 1569 (2017).
3. H. Derikvandi, A. Nezamzadeh-Ejhieh, *J. Haz. Mater.*, **321**, 629 (2017).
4. F. Tian, Y. Liu, *Scripta. Mater.*, **69**, 417 (2013).
5. S. B. A. Hamid, S. J. Teh, C. W. Lai, *Catalysts*, **7**, 93 (2017).
6. M. A. Johar, R. A. Afzal, A. A. Alazba, U. Manzoor, *Adv. Mater. Sci. Eng.*, 934587 (2015).
7. E. D. Sherly, J. Judith Vijaya, L. John Kennedy, B. Sreedhar, *J. Nanosci. Nanotechnol.*, **16**, 9784 (2016).
8. Z. Zhang, C. Shao, X. Li, C. Wang, M. Zhang, Y. Liu, *ACS Appl. Mater. Interfaces*, **2**, 2915 (2010).
9. M. A. M. Adnan, N. M. Julkapli, S. B. A. Hamid, *Rev. Inorg. Chem.*, **36**, 77 (2016).
10. C. Luo, D. Li, W. Wu, Y. Zhang, C. Pan, *RSC Adv.*, **4**, 3090 (2014).
11. P. Ameta; A. Kumar, R. Ameta, R. K. Malkani, *Iran. J. Chem. Chem. Eng.*, **29**, 43 (2010).
12. D. Dey, S. Das, M. Patra, N. Kole, B. Biswas, *J. Org. Inorg. Chem.,* **1**, 1 (2015).
13. I. A. Rahman, M. T. M. Ayob, S. Radiman, *J. Nanotechnol.*, 212694 (2014).
14. M. A. Kanjwal, I. S. Chronakis, N. A. M. Barakat, *Ceram. Int.*, **41**, 12229 (2015).
15. V. Karthikeyan, A. Padmanaban, T. Dhanasekaran, S. Praveen Kumar, G. Gnanamoorthy, V. Narayanan, *Mech. Mater. Sci. Eng.*, **9,** 55 (2017).
16. J. Li, F. Zhao, L. Zhang, M. Zhang, H. Jiang, S. Li, J. Li, *RSC Adv.*, **5,** 67610 (2015).
17. R. Chauhan, A. Kumar, R. Chaudhary, *J. Optoelectron. Biomed. Mater.*, **3**, 17 (2011).
18. X. Cai, Y. Cai, Y. Liu, H. Li, F. Zhang, Y. Wang, *J. Phys. Chem. Solid.,* **74**, 1196 (2013).
19. P. Dai, T. Yan, X. Yu, Z. Bai, M. Wu, *Nanoscale Res. Lett.*, **11**, 226 (2016).
20. B. M. Keyes, L. M. Gedvilas, X. Li, T. J. Coutts, *J. Cryst. Growth*, **281**, 297 (2005).
21. R. M. Alwan, Q. A. Kadhim, K. M. Sahan, R. A. Ali, R. J. Mahdi, N. A. Kassim, A. N. Jassim, *Nanosci. Nanotechnol.*, **5**, 1 (2015).
22. S. Musić, S. Popović, M. Maljković, D. Dragčević, *J. Alloys Comp.*, **347**, 324 (2002).
23. R. Y. Hong, J. H. Li, L. L. Chen, D. Q. Liu, H. Z. Li, Y. Zheng, J. Ding, *Powder Technol.*, **189**, 426 (2009).
24. M. Gancheva, I. Uzunov, R. Iordanova, K. Papazova, *Mater. Chem. Phys.,* **164**, 36 (2015).
25. T. Teka, A. Reda, *Int. J. Technol. Enhanc. Merg. Eng. Res.,***2**, 6 (2014).

СИНТЕЗ И ИЗСЛЕДВАНЕ НА КОМПОЗИТНИ ФОТОКАТАЛИЗАТОРИ НА ОСНОВАТА НА СМЕС ОТ НИКЕЛОВ ОКСИД И ЦИНКОВ ОКСИД

К. И. Миленова[1]*, К. Л. Захариева[1], С. В. Василев[2], С. С. Димова[3], И. Д. Стамболова[4], В. Н. Блъсков[4]

[1] *Институт по катализ, Българска академия на науките, ул. „Акад. Г. Бончев“, бл. 11, 1113 София, България*

[2] *Институт по електрохимия и енергийни системи, Българска академия на науките, ул. „Акад. Г. Бончев“, бл. 10, 1113 София, България*

[3] *Институт по полимери, Българска академия на науките, ул. „Акад. Г. Бончев“, бл. 103А, 1113 София, България*

[4] *Институт по обща и неорганична химия, Българска академия на науките, ул. „Акад. Г. Бончев“, бл. 11, 1113 София, България*

(Резюме)

Сравнена е фотокаталитичната активност на $NiO_{0.8}ZnO_{0.2}$-ZnO образци, получени при утаяване от различни изходни материали (хлориди и нитрати), последвано от термична обработка при две различни температури (450 °C или 650 °C). Рентгенов анализ и инфрачервена спектроскопия с Фурие трансформация са използвани за охарактеризиране на изследваните катализатори. Изучено е окислителното фоторазграждане на багрилото Малахитово Зелено върху $NiO_{0.8}ZnO_{0.2}$-ZnO образци за период от 2 часа, използвайки ултравиолетова светлина. Степените на разграждане на багрилото Малахитово Зелено от $NiO_{0.8}ZnO_{0.2}$-ZnO образци, получени от хлориди, третирани при 450 °C и 650 °C, са съответно 89 и 86%. Образците, получени от нитратни прекурсори обработени при 450 °C и 650 °C проявяват по-висока степен на фотокаталитична деградация (съответно 99% и 94%).

Photocatalytic behaviour of NiMnO$_3$/Mn$_2$O$_3$ materials for degradation of Malachite Green and Methylene Blue dyes under UV irradiation

K. L. Zaharieva[1*], K. I. Milenova[1], S. V. Vassilev[2], S. S. Dimova[3], I. D. Stambolova[4], V. N. Blaskov[4]

[1] *Institute of Catalysis, Bulgarian Academy of Sciences, Acad. G. Bonchev St., Bldg. 11, 1113 Sofia, Bulgaria*

[2] *Institute of Electrochemistry and Energy Systems, Bulgarian Academy of Sciences, Acad. G. Bonchev St., Bldg. 10, 1113, Sofia, Bulgaria*

[3] *Institute of Polymers, Bulgarian Academy of Sciences, Acad. G. Bonchev St., Bldg. 103A, 1113 Sofia, Bulgaria*

[4] *Institute of General and Inorganic Chemistry, Bulgarian Academy of Sciences, Acad. G. Bonchev St., Bldg. 11, 1113 Sofia, Bulgaria*

The present work describes a study of the photocatalytic behaviour of NiMnO$_3$/Mn$_2$O$_3$ materials for degradation of Malachite Green (MG) and Methylene Blue (MB) dyes as model contaminants under UV light irradiation. Samples were prepared by precipitation using nickel and manganese acetates as starting materials and sodium hydroxide precipitant, and then thermally treated at a different temperature – 450 and 650 °C. Powder X-ray diffraction analysis and Fourier-transform infrared spectroscopy were applied to study phase composition and structure of synthesized NiMnO$_3$/Mn$_2$O$_3$ samples. Photocatalytic measurements were carried out using MG or MB aqueous solution with starting concentration of 5 ppm. According to experiments using NiMnO$_3$/Mn$_2$O$_3$ photocatalysts calcined at 450 and 650 °C the degree of degradation of Malachite Green and Methylene Blue dyes after 120 minutes was increased as follows: NiMnO$_3$/Mn$_2$O$_3$, 450 °C, MB (10%) < NiMnO$_3$/Mn$_2$O$_3$, 650 °C, MB (13%) < NiMnO$_3$/Mn$_2$O$_3$, 650 °C, MG (67%) < NiMnO$_3$/Mn$_2$O$_3$, 450 °C, MG (78%). It was established that the NiMnO$_3$/Mn$_2$O$_3$ samples showed a much higher photocatalytic ability for degradation of Malachite Green relative to Methylene Blue dye under UV illumination..

Keywords: Malachite Green, Methylene Blue, degradation, NiMnO$_3$/Mn$_2$O$_3$, photocatalytic ability.

INTRODUCTION

Metal oxides can demonstrate an enormous number of structural geometries with an electronic structure that can possess semiconductor, metallic or insulator character and consequently show a very important role in various fields of physics, chemistry, and materials science [1]. Manganese oxides are famous to be active catalysts for various chemical processes such as dye degradation, water oxidation, organic synthesis, and CO and NO$_x$ removal from waste gases [2]. Heterogeneous photocatalysis using metal oxides due to its potential application to both organic synthesis and environmental applications has attracted considerable attention [1,3].

Catalytic oxidation of Methylene Blue by H$_2$O$_2$ has been tested on manganese oxide loaded hollow silica particles (MHSPs). The MHSPs with hollow structure and high surface areas enhance the catalytic activity compared to the matching manganese oxide solid particles (MSPs) [2]. Xia *et al*. have prepared Mn$_2$O$_3$ microspheres by a two-step method in ethylene glycol system. The obtained samples were tested for photodegradation of Methylene Blue solution in the presence of H$_2$O$_2$ under ultraviolet illumination. The Mn$_2$O$_3$ microspheres exhibited moderate photocatalytic ability due to their particular structure [4]. In addition, Mn$_2$O$_3$ microspheres obtained by a hydrothermal route have been studied for purification of water polluted with Methylene Blue dye [5].

Han *et al*. have investigated a Mn$_2$O$_3$/MCM-41 composite for degradation of Methyl Orange (MO), Congo Red (CR), Methylene Blue (MB), and Rhodamine B (RB) with/without visible light irradiation at room temperature. The Mn$_2$O$_3$/MCM-41 composite demonstrated superb removal efficiency for RB and MB [6]. A Ni/α-Mn$_2$O$_3$ catalyst has been tested for reduction in aqueous phase of 4-nitrophenol and organic dye pollutants - Rhodamine B, Methylene Blue, Rose Bengal, Congo Red, and Methyl Orange in the presence of a mild reducing agent, NaBH$_4$ [7]. Yang *et al*. have prepared single-crystalline nanorods of beta-MnO$_2$, alpha-Mn$_2$O$_3$, and Mn$_3$O$_4$ using heat-treatment of γ-MnOOH nanorods obtained by a hydrothermal method. The synthesized manganese oxide nanorods manifested catalytic ability to oxidise and decompose Methylene Blue dye with H$_2$O$_2$ [8].

Preparation of NiMnO$_3$/Mn$_2$O$_3$ powders using MnSO$_4$·H$_2$O and NiSO$_4$·6H$_2$O precursors has been reported by Gao *et al.* [9]. Mn$_2$O$_3$ is a semiconductor metal oxide [10]. Kakvand *et al.* have prepared NiMnO$_3$/C nanocomposite electrode materials for electrochemical capacitors [11]. NiMnO$_3$ and NiMnO$_3$/nitrogen-doped graphene nanocomposites have been investigated as super-capacitors [12]. Gnanam *et al.* have determined the band gap energy (3.49, 3.43, 3.38, and 3.36 eV) of α-Mn$_2$O$_3$ nanoparticles prepared using sodium dodecyl sulphate (SDS) or different surfactants such as polyethylene glycol (PEG), cetyl trimethyl ammonium bromide (CTAB), and citric acid (CA) [13].

The present paper deals with a study of the photocatalytic efficiency of NiMnO$_3$/Mn$_2$O$_3$ materials about degradation of aqueous solutions of Malachite Green and Methylene Blue dyes under UV irradiation. Samples were obtained using precipitation technique by nickel and manganese acetates, followed by calcination at 450 and 650 °C. The synthesized products were characterized by powder X-ray diffraction analysis and FTIR spectroscopy.

EXPERIMENTAL

Synthesis and physicochemical characterization of NiMnO$_3$/Mn$_2$O$_3$ materials

NiMnO$_3$/Mn$_2$O$_3$ samples were prepared by precipitation technique using 0.25M Ni(CH$_3$COO)$_2$·4H$_2$O and 0.25M Mn(CH$_3$COO)$_2$·4H$_2$O mixed at a ratio of 1:2. 0.75M NaOH precipitant was added dropwise to a mixture of aqueous solutions of acetate precursors until pH reached 12 under continuous stirring. After precipitation, the suspension was further agitated for one hour. The precipitate was filtered and washed with distilled water several times. Finally, it was dried at 35 °C and calcined at 450 °C and 650 °C for 3 hours and 30 minutes in air atmosphere.

FTIR spectra of the synthesized materials were recorded on a Bruker-Vector 22 Fourier transform infrared spectrometer in the range of 400–4000 cm^{-1} using KBr tablets. Powder X-ray diffraction analysis (PXRD) of the investigated samples was performed by means of Philips PW 1050 instrument with Cu K$_α$-radiation. Phases in the prepared materials were established using ICDD database.

Photocatalytic study

The photocatalytic tests of degradation of Malachite Green (MG) and Methylene Blue (MB) with initial concentration of aqueous solution of the dye - 5 ppm were performed under UV-A illumination (18 W). The catalytic experiment was carried out in semi-batch slurry reactor using 0.15 g catalyst and 150 ml of dye solution under air flowing and stirring. To reach adsorption-desorption equilibrium state NiMnO$_3$/Mn$_2$O$_3$ powders were left in the dark for half an hour before turning on the UV light for period of time - 2 hours. The powder was divided from the aliquot solution by centrifugation. After that the change of absorbance during the photocatalytic investigation was monitored by UV-Vis absorbance spectrophotometer UV-1600PC in the wavelength range from 200 to 800 nm ($λ_{max}$ = 615 nm for Malachite Green and 664 nm for Methylene Blue). The degree of dye degradation was computed using $((C_0–C)/C_0)\times100$, where C_0 and C were initial concentration before turning on the illumination and residual concentration of the dye solution after illumination for selected time interval.

RESULTS AND DISCUSSION

Results obtained by powder X-ray diffraction analysis are shown in figure 1. Two phases - NiMnO$_3$ (PDF-653695; PDF-895878) and Mn$_2$O$_3$ (PDF-721427; PDF-651798) were registered in the X-ray diffraction patterns of materials synthesized at 450 °C and 650 °C. In the powders, treated at 450 °C, the NiMnO$_3$ crystallographic phase prevails over other phase.
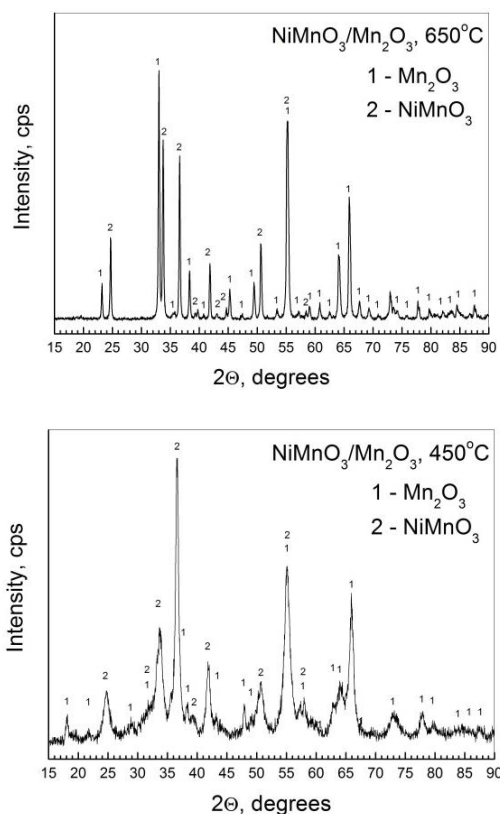
Fig. 1. PXRD patterns of NiMnO$_3$/Mn$_2$O$_3$ samples thermally treated at 450 and 650 °C.

Figure 2 displays FTIR spectra of investigated samples. Characteristic bands recorded in the range of 520−606 cm^{-1} are due to vibrations of the metal oxides [14−16]. The bands at about 3400 cm^{-1} and 1631 cm^{-1} arise from stretching and bending vibrations of OH groups of absorbed water molecules [16,17]. The vibrations observed at 1051, 1058, and 1197 cm^{-1} are probably due to the presence of other admixtures in the studied materials. The data acquired by FTIR spectroscopy are in agreement with results established using powder X-ray diffraction analysis.
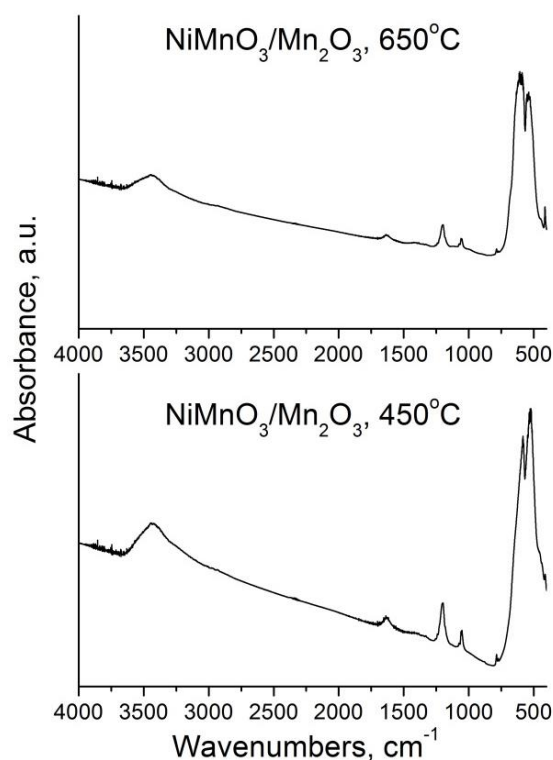
Fig. 2. FTIR spectra of NiMnO₃/Mn₂O₃ materials thermally treated at 450 and 650 °C.

Results from photocatalytic degradation measurements of model pollutant Malachite Green and Methylene Blue dyes under UV light using synthesized NiMnO₃/Mn₂O₃ as photocatalysts are shown and discussed in the following lines.

Calculated adsorption capacities and apparent rate constants of the investigated photocatalytic systems are presented in figure 3 and table 1, respectively.

The following formula was used to estimate adsorption capacity:

$$Q = \frac{(C_0 - C).V}{m},$$

where C_0 is initial dye concentration, C is dye concentration after 30 min in the dark, V is solution volume, and m is sample mass.
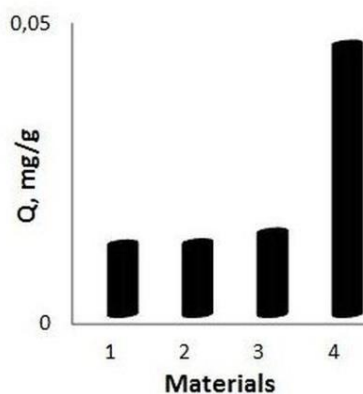
Fig. 3. Comparison of adsorption capacities of materials tested as photocatalysts for degradation of Malachite Green and Methylene Blue dyes: 1-NiMnO₃/Mn₂O₃, 650 °C, MG; 2-NiMnO₃/Mn₂O₃, 450 °C, MB; 3-NiMnO₃/Mn₂O₃, 450 °C, MG; 4-NiMnO₃/Mn₂O₃, 650 °C, MB.

Table 1. Calculated apparent rate constants (k) of tested photocatalysts and degree of degradation of investigated dyes after 120 minutes.

Sample	Used dye	k (×10^{-3} min^{-1})	Degree of degradation, %
NiMnO₃/Mn₂O₃, 450 °C	MG	11.6	78
NiMnO₃/Mn₂O₃, 650 °C	MG	7.9	67
NiMnO₃/Mn₂O₃, 450 °C	MB	0.7	10
NiMnO₃/Mn₂O₃, 650 °C	MB	0.5	13

The adsorption capacity of the investigated materials decreased in the following order: NiMnO₃/Mn₂O₃, 650 °C, MB (0.0450 mg/g) > NiMnO₃/Mn₂O₃, 450 °C, MG (0.0138 mg/g) > NiMnO₃/Mn₂O₃, 450 °C, MB (0.0120 mg/g) > NiMnO₃/Mn₂O₃, 650 °C, MG (0.0118 mg/g).

Apparent rate constants which followed pseudo first-order kinetics, were calculated using a logarithmic linear dependence −ln(C/Co) = k.t. The apparent rate constants of samples calcined at 450 °C were higher than those calcined at 650 °C for degradation of Malachite Green dye (11.6×10^{-3} min^{-1} and 7.9×10^{-3} min^{-1}) and Methylene Blue (0.7×10^{-3} min^{-1} and 0.5×10^{-3} min^{-1}) were.

C/C$_0$ concentration changes of Malachite Green and Methylene Blue dye degradation as a function of UV illumination time are shown in figure 4. The calculated degree of degradation (Table 1) after 120 min UV illumination of Malachite Green dye is superior (67–78%) than that of Methylene Blue dye (10–13%) over the investigated NiMnO₃/Mn₂O₃ samples. The NiMnO₃/Mn₂O₃ materials demonstrated an enhanced photocatalytic efficiency toward photocatalytic degradation of Malachite Green dye compared to Methylene Blue dye.

It could be supposed that the MG degraded faster than the MB taking into account the chemical structure of the dyes. According to Berberidou *et al.* the degradation of MG may proceed in two pathways. The first involves a hydroxyl radical attack to the central carbon atom of MG, while in the second pathway the hydroxyl radical hits the N,N-dimethyl-amino group of MG producing a reactive cationic radical [18]. Methylene blue dye decolourizes slower due to difficult destruction of the single benzene rings in comparison with MG degradation.
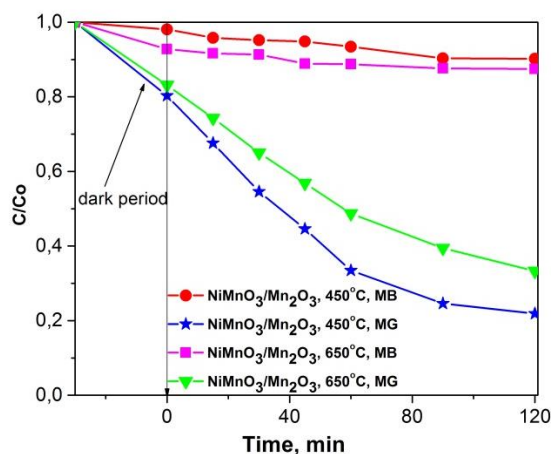
Fig. 4. C/C_0 concentration ratio of Malachite Green and Methylene Blue dyes as a function of UV irradiation time.

CONCLUSIONS

$NiMnO_3/Mn_2O_3$ materials were successfully prepared by precipitation technique using acetates as starting materials followed by thermal treatment at a different temperature of 450 °C and 650 °C. $NiMnO_3$ and Mn_2O_3 phases' occurrence was determined by powder X-ray diffraction analysis and FTIR spectroscopy. The photocatalytic behaviour of synthesized $NiMnO_3/Mn_2O_3$ samples was investigated in degradation reactions of aqueous solutions of Malachite Green and Methylene Blue dyes under UV irradiation for 120 minutes. In degrading Malachite Green dye the $NiMnO_3/Mn_2O_3$ samples exhibited a significantly higher photocatalytic efficiency than that in the case of Methylene Blue. The highest photocatalytic ability possessed a $NiMnO_3/Mn_2O_3$ catalyst calcined at 450 °C for degradation of Malachite Green dye (78%) in comparison with other studied samples.

REFERENCES

1. M. Amini, M. Ashrafi, *Nanochem. Res*., **1**, 79 (2016).
2. Q. Meng, S. Xiang, W. Cheng, Q. Chen, P. Xue, K. Zhang, H. Sun, B. Yang, *J. Colloid Interf. Sci.*, **405**, 28 (2013).
3. H. H. Logita, A. Tadesse, T. Kebede, *Afr. J. Pure Appl. Chem.*, **9**, 211 (2015).
4. Xia H.-Y., Hu L., Yao Q.-Z., *J. Inorg. Mater.*, **26**, 317 (2011).
5. P. Kar, S. Sardar, S. Ghosh, M. R. Parida, B. Liu, O. F. Mohammed, P. Lemmens, S. K. Pal, *J. Mater. Chem. C*, **3**, 8200 (2015).
6. B. Han, F. Zhang, Z. Feng, S. Liu, S. Deng, Y. Wang, Y. Wang, *Ceram. Int.*, **40**, 8093 (2014).
7. P. Deka, P. Sarmah, R. C. Deka, P. Bharali, *ChemistrySelect*, **1**, 4726 (2016).
8. Z. H. Yang, Y. C. Zhang, W. X. Zhang, X. Wang, Y. T. Qian, X. G. Wen, S. H. Yang, *J. Solid State Chem.*, **179**, 679 (2006).
9. J. Gao, J. Li, C. Jiang, C, Wan, *J. Electrochem. Soc.*, **157**, A899 (2010).
10. A. Sharma, A. Sharma, R. Sharma, *Clean Technol.*, 96 (2010).
11. P. Kakvand, M. S. Rahmanifar, M. F. El-Kady, A. Pendashteh, M. A. Kiani, M. Hashami, M. Najafi, A. Abbasi, M. F. Mousavi, R. B Kaner, *Nanotechnology*, **27**, 315401 (2016).
12. S. Giri, D. Ghosh, C. K. Das, *Dalton Trans.*, **42**, 14361 (2013).
13. S. Gnanam, V. Rajendran, *J. Alloys Comp.*, **550**, 463 (2013).
14. C. R. Indulal, G. S. Kumar, A. V. Vaidyan, R. Raveendran, *J. Nano-Electron. Phys.*, **3**, 170 (2011).
15. F. Kovanda, T. Grygar, V. Dorničák, *Solid State Sci.*, **5**, 1019 (2003).
16. M. Pudukudy, Z. Yaakob, *J. Nanopart.*, 1 (2016).
17. M. Salavati-Niasari, M. Esmaeili-Zare, M. Gholami-Daghian, *Adv. Powder Technol.*, **25**, 879 (2014).
18. C. Berberidou, I. Poulios, N. P. Xekoukoulotakis, D. Mantzavinos, *Appl. Catal. B: Environ.*, **74**, 63 (2007).

ФОТОКАТАЛИТИЧНО ПОВЕДЕНИЕ НА NiMnO$_3$/Mn$_2$O$_3$ МАТЕРИАЛИ ЗА РАЗГРАЖДАНЕ НА БАГРИЛАТА МАЛАХИТОВО ЗЕЛЕНО И МЕТИЛЕНОВО СИНЬО ПОД УВ ОБЛЪЧВАНЕ

К. Л. Захариева[1]*, К. И. Миленова[1], С. В. Василев[2], С. С. Димова[3], И. Д. Стамболова[4], В. Н. Блъсков[4]

[1] *Институт по катализ, Българска академия на науките, ул. „Акад. Г. Бончев“, бл. 11, 1113 София, България*
[2] *Институт по електрохимия и енергийни системи, Българска академия на науките, ул. „Акад. Г. Бончев“, бл. 10, 1113 София, България*
[3] *Институт по полимери, Българска академия на науките, ул. „Акад. Г. Бончев“, бл. 103А, 1113 София, България*
[4] *Институт по обща и неорганична химия, Българска академия на науките, ул. „Акад. Г. Бончев“, бл. 11, 1113 София, България*

(Резюме)

В настоящата работа е изследвано фотокаталитичното поведение на NiMnO$_3$/Mn$_2$O$_3$ материали под действието на УВ облъчване за разграждане на багрилата малахитово зелено (МЗ) и метиленово синьо (МС) като моделни замърсители. Получени са образци чрез утаяване използвайки никелов и манганов ацетат и утаител натриева основа и след това термична обработка при различна температура - 450 и 650 °C. Рентгенов фазов анализ и инфрачервена спектроскопия с Фурие преобразуване бяха използвани за да се изследва фазовия състав и структурата на синтезираните NiMnO$_3$/Mn$_2$O$_3$ образци. Фотокаталитичните изследвания бяха проведени използвайки воден разтвор на багрилата МЗ и МС с начална концентрация 5 ppm. От фотокаталитичните тестове се установи, че степента на разграждане на багрилата малахитово зелено и метиленово синьо след 120 минути използвайки NiMnO$_3$/Mn$_2$O$_3$ фотокатализатори, накалени при 450 и 650 °C, нараства както следва: NiMnO$_3$/Mn$_2$O$_3$, 450°C, МС (10%) < NiMnO$_3$/Mn$_2$O$_3$, 650°C, МС (13%) < NiMnO$_3$/Mn$_2$O$_3$, 650°C, МЗ (67%) < NiMnO$_3$/Mn$_2$O$_3$, 450°C, МЗ (78%). Установено е, че NiMnO$_3$/Mn$_2$O$_3$ образци показват много по-висока фотокаталитична способност за разграждане на малахитово зелено отколкото на метиленово синьо под действието на УВ облъчване.

Investigations of abiotic and biotic materials based on iron oxyhydroxides for photocatalytic decolourization of dyes in aqueous solutions

K. L. Zaharieva[1],*, M. G. Shopska[1], K. I. Milenova[1], R. Angelova[2], M. Iliev[2], G. B. Kadinov[1]

[1] *Institute of Catalysis, Bulgarian Academy of Sciences, Acad. G. Bonchev St., Bldg. 11, 1113 Sofia, Bulgaria*
[2] *Faculty of Biology, St. Kliment Ohridski University of Sofia, 8 Dragan Tsankov Blvd., 1000 Sofia, Bulgaria*

Photocatalytic ability of abiotic and biotic materials was investigated in the reaction of decolourization of Methylene Blue and Malachite Green dyes under UV illumination. Tests were carried out with aqueous solution of studied dyes at a concentration of 5 ppm. Biotic material containing lepidocrocite was synthesized by cultivation of *Leptothrix* genus of bacteria in a *Sphaerotilus-Leptothrix* group bacteria isolation medium (ICCL). A reference abiotic sample was prepared in a sterile ICCL not infected by bacteria. Photocatalytic efficiency of examined materials was compared with lepidocrocite synthesized by precipitation. Abiotic, biotic, and synthesized materials were studied by infrared spectroscopy. The biotic material demonstrated a higher photocatalytic activity in Methylene Blue dye decolourization than abiotic sample. In contrast, a higher decolourization degree for Malachite Green dye (83%) was determined using abiotic material in comparison with a biotic sample (70%). Synthesized lepidocrocite demonstrated a higher degree of decolourization of Malachite Green dye (89%) in comparison with that of Methylene Blue dye for the same period of 120 minutes.

Key words: photocatalytic discolouration, Malachite Green, Methylene Blue, lepidocrocite, biogenic material.

INTRODUCTION

In the field of heterogeneous catalysis, materials synthesis by biogenic or biomorphic methods may provide promising resources. Biogenically obtained iron oxyhydroxides and iron oxides have been attractive objects in view of their catalytic application. Interesting subjects of study have been iron oxyhydroxides produced by *Leptothrix sp. Leptothrix* is a filamentous bacterium and its sheath can be coated with iron oxyhydroxide or analogous manganese compounds [1].

Water is very important for life and the presence of undesirable chemical components leads to its pollution and makes it unsuitable for use by living organisms. Industrial effluents containing dyes and going into aquatic ecosystems cause environmental pollution. Dyes may induce harmful effects on plants and animals [2–5]. Photocatalytic oxidation is an efficient method for removal of various contaminants [6].

Using photocatalytic oxidation of Fe(II) in the presence of traces of citric acid Chen *et al.* have synthesized Lepidocrocite (γ-FeOOH) under visible light illumination [7]. The obtained low-crystalline γ-FeOOH was easily dissolved in aqueous solution and demonstrated high ability for degradation of Orange II dye by homogeneous photo-Fenton reaction [7]. Jelle *et al.* have prepared and investigated the relationship among goethite (α-FeOOH), akaganeite (β-FeOOH), lepidocrocite (γ-FeOOH), and feroxyhyte (δ-FeOOH) and their photocatalytic properties for degradation of Methylene Blue dye under visible light irradiation [8]. Chen *et al.* have studied adsorption and degradation of Rhodamine B dye during lepidocrocite formation by air oxidation of $Fe(OH)_2$ under visible light illumination in the presence of trace ethylenediaminetetracetic acid (EDTA) [9]. Sheydaei *et al.* have prepared nano-sized lepidocrocite using iron(II) sulphate solution. These authors reported that optimum adsorption conditions of Lanacron Brown S-GL dye (LBS-GL) removal from aqueous solution involved lepidocrocite dosage of 0.015 g, pH 3.5, temperature of 38 °C, and contact time of 100 min [10]. Lin *et al.* have obtained lepidocrocites by aerial oxidation using a ferrous solution under different LED visible light in the presence of trace EDTA. Catalytic studies have shown the ability of lepidocrocite about decolourization of Crystal Violet dye with traces of H_2O_2 under visible light illumination [11].

Many researchers have yet synthesized lepidocrocite using $FeCl_2 \cdot 4H_2O$, $FeSO_4 \cdot 7H_2O$, and other salts by different techniques [12-16]. Ristić *et al.* synthesized γ-FeOOH, α-FeOOH, and α-Fe$_2$O$_3$ by hydrolysis of Fe^{3+} ions in aqueous solution of perchlorate [17].

The present work deals with investigations of photocatalytic efficiency of abiotic and biotic iron-containing substances obtained in sterile medium and infected ICCL medium by *Leptothrix* bacteria, respectively. Particularly synthesized lepidocrocite activity is reported for photocatalytic decolourization of model pollutants as Malachite Green and Methylene Blue dyes under UV illumination.

EXPERIMENTAL

Biogenic material was synthesized by cultivation of *Leptothrix* genus of bacteria in a *Sphaerotilus-Leptothrix* group bacteria isolation medium (ICCL). A reference abiotic sample (AR) was prepared in a bacteria-uninfected sterile ICCL. The medium contained glucose, $(NH_4)_2SO_4$, $Ca(NO_3)_2$, K_2HPO_4, $MgSO_4$, KCl, $CaCO_3$, vitamin B12, and vitamin B1. An abiotic (synthetic) material (AS) was prepared using a modified procedure described elsewhere [12, 14–16] by precipitation technique from 0.05M aqueous solution of $FeCl_2 \cdot 4H_2O$ (Sigma Aldrich, p.a.) and 0.8M NaOH (Valerus Co.) as precipitating agent. NaOH was added to reach pH = 6. After that, the mixture underwent continuous stirring in air flow for three hours. The precipitate was filtered and washed with distilled water several times and dried in air at room temperature.

Infrared (IR) spectra of the samples were collected on a Nicolet 6700 FTIR spectrometer (Thermo Electron Corporation, USA) using dilution of studied material (0.5%) in a KBr pellet. The spectra were recorded in the middle IR range using 50 scans at a resolution of 4 (data spacing 1.928 cm^{-1}).

The photocatalytic study concerned oxidative decolourization of model pollutants Malachite Green (MG) and Methylene Blue (MB) dyes under UV light for 2 hours. Initial dye concentration in aqueous solution was 5 ppm. A semi-batch slurry reactor containing 150 ml of dye solution was used for tests under constant air flow and stirring. The amount of used catalyst was 0.15 g for biogenic and synthetic (AS) materials and 0.12 g for abiotic reference material. Examined systems were left in the dark for about 30 min in order to reach adsorption-desorption equilibrium. Periodically, after different time intervals of UV illumination, 4 ml of the investigated suspension were taken out of the reactor and centrifuged to separate the powder from the aliquot solution. Absorbance of aliquot solutions during the photocatalytic tests was monitored by UV-1600PC UV-Vis absorbance spectrophotometer in the wavelength range from 200 to 800 nm. Dye concentrations C_0 and C were evaluated from the calibration lines of the absorbance maxima (615 and 664 nm of

MG and MB). Dye decolourization degree was determined following a decrease of absorbance maximum at 615 and 664 nm of MG and MB dye, respectively.

RESULTS AND DISCUSSION

Infrared spectra of abiotic and biotic Fe-containing materials are displayed in figure 1. The bands of lepidocrocite (γ-FeOOH) observed in the region 459–3228 cm^{-1} [9,10,15,17] are marked as 'γ'. The bands at about 3400 and 1631 cm^{-1} are due to stretching vibrations of H-bonded OH groups and bending vibrations of physisorbed water molecules, respectively [15]. The band registered at about 1401 cm^{-1} could be attributed to some components of ICCL medium in which the abiotic reference (AR) and biotic materials were obtained. The vibrations at about 1384 and 1976 cm^{-1} could be assigned to impurities obtained during synthesis of lepidocrocite (AS).
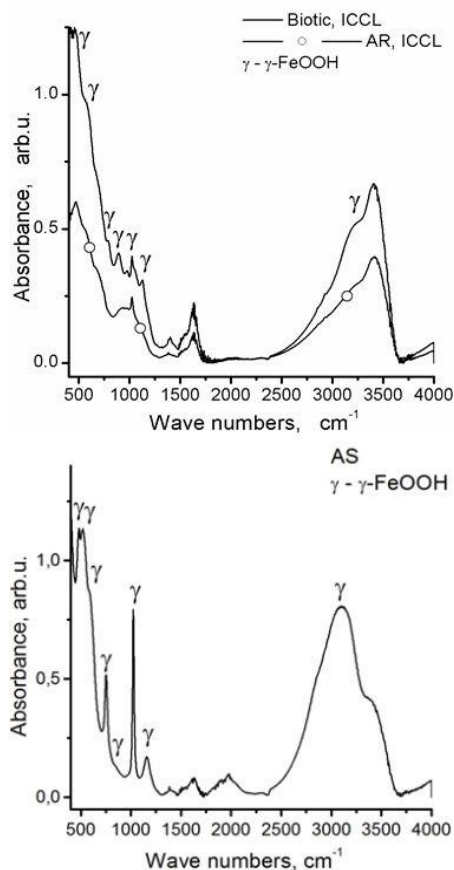
Fig. 1. IR spectra of biotic and abiotic Fe-containing materials.

Photocatalytic ability of biotic, synthetic lepidocrocite (AS), and abiotic control material (AR) was tested in UV-light decolourization of aqueous solution of two model pollutants, Malachite Green (MG) and Methylene Blue (MB), which are used as

textile dyes. Adsorption capacities, apparent rate constants of investigated reaction, and decolourization degree of MG and MB dyes are presented in table 1.

Adsorption capacity of the materials was calculated using the formula (1):

$$Q = \frac{(C_0 - C).V}{m} \qquad (1)$$

where C_0 is initial dye concentration, C is dye concentration after 30 min in the dark, V is solution volume, and m is sample mass. The abiotic reference material (AR) possessed the highest adsorption capacity for both MB and MG dyes – 0.335 and 0.269 mg/g, respectively.

Table 1. Calculated adsorption capacities, apparent rate constants of abiotic and biotic materials, and decolourization degree of MG and MB dyes.

Material	Used dye	Adsorption capacity, (mg/g)	Rate constant k ($\times 10^{-3}$ min^{-1})*	Degree of decolourization, (%)
abiotic (AR), ICCL	MB	0.335	-	-
abiotic (AR), ICCL	MG	0.269	12.8	83
biotic, ICCL	MB	0.266	-	-
abiotic (AS)	MB	0.215	-	-
biotic, ICCL	MG	0.018	10.1	70
abiotic (AS)	MG	0.027	10.7	89

*Apparent rate constant (k) calculated from slope of logarithmic linear dependence until UV irradiation time 60 minutes.

Concentration changes of MG and MB dyes and decolourization degree with the time under UV irradiation using abiotic and biotic Fe-containing samples are displayed in figures 2 and 3, respectively. The results definitely show that all studied materials were not active in decolourization of Methylene Blue dye. Kinetic curves show that the activity of the materials for decolourization of Malachite Green is not high. Bearing in mind these results, the apparent rate constants (Table 1) of the photocatalytic process with studied materials were estimated using logarithmic linear dependence only for the decolourization of MG dye:

$$-ln(C/C_0) = k.t \qquad (2)$$

A clearly lower rate constant of the MG decolourization reaction on the biogenic material could be due to adsorption of the dye, reaction products on biogenic impurities, or some influence of adsorbed components of the ICCL medium.

Iron (hydr)oxides were used as catalysts for purification of waste waters in Fenton-like processes, where reactive species (hydroxyl radicals) are generated at room temperature under atmospheric pressure. Iron oxides (magnetite, maghemite and hematite) were more successful at initiating dye photodegradation than the iron (hydr)oxides [18]. Lepidocrocite was studied for environmental remediation procedures in water treatment for the removal of toxic ions [19].
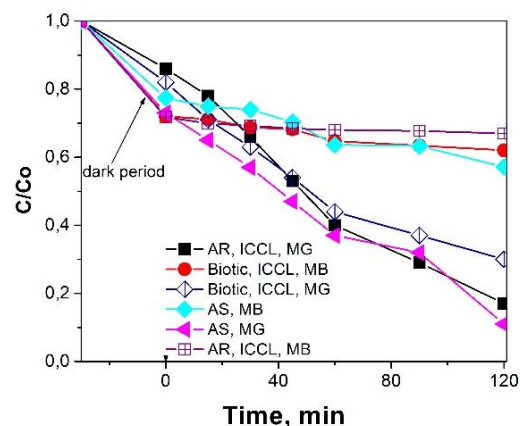
Fig. 2. Concentration C/C_0 ratio of MG and MB dyes in aqueous solution with time under UV illumination using abiotic and biotic Fe-containing samples.
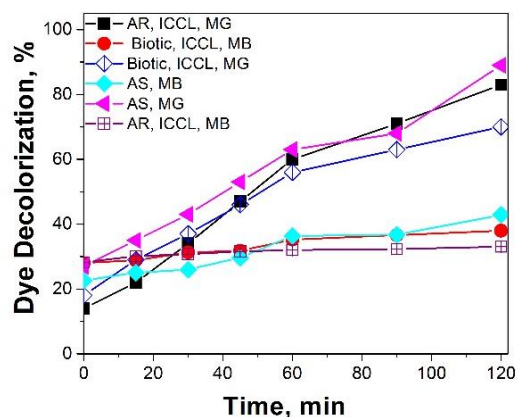
Fig. 3. Decolourization of MG and MB dyes in aqueous solution with time under UV illumination using abiotic and biotic Fe-containing samples.

CONCLUSIONS

Photocatalytic tests of biogenic material from cultivation of *Leptothrix* bacteria in ICCL medium, abiotic (formed in sterile medium), and synthesized iron oxyhydroxide(s) samples, revealed that they were not active in photocatalytic decolourization of Methylene Blue dye. A low decolourization activity of the same substances in aqueous solutions of Malachite Green dye was registered. The presence of bacterial rests so as some ICCL medium components could have a decreasing effect on catalytic activity.

REFERENCES

1. J. S. J. Hargreaves, A. I. Alharthi, *J. Chem. Technol. Biotechnol.*, **91**, 296 (2016).
2. R. Ameta, J. Vardia, P. B. Punjabi, S. C. Ameta, *Indian J. Chem. Technol.*, **13**, 114 (2006).
3. B. H. Hameed, M. I. El-Khaiary, *J. Hazard. Mater.*, **154**, 237 (2008).
4. A. Safavi, S. Momeni, *J. Hazard. Mater.*, **201–202**, 125 (2012).
5. A. R. Khataee, M. B. Kasiri, *J. Mol. Catal. A: Chem.*, **328**, 8 (2010).
6. O. Brahmia, *International Journal of Advances in Chemical Engineering and Biological Sciences (IJACEBS)* 3, 225 (2016).
7. R. Chen, S. Zhao, H. Liu, X. Song, Y. Wei, *J. Photochem. Photobiol. A: Chemistry*, **312**, 73 (2015).
8. A. A. Jelle, M. Hmadeh, P. G. O'Brien, D. D. Perovic, G. A. Ozin, *ChemNanoMat*, **2**, 1047 (2016).
9. R. Chen, J. Zhao, H. Liu, Y. Wei, *J. Environ. Chem. Eng.*, **3**, 202 (2015).
10. M. Sheydaei, S. Aber, *Clean-Soil, Air, Water*, **41**, 890 (2013).
11. Y. Lin, Y. Wei, Y. Sun, *J. Mol. Catal. A: Chemical*, **353–354**, 67 (2012).
12. G. Navarro, R. Acevedo, A. Soto, M. Herane, (in: XV Chilean Physics Symposium, 2006, IOP Publ. Ltd, 2008) *J. Phys.: Conf. Ser.*, **134**, 012023 (2008).
13. U. Schwertmann, H. Fechter, *Clay Miner.*, **29**, 87 (1994).
14. E. Mlirad, U. Schwertmann, *Miner. Mag.*, **48**, 507 (1984).
15. S. Rahimi, R. M. Moattari, L. Rajabi, A. Ashraf Derakhshan, M. Keyhani, *J. Ind. Eng. Chem.*, **23**, 33 (2015).
16. R. M. Cornell, U. Schwertmann, The Iron Oxides: Structure, Properties, Reactions, Occurences and Uses, Wiley-VCH Verlag GmbH & Co. KGaA Weinheim, 2003.
17. M. Ristić, S. Musić, M. Godec, *J. Alloys Comp.*, **417**, 292 (2006).
18. M. C. Pereira, L. C. A. Oliveira, E. Murad, *Clay Miner.*, **47**, 285 (2012).
19. M. Mohapatra, S. Anand, *Int. J. Eng. Sci. Technol.*, **2**, 127 (2010).

ИЗСЛЕДВАНИЯ НА АБИОТИЧНИ И БИОТИЧНИ МАТЕРИАЛИ НА ОСНОВАТА НА ЖЕЛЕЗНИ ОКСИХИДРОКСИДИ ЗА ФОТОКАТАЛИТИЧНО ОБЕЗЦВЕТЯВАНЕ НА БАГРИЛА ВЪВ ВОДНИ РАЗТВОРИ

К. Л. Захариева[1,*], М. Г. Шопска[1], К. И. Миленова[1], Р. Ангелова[2], М. Илиев[2], Г. Б. Кадинов[1]

[1] *Институт по катализ, Българска академия на науките, ул. „Акад. Г. Бончев", бл. 11, 1113 София, България*
[2] *Биологически факултет, Софийски университет „Св. Климент Охридски", бул. „Драган Цанков" 8, 1000 София, България*

(Резюме)

Фотокаталитичната способност на абиотичен и биогенен материал е изследвана в реакцията на обезцветяване на багрилата метиленово синьо и малахитово зелено под действието на УВ облъчване. Опитите са проведени във водни разтвори на изследваните багрила с концентрация 5 ppm. Биогенният материал съдържащ лепидокрокит е получен при култивиране на бактерии *Leptothrix* в изолационна среда за бактерии от групата *Sphaerotilus-Leptothrix* (ИССЛ). Абиотичен сравнителен материал (AR) е получен в стерилна ИССЛ (незаразена с бактерии). Фотокаталитичната способност на тестваните материали беше сравнена с тази на синтезиран чрез утаяване лепидокрокит (AS). Абиотичният, биогенният и синтезираният материал бяха изследвани посредством инфрачервена спектроскопия. Биогенният материал демонстрира по-висока фотокаталитична активност в обезцветяването на метиленово синьо от абиотичния сравнителен материал. Обратното бе наблюдавано при обезцветяване на малахитово зелено, като регистрираният ефект е много по-голям (83% с абиотичния сравнителен материал, 70% с биогенния материал). Синтезираният лепидокрокит показа по-висока степен на обезцветяване на разтвора с малахитово зелено (89%) в сравнение с тази на разтвора с метиленово синьо за еднакъв период от 120 минути.

Enhancing the PMS activation ability of Co_3O_4 by doping with Bi and Mg

V. V. Ivanova-Kolcheva, M. K. Stoyanova*

Department of Physical Chemistry, University of Plovdiv, 24 Tsar Asen St., 4000 Plovdiv, Bulgaria

A series of Co-Bi and Co-Mg composite oxides were prepared by co-precipitation method and their catalytic activity for heterogeneous peroxymonosulphate (PMS) activation was investigated through Acid Orange 7 (AO7) degradation in aqueous solutions. The as-prepared catalysts were characterized by XRD, XPS, TEM, and ICP-OES. A significant increase in catalytic activity of Co_3O_4 by modifying with Bi and Mg oxides was registered. Composites with 50 wt.% Co_3O_4 content displayed the best catalytic activity by achieving complete removal of 50 mg dm^{-3} AO7 within 12–15 minutes under the reaction conditions of 0.1 g dm^{-3} catalyst and PMS/AO7 molar ratio of 6:1. The enhanced PMS activation functionality of the composite catalysts was ascribed to an increased amount of surface hydroxyl groups because of modifying with the basic oxides. Surface hydroxyls favoured the formation of a surface Co(II)-OH intermediate and thus the generation of sulphate radicals (SRs) from PMS was accelerated. AO7 degradation was found to follow first order kinetics. The quenching study clearly indicated that oxidative degradation of AO7 is a radical-involved process with SRs being the dominant radical species. The Co-Bi and Co-Mg composite oxides presented stable performance with minor cobalt leaching even under acidic conditions.

Key words: composite oxides, Co_3O_4, Bi_2O_3, MgO, peroxymonosulphate, AO7 degradation.

INTRODUCTION

In recent decades, advanced oxidation processes (AOPs) based on *in situ* generation of highly reactive radical species by activation of inorganic peroxides have emerged as a promising technology for degradation of refractory organic compounds to harmless products in water at ambient conditions [1–3]. Despite promising performance and cost-effectiveness of the conventional Fenton process, several significant drawbacks limit its practical applications such as a low pH range (2–4), a large catalyst dosage, and large amount of iron sludge produced [4]. Sulphate radical induced AOPs are regarded as a more feasible and effective alternative to the Fenton process, owing to comparative standard reduction potential, longer half-life, and better selectivity of SRs than hydroxyl radicals, to remove or even mineralize organic pollutants [5,6].

Homogeneous activation of unsymmetrical peroxide PMS by transition metal ions is proven an efficient route for production of SRs with cobalt ions being the best activator [7]. However, the adverse effect of dissolved cobalt ions on animals and human beings raise a great concern. Hence, the development of cobalt-based heterogeneous catalysts of high PMS activating ability to conduct catalytic oxidation of organic pollutants is highly desirable. For the first time Anipsitakis *et al.*

explored the possibilities of CoO and Co_3O_4 in activation of PMS for 2,4-dichlorophenol degradation in replacing homogeneous Co(II)/PMS [8]. Nano-sized Co_3O_4 catalyst was found to exhibit an excellent long-term stability and low dissolved Co ions, especially under neutral conditions in degradation of AO7 by PMS activation [9]. Although Co_3O_4 nanoparticles present good catalytic performance, they can easily agglomerate during catalytic reaction to cause a drop of the catalytic efficiency. To tune the surface properties, and therefore improve the catalytic activity, various supports such as TiO_2, Al_2O_3, SiO_2, carbon materials, MgO, etc. have been used to prepare supported cobalt catalysts [10−12]. Among these, metal oxides with abundant surface basic sites such as MgO and TiO_2 were reported to lead to a relative high catalytic activity. Besides, supports can also act as components with synergistic and hybrid property dramatically boosting the catalytic efficiency [13]. Mixed metal catalysts have improved stability (reduced leaching), multifunctionality (e.g. photoactive, magnetically separable, etc.), high redox activity, and better catalytic activity compared to single metal [14]. Many cobalt composite catalysts that have been used as PMS activators including $CoFe_2O_4$ [15], $CoMn_2O_4$ [16], $CuFe_2O_4$ [17], and $CuBi_2O4$ [18] were found to exhibit a much stronger catalytic activity in PMS oxidation process than Co_3O_4. As PMS activation is favoured on a basic surface, modification of the Co_3O_4 with basic metal oxides would have a promotional effect on its PMS

---

* To whom all correspondence should be sent
E-mail: marianas@uni-plovdiv.bg

activation ability. AO7 is a representative azo dye widely used for the dyeing of textiles, food, and cosmetics. It is reported that AO7 shows good resistance to biodegradation, thus it is normally not amenable for the conventional wastewater treatment process [19].

The aim of the present work was to examine the effect of Bi and Mg oxides addition to Co3O4 on the catalytic performance in PMS activation for degrading Acid Orange 7 as a model water pollutant.

EXPERIMENTAL

Co$_3$O$_4$-MgO and Co$_3$O$_4$-Bi$_2$O$_3$ composite catalysts of various Co$_3$O$_4$ content (20, 50, and 80 wt.%) were synthesised by co-precipitation method using NaOH as a precipitation agent and subsequent annealing of the precursor at 773 K. In a typical procedure, 0.8 mol l^{-1} NaOH were added dropwise at 333 K into a certain volume of aqueous solution containing fixed amounts of cobalt nitrate and magnesium or bismuth nitrate under vigorous stirring until solution pH reached 10. The obtained precipitate was further aged at 333 K for 30 minutes under continuous stirring. The solid product was collected by filtration, washed with deionised water and ethanol several times to neutral pH, dried at 378 K overnight, and finally calcined at 773 K for 3 h in static air. For comparative purposes, pristine Co$_3$O$_4$, MgO, and Bi$_2$O$_3$ were also prepared by the same synthesis procedure.

The amount of Co, Bi, and Mg in the prepared samples as well as the concentration of leached cobalt ions after the reaction were measured by ICP-OES analysis (iCAP 6300 Thermo Scientific). XRD analysis was performed using Bruker D8 Advance diffractometer with Cu Kα radiation and LynxEye detector. Phase identification was accomplished by Diffrac*plus* EVA using ICDD-PDF2 Database. Catalyst morphology was determined on a JEOL JEM 2100 high-resolution transmission electron microscope using an accelerating voltage of 200 kV. Two basic regimes of microscope mode were used: bright field transmission microscopy (TEM) and selected area electron diffraction (SAED). X-ray photoelectron spectroscopy (XPS) measurements were carried out on an AXIS Supra photoelectron spectrometer (Kratos Analytical Ltd.) using monochromatic AlKα radiation with photon energy of 1486.6 eV. The binding energies (BEs) were determined with an accuracy of ±0.1 eV utilising the C1s line of adventitious carbon as a reference with energy of 285.0 eV. The pH of the point of zero charge (pH$_{PZC}$) of the catalysts was determined by pH drift method [20].

Degradation experiments were carried out in a 400-cm^3 glass reactor at 293 K under constant stirring at around 400 rpm. In a typical run, a fixed amount of PMS (in the form of Oxone, 2KHSO$_5$.KHSO$_4$.K$_2$SO$_4$) was added into a 200-cm^3 aqueous solution (50 mg dm^{-3} AO7) to attain a predefined PMS/AO7 molar ratio and stirred until dissolved. Degradation reaction was initiated by adding a specified amount of catalyst. Aliquots of 4.0 cm^3 were taken at given time intervals, immediately mixed with 1 ml methanol to quench the reaction, and centrifuged at 4000 rpm for 1 min to remove the catalyst. The AO7 concentration was determined by measuring the absorbance at a fixed wavelength of 486 nm using UV-Vis spectrophotometer (Cintra 101, GBS). All tests were conducted in triplicate to ensure the reproducibility of experimental results. For quenching experiments, prior to addition of oxidant and catalyst, a known amount of the alcohol quencher (ethanol or tert-butyl alcohol) was added into the AO7 solution to obtain a required molar ratio of alcohol to PMS.

RESULTS AND DISCUSSION

Calculated Co$_3$O$_4$ content in the synthesised composite materials based on ICP-OES results and XRD characterisation is given in Table 1 along with preparation parameters for comparison.

Table 1. ICP-OES results for Co, Bi, and Mg content in synthesised catalysts

Catalyst	Co$_3$O$_4$ content (wt.%)	
	Preparation	ICP-OES
X% Co$_3$O$_4$-MgO	20	21.6
	50	47.1
	80	74.3
X% Co$_3$O$_4$-Bi$_2$O$_3$	20	23.8
	50	45.1
	80	79.2

Fig. 1 shows XRD pattern of the 20% Co$_3$O$_4$-Bi$_2$O$_3$ catalyst in comparison with Bi$_2$O$_3$ and Co$_3$O$_4$ as reference compounds. The diffraction peaks of the pristine metal oxides can be indexed to single-phase monoclinic α-Bi$_2$O$_3$, (JCPDS 41-1449) and cubic spinel-type Co$_3$O$_4$ (JCPDS 42-1467), respectively. Reflexes typical of the two individual metal oxides were observed in the spectrum of the composite sample, which indicated the presence of Co$_3$O$_4$ and Bi$_2$O$_3$ in the catalyst. Notably, the intensity of peaks associated with cobalt species was very weak, suggesting good dispersion of the Co$_3$O$_4$ particles in the resulting product. Similarly, the peaks corresponding to the MgO were clearly observed and domi-

nant for the 20% Co_3O_4-MgO sample (not shown).
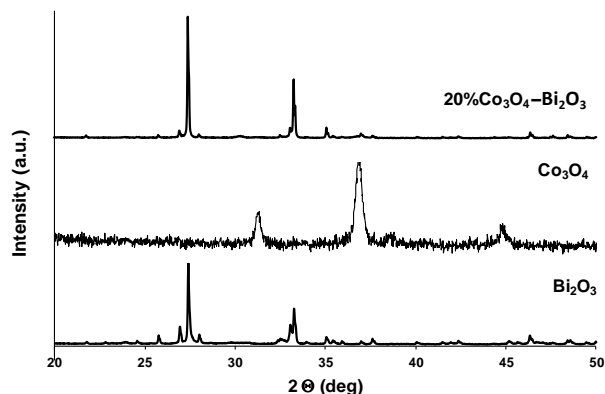
Fig. 1. XRD patterns of 20% Co_3O_4-Bi_2O_3, Co_3O_4, and Bi_2O_3.

Bright field TEM images (Fig. 2a) of the 20% Co_3O_4-MgO and 20% Co_3O_4-Bi_2O_3 catalysts indicate that the particles in both samples are predominantly flat with a near-rectangular shape. Particles with elongated rod-like shape were also observed. The diffraction patterns of both samples (Fig. 2b) reveal their polycrystalline nature with a good degree of crystallisation. Indexations of the SAED patterns confirm the presence of two metal oxide phases in each catalyst, indicated by arrows in Fig. 2b.
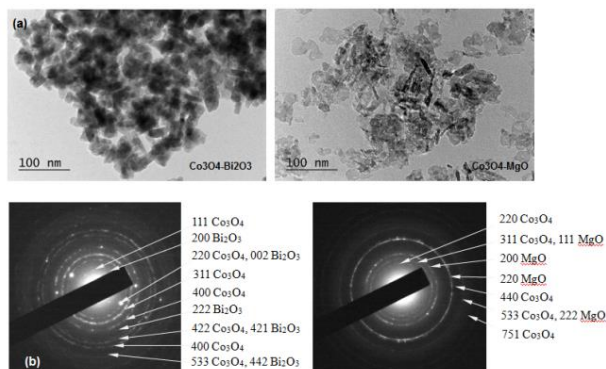
Fig. 2. (a) Bright field TEM (50k) and (b) SAED patterns of 20% Co_3O_4-MgO and 20% Co_3O_4-Bi_2O_3.

The particle size distribution of both composite catalysts was close to normal (Gaussian), but being more homogeneous in the 20% Co_3O_4-MgO sample (not shown). Particle sizes in both samples were mainly concentrated in the range of 7–20 nm. The average crystallite size of 20% Co_3O_4-MgO and 20% Co_3O_4-Bi_2O_3 was estimated to be 10.1 and 13.7 nm, respectively.

Wide-scan XPS spectra of the composite catalysts show that both Co and Mg or Bi elements are present on the surface (Fig. 3a). Deconvolution of the Co (2p) envelopes (not shown) indicated that the cobalt species were present in Co(II) and Co(III) oxidation states at atomic ratio close to 2, which is typical of Co_3O_4. A pronounced asymmetry of the

146

O1s spectra implies for simultaneous presence of two types of oxide particles in the composite catalysts. Two subpeaks could be resolved with BE of 529.4 and 531.1 eV, which were assigned to lattice oxygen and surface hydroxyl species, respectively (Fig. 3b). Based on both peak areas, the ratio of hydroxyl to oxide groups in the Co-Mg composite was calculated to be 62:38 indicating that OH groups dominantly covered the catalyst surface. The relative content of the surface hydroxyl oxygen in the Co-Bi composite was lower (*ca.* 21% of total oxygen), but was twice higher than estimated for Co_3O_4 (11%). A higher extent of surface hydroxylation of the composite catalysts compared to the Co_3O_4 could be due to a higher pHpzc of MgO (11.8) and Bi_2O_3 (9.2) than that of non-modified cobalt oxide (7.3). More surface basic sites available of in composite catalysts can promote the formation of surface Co(II)-OH complexes that was considered crucial for radical generation in the subsequent step of PMS activation [11].

Control experiments were conducted to compare AO7 removal efficiencies by various processes. As shown in Fig. 4a, no obvious degradation of AO7 by PMS alone was observed in the investigated time scale although PMS is a strong oxidizsing agent (φ^0 = +1.82 V). Less than 1% colour removal was reached after 8 h to imply that chemical oxidation process is most likely to occur through a non-radical mechanism. In the presence of composite catalysts without PMS addition *ca.* 5% extent of decolourisation of the solution was attained in 10 min pointing out that AO7 adsorption on the catalysts was less effective to remove it from the water. Similar decolourisation efficiency was observed with the Bi_2O_3/PMS system showing that the pure Bi_2O_3 could not activate the PMS to degrade the dye. However, AO7 degradation was found more significant for the MgO/PMS system under the same conditions with around 63% extent of oxidation suggesting that bare MgO can decompose PMS into active radicals. There was still 55% of AO7 remaining after 15 min, when pure Co_3O_4 was used as the PMS activating catalyst, and a complete discolouration of the solution was achieved for 90 min. However, when the composite oxides even with lowest MgO or Bi_2O_3 content (20 wt.%) were added as a catalyst, the dye pollutant was oxidised rapidly achieving up to 99% colour removal in 15 min even at a very low catalyst concentration of 0.10 g/l. These results confirmed that the degradation process was a radical-involved process and the active radical species were generated much faster in the presence of hybrid catalysts than bare Co_3O_4 (100% active phase).
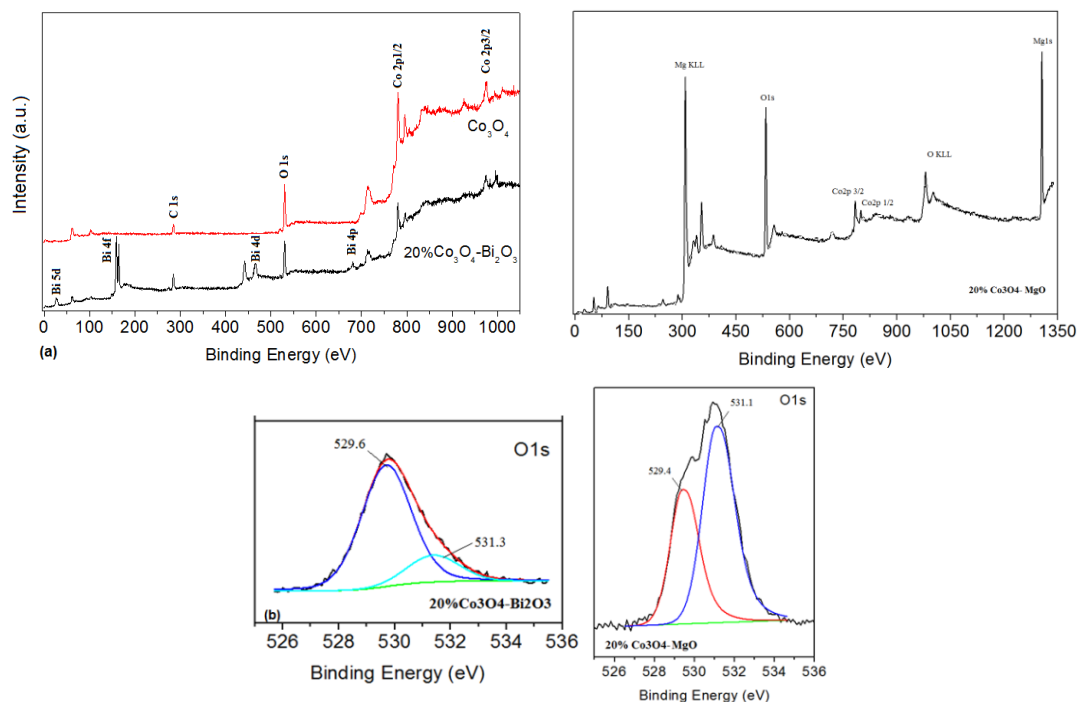
Fig. 3. (a) Wide scan XPS spectra of the 20% Co$_3$O$_4$-Bi$_2$O$_3$ and 20% Co$_3$O$_4$-MgO catalysts and (b) their O1s envelopes (with deconvolution).
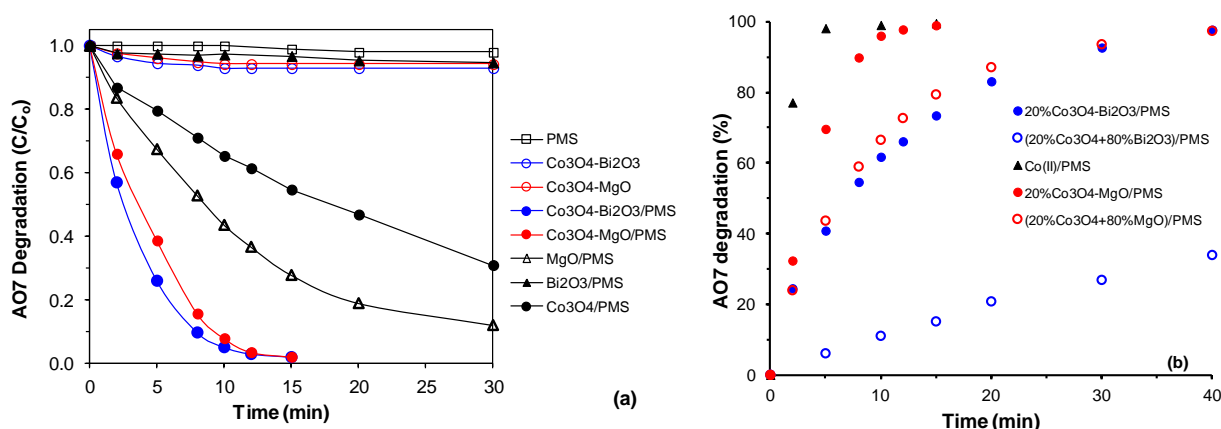
Fig. 4. AO7 degradation with time in different systems. Reaction conditions: 50 mg dm^{-3} AO7; 0.1 g dm^{-3} catalyst loading; PMS/AO7 = 6/1; pH = 4.0. Co$_3$O$_4$ content in composite catalysts was 80 wt.%.

A much higher catalytic activity presented by Co-Bi and Co-Mg composite oxides for AO7 degradation suggests a synergistic effect of both oxide components in the catalysts. The observed synergism supports a hypothesis of the important role of the basic dopants (Bi$_2$O$_3$ and MgO) in facilitating the formation of functional Co(II)-OH complexes through direct interaction of surface cobalt species with the nearby surface of dopant OH groups. Besides, a better dispersion of the Co$_3$O$_4$ active species in the composites because of their smaller size ensures more effective sites on the surface to generate radicals.

The key role of close contact between metal oxide components of the composite catalysts was con-firmed by a much weaker catalytic performance exhibited by mechanical mixture of bismuth oxide/magnesium oxide and Co$_3$O$_4$ (Fig. 4b). In fact, in the presence of 20% Co$_3$O$_4$-MgO complete AO7 degradation was achieved in 10 min, while for the same reaction period around 40% of dye did not undergo conversion under the catalytic action of matching mechanical mixture despite the same amount of Co$_3$O$_4$. The decrease in activity was more pronounced for the mechanical mixture of 20% Co$_3$O$_4$ and 80% Bi$_2$O$_3$ due to inability of the

147

Bi_2O_3 to induce PMS activation to produce radicals. For the 20% Co_3O_4-Bi_2O_3/PMS system, 50 min were required for complete discolouration of the dye solution while for the same time only 43% removal efficiency was attained using a mixture of both oxides. Besides, a linear rate of AO7 decay over mechanical mixture suggests that the rate-limiting step of the oxidation process is decomposition of PMS to radical species rather than destruction of the dye molecules by the radicals formed.

It should be noted that the homogeneous Co(II)/PMS system showed faster oxidation kinetics. At a concentration of Co(II) ions equivalent to the cobalt content in composites, complete discolouration of dye solution was achieved within 5 min. Although the homogeneous approach is more efficient for destroying dye molecules, its practical application is restricted due to potential health hazards caused by cobalt ions released in water as well as to the inability to separate the catalyst from the solution and reuse. The registered difference in degradation kinetics of AO7 under homogeneous and heterogeneous oxidation mode as well as negligible cobalt leaching into the solution (less than 1%) suggests that the activation of PMS is heterogeneously conducted on the catalyst surface.

Figure 5a shows the change in the UV-Vis absorption spectra of the AO7 solution during 80% Co_3O_4-Bi_2O_3-mediated catalytic oxidation with PMS as a function of reaction time. As the reaction progressed the intensity of the absorption peak at 486 nm decreased due to degradation of the chromophore azo bond. In addition, a simultaneous decrease of the absorbance at 230 and 310 nm, ascribed to $\pi-\pi^*$ transitions in the benzene and naphthalene rings of dye, respectively, is considered evidence of a break-up of the conjugated π-system of the dye molecule. In the meantime, a new

absorbance band at about 255 nm appeared in the ultraviolet region at the very beginning of reaction (even at 2 min) and then started to drop slowly. This indicate that a new structure unit was formed from chromophore cleavage, which further was also degraded. 1,2-Naphthoquinone was identified to contribute to the peak by comparing spectra of the reaction mixture and a standard solution containing the expected degradation intermediates (Fig. 5b). Similar UV–vis spectra profiles were observed also in experiments carried out in the presence of other composite catalysts.

Catalytic oxidation of AO7 over synthesised composite catalysts follows first-order kinetics model, thereby implying that the oxidation process was not controlled by the radicals generation step. Table 2 gives reaction rate constants (k) and corresponding regression coefficients (R^2) of the model fitting.

Table 2. Kinetic parameters of AO7 degradation in different catalyst – PMS systems

Catalyst	Co_3O_4 (wt.%)	k (min^{-1})	R^2
Co_3O_4	100	0.039	0.992
Co_3O_4-MgO	20	0.315	0.991
	50	0.334	0.989
	80	0.237	0.991
Co_3O_4- Bi_2O_3	20	0.091	0.984
	50	0.374	0.992
	80	0.257	0.996

Because Co_3O_4 is the component of the composite catalysts that basically determines their PMS activation functionality, the lowest AO7 degradation rate was observed for the samples with lowest Co_3O_4 content. However, the 20% Co_3O_4-MgO catalyst produced faster and complete AO7 degradation with a rate constant being more three-fold that using Co-Bi analogue.
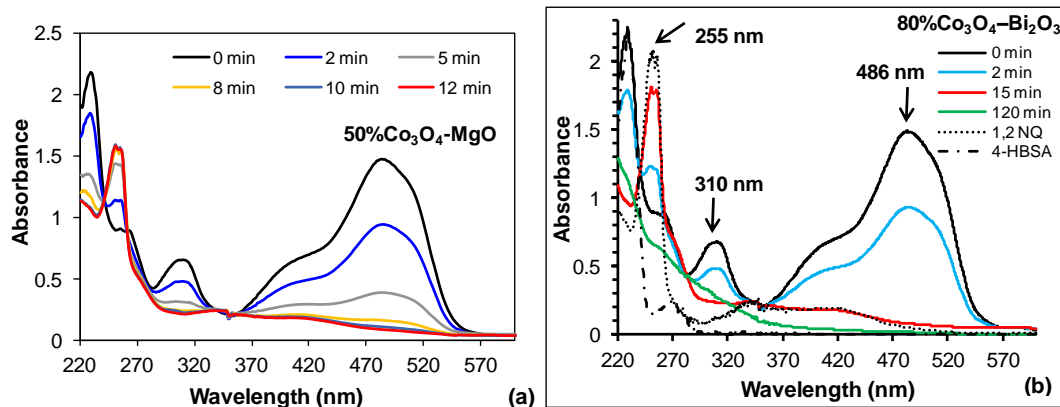
Fig. 5. (a) The UV-Vis spectral changes of AO7 in 50% Co_3O_4-MgO/PMS process. (b) Comparative UV-Vis spectra of the AO7 solution during oxidation over 80% Co_3O_4-Bi_2O_3 and standard solutions of 1,2-naphthoquinone (NQ), and 4-hydroxybenzenesulphonic acid (4HBSA). Reaction conditions were the same as those indicated in Fig. 4.

The difference in activity could be explained by a stronger basic surface of MgO than Bi$_2$O$_3$, which provides formation of more Co(II)-OH complexes and consequently generation of more active radicals for a shorter time. The increase of Co$_3$O$_4$ content up to 50 wt.% favoured the AO7 degradation rate, which was contributed to the higher activation rate of PMS. A further increase of the Co$_3$O$_4$ amount caused a decrease in degradation activity that could be attributed to a lesser amount of hydroxyl groups on the catalyst surface as well as to aggregation of Co$_3$O$_4$ particles resulting in less active sites for PMS activation.

Catalytic activation of PMS mediated by transition metals or metal oxides could generate three main types of reactive radicals, viz., sulphate (SO$_4^{\bullet-}$), hydroxyl (•OH), and peroxymonosulphate (SO$_5^{\bullet-}$) [1,11]. Due to SO$_5^{\bullet-}$ very low redox potential, sulphate radicals and hydroxyl radicals were regarded as active species in the catalytic PMS oxidation.

Ethanol (EtOH) and *tert*-butyl alcohol (TBA) were used as radical scavengers to evaluate the contribution of SO$_4^{\bullet-}$ and •OH in the oxidation. According to the literature, EtOH readily reacts with both hydroxyl and sulphate radicals at high and comparable rates whereas TBA mainly reacts with hydroxyl radicaland about 1000-fold slower with sulphate radicals [1]. The inhibition of the degradation process brought by the two quenching agents is shown in Fig. 6. It is obvious that addition of EtOH to the reaction mixture inhibited AO7 degradation, whereas the process was negligibly affected in the presence of TBA. Based on the results it may be concluded that sulphate radicals played a major role throughout the AO7 degradation process on the composite catalysts. The retarding effect of EtOH can be explained by competitive reactions of generated radicals with AO7 and radical quenching agent.
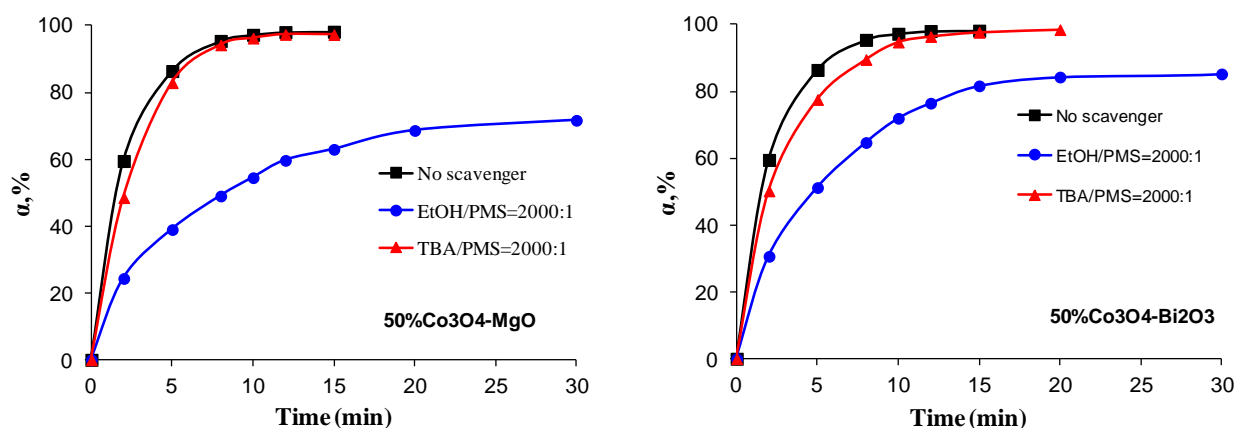
Fig. 6. Influence of ethanol and TBA addition on the AO7 degradation efficiency in composite catalyst-PMS system.

CONCLUSIONS

In this study, Co$_3$O$_4$-Bi$_2$O$_3$ and Co$_3$O$_4$-MgO composite oxides with different Co$_3$O$_4$ content were synthesised and used as heterogeneous catalysts to activate PMS for degrading AO7 in aqueous solution. The formation of the composites was confirmed by XRD and TEM characterisation. It was found that the as-prepared catalysts manifested a superior catalytic activity toward PMS than pristine Co$_3$O$_4$. Composites containing 50 wt.% Co$_3$O$_4$ exhibited the best catalytic performance. In the presence of PMS, they induced fast and complete degradation of AO7 (50 mg dm^{-3}) with the rate constant being 8 times higher than that over unmodified Co$_3$O$_4$. The presence of Mg and Bi was found to be beneficial for enhancing the content of hydroxyl groups on the catalyst surface that form Co(II)-OH complexes critical for heterogeneous PMS activation. Radical quenching studies demonstrated that sulphate radicals are the dominating species formed by the catalyst-PMS interaction, and hence those that are responsible for effective AO7 degradation.

REFERENCES

1. G. P. Anipsitakis, D. D. Dionysiou, *Environ. Sci. Technol.*, **37**, 4790 (2003).

2. W. Zhang, H. Tay, S. Lim, Y. Wang, Z. Zhong, R. Xu, *Appl. Catal. B: Environ*, **95**, 93 (2010).

3. P. Shukla, H. Sun, S. Wang, H. Ang, M. Tadé, *Sep. Purif. Technol.*, **77**, 230 (2011).

4. A. Hu, X. Li, Sh. Ye, G. Yin, Q. Zeng, *Appl. Catal. B: Environ.*, **102**, 37 (2011).

5. Y. Gao; Z. Zhang; S. Li, L. Liu, L. Yao, Y. Li, H. Zhang, *Appl. Catal. B: Environ.*, **185**, 22 (2016).

6. L. Xu, R. Yuan, Y. Guo, D. Xiao, Y. Cao, Z. Wang, J. Liu, *Chem. Eng. J.*, **217**, 169 (2013).

7. S. Yang, P. Wang, X. Yang, L. Shan, W. Zhang, X. Shao, R. Niu, *J. Hazard. Mater.,* **179** 552 (2010) 552.

8. G. Anipsitakis, E. Stathatos, D. Dionysiou,, *J. Phys. Chem. B*, **109**, 13052 (2005).

9. X. Chen, J. Chen, X. Qiao, D. Wang, X. Cai, *Appl. Catal. B: Environ.*, **80**, 116 (2008).

10. P. Shukla, H.Q. Sun, S. B. Wang, H. M. Ang, M. O. Tade, *Catal. Today,* **175**, 380 (2011).

11. Q. Yang, H. Choi, Y. Chen, D. D. Dionysiou, *Appl. Catal. B: Environ.,* **77**, 300 (2008).

12. E. Saputra, S. Muhammad, H. Sun, H. M. Ang, M. O. Tade, S. Wang, *J. Colloid Interface Sci.,* **407**, 467 (2013).

13. J. Deng, Sh. Feng, K. Zhang, J. Li, H. Wang, Z. Wang, T. Zhang, X. Ma, *Chem. Eng. J.*, **308**, 505 (2017).

14. W. Wu, Z.-H. Huang, T.-T. Lim, *Appl. Catal. A: Gen.*, **480**, 58 (2014).

15. Q. Yang, H. Choi, S. Al-Abed, D. Dionysiou, *Appl. Catal. B: Environ,* **88**, 462 (2009)

16. Y. Yao, Y. Cai, G. Wu, F. Wei, H. Chen, S. Wang, *J. Hazard. Mater.,* **296**, 128 (2015).

17. Y. Feng, J. Liu, D. Wu, Z. Zhou, Y. Deng, T. Zgang, K. Shih, *Chem. Eng. J.*, **280**, 514 (2015).

18. W.-D. Oh, S. K. Lua, Z. Dong, T.-T. Lim, *Nanoscale*, **8**, 2046 (2016).

19. J. Deng, Sh. Feng, X. Ma, Ch. Tan, H. Wang, Sh. Zhou, T. Zhang, J. Li, *Sep. Purif. Technol.*, **167**, 181 (2016).

20. P. Faria, J. Órfão, M. Pereira, *Water Res.*, **38**, 2043 (2004).

ПОВИШАВАНЕ НА PMS-АКТИВАЦИОННАТА СПОСОБНОСТ НА Co₃O₄ ЧРЕЗ ДОТИРАНЕ С Bi И Mg

В. В. Иванова-Колчева, М. К. Стоянова*

Катедра „Физикохимия“, Пловдивски университет „Паисий Хилендарски“, ул. „Цар Асен“, № 24, 4000 Пловдив, България

(Резюме)

Синтезирани са серия от композитни Co-Bi и Co-Mg оксиди чрез метод на съутаяване и е изследвана каталитичната им активност за хетерогенно активиране на пероксимоносулфат (PMS) за разграждане на Кисело Оранжево 7 (AO7) във водни разтвори. Катализаторите са охарактеризирани чрез XRD, XPS, TEM, и ICP-OES. Установено е съществено увеличаване на каталитичната активност на Co₃O₄ чрез модифициране с Bi₂O₃ и MgO. Композитите с 50% тегловно съдържание на Co₃O₄ показват най-висока каталитична активност, постигайки пълно разграждане на 50 mg dm⁻³ AO7 в рамките на 12−15 минути при концентрация на катализатора 0.1 g dm⁻³ и молно съотношение PMS/AO7 = 6:1. Повишената PMS-активационна функционалност на композитните катализатори се дължи на по-високото съдържание на повърхностни хидроксилни групи вследствие модифицирането с базичните оксиди. Хидроксилните групи върху катализаторната повърхност благоприятстват образуването на повърхностни Co(II)-OH комплекси, което ускорява генерирането на сулфатни радикали (SRs) от PMS. Разграждането на AO7 се подчинява на кинетичните закономерности на реакции от първи порядък. Експериментите с добавяне на радикал-улавящи агенти показват, че окислителното разграждане на AO7 е радикалов процес, като SRs са доминиращите радикалови частици. Co-Bi и Co-Mg композитните оксиди демонстрират устойчива активност с ниска разтворимост на Co дори в кисела среда.

Green seed-assisted fly ash zeolitisation at room temperature

B. Z. Barbov[1], Yu. A. Kalvachev[2]*

[1] *Institute of Mineralogy and Crystallography, Bulgarian Academy of Sciences, Acad. G. Bonchev St., Bldg. 107, 1113 Sofia, Bulgaria*
[2] *Institute of Catalysis, Bulgarian Academy of Sciences, Acad. G. Bonchev St., Bldg. 11, 1113 Sofia, Bulgaria*

Zeolite X has been successfully synthesised from fly ash produced by combustion of lignite coal at Maritsa Iztok 2 thermal power plant using a two-stage process: fusion with sodium hydroxide followed by hydrothermal treatment at room temperature. NaX zeolite crystallisation started later by decreasing NaOH amount. In order to optimise synthesis process a seed-assisted procedure was introduced. Preliminary synthesised zeolite X from pure chemicals was used as a seed material. On the one hand, seed addition affected synthesis direction to the desired zeolite structure (a monophase zeolite X product) and resulted in reduced synthesis time, but also reduced sodium hydroxide amount upon melting. In this way, zeolitisation may increase cost-effectiveness and eco-efficiency.

Key words: zeolite X, fly ash, zeolite synthesis, seed, green synthesis.

INTRODUCTION

Coal-fired thermal power plants (TPP) are a major source of fly ash (FA). Depending on the type of source and composition of the combustion coal, solid by-product components may vary significantly, but all types of FA include large amounts of silica (amorphous and crystalline) and alumina, both of which are constituent parts of many coal bedrocks. FA world production is over 750 million tons per year [1]. The areas where the production waste from the TPPs is deposited are huge terrains. Due to dusting during drying and release of harmful substances, FA represents an environmental hazard for soils, waters, and air. Discharges of the ash create environmental risks due to increased acid content and infiltration of heavy metals and radioactive elements in the soil. Toxic components in FA depend on the specific structure of the deposit and they may include a variety of the following elements found in negligible quantities: arsenic, beryllium, boron, cadmium, chromium, cobalt, lead, mercury, selenium, thallium, and vanadium. Many approaches to the use of FA have been developed, given their composition and degree of crystallinity. Part of deposited ash is used in the construction of roads and buildings, in the form of gypsum, gypsum board, cement, and concrete, in the ceramic industry, and other building mixes. Zeolite synthesis is another solution to utilise FA [2,3]. Zeolite production from FA results in a good practice with higher added value compared to ash usage as a cement additive [4–6]. In recent years, many studies have also been accomplished on zeolite synthesis from other alternative sources of SiO_2 and Al_2O_3 because the production of synthetic zeolites from pure silica and alumina sources is quite expensive. For alternative sources of silicon and aluminium, industrial waste or geothermal materials rich in Si and Al [7–14] may be used, as well as FA, which is largely composed of silicon and aluminium units. So naturally, one of the approaches to use FA is their zeolitisation. Zeolites synthesised from fly ash have many applications, including ion exchangers, molecular sieves, and adsorbents, similar to the zeolites obtained by conventional methods.

Generally, zeolites represent a group of natural or synthetic crystalline microporous aluminasilicates having a pore size of 0.3 to 2.0 nm [15]. Zeolite pores form a system of channels and cavities with well-defined shape and dimensions. These micro-porous materials are used as adsorbents [16,17], for ion exchange processes [18], and in catalysis [19–22]. Thus, from an environmental point of view the synthesis of coal ash zeolites and their use as adsorbents, catalysts, and ion exchangers is considered one of the most effective applications of fly ash.

FA is fine particles that are trapped by the TPP filters. They are collected by electrostatic or mechanical precipitation. The ash mainly contains amorphous and crystalline silica as well as hematite, mullite, and magnetite [3,23–25]. It has been found that different zeolite structures can be synthesised from the same ash but under different crystallisation conditions, the A, NaX, and NaY zeolites being of utmost importance [26]. One of them, namely NaX

---

* To whom all correspondence should be sent
E-mail: kalvachev@ic.bas.bg

zeolite, which is an analogue to the natural faujasite, has a great ecological application. This zeolite, characterised by a highly developed specific surface area and numerous pores ranging in size from 5.0 to 7.5 Å, facilitates adsorption of 3.2-Å carbon dioxide molecules. Primarily, NaX zeolite is used as a catalyst in biodiesel production and CO_2 adsorption [27,28].

The purpose of the present work was to synthesise a NaX zeolite structure from fly ash obtained after the combustion of lignite coal at Maritsa Iztok 2 TPP by using a two stages process: fusion with sodium hydroxide followed by hydrothermal synthesis at room temperature. The first step, fusion of the alkaline-ash mixture led to the formation of soluble sodium aluminate and sodium silicate, enhanced zeolite formation, and facilitated the complete utilisation of the waste as a raw material [29, 30]. Hydrothermal activation is the second stage, which usually is held at a relatively high temperature (90–120 °C). The goal of the present study was to perform this stage at room temperature. Synthesis time at room temperature was between two weeks and one month, whereas the crystallisation process at 90 °C took a few hours (4–8). In order to reduce crystallisation time, a seed-induced synthesis procedure was applied. Prelimi-nary synthesised zeolite X from pure chemicals was used as a seed material.

EXPERIMENTAL

Sample preparation

Ash residues, containing 52.66 and 23.37 mass% of silica and alumina, respectively, were subjected to a dual stage fusion-hydrothermal transformation.

Initially, the coal ash was thoroughly homogenised with sodium hydroxide, and then the resulting mixture was poured into a nickel pot. Melting was carried out in a furnace at a temperature of 550 °C for a period of 1 hour. Then distilled water and the seed material were added to the preconditioned sample, and the resulting mixture was placed into a polypropylene vessel. Depending on the NaOH/fly ash ratio and the amount of crystal seed added to the resulting mixture the crystallisation of zeolite NaX was conducted at room temperature from 15 days to two months. The separated sample was filtered and allowed to dry at room temperature. In order to reduce crystallisation time and increase the yield, 1, 2, and 5 wt.% crystalline seed of zeolite NaX were used. Weight percentage was calculated regarding silica and alumina in the fly ash. The obtained solid substance was carefully washed with distilled water and then dried at 105 °C for an hour.

Zeolite seeds were synthesised at 90 °C for 8 h

by using pure chemicals from initial gel with the following molar composition: $NaAlO_2$:$4SiO_2$: $16NaOH$:$325H_2O$.

Samples characterization

Product morphology was observed by scanning electron microscopy (SEM) on a JEOL JSM6390 microscope coupled with an energy-dispersive X-ray (EDX) analyser (Oxford Instruments). Phase identification was performed by X-ray diffraction (XRD) technique on a Brucker D2 Phaser diffractometer with CuK_α radiation and a Ni filter.

RESULTS AND DISCUSSIONS

The hydrothermal synthesis of NaX zeolite from fly ash was carried out at room temperature. In these experiments, synthesis duration varied between 15 and 60 days. Table 1 provides data on the crystallisation time of zeolite X obtained from fly ash without seed and with 1, 2, and 5% seed, respectively, at a different NaOH/FA ratio. The NaOH/FA ratios used were 1.2/1, 1.0/1, 0.8/1, and 0.6/1 (Table 1). Higher amounts of NaOH caused NaX zeolite crystallisation to start much earlier. X-ray powder patterns indicate that the best results were obtained when the amount of sodium hydroxide was higher with NaOH/FA ratio of 1.2/1 or 1.0/1. Such a result could be expected because in this case sodium hydroxide brings about larger amounts of soluble silicates and aluminates from the silica and alumina phases, respectively, present in the fly ash. The latter phases increase their mobility to become able to form zeolite nuclei around which crystal growth takes place to build a zeolite structure. On using a lower amount of sodium hydroxide, however, NaX zeolite synthesis was not successful. X-ray powder patterns of the resulting products synthesised at a NaOH/FA ratio of 1/1 show that a crystalline phase emerged around the 29th day after crystallisation at room temperature (Fig. 1) and a high crystalline product of this zeolite was only reached by the 45th day of synthesis.

On employing a NaOH/FA ratio of 1.2/1 in the studies, the crystallisation of NaX zeolite began about 25 days after synthesis onset.

To reduce crystallisation time and direct synthesis to the desired zeolite structure, a seed-assisted synthesis of NaX zeolite from fly ash was applied by means of 1, 2 or 5 wt.% crystalline NaX zeolite. The weight percentage was calculated regarding the total amount of silica and alumina in the fly ash. NaX zeolite crystallisation at a NaOH/FA ratio of 1.2/1 started earlier on using 1, 2, and 5% seed. Comparing seed-assisted with seed-free NaX zeolite

synthesis, crystallisation with the latter started later for the same NaOH/FA ratio. By applying 1, 2 or 5% by weight of crystalline seed crystals, zeolite crystallisation started 21 days after synthesis onset at room temperature.

Table 1. Dependence of the NaOH/FA ratio on the crystallisation time of NaX zeolite synthesised from fly ash in the presence of 1, 2 or 5% seed at room temperature

NaOH/FA	No seeds	1% crystal seed	2% crystal seed	5% crystal seed
1.2/1	25 days	21 days	21 days	21 days
1	29 days	29 days	29 days	21 days
0.8/1	-	37 days	37 days	24 days
0.6/1	-	-	43 days	37 days
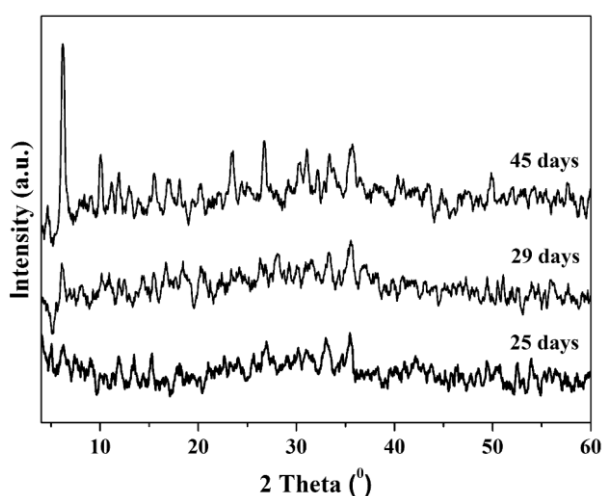
Fig. 1. X-ray powder patterns of NaX zeolite after seed-free synthesis from fly ash at room temperature at a NaOH/FA ratio of 1/1.

On employing a NaOH/FA ratio of 1.2/1 in the studies, the crystallisation of NaX zeolite began about 25 days after synthesis onset.

At a NaOH/FA ratio of 1.2/1 even small amounts of seed made the synthesis of zeolite X most sensitive. Upon addition of 1% seed, the crystallisation time decreased to 21 days, whereas without seed, crystallisation arose after the 25th day. Use of 5 wt.% seed led to a higher degree of crystallinity.

If the NaOH/FA ratio was 1/1 and crystallisation occurred in the presence of 1 or 2% seed, the NaX zeolite started to crystallise before the 29th day. At a higher amount of seed (5%), the crystallisation started earlier than the case with 1 or 2% crystal seed. X-ray powder patterns of the synthesised products give evidence that the NaX zeolite began to crystallise before the 21st day of synthesis (Fig. 2). From these results, it can be concluded that the use of a larger amount of crystal seed favoured a significant decrease in crystallisation time.
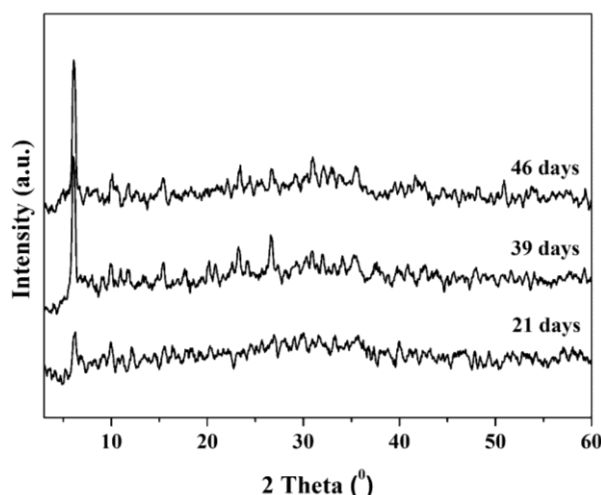
Fig. 2. X-ray powder patterns of NaX zeolite synthesised from fly ash at room temperature in the presence of 5% seeds at a NaOH/FA ratio of 1/1.

Scanning electron microscopy (SEM) was applied to investigate the morphology and size of the crystal particles of NaX zeolite. In Figure 3, a SEM image of NaX zeolite synthesised from fly ash and sodium hydroxide at a ratio of 1/1 in the presence of 5% crystalline seed is presented. From the micrographs, it can be seen that aggregates were formed. The size of the NaX zeolite aggregates varies between 1 and 10 μm, whereas some aggre-gates have sizes in the submicron range (500–1000 nm).
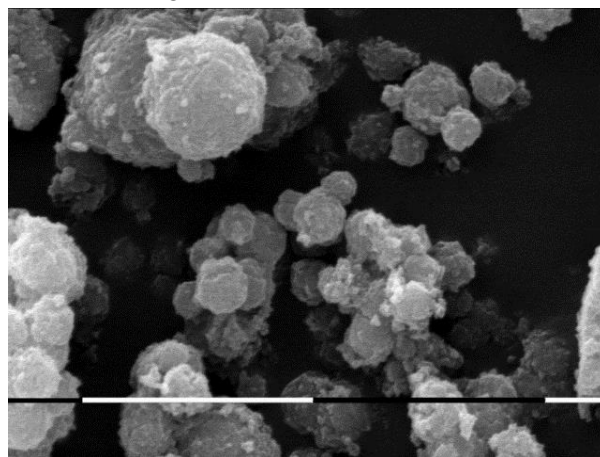
Fig. 3. SEM micrograph of NaX zeolite synthesised from fly ash at room temperature in the presence of 5% of seeds at a NaOH/FA ratio of 1/1 and crystallisation time of 39 days. Bar length 10 μm, magnification 5000.

When the crystallisation time was extended to about 70 days, a product of higher crystallinity was formed. Figure 4 displays an X-ray powder pattern of a product synthesised over a period of 70 days at NaOH/FA ratio of 1/1 in the presence of 2% seeds. It is observed that the product obtained exhibits a higher crystallinity compared with those synthesised for a shorter period.
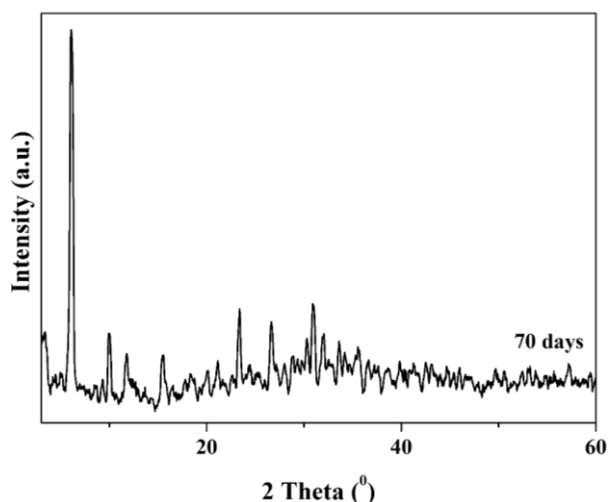
Fig. 4. X-ray powder patterns of NaX zeolite synthesised from fly ash at room temperature in the presence of 2% seeds at a NaOH/FA ratio of 1/1.

On using less sodium hydroxide at NaOH/FA of 0.8/1 without seed, NaX zeolite synthesis failed despite the long crystallisation period of 50 days (Table 1). By adding 1 or 2% crystalline seed to the reaction mixture, the NaX zeolite started to crystallise on the 37th day after synthesis. By use of a larger amount of crystalline seed (5%), significant crystallisation of the zeolite began much earlier, as of the 24th day. Despite the use of a larger amount of seed and crystallisation for nearly 50 days, a completely crystallised NaX zeolite phase was not observed. Figure 5 presents X-ray powder patterns of products synthesised in the presence of 5% seed.
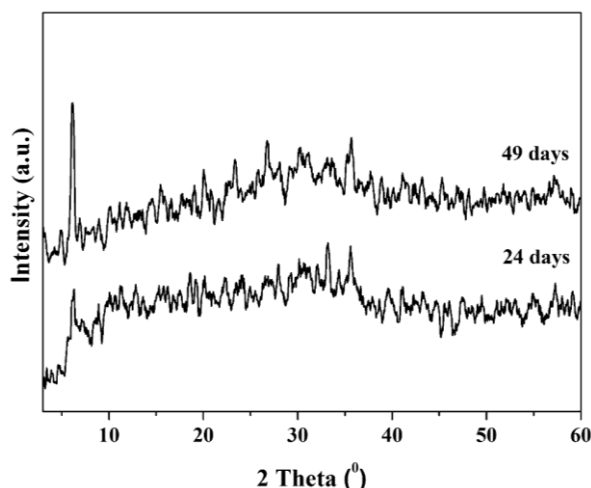
Fig. 5. X-ray powder patterns of NaX zeolite synthesised from fly ash at room temperature in the presence of 5% of seeds at a NaOH/FA ratio of 0.8/1.

At a NaOH/FA ratio of 0.6/1, studies of NaX zeolite synthesis without seed or in the presence of 1% seed were unsuccessful. In these experiments, zeolite crystallisation was not observed despite the long synthesis period of 50 days.

Figure 6 shows X-ray powder patterns of the resulting products synthesised in the presence of 5% crystalline seed. Upon synthesis in the presence of 2% seed, the NaX zeolite started to crystallise only 43 days after synthesis. X-ray powder patterns of the products synthesised in the presence of a higher amount of crystalline seed (5%) indicate that zeolite crystallisation started somewhat earlier, as of the 37th day. From the results obtained, it can be concluded that a larger amount of seed contributes to earlier formation of a zeolite phase.
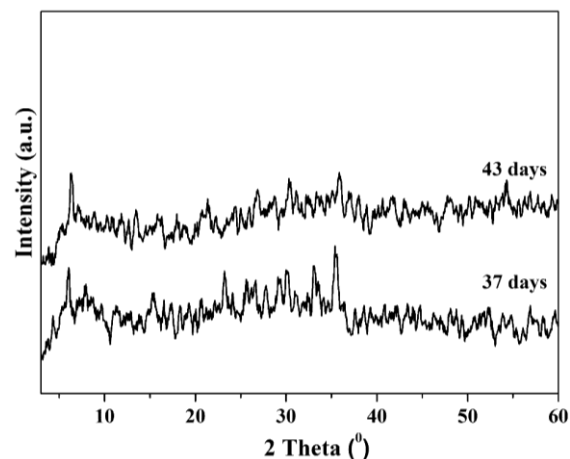
Fig. 6. X-ray powder patterns of NaX zeolite synthesised from fly ash at room temperature in the presence of 5% of seeds at a NaOH/FA ratio of 0.6/1.

It is evident that the lowest NaOH/FA ratio, at which the NaX zeolite is successfully synthesised at room temperature without the presence of seeds, is 1/1. Further reduction of the sodium base at this ratio did not result in a crystalline phase of the zeolite. It was found that by adding crystalline seed to the reaction mixture it is possible to use less NaOH in the zeolite synthesis at room temperature. The results obtained with NaOH/FA ratios of 0.8/1 and 0.6/1 indicate that seeds may result in a crystalline product for longer crystallisation periods of 37–50 days.

CONCLUSIONS

Zeolite X was successfully synthesised from fly ash produced by combustion of lignite coal at Maritsa Iztok 2 TPP using a two-stage process: fusion with sodium hydroxide followed by hydro-thermal treatment at room temperature. Added seed directed synthesis to the desired zeolite structure (mono-phase zeolite X), and reduced both synthesis time and used sodium hydroxide amount upon melting. In this way, the process of zeolitisation is economically cost-effective and better eco-efficient.

Seed-assisted crystallisation at room temperature using NaOH/FA ratios of 1.2/1, 1/1, and 0.8/1

provided successful synthesis of the NaX zeolite. Zeolite crystallisation started later on reducing the amount of sodium hydroxide.

REFERENCES

1. A. M. Cardoso, A. Paprocki, L. S. Ferret, C. M. N. Azevedo, M. Pires, *Fuel*, **139**, 59 (2015).
2. Z. T. Yao, X. S. Ji, P. K. Sarker, J. H. Tang, L. Q. Ge, M. S. Xia, Y. Q. Xi, *Earth Sci. Rev.*, **141**, 105 (2015).
3. A. A. Ramezanianpour, Cement Replacement Materials - Properties, Durability, Sustainability, Springer, 2014.
4. N. Murayama, H. Yamamoto, J. Shibata, *J. Chem. Technol. Biotechnol.*, **77**, 280 (2002).
5. X. Querol, N. Moreno, J. C. Uman, A. Alastuey, E. Herna´ndez, A. Lo´pez-Soler, F. Plana, *Int. J. Coal Geol.*, **50**, 413 (2002).
6. X. Querol, F. Plana, A. Alastuey, A. Lopez-Soler, *Fuel*, **76**, 793 (1997).
7. S. N. Azizi, S. Ghasemi, S. Kavian, *Biosens. Bioelectron.*, **62**, 1 (2014).
8. T.Wajima, K. Kuzawa, H. Ishimoto, O. Tamada, T. Nishiyama, *Am. Mineral.*, **89**, 1694 (2004).
9. C. Belviso, F. Cavalcante, A. Lettino, S. Fiore, *Appl. Clay Sci.*, **80–81**, 162 (2013).
10. N. M. Musyoka, R. Missengue, M. Kusisakana, L. F. Petrik, *Appl. Clay Sci.*, **97–98**, 182, (2014).
11. A. Baccouche, E. Srasra, M. El Maaoui, *Appl. Clay Sci.*, **13**, 255 (1998).
12. G. E. Christidis, H. Papantoni, *Open Mineral. J.*, **2**, 1 (2008).
13. D. Hoellen, D. Klammer, I. Letofsky-Papst, M. Dietzel, *Mater. Sci. Eng. B: Solid-state Mater. Adv. Technol.*, **2**, 523 (2012).
14. S. K. Masoudian, S. Sadighi, A. Abbasi, *Bull. Chem. React. Eng. Catal.*, **8**, 54 (2013).
15. W. M. Meier, *Pure Appl. Chem.*, **58**, 1323 (1986).
16. H. V. Thang, L.Grajciar, P. Nachtigall, O Bludsk´yb, C. O. Areán, E. Fr´ydová, R. Bulánek, *Catal. Today*, **227**, 50 (2014).
17. C.-H. Yu, C.-H. Huang, C.-S. Tan, *Aerosol Air Qual. Res.*, **12**, 745 (2012).
18. C. Y. Pathak, D. Roy, S. Das, *World J. Civil Eng. Construction Technol.*, **1**, 2 (2014).
19. Q. Cui, Y. Zhou, Q. Wei, G. Yu, L. Zhu, *Fuel Process. Technol.*, **106**, 439 (2013).
20. J. Weitkamp, *Solid State Ionics*, **131**, 175 (2000).
21. M. Khalid, G. Joly, A. Renaud, P. Magnoux, *Ind. Eng. Chem. Res.*, **43**, 275 (2004).
22. D. Bastani, N. Esmaeili, M. Asadollahi, *J. Ind. Eng. Chem.*, **19**, 375 (2013).
23. S. V. Vassilev, C. G. Vassileva, *Energy Fuels*, **19**, 1084 (2005).
24. S. V. Vassilev, C. G. Vassileva, *Fuel Process. Technol.*, **47**, 261 (1996).
25. S. V. Vassilev, C. G. Vassileva, *Fuel Process. Technol.*, **48**, 85 (1996.
26. X. Querol, J. C. Uman, F. Plana, A. Alastuey, A. Lopez-Soler, A. Medinaceli, A. Valero, M. J. Domingo, E. Garcia-Rojo, *Fuel*, **80**, 857 (2001).
27. A. Derkowski, W. Franus, E. Beran, A. Czímerová, *Powder Technol.*, **166**, 47 (2006).
28. C.-H. Lee, S.-W. Park, S.-S. Kim, *Korean J. Chem. Eng*, **31**, 179 (2014).
29. K. Ojha, N. C. Pradhan, A. N. Samanta, *Bull. Mater. Sci.* , **27**, 555 (2004).
30. T. Klamrassamee, P. Pavasant, N. Laosiripojana, *Eng. Min. J.*, **14**, 37 (2010).

ЗЕЛЕН СИНТЕЗ НА ЗЕОЛИТ ОТ ВЪГЛИЩНА ПЕПЕЛ В ПРИСЪСТВИЕТО НА ЗАРОДИШИ

Б. Барбов[1], Ю. Кълвачев[2]*

[1] *Институт по минералогия и кристалография, Българска академия на науките, ул. „Акад. Г. Бончев", бл. 107, 1113 София, България*

[2] *Институт по катализ, Българска академия на науките, ул. „Акад. Г. Бончев", бл. 11, 1113 София, България*

(Резюме)

Успешно е синтезиран зеолит X от въглищна пепел, получена чрез изгаряне на лигнитни въглища в ТЕЦ „Марица Изток 2", използвайки двуетапен процес - стапяне с натриев хидроксид, последвано от хидротермален синтез при стайна температура. При намаляване на количеството на NaOH, кристализацията на зеолит NaX започва по-късно. За оптимизиране на процеса на синтез е въведена процедура с използване на зародиши. Кристали от предварително синтезиран зеолит X от чисти химикали се използват като зародиши. Добавянето на зародиши води не само до насочването на синтезата към желаната зеолитна структура (получаване на моно-фазен зеолит X) и до намаляване на времето за синтез, но също и до намаляване на количеството NaOH при стапяне. По този начин процесът на зеолитизация е икономически по-рентабилен и екологично ефективен.

Preparation and application of nanosized zeolite as a carrier for a lipolytic enzyme

M. D. Dimitrov[1], M. Guncheva[1]*, D. G. Kovacheva[2]

[1] Institute of Organic Chemistry with Centre of Phytochemistry, Bulgarian Academy of Sciences, 1113 Sofia, Bulgaria
[2] Institute of General and Inorganic Chemistry, Bulgarian Academy of Sciences, 1113 Sofia, Bulgaria

Porous inorganic materials have been extensively applied as enzyme carriers due to their high mechanic stability and high specific surface area, resistance to microbial attack, stability in organic solvents, and stability upon heating. In recent years, enzymes immobilised on nanosized materials have attracted scientist attention with regard to new emerging applications such as biosensing and medical diagnostics. This research aims to investigate the potential of a nanosized and mostly mesoporous zeolite (nano-Zeo) as a suitable carrier for lipase from porcine pancreas (PPL). For comparative purpose, a nanosized MCM-41 silica material with spherical morphology was studied. The latter was used as a starting material to prepare the nanosized zeolite by densification of the initial amorphous MCM-41 silica nanospheres in presence of a diluted solution of tetrapropylammonium hydroxide, the nanospheres being further transformed into MFI-type of zeolite *via* steam-assisted crystallisation. Both the starting material and the nano-Zeo particles were characterised by means of X-ray diffraction, nitrogen physisorption, and scanning electron microscopy techniques. Loaded protein amount was comparable for the two carriers: 64.0±2.3 and 80.4±3.4 mg/g for MCM-41 and nano-Zeo, respectively. However, nano-Zeo showed over twofold higher specific loading with regard to the mesoporous specific surface area of the studied materials. Besides, monolayer surface distribution and a higher specific lipase activity were estimated for the nano-Zeo-PPL preparation, which is probably due to lipase molecules attached in a proper orientation.

Key words: porcine pancreas lipase (PPL), nanosized zeolite carrier, MCM-41 silica nanospheres, immobilization.

INTRODUCTION

Lipases are industrially applied enzymes in lipid modification, esterification, resolution of racemic mixtures, epoxidation, and other processes [1]. However, they find a limited application due to their high price and low stability under harsh process conditions (presence of detergents, solvents, substrate or product inhibition, high temperatures and low pressures) [2]. On the other hand, adsorption or deposition of the enzymes onto a porous support has proved to be a useful technique for improving their activity and stability [3]. Immobilisation facilitates enzyme recovery from the reaction mixture and allows multiple usages without a significant loss of activity, which makes the process cost-effective. In addition, enzymes immobilised on solid supports have many advantages over their free counterparts, namely, continuous performance and rapid termination of enzymatic reactions, controlled product formation, and easy enzyme removal from the reaction mixture. Compared with polymeric materials inorganic enzyme carriers are structurally more stable, environmentally tolerable, and resistant to organic solvents and microbial attack [4]. Besides, in recent years, enzymes immobilised on nanosized materials have attracted attention with regard to new emerging applications such as biosensing and medical diagnostics [5].

The present study aims to investigate the potential of a nanosized and mostly mesoporous zeolite (nano-Zeo) as a suitable carrier for lipase from porcine pancreas. For comparative purpose a nanosized MCM-41 silica material with spherical morphology was studied, which was used as a starting material to prepare the nanosized zeolite. This is a new idea that utilises a simple procedure to prepare zeolites with nano dimensions by transforming already pre-prepared and geometrically well-defined amorphous silica particles into crystalline entities of similar shape, diminished size, and increased density [6]. Both initial MCM-41 and nano-Zeo materials were characterised by X-ray diffraction, nitrogen physisorption, and scanning electron microscopy techniques. The activity of the immobilised preparations was estimated using 4-nirophenyl palmitate as a substrate.

EXPERIMENTAL

Materials

Nano-Zeo material was synthesised by a two-step procedure. In the first step, MCM-41 silica with

---

* To whom all correspondence should be sent
E-mail: *maiag@orgchm.bas.bg*

spherical morphology was synthesised using TEOS as a silica source and hexadecyltrimethylammonium bromide as a structure-directing reagent [7]. Then, in the second step, the obtained MCM-41 spheres were treated with a dilute solution of tetrapropyl-ammonium hydroxide and densified for 24 h at 383 K *via* a steam-assisted crystallisation under hydro-thermal conditions [6]. Lipase from porcine pancreas (15–30 U/mg, 20% protein content) from Sigma was used to assess protein absorption capacity of the novel zeolitic material and the initial MCM-41 silica nanospheres.

Methods of characterization

Both the starting MCM-41 silica and the nano-Zeo material were characterised by X-ray diffraction, nitrogen physisorption, and scanning electron microscopy techniques. Powder X-ray diffraction patterns were collected on a Bruker D8 Advance diffractometer equipped with Cu Kα radiation and LynxEye detector. Nitrogen sorption measurements were recorded on Quantachrome NOVA 1200e and Quantachrome Autosorb iQ MP instruments at 77 K. Before physisorption measurements, the samples were outgassed overnight at 423 K under vacuum. Pore size distributions and pore diameters were calculated by non-local density functional theory (NLDFT). Scanning electron microscopy (SEM) images were obtained with FEI Quanta FEG 250 and JEOL-JSM-6390 scanning electron microscopes. Lipase from porcine pancreas was immobilised via physical adsorption. In a typical procedure, 20 mg of the carriers were gently shaken with 1 mL of PPL (1–20 mg/ml) dissolved in sodium phosphate buffer (pH 7.0) After 12 h in-

cubation, the immobilised preparations were filtered, washed twice with 0.5 ml of sodium phosphate buffer, freeze dried, and their activity was tested in assay reaction. Protein content in the initial PPL solutions and in the supernatant after immobilisation was estimated using Lowry's method [8]. For both materials, the absorption capacity (1) and the immobilisation yield (2) were determined following the equations:

$$\text{Absorption capacity} = \frac{(C_o - C_f)}{m} V, \text{ mg/g}_{\text{carrier}} \quad (1)$$

$$\text{Immobilisation yield} = \frac{(C_0 - C_f)}{C_0} 100, \% \quad (2)$$

where C_o and C_f are the initial and final concentration of the protein in the solutions in mg/ml, respectively, V is the volume of the loading enzyme solution in mL, and m is carrier weight.

The activity of the immobilised preparations was estimated using 4-nirophenyl palmitate as a substrate. One unit is the amount of protein, which catalyses the conversion of 1 μM substrate for 1 minute at 25 °C.

RESULTS AND DISCUSSION

X-ray diffraction (XRD) technique was applied to determine sample mesoporous ordering, crystallinity, and phase composition (Fig. 1). Small angle X-ray diffraction patterns of the calcined materials are presented in Fig. 1a. A MCM-41 sample shows one main reflection (100) at 2.64 2θ and two small reflections with maxima at 4.64 and 5.28 2θ, respectively, arising from quasi-regular long-range hexagonal arrangement of the obtained mesopores that are characteristic of the MCM-41 structure.
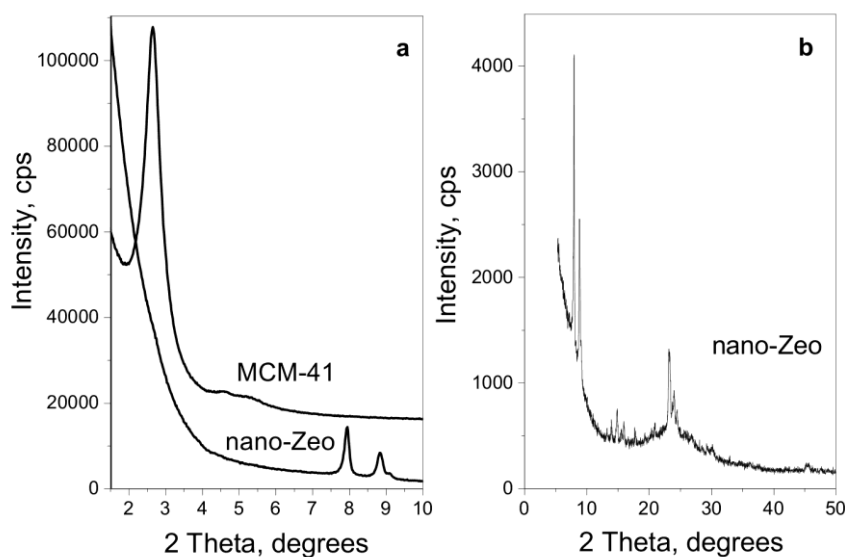
Fig. 1. XRD patterns of the studied samples.

At the same time, the pattern of the nano-Zeo sample displays no reflections of the initial MCM-41 material to indicate transformation of the latter. However, two new reflections are observed at about 7.9 and 8.8 2θ (Fig. 1a). Further information about the newly found structure was obtained from wide-angle XRD pattern of the nano-Zeo sample (Fig. 1b). The observed reflections are characteristic of a MFI zeolite structure [6]. Hence, a complete transformation of the initial amorphous MCM-41 silica material into a crystalline MFI-type zeolite was realised. To follow changes of the textural characteristics of both studied samples two additional techniques were used: nitrogen physic-sorption and scanning electron microscopy (Figs. 2 and 3). Besides, some physicochemical characteristics of the obtained samples are presented in Table 1.

Data on nitrogen physisorption measurements of the studied samples are displayed in Fig. 2 and Table 1. The initial MCM-41 sample manifests a typical isotherm that is characteristic of this type of mesoporous silica materials with a narrow adsorption/desorption step within 0.2-0.3 relative pressure (Fig. 2a). It is characterised by a high specific surface area (985 m^2/g), total pore volume of 0.47 cm^3/g, and narrow pore size distribution with main pore diameter of 2.9 nm (Fig. 2 and Table 1).

SEM analysis showed that this material is composed of well-defined spherical nanoparticles of relatively equal size, most of which are in the range of 400-600 nm (Fig. 3). However, after steam-assisted crystallisation certain changes occurred with the MCM-41 starting material. The isotherm of

the nano-Zeo sample is also of type IV that is characteristic of mesoporous materials (Figure 2a). Yet, a much broader adsorption/desorption step within 0.5-0.9 relative pressure was registered for this sample accompanied by a hysteresis loop most probably owing to interparticle mesoporosity (Fig. 2a). Besides, the nano-Zeo material loses part of the very high specific surface area of the initial MCM-41 sample at the expense of the appearance of certain microporosity (270 m^2/g), however, the mesopore volume increases to 0.68 cm^3/g due to the presence of very broad pore size distribution and much larger mesopores (Fig. 2b, Table 1). At the same time, the SEM image proves preservation of the spherical morphology accompanied by some size reduction phenomena as expected during transformation from amorphous to crystalline phase (Fig. 3). However, larger spherical particles are also found with the nano-Zeo sample that we ascribe to agglomeration of some initial MCM-41 spherical particles during transformation (Fig. 3).

1,3-specific lipase from porcine pancreas was selected to evaluate the absorption capacity of the two silica supports. Industrial application of this enzyme is limited due to its lability in organic solvents and upon heating above 45°C; therefore, methods for PPL stabilisation are of current research interest. The enzyme structure is compact with dimensions *ca*. 4.6×2.6×1.1 nm^3, and earlier studies by other authors have shown that pore size is one of the major factors that should be considered upon selection or design of the excellent enzyme supports [9].

Table 1. Textural characteristics of the obtained materials

Sample	S_{BET},[a] m^2/g	V_{total},[c] cc/g	S_{micro},[b] m^2/g	V_{micro},[d] cc/g	dDFT,[e] nm	D_{SEM},[f] nm
nano-Zeo	728	0.80	270	0.12	2.3; 4.5; 10.5	200–800
MCM-41	985	0.47	-	-	2.9	400–600

a - BET specific surface area; b - Micropore surface area by t-method; c - Total pore volume; d - Micropore volume by t-method; e - Main pore diameter evaluated using NLDFT method, f - Particle sizes evaluated by SEM analysis.
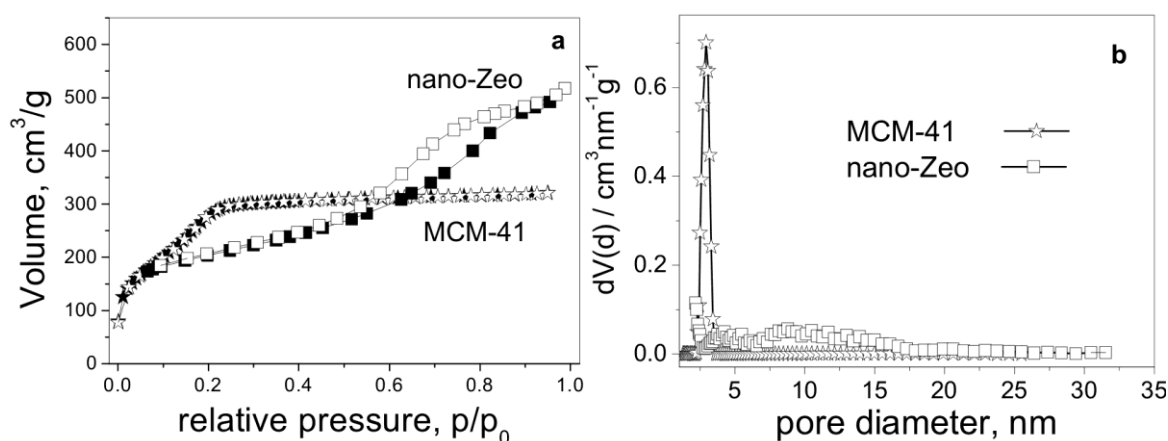
Fig. 2. Nitrogen adsorption/desorption isotherms (a) and pore size distribution (b) of the studied samples.
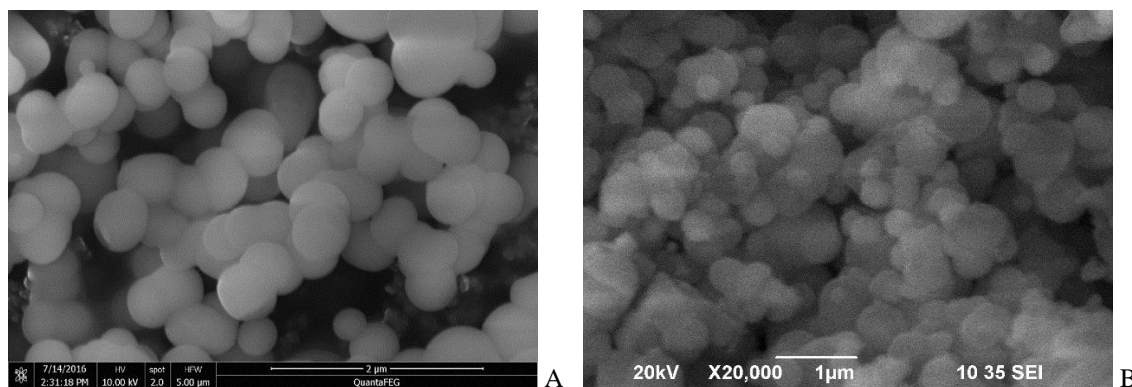
Fig. 3. SEM images of MCM-41 (left) and nano-Zeo (right) samples.

Table 2. Amount of the immobilised porcine pancreas lipase on the two supports and biocatalyst activity

Sample	Absorption capacity, mg prot./g carrier	Specific capacity[a], mg prot./m^2 carrier	Specific activity, U/mg prot.	Immobilization yield, %
MCM-41	64.0 ± 2.3	0.065	170	32
nano-Zeo	80.4 ± 3.4	0.176	238	40

[a] To estimate the specific capacity the absorption capacity of the carrier was divided by its specific surface area (m^2/g$_{carrier}$).

The absorption capacity of the two carriers is given in Table 2. Novel nano-Zeo proves to be a 1.25-times more efficient support than the MCM-41 precursor, most probably due to higher porosity and larger pore sizes. The two carriers were less efficient as compared to literature data on PPL adsorption on SBA-15 for which enzyme loading was between 100 and 920 mg enzyme per gram carrier regarding carrier textural characteristics and reaction conditions [10,11]. However, a monolayer deposition of the PPL on nano-Zeo and MCM-41 was observed, which resulted in a preserved (or even enhanced) lipolytic activity of the nano-Zeo-PPL and MCM-41-PPL in comparison with the free enzyme.

MCM-41-PPL and nano-Zeo-PPL were examined in the reaction of 4-nitrophenyl palmitate hydrolysis. Tested in several consecutive cycles, a fast drop of activity was observed even after the first cycle with the two immobilised preparations, which is due to enzyme leakage or desorption in the aqueous medium (Fig. 4). Functionalisation of the supports and subsequent covalent bonding of the PPL or application of these biocatalysts in esterification reactions in non-solvent or organic media could be a possible solution to enhance enzyme performance.

CONCLUSIONS

Nanosized zeolite material with MFI structure and spherical morphology was successfully synthesised from MCM-41 mesoporous spheres *via* a steam-assisted crystallisation under hydrothermal conditions at 383 K. The novel zeolite material exhibited high specific surface area and high total pore volume due mainly to very high mesoporosity

characterized by broad mesopore size distribution and high amount of mesopores. Over twofold higher adsorption capacity for lipolytic enzyme from porcine pancreas was found with the novel nano-sized zeolite in comparison with the initial MCM-41 material regarding the specific mesoporous surface area of both carriers. A higher adsorption capacity and monolayer surface distribution and a higher specific lipase activity was also estimated for the nano-Zeo-PPL preparation, which is probably due to lipase molecules attached in suitable orientation.
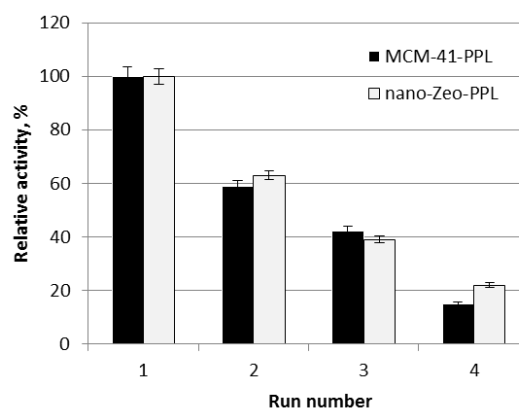
Fig. 4. Relative activity of MCM-41-PPL and nano-Zeo-PPL in the assay reaction of hydrolysis of 4-nitrophenylpalmitate.

REFERENCES

1. F. Hasan, A. A. Shah, A. Hameed, *Enz. Microb. Tech.,* **39**, 235 (2006).
2. A. Houde, A. Kademi, D. Leblanc, *Appl. Biochem. Biotech.,* **118**, 155 (2004).
3. T. Jesionowski, J. Zdarta, B. Krajewska, *Adsorption,* **20**, 801 (2014).

4. S. Y. Lee, J. Lee, J. H. Chang, J. H. Lee, *BMB Rep.,* **44**, 77 (2011).

5. M. Leitgeb, Ž. Knez, K. Vasić, Micro- and Nano-carriers for Immobilization of Enzymes, in: Nanotechnology and Nanomaterials "Micro and Nanotechnologies for Biotechnology", S. G. Stanciu (ed.), CC BY 3.0 license, 2016, Ch. 2.

6. A. G. F. Machoke, B. Apeleo Zubiri, R. Leonhardt, V. R. R. Marthala, M. Schmiele, T. Unruh, M. Hartmann, E. Spiecker, W. Schwieger, *Chem. Eur. J.*, **23**, 10983 (2017).

7. M. Guncheva, M. Dimitrov, P. Ossowicz, E. Janus, *J. Porous Mater.* (2017), https://doi.org/10.1007/s10934-017-0505-z

8. O. H. Lowry, N. J. Rosebrough, A. L. Farr, R. J. Randall, *J. Biol. Chem.*, **193**, 275 (1951).

9. H. Ma, J. He, D. G. Evans, X. Duan, *J. Mol. Cat. B: Enzym.*, **30**, 209 (2004).

10. Y. Li, G. Zhou, W. Qiao, Y. Wang, *Mat. Sci. Eng. B*, **162,** 120 (2009).

11. G. D. Yadav, S. R. Jadhav, *Micro. Meso. Mat.,* **86**, 215 (2005).

ПОЛУЧАВАНЕ И ПРИЛОЖЕНИЕ НА НАНОРАЗМЕРЕН ЗЕОЛИТ КАТО НОСИТЕЛ ЗА ЛИПАЗА

М. Д. Димитров[1], М. Гунчева[1]*, Д. Г. Ковачева[2]

[1] Институт по органична химия с Център по фитохимия, БАН, 1113 София, България
[2] Институт по обща и неорганична химия, БАН, 1113 София, България

(Резюме)

Порестите неорганични материали се прилагат широко като носители на ензими, поради тяхната висока механична стабилност и висока специфична повърхност, устойчивост на микробиална атака, стабилност в органичните разтворители и стабилност при нагряване. През последните години ензимите, имобилизирани върху наноразмерни материали, са атрактивни обекти за изследване поради разширяването на областта им на приложение, например като биосензори или в медицинската диагностика.

Настоящото изследване е фокусирано върху проучване на потенциала на наноразмерен и преобладаващо мезопорест зеолит (nano-Zeo) като подходящ носител за липаза от свински панкреас (PPL). За сравнение проведохме експерименти и с наноразмерен MCM-41 силикат със сферична морфология на частиците, който е изходен материал за получаване на наноразмерния зеолит посредством процес на "уплътняване" на изходните аморфни MCM-41 наночастици в присъствието на разреден разтвор на тетрапропиламониев хидроксид и последващото им превръщане в зеолит тип MFI чрез кристализация в присъствие на водна пара. Материалите са охарактеризирани с помощта на рентгенова дифракция, физична адсорбция на азот и сканираща електронна микроскопия. Количеството на натоварения протеин е съизмеримо за двата носителя и е съответно 64,0 ± 2,3 mg/g за MCM-41 и 80,4 ± 3,4 mg/g за nano-Zeo. Струва да се отбележи, че нанозеолитът показва повече от два пъти по-голямо специфично натоварване по отношение на мезопорестата повърхност на изследваните материали. Освен това, за nano-Zeo-PPL бяха отчетени монослойно повърхностно разпределение и по-висока специфична хидролитична активност, което вероятно се дължи на закрепването на липазните молекули в по-подходяща ориентация за този носител.

Improved catalyst performance of Ni/SiO$_2$ in vegetable oil hydrogenation: impact of Mg dopant

M. V. Gabrovska[1]*, D. A. Nikolova[1], J. B. Krstić[2], D. R. Loncarević[2], P. T. Tzvetkov[3], M. G. Shopska[1], V. D. Radonjić[2], M. V. Stanković[2], D. M. Jovanović[2], L. T. Spasov[1], D. B. Simeonov[3]

[1] *Institute of Catalysis, Bulgarian Academy of Sciences, Acad. G. Bonchev St., Bldg. 11, 1113 Sofia, Bulgaria*

[2] *University of Belgrade, Institute of Chemistry, Technology and Metallurgy, Department of Catalysis and Chemical Engineering, Belgrade 11000, Republic of Serbia*

[3] *Institute of General and Inorganic Chemistry, Bulgarian Academy of Sciences, Acad. G. Bonchev St., Bldg. 11, 1113 Sofia, Bulgaria*

Mg-doped co-precipitated Ni/SIG precursors were studied as edible sunflower oil hydrogenation catalysts applying two types of commercial silica gels (SIG) as supports of different texture characteristics: a microporous type (SIG-A) and a mesoporous type (SIG-C). It was found that texture parameters of both the silica gels and magnesium addition allow obtaining of catalysts of various hydrogenation activities and fatty acid composition of the products. The results reveal the highest hydrogenation activity of MgNi/SIG-C catalyst because of higher amount and accessibility of metal nickel particles on the catalyst surface generated through reduction procedure. A dominant activity of MgNi/SIG-C catalyst is ascribed to appropriate mesoporosity, which controls diffusion. It was established that Mg-doped Ni/SIG-C possessed a capacity for use as an efficient edible vegetable oil hydrogenation catalyst due to high hydrogenation activity, high saturation level of linoleic acid (C18:2*cis*), moderate amounts of C18:1*trans* fatty acids, and C18:0 stearin acid formation in the partially hydrogenated sunflower oil.

Key words: Ni catalyst; silica gel; Mg additive; hydrogenation; sunflower oil; *trans*-isomers.

INTRODUCTION

Metal nickel (21–25 wt.% Ni) supported on silica represents one proven and thereat widely produced and practiced catalyst in the partial hydrogenation of vegetable oils. The process continues to be applied as universal method in modern food industry to enhance oxidation and thermal stability of the hydrogenated products by decreasing unsaturation of the naturally occurring triacylglycerides and changing solidification characteristics and plasticity of the hydrogenated oils [1]. Nickel has been selected due to its high activity, inert nature relative to oil, availability, and economic price, which makes it superior over other metals [2].

During hydrogenation of fatty acids (FAs), several simultaneous processes can be distinguished, such as saturation, migration, and geometric isomerisation of double bonds. Some unsaturated FAs that are normally in *cis*-configuration may be isomerised into *trans*-FAs [3]. In the light of recent recommendations issued by international food associations, the formation of *trans*-FAs during hydrogenation using conventional nickel catalysts is considered undesirable. Conventional partial hydro-genation results in the formation of up to 40% of *trans*-FAs in the hardened products. None of the commercially available catalysts enable the production of partially hydrogenated sunflower oil having insignificant *trans*-FAs content [4].

While numerous studies have been focused on improving catalyst preparation, there are only scarce attempts to elucidate the role of additives or modifiers on the structural and textural properties of nickel catalyst precursors, particularly those, which might form compounds similar to those of the parent metal [4,5]. Moreover, the effect of dopants on the catalytic performance in vegetable oil hydrogenation is rarely discussed in the literature [6].

To promote *cis*-FA selectivity it is necessary to dope Ni-containing catalysts with a suitable pro-motor or modifier [7].

Alkaline, alkaline earth, and rare earth metals are generally employed as promoters. The impact of promoters is mostly related to the following aspects: altering catalyst surface acid-base property, im-proving dispersion of active species, and consi-dering the type and extent of active species-support interactions. An alkaline earth metal could affect the reducibility, the morphology, and the electronic properties of catalysts [8]. In this connection, doping Ni-based catalysts by Mg alkaline earth

metal may alter the structure, texture, basicity, and reducibility of the Ni^{2+} ions, the overall impact on catalyst hydrogenation activity, and its *cis/trans*-selectivity.

Based on these considerations, a partial isomorphous replacement of Ni^{2+} with Mg^{2+} ions in Ni-phyllosilicate structure was accomplished aimed at improving the performance of Ni/SiO₂ catalyst in sunflower oil hydrogenation by increasing hydrogenation activity and oleic acid selectivity, tuning the level of *cis-trans* isomerisation, and minimising stearic acid content in the products of hydrogenation.

EXPERIMENTAL

Sample preparation

Two types of commercial silica gels (SIG) of different texture characteristics, microporous SIG-A and mesoporous SIG-C [9] of 0.8–1.0-mm size, were applied as supports for sample synthesis.

The precursors were obtained with identical composition (SiO₂/Ni = 1.0 and Mg/Ni = 0.1) by co-precipitation of aqueous solutions of nickel nitrate hexahydrate, $Ni(NO_3)_2 \cdot 6H_2O$, and magnesium nitrate hexahydrate, $Mg(NO_3)_2 \cdot 6H_2O$, with anhydrous sodium carbonate, Na_2CO_3, over silica gels suspended in distilled water. The initial salts of analytical grade, provided by Alfa Aesar (USA), were used as received without further purification.

By analogy with non-modified Ni/SIG samples, the same preparation procedure was used which is described in detail elsewhere [10]. It should be noted that because of magnesium presence synthesis procedure was performed at pH = 10.0.

After drying at 120 °C for 20 h the precursors were designated as (Mg)Ni/SIG-X, where X is A or C and represents the type of used silica gel.

This paper reports refined preliminary partially published results [11–13] and new data on FA composition and *cis/trans*-selectivity of non-doped and Mg-doped Ni/SIG catalysts. The properties of the Mg-doped precursors and catalysts were compared with the non-doped counterparts. The effects of magnesium modification on the structure, texture, reducibility, and catalytic performance of the materials will contribute to select a promising candidate for an active edible vegetable oil hydrogenation catalyst.

Sample characterization

Powder X-ray diffraction (PXRD) patterns were recorded on a Bruker D8 Advance powder diffractometer employing CuKα radiation. The crystalline phases were identified using International Centre for Diffraction Data (ICDD) powder diffraction files.

FTIR spectra within the range of 4000–400 cm⁻¹ were recorded on a Nicolet 6700 FTIR spectrometer (Thermo Electron Corporation, USA) at 0.4 cm⁻¹ resolution and 50 scans, using KBr pressed disk technique with sample concentration of ~0.5 wt.%.

Texture characteristics were determined by nitrogen adsorption–desorption measurements conducted at a low temperature (77.4 K) with a Sorptomatic 1990 (Thermo Finnigan) apparatus. Specific surface area (S_{BET}) values were calculated according to the BET method from the linear part of the N₂ adsorption isotherms. Mesopore volume (V_{meso}) data were acquired from isotherms adsorption branch by means of the Dollimore-Heal method. Micropore volume (V_{micro}) values were calculated using the Dubinin-Radushkevich method.

Temperature-programmed reduction (TPR) experiments were accomplished using a Thermo Scientific TPRDO1100 system by a 5% H₂/Ar gas mixture at a flow rate of 20 cm³/min and a heating rate of 10 °C/min in the temperature range 50–900 °C. Two TPR approaches were used: (i) normal TPR and (ii) reTPR – TPR after reduction of the samples at 430 °C for 2 h.

'Dry reduction' of preliminary dried precursors (110 °C/16 h) was performed in a laboratory set-up with a gas mixture of H₂/N₂ (1/1 v/v), flow rate of 10 L/h, and a heating rate of 1.5 °C/min from 110 to 430 °C and held constant for 5 h to avoid sintering of the reduced metal nickel. After cooling down to room temperature in H₂/N₂ stream, the gas line was switched to argon. Then, the reduced precursors were impregnated with argon-purged paraffin oil to prevent oxidation of metal nickel.. Finally, after vacuum filtration of paraffin oil excess, the resulting catalysts (reduced precursor coated with some amount of paraffin oil) were collected.

Partial hydrogenation of commercially available refined edible sunflower oil was performed in a 1000-cm³ jacketed glass reactor Series 5100 (Parr, USA) with a computer coupled with Mass Flow Controller F-201C and Pressure Meter F-502C (Bronkhorst, Netherlands). In all experiments, the conditions were the same: oil mass - 900 g; catalyst concentration - 0.06 wt.% of Ni with respect to oil amount; stirring rate of 1200 rpm; hydrogenation temperature – 160 °C, and H₂ pressure of 0.2 MPa. FA composition of a starting sunflower oil (mol%) was: C16:0 = 7.2; C18:0 = 4.0; C18:1-*cis* = 26.0; C18:1-*trans* = 0.02; C18:2-*cis* = 62.2; C18:2-*trans* = 0.06; C18:3-*cis* = 0.10; C20:0 = 0.22; C22:0 = 0.20. The hydrogenation activity of the catalysts was evaluated by measuring the changes in the Refraction Index (RI) at 50 °C [13] (RX-5000α,

Atago) of the starting oil and periodically collected samples of partially hydrogenated oil in conformity with ISO 6320:2017 [14]. The quantity of the consumed hydrogen during the hydrogenation process was determined by post processing through integrating the differential data from the mass flow controller.

FA composition of the starting and partially hydrogenated sunflower oils was quantitatively determined using a Thermo Scientific Trace GC Ultra gas chromatograph equipped with a FID and a TriPlus auto sampler. The triglycerides were first converted into their fatty acid methyl esters (FAME) following the standardised procedure according to AOCS Official Method Ce 2-66 (1997) [15]. Split injection (split ratio of 1:80) of prepared 1 µl FAME was performed with helium as a carrier gas at a flow rate of 0.8 ml/min. The column temperature (fused silica capillary column HP-88, 100 m x 0.25 mm i.d. with a 0.20-µm film thickness, J&W Scientific – Agilent) was maintained at 170 °C for 75 min of analysis time. The injection part and detector temperatures were 240 and 250 °C, respectively.

RESULTS AND DISCUSSION

PXRD patterns of the as-prepared non-Mg doped samples (Fig. 1a) reveal the presence of a single phase that can be attributed to nickel silicate hydroxide (Pecoraite, $Ni_3Si_2O_5(OH)_4$, ICDD-PDF file 00-049-1859), a nickel analogue of Chrysotile. Chrysotile ($Mg_3Si_2O_5(OH)_4$), a monoclinic Mg-silicate represents a group of polymorphous minerals of the same chemical composition but different crystal system, namely Lizardite $Mg_3Si_2O_5(OH)_4$ (hexagonal), Antigorite, $Mg_3Si_2O_5(OH)_4$ (monoclinic), Pecoraite, $Ni_3Si_2O_5(OH)_4$ (monoclinic), etc.

The concept of Ni substitution for Mg is an important phenomenon in the structure of nickel-bearing minerals. Having isomorphous substitution because of identical charge and close ionic radii of Ni^{2+} (r = 0.069 nm) and Mg^{2+} (r = 0.072 nm) ions [16] it may be expected that Ni^{2+} ions can readily replace six-coordinated Mg^{2+} entities in hydrous Ni-Mg silicates, such as Nepouite, $(Ni,Mg)_3Si_2O_5(OH)_4$ (orthorombic). Nepouite and Pecoraite possess a layered structure that consists of a tetrahedral sheet joined to an octahedral one. In octahedral sites, a complete solid solution is possible between divalent cations of Mg and Ni with a general formula $(Mg,Ni)_{3-x}Si_2O_5(OH)_4$ [17]. Therefore, the patterns of Mg-doped samples (Fig. 1a) show a simultaneous occurrence of the Pecoraite and Nepouite phases (ICDD-PDF file 00-025-0524). Because of turbostratic structure of the registered phases [18], the

diffraction lines of all XRD patterns were not clearly organised, however, they were better defined with the Mg-doped samples, particularly in MgNi/SIG-A.
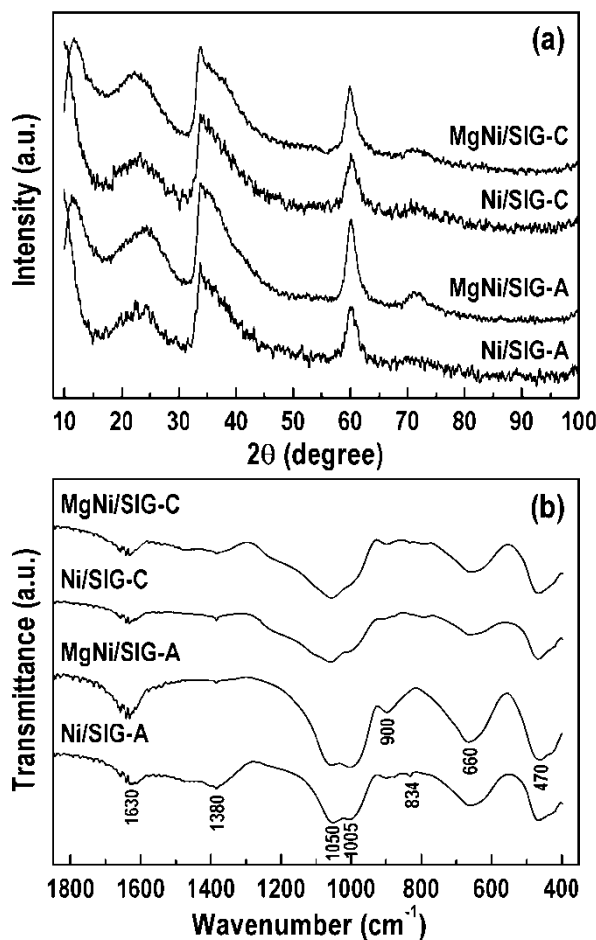
Fig. 1. PXRD patterns (a) and FTIR spectra (b) of the as-prepared precursors.

FTIR spectra of the studied precursors are displayed in the frequency range of 1800–400 cm⁻¹ since variations in the absorption profiles characterising the Ni-O-Si interactions are observed in this region (Fig. 1b). Typical bands of the silica network are absent [10]. A doublet at 1050 and 1005 cm⁻¹, and a band at ~660 cm⁻¹ are related to generated Ni-phyllosilicate structure (−Si−O−Ni−), which covers the surface of the support particles [17,19], formed most significantly in MgNi/SIG-A. A low intensity band at ~900 cm⁻¹ can be ascribed to the stretching vibrations of free Si-OH groups on the solid surfaces. Bands assigned to CO_3^{2-} anions (~1380 cm⁻¹) and to bending vibrations of H_2O molecules at ~1630 cm⁻¹ were also detected [19,20].

Close inspection of the bands gives evidence for creation of different Ni^{2+} species on sample surfaces. A well expressed band at ~1380 cm⁻¹ and a weak one at ~834 cm⁻¹ in the spectrum of Ni/SIG-A are attributed to the presence of a basic nickel

carbonate phase located on the surface of the Ni-phyllosilicate [10,21]. However, these bands were not registered with MgNi/SIG-A thus signifying the formation of a strongly bonded Ni,Mg-phyllosilicate phase.

The effect of Mg modification on the textural properties of the Ni/SIG precursors was investigated by N_2 adsorption–desorption analysis. It has been shown that the SIG-A support is a microporous material with Ib isotherm while the SIG-C support is typically mesoporous with larger mesopores of IV type with H2 hysteresis loop from interconnected network of pores being different in size and shape [9]. Incorporation of Ni leads to a dramatic texture transformation, therefore, the isotherm of Ni/SIG-A (Fig. 2a) is characterised by complicated hysteresis. Registered hysteresis discloses the formation of mesoporous Ni-phyllosilicate phase on the SIG-A microporous surface. Such isotherms are classified as type IIb with type H3 hysteresis generated from aggregates of plate-like particles, which possess non-rigid slit-shaped pores [22]. Mg dopant provokes widening of H3 hysteresis for MgNi/SIG-A as a bimodal porosity is preserved. This view of isotherm confirms generation of a new mesopore system from the Ni,Mg-phyllosilicate phase. The isotherm type of the SIG-C support [9] was preserved in Ni/SIG-C (Fig. 2b) with observation of a step-wise hysteresis character, namely a combination of H2 and H3 at higher and average pressures, respectively. Isotherm type was preserved after incorporation of Mg in the Ni-phyllosilicate structure (MgNi/SIG-C); however, the isotherm position indicates a better filling of SIG-C pores compared to the Mg non-doped Ni/SIG-C sample.

All these observations were confirmed from the texture characteristics of the precursors collected in Table 1, namely S_{BET} for MgNi/SIG-A increased relative to non-doped Ni/SIG-A due to formation of additional micro- and mesoporous system, which is presented by an increase in V_{micro} and V_{meso}.

Table 1. Textural characteristics of the as-prepared precursors

Sample	S_{BET} (m²/g)	V_{micro} (cm³/g)	V_{meso} (cm³/g)	d_{aver} (nm)
Ni/SIG-A	269	0.10	0.32	8.8
MgNi/SIG-A	341	0.13	0.35	9.2
Ni/SIG-C	367	0.13	0.46	10.2
MgNi/SIG-C	197	0.07	0.35	15.1

It can be seen that the S_{BET} surface area of MgNi/SIG-C was diminished approximately twice compared to Ni/SIG-C because of a two-fold decrease in V_{micro} as well as a decrease in V_{meso}.
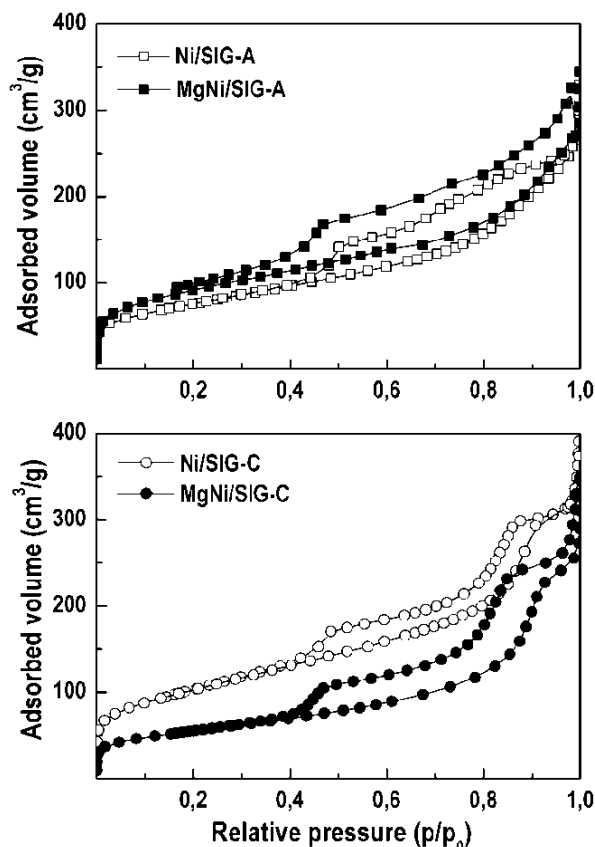
Fig. 2. Adsorption–desorption isotherms of the as-prepared precursors

It is interesting to note that the presence of magnesium provokes enlargement of the average pore diameter (d_{aver}) value to 15.1 nm for MgNi/SIG-C unlike 9.2 nm for MgNi/SIG-A. The explanation of d_{aver} growth in MgNi/SIG-C is illustrated on the differential curves by existence of mesopores having sizes between 15 and 30 nm with two maxima at 18 and 22 nm (Fig. 3). This finding may enable better accessibility of bulky triglyceride molecules to the catalyst surface.
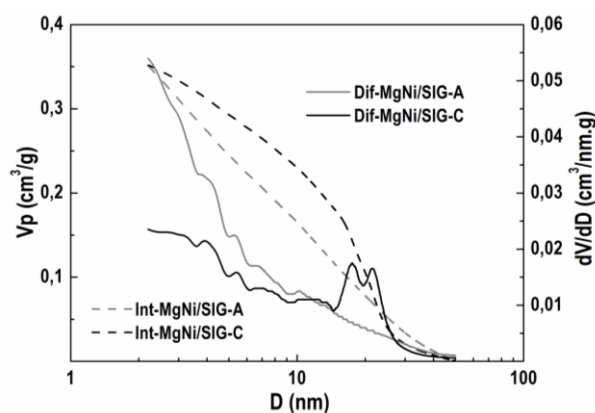
Fig. 3. Integral mesopore curves (Int) and pore size distribution differential curves (Dif) of the Mg-doped precursors.

Pore size distribution (PSD) differential curves (Fig. 3) show a different distribution of pores generated from the created Mg,Ni-phyllosilicate phase. More pores in the range 4–10 nm were recorded for MgNi/SIG-A unlike MgNi/SIG-C, which is in accordance with a higher S_{BET} of MgNi/SIG-A.

Catalyst activity in the sunflower oil hydrogenation was evaluated by measuring the Refraction Index (RI) at 50 °C. Experimental curves expressing the change of crude oil RI (1.46365) as a function of hydrogenation time are displayed in Figure 4. Collected information discloses that the catalysts hydrogenate the oil to different RI levels, consume diverse amount of hydrogen, and need different reaction time. Diminution of the crude oil RI value at the end of the hydrogenation reaction follows the order: MgNi/SIG-C (1.45495) > MgNi/SIG-A (1.45582) > Ni/SIG-A (1.45674) > Ni/SIG-C (1.45783), which corresponds to the quantity of consumed hydrogen (cm^3), namely: MgNi/SIG-C (61395) > MgNi/SIG-A (54868) > Ni/SIG-A (48013) > Ni/SIG-C (40632).
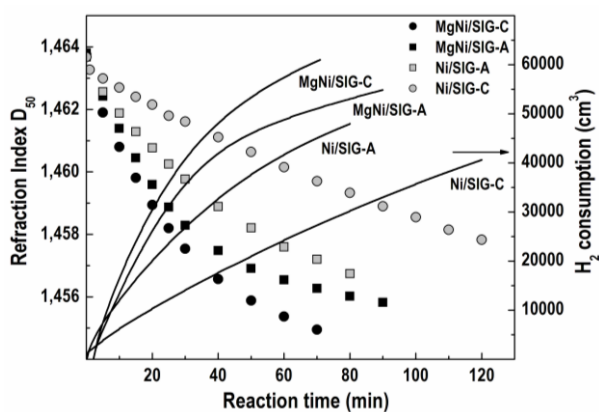
Fig. 4. Changes of RI value and amount of consumed hydrogen *vs.* reaction time.

Hydrogen consumption of the Ni/SIG-A, MgNi/SIG-A, and MgNi/SIG-C catalysts after 70 minutes of hydrogenation reveals higher values by 1.65, 1.87, and 2.23 times, respectively, with reference to the most inactive Ni/SIG-C catalyst. The data point out a higher activity of the Mg-doped catalysts and show the dominant behaviour of MgNi/SIG-C.

As reported in own papers [9,10,23], differences in hydrogenation activity of non-Mg doped catalysts are ascribed to texture parameters of the carriers which induce creation of two types of Ni^{2+} species in the precursors: Ni-phyllosilicate situated in the pores of the supports and basic carbonate-like nickel located on the Ni-phyllosilicate surface [9]. Such an effect leads to a diverse coordination level of the Ni^{2+} ions by the surface oxygen atoms resulting in different Ni-O and Ni-O-Si bond strength, and

hence, different reducibility [10]. Thus, a lower activity of the Ni/SIG-C catalyst was attributed to hardly reducible or non-reducible Ni^{2+} species from the Ni-phyllosilicate phase and to the catalyst pore system, which does not favour accessibility of the reactant molecules to the active Ni^0 sites. A higher activity of the Ni/SIG-A catalyst was attributed to facilitated reduction of the Ni^{2+} species at 430 °C and to creation of adequate number of accessible Ni^0 active sites on the catalyst surface. Obviously, the SIG-A support (microporous-type) contributes to the formation of readily reducible Ni^{2+} species from the basic nickel carbonate-type phases, which after reduction at 430 °C generate a sufficient number of accessible Ni^0 active sites on the catalyst surface.

A possible understanding of the demonstrated activity of the Mg-containing catalysts could be found in TPR experiments accomplished by two consecutive procedures: normal TPR and TPR after reduction of the samples at 430 °C for 2 h denoted as ReTPR. The former procedure with MgNi/SIG-A precursor resulted in a symmetric profile with a temperature maximum T_{max} at 445 °C as well as a high-temperature shoulder at ~600 °C (Fig. 5).
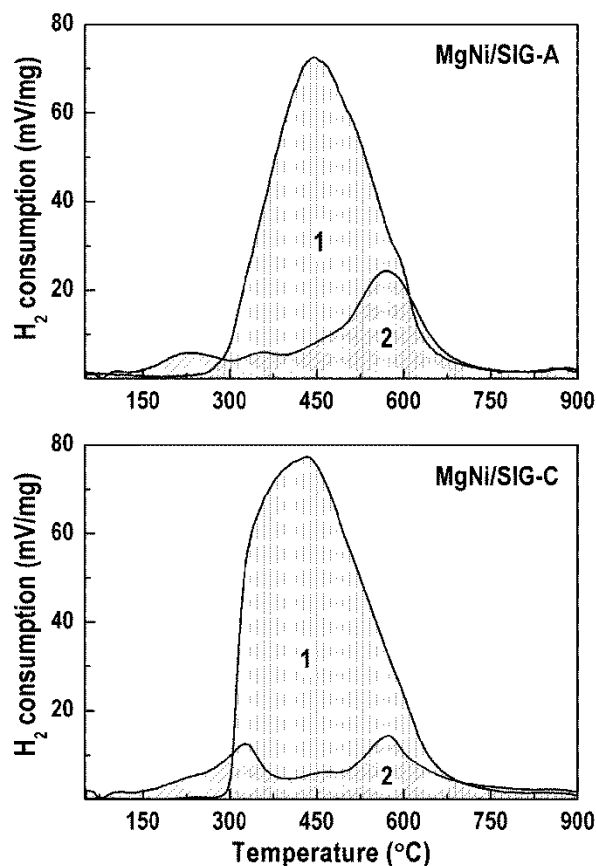
Fig. 5. Normal TPR (1) and ReTPR (2) profiles of the Mg-doped precursors.

The normal TPR profile of MgNi/SIG-C is asymmetric and displayed a well-resolved T_{max} at

430 °C and a negligible high-temperature shoulder also at ~600 °C. Calculated total peak area of both precur-sors showed higher reducibility of the Ni^{2+} species in MgNi/SIG-C by 17.1% compared to MgNi/SIG-A. Considering that chemical analysis of the precursors confirmed a similar concentration of Ni^{2+} for both samples, a likely interpretation is the existence of hardly reducible Ni^{2+} species in MgNi/SIG-A.

The aim of the ReTPR procedure was to indicate catalyst status after reduction at 430 °C for 2 h, namely the presence of unreducible or hardly reducible species, and their quantity, etc. Actually, ReTPR profiles propose a facilitated reduction of the Ni^{2+} species in MgNi/SIG-C up to 430 °C. A smaller area of the ReTPR curve signifies a lesser amount of unreducible species. This phenomenon specifies higher reducibility efficiency in first run (up to 430 °C) and a greater quantity of readily reducible species. Calculations showed that only 11.8% of the Ni^{2+} species in MgNi/SIG-C precursor remained unreduced vs. 26.1% for MgNi/SIG-A. Bearing in mind that the final catalyst was obtained after reduction also at 430 °C, it is correct to assume that the higher MgNi/SIG-C activity originates from a higher amount of metal Ni^0 particles generated during reduction.

It is worth noting that the higher hydrogenation activity of MgNi/SIG-C can be related not only to the presence of a larger number of Ni^0 active sites on the catalyst surface but also to a larger average pore diameter of the MgNi/SIG-C precursor compared to MgNi/SIG-A (Table 1). A larger pore diameter permits a faster diffusion rate of the reactant molecules through the pore system of the catalyst reflecting on a higher reaction rate. In addition, the polydisperse character of the PSD in the whole mesoporous region for the MgNi/SIG-C precursor (Fig. 3) may further contribute to a faster rate of the reaction and a higher hydrogenation activity. Moreover, a twofold smaller amount of micropores (V_{micro}) with MgNi/SIG-C than MgNi/SIG-A (Table 1) may also affect hydro-genation effectiveness. According to Balakos and Hernandez [2], micropores inhibit the participation of triglyceride molecules in the reaction because of limited access to the active sites. In addition to the diffusion limitations due to the presence of micro-pore system, which does not contribute to reaction progress, the lower activity of the MgNi/SIG-A catalyst is explained by existence of hardly reducible Ni^{2+} species, which was evidenced by the TPR and ReTPR results.

The different activity of the catalysts reflects on the different FA profiles and different FA composi-

tions obtained during hydrogenation (Fig. 6). The hydrogenation of linolenic acid (C18:3*cis*) was not considered due to its low initial concentration in the sunflower oil (0.1%)
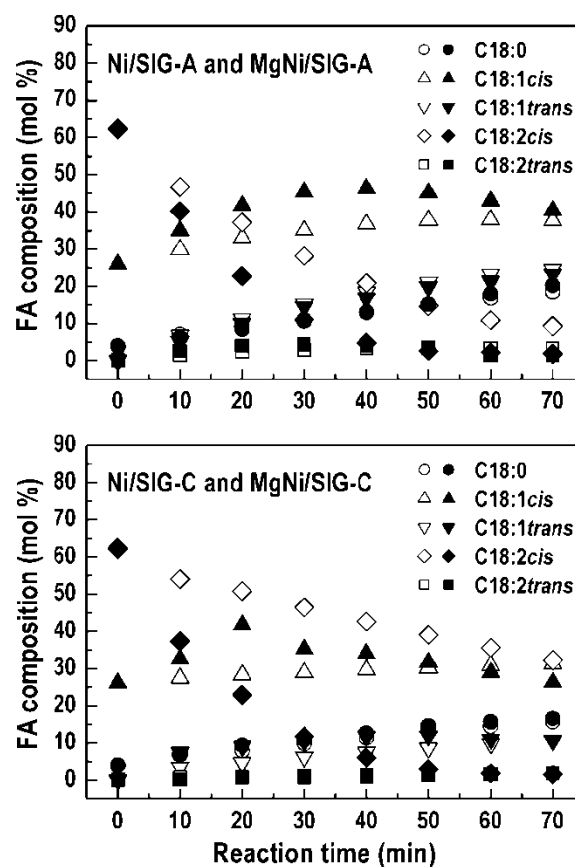
Fig. 6. FA composition obtained during hydrogenation over non-doped catalysts (open symbols) and Mg-doped catalyst (closed symbols).

The overall vegetable oil hydrogenation includes consecutive saturation of linolenic acid (C18:3*cis*) to linoleic acid (C18:2*cis*), then to oleic acid (C18:1*cis*), and finally to stearic acid (C18:0). Except increasing the hydrogenation activity, a goal of this study was to decrease linolenic acid (C18:3*cis*) and linoleic acid (C18:2*cis*) FA contents. From this point of view, FA compositions obtained after 70 min of hydrogenation (end-point of the reaction over the MgNi/SIG-C catalyst) demon-strated a decrease of the linoleic acid C18:2*cis* (mol%) in the order: 1.4 (MgNi/SIG-C) < 1.9 (MgNi/SIG-A) < 9.4 (Ni/SIG-A) << 32.2 (Ni/SIG-C) (Fig. 6). Apparently, modification of the Ni/SIG systems by Mg increases the conversion of C18:2*cis* FA. The results give evidence for a high selectivity of the MgNi/SIG-C catalyst to C18:1*cis*, hydroge-nation being almost complete. This finding could be explained by much faster diffusion of the trigly-ceride molecules through the pores. It is well known that linoleic acid, C18:2*cis*, is one of the essential

fatty acids. Small amounts are sufficient for human nutrition and allowable in the edible hydrogenated oils.

As mentioned above, along with saturation of the double bonds during hydrogenation, two reversible reactions of *cis*-FA to *trans*-FA isomerisation take place: linoleic (C18:2*cis*) → (C18:2*trans*) and oleic (C18:1*cis*) → (C18:1*trans*), which lead to a broad product distribution [1,3]. Due to increasing concern about the negative effect of *trans*-FA on human health, it is desirable to reduce the formation of *trans*-FA isomers [24] and significantly impede stearic acid FA C18:0 formation in the hydrogenated vegetable oil. The latter is better exhibited by the MgNi/SIG-A catalyst than MgNi/SIG-C (Figure 6) and is therefore a promising feature.

Concerning the content of all C18*trans* FA isomers, the MgNi/SIG-C catalyst demonstrated a lower value by 46% than MgNi/SIG-A under the same operating conditions and for the same activity. In this case, the activity was compared for approximately the same value of H₂ consumption, namely: 41 900 cm³ for MgNi/SIG-A reached for 40 min and 40 723 cm³ for MgNi/SIG-C reached for 30 min. The content of all C18*trans* with MgNi/SIG-A for 40 min was 20.78 mol.%, whereas MgNi/SIG-C manifested 11.22 mol.% for 30 min. It is known that the *trans*-isomers are formed when the triglyceride desorbs from the catalyst surface without being hydrogenated [2]. The increase of *trans*-FA amount with the MgNi/SIG-A catalyst could be explained by mass-transfer limitations due to twofold higher microporosity as compared to MgNi/SIG-C (Table 1). Veldsink et al. [3] who stated that an increase of trans-isomer content might be caused by pore diffusion resistance sustained this standpoint.

It was testified that modifying the electronic density of the metallic phase may alter the adsorption-desorption strength of reactants and/or products [7,25]. A lower amount of C18:1*trans* FA isomers formed by the MgNi/SIG-C catalyst relative to the MgNi/SIG-A catalyst can be interpreted also in terms of a greater number of Ni⁰ sites on the catalyst surface, which leads to higher electron density of Ni because of an electron transfer from the basic Mg promotor. The increase in electron density of nickel induces a weak interaction of the adsorbed and hydrogenated molecules, and makes easier theirs desorption to minimise the transformation from *cis*- to *trans*-FA isomers [7,25].

It may be summarised that Mg-doping has a measurable impact on the characteristics of the catalysts affecting the hydrogenation activity as well as the quality of the hydrogenated products.

CONCLUSIONS

Results obtained in this study reveal that both the application of silica gels of different texture parameters and magnesium addition results in catalysts of different hydrogenation activity and variation in fatty acid composition of the reaction products.

A considerable effect of magnesium dopant was established on the reducibility of Ni²⁺ ions from MgNi/SIG-C precursor thus contributing to a greater quantity of readily reducible Ni²⁺ species and generating a sufficient number of accessible metal nickel active sites on the catalyst surface through applied reduction procedure.

The role of the magnesium on catalyst performance in sunflower oil hydrogenation was clearly demonstrated by the MgNi/SIG-C catalyst. A dominant activity and lower amount of formed C18*trans* isomers could be attributed to formation of suitable catalyst mesoporosity, thereby, restricting diffusion effects.

In conclusion, Mg-doping of Ni/SIG-C is promising for use to obtain an efficient edible vegetable oil hydrogenation catalyst of high activity, high saturation value of linoleic (C18:2*cis*) acid, and moderate amounts of C18:1*trans* and C18:0 stearin FA in partially hydrogenated sunflower oil

Note: This study was realised in the frame of inter-academic collaboration between Institute of Catalysis, Bulgarian Academy of Sciences, Sofia, Bulgaria and University of Belgrade, Institute of Chemistry, Technology and Metallurgy, Department of Catalysis and Chemical Engineering, Belgrade, Serbia through the project "*Layered systems as precursors of nanosized catalysts applied to clean fuels and healthy foods production*".

REFERENCES

1. M. Fernández, G. Tonetto, G. Crapiste, D. Damiani, *J. Food Eng.*, **82**, 199 (2007).
2. M. Balakos, E. Hernandez, *Catal. Today*, **35**, 415 (1997).
3. J. Veldsink, M. Bouma, N. Schöön, A. Beenackers, *Catal. Rev. - Sci. Eng.*, **39**, 253 (1997).
4. Vegetable Oils in Food Technology: Composition, Properties and Uses, Second Edition. Edited by Frank D. Gunstone, Blackwell Publishing Ltd., 2011, pp. 353.
5. G. Babu, K. Ghuge, S. Rammohan, V. Krishnan, A. Bhat, *Catal. Lett.*, **15**, 95 (1992).

6. E. Jang, M. Jung, D. Min, *Compr. Rev. Food Sci. F.*, **1**, 22 (2005).
7. G. Tonetto, M. Sánchez, M. Ferreira, D. Damiani, *J. Mol. Catal. A: Chem.*, **299**, 88 (2009).
8. J. Zhu, X. Peng, L. Yao, J. Shen, D. Tong, C. Hu, *Int. J. Hydrogen Energy*, **36**, 7094 (2011).
9. D. Nikolova, J. Krstić, L. Spasov, D. Simeonov, D. Lončarević, Pl. Stefanov, D. Jovanović, *Russ. J. Phys. Chem. A*, **85**, 2380 (2011).
10. M. Gabrovska, J. Krstić, P. Tzvetkov, K. Tenchev, M. Shopska, N. Vukelić, D. Jovanović, *Russ. J. Phys. Chem. A*, **85**, 2392 (2011).
11. M. Gabrovska, D. Nikolova, M. Shopska, P. Tzvetkov, L. Spasov, D. Simeonov, D. Jovanović, Physical Chemistry 2014 (Proc. 12th Int. Conf. Fundamental and Applied Aspects of Physical Chemistry, September 22−26, 2014, Belgrad, Serbia), Eds., Z. Cupić, S. Anić, Society of Physical Chemists of Serbia, vol. 1, p. 235.
12. J. Krstić, V. Radonjić, M. Gabrovska, D. Nikolova, L. Bilyarska, K. Tenchev, N. Vukelić, Physical Chemistry 2014 (Proc. 12th Int. Conf. Fundam. Appl. Aspects Phys. Chem., September 22−26, 2014, Belgrade, Serbia), Eds., Z. Cupić, S. Anić, Society of Physical Chemists of Serbia, vol. 1, p. 276.
13. J. Krstić, M. Gabrovska, D. Lončarević, D. Nikolova, V. Radonjić, N. Vukelić, D. M. Jovanović, *Chem. Eng. Res. Des.,* **100**, 72 (2015).
14. ISO 6320:2017, Animal and vegetable fats and oils - Determination of refractive index.
15. AOCS Official Method Ce 2-66, 1997, Preparations of Methyl Esters of Fatty Acids.
16. R. Shannon, *Acta Crystallogr. A*, **32**, 751 (1976).
17. B. Reddy, R. Frost, M. Dickfos, *Spectrochim. Acta Part A*, **71**, 1762 (2009).
18. K. Ghuge, A. Bhat, G. Babu, *Appl. Catal. A: Gen.*, **103**, 183 (1993).
19. J. Sohn, *Catal. Today*, **73**, 197 (2002).
20. R. Lenza, W. Vasconcelos, *Mater. Res.*, **4**, 189 (2001).
21. O. Solcova, D.-C. Uecker, U. Steinike, K. Jiratova, *Appl. Catal. A: Gen.*, **94**, 153 (1993).
22. F. Rouquerol, J. Rouquerol, K. Sing, in: Adsorption by Powders and Porous Solids, Principle, Methodology and Applications, Academic Press, New York, 1999.
23. J. Krstić, M. Gabrovska, D. Lončarević, D. Nikolova, D. Simeonov, M. Stanković, N. Vukelić, Physical Chemistry 2012 (Proc. 11th Int. Conf. Fundam. Appl. Aspects Phys. Chem., September 24−28, 2012, Belgrade, Serbia), Eds., Z. Cupić, S. Anić, Society of Physical Chemists of Serbia, vol. 1, p. 175.
24. H. Choo, K. Liew, H. Liu, C. Seng, *J. Mol. Catal. A: Chem.,* **165**, 127 (2001).
25. C. Thunyaratchatanon, J. Jitjamnong, A. Luengnaruemitchai, N. Numwong, N. Chollacoop, Y. Yoshimurda, *Appl. Catal. A: Gen.*, 520, **170** (2016)

ПОДОБРЕНО КАТАЛИТИЧНО ПОВЕДЕНИЕ НА Ni/SiO$_2$ ПРИ ХИДРОГЕНИРАНЕ НА РАСТИТЕЛНИ МАСЛА: ВЛИЯНИЕ НА ДОБАВКАТА ОТ Mg

М. В. Габровска[1]*, Д. А. Николова[1], Ю. Б. Кръстич[2], Д. Р. Лонцаревич[2], П. Цв. Цветков[3], М. Г. Шопска[1], В. Д. Радонич[2], М. В. Станкович[2], Д. М. Йованович[2], Л. Т. Спасов[1], Д. Б. Симеонов[3]

[1] Институт по катализ, Българска академия на науките, ул. „Акад. Г. Бончев“, бл. 11, 1113 София, България
[2] Белградски университет, Институт по химия, технология и металургия,
Център по катализ и инженерна химия, ул. Ньегошева 12, 11000 Белград, Сърбия
[3] Институт по обща и неорганична химия, Българска академия на науките, ул. „Акад. Г. Бончев“, бл. 11, 1113 София, България

(Резюме)

Изследвани са Ni-Mg/SIG катализатори за хидрогениране на слънчогледово масло за хранителни цели, получени чрез съутаяване на прекурсори върху носители от търговски силикагели с различни текстурни характеристики - SIG-A (микропорест тип) и SIG-C (мезопорест тип). Установено е, че двата фактора – текстурните параметри на силикагелите и добавката от магнезий – водят до получаване на катализатори с различна хидрогенираща активност и различен състав на мастните киселини в реакционните продукти. Получените резултати разкриват висока хидрогенираща активност на Ni-Mg/SIG-C катализатор като резултат от по-голямо количество и достъпност на метални никелови частици в катализатора, образувани с процедурата на редукция. По-високата активност на MgNi/SIG-C катализатор може да се отдаде на неговата мезопорестост, благодарение на която се избягват дифузионните ограничения. Добавката от Mg подобрява качествата на прекурсора Ni-Mg/SIG-C за получаване на ефективен катализатор за хидрогениране на растителни масла за хранителни цели с висока активност, висока степен на насищане на линоловата киселина (C18:2*cis*) и присъствие на умерени количества от олеинова (C18:1*trans*) и стеаринова (C18:0) киселини в частично хидрогенираното слънчогледово масло.

Synthesis of polyphenylacetylene by iron(III) chloride catalyzed carbonyl olefin metathesis polymerization of chalcone

H. Penchev[1], S. S. Dimova[1,*], K. L. Zaharieva[2], F. S. Ublekov[1], Ch. Novakov[1], V. Sinigersky[1]

[1] *Institute of Polymers, Bulgarian Academy of Sciences, Acad. G. Bonchev St., Bldg. 103A, 1113 Sofia, Bulgaria*
[2] *Institute of Catalysis, Bulgarian Academy of Sciences, Acad. G. Bonchev St., Bldg. 11, 1113 Sofia, Bulgaria*

Carbon-carbon bond formation is a fundamental reaction in organic synthesis, one of its most important applications being synthesis of polymers and copolymers. Studies of the olefin metathesis reaction have resulted in extensive knowledge regarding synthesis of molecules applied in agricultural, petroleum, and pharmaceutical industries. The most commonly used catalysts for this purpose are ruthenium, molybdenum, and tungsten-based complexes.

Recently, Ludwig et al. have successfully conducted iron(III)-catalysed carbonyl-olefin metathesis reaction for synthesis of low molecular weight compounds.

In this study, we demonstrate for the first time that the carbonyl-olefin metathesis reaction, catalysed by anhydrous iron(III) chloride, can also be effectively applied in polymerization mode by using a single bifunctional monomer as chalcone. Polymerization was performed in a simple and efficient way under mild reaction conditions in solvents of various polarity, such as 1,2-dichloroethane and toluene. The average molecular mass of the synthesized oligomers reached 5000 g.mol^{-1}, which was higher than reference values so far reported. In situ doping of the as synthesized polyphenylacetylenes with FeCl$_3$ represents another advantage of selected synthetic approach.

Obtained products were characterized by gel permeation chromatography, ^{1}H NMR, and FTIR spectroscopy. The structure of the obtained oligomers was studied by X-ray diffraction analysis.

Key words: carbonyl olefin metathesis polymerization, Iron(III) chloride, polyphenylacetylenes, chalcone, catalyst dopant.

INTRODUCTION

During the last decade, a new synthetic route for the preparation of oligomeric products based on carbonyl-olefin exchange reaction and reductive coupling of conjugated compounds has been developed using novel catalyst systems. The control over the polymer structure provided by metathesis polymerization makes fine-tuning of polymer properties and functionality possible.

Carbonyl olefin metathesis (COM) has been reported for the first time by Schopov *et all.* [1]. COM has been applied for polymerization of α,β-unsaturated carbonyl compounds in the presence of WCl$_6$ [2]. It has been shown that treatment of α,β-unsaturated carbonyl compound as 1,3-diphenyl-prop-2-en-1-one (chalcone) with WCl$_6$ resulted in the formation of polyphenylacetylene. Using this procedure several substituted α,β-unsaturated carbonyl compounds were polymerized. A series of substituted polyacetylenes (polyphenylacetylene, polydiphenylacetylene, polymethylacetylene, poly-camphor, etc.) was obtained. The most commonly used catalysts for this purpose are ruthenium,

molybdenum, and tungsten-based complexes. Until now, COM has not been widely applied. The requirement of stoichiometric amounts of transition metals with concurrent formation of inert metal oxo species, which preclude regeneration of the active metal catalyst, has probably been the main reason for obscurity of the carbonyl-olefin metathesis reaction [3]. Finding mild catalytic conditions to perform carbonyl olefin metathesis has always been a significant challenge.

Remarkable innovations have been made in the field of olefin metathesis concerned with design and preparation of new catalysts. Considerable break-through has been achieved exploring iron(III)-catalysed carbonyl-olefin metathesis reactions. This approach is characterized by operational simplicity, high functional group compatibility, and region-selectivity using anhydrous FeCl$_3$ as a cheap, non-toxic, and environmentally friendly compound. Ludwig and co-workers have successfully demonstrated iron(III)-catalysed carbonyl-olefin ring-closing metathesis reaction for synthesis of low-molecular cyclic compounds [4, 5].

The goal of the present work was to synthesise polyphenylacetylene by iron(III)-catalysed carbonyl olefin metathesis polymerization of chalcone. Struc-

---

ture and chemical composition of the obtained products were studied by GPC, ^{1}H NMR, FTIR, and XRD analysis.

EXPERIMENTAL

Materials and methods

Chalcone ≥98.0% (Sigma-Aldrich) was used as received. Anhydrous $FeCl_3$ (98%) was purchased from Alfa Aesar. 1,2-Dichloroethane and toluene *ppa* grade were purchased from Valerus company, Bulgaria. 1,2-Dichloroethane was dried over CaH_2 and distilled; toluene was dried over CaH_2 and stored with metal sodium wire.

Characterization

The products prepared by metathesis polymerization were studied by several analytical techniques. ^{1}H-NMR ($CDCl_3$, dioxane) spectroscopy was performed on a Bruker Avance DRX 600 spectrometer, 600 MHz. FTIR spectra were recorded by means of a Bruker-Vector 22 spectrometer using thin films applied on KBr discs. GPC analysis was carried out on a Shimadzu Nexera XR LC20ADXR liquid chromatograph equipped with a DGU-20A5R degasser, a SIL-20ACHT auto sampler, a RID-20A refractive index detector, and a set of PLgel GPC columns: 5 µm 50 A, 500 A, and 10 µm Mixed-B. Tetrahydrofuran (THF) was used as eluent at a flow rate of 1 ml.min^{-1} at 40 °C. Samples were prepared as solutions in THF. Molecular weight characteristics as number average and weight average molecular masses and polydispersity index of the copolymers were calculated using a calibration curve constructed with monodisperse polystyrene standards. Data acquisition and processing were performed using LabSolutions v.5.54 GPC software.

Morphology of the obtained oligomers was studied by X-ray diffraction analysis. X-ray diffraction patterns were recorded on a Bruker D8 Advance ECO diffractometer in reflection mode with Ni-filtered Cu Kα radiation over the 2θ range of 10–60° at 40 kV. ICDD database was used to establish the phases.

Synthetic procedure

Polymerization was conducted in a Schlenk flask equipped with a three-way stopcock under argon, chalcone being dissolved at room temperature. Then the solution was heated according to applied medium: 60 °C for 1,2-dichloroethane and 90 °C for toluene. Almost immediately after addition of the $FeCl_3$ catalyst, a distinguished benzaldehyde smell was perceived. Best results were obtained for reaction time within 12–24 hours. At the first step 10

wt.% chalcone solutions in 1,2-dichloroethane ($C_2H_4Cl_2$) or toluene were obtained. Then anhydrous $FeCl_3$ preliminary dissolved in an appropriate amount of solvent was added. The solution immediately turned brown-reddish in colour as the viscosity was increased. Synthesis conditions are summarized in Table 1.

Table 1. Preparation conditions of polyphenylacetylenes

Sample	Solvent	$FeCl_3$, mole%	Yield, %
PA-1	1,2-dichloroethane	7.5	43
PA-2	1,2-dichloroethane	15	76
PA-3	Toluene	15	81
PA-4	Toluene	45	68

All experiments were carried out for 24 h.

The products were purified by precipitation in methanol, filtering and abundant washing with conc. HCl, washing with distilled water, neutralization with 0.1M $NaHCO_3$, and final washing with water to neutral pH of the filtrate (removal of catalyst and reaction rests). Purified polyphenylacetylene powder was pale yellow in colour while the $FeCl_3$-doped product was reddish-brown.

RESULTS AND DISCUSSION

The aim of this study was to use anhydrous $FeCl_3$ as a cheap and widely available catalyst for metathesis polymerization of chalcone and to characterize the obtained product – oligomeric polyphenylacetylene. Resonance structures of the synthesized oligomeric polyphenylacetylene are given in Scheme 1.

The products are stable in air, well soluble in common volatile solvents like chlorinated hydrocarbons, and exhibit the physical properties of conjugated polymers. GPC analysis of PA-4 sample showed a multimodal molar mass distribution with dispersity index of 2.5. Representative GPC traces are displayed in figure 1. It should be pointed out that the molar mass of the obtained oligomers strongly depended on the polarity of solvent used as polymerization medium. The polymerization carried out in 1,2-dichloroethane resulted in formation of predominantly trimeric product, irrespective of catalyst amount and polymerization time, while when performing the reaction in solvent of lower polarity like toluene, fractions of molecular masses up to 5000 g.mol^{-1} were registered.

FTIR spectra of the products are presented in figure 2. All oligomers showed a band at 1656 cm^{-1} assigned to C=O bond (conjugated ketone end group). In the spectrum of PA-2 sample, the double bond for -C=C- from the phenylene ring appeared around 1597 cm^{-1}, the =C-H aromatic vibrations
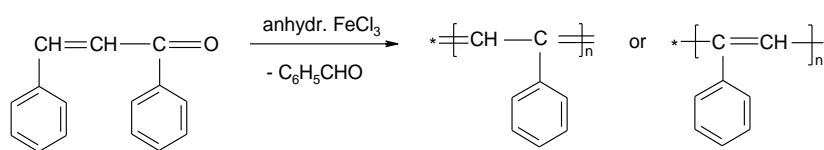
Scheme 1. Fe(III) chloride catalyzed carbonyl olefin metathesis polymerization of chalcone.
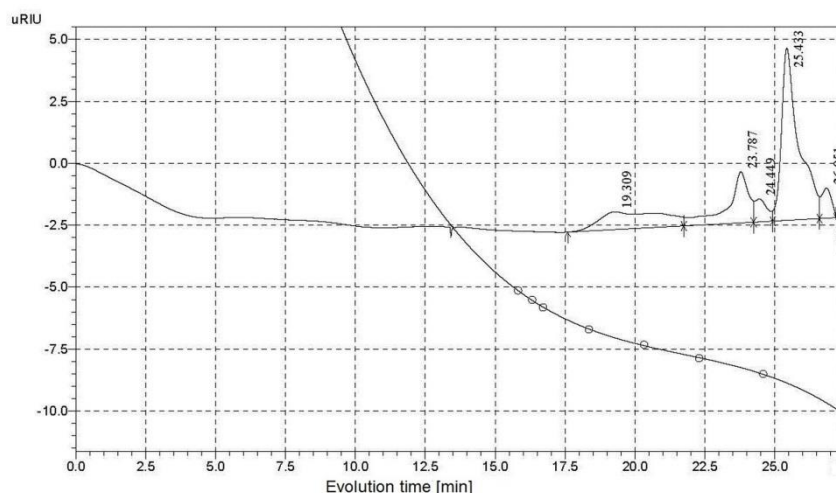
Fig. 1. GPC traces of sample PA-4 (eluent THF).

were in the range of 1180–1029 cm^{-1}, while the =CH- vibration from the polymer backbone was at 1448 cm^{-1} [6].
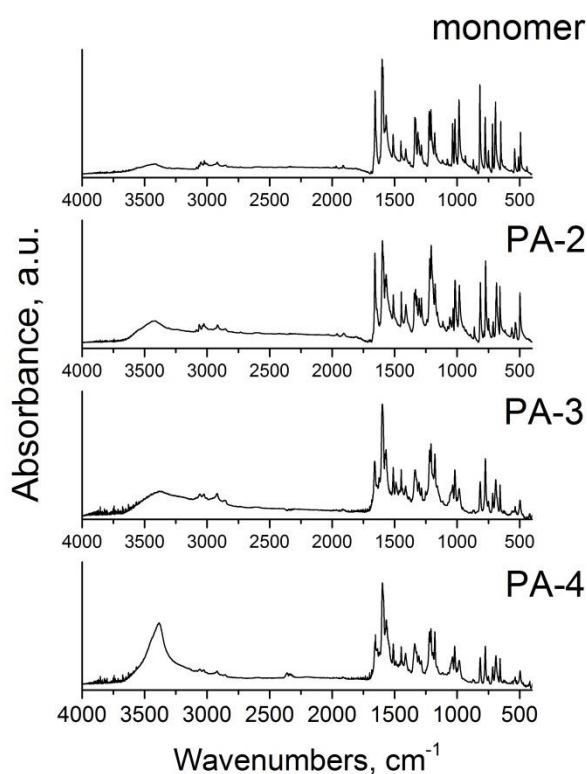
Fig. 2. IR spectra of monomer, PA-2, PA-3, and PA-4.

^{1}H NMR spectra of the synthesized polyphenyl-acetylenes are shown in figures 3 and 4. ^{1}H-NMR (in CDCl$_3$) of PA-2 manifested a characteristic chemical shift for double bonds at 5.37 ppm. Signals in the region 7.3–8 ppm are assigned to protons characteristic of aromatic rings. The chemical shifts between 1.8–2.5 ppm are attributed to =CH- protons from the backbone.

In the ^{1}H NMR spectrum of dominating *cis*-polyphenylacetylene PA-2, the peak characteristic of proton attached to the *cis*-conformation of the double bond was observed at 5.4 ppm. It is known that if W, Mo, and Rh catalyse the polymerization of arylacetylenes a *cis*-transoidal structure is mainly obtained [7–9]. Sample PA-2 showed a singlet at δ = 5.37 ppm that has to be assigned to olefinic protons in the *cis*-transoidal main chain.

X-ray diffraction pattern of the polymerization product in toluene is displayed in figure 5. The diffractogram shows a broad maximum around 2θ ~ 12.5°, which confirms predominant amorphous structure of the sample. However, sharpening of two peaks at 26.6° and 32.8° was observed. This indicates that synthesized oligomer is susceptible to some structural ordering. [10]. The area of these two peaks is negligible in comparison with the amorphous halo. For this reason, the crystallinity is close to zero.
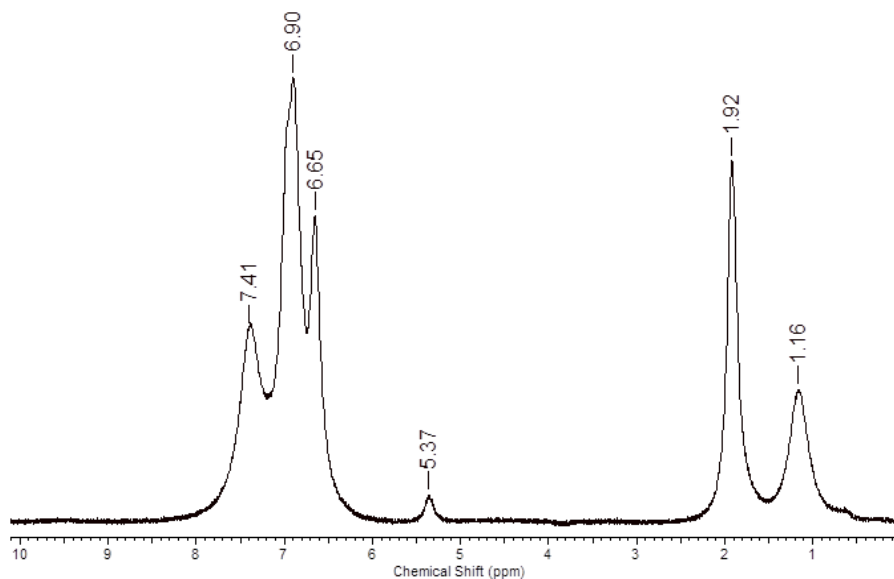
Fig. 3. ^{1}H NMR spectrum of PA-2.
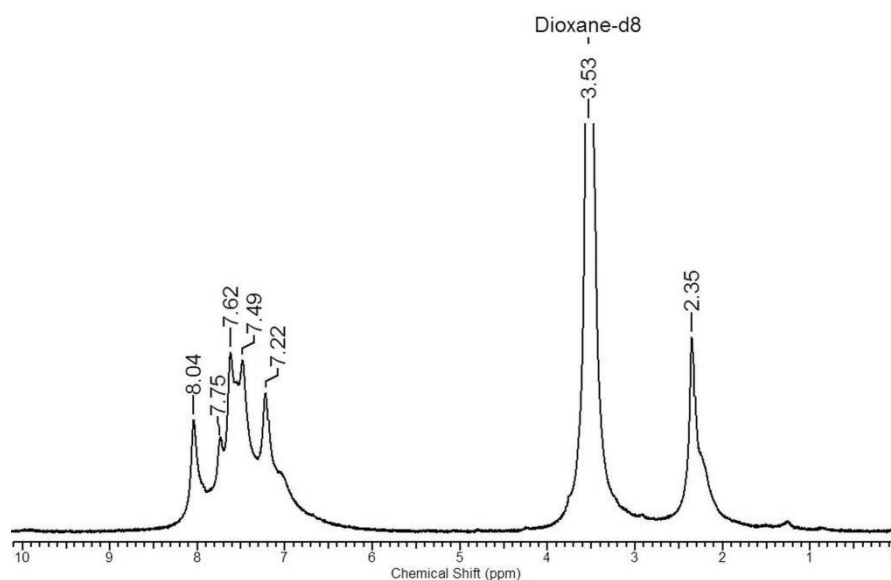
Fig. 4. ^{1}H NMR spectrum of PA-4.

In previous pioneering studies, Jossifov *et al*. performed carbonyl-olefin exchange reaction of chalcone using WCl_6 as catalyst and obtained poly-phenylacetylenes, however, the WCl_6 catalyst is expensive and toxic [11,12]. Binary systems like $WCl_6 + AlCl_3$, $WOCl_4 + AlCl_3$ and others were also used as Friedel-Crafts type catalysts [11,12]. In our study, we performed polymerization of chalcone in solution using anhydrous $FeCl_3$. Iron(III) chloride was selected as a cheap and green catalyst alternative to traditionally used tungsten-based catalyst systems. Another advantage that could be emphasized is conducting the metathesis polymerization in common volatile organic solvents and using low concentrations of $FeCl_3$.
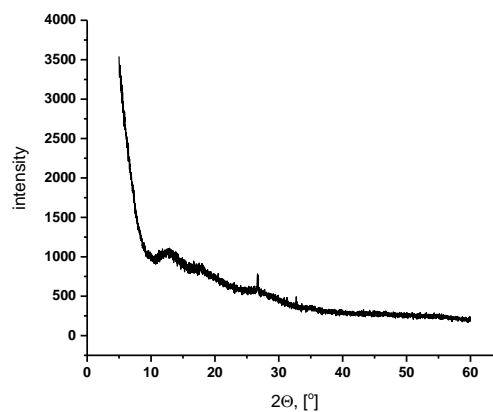
Fig. 5. XRD pattern of the polymerization product in toluene.

CONCLUSIONS

A simple and efficient procedure for synthesis of polyphenylacetylene by iron(III)-catalysed carbonyl olefin metathesis polymerization of chalcone is described for the first time. This procedure could be applied to prepare a broad range of functionalized benzalacetophenone derivatives with high chemo- and regioselectivity. High selectivity, mild reaction conditions, and easy available starting materials can be pointed out as considerable advantages.

The catalytic carbonyl-olefin metathesis reaction enables direct carbon-carbon bond formation between carbonyl and olefin entities by using anhydrous iron(III) chloride as catalyst. Depending on the polarity of the reaction medium, oligomeric products with different molecular mass can be obtained. The procedure can render *in situ* FeCl$_3$-doped conjugated oligomers. The chemical structure of the synthesized polyphenylacetylenes was studied by ^{1}H-NMR, FTIR spectroscopy, XRD analysis, and GPC. The proposed procedure provides *in situ* FeCl$_3$-doped polyphenylacetylene.

REFERENCES

1. I. Schopov, C. Jossifov, L. Mladenova, *Makromol. Chem., Rapid Commun*., **6**, 659 (1985).
2. C. Jossifov, R. Kalinova, in: Green Metathesis Chemistry (Dragutan V., Demonceau A., Dragutan I., Finkelshtein E. S., eds.), NATO Science for Peace and Security Series A: Chemistry and Biology, Springer, Dordrecht, 2010, p. 305
3. C. Sa, *Angew. Chem. Int. Ed*., **55**, 2 (2016).
4. J. R. Ludwig, P. M. Zimmerman, J. B. Gianino, C. S. Schindler, *Nature*, **533** (7603), 374 (2016).
5. J. R. Ludwig, S. Phan, C. C. McAtee, P. M. Zimmerman, J. J. Devery III, C. S. Schindler, *J. Am. Chem. Soc*., **139** (31), 10832 (2017).
6. S. Dimova, K. Zaharieva, V. Sinigersky, Z. Cherkezova-Zheleva, I. Mitov, *Materials, Methods & Technologies*, **8**, 233 (2014).
7. T. Masuda, *J. Polym. Sci. Part A: Polym. Chem*., **45**, 165 (2007).
8. T. Masuda, N. Sasaki, T. Higashimura, *Macromolecules*, **8** (6), 717 (1975).
9. M. Shiotiuki, F. Sanda, T. Masuda, *Polym. Chem*., **2**, 1044 (2011).
10. R. Kamashi, B. S. R. Reddy, *J. Polym. Sci. Part A: Polym. Chem*., **46**, 1521 (2008).
11. C. Jossifov, in: Ring Opening Metathesis Polymerisation and Related Chemistry (Khosravi E., Szymanska-Buzar T., eds.). NATO Science Series (Series II: Mathematics, Physics and Chemistry), vol. 56, Springer, Dordrecht, 2002, p. 425.
12. C. Jossifov, R. Kalinova, in: Metathesis Chemistry: From Nanostructure Design to Synthesis of Advanced Materials (Y. İmamoğlu, V. Dragutan, eds.), Springer, 2007, p. 461.

СИНТЕЗ НА ПОЛИФЕНИЛАЦЕТИЛЕНИ ПОЛУЧЕНИ ЧРЕЗ КАРБОНИЛ ОЛЕФИНОВА МЕТАТЕЗНА ПОЛИМЕРИЗАЦИЯ НА ХАЛКОН КАТАЛИЗИРАНА ОТ ЖЕЛЕЗЕН(III) ХЛОРИД

Хр. П. Пенчев[1], С. С. Димова[1,*], К. Л. Захариева[2], Ф. С. Ублеков[1], Хр. Новаков[1], В. Синигерски[1]

[1] Институт по полимери, Българска академия на науките, ул. „Акад. Г. Бончев", бл. 103А, 1113 София, България
[2] Институт по катализ, Българска академия на науките, ул. „Акад. Г. Бончев", бл. 11, 1113 София, България

(Резюме)

Образуването на въглерод-въглеродна връзка е фундаментална реакция в органичния синтез като едно от най-важните приложения е получаването на полимери и съполимери. Изследването на реакцията на олефиновата метатеза води до задълбочени познания по отношение на синтеза на молекулите, прилагани в селското стопанство, нефтената и фармацевтичната промишленост. Най-често използваните катализатори за тази цел са комплекси на базата на рутений, молибден и волфрам.

Лудвиг и сътр. успешно осъществяват карбонил олефин метатезна реакция, катализирана от желязо(III), за синтез на нискомолекулни съединения.

В това изследване ние показваме за първи път, че карбонил олефинова метатезна реакция, катализирана от безводен железен(III) хлорид, може успешно да се прилага и в полимеризационен режим чрез използване на бифункционален мономер - халкон. Полимеризацията се извършва по прост и ефективен начин при умерени реакционни условия в разтворители с различна полярност като 1,2-дихлороетан и толуен. Средната молекулна маса на синтезираните олигомери достига 5000 g.mol^{-1}, което е по-високо от посоченото в литературата досега. In-situ дотирането на получените полифенилацетилени с FeCl$_3$ е друго предимство на избрания от нас синтетичен подход.

Adsorption of thiophene and its polyaromatic derivatives from model fuel on pyrolyzed rice husks: kinetics and equilibrium

S. A. Uzunova[1], I. M. Uzunov[2,*], I. R. Ivanov[1], D. B. Angelova[1]

[1] *University of Chemical Technology and Metallurgy, 8 Kliment Ohridski Blvd., 1756 Sofia, Bulgaria*

[2] *Institute of General and Inorganic Chemistry, Bulgarian Academy of Sciences, Acad. G. Bonchev St., Bldg. 11, 1113 Sofia, Bulgaria*

Kinetics of fuel adsorptive desulphurisation was studied using a model fuel containing thiophene, benzothiophene, and dibenzothiophene of initial total sulphur content (S_{in}) of 415, 218, and 111 wppm over pyrolyzed rice husks (PRH) under batch mode conditions. Total sulphur content was determined by X-ray fluorescence analysis. Second order kinetics, intraparticle diffusion model, and Elovich equation were used to analyse kinetic data. It was found that a second-order kinetics model adequately described adsorption of the three sulphur compounds on pyrolyzed rice husks. The equation provided the best fit between calculated and experimentally determined values of adsorption capacity. Value differences varied between 1.3% for S_{in} 111 ppm and 5.9% for S_{in} 415 ppm. Adsorption affinity of the three sulphur compounds as well as equilibrium adsorption capacity of pyrolyzed rice husks were investigated by determination of adsorption isotherm. Analysis of experimental data was conducted by using the isotherms of Langmuir, Temkin, and Freundlich. Data from multiple linear regression analysis pointed out that Freundlich isotherm described most adequately the adsorption equilibrium of polyaromatic sulphur heterocycles in the system fuel/PRH.

Key words: desulphurization, adsorption, aromatic sulphur heterocycles, pyrolyzed rice husks, kinetics, adsorption isotherm.

INTRODUCTION

Depletion of the fossil fuel deposits, periodically emerging economic or political crises, and environmental pollution in recent decades imposed demand and development of alternative energy sources. However, the part of energy obtained from fossil feedstocks remains significant, more than 82% and half of them are produced from the crude oil [1]. Intense oil production worldwide leads to depletion of old and commissioning of new oil fields, containing increasingly high sulphur quantity. This in turn leads to new challenges related to technological and environmental problems in removal of the sulphur compounds in oil refinery streams. Conventional hydrodesulphurisation (HDS) of high sulphur feedstocks is unable to ensure sulphur levels, close to the limit ones whereas preserving other important quality indicators, such as content of polycyclic arenes, cetane number, density, etc. The process is not effective with respect to the deep removal of the polycyclic aromatic sulphur compounds such as thiophene (T) and its derivatives. Hereby, the sulphur compounds are passed into the industrial and automotive fuels. This leads to emissions of sulphur oxides, with all the resulting harmful effects on the environment and human health. The presence of organic sulphur compounds in the automotive fuels also reduces largely catalyst system efficiency in modern cars. In addition, the tendency in recent years aimed at developing the so-called 'hydrogen economy' is closely connected with the production of fuel cells but they require <1 ppm sulphur-hydrogen containing feeds [2]. Considering the importance of the problem concerning the emissions of sulphur oxides EU adopted a number of directives and decisions to control total sulphur in fuels [3,4]. Implementation of these directives is a major challenge and requires improving of the existing purification technologies to minimize sulphur content in petroleum derivatives. In addition to their effectiveness, the methods must ensure well-balanced prices of the final products. Research in the field over the last decade has been focused on the development of alternative methods for deep or ultra-deep fuel purification from sulphur. Most often these methods accompany conventional purification by HDS and provide fuels production with a total sulphur content of up to and below 10 ppm. The so-called non-HDS based desulphurisation processes refer to desulphurisation by extraction [5–8], olefinic alkylation of thiophenic sulphur (OATS process) [9], selective oxidative desulphurisation [10], and desulphurisation *via* precipitation [11].

Among the alternative methods for the purification of fuels, particular attention is given to the method of adsorptive desulphurisation (ADS), which is based on selective adsorption of organic sulphur compounds from the fuel onto different by nature solid adsorbents [12–14]. The process is provided under soft conditions, such as moderate temperature and atmospheric pressure. Additional advantages of the process are high efficiency, molecular hydrogen free process, simple technology and equipment, complex, inexpensive capital and operating costs, and high level of labour safety. Extraction of the adsorbed organic sulphur compounds and their subsequent utilization provide a real ecological solution for regulation of a part of the refinery hazardous wastes. Recently published results concerning adsorptive desulphurisation confirm that heterogeneous adsorption is an attractive method for improving the quality of hydrocarbon fuels [15–22]. The method provides low content of sulphur and polyaromatic compounds content in the fuels in order to meet the requirements of modern quality standards. The ADS method is also attractive by the fact that various inexpensive and available raw materials are increasingly used for production of effective adsorbents [16–22]. From this point of view processing of rice husks waste to obtain proper materials for selective adsorption of aromatic sulphur compounds from fuels is of interest. Kumagai and co-workers have reported removal of dibenzothiophenes from kerosene on rice husk activated carbons in terms of their textural and chemical characteristics [23]. Uzunova *et al*. [24] have investigated some factors of influence upon selective adsorption of thiophene on pyrolyzed rice husks (PRH).

The purpose of the present study was to determine adsorption kinetics of a model fuel mixture of thiophene, benzothiophene (BT), and dibenzothiophene (DBT) of different initial sulphur concentration in solution onto pyrolyzed rice husks. Some kinetic models were used, such as second order kinetics; intraparticle diffusion model, and Elovich equation for data analysis to determine phenomenological adsorption mechanism of aromatic sulphur heterocycles (ASHs) onto pyrolyzed rice husks. The kinetics is directly related to achieving adsorption equilibrium in the system PRH/fuel. Adsorption affinity with respect to the mixture of the three sulphur compounds and equilibrium adsorption capacity of pyrolyzed rice husks were determined by use of adsorption isotherm.

Such an investigation deep inside the nature of the adsorptive desulphurisation by pyrolyzed rice husks offers a possibility to optimize the process from laboratory conditions to industrial scale-up.

MATERIALS AND METHODS

Preparation and characterization of pyrolyzed rice husks

The material used in the investigation was prepared by slow pyrolysis of rice husks provided from Pazardzhik region (Bulgaria). Rice husks prewashed several times with water and dried at 110 °C were pyrolyzed at 480 °C in a fixed bed stainless steel reactor under vacuum of 1.33 Pa. The heating rate was 4 °C.min^{-1}, the retention time being 3 h. Porous structure of the material was determined by mercury porosimetry. For the purpose, a Micromeritics Auto-Pore 9200 apparatus was used. The specific surface area was assessed by BET nitrogen adsorption measured by a Strohlein Area Meter static volumetric device. Ash content of the pyrolyzed rice husks was determined by thermogravimetric analysis on a SETARAM LABSYS Evo apparatus in a corundum crucible at a heating rate of 10 °C.min^{-1} in air. Structural characteristics of the pyrolyzed rice husks are summarized in table 1.

Table 1. Characteristics of the pyrolyzed rice husks

Characteristics	Value
total pore volume, cm^3.g^{-1}	1.05
porosity, %	57.1
total pore surface, m^{2}g^{-1}	5.9
average pore diameter, μm	0.72
bulk density, kg.m^{-3}	102
BET specific surface area, m^2.g^{-1}	253
mass yield, wt %	38
carbonaceous material/ash wt. ratio	0.96

As can be seen, the samples are characterized by high specific surface area, over 50% porosity, and total pore volume of 1.0 cm^3.g^{-1}. A differential pore size distribution shows that the porous structure of the pyrolyzed rice husks is formed predominantly by mesopores and macropores (Fig. 1) [25].
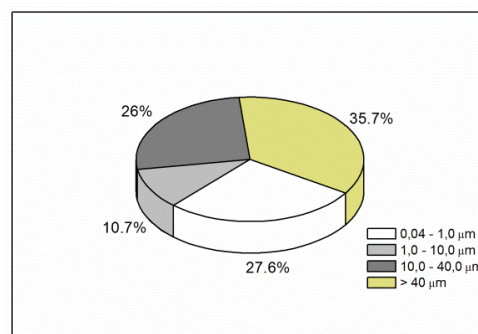
Fig. 1. Percentage of pore size distribution *vs.* total pore volume.

Adsorptive desulphurisation

Preparation of model fuel. To determine the influence of initial sulphur content and contact time

on adsorption kinetics, model fuel (MF) samples containing total sulphur of 415, 218, and 111 wppm were prepared by mixing thiophene, benzothiophene, and dibenzothiophene in octane at a 1:1:1 mass ratio. Fuel samples containing total sulphur of 415, 950, 1945, and 4600 wppm were prepared for determination of adsorption isotherm. The mixtures were percentage of pore size distribution having in mind that sulphur content in the thiophene, benzothiophene, and dibenzothiophene was 38.1, 23.9, and 17.4 mass%, respectively.

The three sulphur compounds and octane were Sigma Aldrich pure grade. Initial solutions were prepared by placing the required amount of thiophene, benzothiophene, or dibenzothiophene in a flask and octane was added up to a total weight of 100 g. Sulphur percentage in the solutions was determined by Sindie OTG Sulfur Analyzer using monochromatic wavelength dispersive X-ray fluorescence.

Adsorption in batch mode. Adsorption experiments were carried out at a constant temperature of 20 °C. Batch mode adsorption was provided by contacting 25.00 ml model fuel (specific gravity of 0.7 g.cm^{-3}) with 3.00 g of adsorbent placed in a stoppered Erlenmeyer flask. The suspensions were agitated on a rotary shaker for 120, 240, 360, 480, and 1440 min. An adsorption isotherm was obtained in order to investigate PRH adsorption capacity and affinity at equilibrium. The time required to reach adsorption equilibrium in the system fuel/PRH at 20 °C was determined by kinetic study.

The mixtures were agitated by shaking for 24 h to attain the equilibrium state. After that, the mixtures were filtered and the filtrates were analysed by XRF to determine adsorbed sulphur amount on the pyrolyzed rice husks. All measurements were performed in triplicate and the arithmetic average $\overline{S_{eq}}$ was calculated.

The adsorption capacity at equilibrium, a_e, was calculated according to the following equation:

$$a_e = \frac{(S_{in} - S_{eq})M}{m}, mg/g \qquad (1)$$

where S_{in} and S_{eq} are the initial and equilibrium sulphur concentration in the fuel (ppmw-S), respectively, M is fuel mass (kg), and m is adsorbent mass (g).

A quantitative measure of PRH efficiency and adsorption capacity is the degree of desulphurisation, φ, which was calculated by the formula:

$$\varphi = \frac{(S_{in} - S_{eq})}{S_{in}} \cdot 100, \% \qquad (2)$$

Kinetic equations. Phenomenological kinetic models are used to establish the rate-limiting step of the adsorption process. Rate-limiting processes for adsorption, occurring in the system liquid/solid usually are diffusion, mass transfer, or possibly chemical interaction between adsorbent and adsorbate. The accuracy of each kinetic model is a function of independent (input) parameters that affect output (measured) parameters. To select the most appropriate kinetic equation for which theoretically calculated and experimentally determined data have the best fit, the multiple linear regression (MLR) method is most commonly used. By establishing the adsorption kinetics, it is intended to optimize the process via regulating the conditions for its performance.

Second order kinetics. A second order equation is applicable to the kinetic region [26]. It usually describes bimolecular reactions with both reactants' concentrations decreasing with time. In this case, one can accept the second decreasing concentration is that of the surface active sites of the adsorbent. The mathematical expression is:

$$\frac{da_t}{dt} = k_2 \left(a_e - a_t \right)^2, \qquad (3)$$

where k_2 is the second order rate constant of adsorp-tion, mg.g^{-1}.min^{-1}.

After integrating equation (3) one obtains:

$$\frac{t}{a_t} = \left(\frac{1}{k_2 \cdot a_e^2} \right) + \left(\frac{t}{a_e} \right), \qquad (4)$$

Initial rate of sorption ($k_2 \cdot a_e^2$) and second order rate constant (k_2) were determined through linear regression method by the slope and interception of the dependence $t/a_t = f(t)$.

Intraparticle diffusion model. Adsorption velocity depends on the diffusion of the sulphur compounds toward and from the surface of the adsorbent. Mass transfer rate is a function of the concentration gradient in the liquid/solid system. In the case when diffusion is a rate-depending step, the process is described satisfactorily by the Weber-Morris equation [27]:

$$a_t = k_{id} \cdot \sqrt{t} + C, \qquad (5)$$

where C is a coefficient accounting the bonding effect between layers and k_{id} is a process rate constant, mg.g^{-1}.min$^{-1/2}$. The values of C and k_{id} are determined by the plot dependence $a_t = f(t^{1/2})$.

Elovich equation. This is one of the most often used models to describe chemisorption kinetics (Eq.

6) [28]. It is also successfully applied to describe the initial adsorption step and multilayer adsorption on a high heterogeneous surface area. The equation is empirical and does not refer to any particular mechanism:

$$\frac{da_t}{dt} = \alpha \cdot \exp(-ba_t), \qquad (6)$$

where α is the initial rate of sorption, mg.g^{-1}.min^{-1}, and b is desorption constant, g.mg^{-1}. Chen and Clayton [29] developed further the equation of Elovich, accepting the assumption ($\alpha.b.t$) >>> 1. For the boundary conditions $a_t = 0$ at $t = 0$ and $a_t = a_e$ at $t = t_e$, Eq. 7 was derived:

$$a_t = \left(\frac{1}{b}\right) \cdot \ln(\alpha b) + \left(\frac{1}{b}\right) \cdot \ln t, \qquad (7)$$

where: b is a constant referred to surface coverage and activation energy of chemisorption mg.g^{-1}, α is equilibrium rate constant, mg.g^{-1}.min^{-1}. The constants α and b in the exponential equation (7) are determined from the intercept and the slope of the dependence a_t *vs* ln$t$. In the case when the correlation between the adsorption capacity and the constant b is negative it is assumed that the adsorbent does not retain the adsorbate.

RESULTS AND DISCUSSION

Adsorption kinetics

Adsorption ability of pyrolyzed rice husks from model solutions containing different initial amount of thiophene, benzothiophene, and dibenzothiophene is presented in figure 2.
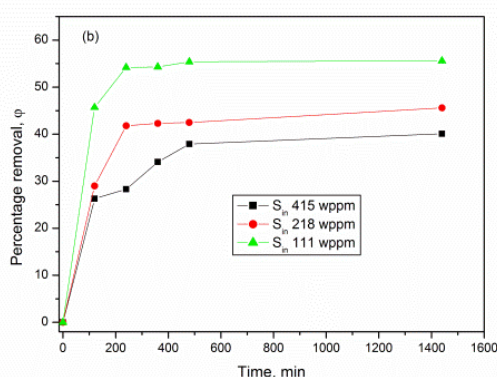
Fig. 2. Adsorption kinetics of aromatic sulphur heterocycles from model fuel on pyrolyzed rice husks.

The type of kinetic curves shows that the process of adsorption of a mixture of thiophene and its aromatic derivatives from fuel on pyrolyzed rice husks was carried out at two distinct stages. The first of them had duration of about 240 min. and is characterised by a sharp increase in the rate of adsorption.

During this stage, a desulphurisation rate between 28 and 54 mass% was achieved depending on the initial content of total sulphur in the fuel. The second stage is related to saturation of the active adsorption sites giving rise to reduction in velocity of the process and establishment of adsorption-desorption equilibrium. The degree of desulphurisation varied between 1 and 12 mass%. The observed relationships are directly related to the structural characteristics of pyrolyzed rice husks. The rate to achieve adsorption-desorption equilibrium determines adsorbent effectiveness, i.e. duration of the first stage is of practical significance.

In order to investigate the dependence between input parameters (initial sulphur concentration in the fuel and contact time between adsorbent and adsorbate) and adsorption rate (output parameter) the above-mentioned four kinetic models were applied to analyse the experimental data. These phenomenological models describe the mechanism by which the adsorption of aromatic sulphur heterocycles from fuel on pyrolyzed rice husks occurred. Model parameters and multiple linear statistics are presented in table 2.

Table 2. Kinetic parameters for thiophene, benzothiophene, and dibenzothiophene adsorption from model fuel

Kinetic constants	Initial sulphur content ,wppm		
	415	218	111
Second order kinetics			
$a_{e,calc}$, mg.g^{-1}	1.033	0.602	0.366
$a_{e,exp}$, mg.g^{-1}	0.971	0.581	0.361
k_2, g.mg^{-1}.min^{-1}	0.0110	0.033	0.177
R^2	0.998	0.999	1.000
Elovich equation			
b, mg.g^{-1}	6.794	13.49	43.74
$1/b$	0.1472	0.074	0.029
α, mg.g^{-1}.min^{-1}	0.096	0.197	210.1
R^2	0.876	0.692	0.601
Intraparticle diffusion model			
C	0.244	0.174	0.137
K_{id}, mg.g^{-1}.min$^{-1/2}$	0.0245	0.014	0.005
R^2	0.757	0.671	0.567

According to the linear regression statistics obtained, high values as 99% of the determination coefficient indicate that adsorption is best fitted to a second order kinetics equation for different initial sulphur concentrations in the fuel. For this kinetic model, a very good match was observed between calculated and experimentally determined values for adsorption capacity, a_e. Value deviation varied from 1 to 6%. On increasing the initial sulphur content in the model fuel the rate constant k_2 decreased by more than one order of magnitude. This is probably due to: (i) competitive adsorption of the three sulphur compounds and (ii) mutual hindrance (steric effects) in the occupation of the active sites on the surface.

Furthermore, with increasing the initial sulphur concentration in the fuel the electrostatic interaction between active adsorption centres decreased causing a decrease in adsorption affinity between adsorbent and adsorbate. As a result, the adsorbed amount decreased from 56% (111 wppm) to 40% (415 wppm). The second order kinetics model indicates that adsorption probably takes place also with the participation of valence forces, i.e. by specific interactions between adsorbent active sites and adsorbate.

Low values of the determination coefficient for the diffusion kinetic model indicate that diffusion cannot be considered a rate-limiting step. The general conditions, when the mass transfer of adsorbate to the adsorbent surface and into its porous structure is rate-determining, are the following: the correlation coefficient (R^2) values are close to 1, and the graphic dependence passes through the origin of the coordinate system, the constant C value being negative. If the experimental data describe not a straight-line dependence, but in fact, a multi-linear one as in the case, this means that sorption is influenced by two or more rate-determining steps, i.e. the process occurs in the kinetic or in the transition region.

Positive values of the constants calculated by Elovich equation give evidence that an active sorption process is really proceeding [29].

Adsorption isotherms

A quantitative measure for maximum depth of fuel purification from sulphur compounds is the adsorption capacity value in equilibrium state. An experimental adsorption isotherm obtained in the concentration range from 415 to 4600 wppm of total sulphur is presented in figure 3. It is obvious that the amount of sulphur adsorbed on pyrolyzed rice husks increased as sulphur initial concentration was increased.
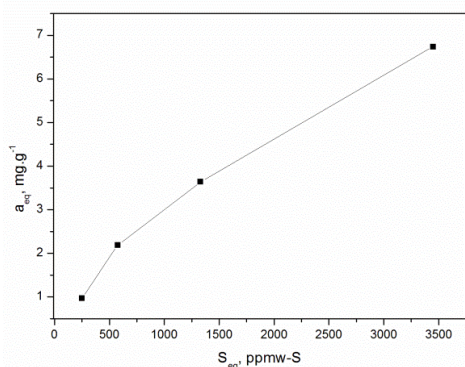
Fig. 3. Adsorption isotherm for simultaneous adsorption of thiophene, benzothiophene, and dibenzothiophene from model fuel.

Adsorption data were analysed using three models:

Langmuir isotherm model. The Langmuir model describes nonlinear adsorption and it is based on the assumption that the process is carried out on a homogeneous surface through the formation of a monolayer by the adsorbate without any interaction between the adsorbed molecules. Langmuir equation has the form:

$$\frac{S_{eq}}{a_e} = \frac{1}{K_L \cdot a_\infty} + \frac{S_{eq}}{a_\infty} \qquad (8)$$

where S_{eq}, ppmw-S; a_e, mg.g^{-1}; a_∞ is maximum adsorption capacity required to form a monolayer on the adsorbent surface, mg.g^{-1}; K_L- is Langmuir constant, kg.mg^{-1}, related to the energy of adsorption. The values of K_L and a_∞ are determined by the relationship:

$$S_{eq}/a_e = f(S_{eq}) \qquad (9)$$

Freundlich isotherm model. This empirical model is based on the assumption that the distribution of adsorption heat on the surface of the adsorbent is not homogeneous. Eq. 10 represents the linear form of the Freundlich isotherm:

$$\log a_e = \log K_F + (1/n).\log S_{eq}, \qquad (10)$$

where K_F, mg.g^{-1}, is the constant of Freundlich isotherm and it is an approximate indicator of adsorption capacity; $1/n$ is a function of adsorption strength. The values of $1/n$ and K_F are determined from the slope and intercept of the following relationship, Eq. 11:

$$\log a_e = f(\log S_{eq}) \qquad (11)$$

Values of adsorption intensity, n, between one and ten indicate favourable physical adsorption [31,32].

Temkin isotherm model.

The model of Temkin is based on the assumption that the energy of all molecules adsorbed in the monolayer decreases linearly in height. The linear dependence of the model is the following (Eq. 12):

$$a_e = B.\ln A + B.\ln S_{eq} \qquad (12)$$

The values of the isotherm constants A and B were determined from the slope and intercept of the graphical dependency (Eq. 13):

$$a_e = f(\ln S_{eq}), \qquad (13)$$

where B is coefficient related to the heat of adsorption (J/mol) and A is Temkin isotherm equilibrium binding factor (kg/g).

Values of the adsorption constants, coefficients for each adsorption isotherm as well as coefficients of determination, R^2, calculated by the multiple linear regression method and standard deviation, S_{RE}, are given in table 3.

Table 3. Isotherms constants and statistical criteria for the adsorption process

Isotherm	Parameters
Langmuir	
a_∞	8.33
K_L	4.1×10^{-4}
R^2	0.906
S_{RE}	62.4
Freundlich	
K_F	0.019
n	1.39
1/n	0.72
R^2	0.987
S_{RE}	0.05
Temkin	
B	2.2
A	5.2×10^{-3}
R^2	0.952
S_{RE}	0.67

According to statistical data, the adsorption of thiophene and its derivatives from fuel is reasonably described by the Freundlich and Temkin isotherms. As can be seen both models provide good correlations for the adsorption, however, the Freundlich isotherm describes the process more adequately. The Freundlich model is valid for heterogeneous surfaces and predicts an increase in concentration of the species adsorbed on the solid surface if species concentration in the liquid phase is increased. Therefore, the adsorption of thiophene and its derivatives on pyrolyzed rice husks obviously takes place on a heterogeneous surface, which may expose various adsorption sites having different affinity to thiophene, benzothiophene, and dibenzothiophene. The equilibrium heat capacity, *B*, calculated from Temkin isotherm is low. The heterogeneity parameter, *1/n*, determined from the Freundlich isotherm is > 1, which indicates favourable adsorption of aromatic sulphur heterocycles onto pyrolyzed rice husks. The process is carried out with predominant participation of non-specific interactions between adsorbent and adsorbate.

4. CONCLUSIONS

The material obtained by slow pyrolysis of renewable agricultural waste as rice husks can successfully be used for additional purification of fuels by adsorptive desulphurisation as a concomitant method of conventional hydrodesulphurisation.

Adsorption of a mixture of thiophene and thiophene aromatic derivatives from model fuel in the studied concentration range predominantly occurred in the kinetic region and is adequately described by a second order kinetics equation. Calculated and experimentally obtained values for adsorption capacity of pyrolyzed rice husks varied from 1 to 6%.

An increase of the initial sulphur content in model fuel caused a decrease of the rate constant of the process by more than one order of magnitude. Probably, this is due to competitive adsorption of the three sulphur compounds and steric effects upon occupation of the active adsorption sites. As a result, adsorbate affinity to the adsorbent was decreased and the adsorbed amount was reduced from 55.6% to 40%.

The equilibrium adsorption of thiophene and its derivatives from fuel was reasonably described by Freundlich isotherm. According to the theory, the model is valid for heterogeneous surfaces and predicts an increase in adsorbate concentration on the solid surface when the concentration of adsorbing entities in the liquid phase is increased. Therefore, adsorption of thiophene and its derivatives on pyrolyzed rice husks takes place on a heterogeneous surface, which may expose various adsorption sites having different affinity to thiophene, benzothiophene, and dibenzothiophene.

REFERENCES

1. Annual Energy Review, Energy Dept., Energy Information Administration, Office of Energy Markets and End Use, DOE/EIA -0384 (2004).
2. C. Song, *Catal.Today*, **77**, 17 (2002).
3. EC Directive, Directive 2008/105/EC of the European parliament and of the Council of 16 December 2008 on environmental quality standards in the field of water policy, amending and subsequently repealing Council Directives 82/176/EEC, 83/513/EEC, 84/156/EEC, 84/491/EEC, 86/280/EEC and amending Directive 2000/60/EC of the European Parliament and of the Council, *Official Journal of the European Union, L 348/84*.
4. EC Directive, Directive 2003/17/EC of the European Parliament and of the Council of 3 March 2003 amending Directive 98/70/EC relating to the quality of petrol and diesel fuels, *Official Journal, L 076 (22/03/2003) 0010 – 0019*.
5. I. Funakoshi, T. Aida, *US Patent* 5,753,102 (1998).
6. J. C. Gentry, F. M. Lee, in: NPRA 2000 Annual Meeting, AM-00-35, San-Antonio, Texas, March 26-28, 16 (2000).
7. R. E. Levy, A. S. Rapas, S. J. DeCanio, V. P. Nero, in: NPRA 2001 Annual Meeting, AM-01-10, New Orleans, March 18-20, 7 (2001).
8. Y. Shiraishi, Y. Taki, T. Hirai, I. Komasawa, *Ind. Engng. Chem. Res.*, **37**, 203 (1998).
9. J. Wiltshire, *BP Technol.Mag.*, **32**, 10 (2000).
10. T. Aida, D. Yamamoto, M. Iwata, K. Sakata, *Rev.*

179

Heteroatom Chem., **22**, 241 (2000).

11. V. Mielle, E. Shulz, M. Vrinat, M. Lemaire, *Chem. Commun.*, 305 (1998).

12. A. B. S. H. Salem, *Ind. Eng. Chem. Res.*, **33**, 336 (1994).

13. D. W.Savage, B. K. Kaul, G. D. Dupre, J. T. O'Bara, W. E. Wales, T. C. Ho, *US Patent* 5,454,933 (1995).

14. R. L. Irvine, B. A. Benson, D. M. Varraveto, R. A. Frye, in: NPRA 1999 Annual Meeting, AM-99-42, San-Antonio, Texas, March 21–23, 1999.

15. J. Bu, G. Loh, C. G. Gwie, S. Dewiyanti, M. Tasrif, A. Borgna, *Chem. Eng. J.*, **166**, 207 (2011).

16. J. Kim, X. Ma, A. Zhou, Ch. Song, *Catal. Today*, **111**, 74 (2006).

17. H. Farag, *J. Colloid Interf. Sci.*, **307**, 1 (2007).

18. I. Dahlan, K. Lee, A. Kamaruddin, A. Mohamed, *J. Hazard. Mater.*, **161** 570 (2009).

19. M. Seredych, J. Lison, U. Jans, T. Bandosz, *Carbon*, **47,** 2491 (2009).

20. K. Lee, A. Mohtar, N. Zainudin, S. Bhatia, A. Mohamed, *Fuel*, **84**, 143 (2005).

21. A. Srivastav, V. Srivastava, *J. Hazard. Mater.*, **170**, 1133 (2009).

22. Z. Cheng, X. Liu, J. Lu, M. Luo, *React. Kinet. Catal. Lett.*, **97** 1 (2009).

23. S. Kumagai, Y. Shimizu, Y. Toida, Y. Enda, *Fuel*, **88**, 1975 (2009).

24. S. Uzunova, L. Minchev, I. Uzunov, V. Toteva, *Chem. Ecol.*, **32**, 976 (2016).

25. J. Rouquerol, D. Avnir, C. Fairbridge, D. Everett, J. Haynes, N. Pernicone, J. Ramsay, K. Sing, K. Unger, *Pure Appl. Chem.*, **66**, 1739 (1994).

26. F. Wu, R. Tseng, R. Juang, *Water Res.*, **35**, 613 (2001).

27. W. Weber, J. Morris, *J. Sanitery Eng. Div. ASCE*, **89**(SA2), 31 (1963).

28. D. Eley, H. Pines, P. Weisz (eds.), in: Advance in Catalysis and Related Subjects, vol. 21, Academic Press, NY, 1970, p. 1.

29. S. Chien, W. Clayton, *Soil Sci. Soc. Am. J.*, **44,** 265 (1980).

30. V. Srihari, A. Das, *Desalination*, **225**, 220 (2008).

31. S. Goldberg, in: Equations and models describing adsorption processes in soils, Chemical Processes in Soils. Soil Science Society of America, 677 S. Segoe Road, Madison, WI 53711, USA, *SSSA* Book Series, 2005, № 8.

32. E. Voudrias, F. Fytianos, E. Bozani, *Global Nest, The Int. J.,* **4,** 75 (2002).

АДСОРБЦИЯ НА ТИОФЕН И НЕГОВИ АРОМАТНИ ПРОИЗВОДНИ ОТ МОДЕЛНО ГОРИВО ВЪРХУ ПИРОЛИЗИРАНИ ОРИЗОВИ ЛЮСПИ: КИНЕТИКА И РАВНОВЕСИЕ

С. А. Узунова[1], И. М. Узунов[2]*, И. Р. Иванов[1], Д. Б. Ангелова[1]

[1] Химикотехнологичен и металургичен университет, бул. „Кл. Охридски" № 8, 1756 София, България
[2] Институт по обща и неорганична химия, БАН, ул. „Акад. Г. Бончев", бл. 11, 1113 София, България

(Резюме)

Изследвано е адсорбционното десулфуриране на горива чрез използване на моделно гориво, съдържащо смес от тиофен, бензотиофен и дибензотиофен при изходно общо съдържание на сяра (S_{in}) 415, 218 и 111 wppm с пиролизирани оризови люспи (ПОЛ) в статични условия. Общото съдържание на сяра в разтвора беше определено чрез рентгенов-флуоресцентен анализ. Кинетиката на процеса бе определена чрез използване на уравнение от втори порядък, дифузионен модел и уравнението на Елович. Установено е, че кинетичният модел от втори порядък описва адекватно адсорбцията на трите серни съединения върху пиролизирани оризови люспи. Това уравнение осигурява и най-добро съвпадение между пресметнатите и експериментално определени стойности на адсорбционния капацитет. Разликата между тях варира от 1.3% при S_{in} 111 ppm до 5.9% за S_{in} 415 ppm. Адсорбционният афинитет на трите серни съединения, както и равновесният адсорбционен капацитет на пиролизирани оризови люспи, бяха определени чрез снемане на адсорбционна изотерма. Опитните данни бяха анализирани чрез използване на изотермите на Лангмюр, Фройндлих и Тьомкин. Данни от регресионния анализ показаха, че изотермата на Фройндлих най-адекватно описва адсорбционното равновесие на полиароматните серни хетеро-циклични съединения в системата гориво/ПОЛ.

Study of Fe₃Mo₃N catalyst for ammonia decomposition

S. F. Zaman*, L. A. Jolaloso, A. A. Al-Zahrani, Y. A. Alhamed, S. Podila, H. Driss, M. A. Daous, L. A. Petrov

Chemical and Materials Engineering Department, Faculty of Engineering, King Abdulaziz University, P.O. Box 80204, Jeddah 21589, Saudi Arabia

A novel synthesis route, using citric acid as a chelating agent, for the preparation of high surface area γ-Mo₂N and Fe₃Mo₃N bulk samples and their application as catalysts for hydrogen production *via* NH₃ decomposition reaction were investigated. Successful formation of high surface area pure bulk phase of Fe₃Mo₃N (S_{BET} = 24.9 m^2 g^{-1}) was confirmed by using XRD, XPS, SEM-EDX, and HRTEM techniques. The Fe₃Mo₃N catalyst showed moderate catalytic activity for ammonia decomposition reaction. It demonstrates 100% conversion of NH₃ at 600 °C at 6000 h^{-1} GHSV. At lower reaction temperatures the Fe₃Mo₃N catalyst has higher catalytic activity than γ-Mo₂N.

Key words: Ammonia decomposition, γ-Mo₂N, Fe₃Mo₃N, Citric acid, Chelating agentл

INTRODUCTION

The high level of environmental pollution and the craving for alternative sustainable clean energy sources is currently a global issue. Hydrogen is a potential alternative fuel due to CO_x-free emissions and its versatility as an energy carrier. Hydrogen has been used as the primary energy source for internal combustion engines or for fuel cells. The problem of using hydrogen as a transportation fuel arises due to the difficulties for finding a proper hydrogen storage system, i.e. as compressed gas or in cryogenic form. Researchers intensively are looking for a suitable hydrogen storage material with high hydrogen density and mild release conditions, which can be safely used in transportation vehicles.

Ammonia, whose synthesis is well matured and in worldwide commercial practice, has been considered as a potential source for the production of hydrogen free of CO_x. NH₃ molecule contains 17.2 wt.% H₂ and agrees with the DOE's criteria to be considered as a commercialisable hydrogen storage material for fuel cell driven transportation vehicles. The cracking of NH₃, an endothermic reaction, must be pursued via a heterogeneous catalytic route. Big number of materials has been tested as catalysts for ammonia decomposition. Unfortunately, ruthenium has been reported to be the most active catalyst [1]. For a short period of time the efforts of the researchers were focused on the ruthenium-based catalysts for ammonia decomposition but considering the cost benefit, the bulk price of ruthenium, which is 50000 times higher than that of iron, thereby calls for the need to develop cheap transition metals-based catalysts with high catalytic performance [2].

Iron is one of the early studied transition metals extensively studied as a catalyst for the decomposition of ammonia reaction for better understanding of ammonia synthesis kinetics over iron based catalysts [3,4]. Very few investigations on iron catalysts for the decomposition of ammonia were reported due to its much smaller activity and stability in contrast to the ruthenium catalysts. This was related to the very strong iron-nitrogen interaction unlike the ruthenium-nitrogen interaction [5]. This strong Fe-N₂ interaction leads to formation subnitrides (stable nitrides) or even bulk nitrides, which were considered in the early studies to be the inhibitors for the ammonia decomposition reaction and eventually deactivating of the catalysts [6–8]. The ammonia decomposition kinetic study reviles that the rate limiting step is the associative desorption of nitrogen over Fe based catalysts [7]. The kinetics follows a Temkin–Pyzhev type rate equation [9].

In this study, we are presenting results of investigation of hydrogen production via ammonia decomposition reaction over high surface area bulk γ-Mo₂N and Fe₃Mo₃N (pure phase) catalysts. Catalysts were prepared using sol-gel method, i.e. using citric acid as a chelating agent. The prepared catalysts were properly characterized using BET, XRD, XPS, SEM-EDX and HRTEM techniques to identify the textural and chemical properties of the prepared catalyst samples.

---

* To whom all correspondence should be sent
E-mail: zfsharif@gmail.com; sfzaman@kau.edu.sa

EXPERIMENTAL

Used chemicals and methods for catalysts preparation

Ammonium heptamolybdate $(NH_4)_6Mo_7O_{24}.4H_2O$, purity $\geq$ 99.9%, was received from Fluka Chemical Industry. Iron(II) nitrate hexahydrate $Fe(NO_3)_2.6H_2O$, purity $\geq$ 99%, was received from Sigma-Aldrich. Citric acid $C_6H_8O_7$, purity $\geq$ 99%, was received from Techno Pharmchem Industry, Haryana, India. All chemicals were used as obtained.

The sol-gel method using citric acid (CA) as a chelating agent, with molar ratio of CA:Metal = 3, was used to prepare both the γ-Mo$_2$N and Fe$_3$Mo$_3$N catalysts. Fe$_3$Mo$_3$N (3.00 g) was prepared by dissolving a desired amount (3.78 g) of ammonium heptamolybdate $(NH_4)_6Mo_7O_{24}.4H_2O$, $Fe(NO_3)_2$ (8.68 g) and citric acid (24.00 g) in 100 cm^3 of deionized water each in separate beakers. Each beaker was placed on a hotplate at 90 °C and stirred uniformly with the help of magnetic stirrer for 30 min. Fe salt solution was then added to the Mo salt solution drop wise and afterwards followed by drop wise addition of CA. The solution mixture was kept on stirring for 4 hours at 90 °C and then the temperature of the hotplate was increased to 150 °C and waited until the solution was turned into a jelly-like substance. The jelly-like solution was then put in a water-bath at 90 °C and aged for 24 hours. After aging, the sample was dried in an oven at 100 °C for 24 hours. The dried sample was pulverized and calcined at 500 °C for 5 hours in stagnant air. The temperature was established by a ramping rate of 5 °C.min^{-1} to form FeMoO$_4$ precursor. Then the precursor underwent nitridation by ammonia to form the Fe$_3$Mo$_3$N catalyst.

The nitridation reaction was performed *via* temperature programmed reaction in pure ammonia stream. The process was carried out in a packed bed quartz reactor filled with 1 g of the precursor charged in the reactor at room temperature. Then pure argon was flown at a flow rate of 30 cm^3.min^{-1} through the reactor. The temperature was ramped at 10 °C.min^{-1} until it reached 120 °C. Then the gas was changed to pure ammonia at a flow rate of 400 cm^3.min^{-1} and temperature was increased with a 1 °C.min^{-1} ramping rate till it reached 350 °C. After that the temperature ramping rate was changed to 0.5 °C.min^{-1} and temperature was increased till it reached 700 °C. This temperature was maintained for 2 h keeping the ammonia flow unchanged. Then the gas flow was changed to argon at 700 °C and the reactor temperature was cooled down to room temperature at a ramp rate of 30 °C.min^{-1}. After reaching the room temperature, the mixture of O$_2$/Ar

containing 1.0% O$_2$ was flown over the catalyst to create a passivated oxidic layer to protect the catalyst from ambient oxygen prior to its exposure to the atmosphere and subjected to catalyst characterization and activity testing experiments.

For the preparation of 2.0 g of γ-Mo$_2$N catalyst, 3.77 g of ammonium heptamolybdate salt was dissolved in 100 cm^3 deionized water and drop wise addition of CA solution (16.70 g in 100 cm^3 deionized water) in it. Rest of the preparation method follows the similar steps as for Fe$_3$Mo$_3$N catalyst.

Characterization Methods

A Nova 2000 Win32 Quantachrome (USA) apparatus was employed to analyze the BET surface area and pore-size distribution of the prepared samples. Each catalyst was degassed at 200 °C for 2 h under vacuum before conducting the measurement.

The Powder X-ray diffraction (XRD) was performed using an Inel Equinox 1000 power diffractometer equipped with a CPS 180 detector (filtered Mo Kα radiation, 40 kV, 30 mA, spinning sample holder). Powder pattern analysis was processed using Match Crystal Impact software (v.1.11e) for phase identification (using both COD and ICSD database), IMAD-INEL XRD software for Rietveld analysis. Data were collected under the same condition for all the samples under investigation. The scanning range was 0 < 2θ < 120 with a step size of 0.0284° at an approximate counting time of 1 second per step.

The XPS measurements were carried out in an ultra-high vacuum multi-technique surface analysis system (SPECS GmbH, Germany) operating at a base pressure of 10^{-10} bar range. A standard dual anode X-ray source SPECS XR-50 with Mg-Kα (1253.6 eV) was used to irradiate the sample surface with 13.5 kV, 150 W X-ray power and a take-off-angle for electrons at 90° relative to sample surface plane. The high energy resolution or narrow scan spectra were recorded at room temperature with a 180° hemispherical energy analyzer model PHOIBOS-150 and a set of nine channel electron multipliers MCD-9. The analyzer was operated in Fixed Analyzer Transmission (FAT) and medium area lens modes at pass energy of 20 eV, step size of 0.05 eV and dwell time of 0.3 sec. As the standard practice in XPS studies, the adventitious hydrocarbon C1s line at Binding Energy (BE) of 284.6 eV corresponds to C–C bond has been used as BE reference for charge correction.

TEM analyses of all the catalyst samples were performed using a Tecnai G2 F20 Super Twin device at 200 kV with a LaB6 emitter. The

microscope was fully equipped for analytical work with an energy-dispersive X-ray (EDX) detector having an S-UTW imaging. The scanning transmission electron microscopy (STEM) imaging and all analytical work were performed with a probe size of 1 nm^2 resulting in a beam current of about 0.5 nA. The TEM images and selected- diffraction area (SAD) pattern were collected on an Eagle 2K HR 200 kV CCD camera. The HAADF-STEM EDX and CCD line traces were collected fully automatically using the Tecnai G2 user interface and processed with Tecnai Imaging an Analysis (TIA) software version 1.9.162.

Catalytic activity measurements

Catalytic activity tests were performed at atmospheric pressure in a PID Eng&Tech automated reactor system (Spain) using a fixed bed quartz tube reactor with an external diameter of 6.0 mm. The reactor was charged with 0.10 g of catalyst mixed with 0.1 g of quartz beads to increase the reaction contact area and was held at the center of the heating zone of the reactor furnace. Prior to the reaction, catalysts were activated at 500 °C under nitrogen flow for 1 hour. This was followed by reduction with hydrogen for 5 hours and flushing again with N_2 for 1 hour at the same temperature. After catalyst activation, the reactor temperature was reduced to 300 °C and pure ammonia gas (reactant) was introduced into the reactor at GHSV of 6000 h^{-1}. Then, the temperature was increased stepwise by 50 °C at a ramping rate of 10 °C.min^{-1}. The catalytic test experiments were carried out within the temperature range of 300–600 °C. At each temperature, the reaction was carried out until a steady state regime was established, verified by a relative percentage difference of less than 5% for two successive runs of effluent gas analysis. Effluent gas analysis was performed using an online-connected gas chromatography (GC-450 Varian, USA) equipped with a thermal conductivity detector and a 2.0 m long Porapak Q column.

RESULTS AND DISCUSSION

Catalyst Characterization

The textural properties of the freshly prepared γ-Mo₂N and Fe₃Mo₃N catalysts were studied using N₂-physisorption. The obtained isotherms and the pore size distributions for Fe₃Mo₃N and γ-Mo₂N catalyst are shown in Fig. 1. The BET surface area and the pore volume of γ-Mo₂N were 110.0 $m^2.g^{-1}$ and 0.071 $cm^3 g^{-1}$. For Fe₃Mo₃N catalyst they were 24.9 $m^2.g^{-1}$ and 0.033 $cm^3.g^{-1}$, correspondingly. Our preparation method has allowed us obtaining Fe₃Mo₃N samples with eight times larger surface area compared to the method used by Srifa *et al.* [10], in which case they have observed BET surface area 8.8 $m^2.g^{-1}$. The increase in surface area is the result of using CA as a chelating agent in the preparation method used by us. CA presence leads to formation of small micelles of metals far apart from each other and thus upon nitridation forming the micro/mesoporous structure.

XRD was used to analyze and identify the phases and crystallinity of the catalysts. Fig. 2 shows the XRD patterns of freshly prepared γ-Mo₂N and Fe₃Mo₃N catalysts (nitridited and passivated). From the analyzed XRD patterns, γ-Mo₂N and MoO₂ phases were registered in the bulk γ-Mo₂N sample. The Mo₂N catalyst had mixed phase of γ-Mo₂N with diffraction peaks (ICSD no. 158843 at 2θ = 43.72, 50.95, 91.00, and 96.27°) and MoO₂ with peaks (ICSD no. 80830 at 2θ = 30.35, 43.31, 63.09, 63.17, 71.29, and 79.36°). The oxidic phase (MoO₂) may arise from the reaction with oxygen present in the atmosphere and also while passivating of the catalysts.

For Fe₃Mo₃N catalyst, only the pure phase of Fe₃Mo₃N (PDF# 01-089-4564) was recorded. No other oxidic or separate Mo or Mo nitride phase was detected as also reported by previous researchers [10,11]. Fig. 2 shows the XRD patterns of fresh and spent γ-Mo₂N and Fe₃Mo₃N catalysts. There are no considerable changes in the structure of Fe₃Mo₃N catalyst except broadening and or increase of the intensity of peaks at some points suggesting that crystallite growth took place in the spent catalyst.

The XPS analysis was done for the freshly prepared nitride catalysts to gain insight view into the oxidation states at the catalyst surface. The XPS spectra for Mo3d region of γ-Mo₂N and Fe₃Mo₃N are shown in Fig. 3a and 3b. The Binding Energies (BE) are tabulated in Table 1. The predominant Mo oxidation states in the γ-Mo₂N catalyst were the Mo^{2+} and/or $Mo^{\delta+}$ which is similar to what was reported by Podila *et al.* [12]. There was also the detection of Mo^{4+} and Mo^{6+} oxidation states in the 3d region. Previous reports [13–15] showed that Mo^{2+} and $Mo^{\delta+}$ oxidation states represent molybdenum nitride. The Mo^{4+} state correspond to MoO_2 while the Mo^{6+} depicts the oxidized form of γ-Mo₂N phase. The piroforic nature of γ-Mo₂N require the sample passivation with 1% O_2/Ar mixture to form a protective layer for the bulk catalyst before it is exposed to the oxygen in the atmosphere for the activity testing and characterization tests, which will inevitably lead to formation MoO_2 phase due to reaction with oxygen.
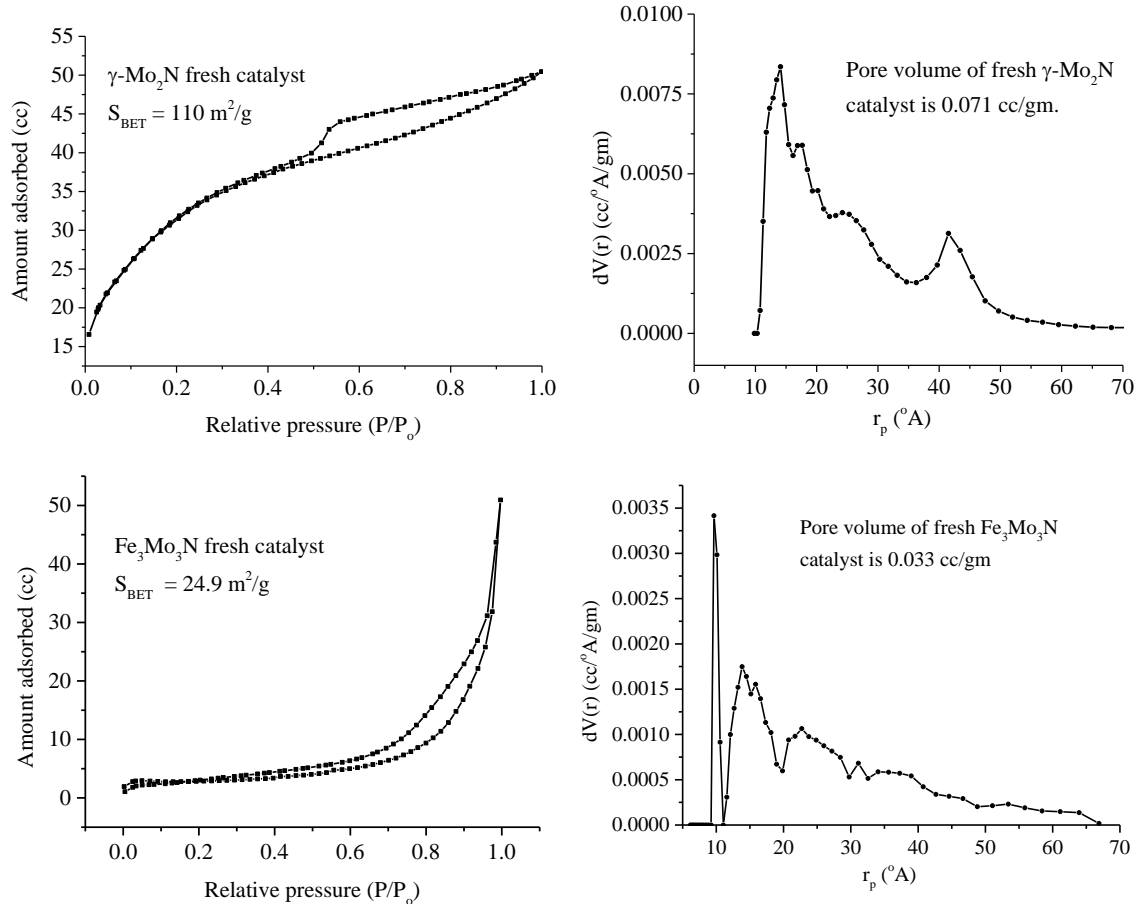
Fig. 1. BET and pore size distribution of γ-Mo$_2$N and Fe$_3$Mo$_3$N catalysts.
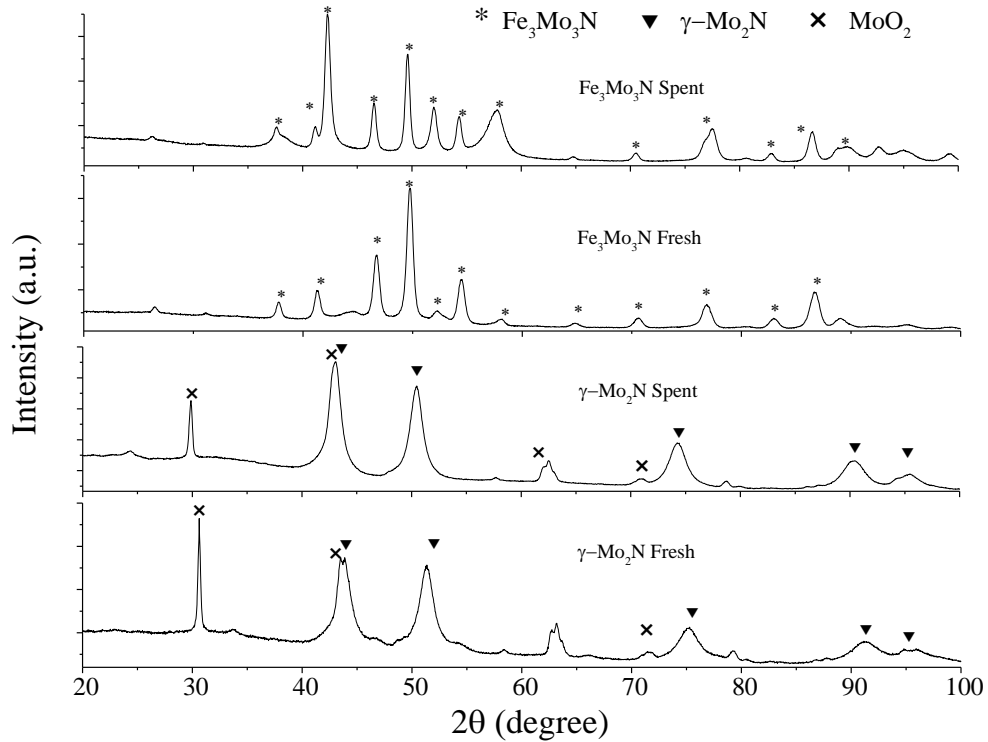
Fig. 2. XRD pattern of fresh and spent Fe$_3$Mo$_3$N and fresh Mo$_2$N catalysts.

For the Mo3d XPS spectra of Fe$_3$Mo$_3$N (Fig. 3b) showed typical mixed oxidation state of molybdenum. Higher oxidation states Mo^{5+} and Mo^{6+} are more pronounced compared to γ-Mo$_2$N sample. The deconvoluted peaks for Mo3d$_{3/2}$ positioned at BE of 227.2, 228.33, and 230.83 eV correspond to Mo^0, Mo$^{+2/\delta}$ and Mo^{+4} oxidation states [16]. According to Perret *et al.* [17] the peak with lower BE of 228.33 eV corresponds to the presence Mo^{+2} ions which represents Fe$_3$Mo$_3$N phase and similar conclusion was also drawn by Hada *et al.* [14]. Fig. 3c (values tabulated in Table 1) shows the Fe2p XPS spectral region, which has a notably split spin-orbit components with a range of 15 eV. The BE of 706.8, 708.23, 709.97, and 711.41 eV are assigned for Fe^0, Fe$_3$O$_4$ (Fe$^{+2/+3}$), FeO (Fe^{+2}) and Fe$_2$O$_3$(Fe^{+3}) oxidation states respectively. The ratio of areas of FeO and Fe$_2$O$_3$ oxidation state signals is 1:1, which might have resulted in the formation of highly dispersed Fe$_3$Mo$_3$N. The dominant phase occurs at BE of 709.97 eV and is due to possible presence of iron in trivalent state, i.e. Fe$_2$O$_3$.

Table 1. Comparison of the oxidation state of Mo3d with their BE for Fe$_3$Mo$_3$N and Mo$_2$N catalysts.

Oxidation state	Mo BE of catalysts, eV					
	Fe$_{23}$Mo$_3$N		γ-Mo$_2$N		Fe2p$_{3/2}$	
	3d$_{3/2}$	3d$_{5/2}$	3d$_{3/2}$	3d$_{5/2}$	Oxidation state	2p$_{3/2}$
Mo^0	230.9	227.8	x	x	x	x
Mo^{2+}	x	x	231.59	228.44	x	x
Mo$^{\delta+}$	231.85	228.75	232.39	229.39	Fe^0	706.8
Mo^{4+}	233.54	230.44	234.01	230.68	Fe^{2+}	709.97
Mo^{5+}	235.04	231.94	x	x	Fe$^{2+/3+}$	708.23
Mo^{6+}	236.34	233.24	235.23	232.61	Fe^{3+}	711.41

SEM-EDS analysis for Fe$_3$Mo$_3$N catalyst are shown in Fig. 4. EDX elemental analysis showed that the atomic ratio of Fe:Mo is ~1.17. The results suggest the possible formation of Fe-Mo-N species by the chemical interaction of molybdenum nitride with Fe species.
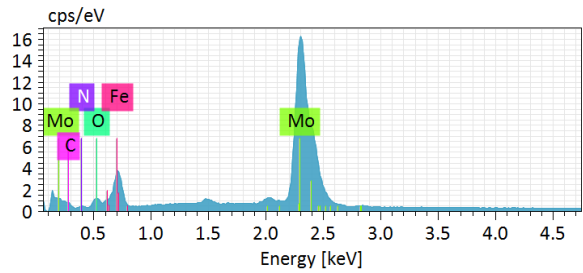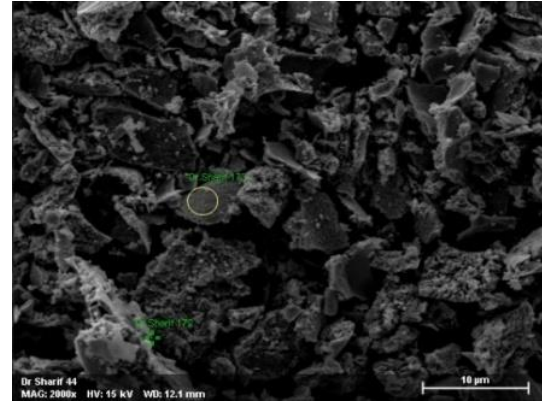
Fig. 4. SEM-EDX analysis of Fe$_3$Mo$_3$N catalyst.

HRTEM and selected-area electron diffraction (SAED) pictures of Fe$_3$Mo$_3$N are shown in the Fig. 5. The nanodomain of the Fe$_3$Mo$_3$N with an average particle size of 5 nm was clearly seen. The selected-area electron diffraction (SAED) pattern of a small representative of Fe$_3$Mo$_3$N particle is shown in the bright-field image confirms the existence of (511), (400), (311), and (331) planes, which are belonging to Fe$_3$Mo$_3$N. The average particle size of Fe$_3$Mo$_3$N measured by HRTEM is 5 nm which is close to the average crystallite size measurement (5.5 nm) using XRD (Mo kα = 0.71 Å) half width data in Scherrer equation.

Fig. 3. XPS spectra: a - Mo3d of γ-Mo$_2$N; b - Mo3d of Fe$_3$Mo$_3$N; c - Fe2p of Fe$_3$Mo$_3$N.
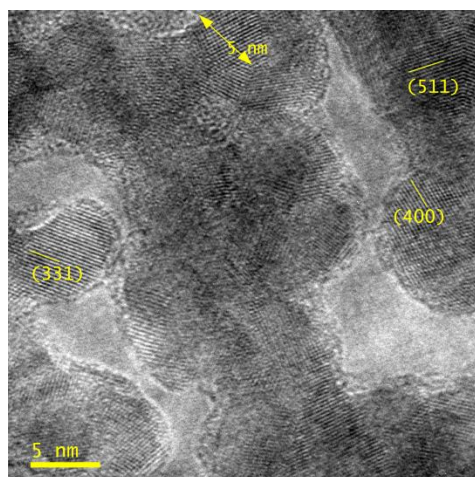
HRTEM image
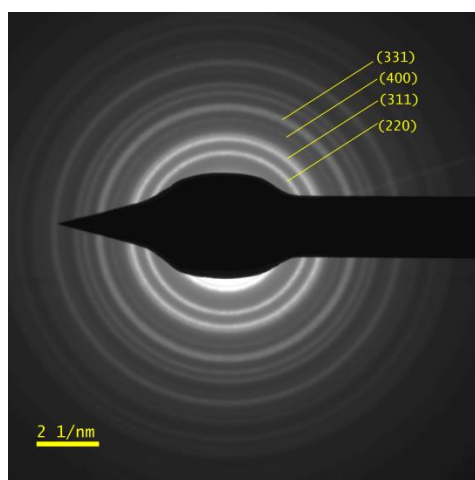
SADE image

Fig. 5. HRTEM and SADE image of Fe_3Mo_3N.

Catalytic activity measurements

The catalytic activity for ammonia decomposition reaction of γ-Mo_2N and Fe_3Mo_3N catalysts was investigated at GHSV of 6000 h^{-1} as a function of temperature at atmospheric pressure. The obtained results are depicted in Fig. 6a. Ammonia decomposition, being an endothermic reaction, showed an increase of ammonia conversion with the increase of temperature. A sharp rise in NH_3 conversion at the beginning of the reaction at 300 °C was observed for Fe_3Mo_3N catalyst, which was not noticed for γ-Mo_2N sample until the reaction temperature reached above 450 °C. At 550 °C the recorded NH_3 conversion over Fe_3Mo_3N, was 78.2%, which is a little better conversion when compared to that reported by Srifa *et al*. [10] at the same temperature and space velocity. On the other hand, at this temperature, γ-Mo_2N catalysts gave only 71.9% conversion. Table 2 shows the experimental data for some previously reported catalysts and the results obtained in this work at 550 °C. The conversion of

ammonia at 600 °C on both the Fe_3Mo_3N and γ-Mo_2N catalysts showed approximately equal value with 97.1% and 97.9% NH_3 conversion, respectively. The better results observed in our work might be attributed to the sol-gel preparation method using a chelating agent which gave higher surface area.

Table 2. Activation Energies and NH_3 conversions on different catalysts at 550 °C and GHSV 6000 h^{-1}.

Catalyst	Ammonia conversion, %	Activation energy Ea, kJ mol^{-1}	Ref.
Fe_3Mo_3N	78.2	72.9	This work
Fe_3Mo_3N	75.1	88.9	11
γ-Mo_2N	69.2	97.4	11
γ-Mo_2N	71.9	131.3	This work

Experimental results of catalytic activity tests of Fe_3Mo_3N catalyst especially at lower temperatures showed that this catalyst had higher activity compared to γ-Mo_2N catalyst which was an indirect indication that the reaction was actually promoted by the addition of Fe as a catalyst component. Consequently, we can come to the conclusion that adding Fe in the molybdenum nitride structure is the key reason for obtaining the high activity for ammonia decomposition reaction. This effect was connected with lowering the nitrogen association energy over the catalyst induced by the electronic distribution disruption of γ-Mo_2N by the addition of Fe. Also at lower temperatures below 500 °C nitrogen association on the surface is the rate limiting step for the NH_3 decomposition reaction as evidenced by kinetic and DFT investigation of several researchers proposing the following rate equation a for NH_3 decomposition:

$$r_{decomposition} = \frac{P_{NH3}^2}{P_{H2}^3 P_{N2} K_{eq}} r_{synthesis} \ [18].$$

Dissociative adsorption of N_2 over Fe based catalyst hindered the ammonia decomposition reaction, whereas Fe modified with Mo and N in the structure enhances the reaction at temperatures about 300 °C suggesting N_2 association is promoted with this structure configuration, i.e. the recombination of N_2 atoms were performed over Fe-Mo-N sites. More experimental evidence is required to confirm the above observation. On the other hand, Srifa *et al*. [10] also reported the decrease in N_2 association energy over $(TM)_xMo_3N$ (TM = Fe, Co, Ni) surfaces compared to Mo_2N surface, which may attribute to the high activity of these bimetallic nitrides compared to γ-Mo_2N for this reaction. This is also in agreement with our observation.

With the increase of temperature higher than 550 °C the inhibition of activity comes from hydrogen

association over the surface (N_2 recombination is no longer a rate limiting step), a well-known phenomenon known as hydrogen poisoning, being the rate limiting step and the two catalysts behave in almost the same way. This is evidenced by kinetic studies conducted by several researchers over different catalysts including Fe based catalysts [7] where ammonia decomposition rate is a function of NH_3 partial pressure of and H_2 only.

The relationship plot of the degree of NH_3 conversion versus temperature for Fe_3Mo_3N and γ-Mo_2N catalysts (Arrhenius plot) is depicted in Fig. 6b. γ-Mo_2N has higher activation energy of 131.29 $kJ.mol^{-1}$ compared to Fe_3Mo_3N, for which the activation barrier drastically reduced to 72.88 $kJ.mol^{-1}$. This may be the main reason for the high activity of Fe_3Mo_3N. Srifa *et al*. [10] reported. The activation energy of 88.9 $kJ.mol^{-1}$ for Fe_3Mo_3N, which is little higher compared to what we have attained.
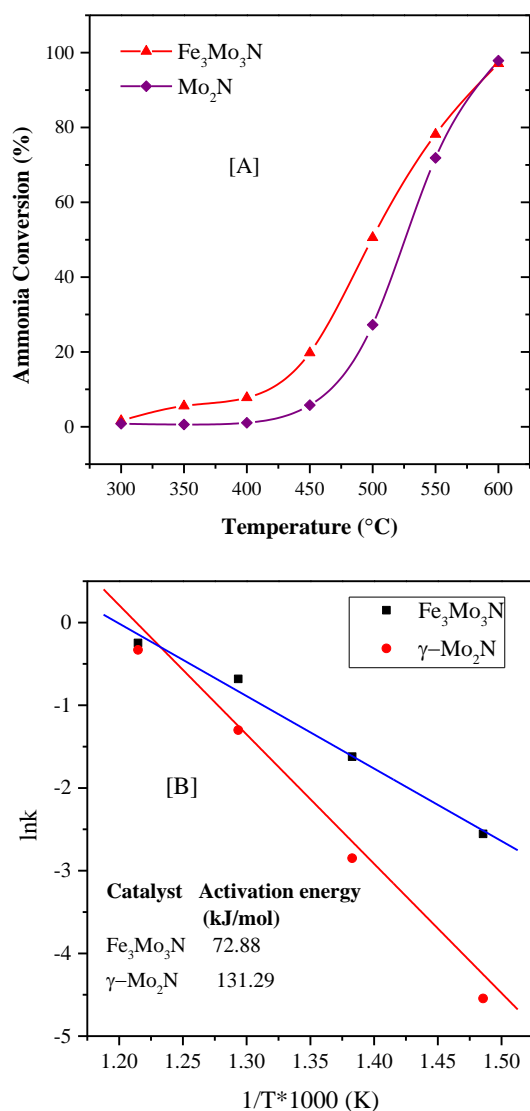
Fig. 6. Catalytic activities (A) and Arrhenius plots (B) of Fe₃Mo₃N and γ-Mo₂N catalysts.

CONCLUSIONS

Ammonia decomposition reaction was investigated using γ-Mo_2N and Fe_3Mo_3N catalysts which were successfully prepared by using sol-gel method and citric acid as a chelating agent. Pure Fe_3Mo_3N phase was successfully obtained from this method of preparation and gave a high surface area of 24.9 m^2g^{-1}. The catalytic activity of this sample was higher compared to catalytic activity of γ-Mo_2N at temperatures below 600 °C.

REFERENCES

1. H. Muroyama, C. Saburi, T. Matsui, K. Eguchi, *Appl. Catal. A:Gen.,* **443-444**, 119 (2012)
2. L. Li, Z. H. Zhu, Z. F. Yan, G. Q. Lu, L. Rintoul, *Appl. Catal. A:Gen.,* **320**, 166 (2007).
3. K. S. Love, P. H. Emmett, *J. Am. Chem. Soc.*, **63**, 3297 (1941).
4. S. Dannstadt, Ullmann's Encyclopedia of Industrial Chemistry, Wiley, Weinheim, 2000.
5. R. Schlögl, Ammonia Synthesis, in: Handbook of Heterogeneous Catalysis, G. Ertl, H. Knozinger, F. Schuth, J. Weitkamp, Eds., Wiley-VCH Verlag GmbH & Co. KGaA, 2008
6. A. Mittasch, W. Frankenburg, Early Studies of Multicomponent Catalysts, in: Advances in Catalysis, vol. 2, V. I. Komarewsky, W. G. Frankenburg, E. K. Rideal, Eds., Academic Press, 1950, p. 81–104.
7. T. E. Bell, L. Torrent-Murciano, *Top. Catal.,* **59** 1438 (2016).
8. W. Zheng, Nanomaterials for Ammonia Decomposition, PhD Thesis, Universität Berlin, 2011.
9. W. Arabczyk, J. Zamlynny, *Catal. Lett.,* **60**, 167 (1999).
10. A. Srifa, K. Okura, T. Okanishi, H. Muroyama, T. Matsui, K. Eguchi, C*atal. Sci. Technol.,* **6**, 7495 (2016).
11. J. H. S. Hargreaves, D. McKay, *J. Mol. Catal. A: Chem.*, **350**, 125 (2009).
12. S. Podila, S. F. Zaman**,** H. Driss, Y. A. Alhamed, A. A. Al-Zahrani, M. A. Daous, L. A. Petrov, *Int. J. Hydrogen Energy,* **42,** 8006 (2017)
13. S. Podila, S. F. Zaman, H. Driss, Y. Alhamed, A. A Al-Zahrani, L. A. Petrov, *Catal. Sci. Technol.,* **6,** 1496 (2016)
14. K. Hada, M. Nagai, S. Omi, *J. Phys. Chem. B,* **105,** 4084 (2001).
15. L. A. Jolaoso, S. F. Zaman, S. Podila, H. Driss, A. A. Al-Zahrani, M. A. Daous, L. Petrov, *Int. J. Hydrogen Energy*, DOI: 10.1016/j.ijhydene.2018.01.092, (2018).
16. C. Castillo, G. Buono-core, C. Manzur, N. Yutronic, R. Sierpe, G. Cabello, B. Chornik, *J. Chil. Chem.*

Soc., **61,** 2816 (2016).

17. N. Perret, A. Alexander, S. T. Hunter, P. Chung, J. S. J. Hargreaves, R. F. Howe, M. A. Keane, *Appl.*

Catal. A: Gen., **488,** 128 (2014).

A. Boisen, S. Dahl, J. K. Nørskov, C. H. Christensen, *J. Catal*., **230,** 309 (2005)..

ИЗСЛЕДВАНЕ НА КАТАЛИЗАТОР Fe₃Mo₃N ЗА РАЗЛАГАНЕ НА АМОНЯК

Ш. Ф. Заман*, Л. А. Жолалозо, А. А. Ал-Захрани, Я. А. Алхамед, С. Подила, Х. Идрис, М. А. Даус, Л. Петров

Департамент по химично инженерство и материалознание, Инженерен факултет, Университет „Крал Абдулазис“, п.к. 80204, 21589 Джеда, Саудитска Арабия

(Резюме)

Предложен е нов метод за синтез на масивни γ-Mo₂N и Fe₃Mo₃N образци с висока специфична повърхност при използване на хелати. Получените катализатори са изследвани в реакцията на разлагане на амоняк с цел получаване на чист водород без съдържание на CO. Получаването на образец Fe₃Mo₃N ($S_{BET} = 24.9$ $m^2.g^{-1}$) с висока специфична повърхност е потвърдено чрез използването на XRD, XPS, SEM-EDX, и HRTEM методи. Катализаторът притежава добра активност. При 600 °C и GHSV 6000 h^{-1} конверсията на амоняк достига 100%. При по ниски температури катализатор Fe₃Mo₃N е по- активен от γ-Mo₂N.

DRIFT study of the mechanism of methanol synthesis from CO_2 and H_2 on CeO_2-supported CaPdZn catalyst

A. S. Malik, S. F. Zaman*, A. A. Al-Zahrani, M. A. Daous, H. Driss, L. A. Petrov

Chemical and Materials Engineering Department, Faculty of Engineering, King Abdulaziz University, P.O. Box 80204, Jeddah 21589, Saudi Arabia

This article reports results of mechanistic DRIFTS study of methanol synthesis from CO_2 and H_2 on CaPdZn/CeO_2 catalyst. The catalyst exhibited superior catalytic performance with ~100% selectivity to methanol and 7.7% conversion of CO_2 at 30 bar and 220 °C. In situ DRIFTS measurements were carried out under experimental conditions and the presence of various surface reaction intermediate species and their subsequent conversion to methanol were carefully monitored. The catalyst was characterised by BET, CO chemisorption, CO_2-TPD, and HRTEM to evaluate the physiochemical properties and structure morphology of fresh and spent samples. DRIFTS investigation confirmed the formation of mono- and bidentate formates, CH_2O, and CH_3O intermediate species suggesting that the reaction mechanism follows formate pathway for the synthesis of methanol from CO_2 hydrogenation over CaPdZn/CeO_2.

Key words: CO_2 hydrogenation, methanol, CaPdZn/CeO_2 catalyst, DRIFTS, reaction mechanism.

INTRODUCTION

Carbon dioxide utilisation as a feedstock for industrial production of valuable chemicals has recently been involved as an active area of catalysis research. The utilisation of CO_2 was addressing the possible solution of critical issues like global warming, depleting of high quality fossil fuel sources, and availability of a cheap and abundant CO_2 raw material for the synthesis of different chemical products [1,2]. Carbon dioxide hydrogenation to methanol is the most viable route for application of the former. Methanol serves as an excellent energy storage material alternative to traditional fossil fuels as well as a fuel for direct methanol fuel cell [3–5].

Palladium-based catalysts have exhibited superior catalytic performance in recent years, especially in the reaction of methanol synthesis from CO_2 and H_2 [6–9]. The properties of these catalysts are strongly influenced by preparation method [10–12] and catalyst reduction procedure [7,8,12,13] as well as by type of support [14–17] and promoter [18,19]. Synergic effects and chemistry of the strong metal support and metal-metal interaction of Pd and ZnO have also been widely studied. Pd/ZnO system appeared to be highly active towards methanol formation from CO_2 [6–9,12,14,20]. The observed high catalytic activity of this system is associated mainly with the formation of PdZn bimetallic alloy, which was formed due to electrons transfer from Pd to ZnO at elevated temperatures over 500 °C of catalyst reduction [6–9,12].

In the present study, we report results of DRIFTS study of methanol synthesis from CO_2 and H_2 on CaPdZn/CeO_2 catalyst. A reaction mechanism was proposed based on evidences obtained from spectroscopic registration of the formation of various intermediate species over the catalyst surface during the reaction of methanol synthesis from CO_2 and H_2.

The catalyst was prepared by the chelating method employing citric acid as a chelating agent. This method was previously used for synthesising nanosized high surface area CeO_2 particles. The citric acid was used as a chelating agent for its well-known positive contribution in controlling the morphology of the metal particles size and useful assistance to avoid sintering of synthesized nano-materials [21–23].

EXPERIMENTAL

Catalyst preparation

A typical preparation procedure of 2.0 g of CaPdZn/CeO_2 sample is presented in the following lines.

Needed amounts of desired catalyst component salts were dissolved in separate beakers containing 30 cm^3 deionised water, i.e. 0.2165 g of Pd (palladium(II) nitrate hydrate ≥99.9%-metal basis, Alfa Aesar), 0.4549 g of Zn (zinc nitrate hexahydrate ≥98%, Aldrich Chemical Company), 0.059 g of Ca (calcium nitrate tetrahydrate, Techno Pharmchem

* To whom all correspondence should be sent
E-mail: zfsharif@gmail.com; sfzaman@kau.edu.sa

≥99.0%), and 4.516 g of Ce (cerium(III) nitrate hexahydrate ≥99.0%, Fluka Analytical).

An aqueous solution of 8.2702 g citric acid (≥99%, Techno Pharmchem, India) at a 1:3 molar ratio of metal ion (Pd, Zn, Ca and Ce) present in a particular catalyst sample to citric acid, was added dropwise into Ce salt solution and heated at 50 °C for 15 min under continuous stirring. Later, Pd, Zn, and Ca salt solutions were added dropwise into the mixture of Ce salt and citric acid and heated at 90 °C for 6 h until a brownish yellow gel-like mixture was formed. The resulting mixed gel was aged for 24 h at 90 °C in a water bath and later placed into an oven for 18 h at 110 °C resulting in a completely dried solid residue. Afterwards, it was crushed into powder and calcined in dry air at 300 °C for 2 h and then at 500 °C for 3 h.

Catalyst characterisation

BET surface area and pore size distribution were analysed by N_2 adsorption-desorption method at liquid nitrogen temperature with N_2 as adsorbate. NOVA 2200e (Surface area & Pore size Analyzer, Quantachrome Instruments) apparatus was used. Before each analysis, samples were dried at 300 °C for 2 h under vacuum.

X-ray diffraction patterns were collected in order to identify the crystal phases contained in the calcined, passivated, and spent samples. An Equinox 1000 (Inel, France) XRD equipment (Co Kα = 1.789 Å X-ray source and generator settings: 30 kV, 30 mA) with the real-time acquisition in 2θ range of 0–110° for 7200 s were used for these measurements.

H_2-TPR experiments were conducted to study the reduction behaviour of the calcined catalysts using Pulsar automated chemisorption analyser (Quantachrome Instruments). In general, 0.1 g of sample was loaded into U-type quartz reactor. Then the temperature was raised and maintained at 120 °C under helium flow for 1 h to remove any entrapped moisture. After cooling the sample back to 40 °C, a 5% H_2 in N_2 mixture was introduced at 15 cm^{3}min^{-1} and the temperature was linearly raised to 800 °C at a 5 °Cmin^{-1} ramping rate. A TCD detector was used to analyse the effluent stream.

CO_2-TPD measurements were employed to examine catalyst sample basicity using Pulsar automated chemisorption analyser (Quantachrome Instruments). Prior to CO_2 adsorption, catalyst samples (0.1 g each) were first reduced at 550 °C under H_2 flow (20 cm^{3}min^{-1}) for 1 h and then brought to room temperature under He flushing (15 cm^{3}min^{-1}) for 2 h. The reduced samples were then saturated with 15% CO_2/N_2 mixture (20 cm^{3}min^{-1}) for 1 h. Afterwards, TPD analysis was prompted at a heating rate of 10 °C/min under He flow (15 cm^{3}min^{-1}n) and desorbed amount of CO_2 was detected by a mass spectrometer. The amount of desorbed CO_2 was calculated by comparing the integrated peak area of CO_2-TPD curve to the area of the CO_2 calibration pulse.

In order to understand and identify the intermediate species and general reaction mechanism, in situ IR spectra were recorded on a Tensor II FTIR spectrometer (Bruker) installed with DRIFT accessories, Harrick praying mantis, and zinc selenide window capable of achieving pressure up to 40 bar. In general, 0.1 g of calcined sample was placed in the IR cell and reduced at 550 °C under H_2 flow (20 cm^{3}min^{-1}) for 1 h. Subsequently, the temperature was lowered back to 230 °C under Ar flow (15 mlmin^{-1}) and a background IR spectrum was recorded after 3 h of Ar flushing of the reaction chamber at reaction temperature. Then, CO_2 and H_2 mixture flow (20 cm^{3}min^{-1}) was introduced with an applied pressure of 30 bar. Totally 91 DRIFT spectra were collected for 3 h at 2 min time interval. Each spectrum was an average of 100 scans at 4 cm^{-1} resolution.

To investigate the catalyst structure and morphology at nanoscale, HRTEM and EDX analyses of freshly reduced CaPdZn/CeO$_2$ catalyst were also performed employing a 200 kV D1234 Super Twin microscope (Technai, Netherlands).

Catalytic activity tests

Activity tests of CaPdZn/CeO$_2$ catalysts were carried out in a MA-Effi reactor (PID Eng & Tech, Spain) equipped with Bronkhorst mass flow controllers and temperature sensors and controllers. A reaction mixture at a flow rate of 20 cm^{3}min^{-1} and pressure of 30 bar and composition of CO_2:H_2 = 1:3 was used. The reactor was charged with 0.5 g of catalyst. Prior to each test, the sample was reduced *in situ* at 550 °C with 20 cm^{3}min^{-1} H_2 gas flow for one hour at atmospheric pressure.

The reaction products were analysed using an Agilent 7890 A gas chromatograph equipped with a TCD detector with HayeSep Q packed column for CO_2, CO, and CH_4 analysis and a FID detector with HP-Pona capillary column (19091S-001E) for methanol and higher hydrocarbons analysis. Reported data on conversion and selectivity were obtained by an average of three independent readings with an error range of ±3% taken after 3 h of reaction run. CO_2 conversion and selectivity of products were defined as follows:

$$CO_2 conv = \frac{(Moles\ CO_{2\ in} - Moles\ CO_{2\ out}) \times 100}{Moles\ CO_{2\ out}}, \% \quad (1)$$

$$CH_3OH\ sel = \frac{Moles\ CH_3OH \times 100}{Moles\ (CH_3OH + CO + CH_4)\ in\ product\ stream}, \% \quad (2)$$

190

RESULTS AND DISCUSSION

Structural properties and catalytic performance

Figure 1 shows XRD profiles of calcined and reduced CaPdZn/CeO_2 samples. Diffraction peaks for CeO_2 phase [PDF 00-034-0394] were observed at 2θ= 33.28, 38.61, 55.74, 66.48, 69.86, 82.77, 92.19, 95.32, 108.13, 118.38, 138.48, 155.87, and 165.31° for calcined and reduced CaPdZn/CeO_2 sample. For reduced CaPdZn/CeO_2 sample, intense peaks at 2θ = 48.19 and 51.74° were detected reflecting the presence of PdZn alloy phase with (111) and (200) crystal planes [PDF 03-065-9523]. This confirms the formation PdZn alloy phase as shown in figure 1. At a higher reduction temperature (>500 °C), metal-to-metal interaction causes the transfer of electrons between metallic palladium and ZnO, hence forming the PdZn-bimetallic alloy. Several previous studies asserted that PdZn alloy phase served as the catalytically active phase for con-verting CO_2 to methanol [6–8, 20].
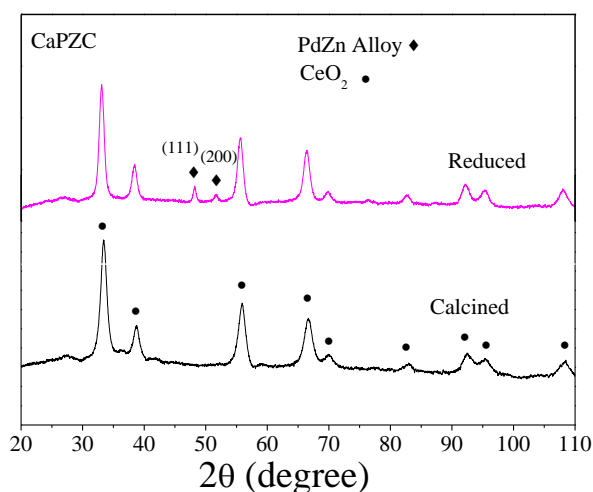
Fig. 1. XRD profile of calcined and reduced CaPdZn/CeO_2 catalyst.

Table 1 lists the physiochemical data and catalytic performance of ceria carrier and CaPdZn/CeO_2 catalyst. Catalyst surface area was 67 m^{2}g^{-1}, being much higher compared to the support CeO_2 which had a surface area of 52 m^{2}g^{-1}.

Table 1. Textural and catalytic properties of the CaPdZn/CeO_2 and CeO_2

Catalyst	Surface area S_{BET} m^2/g	Pd Dispersion %	Desorbed CO_2 μmole/g$_{cat}$	CO_2 conversion %	CH_3OH Selectivity %
CaPdZn/CeO_2	67	7.6	88.0	7.7	100.0
CeO_2	52	-	42.0	-	-

The increase of surface area with the insertion of various metals over CeO_2 support might be attributed to the chelating preparation procedure. Basicity of the CaPdZn/CeO_2 sample was also enhanced as the desorbed amount of CO_2 from the catalyst (88 μmolg$_{cat}^{-1}$) was much larger than the amount of CO_2 desorbed from catalyst support, CeO_2 (42 μmolg$_{cat}^{-1}$).

Figure 2 displays a HRTEM image of reduced CaPdZn/CeO_2 sample. PdZn alloy particles, formed at high temperature reduction, were well dispersed and uniformly distributed over CeO_2 support which was confirmed by HRTEM. Figure 3 illustrates the EDS image of reduced CaPdZn/CeO_2 catalyst enlisting elemental composition of Pd, Ce, Zn, and Ca, which agrees with the amounts used for catalyst synthesis.
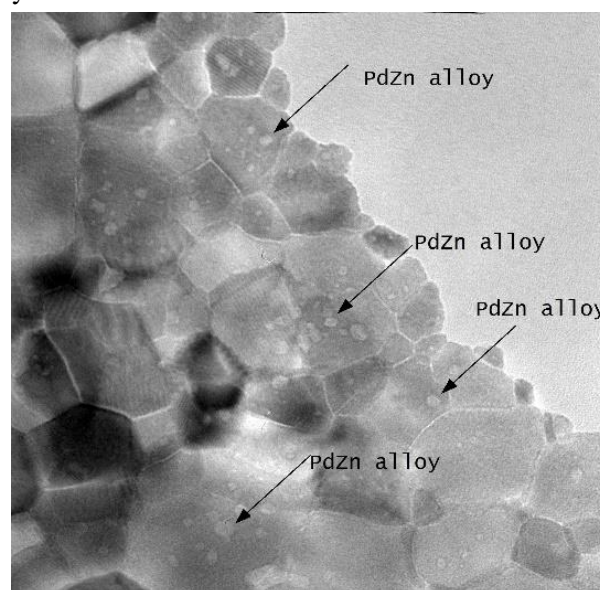
Fig. 2. HRTEM image of reduced CaPdZn/CeO_2 catalyst.
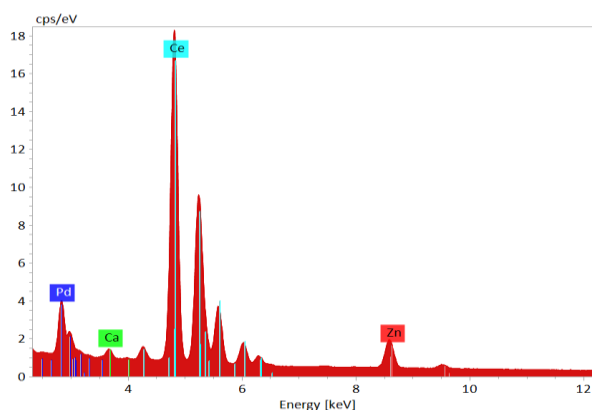
Fig. 3. EDS of reduced CaPdZn/CeO_2 catalyst. (Bruker Quantax XFalsh 6 solid angle of a 30-mm^2 active area chip energy resolution 123 eV at Mn Kα, 45 eV at C).

Catalytic activity testing

The catalytic activity of CaPdZn/CeO₂ samples was tested at different temperatures in the range of 220–270 °C and pressure of 30 bar. The conversion of CO_2 was improved appreciably with the increase of temperature but methanol selectivity was decreased as presented in Table 2. Methanol selectivity decrease may have occurred mainly due to reverse water-gas shift (RWGS) reaction, forming CO as a by-product at elevated temperatures above 220 °C. Generally, at higher temperatures, RWGS reaction (Eqn. 3) dominates and hinders methanol formation due to thermodynamic constrains [21].

$$CO_{2(g)} + H_{2(g)} \leftrightarrow CO_{(g)} + H_2O_{(g)}; \Delta H_{298\,K} = 41 \text{ kJ/mol} \tag{3}$$
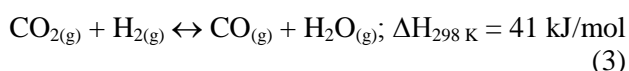
Table 2. Catalytic activity of CaPdZn/CeO₂ catalyst

	220 °C	230 °C	250 °C	270 °C
Conversion (%X)	7.7	8.3	10.8	11.25
Methanol selectivity (%S)	~100	97.4	90.0	78.0

(Reaction conditions: Catalyst weight = 0.5 g; Pressure = 30 bar, reaction mixture composition H₂:CO₂ = 3:1, flow rate = 20 cm³min⁻¹. Reduction temperature 550 °C)

In situ DRIFTS analysis

We have selected the temperature of 230 °C for DRIFT mechanistic study as at this point, we have observed moderate CO_2 conversion and high methanol (>97%) selectivity. *In situ* DRIFTS analysis was carried out to evaluate the emergence of various intermediate species formed over the catalyst surface with time at 230 °C and pressure of 30 bar for CO_2 hydrogenation to methanol. DRIFTS results assisted in developing a perception of the actual reaction sequence occurred over the surface of the tested catalyst and helped to distinguish the surface species relevant to the mechanism of selective formation of methanol.

DRIFT spectra, which were registered for reaction time of 180 minutes at interval of 5 minutes, exhibited unique characteristics of emerging intermediate surface species as presented in figure 4. Surface concentrations of the intermediate species were gradually increased at the beginning of the reaction and reached a maximum for 90 minutes after introduction of the reaction mixture to the DRIFT chamber. The DRIFT spectral range of acquisition was divided into five regions (R1-R5 as shown in figure 4) based on the unique band characteristics of various detected surface species. Figure 5 shows an enlarged image of IR spectral acquisition at different time intervals with the evolution of different surface species. Carbonates (bridged, monodentate and bidentate) and inorganic carboxylate species, which usually appear at low tempera-

192

ture CO_2 adsorption on ceria [24], could not be observed as they normally were converted to corresponding formate species at temperature above 200 °C in a very short time [25].

At the beginning of the registration of IR spectra, no characteristic bands due to the presence of formates were registered. After 5 min onward, IR bands appeared at 1640, 1575, and 1340 cm⁻¹ (Region R2) indicating the emergence of monodentate (m-HCOO) and bidentate (b-HCOO) formate species [26–28] attributed to hydrogenation of carbonaceous species at elevated temperature. IR bands at 1746 and 2843 cm⁻¹ corresponded CO-stretching vibrations (Region R3) and CH₂-stretching vibration ascribed to gas phase CH₂O species. IR bands at 2831, 2942, and 3077 cm⁻¹ (Region R5) may be assigned to methoxy (CH₃O) species [26,29,30], which was evolved by stepwise hydrogenation of formate and CH₂O species. A strong feature for CO_2 (gas phase non-dissociative adsorption over CeO₂ surface) can also be observed between 2250 and 2400 cm⁻¹ (Region R4). Band intensity in this region was consistent throughout the reaction time showing a strong interaction of CeO₂ with acidic CO_2. IR bands appearing at 2090 and 2177 cm⁻¹ (Region R3) may be attributed to linearly adsorbed CO (CO_L) on Ce⁺⁴ [24] and gas phase CO, respectively, due to the adsorption of CO_2 on oxygen vacancies over the surface of ceria support. Formation of gaseous methanol was also evident (almost after 5 min of introducing reaction mixture at reaction conditions) from the bands arisen at 1005, 1031, and 1055 cm⁻¹ (gaseous methanol) and 2844 cm⁻¹ (gas phase CH₃ *s*-stretching), and 3000 cm⁻¹ (gas phase CH₃ *d*-stretching) corresponding to methanol formation.
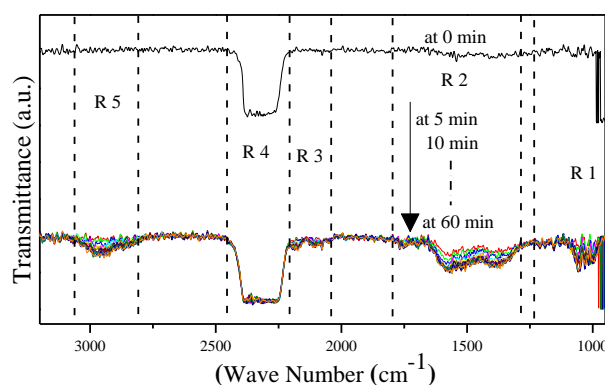
Fig. 4. DRIFT spectral acquisition at different time intervals of reduced CaPdZn/CeO₂ catalysts at 230 °C and 30 bar.

Figure 5 presents the appearance of gaseous CH₃OH species with time during the CO_2 hydrogenation reaction. The band at 1055 cm⁻¹ was used to analyse the dynamics of CH₃OH rise with time

(Fig. 6). It has been reported that PdZn alloy formation assists the selective formation of methanol [7,8]. It is well known that the type of preparation method, used support, and promoters may influence strongly the catalytic performance of the catalyst. Metal-support interaction also enhances the catalytic performance in the case of supported Pd catalysts

and this phenomenon was also observed in our CaPdZn/CeO_2 catalyst [6,9]. It may be assumed that the adsorption ability of CO_2 and oxygen-containing intermediate species (such as OH^-, HCO^-, H_2CO, H_2COO, $HCOO$, and H_3CO) is higher at CaPdZn/CeO_2 interface. A density functional study is required to prove this claim though.
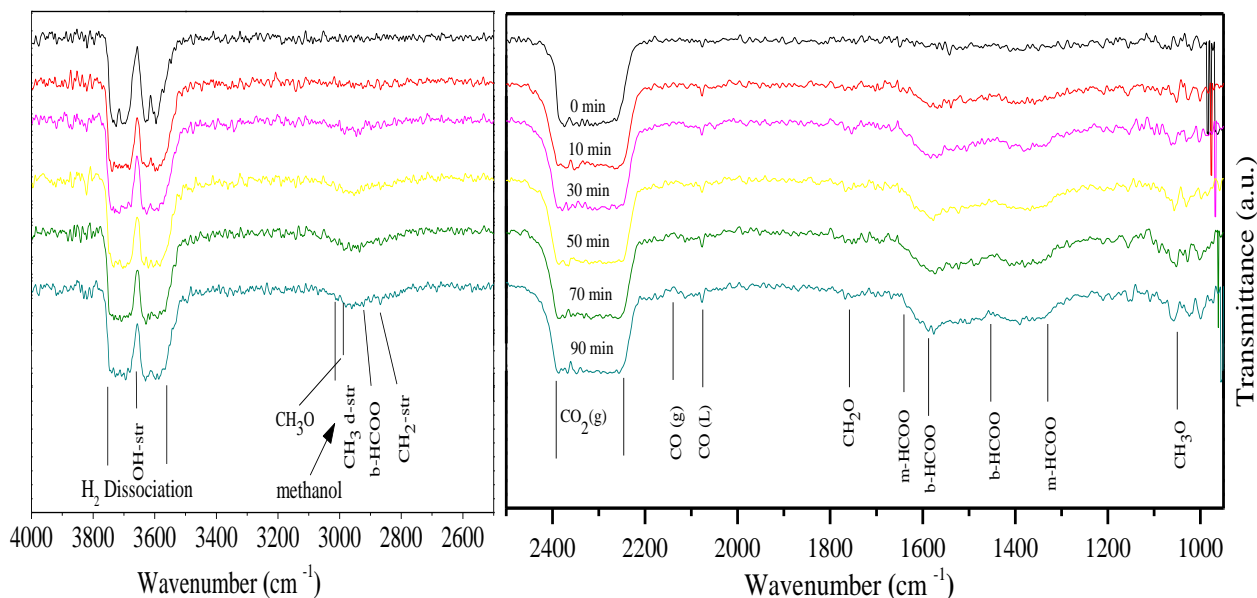
Fig. 5. Identification of various surface species for methanol synthesis from CO_2 using CaPdZn/CeO_2 catalysts at 230 °C and 30 bar pressure.
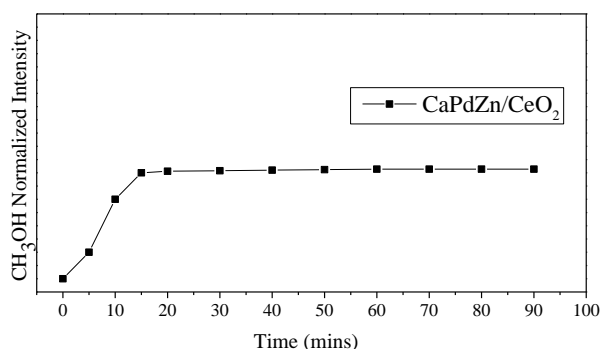
Fig. 6. Band intensity of gaseous methanol in the reaction products as a function of reaction time over CaPdZn/CeO_2 catalyst.

Reaction mechanism

In situ DRIFT study provided the necessary evidence required to propose a general reaction mechanism of CH_3OH formation over CaPdZn/CeO_2 catalyst. Formation of m-HCOO, b-HCOO, CH_2O, and CH_3O were kinetically favourable over the catalyst surface. Furthermore, no clear evidence of COOH species formation was observed indicating that the CaPdZn/CeO_2 system inhibits the RWGS reaction

and leads the reaction sequence to follow the formate pathway. Dissociative adsorption of hydrogen on PdZn alloy generated activated H adatoms, which ultimately lowered the reaction energy barrier for HCOO pathway. A strong metal support interaction (SMSI) between PdZn bimetallic alloy and CeO_2 allowed activation of CO_2 over the catalyst surface and facilitated spillover of H adatoms onto the support thereby increasing the hydrogenation rate of adsorbed carbonaceous species. These results were in line with previous reports on Pd-based systems for CO_2 hydrogenation [25,31,32]. Based on our findings, we may suggest a dual-site (bifunctional) reaction mechanism for CO_2 hydrogenation over CaPdZn/CeO_2 yielding CH_3OH and CO only as also discussed elsewhere [25,31,33]. Adsorbed carbonaceous species (monodentate, bidentate, and polydentate carbonate, etc.) over CeO_2 were stepwise hydrogenated to formates (m-HCOO and b-HCOO) with the supply of H adatoms from the dissociation of H_2 on PdZn alloy. This formate species was further hydrogenated to CH_2O, methoxy CH_3O species, and finally to methanol and CO. A general reaction mechanism is illustrated in Scheme 1.
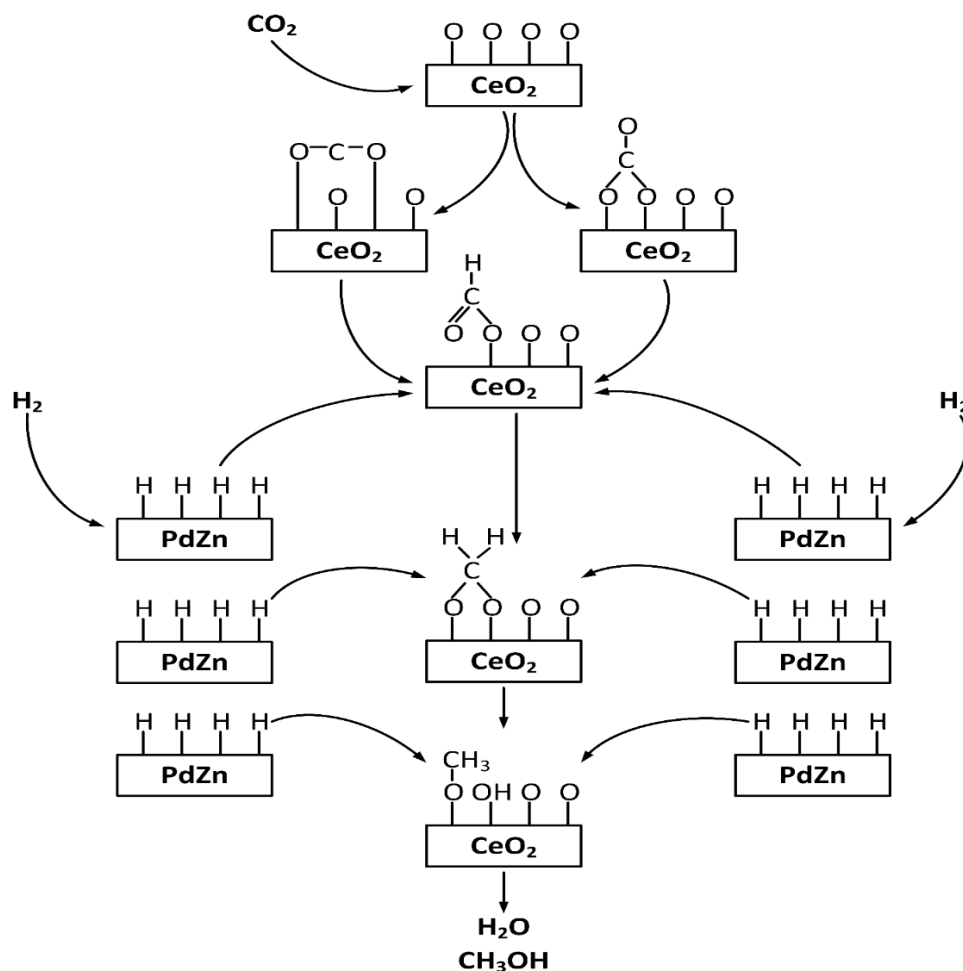
Scheme 1. Proposed reaction mechanism based on *in situ* DRIFTS data on methanol synthesis from CO_2 and H_2 over CaPdZn/CeO$_2$ catalyst.

CONCLUSIONS

The CaPdZn/CeO$_2$ catalyst exhibits ~100% selectivity to methanol and 7.7% of CO_2 conversion at low temperature of 220 °C and pressure of 30 bar. The reason for this excellent selectivity and activity lies in the strong H_2 dissociation ability of PdZn alloy to actively hydrogenate the adsorbed carbonaceous species as well as the strong adsorption of CO_2 over CeO$_2$ support as it provides a platform and stability to carbonaceous species formed over the catalysts surface. *In situ* DRIFT analysis confirmed the formation of formate species and its subsequent conversion to methoxy species, and then finally to methanol, suggesting a formate pathway for methanol synthesis from CO_2 hydrogenation using CaPdZn/CeO$_2$ under tested reaction conditions.

REFERENCES

1. F. T. Zangeneh, S. Sahebdelfar, M. T. Ravanchi, *J. Nat. Gas Chem.*, **20**, 219 (2011).
2. G. A. Olah, *Catal. Lett.*, **93**, 1 (2004).
3. F. Pontzen, W. Liebner, V. Gronemann, M. Rothaemel, B. Ahlers, *Catal. Today*, **171**, 242 (2011).
4. F. Liao, Z. Zeng, C. Eley, Q. Lu, X. Hong, S. C. E. Tsang, *Angew. Chem. Int. Ed.*, **51**, 5832 (2012).
5. J. Nakamura, T. Uchijima, Y. Kanai, T. Fujitani, *Catal. Today*, **28**, 223 (1996).
6. H. Bahruji, M. Bowker, J. Hayward, G. Hutchings, W. Jones, J. R. Esquius, *Farad. Disc.*, **197**, 309 (2017).
7. H. Bahruji, M. Bowker, G. Hutchings, N. Dimitratos, P. Wells, E. Gibson, W. Jones, C. Brookes, D. Morgan, G. Lalev, *J. Cat.*, **343**, 133 (2016).
8. X.-L. Liang, X. Dong, G.-D. Lin, H.-B. Zhang, *Appl. Catal. B: Environ.*, **88**, 315 (2009).
9. J. Xu, X. Su, X. Liu, X. Pan, G. Pei, Y. Huang, X. Wang, T. Zhang, H. Geng, *Appl. Catal. A: Gen.*, **514**, 51 (2016).
10. L. Fan, K. Fujimoto, *J. Catal.*, **150**, 217 (1994).
11. L. Fan, K. Fujimoto, *J. Catal.*, **172**, 238 (1997).

12. C.-H. Kim, J. S. Lee, D. Trimm, *Top. Catal.*, **22**, 319 (2003).
13. L. Fan, K. Fujimoto, *Appl. Catal. A: Gen.*, **106**, L1 (1993).
14. Y. A. Ryndin, R. Hicks, A. Bell, Y. I. Yermakov, *J. Catal.*, **70**, 287 (1981).
15. T. Fujitani, M. Saito, Y. Kanai, T. Watanabe, J. Nakamura, T. Uchijima, *Appl. Catal. A: Gen.*, **125**, L199 (1995).
16. W.-J. Shen, M. Okumura, Y. Matsumura, M. Haruta, *Appl. Catal. A: Gen.*, **213**, 225 (2001).
17. P. J. Berlowitz, D. W. Goodman, *J. Catal.*, **108**, 364 (1987).
18. J. Driessen, E. Poels, J. Hindermann, V. Ponec, *J. Catal.*, **82**, 26 (1983).
19. V. Ponec, *Surf. Sci.*, **272**, 111 (1992).
20. N. Iwasa, H. Suzuki, M. Terashita, M. Arai, N. Takezawa, *Catal. Lett.*, **96**, 75 (2004).
21. J. Trujillo-Reyes, A. Vilchis-Nestor, S. Majumdar, J. Peralta-Videa, J. Gardea-Torresdey, *J. Haz. Mat.*, **263**, 677 (2013).
22. T. Masui, H. Hirai, N. Imanaka, G. Adachi, T. Sakata, H. Mori, *J. Mat. Sci. Lett.*, **21**, 489 (2002).
23. C. H. Wang, S. S. Lin, *Appl. Catal. A: Gen.*, **268**, 227 (2004).
24. C. Li, Y. Sakata, T. Arai, K. Domen, K.-I. Maruya, T. Onishi, *J. Chem. Soc. Faraday Trans. 1*, **85**, 929 (1989).
25. S. E. Collins, M. A. Baltanás, A. L. Bonivardi, *J. Catal.*, **226**, 410 (2004).
26. G. C. Cabilla, A. L. Bonivardi, M. A. Baltanás, *J. Catal.*, **210**, 213 (2001).
27. D. H. Gibson, *Coord. Chem. Rev.*, **185**, 335 (1999).
28. R. Burch, S. Chalker, J. Pritchard, *J. Chem. Soc., Faraday Trans.*, **87**, 193 (1991).
29. J. Weigel, R. Koeppel, A. Baiker, A. Wokaun, *Langmuir*, **12**, 5319 (1996).
30. L. J. Burcham, L. E. Briand, I. E. Wachs, *Langmuir*, **17**, 6164 (2001).
31. S. E. Collins, J. J. Delgado, C. Mira, J. J. Calvino, S. Bernal, D. L. Chiavassa, M. A. Baltanás, A. L. Bonivardi, *J. Catal.*, **292**, 90 (2012).
32. N. Rui, Z. Wang, K. Sun, J. Ye, Q. Ge, C.-J. Liu, *Appl. Catal. B: Environ.*, **218**, 488 (2017).
33. X. Guo, D. Mao, G. Lu, S. Wang, G. Wu, *J. Mol. Cat. A: Chem.*, **345**, 60 (2011)...

ИЗСЛЕДВАНЕ С ДОИЧС НА МЕХАНИЗМА НА СИНТЕЗ НА МЕТАНОЛ ОТ CO₂ И ВОДОРОД С КАТАЛИЗАТОР CaPdZn/CeO₂

А. С. Малик*, Ш. Ф. Заман[1], А. А. Ал-Захрани, М. А. Даус, Х. Идрис, Л. А. Петров

Департамент по инженерна химия и материалознание, Инженерен факултет, Университет „Крал Абдулазис", п.к. 80204, 21589 Джеда, Саудитска Арабия

(Резюме)

В настоящата работа са представени резултати от DRIFTS изследване на механизма на синтез на метанол от CO₂ и H₂ върху катализатор CaPdZn/CeO₂. Катализаторът притежава превъзходни каталитични свойства. Селективността на процеса при 220 °C и налягане 30 атм. е 100% при 7.7% конверсия на CO₂. Измерванията с DRIFTS са проведени *in situ* при налягане 30 атм. и са проследени във времето промените в концентрациите на повърхностните междинни съединения. Катализаторът и използваният носител са охарактеризирани с метода БЕТ, хемосорбция на CO, ТПД на CO₂, рентгеноструктурен анализ и ТЕМ с висока разделителна способност. Установено е формирането на моно- и бидентантни формиати, CH₂O и CH₃O, което сочи че синтеза на метанол протича през формирането на формиати. Предложен е и вероятен механизъм на процеса на синтез на метанол от CO₂ и водород.

Ionic gold and catalytic activity of gold catalysts for CO oxidation

A. M. Ali

Department of Chemical and Materials Engineering, Faculty of Engineering, King Abdulaziz University
P.O. Box 80204, Jeddah 21589, Kingdom of Saudi Arabia

This study is aimed to investigate the catalytic activity of freshly prepared gold catalysts supported on three metal oxide supports CeO_2, ZrO_2 and mechanically mixed CeO_2+ZrO_2 (DOS) for the CO oxidation under atmospheric pressure. The catalytic activity of both Au/CeO_2 and Au/DOS were nearly the same and far higher than that of an Au/ZrO_2 sample. The higher catalytic activity of both the Au/CeO_2 and Au/DOS catalysts is attributed to the presence of Au^{+1} and Ce^{+4} ions as well as to enhanced CeO_2 oxygen mobility in the presence of ZrO_2.

Key words: gold catalyst, ionic gold, ceria, CO oxidation.

INTRODUCTION

Traditionally, gold was considered one of the most stable metals [1]. In 1987, Haruta *et.al* found that gold nanoparticles have high catalytic activity for the CO oxidation, and overturned the conventional paradigm about the gold [2,3]. Currently gold catalysts has become one of the most studied catalysts, due to their high activity in many oxidation reactions at low temperatures [4]. This allows reduction of energy costs in the industry and offers low-cost solutions of many global environmental issues [5–9]. Additionally, the gold catalysts exhibit unusual selectivity in many important reactions [10,11]. Further, it is also cost-effective to use the gold catalysts for the industries [4,12].

It has been widely accepted that the performance of the gold catalysts depend on the size distribution of the gold particles, gold-support interaction and on the electronic properties of both gold and support [1, 4, 13–18]. Also, many other parameters such as nature of the support [3,19–21], preparation method [1,22,23], calcination conditions [24–28], as well as the pH [29] and the precipitating agent [30, 31] have strong influence on the catalytic behavior of the gold catalysts.

CO oxidation is one of the most widely studied fields of application of the gold catalysts [32–36] because of many important applications for this reaction at low temperature, such as gas sensors [37], carbon monoxide laser [30] and air purification [38], etc. Among the catalyst supports, ceria is one of the most widely studied carriers for gold catalysts, due to its ability to maintain high Au dispersion. In addition, stabilized cationic Au species on the CeO_2 surface, and ceria redox property to exchange the available oxygen are very useful to produce a strong promoting effect on gold oxidation state [39–42]. Further, the catalytic performance of Au/CeO_2 can be improved by several methods such as doping with other metals, nano-crystallisation and mixing with other metal oxides [39,40,43]. Among these, mixing ceria with other metal oxides is found to be beneficial for the enhanced catalytic activity of gold catalysts. For example, the catalytic performance of Au/CeO_2-Co_3O_4 in the CO oxidation has been reported to be much higher than that of Au/CeO_2 [44]. Zirconia is another interesting metal oxide to mix with CeO_2, because it can retard ceria degradation, improve the redox property of the latter, and preserve the oxygen defects in the metal oxide structure [45].

Based on available literature and as per author's best knowledge, none of the study results have been reported on the possible catalytic activity of gold catalysts supported on a mixture of two metal oxides (CeO_2 and ZrO_2) and/or their comparison to each metal oxide as support during CO oxidation.

Therefore, the aim of this study is to investigate the impact of support type and the possible role of ionic gold during CO oxidation on the gold catalyst.

EXPERIMENTAL

Catalyst preparation

Precisely calculated 10 g of each pure CeO_2 (Rhodia) and pure ZrO_2 (Rhodia) or 10 g DOS [CeO_2 : ZrO_2 = 3:1] were mechanically mixed in a Power Sonic instrument. Well-dried support at 120 °C was further used in a Mettler Toledo Labmax reactor for gold deposition. 13.5 cm^3 of 0.1M KOH

---

* To whom all correspondence should be sent
E-mail: amsali@kau.edu.sa

and 3.86 cm^3 of deionised water (DIW) for each gram of the support were added to the reactor. Under controlled temperature (60 °C) and pH of 8.5, HAuCl$_4$.3H$_2$O was used as the gold precursor. The system was aged for 1 h at 60 °C and 180 rpm. The freshly prepared sludge was rinsed multiple times with lukewarm DIW under vacuum to remove any chloride ions. Details on six different freshly prepared catalysts are enlisted Table 1.

Catalytic activity testing

The catalytic activity studies were performed in a PID Microactivity Reference reactor system. The CO oxidation was carried out in a 4-mm-ID quartz reactor charged with 0.5 g of catalyst at 12000 GHSV under different temperatures. Gaseous flow rates were controlled by Bronkhorst mass flow controllers. A ramping rate of 10 °C/min was used to increase the reaction temperature. The catalytic activity at a particular temperature was measured under steady state temperature regime throughout the catalytic experiment by applying PID Micro-activity Reference software. The concentrations of both CO and CO$_2$ reaction products were monitored by employing an online Agilent 7890A gas chromatography instrument. A GC ChemStation$^®$ B.04.03 (54) was applied to analyse and process the reaction data obtained by using HayeSep Q (8 ft) columns and N$_2$ as carrier gas. In addition, all the catalysts were tested twice to check reproducibility under set parameters of the PID Microactivity reference reactor.

Catalyst characterisation

Catalyst surface area was measured by means of Quantachrome Nova 2000 under standard operating conditions (see Table 1).

The XPS method was applied to identify the possible oxidation states of each element by using multi-technique surface analysis system (SPECS GmbH, Germany). The sample was irradiated with 13.5 kV under electron take-off-angle perpendicular to the sample surface plane. The charge correction was performed by sing C1s line (284.6 eV). A

SPECS XR-50 with Mg-Kα was used as an X-ray source.

XRD analysis was conducted by Equinox system Inel CPS 180 powder diffractometer. X-ray diffraction patterns were obtained from CoKα under 30 kV and 30 mA. Both COD and ICCD databases were used to identify existing phases.

RESULTS AND DISCUSSION

Catalytic activity results

The catalytic activity of three samples of CeO$_2$, ZrO$_2$, and DOS supports is shown in Fig. 1. Up to 175 °C, all the studied supports showed practically negligible catalytic activity. However, in the temperature range of 175 to 250 °C, the catalytic activity of both ceria and DOS started to increase, whereas the catalytic activity of zirconia did not show any significant change. Up to 250 °C, the CO conversions over both CeO$_2$ and DOS were ~7%, whereas, at temperatures up to 250 °C, the zirconia sample manifested only ~3% CO conversion. In the temperature range of 250–300 °C, the CO conversion over the three supports reached almost 85% and remained almost stable upon further temperature rise. In general, the catalytic activities of both ceria and DOS were almost the same and were higher that of zirconia.
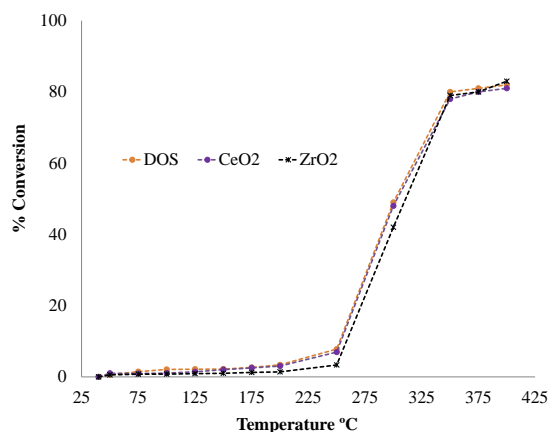
Fig. 1. Catalytic activity of the gold catalysts supports: DOS, CeO$_2$, and ZrO$_2$.

Table 1. Summary of the prepared catalysts

Catalyst Composition	Notation	Surface area (m^{2}g^{-1})	Gold particle size (nm)	Gold dominant oxidation state
100% CeO$_2$	CeO$_2$	131.1	-	-
100% ZrO$_2$	ZrO$_2$	80	-	-
75% CeO$_2$ + 25% ZrO$_2$	DOS	118.9	-	-
1% Au-CeO$_2$	Au/CeO$_2$	132	~ 5.1	Au^0, Au^{+1}
1% Au-ZrO$_2$	Au/ZrO$_2$	80.3	~ 4.5	Au^0, Au^{+1}
1% Au-CeO$_2$-ZrO$_2$	Au/DOS	120.1	~ 4.0	Au^0, Au^{+1}, Au^{+3}

CO conversions on three gold catalysts Au/DOS, Au/CeO$_2$, and Au/ZrO$_2$ are shown in Fig. 2. The gold catalysts are much more active in comparison with used metal oxide supports. In addition, catalyst carrier nature plays a crucial role to catalytic activity of the supported gold catalysts. In the case of Au/ZrO$_2$ catalyst, the conversion of CO was significantly increased. A maximum conversion was obtained above 150 °C. The Au/CeO$_2$ catalyst exhibited a much higher activity as to that of the Au/ZrO$_2$ catalyst.

The Au/DOS catalyst had almost similar catalytic activity with regard to the Au/CeO$_2$ catalyst. This is an indication that the addition of zirconia to the catalyst support slightly improves the catalytic activity of Au/DOS. In general, Au/DOS showed a maximum CO conversion at 150 ºC.
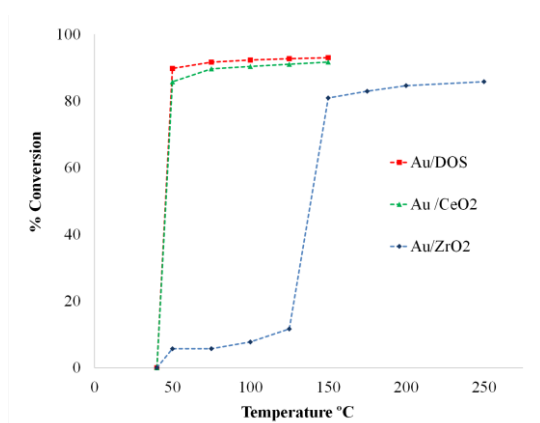
Fig. 2. Catalytic activity of the gold catalysts: Au/DOS, Au/CeO$_2$ and Au/ZrO$_2$.

XPS study

A detailed comparison of the overlay Au 4f XPS spectra of the Au/CeO$_2$, Au/ZrO$_2$, and Au/DOS catalysts is shown in Fig. 3. The binding energy (BE) for metallic gold (Au^0) is 84.0 eV. While the oxidized Au species Au^{+1} have a BE of 85.5 eV, Au^{+3} shows a BE of 86.3 eV [46]. Metallic gold (Au^0) and ionic gold (Au^{+1}) were the only species present in all the studied gold catalysts. The binding energy of the Au^0/CeO$_2$ and Au^0/DOS catalysts was found to be almost the same. Nevertheless, the binding energy of the Au/ZrO$_2$ catalyst was about 0.4 eV lower than that of the Au/CeO$_2$ and Au/DOS catalysts.

According to the literature [47], it is evident that the concentration of oxidized gold on the Au/ZrO$_2$ catalyst is lower as to that of the Au/CeO$_2$ and Au/DOS catalysts. Cerium is mainly present as Ce^{4+} in all the gold catalysts. It is well known that ceria can be partially reduced under X-ray radiation in the XPS instrument. However, the Ce^{3+} ions are formed also by influence of both gold species and zirconia. This result confirms that ceria can easily exchange oxygen with medium, and zirconia can improve the redox property of ceria, which play a key role in the CO oxidation.

XRD study

XRD analysis of all the gold catalysts (see Fig. 4) exhibited almost similar patterns as to that of support. It was found that after thermal treatment in the preparation procedure zirconia and ceria interact and form a mixed oxide Ce$_{0.25}$OZr$_{0.75}$O$_4$. The amount of the latter oxide is very small. This phase was registered after 24 h scanning of the sample. However, the addition of gold does not impart any significant changes to crystal structure. Therefore, only the Au oxidation states are the key reasons to enhance the catalytic activity of the studied gold catalyst.
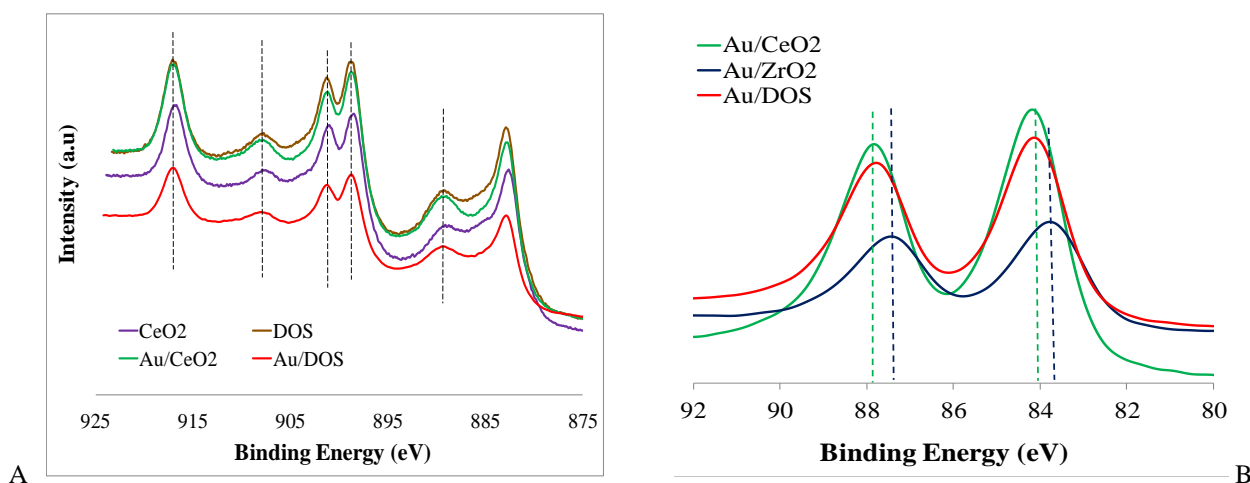
Fig. 3: Comparison of overlay XPS spectra: A - Ce 3d in CeO$_2$, DOS, Au/CeO$_2$, and Au/DOS catalysts;
B - Au 4f for Au/DOS, Au/CeO$_2$, and Au/ZrO$_2$ catalysts.
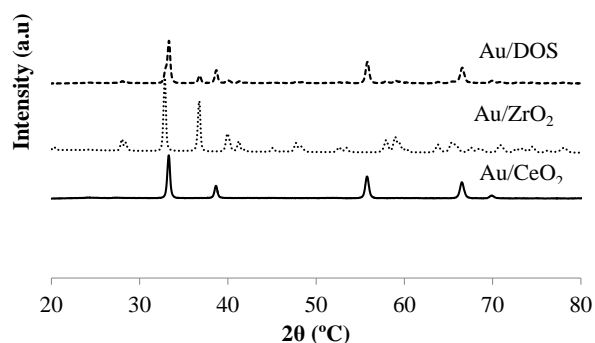
Fig. 4. XRD comparison of Au/DOS, Au/ZrO$_2$, and Au/CeO$_2$ catalysts.

CONCLUSIONS

All the studied gold catalysts showed a higher catalytic activity in comparison with applied support. Both the Au/CeO$_2$ and Au/DOS catalysts exhibited nearly the same catalytic activity for the CO oxidation at low temperature under atmospheric pressure, which was much higher than that of Au/ZrO$_2$. Under similar reaction conditions, the catalytic activity of the three supports (CeO$_2$, ZrO$_2$, and DOS) was nearly zero. The higher catalytic activity of both Au/CeO$_2$ and Au/DOS is because of the presence of ionic gold Au^{+1} and Ce^{+4}. Zirconia presence slightly improved ceria redox ability in the presence of gold. Further, this is helpful in promoting the oxidised gold species, which lead to enhanced catalytic activity.

REFERENCES

1. G. C. Bond, D. T. Thompson, *Catal. Rev.*, **41**, 319 (1999).
2. M. Haruta, T. Kobayashi, H. Sano, N. Yamada, *Chem. Lett.*, 405 (1987).
3. M. Haruta, H. Sano, T. Kobayashi, Google Patents, 1987.
4. G. C. Bond, C. Louis, D. T. Thompson, ICP, 2006.
5. L. Delannoy, K. Fajerwerg, P. Lakshmanan, C. Potvin, C. Méthivier, C. Louis, *Appl. Catal., B*, **94**, 117 (2010).
6. B. Solsona, T. Garcia, E. Aylón, A. M. Dejoz, I. Vázquez, S. Agouram, T. E. Davies, S. H. Taylor, *Chem. Eng. J.*, **175**, 271 (2011).
7. B. Solsona, T. Garcia, E. Aylón, A. M. Dejoz, I. Vázquez, S. Agouram, T. E. Davies, S. H. Taylor, *Chem. Eng. J.*, **175**, 271 (2011).
8. J. Mellor, A. Palazov, B. Grigorova, J. Greyling, K. Reddy, M. Letsoalo, J. Marsh, *Catal. Today*, **72**, 145 (2002).
9. M. Haruta, *Gold Bull.*, **37**, 27 (2004).
10. M. M. Schubert, M. J. Kahlich, H. A. Gasteiger, R. J. Behm, *J. Power Sources*, **84**, 175 (1999).
11. D. L. Trimm, *Appl. Catal. A*, **296**, 1 (2005).
12. D. Cameron, R. Holliday, D. Thompson, *J. Power Sources*, **118**, 298 (2003).
13. M. Haruta, *Cattech*, **6**, 102 (2002).
14. M. Haruta, *Chem. Rec.*, **3**, 75 (2003).
15. H. Liu, A. I. Kozlov, A. P. Kozlova, T. Shido, K. Asakura, Y. Iwasawa, *J. Catal.*, **185**, 252 (1999).
16. A. M. Ali, M. A. Daous, A. A. M. Khamis, H. Driss, R. Burch, L. A. Petrov, *Appl. Catal. A*, **489**, 24 (2015).
17. B. Skårman, L. R. Wallenberg, P.-O. Larsson, A. Andersson, J.-O. Bovin, S. N. Jacobsen, U. Helmersson, *J. Catal.*, **181**, 6 (1999).
18. J. Papavasiliou, G. Avgouropoulos, T. Ioannides, *J. Catal.*, **251**, 7 (2007).
19. M. Haruta, S. Tsubota, T. Kobayashi, H. Kageyama, M. J. Genet, B. Delmon, *J. Catal.*, **144**, 175 (1993).
20. S. Carabineiro, S. Bastos, J. Órfão, M. Pereira, J. Delgado, J. Figueiredo, *Appl. Catal. A*, **381**, 150 (2010).
21. D. Widmann, Y. Liu, F. Schüth, R. Behm, *J. Catal.*, **276**, 292 (2010).
22. D. Wang, Z. Hao, D. Cheng, X. Shi, C. Hu, *J. Mol. Catal. A: Chem.*, **200**, 229 (2003).
23. G. R. Bamwenda, S. Tsubota, T. Nakamura, M. Haruta, *Catal. Lett.*, **44**, 83 (1997).
24. F. Boccuzzi, A. Chiorino, M. Manzoli, P. Lu, T. Akita, S. Ichikawa, M. Haruta, *J. Catal.*, **202**, 256 (2001).
25. M. Daté, Y. Ichihashi, T. Yamashita, A. Chiorino, F. Boccuzzi, M. Haruta, *Catal. Today*, **72**, 89 (2002).
26. V. I. Sobolev, L. V. Pirutko, *Catal. Commun.*, **18**, 147 (2012).
27. T. Takei, I. Okuda, K. K. Bando, T. Akita, M. Haruta, *Chem. Phys. Lett.*, **493**, 207 (2010).
28. V. Choudhary, D. Dumbre, N. Patil, B. Uphade, S. Bhargava, *J. Catal.*, **300**, 217 (2013).
29. F. Moreau, G. C. Bond, A. O. Taylor, *J. Catal.*, **231**, 105 (2005).
30. M. Haruta, *Catal. Today*, **36**, 153 (1997).
31. S. Tsubota, D. A. H. Cunningham, Y. Bando, M. Haruta, in: Preparation of Catalysis VI. Scientific Bases for the Preparation of Heterogeneous Catalysts (Proc. 6th Int. Symp., Louvain-La-Neuve, 5–8 September 1994, Eds. G. Poncelet, J. Martens, B. Delmon, P. A. Jacobs and P. Grange) *Stud. Surf. Sci. Catal.*, **91**, 227 (1995)
32. M. Dekkers, M. Lippits, B. Nieuwenhuys, *Catal. Lett.*, **56**, 195 (1998).
33. S. A. C. Carabineiro, N. Bogdanchikova, P. B. Tavares, J. L. Figueiredo, *RSC Adv.*, **2**, 2957 (2012).
34. H. Xu, W. Chu, J. Luo, T. Zhang, *Chem. Eng. J.*, **170**, 419 (2011).
35. S. A. C. Carabineiro, N. Bogdanchikova, M. Avalos-Borja, A. Pestryakov, P. B. Tavares, J. L. Figueiredo, *Nano Res.*, **4**, 180 (2011).
36. C. L. Peza-Ledesma, L. Escamilla-Perea, R. Nava, B. Pawelec, J. L. G. Fierro, *Appl. Catal., A*, **375**, 37 (2010).
37. S. A. C. Carabineiro, A. M. T. Silva, G. Dražić, P. B.

Tavares, J. L. Figueiredo, *Catal. Today*, **154**, 21 (2010).

38. T. Kobayashi, M. Haruta, S. Tsubota, H. Sano, B. Delmon, *Sens. Actuator B-Chem.*, **1**, 222 (1990).
39. M. Ikegami, T. Matsumoto, Y. Kobayashi, Y. Jikihara, T. Nakayama, H. Ohashi, T. Honma, T. Takei, M. Haruta, *Appl. Catal. B*, **134**, 130 (2013).
40. S. Carrettin, P. Concepción, A. Corma, J. M. Lopez Nieto, V. F. Puntes, *Angew. Chem. Int. Ed.*, **43**, 2538 (2004).
41. O. H. Laguna, F. Romero Sarria, M. A. Centeno, J. A. Odriozola, *J. Catal.*, **276**, 360 (2010).
42. T. Tabakova, G. Avgouropoulos, J. Papavasiliou, M. Manzoli, F. Boccuzzi, K. Tenchev, F. Vindigni, T. Ioannides, *Appl. Catal. B*, **101,** 256 (2011).
43. H.-F. Li, N. Zhang, P. Chen, M.-F. Luo, J.-Q. Lu, *Appl. Catal. B*, **110,** 279 (2011).
44. E. Smolentseva, A. Simakov, S. Beloshapkin, M. Estrada, E. Vargas, V. Sobolev, R. Kenzhin, S. Fuentes, *Appl. Catal. B*, **115-116,** 117 (2012).
45. H. Wang, H. Zhu, Z. Qin, G. Wang, F. Liang, J. Wang, *Catal. Commun.*, **9,** 1487 (2008).
46. E. Mamontov, T. Egami, R. Brezny, M. Koranne, S. Tyagi, *J. Phys. Chem. B*, **104,** 11110 (2000).
47. G. J. Hutchings, M. S. Hall, A. F. Carley, P. Landon, B. E. Solsona, C. J. Kiely, A. Herzing, M. Makkee, J. A. Moulijn, A. Overweg, *J. Catal.*, **242,** 71 (2006).
48. K. M. Parida, N. Sahu, P. Mohapatra, M. S. Scurrell, *J. Mol. Catal. A: Chem.*, **319,** 92 (2010).

ЗЛАТНИ ЙОНИ И КАТАЛИТИЧНА АКТИВНОСТ НА ЗЛАТНИ КАТАЛИЗАТОРИ ЗА ОКИСЛЕНИЕ НА CO

А. М. Али

Департамент по инженерна химия и материали, Инженерен факултет, Университет „Крал Абдулазис“, п.к. 80204, Джеда 21589, Кралство Саудитска Арабия

(Резюме)

Изследвани са прясно приготвени златни катализатори нанесени върху три оксидни носителя CeO_2, ZrO_2 и тяхна механична смес CeO_2+ZrO_2 (DOS) като катализатори за реакцията на окисление на CO при атмосферно налягане. Каталитичната активност на образци от Au/CeO_2 и Au/DOS е приблизително равна и е значително по-висока от активността на Au/ZrO_2 катализатор. Активността на изследваните златни катализатори се дължи на присъствието на златни Au^{+1} йони, на Ce^{+4} и на високата мобилност на кислорода в цериевия диоксид.

A DFT study of ammonia dissociation over Mo_3N_2 cluster

S. F. Zaman

Chemical and Materials Engineering Department, Faculty of Engineering, King Abdulaziz University,
P.O. Box 80204, Jeddah 21589, Saudi Arabia

Density functional theory (DFT) calculations were performed to generate the potential energy surface of ammonia decomposition over a Mo_3N_2 cluster by investigating elementary surface reaction steps of the dehydrogenation pathway of NH_3. Ontop adsorption of NHx (x = 0–3) species over an Mo atom was found to be the most favourable adsorption arrangement. The rate limiting step for NH_3 dissociation was the abstraction of the 2nd hydrogen according to the following surface elementary reaction (NH_2*ad → NH*ad + H*ad) with an activation energy of 41.2 kcal/mol and an endothermic heat of reaction of 28.05 kcal/mol. The Nitrogen dissociation energy 35.19 kcal/mol over the cluster is much higher than over the Ru(0001) surface.

Key words: DFT, NH_3 dissociation, Mo_3N_2 cluster, adsorption energy, potential energy surface.

INTRODUCTION

Hydrogen is the ideal fuel that can mitigate environmental problems connected with energy production, since the water is the only combustion product. The use of clean hydrogen containing low (< 10 ppm) concentration of CO as a fuel in proton exchange membrane fuel cells (PEMFC) is a very effective way to produce eclectic energy with efficiency up to 60% [1–3]. The fuel cell generators are noiseless devices, which have no harmful emissions generation. The main obstacle for practical application of hydrogen as a fuel for on board devices is the very low energy capacity per unit hydrogen gas volume. Therefore, the hydrogen storage is a problem of crucial importance for the future practical use of hydrogen in on board devices. One of the possible ways to overcome this negative circumstance is the production of clean hydrogen by NH_3 decomposition in on board catalytic reactors. NH_3 molecule is the richest for hydrogen molecule. It contains 17.8 wt.% hydrogen. This means that at 20 °C and 8.6 bar from one m^3 liquid NH_3 108 kg H_2 can be produced [4]. The use of liquid NH_3 as a hydrogen storage also offers a number of technological advantages. Because of the fact that obtained hydrogen does not contain any traces of CO. Thus the use of NH_3 for on board preparation of clean hydrogen is very promising technology. Thermodynamic data shows that at atmospheric pressure and 400 °C the possible achievable degree of conversion of NH_3 is 99.0%. However, in the catalytic experiments with different types of catalysts obtained degrees of conversion are lower at much higher temperatures.

Supported Ru is the most active catalyst [5], but Ru scarce availability in nature and very high price make it not suitable for wide applications. The decomposition catalysts have different chemical nature i.e. metals from Group VIII (Fe, [6–9] Co, Ni [10–13], Ru [13–20] or supported on oxides or on MWCNTs, metal carbides and nitrides like MoNx, VCx, MoCx, VNx, etc. Therefore, it is of great importance to receive information about some of the elementary steps of the mechanism of this reaction. NH_3 decomposition is a reversible endothermic reaction given by the following equation:

$$NH_3 = 0.5\ N_2 + 1.5\ H_2\ \ [\Delta Hr = +46\ kJ/mol]$$
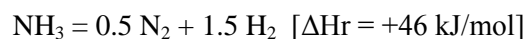
Recently, the reaction of NH_3 decomposition has attracted much attention. Several studies have been reported results from ammonia dissociation studies on different catalyst surfaces using DFT approach [22–28]. Interestingly, no DFT work is reported for Mo_2N based catalysts.

This paper presents the results of DFT study of the ammonia dissociation mechanism on a simple Mo_3N_2 cluster. This cluster was selected for two reasons. (i) The Mo_3N_2 cluster can be used as a simple model of the Mo_2N catalyst surface. Therefore, by the studying Mo_3N_2 cluster we can obtain reliable information about surface reaction steps and we will be able to determine the potential energy surface (PES) for this dissociation reaction. (ii) The use Mo_3N_2 cluster leads to substantial reduction of the computational cost.

CALCULATION PROCEDURE

The DMol3 module of Material Studio (version 7.0) from Accelrys Inc. (San Diego, CA, USA) was used to perform the DFT calculations. Accordingly, the electronic wave functions are expanded in numerical atomic basis sets defined on an atomic-centered spherical polar mesh. The double-numerical plus P-function (DNP) of all electron basis set, was used for all the calculations. The DNP basis set includes one numerical function for each occupied atomic orbital and a second set of functions for valence atomic orbitals, plus a polarization p-function on all atoms. Each basis function was restricted to a cutoff radius of 4.9 Å, allowing for efficient calculations without loss of accuracy. The Kohn-Sham equations [29] were solved by a self-consistent field procedure using PW91 functional with GGA for exchange correlation [30-32]. The techniques of direct inversion in an iterative subspace with a size value of six and thermal smearing of 0.005 Ha were applied to accelerate convergence. The optimization convergence thresholds for energy change, maximum force and maximum displacement between the optimization cycles were 0.00001 Ha, 0.002 Ha/Å and 0.005 Å, respectively. The k-point set of (1x1x1) was used for all calculations. The activation energy of interaction between two surface species was identified by complete linear synchronous transit and quadratic synchronous transit search methods [33] followed by TS confirmation through the nudge elastic band method [34]. Spin polarization was imposed in all the calculations. The adsorption energy of an element (i.e. molecule or atom) was found according to the following formula:

$$E_{ad} = 1/n \left[E_{slab+element} - \{ E_{empty\ slab} + E_{element} \} \right],$$

where n is the number of adsorbed species.

Mo_3N_2 CLUSTER FORMATION

The Mo_3N_2 cluster, comprising of five atoms, is depicted in Fig. 1, where Mo atoms are indexed as $Mo_{(1)}$, $Mo_{(2)}$ and $Mo_{(3)}$ and nitrogen atoms as $N_{(4)}$ and $N_{(5)}$. The cluster structure was optimized using geometric optimization imposing no constraints on atomic position. After geometric optimization the cluster atomic position was fixed to investigate NH_3 decomposition. The optimised distance between $Mo_{(1)}$–$Mo_{(2)}$ is 2.236 Å, $Mo_{(1)}$–$Mo_{(3)}$ is 2.753 Å, $Mo_{(2)}$–$Mo_{(3)}$ is 2.842 Å, $Mo_{(1)}$–$N_{(4)}$ is 2.042 Å, and $Mo_{(1)}$–$N_{(5)}$ is 2.042 Å. The angle, $\angle\ Mo_{(1)}$–$N_{(4)}$–$Mo_{(2)}$ is 66.95°, $\angle\ Mo_{(1)}$–$N_{(4)}$–$Mo_{(3)}$ is 88.36°, $\angle\ Mo_{(2)}$–$N_{(4)}$–$Mo_{(3)}$ is 92.26°, $\angle\ Mo_{(1)}$–$N_{(4)}$–$Mo_{(2)}$ is 66.57°, $\angle\ Mo_{(1)}$–$N_{(4)}$–$Mo_{(3)}$ is 88.37°, $\angle\ Mo_{(2)}$–$N_{(5)}$–$Mo_{(3)}$ is

92.28°. The reaction sequence investigated on Mo_3N_2 cluster is as follows:

$$NH_3*ad \rightarrow NH_2*ad + H*ad \qquad (1)$$

$$NH*ad \rightarrow NH*ad + H*ad \qquad (2)$$

$$NH*ad \rightarrow N*ad + H*ad \qquad (3)$$
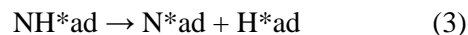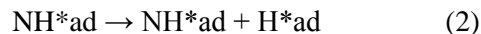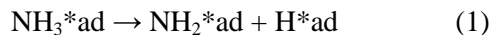
Also the nitrogen molecule decomposition over the cluster was investigated

$$N_2*ad \rightarrow N*ad + N*ad. \qquad (4)$$
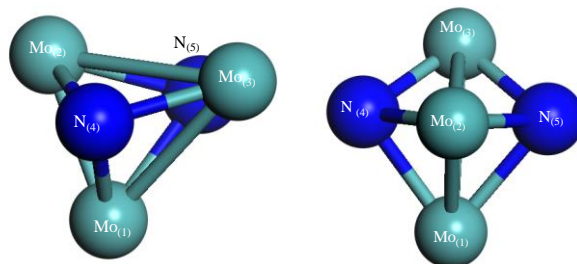
Fig. 1. The optimized Mo_3N_2 cluster structure with atom indexing.

AMMONIA (NH_3) ADSORPTION ON THE CLUSTER

Ammonia molecule was placed on the three different Mo atoms of the cluster (indexed as 1, 2, 3) to seek the preferred adsorption position or the minimum energy configuration (Fig. 2). It was found that NH_3 was absorbed on-top position over Mo atom. The adsorption energy on different Mo atoms indexing (1), (2) and (3) was −25.35 kcal/mol, −21.49 kcal/mol, and −20.48 kcal/mol, and the bond length between $Mo_{(x)}$ and N atom (of NH_3) was 2.33 Å, 2.34 Å and 2.36 Å, respectively. $Mo_{(1)}$ atom is the preferred adsorption location for the NH_3 molecule. The adsorption arrangements are shown in Fig. 2. Researchers previously reported the value of NH_3 adsorption energy on Ni (110) surface of 20.75 kcal/mol [35], 17.29 kcal/mol on Ni (111) surface [36], 15.78 kcal/mol on Co (111) surface [36] and on an Fe cluster 8.83 kcal/mol [37]. So NH_3 is more strongly adsorbed on the Mo_3N_2 cluster compared to other potential NH_3 decomposition catalyst surfaces. Table 1 shows the charge distribution on the cluster atoms and on the N atom of NH_x (x = 1–3) species prior to and after being adsorbed on the cluster. After adsorbing NH_3 on the cluster at the $Mo_{(1)}$ atom there was a decrease in positive charge on $Mo_{(1, 2, 3)}$ atom of the cluster, and the negative charge on the $N_{(4)}$ and $N_{(5)}$ atoms decreased compared to the empty cluster. The negative charge on the N atom of NH_3 increased upon adsorption. Clearly electron transferred from the $N_{(5)}$ and $N_{(4)}$ atoms (of the cluster) to the nitrogen atom (NH_3 species) and Mo

atoms of the cluster during the surface bond formation.

FIRST HYDROGEN ATOM ABSTRACTION FROM AMMONIA

The abstraction of the 1st hydrogen (Fig. 2) was investigated according to the elementary surface reaction $NH_3*ad \rightarrow NH_2*ad + H*ad$. NH_3 adsorbed on $Mo_{(1)}$ atom was taken as the reactant configuration as it has the lowest energy configuration. The NH_2 species was adsorbed on $Mo_{(1)}$ atom. Preferred hydrogen co-adsorption location was investigated on $Mo_{(2)}$ and $Mo_{(3)}$ and $N_{(4)}$ atom. The $[NH_2*ad + H*ad]$ configuration had the lowest energy configuration when NH_2 species was adsorbed on $Mo_{(1)}$ and the H atom adsorbed on $Mo_{(3)}$, with an adsorption energy of -77.70 kcal/mol. The distance between $Mo_{(1)}$ and N of NH_2 species is 2.007 Å and $Mo_{(3)}$ and H is 1.791 Å. A very similar adsorption energy, -77.41 kcal/mol, was found when the H atom was adsorbed on $Mo_{(2)}$. The distance between $Mo_{(1)}$ and N of NH_2 species is 2.07 Å and $Mo_{(2)}$ and the H is 1.787 Å. The H atom is adsorbed on $N_{(4)}$ atom showed the largest adsorption energy

among the three arrangements, -70.99 kcal/mol, and is least favourable. The transition state search was performed for the first two arrangements. Fig. 2 shows the adsorption configuration and adsorption energies and atomic distances.

The activation barrier for the product arrangement NH_2 on $Mo_{(1)}$ and H on $Mo_{(3)}$ was found to be 18.41 kcal/mol with an exothermic heat of reaction of -16.47 kcal/mol. The activation barrier for the product arrangement NH_2 on $Mo_{(1)}$ and H on $Mo_{(2)}$ was found to be 18.19 kcal/mol with an exothermic heat of reaction of -15.88 kcal/mol. The energy difference is very small but for the 2nd arrangement where the H atom is adsorbed on $Mo_{(2)}$, less activation energy is required. Hence it is a much more favourable dissociation path for the 1st H abstraction. The activation barrier of the 1st hydrogen abstraction on Ni (110) surface it is 22.14 kcal/mol [35], on Co (111) surface it is 23.29 kcal/mol [36], on an Fe cluster it is 34.13 kcal/mol [37] and on Pt (111) surface 26.76 kcal/mol [38]. The Mo_3N_2 cluster is more reactive towards first hydrogen abstraction compared to other active catalysts for ammonia dissociation, which is an important characteristic of the Mo_3N_2 cluster.

NH₃ on Mo₍₁₎ of Mo₃N₂ cluster

E_{ad} = -25.35 kcal/mol
$d_{Mo(1) - N}$ = 2.33 Å

NH₃ on Mo₍₂₎ of Mo₃N₂ cluster

E_{ad} = -21.49 kcal/mol
$d_{Mo(1) - N}$ = 2.34 Å

NH₃ on Mo₍₃₎ of Mo₃N₂ cluster

E_{ad} = -20.48 kcal/mol
$d_{Mo(1) - N}$ = 2.36 Å

NH₂ on Mo₍₁₎ and H atom on Mo₍₂₎ of Mo₃N₂ cluster

E_{ad} = -77.41 kcal/mol
$d_{Mo(1) - N}$ = 2.007 Å
$d_{Mo(2) - H}$ = 1.787 Å

NH₂ on Mo₍₁₎ and H atom on Mo₍₃₎ of Mo₃N₂ cluster

E_{ad} = -77.71 kcal/mol
$d_{Mo(1) - N}$ = 2.007 Å
$d_{Mo(2) - H}$ = 1.791 Å

NH₂ on Mo₍₁₎ and H atom on N₍₄₎ of Mo₃N₂ cluster

E_{ad} = -70.99 kcal/mol
$d_{Mo(1) - N}$ = 2.020 Å
$d_{Mo(2) - H}$ = 1.029 Å

Fig. 2. Reactant and product configuration, adsorption energies and atomic distance for 1st hydrogen abstraction from NH_3 over Mo_3N_2.

NH₂ ADSORPTION ENERGY

The NH₂ species was strongly adsorbed ontop of the $Mo_{(1)}$ atom of Mo_3N_2 cluster (Fig. 3), compared to NH_3 molecule, with an adsorption energy of −92.33 kcal/mol. The distance between $Mo_{(1)}$ and N (NH_2 species) is 2.022 Å. A bridge adsorption mode of NH_2, where the N atom (of NH_2 species) was bound to $Mo_{(1)}$ and $Mo_{(2)}$ has adsorption energy of −80.11 kcal/mol, which is much less than on-top adsorption mode. NH_2 species prefer a bridge position having an adsorption energy of −73.33 kcal/mol on Ni (110) surface [35], on Fe(110) surface adsorption energy is −73.10 kcal/mol [38], on Co (111) surface adsorption energy is −63.78 kcal/mol [36] and on Ni (111) surface adsorption energy is −62.95 kcal/mol [36]. NH_2 species is more strongly bound to the Mo_3N_2 surface. The charge distribution over the cluster atoms and NH_2 species are reported in Table 1. There is an increase in positive charge over the Mo atoms suggesting electron transfer from the Mo atoms of the cluster for the surface bond formation which is confirmed by the increase in

negative charge on the N atom (of NH_2 species). The charge on the cluster N atoms undergoes a small increase in negative charge compared to the empty cluster.

Table 1. Mulliken atomic charge over the atoms in the Mo_3N_2 cluster and the adsorbed species during ammonia decomposition.

Atom (index) in the cluster and adsorbed species	Empty Cluster [e]	Adsorbed NH_3 on $Mo_{(1)}$ [e]	Adsorbed NH_2 on $Mo_{(1)}$ [e]	Adsorbed NH on $Mo_{(1)}$ [e]
Mo (1)	0.585	0.447	0.783	0.858
Mo (2)	0.420	0.355	0.442	0.486
Mo (3)	0.585	0.528	0.656	0.655
N (4)	-0.711	-0.717	-0.729	-0.728
N (5)	-0.711	-0.571	-0.730	-0.728
N (Adsorbed NH_x species on Cluster)	-	-0.571	-0.786	-0.701
N (Free NH_x Species)	-	-0.430	-0.331	-0.167

NH₂ on $Mo_{(1)}$ of Mo_3N_2 cluster

E_{ad} = -92.33 kcal/mol
$d_{Mo(1) - N}$ = 2.022 Å

NH on $Mo_{(1)}$ and H atom on $Mo_{(2)}$ of Mo_3N_2 cluster

E_{ad} = -81.35 kcal/mol
$d_{Mo(1) - N}$ = 1.818 Å
$d_{Mo(2) - H}$ = 1.775 Å

NH on $Mo_{(1)}$ and H atom on $Mo_{(3)}$ of Mo_3N_2 cluster

E_{ad} = -81.95 kcal/mol
$d_{Mo(1) - N}$ = 1.820 Å
$d_{Mo(2) - H}$ = 1.787 Å

NH on $Mo_{(1)}$ and H atom on $N_{(4)}$ of Mo_3N_2 cluster

E_{ad} = -78.77 kcal/mol
$d_{Mo(1) - N}$ = 1.830 Å
$d_{Mo(2) - H}$ = 1.028 Å

NH on $Mo_{(1)}$ of Mo_3N_2 cluster

E_{ad} = -105.91 kcal/mol
$d_{Mo(1) - N}$ = 1.828 Å

N on $Mo_{(1)}$ and H atom on $Mo_{(2)}$ of Mo_3N_2 cluster

E_{ad} = -82.40 kcal/mol
$d_{Mo(1) - N}$ = 1.728 Å
$d_{Mo(2) - H}$ = 1.766 Å

N on $Mo_{(1)}$ and H atom on $Mo_{(3)}$ of Mo_3N_2 cluster

E_{ad} = -83.14 kcal/mol
$d_{Mo(1) - N}$ = 1.723 Å
$d_{Mo(2) - H}$ = 1.749 Å

N on $Mo_{(1)}$ and H atom on $N_{(4)}$ of Mo_3N_2 cluster

E_{ad} = -81.60 kcal/mol
$d_{Mo(1) - N}$ = 1.772 Å
$d_{Mo(2) - H}$ = 1.029 Å

Fig. 3. Reactant and product configuration, adsorption energies and atomic distance for 2nd and 3rd hydrogen abstraction fromNH₃ over Mo₃N₂.

SECOND HYDROGEN ATOM ABSTRACTION

The abstraction of the 2nd hydrogen was investigated according to the elementary surface reaction $NH_2*ad \rightarrow NH*ad + H*ad$. $NH*$ species adsorbed on the $Mo_{(1)}$ atom was taken as the reactant configuration (Fig. 3). For the product configuration, three different surface arrangement were investigated with NH species on $Mo_{(1)}$ and H on three different positions, $Mo_{(2)}$, $Mo_{(3)}$ and $N_{(4)}$ atom. The binding energies are −95.98 kcal/mol, 81.95 kcal/mol and −78.78 kcal/mol, respectively. Hence NH species on $Mo_{(1)}$ and H atom on $Mo_{(2)}$ is energetically the most favourable product configuration where the atomic distance between $Mo_{(1)}$ and N (NH species) is 1.818 Å and between $Mo_{(2)}$ and H atom is 1.775 Å. Fig. 3 shows the adsorption configuration and adsorption energies and atomic distances. A transition state search found that the dissociation energy barrier is 41.20 kcal/mol with an endothermic reaction energy of 28.08 kcal/mol. X. Duan *et al.* [35] reported an activation barrier of 37.59 kcal/mol over Ni(110) plane, over Pt (111) surface the barrier is 36.09 kcal/mol [38], over Co (111) surface the barrier is 4.84 kcal/mol [36] and over Fe cluster the barrier 20.75 kcal/mol [37].

NH ADSORPTION ENERGY

The NH species is strongly adsorbed ontop of the $Mo_{(1)}$ atom of the Mo_3N_2 cluster (Fig. 3) compared to NH_3 and NH_2, with an adsorption energy of -105.91 kcal/mol. The distance between $Mo_{(1)}$ and N (NH species) is 1.828 Å. A bridge adsorption mode of NH, where the N atom is bound to $Mo_{(1)}$ and $Mo_{(2)}$, has an adsorption energy of -94.79 kcal/mol, which is much less than the on-top adsorption mode. The NH species prefer a bridge position having an adsorption energy of −91.08 kcal/mol on Ni(110) [35], on Co(111) surface, the hcp location has adsorption energy of -106.76 kcal/mol [36] and on Ni(111) surface, the fcc location has adsorption energy of −105.38 kcal/mol [36]. There is an increase in positive charge over the cluster Mo atoms, especially on the $Mo_{(1)}$ and $Mo_{(3)}$ suggesting the electron transfer from the Mo atoms of the cluster for the surface bond formation with NH species, which is confirmed by the increase in negative charge on the N atom (of NH species). The charge on the cluster N atoms undergoes small increase in negative charge.

THIRD HYDROGEN ATOM ABSTRACTION

The abstraction of the 3rd hydrogen atom from NH_3 was investigated according to the elementary surface reaction $NH*ad \rightarrow N*ad + H*ad$ (Fig. 3).

The NH species adsorbed on the $Mo_{(1)}$ atom was taken as the reactant configuration. For the product configuration three different surface arrangements were investigated with N species on $Mo_{(1)}$ and H on three different positions, $Mo_{(2)}$, $Mo_{(3)}$ and $N_{(4)}$ atom with binding energy −82.40 kcal/mol, −83.14 kcal/mol and −77.41 kcal/mol, respectively. Hence the N species on $Mo_{(1)}$ and the H atom on $Mo_{(3)}$ is energetically the most favourable product configuration where the atomic distance between $Mo_{(1)}$ and N (NH species) is 1.723 Å and $Mo_{(2)}$ and H is 1.749 Å. Fig. 3 shows the adsorption configuration, adsorption energies and atomic distances. A transition state search found that the dissociation energy barrier is 33.89 kcal/mol with the endothermic reaction energy of 28.38 kcal/mol. Duan X. *et al.* [35] reported an activation barrier 20.52 kcal/mol over Ni(110) plane, over Pt(111) surface the barrier is 34.42 kcal/mol [38], over Co(111) surface the barrier is 24.44 kcal/mol [36] and over Fe cluster 7.84 kcal/mol [37]. Charges on atoms of the cluster and on the adsorbed molecules are tabulated in Table 1.

POTENTIAL ENERGY SURFACE OF NH_3 DISSOCIATION

The activation barrier and reaction energies of the surface elementary reactions of ammonia decomposition for the Mo_3N_2 cluster and some other potential surfaces are tabulated in Table 2 and the potential energy surface on the Mo_3N_2 cluster is depicted in Fig. 4, taking free Mo_3N_2 cluster and free NH_3 molecule as the zero energy reference. Only the 1st hydrogen abstraction step is exothermic (-15.88 kcal/mol) and the other two are highly endothermic (28.05 and 28.35 kcal/mol for the 2nd and 3rd abstraction respectively), make the overall hydrogen abstraction process highly endothermic (15.12 kcal/mol). The activation barrier has the highest value for the 2nd hydrogen abstraction step ($NH_2*ad \rightarrow NH*ad + H*ad$), 41.2 kcal/mol (172.21 kJ/mol), and this is the rate limiting step for NH_3 dissociation over Mo_3N_2 cluster. Offermans *et al.* [38] also reported the 2nd hydrogen abstraction as the rate limiting step for Pt (111) surface and also found the same rate limiting step was reported by Duan *et al.* [36] for Ni (110) and by Mhadeshwar *et al.* [39] over Ru (0001) plane. Lanzania [37] reported the 1st hydrogen abstraction as the rate limiting step for NH_3 dissociation on nanosized iron cluster and Duan *et al.* [36] reported the 3rd hydrogen abstraction step as the rate limiting step. Mo_3N_2 cluster resembles Pt (111), Ru (0001) and Ni (111) plane regarding the rate-limiting step.
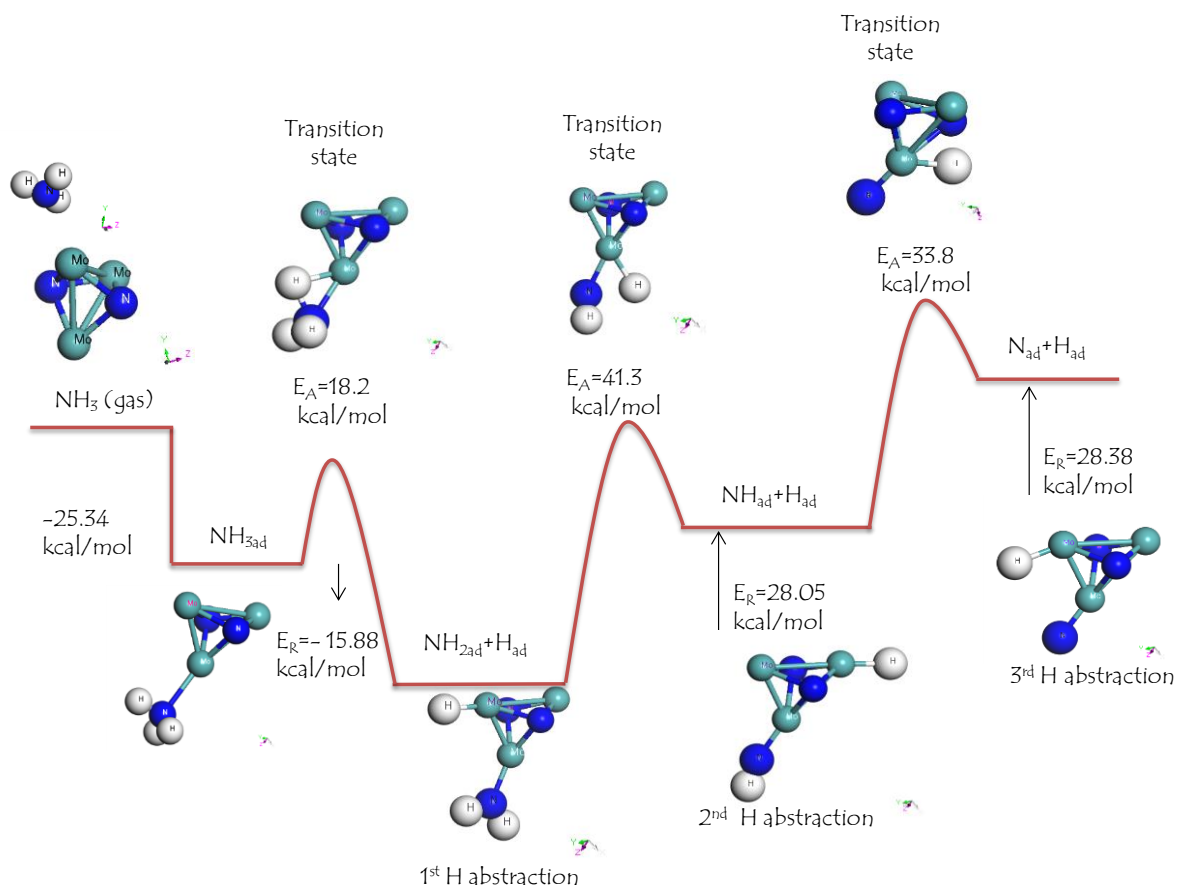
Fig. 4. Potential energy surface of ammonia dissociation over Mo3N2 cluster.

Table 2. Activation and reaction energies of hydrogen abstraction step for ammonia dissociation

Elementary reaction	Mo_3N_2 cluster		Pt(111) [38]		Ni(110) [35]		Fe cluster [37]		Co(111) [36]	
	Activation energy (ΔE_A) [kcal/mol]	Reaction energy (ΔE_R) [kcal/mol]	Activation energy (ΔE_A) [kcal/mol]	Reaction energy (ΔE_R) [kcal/mol]	Activation energy (ΔE_A) [kcal/mol]	Reaction energy (ΔE_R) [kcal/mol]	Activation energy (ΔE_A) [kcal/mol]	Reaction energy (ΔE_R) [kcal/mol]	Activation energy (ΔE_A) [kcal/mol]	Reaction energy (ΔE_R) [kcal/mol]
$NH_3^* \rightarrow NH_2^* + H^*$	18.2	-16.47	26.77	16.25	22.14	-5.76	34.13	-2.77	23.29	-3.23
$NH_2^* \rightarrow NH^* + H^*$	41.2	28.08	36.09	2.15	37.59	12.45	20.76	8.53	4.84	-10.15
$NH^* \rightarrow N^* + H^*$	33.8	28.38	34.42	18.88	20.52	6.68	7.84	-8.76	24.44	2.31
$N_2^* \rightarrow N^* + N^*$	35.19	22.44	x	x	38.74	0.59	x	x	42.89	14.30

N atom adsorption on $Mo_{(1)}$
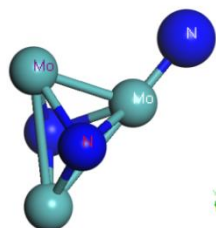
Ea = -106.35 kcal/mol
$d_{Mo(1) - N}$ = 1.70 Å

N₂ adsorption on $Mo_{(1)}$
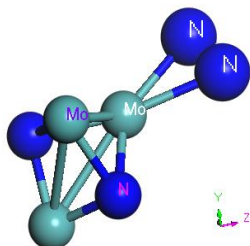
Ea = -19.75 kcal/mol
$d_{Mo(1) - N}$ = 1.24 Å

Dissociative adsorption of N_2
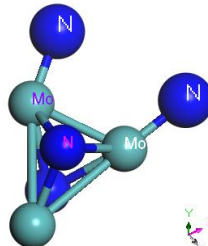
Ea = -103.17 kcal/mol
$d_{Mo(1) - N}$ = 1.73 Å

Transition State
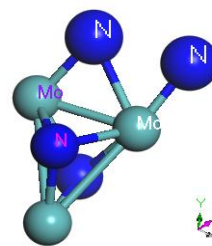
ΔEa = 35.19 kcal/mol
ΔEr = 49.31 kcal/mol

Fig, 5. Nitrogen adsorption and dissociation over Mo3N2 cluster.

NITROGEN ADSORPTION AND DISSOCIATION

Fig. 5 depicts the adsorption and dissociation of the nitrogen molecule. Atomic adsorption of the N atom on the Mo$_{(1)}$ atom of the cluster is −106.35 kcal/mol and when two N atoms adsorb on two different Mo atoms, Mo$_{(1)}$ and Mo$_{(2)}$, the adsorption energy is −103.73 kcal/mol, showing a small decrease due to interaction effects. The N$_2$ molecule adsorbed on the Mo$_{(1)}$ atom making a bond with two N atoms has an adsorption energy of −19.75 kcal/mol. The molecular nitrogen dissociation energy has an activation barrier of 35.19 kcal/mol and an endothermic reaction energy of 49 kcal/mol. The dissociation barrier of the N$_2$ molecule is 38.78 kcal/mol on Ni (110) surface [35], 43.82 kcal/mol on terraces of Ru (0001) surface [40], and 9.42 kcal/mol on steps of Ru(0001) [40] and 9.42 kcal/mol on V(110) surface [41]. Nitrogen dissociation is much more difficult on the Mo$_3$N$_2$ cluster compared to the other promising catalyst surfaces, which suggests that the ammonia decomposition follows the Tamaru mechanism over the Mo$_3$N$_2$ cluster, where ammonia activation and nitrogen desorption are rate limiting, similar to VN catalysts reported by Oyama *et al.* [42].

CONCLUSIONS

A DFT study was employed to determine the adsorption energy of NH$_x$ (x = 1–3) and the transition state and the activation barrier of NH$_3$ dehydrogenation and N$_2$ dissociation over the Mo$_3$N$_2$ cluster. The results of calculations have shown that On-top adsorption configuration was the preferred adsorption arrangement for NH$_x$ species over an Mo atom. The rate-limiting step for NH$_3$ decomposition is the second hydrogen abstraction step according to the following surface elementary reaction (NH$_2$*ad → NH*ad + H*ad) having an activation energy of 41.2 kcal/mol with an endothermic heat of reaction of 28.05 kcal/mol. Nitrogen dissociation has a barrier of 35.19 kcal/mol on the Mo$_3$N$_2$, which is much higher than on Ru and V catalysts.

REFERENCES

1. B. L. Yi, Fuel Cells – Principle, Technology and Application, Chemical Industrial Publisher, Beijing, 2003.
2. A. S. Chellappal, C. M. Fischer, W. J. Thomson, *App. Catal. A*, **227**, 231 (2002).
3. L. F. Brown, *Int. J. Hydrog. Energy*, **26**, 381 (2001).
4. C. Zamfirescu, I. Dincer, *Fuel Proc. Tech.*, **90**, 729 (2009).
5. S. F. Yin, B. Q. Xu, C. F. Ng, C. T. Au, *App. Catal. B: Environ.*, **52**, 287 (2004).
6. S. F. Yin, B. Q. Xu, X. P. Zhou, C. T. Au, *Appl. Catal. A*, **277**, 1 (2004).
7. J. Zhang, M. Comotti, F. Schuth, R. Schlogl, D. S. Su, *Chem. Commun.*, **17**, 1916 (2007).
8. R. Pelka, I. Moszynska, W. Arabczyk, *Catal. Lett.*, **128**, 72 (2009).
9. Y. Liu, H. Wang, J. F. Li, Y. Lu, Q. S. Xue, J. C. Chen, *AIChE*, **53**, 1845 (2007).
10. Y. Lu, H. Wang, Y. Liu, Q. S. Xue, J. C. Chen, M. Y. He, *Lab Chip.*, **7**, 133 (2007).
11. X. K. Li, W. J. Ji, J. Zhao, S. J. Wang, C. T. Au, *J. Catal.*, **236**, 181 (2005).
12. T. V. Choudhary, D. C. Svammonia, D. W. Goodman, *Catal. Lett.*, **72**, 197 (2001).
13. M. E. E. Abashar, Y. S. Al-Sughair, I. S. Al-Mutaz, *Appl. Catal. A.*, **236**, 35 (2002).
14. A. Hellman, K. Honkala, I. N. Remediakis, D. A. Logammonia, A. Carlsson, S. Dahl, H. Christensen, J. K. Norskov, *Surf. Sci.*, **603**, 1731 (2009).
15. S. Dahl, D. A. Logammonia, R. C. Egeberg, J. H. Larsen, I. Chorkendorff, E. Tornqvist, J. K. Norskov, *Phys. Rev. Lett.*, **83**, 1814 (1999).
16. S. Dahl, E. Tornqvist, I. Chorkendorff, *J. Catal.*, **192**, 381 (2000).
17. P. F. Ng, L. Li, S. B. Wang, Z. H. Zhu, G. Q. Lu, Z. F. Yan, *Environ. Sci. Technol.*, **41**, 3758 (2007).
18. A. Klerke, S. K. Klitgaard, R. Fehrmann, *Catal. Lett.*, **130**, 541 (2009).
19. S. R. Deshmukh, A. B. Mhadeshwar, D. G. Vlachos, *Ind. Eng. Chem. Res.*, **43**, 2986 (2004).
20. A. M. Karim, V. Prash, G. Mpourmpakis, W. W. Lonergan, A. I. Frenkel, J. G. Chen, D. G. Vlachos, *J. Am. Chem. Soc.*, **131**, 12230 (2009).
21. W. Q. Zheng, J. Zhang, H. Y. Xu, W. Z. Li, *Catal. Lett.*, **119**, 311 (2007).
22. C. W. Seabury, T. N. Rhodin, R. J. Purtell, R. P. Merrill, *Surf. Sci.*, **93**, 117 (1980).
23. C. Egawa, T. Nishida, S. Naito, K. Tamaru, *J. Chem. Soc. Faraday Trans. I*, **80**, 1595 (1984).
24. F. Frechard, R .A. van Santen, A. Siokou, J. W. Niemantsverdriet, J. Hafner, *J. Chem. Phys.*, **111**, 8124 (1999).
25. S. Stolbov, T. S. Rahman, *J. Chem. Phys.*, **123**, 204716 (2005).
26. W. P. Krekelberg, J. Greeley, M. Mavrikakis, *J. Phys. Chem. B*, **108**, 987 (2004).
27. X. Z. Xiao, Y. L. Cao, Y. Y Cai, *Surf. Sci.*, **605**, 802 (2012).
28. W. Tsai, W. H. Weinberg, *J. Phys. Chem.*, **91**, 5302 (1987).
29. W. Kohn, L. J. Sham, *Phys. Rev.*, **140**, A1133 (1965).
30. J. P. Perdew, J. A. Chevary, S. H. Vosko, K. A. Jackson, M. R. Pederson, D. J. Singh, C. Fiolhais, *Phys. Rev. B*, **46**, 6671 (1992).
31. A. D. Becke, *J. Chem. Phys.*, **88**, 2547 (1988).

32. J. P. Perdew, Y. Wang, *Phys. Rev. B*, **45**, 13244 (1992).
33. T. A. Halgren, W. N. Lipscomb, *Chem. Phys. Lett.*, **49**, 225 (1977).
34. S. Bell, J. S. Crighton, *J. Chem. Phys.*, **80**, 2464 (1983).
35. X. Duan, G. Qian, C. Fan, Y. Zhu, X. Zhou, D. Chen, W. Yuan, *Surf. Sci.*, **606**, 549 (2012).
36. G. Lanzania, K. Laasonen, *Int. J. Hydrog. Energy*, **35**, 6571 (2010).
37. X. Duan, J. Ji, G. Qian, C. Fan, Y. Zhu, X. Zhou, D. Chen, W. Yuan, *J. Mol. Catal. A: Chem.*, **357**, 81

38. W. K. Offermans, A. P. J. Jansen, R. A. van Santen, G. Novell-Leruth, J. M. Ricart, J. Pérez-Ramírez, *J. Phys. Chem. C*, **111**, 17551 (2007).
39. A. B. Mhadeshwar, J. R. Kitchin, M. A. Barteau, D. G. Vlachos, *Catal. Lett.*, **96**, 13 (2004).
40. A. Logadottir, J. K. Norskov, *J. Catal.*, **220**, 273 (2003).
41. P. Rochana, K. Lee, J. Wilcox, *J. Phys. Chem. C*, **118**, 4238 (2014).
42. J. J. Spivey, K. M. Dooley, *Catalysis*, **19**, 84 (2006).

(2012).

ИЗСЛЕДВАНЕ С ТФП НА ДИСОЦИАЦИЯТА НА АМОНЯК ВЪРХУ КЛЪСТЕР Mo₃N₂

Ш. Ф. Заман

Chemical and Materials Engineering Department, Faculty of Engineering, King Abdulaziz University, P.O. Box 80204, Jeddah 21589, Saudi Arabia

(Резюме)

С метода на ТФП е изследван механизма на процеса на разлагане на амоняк върху Mo₃N₂ клъстер. Моделирани са елементарните стадии на повърхностните реакции след адсорбция на NH$_x$ (x = 0–3) частици "on-top" върху Mo атоми. Тази конфигурация на повърхностните активни комплекси е енергитично най-изгодна. Скорост определящият стадий на разлагането на амоняка (NH₂*ad → NH*ad + H*ad) е с активираща енергия от 41.2 kcal/mol и ендотермична топлина на стадия 28.1 kcal/mol. Енергията на дисоцияция на адсорбирания N₂ е 35.19 kcal/mol и е значително по-висока от тази на N₂ адсорбиран на Ru(0001).

Rapid synthesis of (3-bromopropyl)triphenylphosphonium bromide or iodide

S. I. Minkovska[1,*], N. T. Burdzhiev[2], A. A. Alexiev[2], T. G. Deligeorgiev[2]

[1] *Institute of Catalysis, Bulgarian Academy of Sciences, Acad. G. Bonchev St., Bldg. 11, 1113 Sofia, Bulgaria;*

[2] *Faculty of Chemistry and Pharmacy, St. Kliment Ohridski University of Sofia, 1, J. Bourchier Blvd., 1164 Sofia, Bulgaria*

A novel rapid method for the preparation of (3-bromopropyl)triphenylphosphonium bromide was developed. The synthesis was accomplished by microwave irradiation of 1,3-dibromopropane with triphenylphosphine at a ratio of 1:1 for 2 minutes in xylene or toluene or without any solvent. The target compound was isolated in good yield (81−93%) and high purity.

Key words: 1,3-dibromopropane, triphenylphosphine, (3-bromopropyl)triphenylphosphonium bromide, (3-bromo-propyl)triphenylphosphonium iodide, solvent effect; microwave irradiation.

INTRODUCTION

(3-Bromopropyl)triphenylphosphonium bromide is a useful compound which can be applied as novel insoluble bactericidal ceramisite filler [1]. Its anti-bacterial activity is used against heterotrophic bacteria in simulated industrial recirculation water. After regenerating, the reused bactericide ceramisite could still purify contaminated water [1]. Aqueous solutions of bromoalkyltriphenylphosphonium bromides react with zero-valent metals, causing their dissolution [2]. The reaction initially follows second-order kinetics, with the rate depending on both metal and bromide concen-trations. Zero-valent metals similarly react with aqueous methylmercuric acetate and other dissolved organo-metals [2]. Positive ion fast atom bombard-ment (FAB) mass spectra were reported [3] for a representative series of mono- and bis-phosphonium halides derived from triphenylphos-phine. The use of laser micro-probe mass spectro-metry (LMMS) for structural characterization of thermolabile quaternary phosphonium salts has been evaluated [4]. From 793 screening compounds with evaluable data, 158 were found, including (3-bro-mopropyl)triphenylphosphonium, bromide to have significant inhibitory effects on ovarian cancer stem-like cells (CSC) [5].

In a paper were reported the synthesis and struct-ural characterization of a new family of stable $R_3P^+(CH_2)nS_2O_3^-$ (R = Ph or Bu, n = 3, 4, 6, 8 or 10), which behave as cationic masked thiolate ligands with application to the functionalisation of gold nanoparticles having potential as new dia-gnostic bio-recognition systems [6]. The hexaflu-orophosphate salt of the (3-bromopropyl)triphenyl-phosphonium compound was synthesized by Guarr *et al.* [7].

In this paper we report a rapid (only for 2 min) method for the preparation of (3-bromopropyl)tri-phenylphosphonium bromide by microwave irra-diation. The conversion of bromide salt into iodide salt was performed in water that is the most popular green solvent [8].

EXPERIMENTAL

Materials

Unless otherwise stated, all reagents and solvents used in the synthesis and analysis were obtained from Sigma-Aldrich (St. Louis, MO, USA), Alfa-Aesar (Haverhill, MA, USA) as commercial products of analytical grade and applied without further purification.

Instrumentation

NMR spectra were recorded on a Bruker Avance III 500 MHz instrument (Rheinstetten, Germany) using $CDCl_3$ at 25 °C. (δ) are reported in ppm and referenced directly to the chemical shift of the TMS peak. Chemical shift of ^{31}P signal is not referenced. Melting point temperatures were determined on a Kofler bench apparatus (DDR, Berlin, Germany) and are uncorrected.

Experimental procedure for the preparation of (3-bromopropyl)triphenylphosphonium bromide or iodide

A 100 ml Erlenmeyer flask was charged with triphenylphosphine **2** (13.10 g, 0.05 mol), 1.3-dibro-mopropane **1** (5.10 ml, 0.05 mol, ratio of 1:1), and 5

* To whom all correspondence should be sent
E-mail: stelamin@ic.bas.bg

ml xylene or toluene. The flask content was heated in MW oven for up to 2 min at 450 W (stop on every 10 s with intervals of 10 s). A vigorous exothermic reaction was observed. Heating was stopped until the exothermic reaction ceased. After cooling to room temperature the reaction mixture was diluted with 20 ml of acetone and 75 ml of diethyl ether. The precipitate was filtered and air-dried. Yield: 81−93%, m.p. 226−227 °C (lit. m.p. 229−230 °C [2]).

The anion of (3-bromopropyl)triphenylphosphonium bromidre could readily be exchanged with iodide. The white precipitate of (3-bromopropyl)triphenylphosphonium bromide (1 g) was dissolved in 5 ml of ethanol and added to 0.012 mol of potassium iodide dissolved in 10 ml of water. The solution was boiled for 10 minutes with stirring and then cooled to room temperature. The resulting white precipitate was filtered and dried in the air. Yield: 80%, m.p. 198−199 °C, no lit. m.p.

^{1}H-NMR (500 MHz, CDCl$_3$): 2.19−2.29 (m, 2H, CH$_2$C*H*$_2$), 3.87 (dt, 2H, J = 1.3, 6.2 Hz, C*H*$_2$Br), 4.09−4.15 (m, 2H, C*H*$_2$P), 7.68−7.76 (m, 6H, Ph*H*), 7.78−7.90 (m, 9H, Ph*H*).

^{13}C-NMR (125 MHz, CDCl$_3$): 21.64 (d, 1C, *J* = 52.5 Hz, P*C*H$_2$), 26.31 (d, 1C, *J* = 2.7 Hz, CH$_2$*C*H$_2$), 33.54 (d, 1C, *J* = 20.4 Hz, Br*C*H$_2$), 117.98 (d, 3C, *J* = 86.4 Hz, Ph*C*), 130.59 (d, 6C, *J* = 12.6 Hz, Ph*C*H), 133.72 (d, 6C, *J* = 10.0 Hz, Ph*C*H), 135.21 (d, 3C, *J* = 3.1 Hz, Ph*C*H) [9]

^{31}P-NMR (202 MHz, CDCl$_3$): 24.20 (s, 1P).

ESI+: m/z 384.055 (M+H, calculated 384.064), 386.034 (M+H, calculated 386.062)

RESULTS AND DISCUSSION

Usually (3-bromopropyl)triphenylphosphonium bromide has been prepared in solvents as xylene or toluene from equimolar quantities of 1,3-dibromopropane and triphenylphosphine for 20 h heating in yield up to 90% [10−12]. Another synthetic pathway involves reaction of triphenylphosphine with halogenoalcohols and subsequent replacement of the OH in alcohols by a halogen [6]. An attempt has been made to develop a green synthesis process. In PEG200/400, which recently have been confirmed as eco-friendly solvents [13], a mixture was obtained from mono- and bis-phosphonium salts. Probably this is due to PEG200/400 polarity. The same was obtained in another green solvent − ethyl L-lactate [14]. We found that this compound could be obtained with xylene (toluene) or without any solvent only for up to 2 min heating the reaction mixture in MW oven at 450 W (Scheme 1). The best yield of (3-bromopropyl)triphenylphosphonium was obtained in xylene and toluene corresponding to the similar dH evap [kJ/mol] of both solvents, 33.3 for toluene and 36.2 for xylene, irrespective of their different boiling points. The temperature obtained using microwaves depends on the dielectric constant of the reagent [15]. Microwave irradiation not only affords better yield (81−93%) than conventional heating, but even leads to acquiring a product of higher purity. Our method is much more rapid than most of the available procedures and greatly simplified as well.

The (3-bromopropyl)triphenylphosphonium bromide was proved by melting point, ^{1}H-NMR (Fig. 1), ^{13}C-NMR (Fig. 2), ^{31}P-NMR (Fig. 3) and mass spectra.

CONCLUSIONS

The new method for synthesis of (3-bromopropyl)triphenylphosphonium bromide or iodide by microwave irradiation has been described. The present procedure has the advantages of short reaction time (up to 2 minutes), high yields of the products, small reaction volume, a highly reproducible approach, a simple experimental work-up procedure, and easy anion replacement. By preparation of larger amount of (3-bromopropyl)triphenylphosphonium bromide part of the diethyl ether, acetone and xylene (or toluene) could be regenerated.
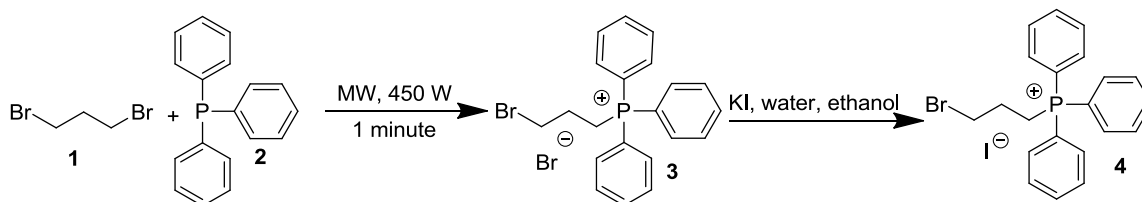
Scheme 1. Preparation of 1-(3-bromopropyl)triphenylphosphonium bromide and iodide.
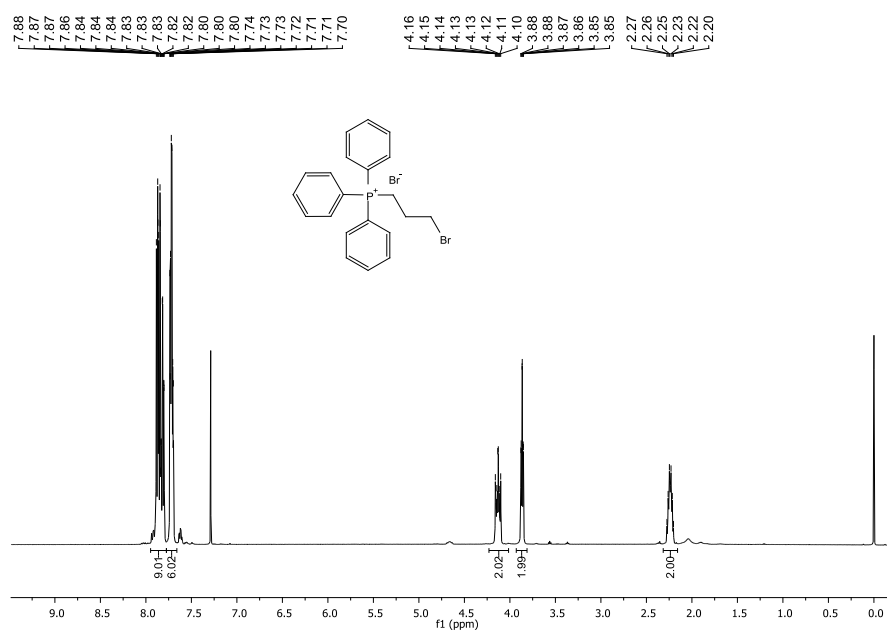
Fig. 1. ^{1}H-NMR spectra of (3-bromopropyl)triphenylphosphonium bromide.
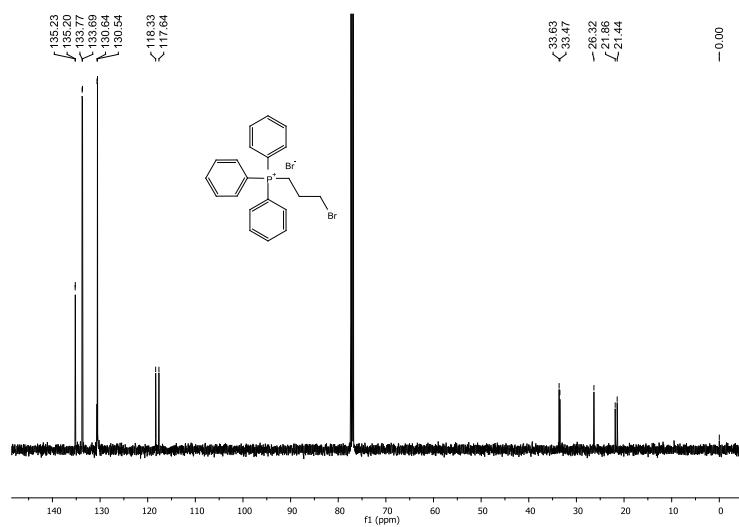
Fig. 2. ^{13}C-NMR spectra of (3-bromopropyl) triphenylphosphonium bromide.
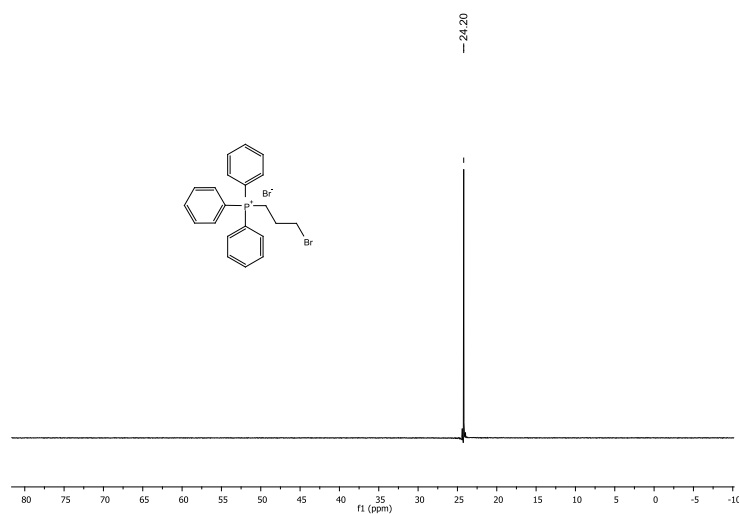
Fig. 3. ^{31}P-NMR spectra of (3-bromopropyl) triphenylphosphonium bromide.

211

REFERENCES

1. X. Zhanga, X. Lü, P. Han, *Desalin. Water Treat.*, **52**, 6016 (2014).
2. J. S. Thayer, *Appl. Organometal. Chem.*, **12**, 571 (1998).
3. J. Claereboudt, W. Baeten, H. Geise, M. Claeys, *Org. Mass Spectrom.*, **28**, 71 (1993).
4. J. Claereboudt, M. Claeys, H. Geise, R. Gijbels, A. Vertess, *J. Am. Soc. Mass. Spectrom.*, **4**, 798 (1993).
5. R. Mezencev, L. Wang, J. F. McDonald, *J. Ovarian Res.*, **5**, 30 (2012).
6. Y. Ju-Nam, N. Bricklebank, D. W. Allen, P. H. E. Gardiner, M. E. Light, M. B. Hursthouse, *Org. Biomol. Chem.*, **4**, 4345 (2006).
7. T. H. Guarr, K. E. Roberts, R. Lin, L. B. Kelvin, A. T. David, G. Punam, M. S. Elizabeth, *US Patent* 20020141032 (2002).
8. A. Filly, A. S. Fabiano-Tixier, C. Louis, X. Fernandez, F. Chemat, *C. R. Chimie*, **19**, 707 (2016).
9. SDBSWeb: http://sdbs.db.aist.go.jp (National Institute of Advanced Industrial Science and Technology, 30.04.2017).
10. T. Bader, H.-U. Bichsel, B. Gilonen, I. Meyer-Wilmes, M. Sundermeier, *DE Patent* WO2007110761 (2008).
11. J. R. Tretter, *US Patent* 3509175 (1970)
12. O. Farooq, *US Patent* 5403955 (1995)
13. J. Chen, S. K. Spear, J. G. Huddleston, R. D. Rogers, *Green Chem.*, **7**, 64 (2005)
14. Y. L. Kua, S. Gan, A. Morris, H. K. Ng, Sustainable *Chem. Pharm.*, **4**, 21 (2016).
15. A. De La Hoz, A. Diaz-Ortiz, A. Moreno, *Curr. Org. Chem.*, **8**, 903 (2004).

БЪРЗ МЕТОД СИНТЕЗ НА (3-БРОМОПРОПИЛ)ТРИФЕНИЛФОСФОНИЕВ БРОМИД ИЛИ ЙОДИД

С. И. Минковска[1,*], Н. Т. Бурджиев[2], А. А. Алексиев[2], Т. Г. Делигеоргиев[2]

[1] *Институт по катализ, Българска академия на науките, ул. „Акад. Г. Бончев“, бл. 11, 1113 София, България*
[2] *Факултет по химия и фармация, Софийски университет „Св. Климент Охридски“, бул. „Джеймс Баучер“ 1, 1164 София, България*

(Резюме)

Разработен е нов бърз метод за получаване на (3-бромопропил)трифенилфосфониев бромид. Синтезът се извършва чрез MW облъчване на 1,3-дибромпропан с трифенилфосфин в съотношение 1:1 за 2 минути в ксилен или толуен или без разтворител. Основното съединение се получава с добър добив (81−93%) и с висока чистота.

CONTENTS

СЪДЪРЖАНИЕ